Joakim Samuel Jestilä

Reductive gas-phase ion chemistry of simple oxocarbons in the presence of alkali and alkaline earth metals

Series of dissertations submitted to the
Faculty of Mathematics and Natural Sciences, University of Oslo
No. 2430

ISSN 1501-7710

Cover: Hanne Baadsgaard Utigard.
Print production: Reprosentralen, University of Oslo.

I Abstract

Efficient utilization of CO_2 as a molecular building block driven by renewable energy is a cornerstone of a circular carbon economy. This entails selective conversion of CO_2 into a wide array of commodity chemicals, materials and fuels, which necessitates extensive knowledge of the mechanisms of CO_2 reduction.

This thesis is the result of a combined mass spectrometric, spectroscopic and computational exploration of fundamental gas-phase interactions between CO_2 and anionic alkali and alkaline earth metals. Existing literature suggests that metal atoms and ions may either reduce CO_2 directly to CO, or react to form a metalated complex MCO_2, the latter considered an important intermediate in the conversion of CO_2. This is corroborated in this work as the reduction of CO_2 to oxalate and CO by the anionic metal species in question is seen to typically proceed *via* this type of complexes. The associated reaction energetics are linked to the structural perturbation and the closely connected reduction of the bound CO_2 moiety. Periodic trends are revealed as more efficient charge transfer from metal to CO_2 is found to generally correlate with lowered barriers for further reactions. Important mechanistic aspects related to the energetic demands are also presented.

Additionally, this work elaborates on the further reduction of CO by homologation to cyclic oxocarbons $C_nO_n^{m-}$ ($n = 3 – 4$, $m = 1 – 2$), viewed from the perspective of upscaling CO_2 to multi-carbon compounds. A critical step for these processes when initiated by e^- or $MgCl^-$ is determined to be the simultaneous reduction and C—C coupling of two CO molecules. Transfer of a single electron to the oxocarbon moiety is found to initiate the cyclooligomerization process while a second electron terminates it, consistent with the fact that the corresponding neutral species are deemed unstable.

These results represent another step towards surveying CO_2-interactions with species throughout the periodic table, and could prove useful for the development of processes utilizing CO_2 efficiently.

II Preface

This thesis would not exist had I not received support from a number of people. It was my supervisor, Einar Uggerud, who first encouraged me to pursue a PhD, thus providing both motivation and opportunity. Over the past years, he has been highly influential on me as a scientist and as a person.

I have long thought that if I spend enough time in the company of highly talented and intelligent people, their qualities are bound to influence myself. Hence, I must extend my gratitude to past and current members of our research group and the Hylleraas Centre for Quantum Molecular Sciences. I am particularly grateful to Mauritz Ryding for his invaluable feedback, especially on the experimental parts of my project and thesis, helping me push beyond practical proficiency. I must also thank Sverre Løyland, Audun Skau Hansen and Thomas Qureishy for providing highly useful feedback on this thesis.

During my thesis work, I was fortunate enough to be part of several collaborations, for which I am humbled and very grateful. First to Sotiris Xantheas and Edoardo Aprá for enabling and guiding me through high-level computations, which have been critical for this thesis. Second, I must thank Mark Johnson and his students for their hospitality and patience, since essentially all I did when I visited their lab was to order them around.

Finally, I would like to thank my significant other, friends and family, who have supported and encouraged me at each step along the way.

III List of papers

Paper I. Characterization of the alkali metal oxalates ($MC_2O_4^-$) and their formation by CO_2 reduction *via* the alkali metal carbonites (MCO_2^-)

Joakim S. Jestilä, Joanna K. Denton, Evan H. Perez, Thien Khuu, Edoardo Aprà, Sotiris S. Xantheas, Mark A. Johnson and Einar Uggerud

Phys. Chem. Chem. Phys., **2020**, *22* (14), 7460-7473.

This paper details the reduction of carbon dioxide to oxalate mediated by alkali metal anions, emphasizing the role of the intermediary metal carbonites, MCO_2^-, studied using mass spectrometric techniques and quantum chemistry. The metal oxalate complexes, $MC_2O_4^-$, were characterized by cryogenic ion vibrational spectroscopy in collaboration with the Mark Johnson research group at Yale University. High-level ab initio quantum chemical methods (CCSD(T)) were employed in collaboration with Sotiris S. Xantheas and Edoardo Aprà at the Pacific Northwestern National Laboratory and University of Washington (for S.S.X.), using high-performance computing (HPC) resources provided by the National Energy Research Scientific Computing Center (NERSC).

Paper II. Computational Exploration of the Direct Reduction of CO_2 to CO Mediated by Alkali Metal and Alkaline Earth Metal Chloride Anions

Joakim S. Jestilä and Einar Uggerud

Organometallics., **2021**, *40* (11), 1735-1743

This was a purely computational investigation, concerning the alternative reaction pathways for CO_2 reduction *via* the metal carbonites, specifically those leading to CO. Herein, the alkaline earth metals are included, also elucidating their role in the formation of oxalate.

Paper III. Unimolecular Dissociation of Hydrogen Squarate ($HC_4O_4^-$) and the Squarate Radical Anion ($C_4O_4^{\bullet-}$) in the Gas Phase and the Relationship to CO Cyclooligomerization

Joakim S. Jestilä and Einar Uggerud

J. Org. Chem., **2019**, *84* (21), 14005–14014.

This paper details the dissociation of hydrogen squarate and the squarate radical anions, investigated with a combination of mass spectrometry and quantum chemistry. The aim was to elucidate mechanistic details and their relevance for the reverse processes.

Paper IV. The unimolecular dissociation of magnesium chloride squarate ($ClMgC_4O_4^-$) and reductive cyclooligomerisation of CO on magnesium

Joakim S. Jestilä, Zsuzsanna Iker, Mauritz J. O. Ryding and Einar Uggerud *Org. Biomol. Chem.*, **2020**, *18* (46), 9499-9510.

The purpose of this study was to expand upon the previous publication, Paper III. Specifically, it was of interest to investigate the effects of magnesium on the anionic squarate system. We strove towards improving upon our methodology for the estimation and assessment of threshold energies during this work.

IV List of contributions

Paper I.

Joakim S. Jestilä: provided key ideas, conducted the experiments in Oslo, did the computational work, wrote the first draft and the final manuscript.

Joanna K. Denton: conducted and analyzed experiments at Yale and contributed to the manuscript.

Evan H. Perez: conducted and analyzed experiments at Yale and contributed to the manuscript.

Thien Khuu: conducted analyzed experiments at Yale and contributed to the manuscript.

Edoardo Aprà: contributed to the actualization of the computational part, and to the manuscript.

Sotiris S. Xantheas: contributed to and supervised the computational part, and contributed to the manuscript.

Mark Johnson: supervised experiments at Yale and contributed to the manuscript.

Einar Uggerud: provided key ideas for the study, supervised its actualization and revised the manuscript.

Paper II.

Joakim S. Jestilä: provided key ideas, did the computations, analyzed the results and wrote the manuscript.

Einar Uggerud: provided the concept for the study, supervised its actualization and revised the manuscript.

Paper III.

Joakim S. Jestilä: provided key ideas, did the experimental and computational work, analyzed the results and wrote the manuscript.

Einar Uggerud: provided key ideas for the study, supervised its actualization and revised the manuscript.

Paper IV.

Joakim S. Jestilä: provided key ideas, did part of the experimental and computational work, analyzed results and wrote the first draft and the final manuscript. Co-supervised the main experiments and initial computational exploration.

Zsuzsanna Iker: conducted the main experiments and initial computational exploration.

Mauritz J. O. Ryding: did part of the experimental work, contributed significantly to its analysis and revised the manuscript.

Einar Uggerud: provided key ideas for the study, supervised its actualization and revised the manuscript.

V Contents

VI List of abbreviations

AO	Atomic orbitals
B3LYP	The Becke 3-parameter exchange and the Lee-Yang-Parr correlation functionals
BO	Born-Oppenheimer approximation
BSSE	Basis set superposition error
CAS	Complete active space
CC	Coupled-cluster
CCS	Carbon capture and sequestration
CCSD(T)	Coupled-cluster singles, doubles and perturbative triples
CI	Configuration interaction
CID	Collision induced dissociation
CRM	Charge residue model
CSF	Configuration state functions
DAC	Direct air capture
DFT	Density functional theory
DZ	Double-zeta
E_{COM}	Center-of-mass collision energy
E_e	Electronic energy
E_{LAB}	Lab-frame collision energy
ESI	Electrospray ionization/ion
E_T	Threshold energy
FI	Fragment ion
FWHM	Full width at half maximum
G4	Gaussian-4 composite method
GGA	Generalized gradient approximation
GTO	Gaussian-type orbitals
H	Hamiltonian
HF	Hartree-Fock
HOMO	Highest occupied molecular orbital
HPC	High-performance computing

IEM	Ion evaporation model
IR	Infrared
IRC	Intrinsic reaction coordinate
IS	In-source
KS	Kohn-Sham
LUMO	Lowest unoccupied molecular orbital
MCO_2	Metal carbonite
MCP	Multichannel plate
mGGA	meta-generalized gradient approximation
MOF	Metal organic framework
MOXIE	Mars oxygen in-situ resource utilization experiment
MP*n*	Møller-Plesset perturbation theory
MR	Multi-reference
MS	Mass spectrometry
MS^n	Tandem mass spectrometry
NBO	Natural bond orbitals
NERSC	National energy research scientific computing center
NF	Neutral fragment
NLS	Natural Lewis structure
oa-TOF	Orthogonal acceleration (reflectron) time-of-flight
PI	Precursor ion
QTOF	Quadrupole-time-of-flight
RF	Radiofrequency
SAC	Single-atom catalyst
SCF	Self-consistent field
S_N2	Bimolecular nucleophilic substitution
SR	Single-reference
STO	Slater-type orbitals
SZ	Single-zeta
TOF	Time-of-flight
TS	Transition state

TZ	Triple-zeta
UHV	Ultra-high vacuum
UV-vis	Ultraviolet-visible
ZPVE	Zero-point vibrational energy

VII List of figures

1 Introduction

1.1 General background

Carbon dioxide, CO_2, is formed in any complete aerobic biological and chemical combustion process. While some of it is converted back to combustible form as part of a natural carbon cycle, a substantial human contribution has resulted in its accumulation in the atmosphere. The latter is linked to a warmer climate, in turn connected to more frequent and extreme weather events, drought, and rising sea levels.[1] Due to the increasing energy demands of a growing global population, it seems at this point infeasible that the anthropogenic contribution is going to be reduced to a level that stagnates the growth in the atmospheric concentration of CO_2. Hence, the most realistic strategy to alleviate the natural cycle is to remove or capture CO_2 before it ends up in the atmosphere. *Direct air capture* (DAC) is a suggested approach for scrubbing CO_2 directly from the atmosphere, while *carbon capture and sequestration* (CCS) involves capturing it from the flue gases of industrial emitters and subsequently storing it. The former approach is highly energy intensive, whereas the usefulness of the latter is largely contingent on the permanency of the selected storage medium—which is uncertain at this point. Mitigation of the latter can be achieved if the gas is instead utilized by converting it to useful compounds.

The utilization of CO_2 is in fact a relatively old technique, emerging with the syntheses of salicylic acid and sodium carbonate developed in the 19th century.[2] Since then, a plethora of applications have been developed, utilizing CO_2 as a carbon source in the production of various compounds.[3] Nonetheless, if all of these applications were implemented today, they would only amount to about 0.3 Gt CO_2/year converted to commodity chemicals, which is a drop in the ocean compared to the 32 Gt CO_2/year released through human activities.[2,4]

Although global oil reserves might seem practically non-depletable due to the development of technologies enabling extraction from previously unavailable locations, they are finite. Carbon dioxide represents a prospective replacement for oil, gas and coal as one of the primary sources of carbon for commodity chemicals, materials and fuels. However, for this to become more than a prospect, an intimate knowledge of the reactivity of CO_2 must be established.

1.2 CO_2 utilization

The carbon atom of CO_2 is in its highest oxidation state, hence utilization of carbon dioxide can be divided into categories depending on the extent of reduction.[2] Generally, reactions that maintain the +IV oxidation state of the carbon, or lower it to +III, have fairly low energy demands, therefore known simply as low-energy processes. Conversely, high-energy reactions lower the oxidation state of the carbon to any number between +II and −IV, and are energetically more demanding. The low-energy category leads to commodity chemicals or materials, while the high-energy category represents a potential source for fuels and chemical feedstock. It should be noted that the market for fuels is much larger than the market for chemicals, the former thus having a much higher potential impact on offsetting CO_2 emissions than the latter.[2] A simple fuel formed directly by CO_2 reduction is methanol:

$$CO_2(g) + 3H_2(g) \rightarrow CH_3OH(aq) + H_2O(l). \quad (1.1)$$

This can be accomplished electrolytically, although electrolytic CO_2 reduction is usually energy-inefficient and requires significant overpotentials.[5] In any case, CO_2 based fuels are only useful in terms of reducing emissions when produced using renewable energy.[2]

Production of fuels, which are in essence molecular energy carriers, has been pioneered by nature through photosynthesis. While it is extremely energy-inefficient by most relevant metrics, photosynthesis is unparalleled in its ability to produce complex organic molecules using solar energy. Humans can harvest solar energy more effectively and produce the chemicals to store it, yet seamless coupling of these processes—as in photosynthesis—is largely missing. Finding this missing link could solve the issue of accumulating CO_2 in the atmosphere by having it replace fossil-fuels both as carbon source and energy carrier.[2,6] Hence, development of highly energy-*efficient* artificial photosynthetic or photocatalytic processes represents a practical way to transition to a circular economy.

Some of the most promising materials for photocatalytic CO_2 reduction are metal-organic frameworks (MOF).[7–10] In spite of this, practical or commercial applications of MOFs are still limited, and several issues need to be addressed before they can be fully implemented.[8] Moreover, the mechanisms for photocatalytic CO_2 reduction are poorly understood, representing a significant bottleneck in this respect.[7]

Traditional heterogeneous catalysts are characterized by having a broad size distribution of metal species on the catalyst surface, yet only a small fraction of these usually act as the active species for the desired reaction.[11,12] While the rest are typically inert, they may in the worst case even trigger unwanted side reactions. Hence, such catalysts suffer from poor metal utilization and selectivity. On the other end of the scale, homogeneous catalysts have well-defined active sites, and are therefore highly tunable and selective. However, these are limited by their low recyclabilities and stabilities.

The emerging single-atom catalysts (SAC) seem to avoid many of the issues mentioned above.[11,12] Single atom catalysts contain isolated metal atoms dispersed on solid supports, which has proven to improve upon the catalytic activity of more traditional heterogeneous designs.[11,13] In addition, their structural simplicity carries over to the characterization and identification of the active sites, elucidation of the operative reaction mechanisms on the molecular level, ultimately enabling highly targeted catalyst designs.

1.3 Scope of thesis

The scope of this thesis is rooted in the molecular level mechanisms of CO_2 reduction due to their implicit relevance for CO_2 utilization. Direct reduction by electrons could conceivably be the first step, but since the isolated CO_2 molecule has a negative electron affinity, the resulting anions are unstable with respect to electron detachment.[14,15] Nevertheless, reduction of CO_2 to the radical anion is likely the first step in electrolytic processes, wherein the anion is stabilized by interactions with the solvent or the electrode surface. Furthermore, complex formation between metal atoms (or anions) and CO_2 in the gas phase leads to reduction of the latter.[16–28] These complexes are formally metal carbonites MCO_2, currently subject to considerable efforts in terms of characterization since they are thought to be important intermediates for CO_2 reduction.[15,29,30] The alkali and alkaline earth metals prefer bidentate coordination of the metal to both oxygen atoms (κ^2-O_2C), while transition metals typically binds to the carbon atom (η^1-CO_2) or in a side-on fashion (η^2-CO_2), see Figure 1. At this point, it must be emphasized these species have only been characterized for a selection of metals, and some only computationally.[16–28,31] Due to a free electron pair on the carbon atom, the κ^2-O_2C complexes are suggested to be carbenic; undergoing C—C bond forming reactions with alkyl halides, acetaldehyde and CO_2. These intermediate species are

therefore potentially important for the upscaling of CO_2 to more complex compounds.[19,28,32,33] Still, rather few reactivity studies have been published on these species in general.

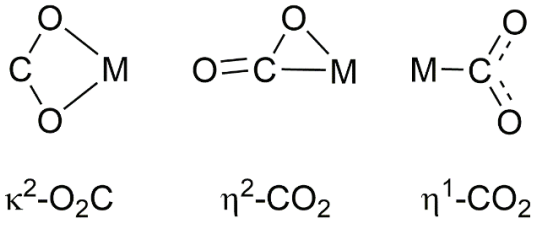

Figure 1. Frequently reported structures for metal carbonites, MCO_2. From Paper II.

Certain highly oxophilic metals do not form MCO_2 complexes in reactions with CO_2, instead undergoing C=O bond metal-insertion followed by CO elimination.[21,22,34–40] Carbon monoxide constitutes an attractive target for the CO_2 utilization scheme outright—yet perhaps even more so as a precursor to more complex chemicals. The remaining oxygen atom may for instance be used to form O_2, as recently demonstrated in the Mars oxygen in-situ resource utilization experiment (MOXIE).[41]

A related interesting class of compounds are the cyclic oxocarbons C_nO_n (n = 3 – 6). While the neutral species are generally unstable, their corresponding dianions, $C_nO_n^{2-}$, are highly stable with moderately aromatic character.[42–44] The tetramer, squarate, $C_4O_4^{2-}$, is a promising anode material for rechargeable lithium battery technology.[45,46] An atom efficient approach for its synthesis involves use of CO as a reactant by reductive cyclooligomerization,

$$4CO + 2e^- \rightarrow C_4O_4^{2-}. \quad (1.2)$$

This was first reported by Summerscales and coworkers, while similar processes have been published for the analogous trimer, deltate, $C_3O_3^{2-}$, involving actinide, lanthanide and alkaline earth metal homogeneous catalysts.[47–50] Cyclooligomerization is highly relevant in the context of CO upscaling, the latter representing a simple product of CO_2 reduction.

1.4 Aims of study

To improve upon our understanding of the reduction of CO_2 and the related reduction of CO, the overarching aim of this study has been to study the fundamental interactions and reactions between these simple oxocarbons and metal centers in detail, with particular attention toward their periodic trends. Specifically, the above can be expressed as:

$$M^- + nCO_2 \rightarrow MC_nO_{2n}^- \qquad n = 1, 2 \qquad (1.3)$$

$$\rightarrow MC_{(n-1)}O_{(2n-1)}^- + CO, \qquad n = 1, 2 \qquad (1.4)$$

where 1.3 describes the reduction and homologation of CO_2 to oxalate, 1.4 the direct reduction of CO_2 to CO. Meanwhile, 1.5 describes the equivalent reduction and homologation (cyclooligomerization) of CO,

$$M^- + nCO \rightarrow MC_nO_n^- \qquad n = 1, 2, 3, 4 \qquad (1.5)$$

The metal carbonite intermediate MCO_2^- has been attributed particular importance for the two first processes,[15] and is therefore given much attention herein. Decarboxylation of several metalated dicarboxylic acids lead to the formation of MCO_2^- and M^-, which in the case of oxalate is expressed by the reverse of Equation 1.3.[51–55] Similarly, the oxocarbon species C_nO_n (n = 3 – 6) typically fragment by consecutive decarbonylations, the reverse of Equation 1.5.[56] Dissociation of the desired products thus provides a facile way to study the mechanisms for their formation, and at the same time, generate relevant reaction intermediates.

This work is limited to investigating the above processes with the alkali and isovalent alkaline earth metal chlorides, M = Li, Na, K, Rb, Cs, and M = BeCl, MgCl, CaCl, SrCl, BaCl, although not all metals were examined in depth due to the time constraints. These metals were chosen due to their abundance, low toxicities (with the exception of Be and Ba), oxophilicities and reducing abilities. Moreover, some of these are already involved in the chemical scrubbing of CO_2.[57,58] Finally, magnesium is present in the reactive center for photosynthetic CO_2 reduction, the mechanisms of which are not fully understood.

1.5 Project outline

Based on the more general aims of study presented in the previous section, a specific project outline is given to provide a bridge between the aims of study and the results. The first and primary part of the project consists of:

a) Experimental and computational characterization of the properties of MCO_2^- complexes where M = Li, Na, K, Rb, Cs and BeCl, MgCl, CaCl, SrCl, BaCl.

Gas phase reactions between metals and CO_2 has been established to either proceed by complexation (to MCO_2) or reduction to CO. Hence, the second part of the project is:

b) Elucidation of the reactivity of the aforementioned metals with CO_2, paying particular attention towards factors governing complexation, C=O bond insertion and CO elimination.

Finally, utilization of CO_2 as chemical feedstock involves production of species of higher complexity, and the final part is thus directed towards C—C bond formation:

c) Study C—C bond formation involving reduced forms of carbon dioxide (MCO_2 and CO).

2 Background

The purpose of this chapter is to give a brief introduction to the carbon dioxide molecule in its various charge states, and to its coordination chemistry. This is followed by a brief description of the reactivity of CO_2, its reduced and metalated analogues. Finally, a short introduction to cyclooligomerization of CO concludes the chapter.

2.1 Carbon dioxide, CO_2

The stability of CO_2 is reflected by its low enthalpy of formation, $\Delta_f H^\circ = -393.5$ kJ/mol. While the ground state molecule is linear and lacks a dipole moment, it does have a quadrupole moment responsible for intermolecular interactions, facilitating the formation of neutral aggregates.[59–64] The infrared (IR) spectrum of CO_2 is well known, and the vibrational modes of solid and aqueous CO_2 are only slightly perturbed from the gas phase analogues, illustrating the relatively weak intermolecular forces at play.[65,66]

The computationally determined, experimentally supported electronic ground state of the molecule is $^1\Sigma_g^+$, and the lowest excited states have been assigned $^3B_2$, $^3A_2$, $^1A_2$ and $^1B_2$, respectively.[59,67–75] Electronic excitation typically elongates the C—O bonds and bends the molecule. For a more detailed account of the changes in geometry with electronic state, see either Aresta[59] or Ma *et al*.[67] Bending of the molecule during excitation is concurrent with an increased electron population of the central carbon atom. This correlation can be rationalized using the Walsh diagram[76] in Figure 2. The oxygen-centered degenerate HOMOs, $1\pi_g$, increase in energy while the carbon-centered degenerate LUMOs, $2\pi_u$, are lowered in energy with decreasing bond angle.

Ground state CO_2 can either react as an oxygen nucleophile or a carbon electrophile, the results of which can also be rationalized with the Walsh diagram.[59] The former results in bonding interactions at the oxygen through donation of electrons from $1\pi_g$ to an electrophilic reaction partner, and the linear geometry is typically more or less retained.[59] This is exemplified by the reaction between CO_2 and a proton, forming the hydroxycarbonyl cation, $HOCO^+$. Both of the possible *trans* and *cis* isomers are only slightly bent, $\angle_{O\text{-}C\text{-}O} = 174$ and 179°, respectively.[77]

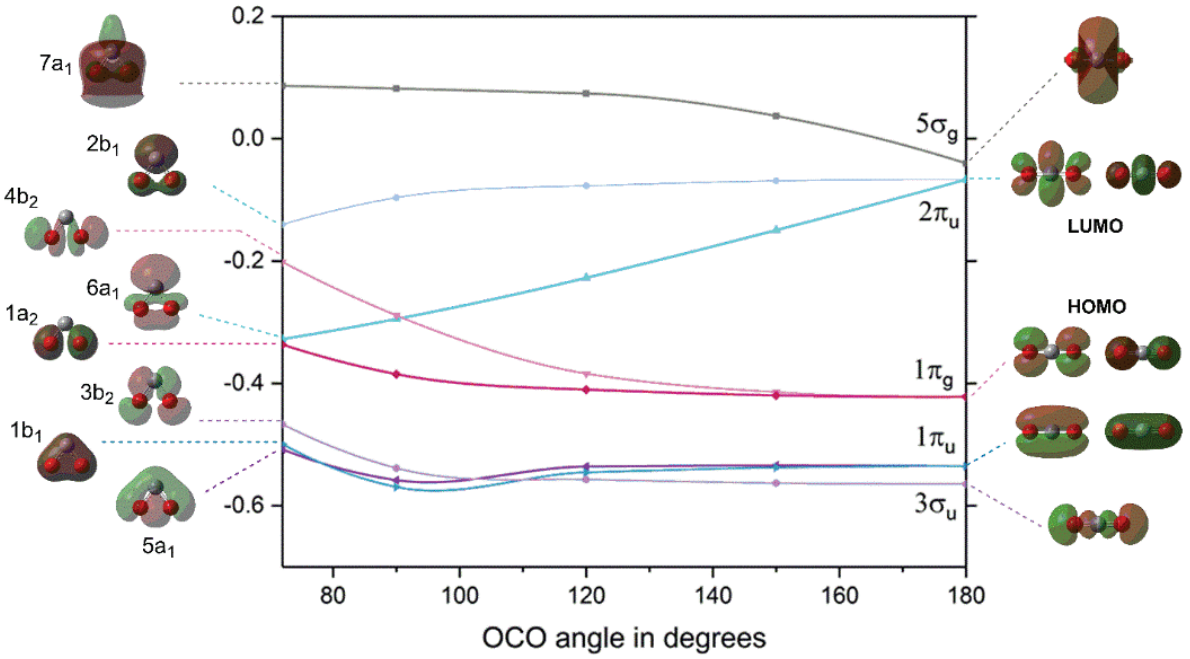

Figure 2. The relative energies of the frontier molecular orbitals of CO_2 as a function of O-C-O bond angle ($\angle_{O\text{-}C\text{-}O}$).

While reactions with electron deficient metals generally only slightly perturb the structure of CO_2, the situation is different when the latter reacts as a carbon electrophile. The resulting increased electron density on the carbon atom bends the molecule, simultaneously destabilizing the $1\pi_g$ orbitals. This enhances the nucleophilicity of the oxygen atoms, in turn favoring interactions with electrophiles. A logical argument is that the reverse must also be true; interactions between the oxygen atoms and electrophiles stabilize the increased electron density on the carbon atom. As long as the system is not electron-deficient, this may even reverse the polarity of the carbon as to render it nucleophilic, known simply as *umpolung*.

2.2 Carbon dioxide radical anion, $CO_2^{\bullet-}$

One-electron reduction of CO_2 leads to formation of the carbon dioxide radical anion:

$$CO_2 + e^- \rightarrow CO_2^{\bullet-}. \qquad (2.1)$$

The anion exists in a shallow local energy minimum with elongated bonds and a bent O-C-O angle, akin to the excited states of the neutral.[78,79] The unpaired electron is located on the carbon atom,

while the negative charge resides mostly on the oxygen atoms.[14] Since isolated CO_2 has a negative electron affinity of approximately −0.6 ± 0.2 eV, the corresponding anion is unstable with respect to electron detachment.[14,80,81] Nevertheless, the radical anion has been observed in several types of mass spectrometric experiments, indicating it has a finite, albeit short lifetime, from at least 50 μs up to several milliseconds.[14,55,81–84] This metastability has been attributed to the fact that an estimated barrier of 0.4 eV separates the potential energy surfaces of the bent anion and the linear neutral molecule.[85] The above suggests that electron attachment occurs at bent geometries; otherwise, the lifetime of the radical anion is reduced to femtoseconds (10^{-15} s). This is consistent with the fact that the anion is usually formed from species with already incorporated bent CO_2 moieties—such as carboxylates.[14,54,55,86] Although metastable as an isolated ion, stabilization is brought by aggregation or solvation.[14,79,87–93] This has enabled measurements of the vibrational spectra of the radical anion in various environments.[17,94,95]

2.3 Carbonite, CO_2^{2-}

The dianion of carbon dioxide, carbonite, is formed by addition of another electron to the radical anion,

$$CO_2^{\bullet-} + e^- \rightarrow CO_2^{2-}. \tag{2.2}$$

This elusive species is thought to be an important intermediate in several reactions.[15,96–101] Although extremely unstable as an isolated ion, carbonite can be studied through its protonated and metalated derivatives, the simplest of which is formic acid,[15]

$$CO_2^{2-} + 2H^+ \rightarrow HCOOH. \tag{2.3}$$

Since the carbon-bound hydrogen in formic acid is formally a hydride, it can be used as a reducing agent.[102] Conceivably, umpolung of the carbon atom as described in section 2.1 can be used to deprotonate formate to carbonite.[100,103] The umpolung effect is also manifested in the tautomerization of formic acid to dihydroxycarbene, $C(OH)_2$, in which the oxocarbon moiety attains a dianionic charge. Despite the fact that dihydroxycarbene is an unstable isomer of formic acid, it has been spectroscopically characterized.[104]

The earliest reported method to generate metalated carbonites is by treatment of CO_2 with the alkali metal atoms in the gas phase,

$$2M + CO_2 \rightarrow M_2CO_2. \qquad M = Li, Na, K, Cs \qquad (2.4)$$

This work was pioneered by Setton with cesium, who concluded that the adduct formed was a formate of cesium, rather than the carbonite.[16] Later, the products of reactions with Li, Na, and K, in addition to Cs, were studied using IR matrix isolation spectroscopy, finding that the species formed were metalated carbonites, M_2CO_2, as well as metalated carbon dioxide radical anions, MCO_2.[17–19,105] The former were seen to have generally more acute O-C-O angles than the latter, and these studies thus established a direct connection between the structure of the CO_2 moiety and the degree of reduction, as being dependent on the specific metal, but also on the number of metal atoms.

Furthermore, carbonite formation is observed in the condensed phase for low-valent transition metal, lanthanide or actinide complexes when allowed to react with CO_2.[27,106–109] This has also been reported for reactions between CO and alkaline earth, lanthanide and actinide metal oxide surfaces.[110–112]

2.4 Coordination modes

Carbon dioxide exhibits a diverse coordination chemistry with metals, but also with other elements.[29,59,84,113–116] The aim of this chapter is not to provide an extensive review, but rather a brief overview of possible coordination modes to illustrate its flexibility as a ligand. The considered species involve both isolated gas-phase as well as solvated compounds. The corresponding idealized structures are shown in Figure 3, adapted from a review by Paparo and Okuda.[29]

As already mentioned, complexes formed in reactions with electron deficient metals typically retain a neutral, linear CO_2 moiety. The interaction between a metal center and an oxygen atom can be either of dative or purely electrostatic character, η^1–OCO (1) or η^1–OCO (2), respectively. In addition, dative interactions may also emerge from the C=O or M=M double bonds, as in η^2–CO_2 (1) or μ–η^1–CO_2, in these cases effecting more pronounced structural changes in the CO_2 moiety ($\angle_{O\text{-}C\text{-}O} = 133°$).[117–119] Carbon dioxide can also act as a doubly bridging ligand, μ-η^1-O:η^1-O (1).[120]

Only three monometallic binding modes have been described for the singly reduced species, $CO_2^{\bullet-}$, all monometallic. The bidentate oxygen coordination mode, κ^2–O_2C (1), has rarely been observed, although the earliest report detailing it was published almost forty years ago.[18,19] As

mentioned in the previous section, alkali metals reduce CO_2 in noble gas matrices, resulting in either the κ^2–O_2C (1) or η^1–OCO structural moieties, respectively. Similar coordination has been suggested for the isovalent $CO_2MgCl_2^{\bullet-}$ and $CO_2CaCl_2^{\bullet-}$ species.[121] Two distinct types of η^1–OCO coordination has been surmised for the radical anion, differing in whether the CO_2 moiety is significantly bent (η^1–OCO (3)) or not (η^1–OCO (4)).[29] Still, it should be mentioned that the latter has only one reported example.[122]

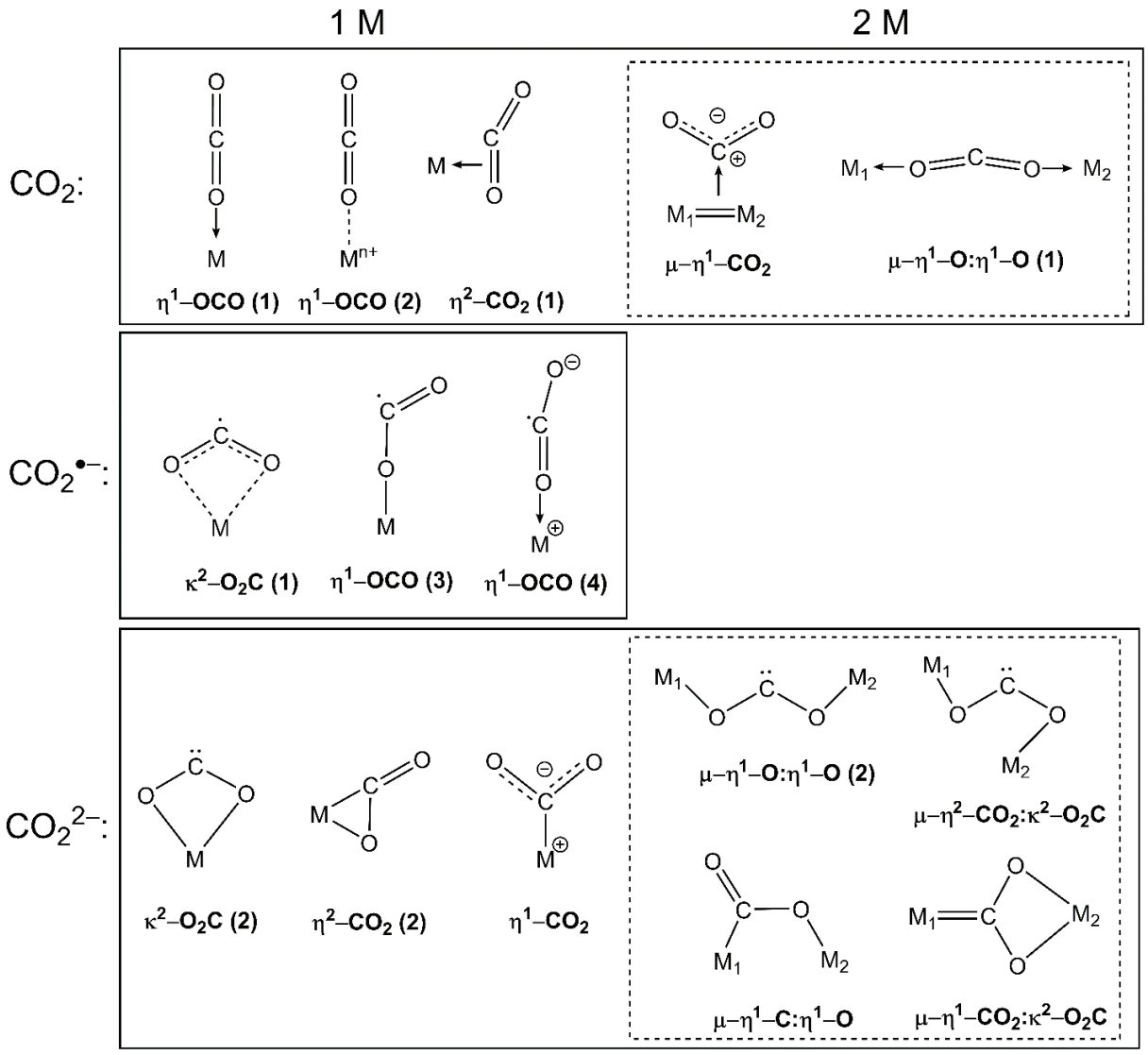

Figure 3. Coordination modes of CO_2, $CO_2^{\bullet-}$ and CO_2^{2-} to one or two metals (*left* and *right*, respectively). Figure adapted from reference [29].

The highest number of binding modes are possible for the carbonite ligand. The higher electron density on CO_2^{2-} leads to generally narrower O-C-O angles than for the neutral molecule and the radical anion complexes. Recall that the increased electron density increases the nucleophilicity of the oxygen atoms, thereby enhancing their affinity for electron-deficient, electrophilic metals. Unsurprisingly, bidentate oxygen coordination κ^2–O_2C (2) has been reported for magnesium, representing one of few spectroscopically characterized examples of this carbenic mode.[31] Nevertheless, several studies have indicated similar bonding for complexes with other alkaline earth metals, and some early transition metals.[27,36,123–125] Conversely, electron-rich species mainly interact in η^1–C fashion through the carbon, and these complexes can therefore be viewed as metalloformates, or metallocarboxylates.[23,26,115,116,126–128] In any case, the most frequently characterized mode of bonding is the mixed oxygen-carbon η^2–CO_2 (2) coordination, which can be thought of as an intermediate structure between the two former types.[27,29,40,59,100,129–135]

Two metal centers further increase the flexibility of carbonite coordination modes. Some of these are analogous to monometallic species, such as the μ–η^1–O:η^1–O (2) and μ–η^2–CO_2:κ^2–O_2C modes—observed for alkali metals—both similar to κ^2–O_2C (2).[18,19] With the exception of the metallocarboxylic ester type mode, μ–η^1–C:η^1–O, all of the bimetallic carbonite modes can be described as carbenic.[136]

Finally, it is worth noting that larger clusters of metals and CO_2 units have been reported, but are outside the scope of this brief overview, urging curious readers to find more information in the given references.[129,134,137,138]

Before proceeding, it is pertinent to mention that while the correct nomenclature for the metalated complexes depend on the specific coordination mode and charge on the CO_2 moiety, the term metal carbonite has been used in a general fashion in this thesis, referring to all MCO_2 species.

2.5 Reactivity of carbon dioxide and metal carbonites

This section builds upon those preceding it by providing a brief overview of the reactivity of CO_2 and MCO_2, both for gas phase and condensed phase species, which is explicitly stated unless obvious. It begins by presenting elimination reactions involving only CO_2 and its ionic counterparts, followed by possible elimination reactions of the metalated analogues. In the second subsection, a selection of addition, disproportionation, and substitution reactions of the metal

carbonites are described. For the latter subsection, a deliberate choice was made to focus on the reactions of the metal coordinated CO_2 due to their explicit relevance to this thesis, excluding reactions involving uncoordinated CO_2. However, photosynthetic CO_2 fixation, the Grignard and the generalized version thereof, the Barbier reactions, should be pointed out as relevant to the topic at hand, and the interested reader is referred to selected literature for more information.[139–141]

2.5.1 Elimination reactions

One of the simplest reactions involving carbon dioxide is cleavage of a C=O bond resulting in the elimination of oxygen, CO + O. Surface crossings between its excited states are thought to be important for this process.[67,68] Specifically, the crossing point between the $^1B_2$ and $^3A_2$ states lies above the $CO(^1\Sigma^+) + O(^3P)$ asymptote, indicating that a C=O bond is cleaved after passing from the former electronic state to the latter.[67,69,142–144] Xantheas and Ruedenberg investigated the potential energy surfaces of the ground and excited states of CO_2 and their decomposition pathways, finding that the route leading to $C(^3P) + O_2(^3\Sigma_g^-)$ involves a carbenic CO_2 intermediate with a ring structure (C_{2v}). Its existence was first proposed by Feller *et al*, also illustrating how electron density is transferred to the carbon when the CO_2 moiety is bent, even when the molecule itself is not reduced.[142,145] Nevertheless, reactions involving solely the isolated neutral CO_2 molecule are prohibitively demanding, exemplified by the least demanding elimination reaction,

$$CO_2(^1\Sigma_g^+) \rightarrow CO(^1\Sigma^+) + O(^3P), \tag{2.5}$$

which is spin-forbidden and endothermic by 526 kJ/mol.[59,124]

Reactions with isolated $CO_2^{\bullet-}$ and CO_2^{2-} species are practically infeasible to study experimentally due to their inherent instabilities. However, reactions between $CO_2^{\bullet-}$ radical anion clusters and methyl iodides in the gas phase has revealed nucleophilic reactivity for the former, although this is outside the scope of this chapter.[146,147]

In contrast to the reactions of isolated CO_2, metal-insertion and subsequent CO elimination,

$$M + CO_2 \rightarrow MCO_2 \rightarrow OMCO \rightarrow MO + CO, \tag{2.6}$$

is exothermic and proceeds practically without a barrier in the gas phase for early transition metal atoms and cations, Pathway 1, Figure 4.[21,22,34–40,95,148–152] In contrast, this is thermodynamically infeasible for the mid- to late transition metals, only forming carbonites.[22,39,129,130,134,135,148–150,153]

Similarly to the latter species, the preferred outcome for the analogous reaction between CO_2 and the alkaline earth metal atoms, M = Be, Mg, Ca, Sr and Ba, is predicted to be metal carbonite formation.[123–125,152,154] With the exception of M = Be, these do not insert into the C=O bond. Elimination of CO thereby proceeds directly from the carbonite, Pathway 2, Figure 4, which is endothermic for the first four metals, yet exothermic for M = Ba. This was rationalized by correlating the reaction energies with M—O bond strengths, with barium forming the strongest bond with oxygen.[125] For other main group species, CO elimination is exothermic for M = B, and slightly endothermic for M = Al, the latter instead preferring formation of the corresponding aluminum carbonite.[155–157] Although the above discussion is based solely on the energetics of the processes, it must be stressed that the partitioning towards MCO_2 formation or CO elimination also depends on the reactant and product spin states, as seen in the given references.[153,158]

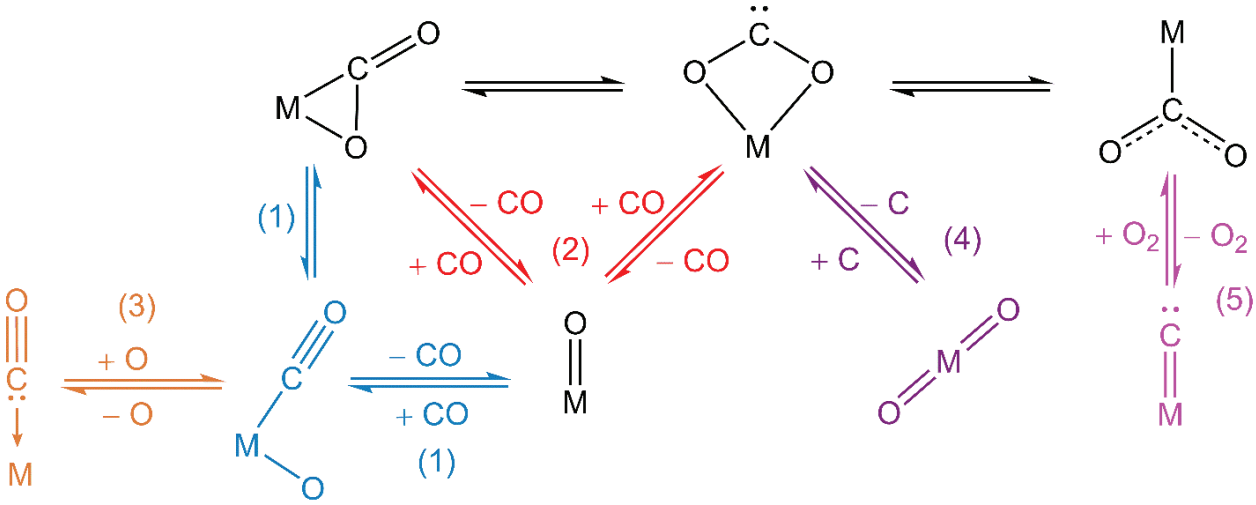

Figure 4. Putative reversible elimination pathways for metal carbonites: (1) metal-insertion and CO elimination, (2) direct CO elimination, (3) oxygen-atom elimination, (4) carbon-atom elimination, and (5) O_2 elimination. Figure partly adapted from reference [29]. Note that this is not an extensive depiction of all pathways, and is only meant to provide a general idea of the possibilities.

It is also conceivable that the metal-inserted product OMCO undergoes oxygen-atom elimination, resulting in metal carbonyl formation, Pathway 3, Figure 4. As one of few explicit examples of this in the literature, a bimetallic titanium bis(pentalene) complex reacts with two equivalents of CO_2 to give one equivalent of a carbonyl complex and one equivalent of a

bis(oxo)bridged dimer, implying that both Pathways 1 and 3 occur simultaneously.[159] An example of the reverse of the latter has also been published, describing the oxidation of metal coordinated carbon monoxide by peroxy acids, resulting in the formation of L_nReCO_2 species.[160] Both of these two latter examples are from the condensed phase.

On a related note, cryogenic matrix isolation studies have recently revealed that the late alkaline earth metals, M = Ca, Sr and Ba, form neutral and ionic metal carbonyls $M(CO)_n$ where $n = 1 – 15$.[161,162] This is particularly interesting for M = Ba, having a highly stable oxide as suggested above; hence the preference of the Ba + CO_2 system towards either BaO or BaCO is not entirely clear.

The fourth possible elimination pathway—carbon-atom elimination—has been reported in a study detailing the electrolytic reduction of CO_2 by elemental cerium,[163]

$$Ce + CO_2 \rightarrow CeO_2 + C. \quad (2.7)$$

This was accomplished using a liquid metal electrocatalyst, resulting in layered solid carbonaceous species. The reactivity of Ce towards CO_2 is perhaps not surprising, as the elemental metal spontaneously ignites when heated in air or CO_2, resulting in CeO_2, noting that similar reactivity is observed in CO_2 streams with alkali and alkaline earth metals.[164] The isodesmic Pathway 5 in Figure 4 has to the best of my knowledge never been reported. Conversely, transition metal carbides are potential catalysts for the reduction of CO_2 to CO.[165,166] Hence, these species are probably more suited to reduce CO_2, rather than constituting products of its reduction.

2.5.2 Addition, disproportionation and substitution reactions

As previously mentioned, metal carbonites are deemed important intermediates in the utilization of CO_2. So far, only their formation, along with their conversion to simpler compounds have been described. The following aims to illustrate the reactivity of these species towards other simple compounds, with specific relevance to the low-energy CO_2 utilization reactions leading to carbonates and carboxylates.

Figure 5 illustrates the reactions between alkali metal atoms and CO_2 in inert gas matrices, highlighting the role of the M_nCO_2 intermediates. In the latter, CO_2 is either reduced by one or two metals (n =1, 2), or equivalently, one or two electrons.[18,19]

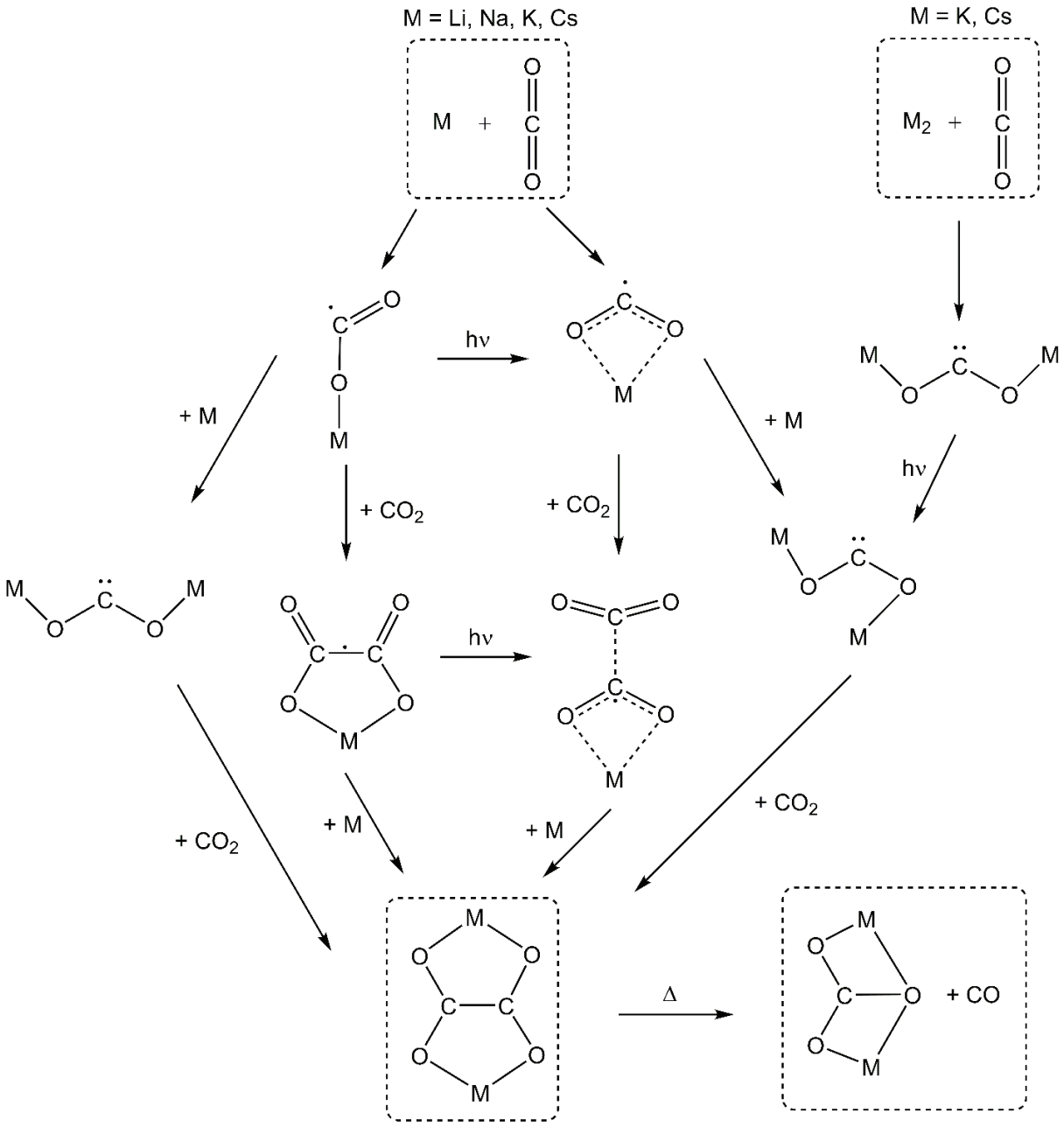

Figure 5. Addition and disproportionation reactions between alkali metal atoms and CO_2 in inert gas matrices, adapted from references [18,19].

Addition of CO_2 to the singly reduced $MCO_2^{\bullet}$ complexes corresponds to one electron reduction of two CO_2 molecules by a metal atom, resulting in the formation of monoanionic oxalate, $C_2O_4^{\bullet-}$, with a weak one-electron C—C bond. In contrast, the reaction between the dianionic carbonite, M_2CO_2, and an additional CO_2 molecule results in the formation of dianionic

oxalate, $C_2O_4^{2-}$, with a normal two-electron covalent C—C bond. Nonetheless, the latter is also formed by addition of another metal atom to $M^+C_2O_4^{\bullet-}$, showing that the number of metal atoms available to react with each CO_2 molecule is a key parameter in controlling the reduction of the latter. The metal oxalate products undergo disproportionation at room temperature, resulting in formation of M_2CO_3 and CO, which is preferred over oxalate formation for the heavier species M = K and Cs, even at cryogenic temperatures.[19] While the reaction steps and species involved for the alkali metal scheme are fairly well established, the detailed mechanisms and corresponding reaction energies are unknown.

The reverse of the above—the unimolecular dissociation of the alkali metal oxalates—have also been studied for the corresponding ionic species using mass spectrometry.[51–53,167] The sole fragmentation pathway for most of the ions is consecutive decarboxylation, resulting in the formation of the somewhat exotic alkali metal anions, M^-. Meanwhile, $LiC_2O_4^-$ displays an additional decarbonylation pathway leading to $LiCO_3^- + CO$.[52] The difference between lithium and the rest of the alkali metals in this context has not been elaborated in literature. Interestingly, decarbonylation is observed for all alkali metals in the similar cationic species, $M_3C_2O_4^+$.[167]

More recently, the $M(\kappa^2\text{–}O_2C)^-$ (M = MgCl, MgBr, MgOH) complexes were shown to react with alkyl halides by nucleophilic substitution (S_N2) in mass spectrometric experiments.[32] The major products of these reactions were the corresponding metal acetates and halide anions, while the minor products were the acetate anion and the corresponding metal halides, Figure 6.

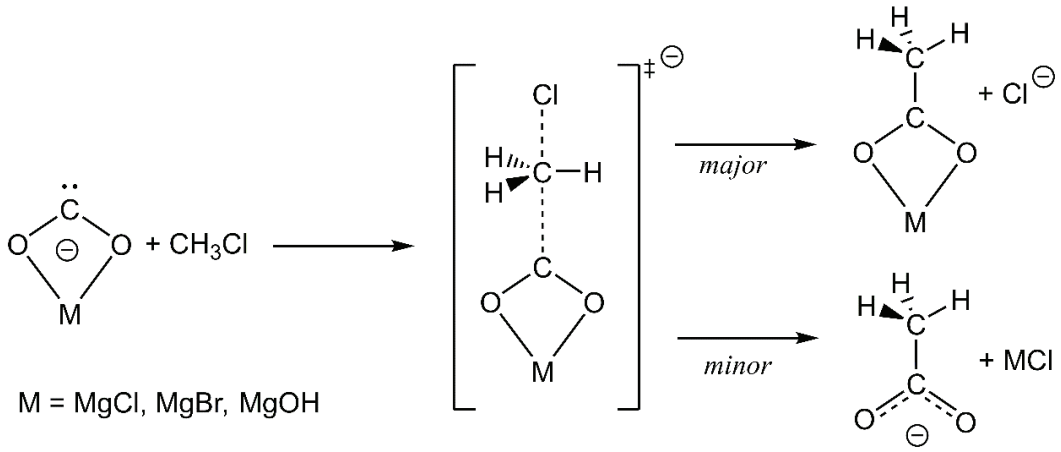

Figure 6. Nucleophilic substitution between methyl chloride and $M(\kappa^2\text{–}O_2C)^-$.[32]

The aforementioned study also showed how the magnesium carbonites were highly reactive towards water, $MCO_2^- + H_2O \rightarrow M(OH)_2 + CO$, attributed to the stability of the hydrated magnesium species. Further studies determined that magnesium and zinc chloride carbonites, $ClM(\kappa^2{-}O_2C)^-$ (M = Mg, Zn) react similarly to the alkali metal species, forming oxalates and carbonates by CO_2 addition and CO elimination, respectively.[28] Moreover, these carbonites react with acetaldehyde by nucleophilic addition to form lactate complexes, but also by electrophilic substitution, thereby eliminating CO as shown in Figure 7. These aforementioned reactions were explored computationally, all found to be exothermic and essentially barrierless.

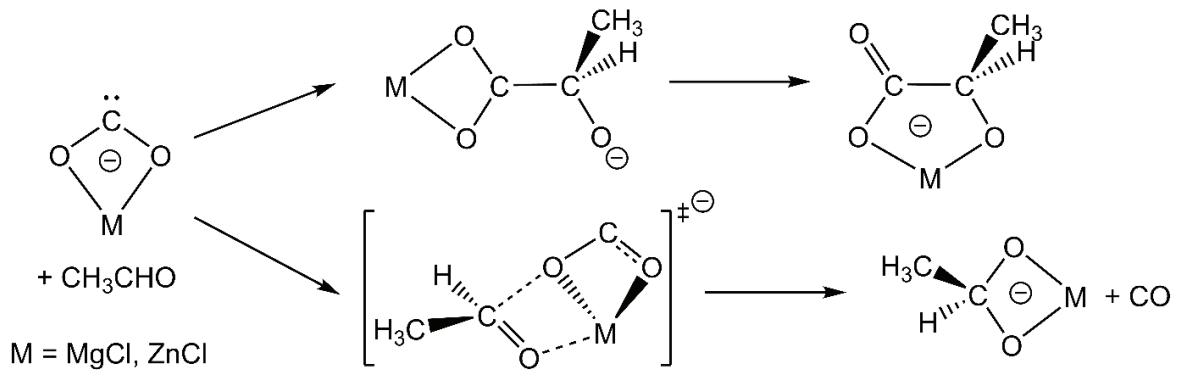

Figure 7. Addition and electrophilic substitution reactions between $M(\kappa^2{-}O_2C)^-$ and acetaldehyde.

The general relevance of the above gas-phase studies is highlighted as formation of oxalates and carbonates is similarly observed in the condensed phase. This has been reported for various monomeric and dimeric transition metal and lanthanide complexes wherein CO_2 binds in the bridging $\mu{-}\eta^1{-}O{:}\eta^1{-}O$, or mixed $\eta^2{-}CO_2$ fashion.[100,168,106,108,169,170] Computational studies on Yb and Sm complexes suggest that the selectivity of the reaction depends on the polarity of the solvent. Polar solvents favor the monomeric metal complexes displaying an increased propensity towards carbonate products, while non-polar solvents favor the bimetallic complexes effecting oxalate formation.[169] Furthermore, selectivity is also influenced by the ancillary ligand, and since these studies have been conducted in a myriad of solvent/ligand environments, derivation of clear, unambiguous trends is rather challenging.[108,131,171] Still, this can be simplified by studying isolated metal carbonites in the gas-phase, providing a window to their intrinsic reactivity. Moreover, rather

few such studies have been published overall. This constitutes one of the major motivations for this work.

2.6 Cyclooligomerization

The cyclic oxocarbons, $C_nO_n^{m-}$ (n = 3 – 6, m = 0 – 2), can be envisioned as products of reductive consecutive C—C coupling of n CO molecules, *i.e.* cyclooligomerization,

$$n\mathrm{CO} + m\mathrm{e}^- \rightarrow \mathrm{C}_n\mathrm{O}_n^{m-}. \tag{2.8}$$

The dianionic species (m = 2) represent an interesting class of compounds, being highly stable due to aromaticity, resulting in unusually strong corresponding acids, $H_2C_nO_n$.[43] In contrast, their neutral counterparts (m = 0) are generally unstable.[44] Squarate, $C_4O_4^{2-}$, is a promising anode material for rechargeable lithium batteries.[46] Since squarate is a reduced cyclic tetramer of carbon monoxide, it makes sense to synthesize it directly from CO under reductive conditions. However, its first reported synthesis in 1956 was atom-inefficient and involved perhalogenated reactants, and while several patents exist on electrochemical cyclooligomerization of CO, these are typically associated with large CO overpressures, difficult product separation and solvent-recycling issues.[172–174]

Some fifty years after its first synthesis, Green *et al*. reported a direct route from four CO molecules to squaric acid catalyzed by a mixed-sandwich U(III) complex.[47] Initial mechanistic studies on the process revealed that formation of the first C—C bond occurs between two CO molecules coordinated to separate complexes.[175] The newly formed ethenedione anion $^{\bullet}O{=}C{=}C{=}O^-$ may react with additional COs to form either deltate, $C_3O_3^{2-}$, or squarate, but it may also relax to the ethynedione structure $^-O{-}C{\equiv}C{-}O^-$, found to be inert towards further reaction with CO. The role of the metal was highlighted, acting both to reduce CO and to bring these into the specific orientations required for further reaction, be that addition of CO or isomerization. A subsequent computational study elaborated on these findings, suggesting that two different pathways were operative for the formation of higher oligomers and the formation of the dimer, as shown in Figure 8.[176] In particular, it was inferred that further reactivity of the dimer was contingent on the inequivalence of the two CO moieties in the complex; nucleophilic attack by CO occurs on the positively polarized carbon atom. Formation of deltate was determined to be preferred thermodynamically, whereas ethynedione constituted the kinetic product. In addition, Yuvaraj and

coworkers recently reported formation of deltate, in this case catalyzed by a bimetallic Mg(I) complex, finding similar mechanisms for this process.[50]

While the reactivity of the cyclic oxocarbons seems straightforward in the sense that they are formed by coupling of *n* CO molecules, this notion was put to the test by Schröder *et al*.[56] In particular, they studied the fragmentation patterns of $C_nO_n^{\bullet-}$ (n = 3 – 6) and found that the deltate radical anion may rearrange to an open-chain structure with a carboxylate group, $^{\bullet}O{-}C{\equiv}C{-}CO_2^{-}$. Nevertheless, complete dissociation into CO molecules was seen to dominate the reactivity of these species.

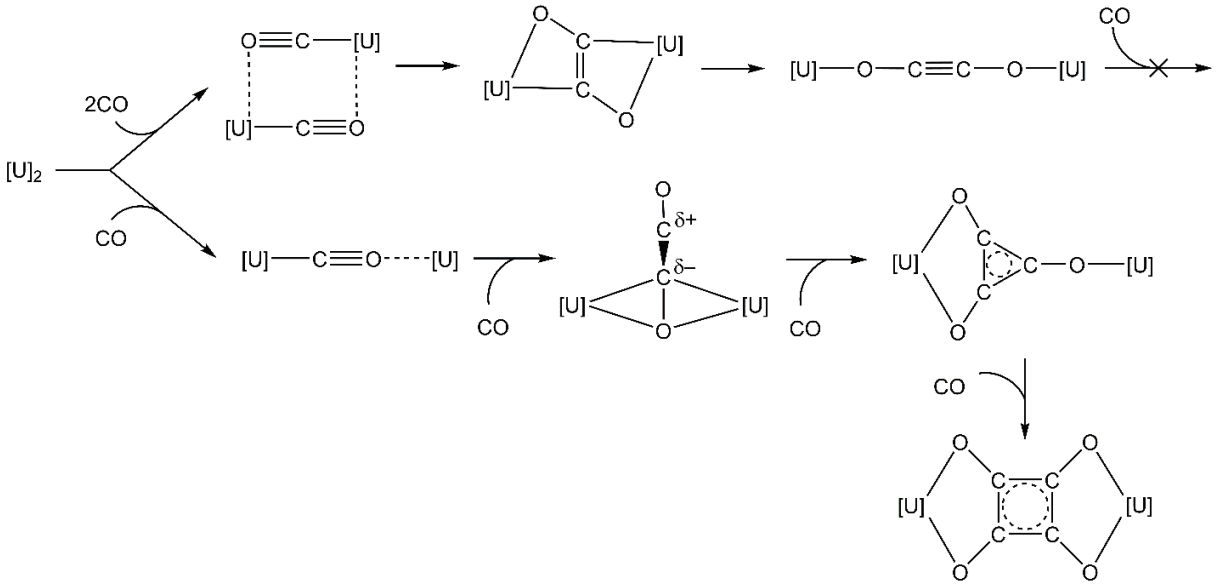

Figure 8. Cyclooligomerization of CO catalyzed by a model uranium (III) complex, [U] = U(η-C_8H_6{SiH_3-1,4}$_2$)(η-Cp) as described in reference [176].

3 Methods

The works in this thesis were realized using a combination of experimental and computational methods. With the exception of the cryogenic ion vibrational spectroscopy,[177] the experiments were conducted using a Quadrupole-time-of-flight (QTOF) mass spectrometer equipped with an electrospray ion source. For the computational part, the results were mainly obtained using the Gaussian/Gaussview Program suite,[178] NWChem[179] and Chemissian.[180] Basis sets that were not included in standard software libraries were retrieved from the Basis Set Exchange web portal.[181–183] High-performance computing (HPC) resources on the computing clusters Abel, Stallo and Saga were provided by Uninett Sigma 2 (NOTUR), and on Cori by the National Energy Research Scientific Computing Center (NERSC). This chapter aims to introduce the relevant fundamental principles of both the experimental and the computational methods, followed by a description of the specific methods employed.

3.1 Mass spectrometry

3.1.1 Fundamentals of mass spectrometry

The movement of ions in vacuum are governed by Newton's second law of motion,

$$\boldsymbol{F} = \mathrm{m}\boldsymbol{a}, \tag{3.1}$$

where $\boldsymbol{F}$ is the force, m is the ion mass and $\boldsymbol{a}$ is its acceleration; and the Lorentz force law,

$$\boldsymbol{F} = ze(\mathbf{E} + \boldsymbol{v}\times\mathbf{B}), \tag{3.2}$$

where z is the charge number, e is the elementary charge, $\boldsymbol{v}$ is the velocity of the ion, while $\mathbf{E}$ and $\mathbf{B}$ are the electric and magnetic fields, respectively. The fundamental equation of motion in mass spectrometry is obtained by equating the two expressions, and rewriting the acceleration term on a differential form, $\boldsymbol{a} = \mathrm{d}\boldsymbol{v}/\mathrm{d}t$,

$$\mathrm{d}\boldsymbol{v}/\mathrm{d}t = ze(\mathbf{E} + \boldsymbol{v}\times\mathbf{B})/\mathrm{m}, \tag{3.3}$$

relating the mass and charge of an ion to its velocity and the forces acting upon it. Moreover, it shows that the velocity of an ion is inversely proportional to its mass and proportional to its charge; hence, heavy ions move slower than light ions and ions with a lower charge move slower than ions with a higher charge. In mass spectrometry, ions are usually accelerated in an electric field between

two or more acceleration plates, imparting kinetic energy equal to the electric potential difference V separating the plates,

$$m\boldsymbol{v}^2/2 = zeV. \tag{3.4}$$

The magnetic force exerted on an ion is a cross product of ion velocity and field strength, thus acting perpendicular to both. This means that a magnetic field cannot alter the speed of an ion, only the direction of its path, which is the working principle behind magnetic sector instruments.

The abovementioned fundamental principles enabled the development of the field of mass spectrometry, where ions are separated according to the ratio between their mass and charge numbers, *m/z*, by definition a dimensionless quantity. The resulting collection of *m/z* signals (or peaks) is a mass spectrum. A quantitative measure of the ability to separate slightly differing *m/z* signals is the resolution *R*,

$$R = M/\Delta M, \tag{3.5}$$

where *M* is the nominal *m/z* of a particular peak and ΔM is the resolving power, typically defined as the width of a peak at a given fraction of its height for instance at 50%, known as the full width at half maximum (FWHM). A higher resolution therefore implies that more closely spaced peaks can be separated, and thereby more precise mass measurements.

3.1.2 The QTOF 2 and its components

The vast majority of the experiments of the included papers were conducted using a Waters/Micromass QTOF 2 mass spectrometer, as shown in Figure 9. It is fitted with an electrospray ion (ESI) source, a linear quadrupole (Q) mass analyzer, a collision cell with a hexapole ion guide, and a combined orthogonal acceleration reflectron time-of-flight (oa-TOF) mass analyzer with a multichannel plate (MCP) detector. These components, along with their working principles and use, will briefly be described in the same order as above.

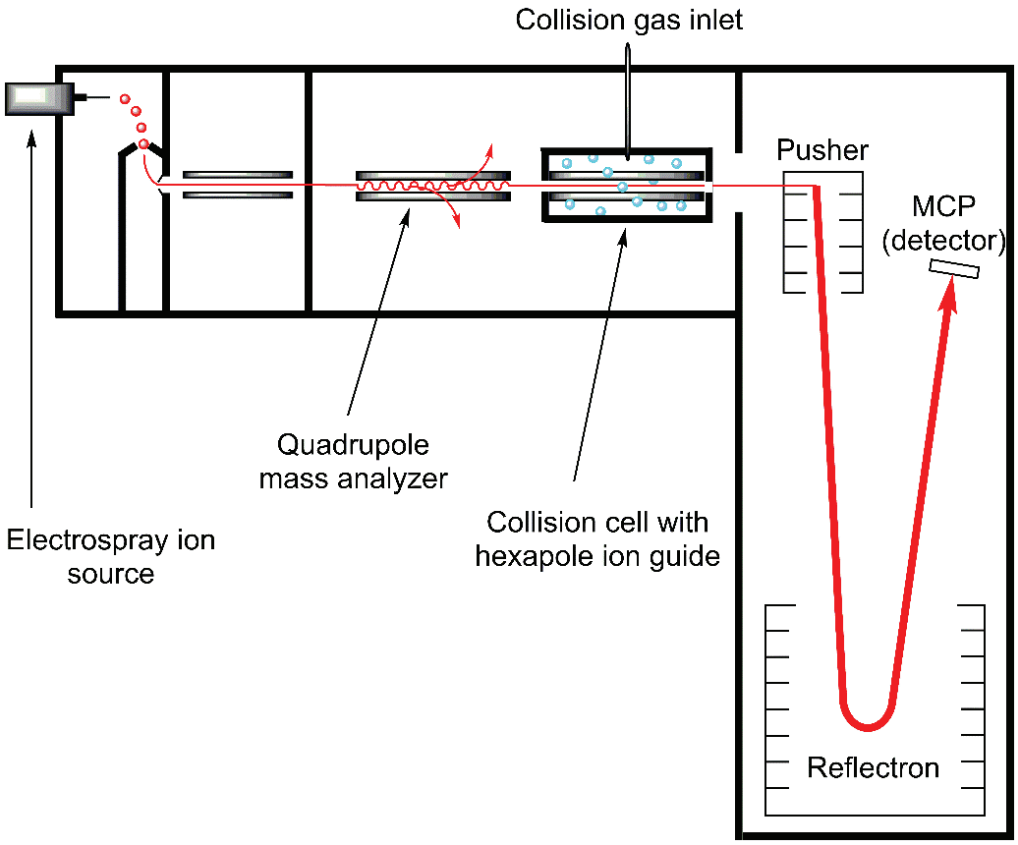

Figure 9. Configuration of the Waters/Micromass QTOF 2 mass spectrometer.

3.1.2.1 Electrospray ion source

Ionization methods are often classified as hard or soft, depending upon the extent of fragmentation effected by the ionization event. The ionized analyte known as the molecular ion, while ions resulting from fragmentation are generally called fragment ions. As a soft ionization method, ESI produces mostly intact molecular ions, typically protonated or deprotonated versions of the neutral species, $[A + H]^+$ and $[A - H]^-$. The electrospray ionization process is illustrated in Figure 10, and can be described in terms of two discrete steps; (1) the formation of charged droplets (~10^{-6} m radius) from a solution containing the species of interest, and (2) the formation of the corresponding naked ions by evaporation of the solvent from these droplets. Both of these steps have been extensively studied, and the reader is referred to the literature for a more complete overview than given below.[184–193]

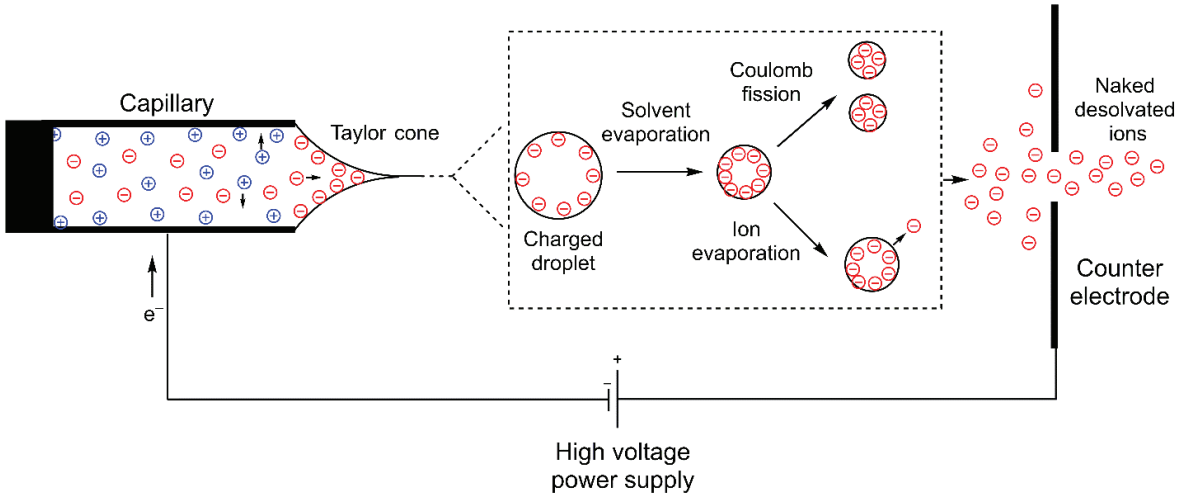

Figure 10. Simplified illustration of the electrospray ionization process (in negative ion mode), assuming full charge separation for clarity.

In an ESI source, a solution containing the sample is pumped into a needle capillary. The capillary and its counter electrode are separated by an electric potential of a few kV, creating a strong electric field. The electric field induces partial separation of positive and negative ions; those of similar polarity as the capillary accumulate at the tip of the needle. The mutual repulsion of the accumulated charge leads to a protrusion of the liquid towards the counter electrode. This protrusion, known as the Taylor cone, is held in place by the surface tension of the solvent, to which the ESI process is highly sensitive.[186,190] Eventually, the mutual repulsion of ions exceeds the surface tension, releasing a fine jet of highly charged liquid subsequently breaking up into a mist of charged droplets. A heated gas in the source region assists both the formation of droplets and solvent evaporation from them.

The exact mechanisms behind the formation of naked, desolvated gas phase ions from these charged droplets are still debated, yet two main models are widely accepted: the ion evaporation model (IEM) and the charge residue model (CRM).[184,185,193] An important parameter in both of these models is the maximum charge that can be held by a droplet of a given size and surface tension, known as the Rayleigh limit.[194] A droplet that surpasses this limit undergoes Coulomb fission producing smaller offspring droplets, thereby increasing the total surface area available for the charge.[192] In the IEM, ions are emitted from droplets assisted by the surrounding electric field, alleviating the excess charge within. In contrast, the CRM states that droplets undergo fission and

solvent evaporation in cycles until all solvent is gone, leaving the analyte molecules with any remaining charge thereby producing desolvated ions. It has been suggested that the IEM better describes the behavior of smaller ions, while the CRM is better suited to larger ions.[193] This can be understood in terms of the uneven distribution of mass and charge between parent and offspring droplets. While the small offspring droplets necessarily contain smaller ions and less charge, more easily extracted by the electric field, the large parent droplets can accommodate larger ions and a higher charge, more susceptible to coulomb fission and solvent evaporation.

As already stated, ESI is a soft ionization method, but the source conditions can still be tuned to increase the internal energy of the ions sufficiently to induce fragmentation, known as in-source (IS) fragmentation. This possibility has been exploited in some of the included papers.

3.1.2.2 Quadrupole mass analyzer

The linear quadrupole in this particular instrumental configuration serves as a mass filter with better than unit mass resolving power. It consists of four parallel cylindrical rods as shown in Figure 11, each at their respective corner of a square when viewed in the direction of ion traversal (*z*-direction). The rods reside between two plates separated by a potential difference along the z-direction, ensuring the forward momentum of the ions. The rods are diagonally paired, with each pair being oppositely polarized. The potential at each pair consists of a constant voltage U modulated by an oscillating radiofrequency (RF) voltage V. This yields the following expression for the quadrupole potential Φ_0,

$$\Phi_0 = U + V\cos(\omega t), \tag{3.6}$$

where ω is the angular frequency of the RF voltage. Combining this expression with the fundamental equations of motion results in the Mathieu equations, describing the movement of ions in a quadrupolar electric field. The solutions to these equations are rather technical, and the reader is referred to literature for further information.[195,196] In contrast, a simple analogy for the stability of an ion trajectory through the quadrupole is that of a ball on top of a rotating saddle: as long as the saddle rotates (the quadrupole potential) with the correct angular speed, the ball (the ion) is kept from falling off.

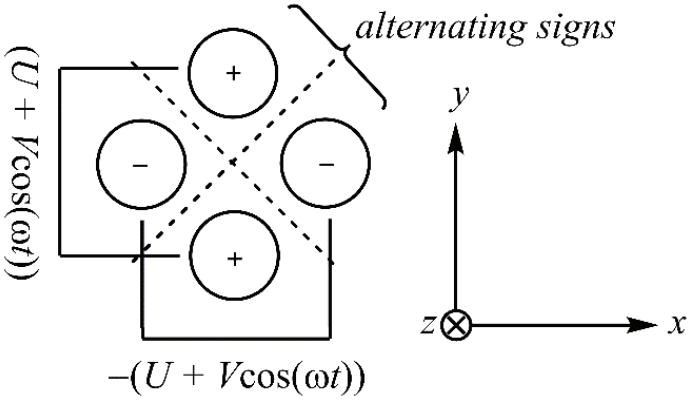

Figure 11. Cross section of the quadrupole mass filter. The potential is zero along the dotted lines. Stable ion trajectories imply transmission of ions in the *z*-direction; ions with unstable trajectories collide with the rods or are ejected in the *xy*-directions.

3.1.2.3 Collision cell

The collision cell in our QTOF 2 enables collisions, or reactions, between our ions and various gaseous molecules. The lab-frame kinetic energy of the ions passing through the cell (E_{LAB}) is tunable *via* an instrument parameter. The collision gas pressure can also be adjusted by means of a retrofitted ultra-high vacuum (UHV) leak-valve; the frequency of ion–gas collisions is to a first approximation proportional to the collision gas pressure. This is due to the inverse dependency between the pressure of the gas and the mean-free path of the ions within the cell. Collision on inert gases (typically Ar or Xe) at relatively high collision energies lead to collision induced dissociation (CID) of the ion whence its specific fragmentation pattern can be obtained. Reactions between ions and reactant gases are usually done at relatively low collision energies.

The CID of an ion—denoted precursor ion in this context—can be conceived simplistically as a two-step process involving an initial collision and activation step, followed by unimolecular dissociation of the activated ion.

A collision between an ion and a neutral molecule is often defined in terms of a critical radius surrounding the former—the capture radius (r_c)—and the trajectory of the molecule relative to a parallel line drawn from the center of the ion—described by the impact parameter (b)—as illustrated in Figure 12.

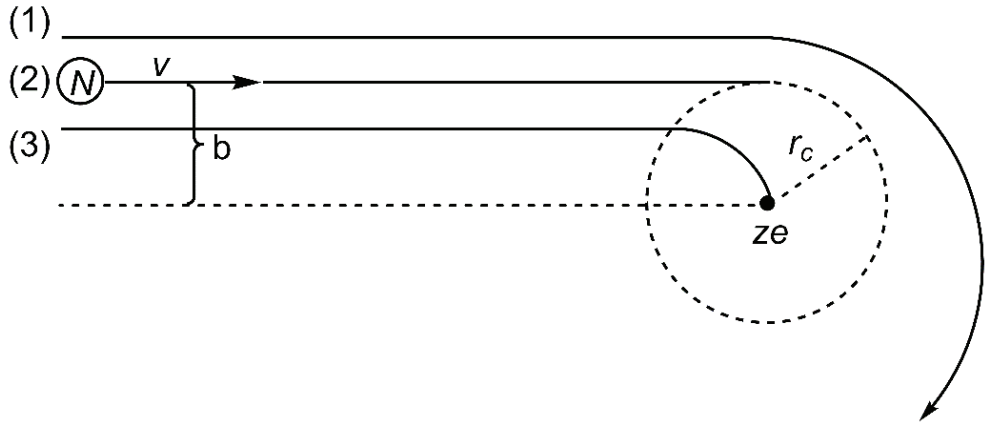

Figure 12. A simple ion-molecule collision model.

When a molecule N of relative velocity $\boldsymbol{v}$ closely approaches an ion with charge ze, three events can be envisioned: (1) its trajectory is altered by the electric field around the ion but there is no collision when $b > r_c$, (2) N is caught in an orbit around the ion when $b = r_c$, or (3) collision occurs when $b < r_c$. The capture radius is a function of the relative velocities between the colliding species, the electric field around the ion, and the properties of the neutral molecule.[197–199] During a collision with a neutral collision gas N, some of the collision energy is transferred to the internal degrees of freedom of the precursor ion PI, leading to a vibrationally excited or activated ion PI*,

$$\mathrm{PI} + N \rightarrow \mathrm{PI}^* + N. \tag{3.7}$$

This process is dominated by impulsive collisions, wherein excitation occurs on the repulsive part of the ion-neutral potential, leading to significant scattering of the involved ions.[200] Excitation can also take place in an ion-neutral complex formed during low energy collisions. The total energy available for activation—and thus reaction—is the center-of-mass collision energy,

$$E_{\mathrm{COM}} = E_{\mathrm{LAB}}(m_N/(m_N + m_{PI})), \tag{3.8}$$

where m_N and m_{PI} denote the masses of the collision gas and precursor ion, respectively. However, the amount of energy transferred in collisions between ions and neutral molecules also depend upon their relative directional movements, internal degrees of freedom and thermal motions. Hence, the precursor ions attain a distribution of internal energies during the collisional activation step.

At a certain point following activation, an activated ion dissociates to a fragment ion FI and a corresponding neutral fragment NF,

$$PI^* \rightarrow FI + NF, \tag{3.9}$$

depending on its internal energy content. The appearance of the FI enables estimation of its threshold energy, the minimum energy needed for the dissociation reaction to take place. This is achieved by monitoring FI abundance as a function of E_{COM}, related to the internal energy content of the activated ion. Note that the rate of unimolecular dissociation of an activated ion *via* a given reaction channel is a function of the internal energy it has in excess of the corresponding energetic barrier. Due to the relatively short residence times within a mass spectrometer, it is possible that activated ions will not have time to decay before reaching the detector unless they have a significant internal energy surplus relative to the energetic barrier. In practice, this leads to the energetic barrier appearing higher than it is, an effect known as the kinetic shift. A related effect is the thermal shift; the apparent lowering of threshold energies relative to the energetic barrier due to the non-zero internal energy content of the precursor ions. In addition to these effects, the scattering of ions within the instrument due to either the collision events or the ion optics leads to decreasing PI signals with increasing collision energy, in turn affecting the appearance of the FI signals. Hence, the estimated threshold energy of a reaction can differ remarkably from the actual energetic barrier. Furthermore, the magnitude of these effects increase with the degrees-of-freedom of the precursor ion and the number of sequential reactions, limiting the quantitative use of threshold energies unless these are taken into account.

As mentioned at the start of this subsection, another use of the collision cell is to study the reactivity of ions. The inert collision gas in the cell can be replaced with a reactant gas having certain characteristics to elucidate the corresponding type of reactivity of the ion. For instance, the cell can be filled with gaseous molecules containing electrophilic sites, enabling investigation of the nucleophilic reactivity of an ion. Whereas CID typically utilizes higher collision energies, this type of experiment requires lower collision energies, otherwise the product ions would simply not form, or they would dissociate prior to observation. At any rate, the product ions contain significant excess energy. This is alleviated by elevating the pressure of the reactant gas, facilitating stabilizing third-body collisions, which incidentally also increases the probability of reactive collisions. It

should be mentioned that while this kind of experiments were conducted during this project, their preliminary character made them unsuitable for publication.

3.1.2.4 Time-of-flight mass analyzer and MCP detector

A second mass analyzer, the time-of-flight (TOF) mass analyzer, follows the collision cell, enabling observation of the products formed in the latter. The coupling of several mass analyzers in sequence is known as tandem mass spectrometry, denoted MS^n, where n is the number of analyzers. A mass spectrometer with at least $n = 2$ enables investigation of specific ions corresponding to a given m/z. The first mass analyser (or mass filter) is then used to select the ions of interest based on their m/z, and the second mass analyser is used to monitor the products of any reaction in which the selected ions is a reactant.

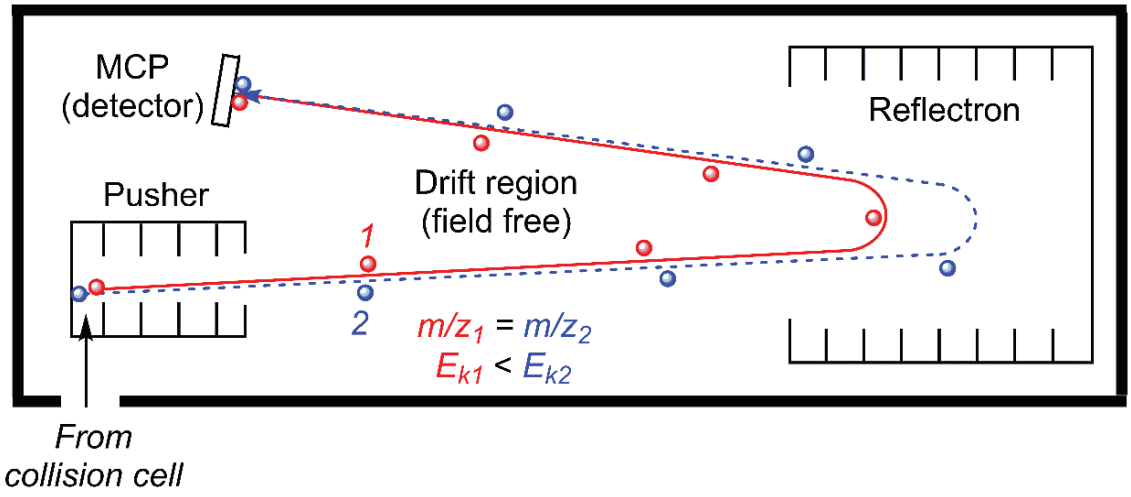

Figure 13. Illustration of the reflectron TOF mass analyzer and the correction of the differing initial kinetic energies of two identical ions by the reflectron.

The principle of a TOF mass analyzer is simple. The velocity of an ion is related to its kinetic energy and corresponds to an accelerating potential energy difference zeV in the TOF. The resulting expression for velocity can be rearranged with respect to m/z, and substituting $\boldsymbol{v} = d/t$ yields

$$m/z = 2eV(t^2/d^2). \tag{3.10}$$

Thus, when the accelerating potential V and the flight distance d is constant, the m/z of an ion is uniquely determined by its flight time. In practice, slightly differing initial conditions for the ions due to processes prior to the TOF component lead to slightly varying flight times for ions of a given m/z. These differing initial conditions are somewhat accounted for in our instrument, as illustrated in Figure 13. At the beginning of the TOF, the ions are accelerated orthogonally to their initial flight path, thereby correcting for differences in their initial velocities. Still, the ions are not accelerated equally due to their spatial distribution in the acceleration region (Pusher). This is corrected by the reflectron, an electrostatic mirror placed opposite to the acceleration region. For a given m/z, ions with higher kinetic energies penetrate deeper into the mirror; the slightly longer flight paths compensates for the greater speed of the ion as illustrated in Figure 13. The use of these two corrective steps, along with a generally longer flight distance, increase the resolution of this TOF configuration compared to a linear TOF.

The MCP detector is the final destination of an ion in this instrument, and functions as a charge multiplier. Specifically, it translates the low charge of an ion—proportional to the fundamental charge e—to a detectable signal. The detector consists of two plates of highly resistive material with multiple individual channels going through the plates at an angle; the two plates are stacked so that the channels form chevrons. When a charged particle hits the detector, it induces secondary emission of electrons within a channel. Subsequently, each electron may induce a new process of electron emission, rapidly multiplying the charge of the initial particle up to several million times.[201]

3.1.3 Yale hybrid Orbitrap/TOF photofragmentation mass spectrometer

Although traditional MS is used as a tool for structural elucidation, it does not provide molecular structures in its own right. To be more specific, the fragmentation patterns of ions can divulge the presence of certain structural and functional groups that can be used to infer the identity of the species of interest confidently, but does not give their spatial arrangements within the overall ion structure. However, the latter is made possible by combining the functionalities of traditional MS and infrared (IR) spectroscopy. Parts of the experiments were therefore done in collaboration with the Mark Johnson Lab at Yale university, employing their state-of-the-art hybrid Orbitrap/TOF photofragmentation mass spectrometer. This subsection contains a brief description of the

instrument and its functioning principles. A schematic of the instrument is shown in Figure 14, and the reader is referred to the relevant publication for a more complete overview.[177]

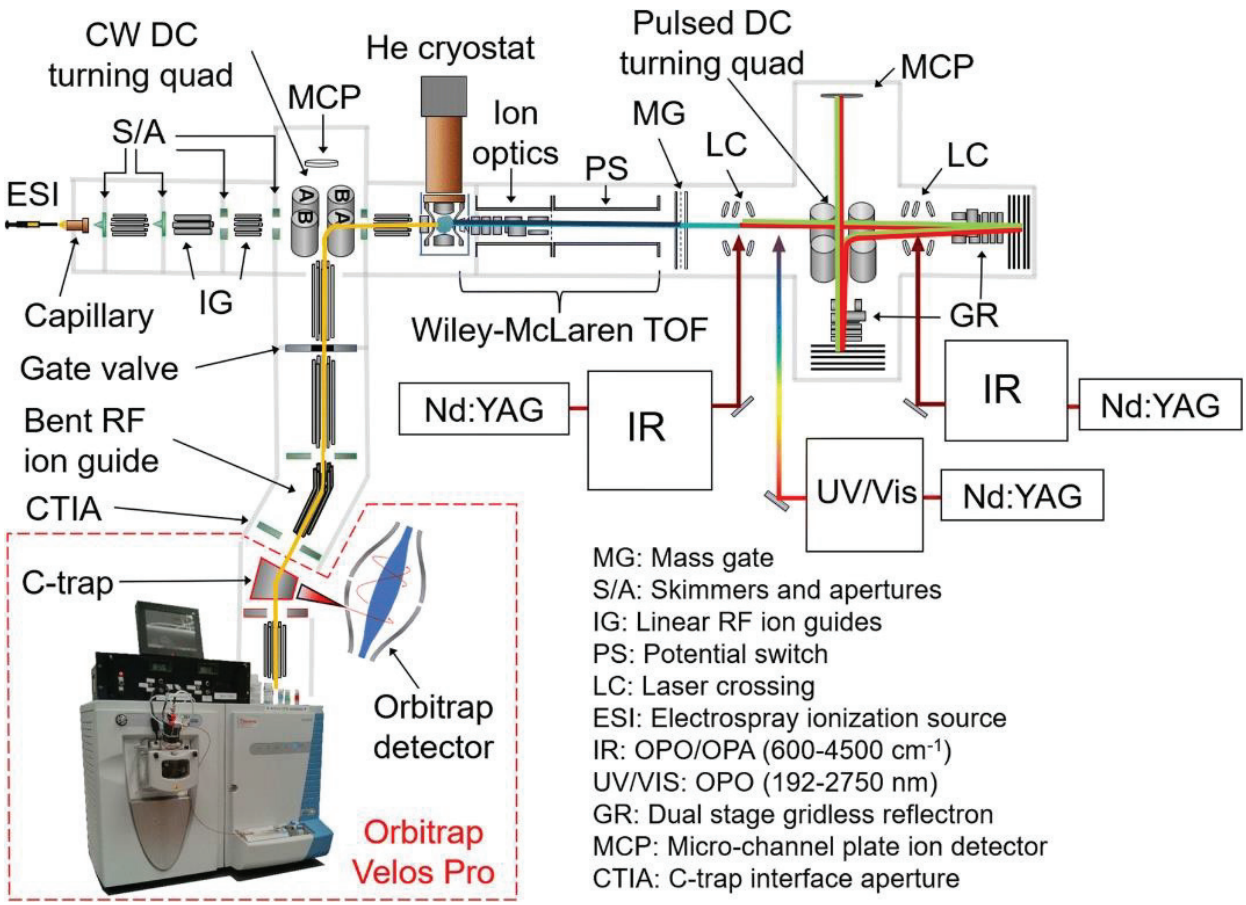

Figure 14. Yale hybrid Orbitrap/TOF photofragmentation MS.[177] Reprinted (adapted) with permission from (Menges, F. S.; Perez, E. H.; Edington, S. C.; Duong, C. H.; Yang, N.; Johnson, M. A. Integration of High-Resolution Mass Spectrometry with Cryogenic Ion Vibrational Spectroscopy. J. Am. Soc. Mass Spectrom. 2019, 30 (9), 1551–1557). Copyright (2021) American Chemical Society.

The instrument combines a high-resolution commercial instrument (Orbitrap Velos Pro) with a cryogenic ion vibrational spectroscopy instrument with both infrared and ultraviolet-visible (UV-Vis) functionalities. This design choice enables vibrational characterization of both intact molecular ions as well as specific fragments thereof, generated by operating the commercial instrument in the MS^2 mode.

Typically, an infrared spectrum is obtained by irradiating a sample containing the compound of interest and measuring the absorption of infrared radiation at specific wavelengths. This is not feasible for isolated ions, mainly due to the fact that absorption depends on the concentration of the irradiated species, which is far too low for isolated ions in high-vacuum to be observed directly by conventional means. Still, this does not mean that these ions do not absorb radiation. The latter is exploited in photofragmentation mass spectrometry, where the fragmentation of ions is induced by electromagnetic radiation, rather than collisions. In the Yale hybrid instruments, this is achieved by first cooling the ions to cryogenic temperatures in a quadrupole ion trap, where they are tagged with an inert gas (typically D_2 or N_2). The resulting weakly bound ion-neutral tag molecule complexes are subsequently irradiated over the spectral range (600-4500 cm^{-1}), enabling the observation of IR absorption by (1) loss of the tag molecule, and (2) the appearance of the untagged ion of interest. The corresponding spectrum is constructed by plotting the signal corresponding to either of these against the scanned IR frequency.

3.1.4 Experimental procedures

This subsection contains an account of the specific experimental procedures employed in this work, starting with the estimation of threshold energies.

3.1.4.1 Estimation of threshold energies by linear extrapolation

As previously mentioned, monitoring the fragment ion intensities as a function of collision energy enables estimation of their threshold energies, related to the corresponding energetic barriers for the reactions leading to the fragments. Consequently, the term threshold energy is used interchangeably with dissociation energy herein. This chapter aims to describe how these energies were estimated in this work.

Some terminology must first be introduced to aid the reader. A plot of the fragment ion signal intensity—or cross section—with collision energy is an appearance curve, while the corresponding plot for the disappearing precursor ion is the breakdown curve. Note that the term breakdown curve is often used interchangeably for the two, also in some of the included publications. The cross section (σ) leading to a particular fragment ion can be calculated from the Lambert–Beer law analogy $\sigma = -\ln(1 - \varphi) / (Lc)$, where φ is the ratio of fragment ion intensity to precursor ion intensity, L is the length of the flight path through the collision cell, and c is the concentration of the collision gas.

The simplest method for threshold energy estimation from appearance curves by linear extrapolation amount to following the tangent of the inflection point to the abscissa, with the corresponding E_{COM} value being interpreted as the threshold energy, as shown in Figure 15.

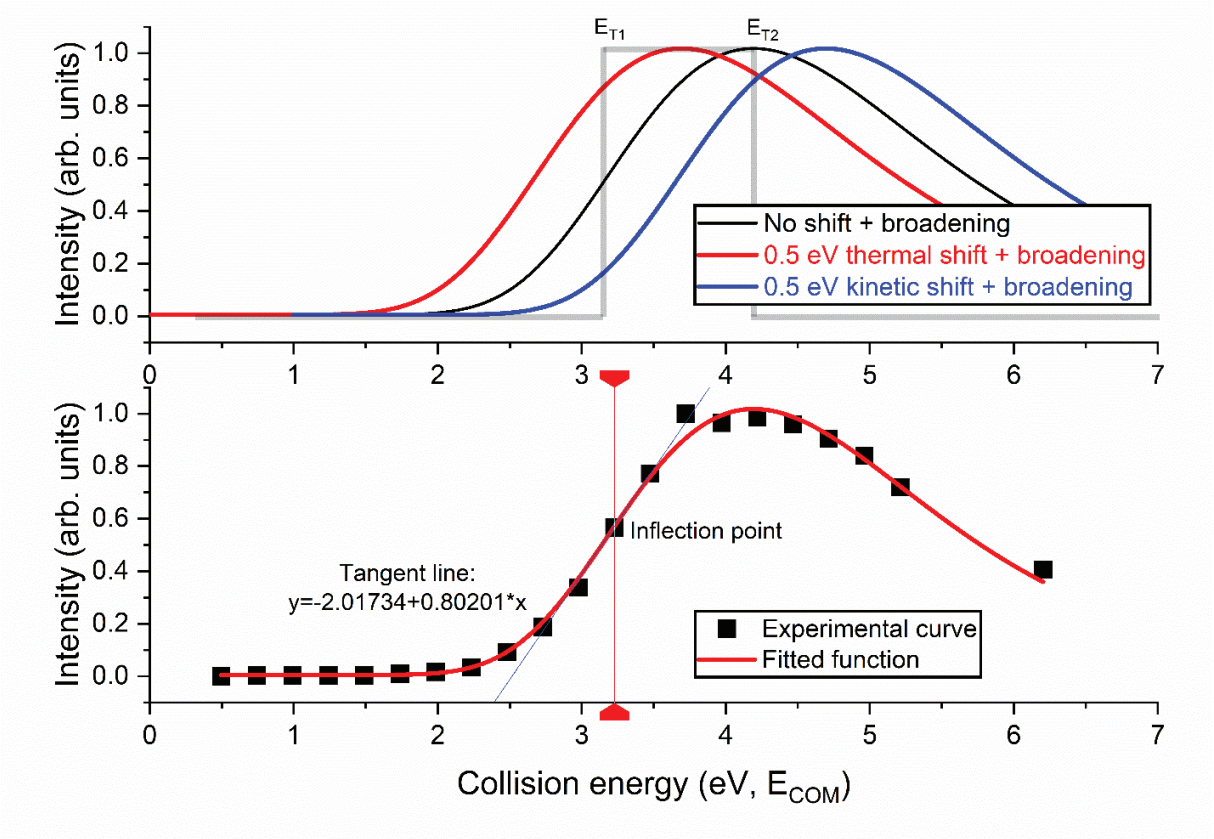

Figure 15. The effects of signal broadening, thermal and kinetic shifts on a hypothetical step function, adapted from the PhD thesis of Glenn B. S. Miller (*top*).[202] Example appearance curve and the corresponding threshold energy estimation procedure using linear extrapolation (*bottom*).

This method, mainly used in Papers I and III, is based on the assumption that the appearance curve is a step function in the absence of physical convolution effects—Doppler broadening, the kinetic and internal ion energy distributions, and the kinetic and the thermal shifts, respectively. Specifically, it is a function that rises linearly from zero to maximum intensity when the internal energy of the precursor ion surpasses the energetic barrier E_{T1} leading to the fragment ion. When the barrier E_{T2} for the next fragment is reached, the intensity returns to zero. The tangent at the inflection point of the experimental appearance curve is thus approximated as the vertical line at

the point where the step function changes its value. Determination of the inflection point is enabled by fitting a (twice differentiable) function to the experimental appearance curve. The relevant onset regions of the curves typically have sigmoidal shapes, hence these kind of functions have often been employed herein.

It should be mentioned that the threshold energy is sometimes interpreted as the energy at 50 % fragmentation in literature, more closely corresponding to the inflection point, as one would expect to be the logical choice after inspection of the above figure. The experience in our lab is that this overestimates the actual energetic demands, whereas similar linear extrapolation schemes as described above come closer to accurate computational values—although this has an explicit dependency on the system at hand. Hence, it can be surmised that in general, the appearance curves obtained with our instrument more closely corresponds to the blue, kinetically shifted curve in Figure 15. The reader is referred to recent studies for relevant examples.[27,54,203]

The main advantage of this method is its straightforwardness, but it should be noted that it works best when the kinetic and thermal shifts are small, as it makes no attempts to compensate for these. More accurate methods account explicitly for the various effects that govern the appearance curves, but are as a result often complex and depend on quantum chemistry for the treatment of kinetics.[204–206]

3.1.4.2 Estimation of threshold energies using L-CID

The L-CID method[206] developed by the Chen group bypasses the need of explicit treatment of the kinetic and thermal shifts as well as use of quantum chemical parameters. Instead, it utilizes Monte-Carlo simulations[207] to model collision events, the results of which are fitted to experimental appearance curves. Critical factors in the CID process from collision to dissociation are introduced to the simulations with physically realistic models. The collision event is treated according to the model described in 3.1.2.3, based on the electrostatic theory by Gioumousis and Stevenson.[197] This model is further expanded upon by including additional terms for the internal energy of the ions, their kinetic energy distribution and the Doppler Effect[208], providing a realistic shape for the simulated appearance curves. The treatment of the dissociation event accounts for the collisional energy transfer process and the kinetic shift. The threshold energy is fitted with a genetic algorithm, finally resulting in the simulated reaction cross section. Hence, the required parameters are the masses of the colliding species, polarizability and temperature of the collision gas, number of

degrees of freedom of the fragmenting ion, as well as the experimental FWHM of the ions kinetic energy distribution. None of these parameters require approximations.

The L-CID method was first implemented in Paper IV as part of an effort to improve upon the standard procedures for threshold energy estimation in our group—typically variants of linear extrapolation—by introducing a more multifaceted approach.

3.1.4.3 Extrapolation to zero-pressure

The accuracies of the abovementioned methods depend on the frequency of collisions the precursors ions are subjected to, which decreases linearly with the collision gas pressure as indicated. Multiple collisions has a similar effect as the thermal shift; leading to the apparent lowering of threshold energies relative to the energetic barrier. To compensate for this, the threshold energies were plotted against the pressure and extrapolated to vacuum. This method was implemented in Paper IV.

3.1.4.4 Signal stability

A stable ion beam (a concise term for the collection of traversing ions) is a prerequisite for the accurate determination of threshold energies due to its influence on the shape of the appearance curves, which has been ensured in two different ways during this project. The first method, employed in Papers I and III, checked for the overall drift in the amount of ions produced in the source by resetting the collision energy to the nominal value of the first measurement following the final measurement of the series. However, this does not capture fluctuations occurring during critical parts of the experiments, *i.e.* the onset regions of the appearance curves. Hence, for paper IV, reference measurements were conducted at a fixed collision energy before and after each energy increment on the appearance curve, and the precursor and fragment ion intensities were plotted relative to their reference measurement values. Additionally, the collision gas pressure was monitored and corrected for fluctuations or drift during measurements.

Any drift observed in the ion beam during the published experiments was usually minor or non-existent, and corrections were therefore found unnecessary.

3.1.4.5 Validation of threshold energies

The accuracies of the outlined methods were tested by employing them on fragmentation reactions with available literature data, termed reference reactions. The main selection criteria for these

reactions were that the available data should include both accurate threshold energy estimates, in addition to thermodynamic data such as enthalpies of formation, enabling comparison of reaction energies determined from multiple sources. Three reactions were employed in total; the decarboxylation of benzoate, dehydration of the ethanol cation, and demetalation of the cesium–15-crown-5 complex.[206] The threshold energy of the first reaction has been estimated by Graul and Squires,[209] and all reaction partners have well-known thermodynamic parameters. The second reaction has been analyzed by several authors, and is somewhat more complicated due to multiple fragmentation pathways.[210–212] Finally, the cesium–15-crown-5 complex has previously been subjected to several energy extraction methods, such as CRUNCH and T-CID developed by Armentrout and coworkers, in addition to L-CID.[205,213,214] Hence, the threshold energy validation measurements for Paper I included the first and second reference reactions, while the first and third reference reactions were used for Paper IV. Correspondingly, the reference reactions were measured under the same conditions, and using the same methods as the main measurements for the respective papers. Validation measurements were not conducted for Paper III, published prior to their implementation.

3.1.4.6 Metastable fragmentation

For the vast majority of cases, the fragmentation of a precursor ion occurs following an impact with the collision gas and prior to the TOF component in the QTOF 2. These fragment ions are observed at the *m/z* corresponding to their actual mass and charge, termed *focused fragments*. For a tiny fraction of the cases, fragmentation occurs after the activated (or metastable) precursor ion has entered the TOF region. Up until the reflectron, the fragment ion formed in the first field-free region will have the same flight time as the precursor, but spends less time inside it since the total kinetic energy is divided between the fragment ion and the corresponding neutral fragment, see Figure 13. These *un-focused fragment* ions are thus observed somewhere between the *m/z* ratios of the focused fragment and the precursor ion. The process itself is simply known as metastable fragmentation, while the term metastable fragments has been used to denote the un-focused fragment ions in the relevant publications, although technically, the term metastable refers to the precursors rather than the fragments. An expression linking the apparent masses of unfocused fragments (M_{uf}) to their corresponding precursor (M_p) and focused (M_f) fragments in reflectron-TOF instruments was proposed by Harvey and coworkers:[215]

$$M_{uf} = M_p \left[\frac{1 + \left(\frac{M_f}{M_p}\right) r}{(1 + r)} \right]^2 \tag{3.11}$$

The instrument-dependent parameter r describes the relative traversal times of an ion through the field-free and the reflectron regions, calibrated by assigning the unfocused fragment M_{uf} to a specific precursor-to-fragment ion (M_p-M_f) reaction. The parameter was calibrated to $r = 0.82$ for the QTOF 2, using the known spontaneous metastable fragmentation of water clusters, Figure 16.

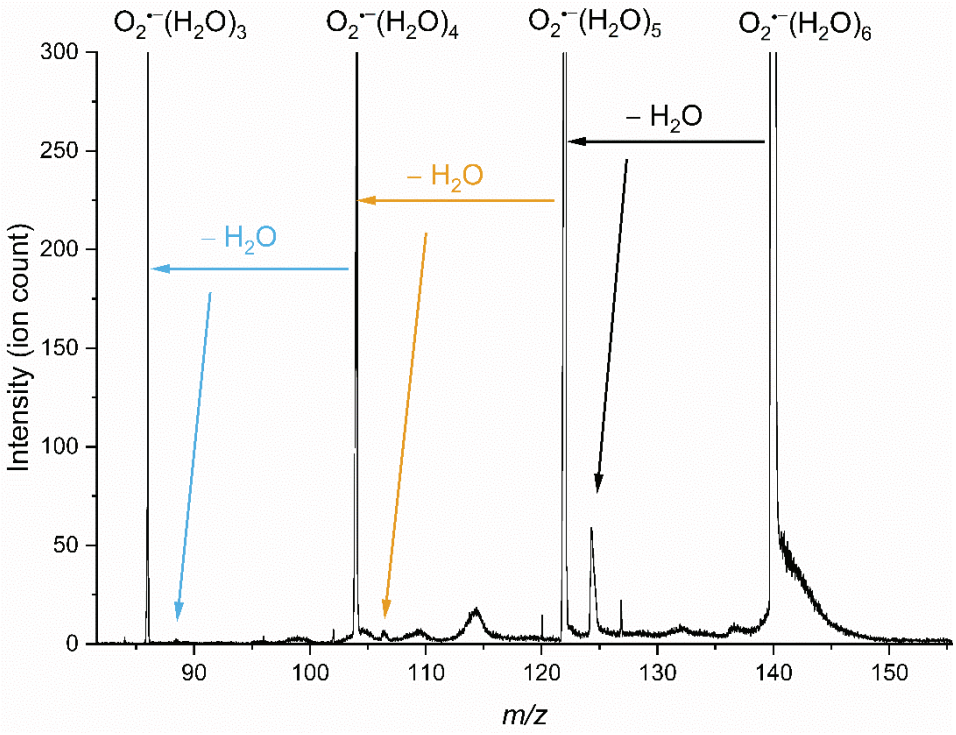

Figure 16. Mass spectrum of mass selected $O_2^{\bullet-}(H_2O)_6$ showing its metastable fragmentation by consecutive water losses. The background pressure in the collision cell was 1.5×10^{-5} mbar Ar. Note that the highest peak corresponding to metastable fragmentation (*m/z* ~124) is only 0.03 % of the precursor ion ($O_2^{\bullet-}(H_2O)_6$) intensity.

While it is conceivable that fragmentation may also occur in either the acceleration or the reflectron regions, the flight times of these fragment ions are difficult to determine confidently—even if the ions do reach the detector. The corresponding signals are likely spread over rather large

portions of the given spectrum, and therefore cannot be easily distinguished from noise. Analysis of metastable fragmentation was done for Papers III and IV.

3.2 Computational

3.2.1 Fundamentals of quantum chemistry

The concept of electrons in atoms and molecules occupying specific orbitals surrounding the nuclei is in fact a purely mathematical construct, known as the molecular orbital approximation. The approximation describes chemistry quite successfully, and most, if not all aspiring chemists are introduced to its formalism at an early point in their education, albeit usually through its results, rather than the underlying mathematics. The purpose of this subsection is to give the reader a brief introduction to the latter, *i.e.* quantum chemistry.

3.2.1.1 Molecular orbitals and the Schrödinger equation

A molecular orbital is defined as a single-electron wave function (ψ_i). To completely describe an electron, its spatial and spin-components must be specified, the product of which is termed a spin orbital (φ_i). When multiple electrons are present, such as in a molecule, the wave function must be antisymmetric with respect to the exchange of the spatial and spin coordinates of any two electrons due to their indistinguishability, changing sign upon permutation of coordinates. Expressing the wave function as a single determinant of individual spin-orbitals—a Slater determinant (Φ)—accomplishes this:

$$\Phi = \frac{1}{\sqrt{N!}} \begin{vmatrix} \varphi_1(1)\varphi_2(1) \dots \varphi_N(1) \\ \varphi_1(2)\varphi_2(2) \dots \varphi_N(2) \\ \vdots \quad \vdots \quad \vdots \\ \varphi_1(N)\varphi_2(N) \dots \varphi_N(N) \end{vmatrix} \tag{3.12}$$

This also introduces exchange effects, correlating the motion of electrons with parallel spins. In this formalism, it is impossible to assign explicitly an electron to a specific orbital, only the fact that N electrons occupy N spin orbitals. At this point, it is relevant to describe how molecular orbitals are constructed in practice from the linear combination of a set of M known basis functions ϕ_i:

$$\Phi = \sum_{i=1}^{M} c_i \phi_i \tag{3.13}$$

This reduces the problem of calculating the unknown molecular orbitals to a problem of finding the expansion coefficients c_i of the basis functions. If the set were complete, this expansion would be exact within molecular orbital approximation. However, basis sets are always finite for computational feasibility, and one must therefore choose a set of functions that describe the chemistry adequately and are computationally efficient. In molecular calculations, the basis functions are typically composed of atomic orbitals (AO) centered at each corresponding nucleus. The most physically accurate basis functions are the termed Slater-type orbitals (STO), but these are computationally demanding since the relevant integrals are costly to evaluate. However, STOs can be approximated as linear combinations of Gaussian-type orbitals (GTO), which are not as accurate, but computationally more efficient. The number of basis functions for each atomic orbital is also critical for an accurate description of the chemical behavior of an atom. A minimal basis set is the smallest possible set, with one function per AO, designated a single-zeta (SZ) basis set. Equivalently, basis sets with two and three functions per AO, termed split-valence, are designated double-zeta (DZ) and triple-zeta (TZ) basis sets, and so forth. Increasing the number of basis functions on each AO increases their flexibility and provides a more accurate description of chemical bonds since the functions have different spatial and directional extents. This description is further improved upon with the addition of polarization functions, whereas the inclusion of diffuse functions is critical for the description of the loosely bound electrons found in anions and excited molecules.

The true molecular wave function Ψ contains all information about the molecular system of interest, often approximated by a Slater determinant. Information about the system can be extracted from the wave function by applying an appropriate operator. In this work, the property of interest is typically the total energy of the system, and the corresponding operator is the Hamilton operator H, or simply the Hamiltonian. Determination of a given property—in this case the total energy E—is an eigenvalue problem involving the non-relativistic time-independent Schrödinger equation,

$$H\Psi = E\Psi \tag{3.14}$$

The total Hamiltonian includes terms for the kinetic energies (T) of both electrons and nuclei; as well as terms for the potential energy (V) of interactions between the various particles, *i.e.* electron-electron, electron-nuclei and nuclei-nuclei interactions, simplistically expressed as

$$H_{tot} = \mathrm{T}_e + \mathrm{T}_n + \mathrm{V}_{ee} + \mathrm{V}_{en} + \mathrm{V}_{nn} \tag{3.15}$$

However, nuclei are much heavier and slower than electrons, and their motions can therefore be treated independently to a good approximation. This is the Born-Oppenheimer approximation (BO), where the wave function is separated into a product of electronic and nuclear wave functions, and it is assumed that these can be solved independently. Consequently, it makes sense to separate the Hamiltonian into electronic and nuclear terms:

$$H_{el} = \mathrm{T}_e + \mathrm{V}_{ee} + \mathrm{V}_{en} \tag{3.16}$$

$$H_{el}\psi_{el} = E_{el}\psi_{el} \tag{3.17}$$

$$H_{nu} = \mathrm{T}_n + \mathrm{V}_{nn} + E_{el} \tag{3.18}$$

$$H_{nu}\psi_{nu} = E_{nu}\psi_{nu} \tag{3.19}$$

The solution to the electronic Schrödinger equation has a parametric dependence on the positions of the nuclei *via* the V_{en} term, whereas the nuclear solution depends on the former, describing the electric field E_{el} induced by the electrons. The total energy of a molecule is thereby found by solving the electronic problem and adding the constant nuclear repulsion for a set of given nuclear coordinates, allowing the determination of the equilibrium geometries of molecules. The nuclear solution describes the vibrational, rotational and translational motions of molecules, in turn important for their thermal properties. Only the electronic problem will be considered henceforth.

3.2.1.2 The Hartree-Fock method

In practical applications of quantum chemistry, the eigenvalue problem involving a Hamiltonian is typically solved—at least prior to more accurate procedures—using the Hartree-Fock (HF) method. HF is variational, meaning that the best approximation for the wave function Ψ is the determinant Φ formed from a set of orthonormal spin orbitals that minimizes the electronic energy:

$$E_0 = \langle \Phi | H_{el} | \Phi \rangle \tag{3.20}$$

The procedure for minimizing the energy yields the HF equations,

$$f_i \Phi = \varepsilon_i \Phi \tag{3.21}$$

where f_i is the Fock operator acting on all *i* electrons and the spin orbitals are eigenfunctions with eigenvalues ε_i corresponding to their energies. The above HF equations are typically transformed

to matrix form and solved iteratively; the spin orbitals obtained from one iteration are used as the guess for the next. This procedure is repeated until the orbitals are invariant between iterations, thereby known as the self-consistent field (SCF) procedure.

The SCF procedure provides an approximation for the true wave function as a single Slater determinant, but does not provide the total energy of the system. At this point, it might be tempting to interpret the sum of orbital energies ε_i as the total HF energy of the system. This would lead to an overestimation equal to the electron-electron repulsion energy—counted twice by the Fock operator—and the HF energy is simply the sum of orbital energies minus this repulsion energy. Although HF accounts for most of the energy of a system, electron-electron interactions are treated in an average way, thus neglecting the electron correlation energy. The missing correlation energy can amount to as much as 100 kJ/mol per electron pair, obviously a significant quantity. Electron correlation is typically split into two types, dynamic and static correlation. The first can be attributed to the movement of electrons in relation to one another, while the second is linked to near-degeneracies of electronic states (occupied and virtual spin-orbitals have similar eigenvalues), meaning that the true wave function is not accurately approximated by a single determinant. Accounting for correlation effects is essential for the accurate description of chemical phenomena, and many *post*-Hartree-Fock methods have been developed for this purpose.

3.2.1.3 Perturbation theory

Møller-Plesset perturbation theory (MPn)[216] recovers most of the dynamic correlation energy. In MPn, the total energy of a system is the sum of an unperturbed zeroth-order energy E_0 and its corrections, each with a corresponding Hamiltonian:

$$(H_0 + H_1 + H_2 + \cdots)\Phi = (E_0 + E_1 + E_2 + \cdots)\Phi \tag{3.22}$$

In this context, the sum of the one-electron Fock operators f_i is the zeroth-order Hamiltonian H_0 with eigenvalue E_0 equal to the sum of orbital energies ε_i of the individual spin orbitals in the determinant,

$$\sum_{i=1}^{N} f_i \Phi = \sum_{i=1}^{N} \varepsilon_i \Phi \tag{3.23}$$

In the chemists' formulation, the first-order correction E_1 is the negative of the electron-electron repulsion energy. This yields the HF energy as stated above, equivalent to the MP1 energy:

$$E_{\mathrm{MP1}} = E_{\mathrm{HF}} = E_0 + E_1 \tag{3.24}$$

The second order correction involves doubly excited determinants, where the occupation of spin orbitals is varied, and provides the MP2 energy. The associated method has been used extensively in this work.[204–207,20] Adding further corrections increases the amount of dynamic correlation recovered, but also computational cost. The higher-level corrections (MP3 and MP4) lead to small improvements over MP2 for various molecular properties, and have only been used as part of the higher level methods, such as the G4 composite method and CCSD(T), described later in the text. The major disadvantages of MP*n* theory stems from the use of the HF determinant, and it is therefore subject to all of its shortcomings. MP*n* theory is not variational, as it cannot be guaranteed that a perturbation does not overshoot the variational limit.

3.2.1.4 Configuration interaction and coupled-cluster theory

The configuration interaction (CI) method constructs the wave function from a linear combination of determinants with different configurations of occupied and unoccupied (virtual) spin orbitals, or configuration state functions (CSF) corresponding to excited electronic states:

$$\Psi_{CI} = \sum_{j=0} C_j \, \Phi_j \tag{3.25}$$

The first term in the expansion $j = 0$ is equivalent to the HF determinant (in the case $C_0 = 1$), from which the rest of the CFSs are obtained. If the expansion includes all possible electron configurations, Ψ_{CI} provides the exact BO solution to the Schrödinger equation for a given basis set. This is only possible for very small molecules, and the operator is therefore truncated at the desired accuracy for systems of interest. The level of truncation is indicated by denoting the relevant number of excitations with a letter following the CI term, *e.g.* CISD for singles and doubles. Configuration interaction is variational like HF, and the optimal CI wave function is the one that minimizes the total energy of the system.

In the coupled-cluster (CC) method, the wave function is a linear combination of excited determinants generated from a HF reference by the cluster operator *T*:

$$\Psi_{CC} = e^{T}\Phi_{\mathrm{HF}} \tag{3.26}$$

$$T = T_1 + T_2 + \cdots + T_N \tag{3.27}$$

Here, the subscripts indicate the number of excitations in each single determinant, *N* corresponding to exciting every single electron to all virtual orbitals, giving equivalently the full configuration interaction (CI) wave function. Similarly to CI, coupled-cluster is usually truncated for computational feasibility; including only singly excited determinants in the CC wave function is termed the coupled-cluster singles (CCS), adding doubly excited determinants gives the singles and doubles (CCSD), while the inclusion of triply excited determinants comprise the singles, doubles and triples (CCSDT) variation of the method. This is computationally demanding, scaling as N^8 with the number of basis functions, but treating the triples contribution non-iteratively using perturbation theory allows computations on moderately sized molecules with a large basis set. This is termed CCSD(T),[217–219] which is considered the "gold standard" in modern applications of quantum chemistry, since it approaches chemical accuracy (errors in relative energy < 4 kJ/mol). The latter has been used for theoretical benchmarking of the metal carbonites, more closely discussed later.

An advantage of CC of over CI is that it is generally size consistent, whereas the latter is not. This means that energy evaluation of a molecule produces the same result for the infinitely separated reactants making up the molecule as the sum of the energies of the isolated reactants. However, the size consistency of CC depends on the adequacy of the underlying HF reference, which is not always a given.

3.2.1.5 Single- and multi-reference character

In all of the theories outlined thus far, the true wave function of a system is approximated using a single reference determinant and its expansions. This type of methods are known as single-reference (SR), and are usually sufficient for molecules dominated by dynamic correlation. However, for systems where static correlation is prominent, *i.e.* when multiple electron configurations are nearly degenerate, the wave function must include contributions from each optimized configuration for an accurate description. In other words, not only are the orbitals in the ground state optimized by the procedure, but also in the excited states. Such methods are termed multi-reference (MR) or multiconfigurational (MC). Several tests have been suggested for the determination of the MR or SR character of a molecule. One of the earliest are based on the CI

method, where this is estimated using the coefficient C_0 of the first term in the expansion, which in effect is the fraction of the CI wave function made up by the HF determinant. A value of $C_0 \geq 0.95$ indicates that the system is mostly SR.[220] Nevertheless, CI is a highly costly method, and the diagnostic even fails to capture the MR character in many cases, in particular where the CI wave function is biased towards the HF determinant.[221] Later, it was proposed that the Frobenius norm of the single excitation amplitudes t_1 in the CCSD wave function could be used, known as the T1 diagnostic. A value of T1 < 0.02 for closed-shell systems, T1 < 0.44 for open shell systems, is often taken as an indication that a SR method performs adequately.[221] The latter has been utilized in this work.

Multi-reference versions of the CI and CC methods, (MRCI and MRCC, respectively) have been developed, but these are computationally much more expensive than single-reference procedures—already limited by cost. However, just as CI and CC can be limited to include fewer excitations, multi-reference methods can be truncated to a rational selection of reference determinants. This is the principle behind the complete-active-space (CAS) methods. In the CAS approach, the selection of reference determinants that comprises the expansion of the wave function involves all configurations arising from a particular combination of electrons, and occupied and virtual orbitals, respectively. This is termed the active space, currently limited to around 18 electrons in 18 orbitals, denoted (18,18).[222] In principle, a CAS wave function can be applied to all of the methods described above. During this work, we have in some instances utilized the MR counterpart to HF—CASSCF. Analogously to the former, the latter does not recover the dynamic correlation of a system, but this can be estimated using perturbation theory (CASPT2).

3.2.1.6 Density functional theory and composite methods

Evaluation of wave functions is a computationally costly endeavor, which would be mitigated if molecular properties were determined by simpler functions. The Hohenberg-Kohn existence theorem states that the ground state properties of a molecule are uniquely characterized by the electron density ρ, a much simpler function than the wave function. This theorem enabled the conception of density functional theory (DFT), concerned with the evaluation of ρ rather than the wave function. Although ρ is a simple three dimensional function, only the orbital description has so far proven to accurately describe it. Hence, this was reintroduced in Kohn-Sham (KS) theory—bringing the dimensionality back to 3N. Density functional theory shares many features with HF

theory (also 3N dimensional), being variational in principle, and treating electron-electron interactions in an average or non-interacting way. Still, it is more efficient than post-HF methods, although not necessarily as accurate. An additional advantage of DFT is that ρ is not subject to antisymmetric constraints. The ground state KS energy,

$$E[\rho] = T_S[\rho] + E_{ne}[\rho] + J[\rho] + E_{xc}[\rho] \tag{3.28}$$

is fully determined by ρ, the latter a function of electron coordinates—whence the term density functional. The first three terms can be exactly solved, corresponding to the non-interacting kinetic energy of the electrons, the effective potential in which they are moving and their Coulombic repulsion. Meanwhile, the true bottleneck for DFT theory lies in estimating the exchange-correlation functional, $E_{xc}[\rho]$. This is split into two parts, one for exchange, one for correlation. While the functionals only depend explicitly on the electron density, a better description is obtained by inclusion of its gradient. The most primitive is the generalized gradient approximation (GGA), improved upon by including the derivative of the gradient, leading to the meta-generalized gradient approximation (mGGA), which can involve fitting parameters for the density function to experimental data. Finally, the exchange and correlation functionals can be combined as desired, or even include a fraction of HF exchange to accurately describe the system of interest, known as hybrid functionals. As an active field of research, a plethora of exchange and correlation functionals has been developed, aimed at accurately describing a given system. Consequently, DFT methods usually require benchmarking against systems similar to the one of interest to ensure their applicability. The popular hybrid functional comprised of the Becke 3-parameter exchange functional and the Lee-Yang-Parr correlation functional, or simply B3LYP, has been used extensively in this work as a first approximation for structures and energies.[223,224]

Another powerful approach is to combine several methods in ways that provide more accurate results at a significantly reduced cost, termed composite methods. Typically, these involve geometry optimization and zero-point energy calculations at a lower level of theory with a relatively large basis set and subsequent single point energies from high-level methods with smaller basis sets, aimed at correcting the deficiencies in the former. Case in point, the Gaussian-4 (G4) method[225] employed extensively herein begins with B3LYP/6-31G(2df,p) for geometry optimization and zero-point vibrational energies, followed by extrapolation to the HF-basis set limit using the aug-cc-pVnZ basis sets. Electron correlation is estimated using MP4 with

corrections for various basis set effects, and subsequently by CCSD(T). Finally, several corrections are added to account for remaining deficiencies in the methods used. While G4 generally provides highly accurate energies,[226] it is unfortunately only available for elements up to the third row, and thus unavailable for several relevant species in this work.

3.2.2 Computational procedures

The previous subsection gave a general description of the underlying theory of computational chemistry. Hence, the following contains an account of the specific computational methods and procedures used during this work.

3.2.2.1 Quantum chemical methods and basis sets

The use of quantum chemical methods in this work is best described as hierarchical. Lower level, computationally more affordable methods were used for initial computations aimed at exploring possible species of interest, whereas higher level, costly methods are used for refining the former.

As mentioned in the previous chapter, B3LYP was often employed for the initial exploration of possible structures and energies, usually combined with a basis set of triple zeta quality including diffuse functions, such as aug-cc-pVTZ or def2-TZVPPD,. Depending on the system at hand, these results were refined upon using either CCSD(T) or G4, and in some cases, both.

The initially determined B3LYP geometries of the alkali and alkaline earth MCO_2^- species were optimized on the CCSD(T)/def2-TZVPPD level of theory, followed by computation of their vibrational frequencies. Single point energies were also obtained on these optimized geometries using the slightly larger def2-QZVPPD, but these results have not been published. This part of the work relied heavily on the advice and guidance of Sotiris S. Xantheas and Edoardo Aprà, as well as their available computational infrastructure at NERSC. The Karlsruhe basis sets were chosen for these groups of species due to their availability over the periodic table from H-Rn. The basis set superposition error (BSSE) was estimated for the metal carbonites using the function counterpoise method,[227–229] including the substantial CO_2 deformation energy in these complexes.[230] The CCSD(T)/def2-TZVPPD results were treated as high-level theoretical benchmarks for subsequent computations, aimed at exploring the metal carbonite reactions at lower levels. Benchmarking of these computations against experiments were limited to the electron

affinities of the alkali metals as well as the geometry and vibrational frequencies of CO_2, although the latter has not been explicitly discussed in any of the included publications. Furthermore, benchmarking could have been done against experimental data on the neutral metal carbonites in rare gas matrices reported by Kafafi *et al.*[18,19]

Consistent periodic trends were deemed highly relevant for the aims of this study. The closest agreement with the CCSD(T) benchmark computations for the trends was achieved using MP2/def2-TZVPPD, see Figure 17. The latter was therefore used to investigate the full reaction pathways of the metal carbonites. The above methods, CCSD(T) and MP2, are most heavily featured in papers I and II.

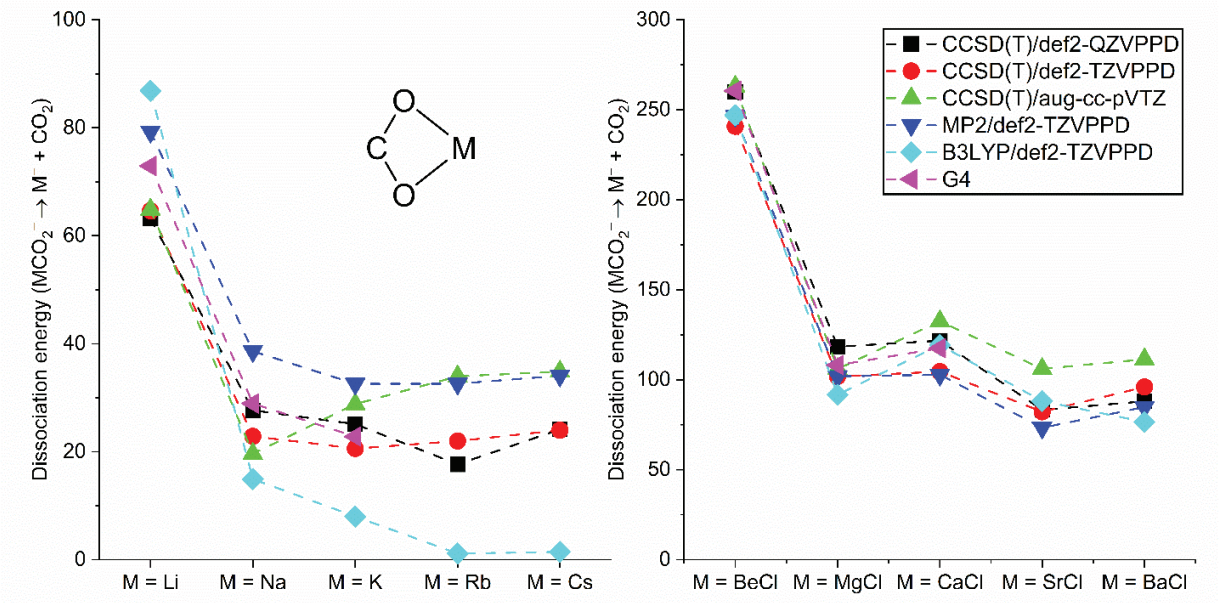

Figure 17. Computed dissociation energies (electronic energy (E_e) + ZPVE) of the bidentate oxygen coordinated metal carbonites $M(\kappa^2\text{-}O_2C)^-$ at various levels of theory. Note the different y-axes for the alkali and alkaline earth metal groups.

For the last two papers included in this thesis, G4 was employed as the high level method, due to being much more affordable than CCSD(T) and available for all of the involved atoms. The G4 method was benchmarked against the experimentally determined electron affinities, bond distances and dissociation energies of CO and MgCl, and found to be in excellent agreement.

Additionally, CASSCF was employed in Paper III for certain fragments of the hydrogen squarate and the squarate radical anions, due to their suspected multi-reference character, although the T1-diagnostic of CCSD was not used first to infer the necessity of a multi-reference treatment. In contrast, the diagnostic was employed for the magnesium chloride squarate species in Paper IV, on the basis of which a single-reference treatment was found adequate.

3.2.2.2 Natural bond orbitals and partial charges

Unlike orbitals, the electron density of a molecule is a physical observable. It can be used to predict various molecular properties, such as sites of nucleophilic/electrophilic reactivity or to quantify the transfer of electrons between from one species to another. The molecular orbitals obtained through quantum chemical computations are highly delocalized, and using these directly to assign charges to particular atoms in molecules is typically inaccurate unless calibrated (such as in Mulliken population analysis). In contrast, *natural bond orbitals* (NBOs) are localized few-center orbitals that provide the most accurate possible Lewis-type structure of the total electron density of a molecule, the *natural Lewis structure* (NLS)—facilitating charge assignment.[231] The natural bond orbitals of a given molecule are determined by searching over all possible ways to draw the bonds and lone pairs to find the combination that accommodates the highest percentage of the total electron density. While this typically accounts for >99.9% of the density for most common molecules, the remaining percentage describes delocalization effects. This analysis has been employed in all of the included papers.

3.2.2.3 Construction of potential energy diagrams

Optimized geometries and their associated energies were typically translated to energy diagrams describing their chemical transformations. This subchapter will briefly illustrate how this was accomplished.

The first step in the construction of a potential energy diagram for a given chemical reaction, or a set of thereof, was to optimize the geometries of the presumed reactants and products. This was followed by a vibrational analysis to ensure that the obtained structures were in fact reactants and products—minima on the potential energy surface. If all vibrational modes are real, *i.e.* there are no imaginary frequencies, the structure constitutes a true minima on the potential energy surface. If it displays one imaginary frequency, it is a transition state (TS); the lowest point on the potential energy pathway separating two minima. The lowest energy pathway from one minimum

to the next, defined as the intrinsic reaction coordinate (IRC), can be followed computationally. Hence, the optimized minimum structures were connected by transition states, the connectivity of which were ensured by following the IRC.

Sometimes, there was no barrier separating reactant from product other than the endothermicity of the reaction, often seen for single bond scission. In these instances, the absence of the barrier—often termed the reverse barrier—was ensured using relaxed potential energy scans. The latter involves changing a geometric variable incrementally from reactant to product, while optimizing the rest of the structure at each increment.

4 Results

This chapter summarizes the main results from the included papers. Their order follows the project outline (Section 1.5) closely, beginning with the two papers describing the metal carbonites and their reactions, followed by the two papers describing the cyclooligomerization of CO. The notations in the next sections generally adhere to those of the respective papers.

4.1 Paper I.

This paper is the result of a combined experimental and computational effort to study the reductive coupling of CO_2 to oxalate *via* the MCO_2^- species, where M = Li – Cs. Due to restrictively low signal intensities for in-source produced M^- and MCO_2^-, the process was studied in reverse, *i.e.*

$$MC_2O_4^- \rightarrow MCO_2^- + CO_2 \rightarrow M^- + 2CO_2, \quad (4.1)$$

employing mass spectrometric techniques. The associated reaction mechanisms were modelled using quantum chemical computations. Finally, the metal oxalates were characterized by vibrational predissociation spectroscopy.

The results of the mass spectrometric and computational investigations of the reactions in Equation 4.1 are summarized in Figure 18 and Table 1. While the experiments indicate that the dissociation energies for both the oxalates and carbonites decrease with increasing metal size, the computations suggest a slight increase from the middle of the group towards the heavier metals. Nevertheless, both methods agree upon the trends for the dissociation energies between M = Li – K. It should be mentioned that the signal corresponding to Li^- (*m/z* 7) cannot be observed in our instrument, having a low-mass cutoff at *m/z* 15, hence it was not possible to estimate the corresponding dissociation energy of $LiCO_2^-$ experimentally.

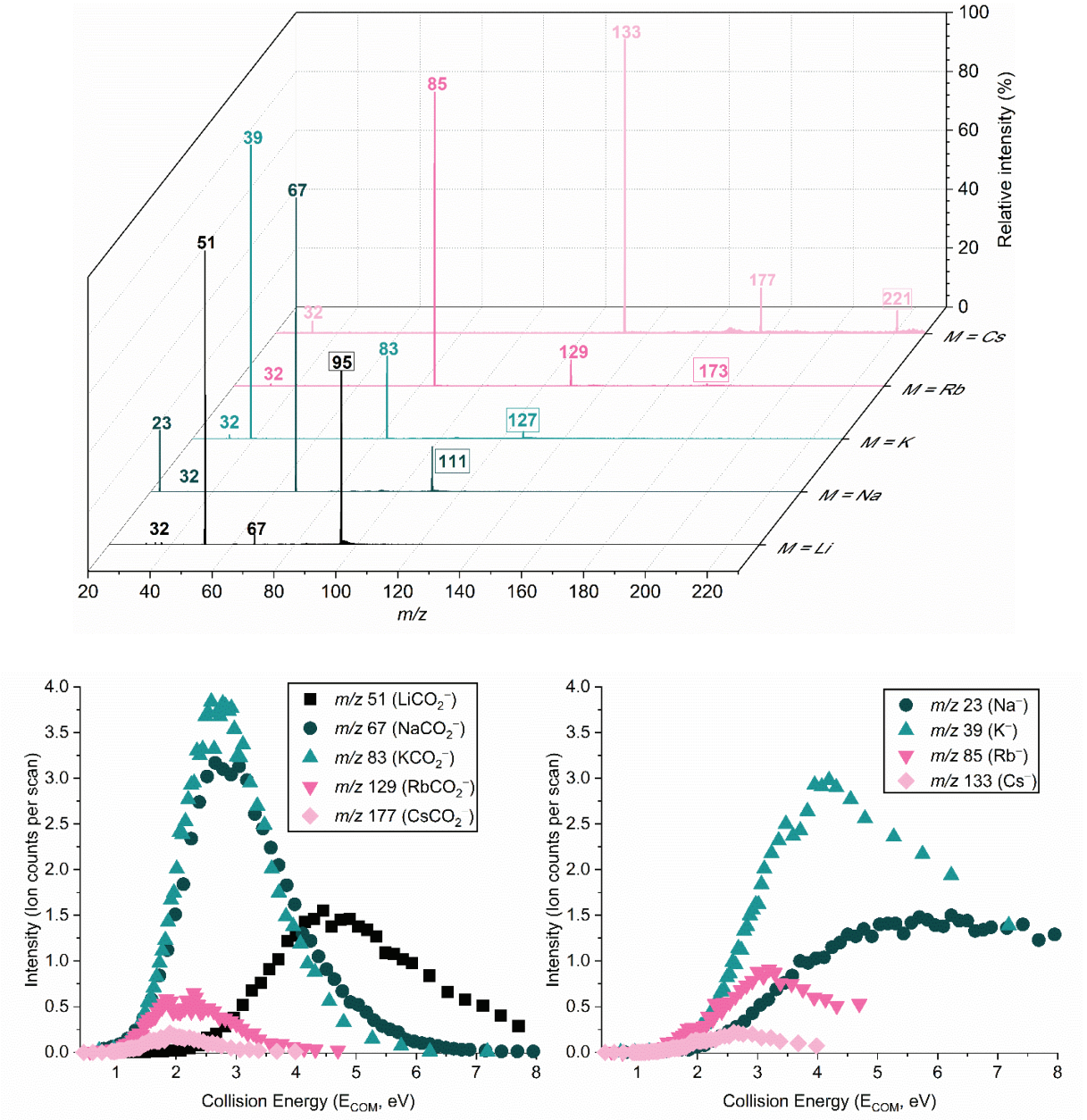

Figure 18. Fragmentation mass spectra of $MC_2O_4^-$ recorded at a collision energy integrated over the range E_{COM} = 3.0 – 5.0 eV under 2.0 × 10^{-4} mbar collision gas (Ar) pressure. The *m/z* values of the mass selected parent ions are enclosed in frames (*top*). Appearance curves for MCO_2^- and M^- recorded for the collision energy interval E_{COM} = 0.4 – 8.0 eV under 2.0 × 10^{-4} mbar collision gas (Ar) pressure (*bottom*). Adapted from Paper I.

Table 1. Experimentally estimated threshold energies for MCO_2^- and M^- in kJ mol^{-1} and MP2/def2-TZVPPD barriers in parentheses. From Paper I.

	M = Li	M = Na	M = K	M = Rb	M = Cs
MCO_2^-	256 ± 14 (238)	157 ± 10 (150)	150 ± 9 (143)	110 ± 6 (145)	109 ± 11 (158)
M^-	n/a (317)	238 ± 45 (192)	200 ± 19(176)	157 ± 16 (181)	139 ± 5 (195)

The trends for the experimental dissociation energies down the alkali metal group finds support in the vibrational analysis of the corresponding metal oxalates. It is widely accepted that the most stable conformation of the isolated oxalate dianion is staggered,[232] and its structure in these complexes is determined by the competing effects of stabilization by interaction with the alkali metal and the additional strain on a planar geometry. We found that the oxalate moiety in the complexes twists from a planar to a staggered structure from M = Li to Cs, which is evident from the concurrent blueshift of the bound C=O vibrational bands (ν_{12} and ν_{13}) down the series, Figure 19.

Consistent with the abovementioned structural change in the oxalate moiety, we found an additional type of transition state for the decarboxylation of the heavier metal oxalates, M = K – Cs. This in turn led us to propose two different types of nucleophilic reactivity for the intermediate metal carbonites; while the lighter, more tightly bound metal carbonites prefer to react as pure carbon-centered nucleophiles, the heavier, more polarizable metals prefer to react as mixed carbon-metal centered nucleophiles. This was attributed to a more complete transfer of electrons from the metal to CO_2—and consequently, the carbon atom—in the more tightly bound carbonite complexes.

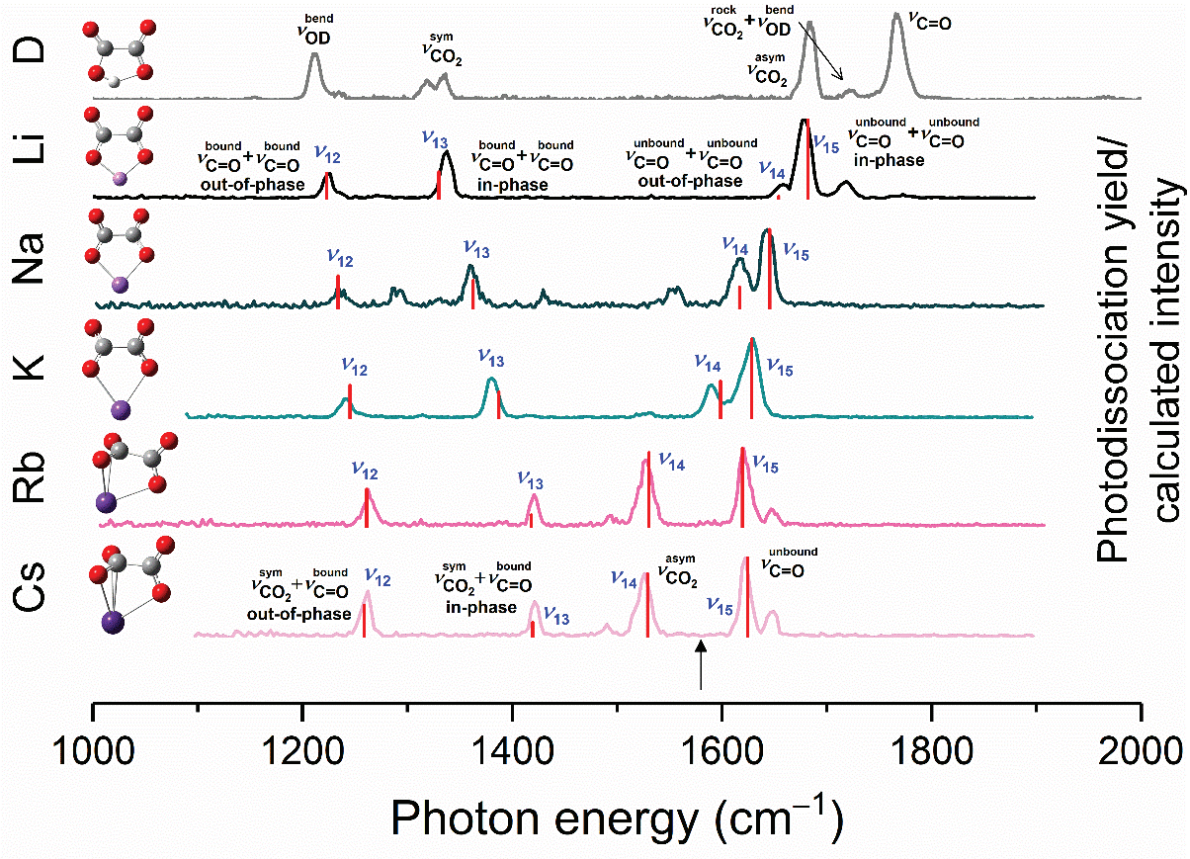

Figure 19. Vibrational predissociation spectra for the $MC_2O_4^-$ (M = D, Li, Na, K, Rb and Cs) complexes "tagged" by either D_2 (M = Li, K and Cs) or H_2 (M = Na and Rb). The deuterium oxalate spectrum is adapted with permission from (Wolke, C. T.; DeBlase, A. F.; Leavitt, C. M.; McCoy, A. B.; Johnson, M. A. Diffuse Vibrational Signature of a Single Proton Embedded in the Oxalate Scaffold, $HO_2CCO_2^-$. J. Phys. Chem. A 2015, 119 (52), 13018–13024.). Copyright (2020) American Chemical Society. The MP2/def2-TZVPPD minimum energy structures are shown to the left, and the corresponding computed vibrational frequencies (scaled by 0.990 for the Li, Na and K, and by 0.985 for the Rb and Cs), are denoted by sticks. The scaling has been determined according to the best fit to the experimental spectra. From Paper I.

Two possible isomers were computed for the metal carbonites, one with bidentate oxygen-metal coordination $M(\kappa^2\text{-}O_2C)^-$, the other with mixed carbon-oxygen coordination, $M(\eta^2\text{-}CO_2)^-$, consistent with literature on the neutral counterparts, Figure 20.[18–20,105]

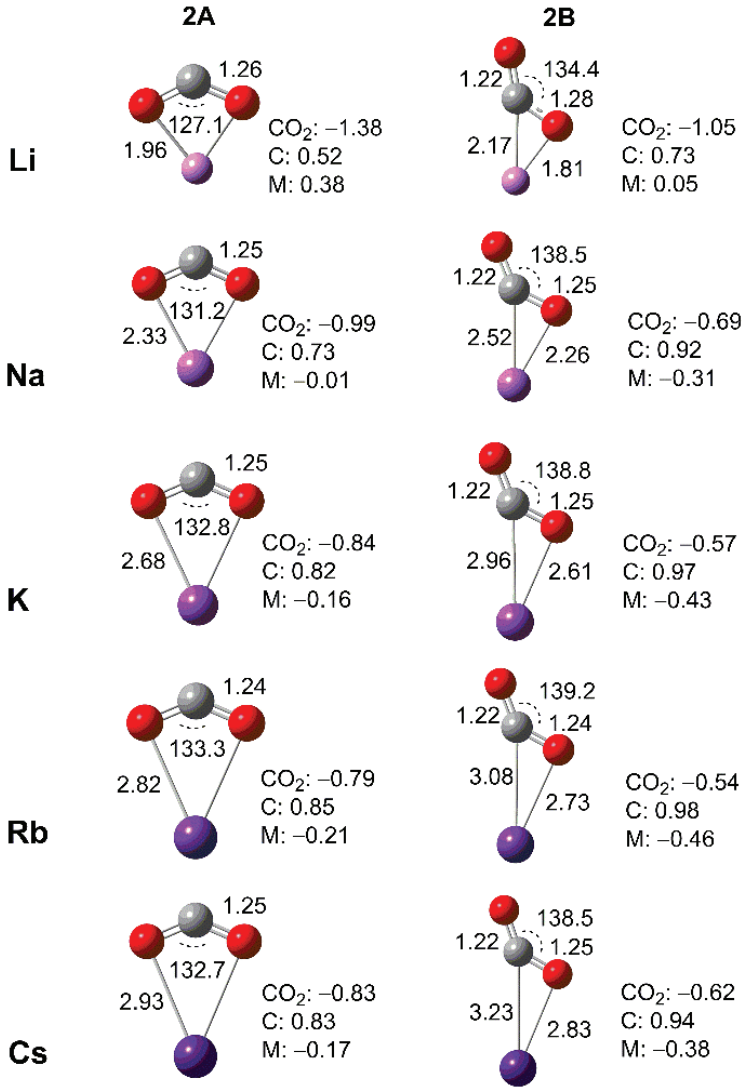

Figure 20. CCSD(T)/def2-TZVPPD optimized geometries of the 2A ($M(\kappa^2\text{-}O_2C)^-$) and 2B ($M(\eta^2\text{-}CO_2)^-$) alkali metal carbonites. Bond lengths in Angstroms (Å) and angles in degrees. The NBO partial charges on the CO_2 moiety as well as the carbon and the metal atoms are also indicated. From Paper I.

Lithium displayed an additional $M(\eta^1\text{-}CO_2)^-$ isomer (not shown), formally a metalloformate. Carbon dioxide typically forms these kind of complexes with transition metals of low oxophilicity, thus strengthening the previously assumed correlation between the mode of coordination and the oxophilicity of the metal.

4.2 Paper II.

Paper I explored reductive C—C coupling of CO_2 to oxalate. In other words, the CO_2 moieties are reduced, but more or less structurally intact as carboxylates. The second paper, which is purely computational, details a more dramatic transformation of CO_2, undergoing C=O bond scission to form CO. This paper was in part motivated by the fact that some metal atoms or anions may add CO_2 to form MCO_2 complexes in gas phase reactions, whereas the early transition metal atoms, Sc, Ti, V and Cr insert into one of the C=O bonds, followed by subsequent CO elimination. In addition, it has been observed that reactions between MCO_2^- (M = MgCl, ZnCl) and CO_2, as well as CID of $LiC_2O_4^-$ lead to the formation of MCO_3^- + CO. Hence, we were interested in obtaining comprehensive mechanistic pictures for the following reactions:

$$M^- + CO_2 \rightarrow MO^- + CO \tag{4.2}$$

$$M^- + 2CO_2 \rightarrow MCO_3^- + CO. \tag{4.3}$$

This was aimed at more closely elucidating the factors that govern the partitioning between metal carbonite formation and CO elimination. Herein, we considered both the alkali metals (M = Li, Na, K, Rb, Cs) and the isovalent alkaline earth metal chlorides (M = BeCl, MgCl, CaCl, SrCl, BaCl), due to their reductive character and chemical similarity to the early transition metals.

It was found that the reduction of a single CO_2 molecule as in 4.2 is generally endothermic, with the exception of M = BeCl. Meanwhile, the reaction involving two CO_2 molecules as in 4.3—corresponding to reductive disproportionation—is exothermic. None of these metal species were seen to undergo $OMCO^-$ formation by C=O bond insertion, in contrast to many early transition metals. Both processes described above involve the metal carbonites as intermediates, see Figure 21. For these intermediates, decarbonylation competes with carboxylation to form the metal oxalates.

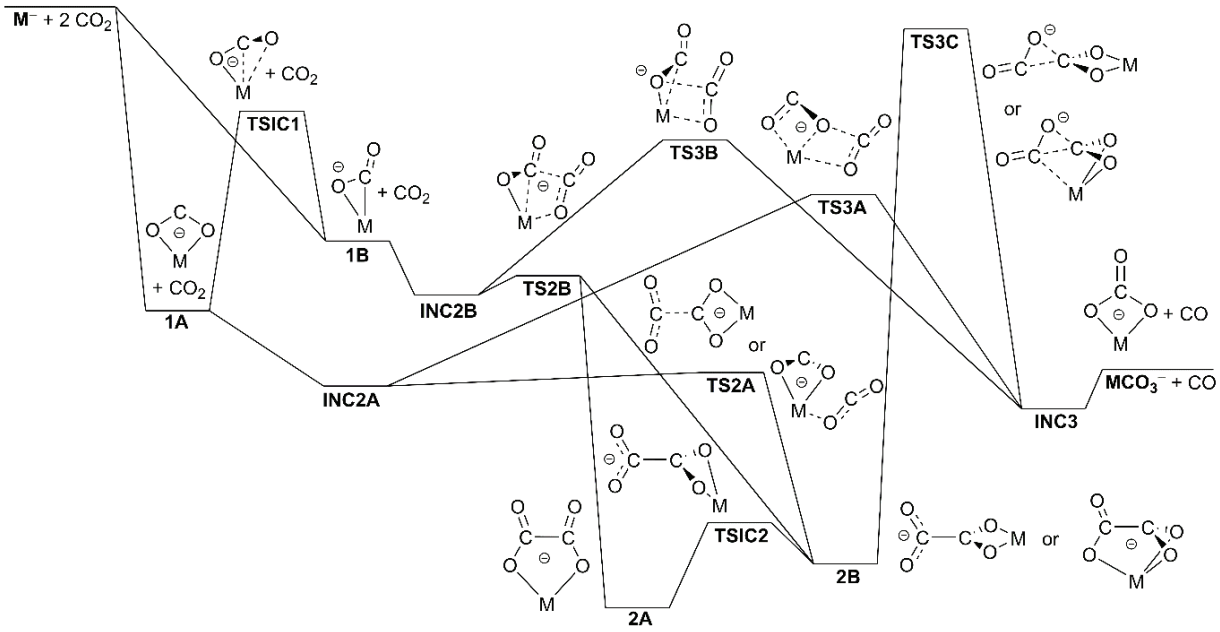

Figure 21. Schematic MP2/def2-TZVPPD potential energy diagram for the reactions between two CO_2 molecules and alkali (M = Li – Cs) and chloride-tagged alkaline earth (M = BeCl – BaCl) metal anions, M^-. From Paper II.

Table 2. Relative ZPVE-corrected [MP2/def2-TZVPPD] electronic energies for $M^- + 2\ CO_2 \rightarrow MCO_3^- + CO$ in kJ/mol. The designation *n.e.* either indicates non-existent minima or, in the case of transition states, that the reaction proceeds with a monotonic increase in potential energy in both directions along the reaction coordinate.

	Li	Na	K	Rb	Cs	BeCl	MgCl	CaCl	SrCl	BaCl
M^- + $2CO_2$	0*	0*	0*	0*	0*	0	0	0	0	0
1A + CO_2	−79*	−39*	−33*	−33*	−34*	−247	−102	−103	−73	−85
TSIC1 + CO_2	−44*	9*	2*	2*	−3*	*n.e.***	6	−35	−32	−45
1B + CO_2	−68*	−11*	−9*	−8*	−14*	−248	−84	−96	−76	−82
INC2A	−102*	−64*	−60*	−61*	−62*	*n.e.*	*n.e.*	*n.e.*	*n.e.*	*n.e.*
INC2B	−92*	−32*	−34*	−36*	*n.e.*	−273	−110	−134	−117	−126
TS2A	−102*	−46*	−26*	−29*	−30*	*n.e.*	*n.e.*	*n.e.*	*n.e.*	*n.e.*
TS2B	−84*	*n.f.*	−34*	−36*	*n.e.*	−244	−105	−130	−113	−123
2A	−317*	−189*	−169*	*n.e.*	*n.e.*	−504	−334	−344	−323	−334
TSIC2	−226*	−134*	−168*	*n.e.*	*n.e.*	−266	−198	−254	−307	−327
2B	−241*	−140*	−172*	−174*	−188*	−357	−232	−315	−312	−335
TS3A	*n.e.*	5	24	11	9	*n.e.*	−120	−140	−121	−127
TS3B	−88	5	*n.e.*	*n.e.*	*n.e.*	*n.e.*	−107	−110	−118	−127
TS3C	−28	84	79	76	56	−198	−41	−66	−63	−89
INC3	−200	−70	−52	−47	−70	−411	−243	−272	−251	−246
MCO_3^- + CO	−181	−48	−20	−14	−41	−399	−228	−239	−216	−226

* from reference [233] ** proceeds by dissociation and reattachment via **INC1**

Generally, the alkaline earth metals have the lowest energetic demands, consistent with the expected shortening of bonds across periods, Table 2. Within groups, however, the energies increase towards the middle, contrasting the expected increase towards the heaviest elements. This was attributed to the increasing d-orbital participation in bonding for the heavier elements, leading to slightly stronger, more covalent bonds in the products. This deviation from the expected trends for groups led us to analyze and compare our reaction energies to corresponding "experimental" values procured form Born Haber cycles, shown in Figure 22. Despite the possibility of systematic errors in our computational treatment of these reactions—especially considering the possible MR character of some of the MO^- species—our results are consistent with the "experimental" estimates, although the uncertainties in the latter are high.

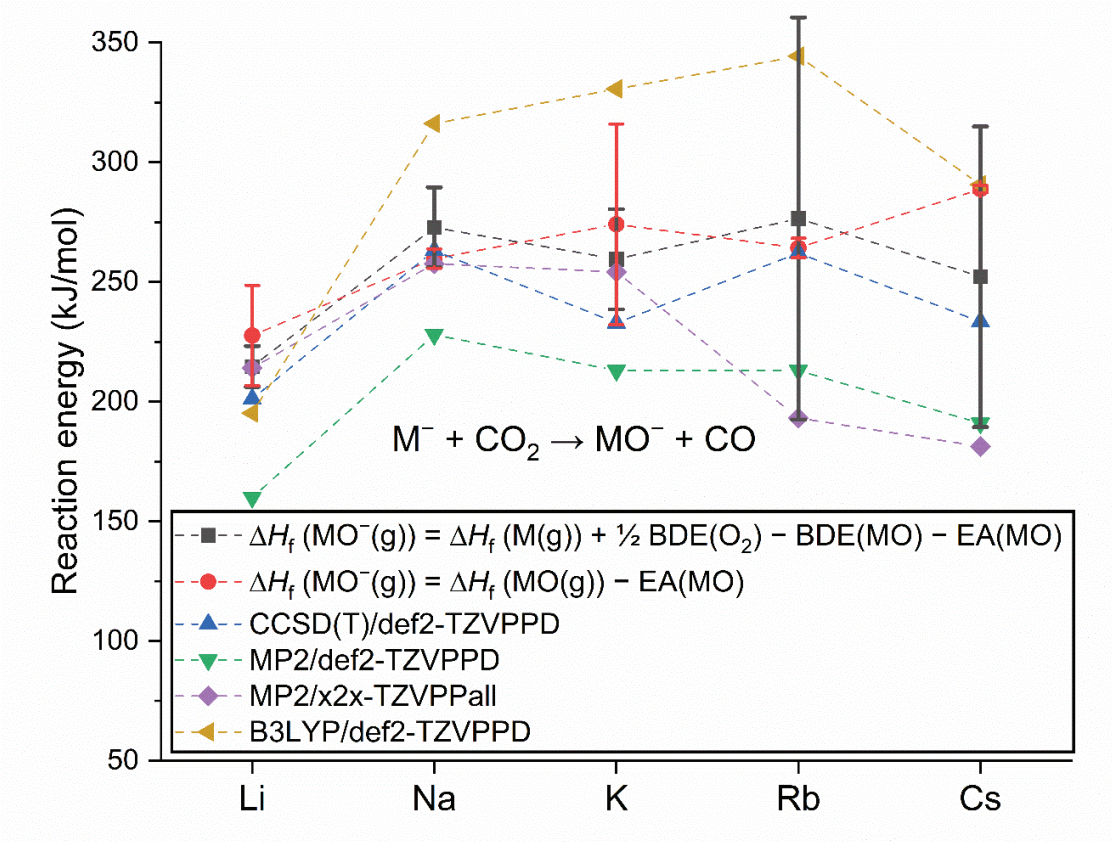

Figure 22. Comparison of "experimental" and computational reaction energies for the reduction of CO_2 to CO by the alkali metals. The connecting lines are meant as a guide to the eye and carry no further significance. For the "experimental" values, the error bars indicate uncertainties. From Paper II.

4.3 Paper III.

This paper was conceived out of our general interest in C—C bond forming reactions leading to the upscaling of CO_2. This kind of reactivity between reduced CO_2 (on the metal carbonite form) and a neutral CO_2 molecule is described in the first two papers herein. The second paper also describes the direct reduction of CO_2 to CO, hence we found it of relevance to investigate C—C bond forming reactions with the latter, in particular *via* cyclooligomerization. While the associated reaction mechanisms have been detailed up to the formation of deltate ($C_3O_3^{2-}$), they have not been reported for squarate, to the best of the authors' knowledge.

Hence, to expand upon the established reaction mechanisms of reductive cyclooligomerization, we studied the process through the corresponding reverse reactions; the collision-induced dissociation of hydrogen squarate, $HC_4O_4^-$ (*m/z* 113), and the squarate radical anion, $C_4O_4^{\bullet-}$ (*m/z* 112). The corresponding fragmentation (CID) mass spectra are shown in Figure 23. Both species undergo consecutive decarbonylation as the primary fragmentation pathway. In 1983, Lednor and Versloot proposed that reductive cyclooligomerization is initiated by electron attachment to CO. This is possible for the hydrogen squarate system, as indicated by the observation of the corresponding HCO^- (*m/z* 29) monomer in our experiments. However, this is impossible for the isolated squarate system due to the negative electron affinity of CO. We observed the reverse reaction sequence $C_4O_4^{\bullet-}$ (*m/z* 112) → $C_3O_3^{\bullet-}$ (*m/z* 84) + CO → $C_2O_2^{\bullet-}$ (*m/z* 56) + 2CO, but no fragments corresponding to $CO^{\bullet-}$ (*m/z* 28). The latter suggests that cyclooligomerization of the isolated system is initiated by formation of the ethynedione radical anion, $C_2O_2^{\bullet-}$. This constitutes the most demanding step for the whole process, as reduction must occur simultaneously with C—C coupling. According to our computations, addition of the third and fourth CO molecules have relatively low barriers and are exothermic. Comparison of model system with the reported cyclooligomerization by U(III) compounds led us to infer a relationship between the number of electrons on the CO-dimer and further reaction. Specifically, Green *et al.* showed that the dianionic ethynedione moiety, $C_2O_2^{2-}$, in their U(III)-complex does not add further CO, while a long lived ethenedione intermediate, $C_2O_2^{\bullet-}$, may cyclooligomerize further in accordance with our simple model system.[175] Thus, cyclooligomerization proceeds by radical addition, thereby avoiding symmetry constraints related to the conservation of orbital symmetry. In contrast to the exothermic anionic process, neutral cyclooligomerization is endothermic, corroborated by the elusive nature of the neutral C_nO_n species. The above findings led us to

conclude that initiation of the cyclooligomerization process requires an electron, while a second electron terminates it.

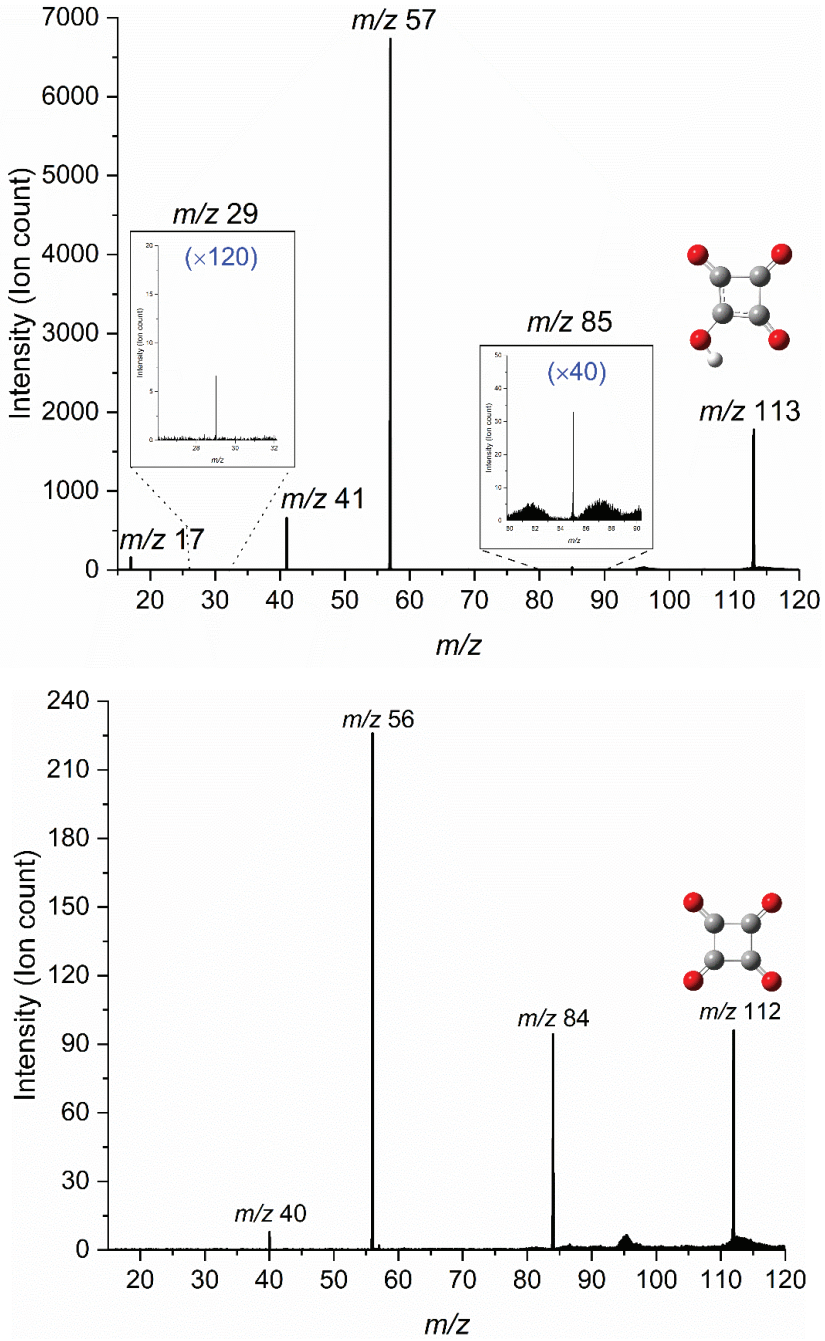

Figure 23. Fragmentation mass spectra of mass selected *m/z* 113 ($HC_4O_4^-$, *left*) and *m/z* 112 ($C_4O_4^{\bullet -}$, *right*) averaged over collision energies from 480 to 560 kJ/mol (E_{COM}) at 2.0 × 10^{-4} mbar collision gas (Ar) pressure. From Paper III.

4.4 Paper IV.

Although cyclooligomerization has been reported for complexes involving uranium, samarium and magnesium, the latter stands out as being neither radioactive nor toxic.[47,48,50] Magnesium is also important for photosynthetic carbon dioxide fixation, and efficiently activates it in the gas-phase as shown in previous work by our group.[28,32] Hence, this paper expands upon the results of Paper III by elucidating the effects of magnesium on the energetics of the reductive cyclooligomerization process for the isolated gas-phase system,

$$ClMg^- + nCO \rightarrow ClMgC_nO_n^-. \quad (4.4)$$

Once again, this was investigated *via* the reverse reactions. Similar to the naked hydrogen squarate and squarate radical anions, the magnesium chloride squarate was found to dissociate by sequential decarbonylation,

$$ClMgC_4O_4^- \rightarrow ClMgC_3O_3^- + CO \rightarrow ClMgC_2O_2^- + 2CO \rightarrow ClMg^- + 4CO, \quad (4.5)$$

i.e. in three discrete steps. No monocarbonyl, $ClMgCO^-$, was observed in our experiments, implying that cyclooligomerization of CO on magnesium chloride must also be initiated by coupling of two CO molecules, simultaneously as they are being reduced by the metal ligand. The energetic demands of each reaction step were estimated using two different methods, L-CID and linear extrapolation for the corresponding threshold energies. In addition, the process was modeled using quantum chemistry (G4), all three yielding results that are consistent with one another.

To fully grasp the role of the metal ligand in the process, a comparison of the potential energy surfaces of the three squarate systems studied (LC_4O_4, where L = e^-,H^- and $MgCl^-$) was made, Figure 24. This revealed that the magnesium system is associated with the lowest overall demands, despite the fact that the first step is less demanding for L = H^-. This follows from the ease at which the corresponding monomer HCO^- is formed. However, the next step, $HCO^- + CO \rightarrow HC_2O_2^-$ has a slightly higher barrier than the first step for $MgCl^-$, while each subsequent step proceeds essentially without barriers for the latter.

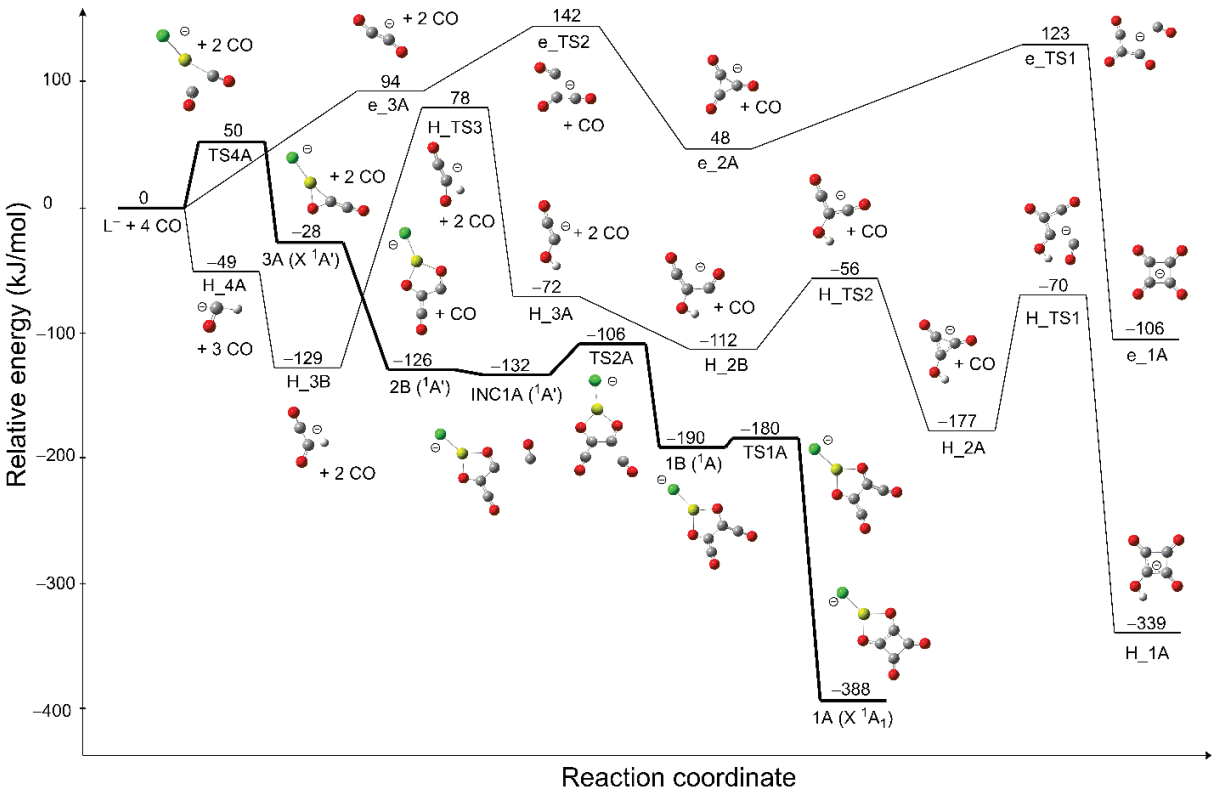

Figure 24. The singlet G4 (0 K) potential energy (electronic + zero-point vibrational energy) diagram for the L + *n*CO → LC_nO_n reactions (L = e^-, H^- or $MgCl^-$). The lowest energy $ClMgC_4O_4^-$ (L = $MgCl^-$) pathway is indicated by lines in bold, while the lowest energy $C_4O_4^{\bullet-}$ and $HC_4O_4^-$ pathways (from Paper III) are indicated by prefixes e and H in the labels, respectively. From Paper IV.

Finally, to elucidate the absence of $ClMgCO^-$ in our experiments, a computational analysis was done on various magnesium monocarbonyl species, Figure 25. It was found that while the former does in fact constitute a shallow minimum on the electronic potential energy surface, it is less stable than the separated reactants $MgCl^-$ + CO due to having a higher zero-point vibrational energy than the latter. Moreover, while the singlet monomers were generally found unstable with respect to dissociation, the triplet monomers were found stable in this regard, and could in principle act as the first step in the cyclooligomerization process. Their relative stability was rationalized by noting that the triplet $MgCl^-$ anion is destabilized more compared to the singlet, than the CO anion compared to the neutral, placing the charge bearing electron on the latter.

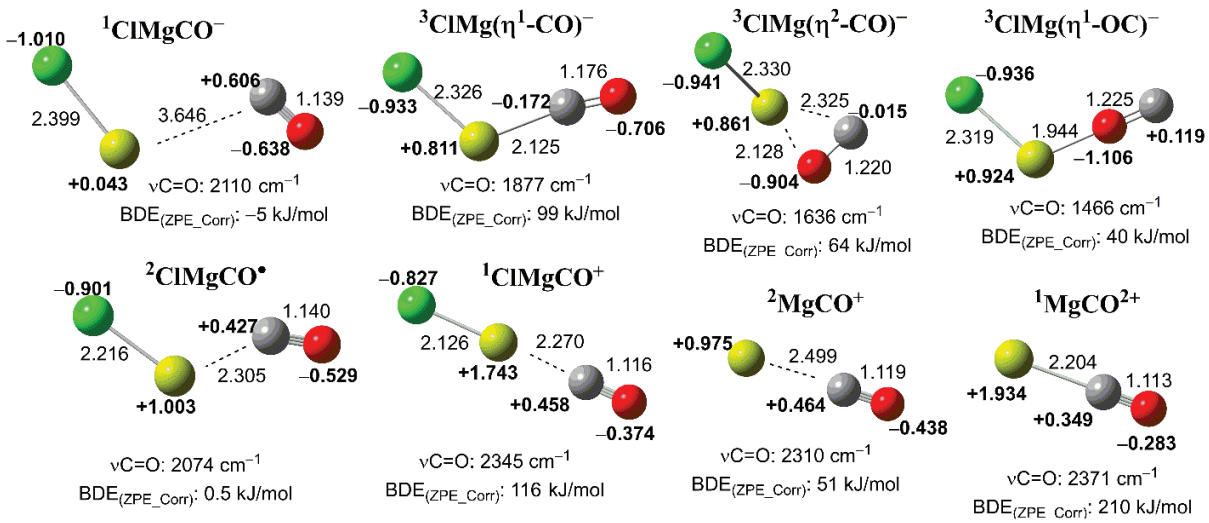

Figure 25. Magnesium chloride monocarbonyls, $ClMgCO^{-/0/+}$, and magnesium monocarbonyls, $MgCO^{+/2+}$, computed on the G4 level of theory (B3LYP/ 6-31G(2df,p) geometries). From Paper IV.

In Paper III, an apparent correlation between the negative charge transferred to the oxocarbon moieties $(CO)_n^-$ and their stability was inferred. This was further elaborated on in this paper by analyzing the NBO partial charges at each reaction step. In particular, a higher negative charge was found to correlate with a higher barrier for the next reaction step in the cyclooligomerization sequence, consistent with the notion that transfer of one electron to the oxocarbon is necessary to initiate the process, whereas a second electron terminates it.

4.5 Unpublished results

Most of the results from the CCSD(T) computations have been published for the alkali metal carbonites (Paper I). The corresponding results for the alkaline earth metal species have only been used to benchmark MP2 computations (Paper II), and have not been published. Hence, their optimized structures, along with relevant NBO partial charges are provided in Figure 26.

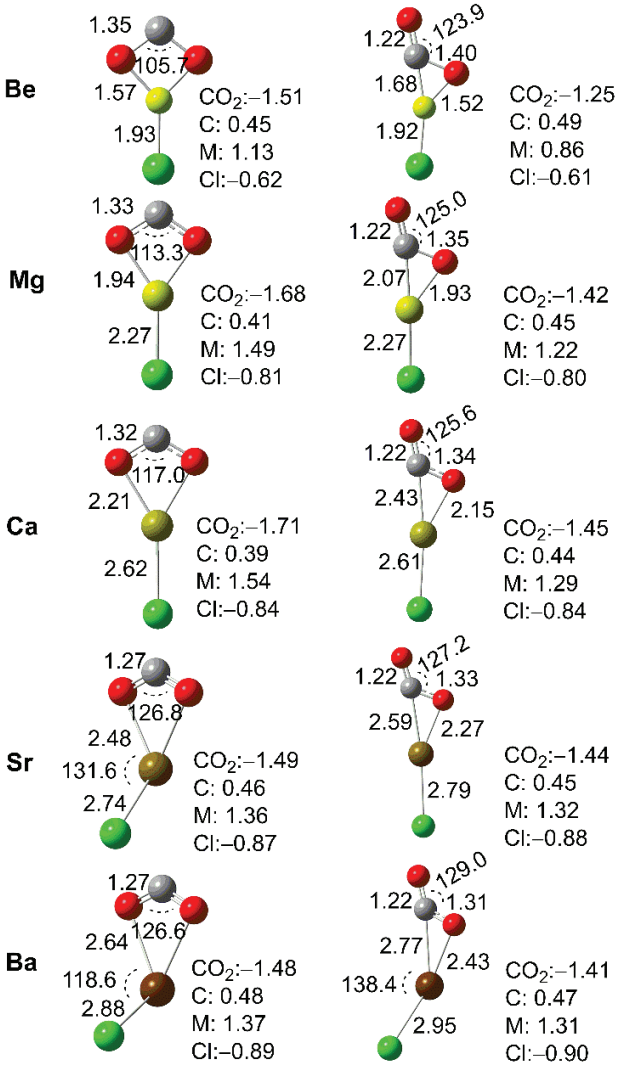

Figure 26. CCSD(T)/def2-TZVPPD optimized geometries of the $M(\kappa^2\text{-}O_2C)^-$ and $M(\eta^2\text{-}CO_2)^-$ alkaline earth metal chloride carbonites. Bond lengths in Angstroms (Å) and angles in degrees. The NBO partial charges on the CO_2 moiety as well as the carbon, metal and chlorine atoms are also indicated.

The structures of the CO_2 moieties in the alkaline earth metal carbonites are seen to be generally more perturbed (105.7˚ – 129.0˚) than with the alkali metals (127.1˚- 139.2˚), see also Figure 20. This can likely be attributed to more efficient charge transfer from metal to CO_2 as noted in Paper II (in referring to the equivalent MP2 results). Charge transfer is seen to be more efficient toward the middle of the group; the most reduced CO_2 moiety is observed for $ClCa(\kappa^2\text{-}CO_2)^-$. The heaviest metal carbonites are bent at the metal, which is more pronounced for barium than strontium. Alkaline earth metal dihalides (CaF_2, SrF_2, $SrCl_2$, BaF_2, $BaCl_2$, BaI_2) have been established as having bent, non-planar structures, suggested to be due to the involvement of the (*n* – 1) *p*- and *d*-orbitals in bonding.[234] This explanation is consistent with the observed evolution of partial charges; the ionic character of the metal-CO_2 bonding increases towards the middle of the alkaline earth metal group.

Furthermore, the results of the associated vibrational analyses have not been included in any of the published papers for either group of metals. The computed frequencies of the asymmetric ($\nu^{as}_{CO_2}$) and symmetric ($\nu^{s}_{CO_2}$) CO_2 displacement modes are given in Table 3. Although the frequencies are classified equally for the two isomers for convenience, the C=O bonds in the mixed carbon-oxygen coordinated species $M(\eta^2\text{-}CO_2)^-$ are inequivalent, and the vibrational motions of the two are thus decoupled. As a result, the asymmetric CO_2 displacement more closely resembles the stretching mode of the terminal C=O bond, whereas the symmetric counterpart corresponds to the stretching mode of the bridging C=O bond.

Table 3. Asymmetric ($\nu^{as}_{CO_2}$) and symmetric ($\nu^{s}_{CO_2}$) CO_2 displacement frequencies in cm^{-1} computed on the CCSD/def2-TZVPPD level.

	M =	Li	Na	K	Rb	Cs	BeCl	MgCl	CaCl	SrCl	BaCl
$M(\kappa^2\text{-}O_2C)^-$	$\nu^{as}_{CO_2}$	1566	1644	1647	1676	1660	1112	1160	1123*	1517	1537
	$\nu^{s}_{CO_2}$	1230	1202	1182	1185	1153	1207	1118	1036*	1245	1425
$M(\eta^2\text{-}CO_2)^-$	$\nu^{as}_{CO_2}$	1725	1777	1781	1790	1780	1728	1654	1615*	1649	1649
	$\nu^{s}_{CO_2}$	1142	1166	1167	1173	1155	1135	1118	927*	955	989

* MP2/def2-TZVPPD frequencies

The preceding analysis based on the computed geometries is corroborated by the vibrational frequencies. It is worth noting how the $\nu_{CO_2}^{as}$ frequencies of the bidentate oxygen coordinated complexes M(κ^2-O_2C)$^-$ range from values characteristic for alcohol C—O single bonds to values characteristic for carbonyl C=O double bonds, highlighting the differences in CO_2 activation by the alkaline earth metals. The analogous frequencies for the mixed carbon-oxygen coordinated complexes M(η^2-CO_2)$^-$ are more difficult to interpret in terms of trends, due to the more intricate bonding situation. The bridging C=O bond is contracted with increasing metal size, in principle leading to a blueshift of the $\nu_{CO_2}^{s}$ frequencies. At the same time, the metal interacting with this particular oxygen atom becomes heavier, counteracting the former effect. Consequently, smaller variations within groups are observed for this particular isomer.

In any case, this preliminary analysis provides a solid stepping stone for future spectroscopic or other experimental efforts to characterize these highly elusive and important intermediates.

5 Concluding remarks

This thesis has presented an extensive investigation on specific molecular level mechanisms for the reduction of CO_2 by the alkali and alkaline earth metal chloride anions, as well as further reduction of CO to cyclic oxocarbons. The described studies were conducted using a combination of mass spectrometric and quantum chemical methods, where the latter has lent heavily to the interpretation of the experimental data.

The metal carbonites have been reaffirmed as critical intermediates for the utilization of CO_2, as its reduction to oxalate, carbonate, and CO proceeds *via.* these intermediates. The two former correspond to low-energy products in the CO_2 utilization scheme, while the latter belongs to the high-level category, and is therefore highly interesting as a simple molecular building block. The associated energetics for these processes are inherently correlated to the involved metal, and it is shown that a metal leading to a more reduced or perturbed CO_2 moiety is generally associated with lower barriers for various reactions. In particular, despite their isovalency, the alkaline earth metal chlorides transfer close to two electrons, whereas the alkali metals only transfer close to one electron during complexation with CO_2. This is manifested in generally lower barriers, as well as a higher exothermicity for reactions involving the former.

The degree of CO_2 reduction and activation in the metal carbonites generally decreases with increasing metal size, determined by threshold energy measurements and computations, and was linked to the experimentally determined structures of the alkali metal oxalates formed in further reactions with CO_2. Two fundamentally different mechanisms were found for the latter process. The first proceeds directly between the incoming CO_2 and the carbon atom of the activated species, while the second involves both the metal and the carbon atom in the transition state. The energetic demands of the former increases with metal size, yet decreases for the second. This led to the assumption that the lighter, more tightly bound metal complexes are more efficient carbon nucleophiles, while complexes with larger, more polarizable metals react more efficiently as mixed metal-carbon centered nucleophiles.

While the experimental results indicate decreasing activation of CO_2 when going down each group, computations suggest that it increases slightly from the middle of the groups. The partial charge on CO_2 decrease towards the middle of the group, slightly increasing towards the heaviest metals, attributed to an increased covalent contribution to the bonding in these complexes.

According to computations, direct reduction of CO_2 to CO by the alkali metal and alkaline earth metal chloride anions is generally endothermic, except by $BeCl^-$, displaying an exothermic, barrierless reaction. However, the equivalent reductive disproportionation reaction, $M^- + 2\ CO_2 \rightarrow MCO_3^- + CO$, is exothermic and competes directly with carboxylation. The formation of carbonates in this manner constitutes the major source of carbon- and energy losses during electrolytical reduction of CO_2. Similar trends are observed for decarbonylation reaction as for carboxylation; the alkali metal complexes undergo generally less exothermic reactions and have higher barriers. These findings could potentially be used to design processes where carbonate formation is avoided by employing less activating metals, such as the alkali metals, rather than the more activating alkaline earth metal species. On the other hand, if the target is CO, a commercially used chemical feedstock, the more activating metals might be preferable due to having lower barriers towards decarbonylation.

Squarate and its derivatives are potential high-value products formed from CO cyclooligomerization. For the naked radical anion, $C_4O_4^{\bullet-}$, the critical step for this process is the simultaneous reduction and coupling of two CO molecules to yield the ethenedione radical anion, $C_2O_2^{\bullet-}$. A similar step is a prerequisite for the process catalyzed by $MgCl^-$, but not for H^-. In any case, the lowest overall energetic demands are found for the magnesium system, where every step following the initial proceeds essentially monotonously downhill with no barriers. It was also inferred that cyclooligomerization is initiated by transfer of a single electron, whereas a second electron terminates the process. These considerations can likely be used to control the overall selectivity of the sequence.

The findings of this thesis are thought to be relevant and useful for the rational design of single-atom catalysts for these processes, but also for the more established electrochemical or chemical approaches.

6 Outlook

One of the main goals of this project was to characterize the metal carbonites and their significance for CO_2 utilization, and many hours were thus spent in the lab trying to coax these elusive species into appearing for me. Towards the end of the project, my efforts were starting to bear fruits in terms of isolating some of these species for more direct reactivity studies, but I did not have the time to refine these preliminary results into anything publishable. Hence, quite a few stones have been left unturned, opening up for potential future projects. To provide some examples, these could involve investigation of substitution or addition reactions between MCO_2^- and more or less reactive carbon atoms to systematically elucidate their nucleophilic reactivity more closely, related to published literature on the magnesium and zinc analogues.[28,32]

To our great disappointment, the collaboration with the Mark Johnson lab was cut short due to a certain airborne pathogen, effectively putting an end to our efforts towards the spectroscopic characterization of the metal carbonites. Therefore, it should definitely be pursued further.

As has become apparent during my thesis work, as well as through previous literature on the interaction of CO_2 with various metals, the degree of activation depends on several factors. These naturally include the specific metal, but also the number of interacting metals. A relevant example is found in a relevant study by Hale *et al*.[167] For instance, while the cationic alkali metal oxalates, $M_3C_2O_4^+$, generally display similar reactivity as the anionic systems detailed herein, the cationic metal carbonites, $M_3CO_2^+$ are computed to be structurally more perturbed than the corresponding MCO_2^- species. It would therefore be highly relevant to study the interplay between number of interacting metals and the activation of the CO_2.

While the complete alkali and alkaline earth metal groups were studied for the metal carbonites, the cyclooligomerization process was only elucidated for the isolated systems ($L = e^-$, H^-), and magnesium. It would therefore be highly interesting to investigate the effects of the other metals on this process, in particular how these affect the first step in the process.

7 Bibliography

(1) Kramer, R. J.; He, H.; Soden, B. J.; Oreopoulos, L.; Myhre, G.; Forster, P. M.; Smith, C. J. Observational Evidence of Increasing Global Radiative Forcing. *Geophys. Res. Lett.* **2021**, *48* (7), e2020GL091585. https://doi.org/10.1029/2020GL091585.

(2) Aresta, M.; Dibenedetto, A.; Angelini, A. The Changing Paradigm in CO_2 Utilization. *J. CO2 Util.* **2013**, *3–4*, 65–73. https://doi.org/10.1016/j.jcou.2013.08.001.

(3) Aresta, M. Carbon Dioxide Reduction and Uses as a Chemical Feedstock. In *Activation of Small Molecules*; John Wiley & Sons, Ltd, 2006; pp 1–41. https://doi.org/10.1002/9783527609352.ch1.

(4) Aresta, M.; Dibenedetto, A. The Contribution of the Utilization Option to Reducing the CO_2 Atmospheric Loading: Research Needed to Overcome Existing Barriers for a Full Exploitation of the Potential of the CO_2 Use. *Catal. Today* **2004**, *98* (4), 455–462. https://doi.org/10.1016/j.cattod.2004.09.001.

(5) Küngas, R. Review—Electrochemical CO_2 Reduction for CO Production: Comparison of Low- and High-Temperature Electrolysis Technologies. *J. Electrochem. Soc.* **2020**, *167* (4), 044508. https://doi.org/10.1149/1945-7111/ab7099.

(6) Blankenship, R.; Tiede, D.; Barber, J.; Brudvig, G.; Fleming, G.; Ghirardi, M.; Gunner, M.; Junge, W.; Kramer, D.; Melis, A.; Moore, T.; Moser, C.; Nocera, D.; Nozik, A.; Ort, D.; Parson, W.; Prince, R.; Sayre, R. Comparing Photosynthetic and Photovoltaic Efficiencies and Recognizing the Potential for Improvement. *Science* **2011**, *332*, 805–809. https://doi.org/10.1126/science.1200165.

(7) Li, D.; Kassymova, M.; Cai, X.; Zang, S.-Q.; Jiang, H.-L. Photocatalytic CO_2 Reduction over Metal-Organic Framework-Based Materials. *Coord. Chem. Rev.* **2020**, *412*, 213262. https://doi.org/10.1016/j.ccr.2020.213262.

(8) Yuan, S.; Feng, L.; Wang, K.; Pang, J.; Bosch, M.; Lollar, C.; Sun, Y.; Qin, J.; Yang, X.; Zhang, P.; Wang, Q.; Zou, L.; Zhang, Y.; Zhang, L.; Fang, Y.; Li, J.; Zhou, H.-C. Stable Metal–Organic Frameworks: Design, Synthesis, and Applications. *Adv. Mater.* **2018**, *30* (37), 1704303. https://doi.org/10.1002/adma.201704303.

(9) Luo, Y.-H.; Dong, L.-Z.; Liu, J.; Li, S.-L.; Lan, Y.-Q. From Molecular Metal Complex to Metal-Organic Framework: The CO_2 Reduction Photocatalysts with Clear and Tunable Structure. *Coord. Chem. Rev.* **2019**, *390*, 86–126. https://doi.org/10.1016/j.ccr.2019.03.019.

(10) Baumann, A. E.; Burns, D. A.; Liu, B.; Thoi, V. S. Metal-Organic Framework Functionalization and Design Strategies for Advanced Electrochemical Energy Storage Devices. *Commun. Chem.* **2019**, *2* (1), 1–14. https://doi.org/10.1038/s42004-019-0184-6.

(11) Chen, Y.; Ji, S.; Chen, C.; Peng, Q.; Wang, D.; Li, Y. Single-Atom Catalysts: Synthetic Strategies and Electrochemical Applications. *Joule* **2018**, *2* (7), 1242–1264. https://doi.org/10.1016/j.joule.2018.06.019.

(12) Liu, J. Single-Atom Catalysis for a Sustainable and Greener Future. *Curr. Opin. Green Sustain. Chem.* **2020**, *22*, 54–64. https://doi.org/10.1016/j.cogsc.2020.01.004.

(13) Qiao, B.; Wang, A.; Yang, X.; Allard, L. F.; Jiang, Z.; Cui, Y.; Liu, J.; Li, J.; Zhang, T. Single-Atom Catalysis of CO Oxidation Using Pt_1/FeO_x. *Nat. Chem.* **2011**, *3* (8), 634–641. https://doi.org/10.1038/nchem.1095.

(14) Schröder, D.; Schalley, C. A.; Harvey, J. N.; Schwarz, H. On the Formation of the Carbon Dioxide Anion Radical $CO_2^{\cdot-}$ in the Gas Phase. *Int. J. Mass Spectrom.* **1999**, *185*, 25–35.

(15) Paparo, A.; Okuda, J. Carbonite, the Dianion of Carbon Dioxide and Its Metal Complexes. *J. Organomet. Chem.* **2018**, *869*, 270–274. https://doi.org/10.1016/j.jorganchem.2017.10.005.

(16) Setton, R. THE REACTION BETWEEN CESIUM AND CARBON DIOXIDE. *Bull Soc Chim Fr.* **1958**, *Vol: No. 11-12*.

(17) Jacox, M. E.; Milligan, D. E. Vibrational Spectrum of CO_2^- in an Argon Matrix. *Chem. Phys. Lett.* **1974**, *28* (2), 163–168. https://doi.org/10.1016/0009-2614(74)80043-6.

(18) Kafafi, Z. H.; Hauge, R. H.; Billups, W. E.; Margrave, J. L. Carbon Dioxide Activation by Lithium Metal. 1. Infrared Spectra of Lithium Carbon Dioxide ($Li^+CO_2^-$), Lithium Oxalate ($Li^+C_2O_4^-$), and Lithium Carbon Dioxide ($Li_2^{2+}CO_2^{2-}$) in Inert-Gas Matrices. *J. Am. Chem. Soc.* **1983**, *105* (12), 3886–3893. https://doi.org/10.1021/ja00350a025.
(19) Kafafi, Z. H.; Hauge, R. H.; Billups, W. E.; Margrave, J. L. Carbon Dioxide Activation by Alkali Metals. 2. Infrared Spectra of $M^+CO_2^-$ and $M_2^{2+}CO_2^{2-}$ in Argon and Nitrogen Matrixes. *Inorg. Chem.* **1984**, *23* (2), 177–183. https://doi.org/10.1021/ic00170a013.
(20) Manceron, L.; Loutellier, A.; Perchard, J. P. Reduction of Carbon Dioxide to Oxalate by Lithium Atoms: A Matrix Isolation Study of the Intermediate Steps. *J. Mol. Struct.* **1985**, *129* (1), 115–124. https://doi.org/10.1016/0022-2860(85)80197-6.
(21) Mascetti, J.; Tranquille, M. Fourier Transform Infrared Studies of Atomic Titanium, Vanadium, Chromium, Iron, Cobalt, Nickel and Copper Reactions with Carbon Dioxide in Low-Temperature Matrices. *J. Phys. Chem.* **1988**, *92* (8), 2177–2184. https://doi.org/10.1021/j100319a020.
(22) Mascetti, J.; Galan, F.; Pàpai, I. Carbon Dioxide Interaction with Metal Atoms: Matrix Isolation Spectroscopic Study and DFT Calculations. *Coord. Chem. Rev.* **1999**, *190–192*, 557–576. https://doi.org/10.1016/S0010-8545(99)00100-9.
(23) Boese, A. D.; Schneider, H.; Glöß, A. N.; Weber, J. M. The Infrared Spectrum of Au^-CO_2. *J. Chem. Phys.* **2005**, *122* (15), 154301. https://doi.org/10.1063/1.1875114.
(24) Knurr, B. J.; Weber, J. M. Solvent-Driven Reductive Activation of Carbon Dioxide by Gold Anions. *J. Am. Chem. Soc.* **2012**, *134* (45), 18804–18808. https://doi.org/10.1021/ja308991a.
(25) Knurr, B. J.; Weber, J. M. Solvent-Mediated Reduction of Carbon Dioxide in Anionic Complexes with Silver Atoms. *J. Phys. Chem. A* **2013**, *117* (41), 10764–10771. https://doi.org/10.1021/jp407646t.
(26) Lim, E.; Kim, S. K.; Bowen, K. H. Photoelectron Spectroscopic and Computational Study of $(M–CO_2)^-$ Anions, M = Cu, Ag, Au. *J. Chem. Phys.* **2015**, *143* (17), 174305. https://doi.org/10.1063/1.4935061.
(27) Blaziak, K.; Tzeli, D.; Xantheas, S. S.; Uggerud, E. The Activation of Carbon Dioxide by First Row Transition Metals (Sc–Zn). *Phys. Chem. Chem. Phys.* **2018**, *20* (39), 25495–25505. https://doi.org/10.1039/C8CP04231D.
(28) Miller, G. B. S.; Uggerud, E. C−C Bond Formation of Mg- and Zn-Activated Carbon Dioxide. *Chem. – Eur. J.* **2018**, *24* (18), 4710–4717. https://doi.org/10.1002/chem.201706069.
(29) Paparo, A.; Okuda, J. Carbon Dioxide Complexes: Bonding Modes and Synthetic Methods. *Coord. Chem. Rev.* **2017**, *334*, 136–149. https://doi.org/10.1016/j.ccr.2016.06.005.
(30) Zheng, H.; Kong, X.; Wang, C.; Wang, T.; Yang, D.; Li, G.; Xie, H.; Zhao, Z.; Shi, R.; Han, H.; Fan, H.; Yang, X.; Jiang, L. Spectroscopic Identification of Transition-Metal $M[\eta^2\text{-}(O,O)C]$ Species for Highly-Efficient CO_2 Activation. *J. Phys. Chem. Lett.* **2021**, *12* (1), 472–477. https://doi.org/10.1021/acs.jpclett.0c03379.
(31) Miller, G. B. S.; Esser, T. K.; Knorke, H.; Gewinner, S.; Schöllkopf, W.; Heine, N.; Asmis, K. R.; Uggerud, E. Spectroscopic Identification of a Bidentate Binding Motif in the Anionic Magnesium-CO_2 Complex ($[ClMgCO_2]^-$). *Angew. Chem.* **2014**, *126* (52), 14635–14638. https://doi.org/10.1002/ange.201409444.
(32) Dossmann Soldi-Lose, H.; Afonso, C.; Lesage, D.; Tabet, J.-C.; Uggerud, E. Formation and Characterization of Gaseous Adducts of Carbon Dioxide to Magnesium, $(CO_2)MgX^-$ (X=OH, Cl, Br). *Angew. Chem. Int. Ed.* **2012**, *51* (28), 6938–6941. https://doi.org/10.1002/anie.201108477.
(33) Thompson, M. C.; Ramsay, J.; Weber, J. M. Solvent-Driven Reductive Activation of CO_2 by Bismuth: Switching from Metalloformate Complexes to Oxalate Products. *Angew. Chem. Int. Ed.* **2016**, *55* (48), 15171–15174. https://doi.org/10.1002/anie.201607445.
(34) Lessen, D. E.; Asher, R. L.; Brucat, P. J. Energy Dependent Photochemistry in the Predissociation of $V(OCO)^+$. *J. Chem. Phys.* **1991**, *95* (2), 1414–1416. https://doi.org/10.1063/1.461122.

(35) Sievers, M. R.; Armentrout, P. B. Potential Energy Surface for Carbon-dioxide Activation by V^+: A Guided Ion Beam Study. *J. Chem. Phys.* **1995**, *102* (2), 754–762. https://doi.org/10.1063/1.469188.
(36) Hwang, D.-Y.; Mebel, A. Theoretical Study on the Reaction Mechanism of Sc Atoms with Carbon Dioxide. *Chem. Phys. Lett.* **2002**, *357* (1), 51–58. https://doi.org/10.1016/S0009-2614(02)00438-4.
(37) Pápai, I.; Hannachi, Y.; Gwizdala, S.; Mascetti, J. Vanadium Insertion into CO_2, CS_2 and OCS: A Comparative Theoretical Study. *J. Phys. Chem. A* **2002**, *106* (16), 4181–4186. https://doi.org/10.1021/jp014034k.
(38) Zhang, Q.; Chen, M.; Zhou, M. Infrared Spectra and Structures of the Neutral and Charged $CrCO_2$ and $Cr(CO_2)_2$ Isomers in Solid Neon. *J. Phys. Chem. A* **2014**, *118* (31), 6009–6017. https://doi.org/10.1021/jp505740j.
(39) Schwarz, H. Metal-Mediated Activation of Carbon Dioxide in the Gas Phase: Mechanistic Insight Derived from a Combined Experimental/Computational Approach. *Coord. Chem. Rev.* **2017**, *334*, 112–123. https://doi.org/10.1016/j.ccr.2016.03.009.
(40) Dodson, L. G.; Thompson, M. C.; Weber, J. M. Titanium Insertion into CO Bonds in Anionic Ti–CO_2 Complexes. *J. Phys. Chem. A* **2018**, *122* (11), 2983–2991. https://doi.org/10.1021/acs.jpca.8b01843.
(41) Hecht, M.; Hoffman, J.; Rapp, D.; McClean, J.; SooHoo, J.; Schaefer, R.; Aboobaker, A.; Mellstrom, J.; Hartvigsen, J.; Meyen, F.; Hinterman, E.; Voecks, G.; Liu, A.; Nasr, M.; Lewis, J.; Johnson, J.; Guernsey, C.; Swoboda, J.; Eckert, C.; Alcalde, C.; Poirier, M.; Khopkar, P.; Elangovan, S.; Madsen, M.; Smith, P.; Graves, C.; Sanders, G.; Araghi, K.; de la Torre Juarez, M.; Larsen, D.; Agui, J.; Burns, A.; Lackner, K.; Nielsen, R.; Pike, T.; Tata, B.; Wilson, K.; Brown, T.; Disarro, T.; Morris, R.; Schaefer, R.; Steinkraus, R.; Surampudi, R.; Werne, T.; Ponce, A. Mars Oxygen ISRU Experiment (MOXIE). *Space Sci. Rev.* **2021**, *217* (1), 9. https://doi.org/10.1007/s11214-020-00782-8.
(42) West, R. *Oxocarbons*; Elsevier, 1980. https://doi.org/10.1016/B978-0-12-744580-9.X5001-5.
(43) Schleyer, P. von R.; Najafian, K.; Kiran, B.; Jiao, H. Are Oxocarbon Dianions Aromatic? *J. Org. Chem.* **2000**, *65* (2), 426–431. https://doi.org/10.1021/jo991267n.
(44) Jiao, H.; Wu, H.-S. Are Neutral Oxocarbons Stable? *J. Org. Chem.* **2003**, *68* (4), 1475–1479. https://doi.org/10.1021/jo026243m.
(45) Okuda, Y.; Iwayasu, N.; Honbou, H. Cathode Active Material and Lithium Ion Rechargeable Battery Using the Material. US8685573B2, April 1, 2014.
(46) Ghosh, A.; Mitra, S. In Situ Surface Coating of Squaric Acid with Conductive Polyaniline for a High-Capacity and Sustainable Lithium Battery Anode. *ChemElectroChem* **2018**, *5* (1), 159–165. https://doi.org/10.1002/celc.201700866.
(47) Summerscales, O. T.; Cloke, F. G. N.; Hitchcock, P. B.; Green, J. C.; Hazari, N. Reductive Cyclotetramerization of CO to Squarate by a U(III) Complex: The X-Ray Crystal Structure of $[(U(\eta\text{-}C_8H_6\{Si^iPr_3\text{-}1,4\}_2)(\eta\text{-}C_5Me_4H)]_2(\mu\text{-}\eta^2\text{:}\,\eta^2\text{-}C_4O_4)$. *J. Am. Chem. Soc.* **2006**, *128* (30), 9602–9603. https://doi.org/10.1021/ja063222r.
(48) Evans, W. J.; Grate, J. W.; Hughes, L. A.; Zhang, H.; Atwood, J. L. Reductive Homologation of Carbon Monoxide to a Ketenecarboxylate by a Low-Valent Organolanthanide Complex: Synthesis and x-Ray Crystal Structure of $[(C_5Me_5)_4Sm_2(O_2CCCO)(THF)]_2$. *J. Am. Chem. Soc.* **1985**, *107* (12), 3728–3730. https://doi.org/10.1021/ja00298a060.
(49) Lalrempuia, R.; Kefalidis, C. E.; Bonyhady, S. J.; Schwarze, B.; Maron, L.; Stasch, A.; Jones, C. Activation of CO by Hydrogenated Magnesium(I) Dimers: Sterically Controlled Formation of Ethenediolate and Cyclopropanetriolate Complexes. *J. Am. Chem. Soc.* **2015**, *137* (28), 8944–8947. https://doi.org/10.1021/jacs.5b06439.
(50) Yuvaraj, K.; Douair, I.; Paparo, A.; Maron, L.; Jones, C. Reductive Trimerization of CO to the Deltate Dianion Using Activated Magnesium(I) Compounds. *J. Am. Chem. Soc.* **2019**, *141* (22), 8764–8768. https://doi.org/10.1021/jacs.9b04085.

(51) Tian, Z.; Chan, B.; Sullivan, M. B.; Radom, L.; Kass, S. R. Lithium Monoxide Anion: A Ground-State Triplet with the Strongest Base to Date. *Proc. Natl. Acad. Sci.* **2008**, *105* (22), 7647–7651. https://doi.org/10.1073/pnas.0801393105.
(52) Curtis, S.; Renaud, J.; Holmes, J. L.; Mayer, P. M. Old Acid, New Chemistry. Negative Metal Anions Generated from Alkali Metal Oxalates and Others. *J. Am. Soc. Mass Spectrom.* **2010**, *21* (11), 1944–1946. https://doi.org/10.1016/j.jasms.2010.08.003.
(53) Attygalle, A. B.; Axe, F. U.; Weisbecker, C. S. Mild Route to Generate Gaseous Metal Anions. *Rapid Commun. Mass Spectrom.* **2011**, *25* (6), 681–688. https://doi.org/10.1002/rcm.4913.
(54) Miller, G.; Fäseke, V.; Uggerud, E. Unimolecular Dissociation of Anions Derived from Maleic Acid (MaH_2) in the Gas Phase: MaH^- and $MaMgCl^-$— Relationship to Grignard Chemistry and Reductive CO_2 Fixation. *Eur. J. Mass Spectrom.* **2015**, *21* (3), 545. https://doi.org/10.1255/ejms.1325.
(55) Jestilä, J. S.; Uggerud, E. Unimolecular Dissociation of Anions Derived from Succinic Acid (H_2Su) in the Gas Phase: HSu^- and $ClMgSu^-$. Relationship to CO_2 Fixation: *Eur. J. Mass Spectrom.* **2018**, *24* (1), 33–42. https://doi.org/10.1177/1469066717729904.
(56) Schröder, D.; Schwarz, H.; Dua, S.; Blanksby, S. J.; Bowie, J. H. Mass Spectrometric Studies of the Oxocarbons C_nO_n (n = 3–6). *Int. J. Mass Spectrom.* **1999**, *188* (1), 17–25. https://doi.org/10.1016/S1387-3806(98)14208-2.
(57) House, K. Z.; Baclig, A. C.; Ranjan, M.; van Nierop, E. A.; Wilcox, J.; Herzog, H. J. Economic and Energetic Analysis of Capturing CO_2 from Ambient Air. *Proc. Natl. Acad. Sci. U. S. A.* **2011**, *108* (51), 20428–20433. https://doi.org/10.1073/pnas.1012253108.
(58) Back, M.; Bauer, M.; Stanjek, H.; Peiffer, S. Sequestration of CO_2 after Reaction with Alkaline Earth Metal Oxides CaO and MgO. *Appl. Geochem.* **2011**, *26* (7), 1097–1107. https://doi.org/10.1016/j.apgeochem.2011.03.125.
(59) Aresta, M.; Angelini, A. The Carbon Dioxide Molecule and the Effects of Its Interaction with Electrophiles and Nucleophiles. In *Carbon Dioxide and Organometallics*; Lu, X.-B., Ed.; Topics in Organometallic Chemistry; Springer International Publishing: Cham, 2016; pp 1–38. https://doi.org/10.1007/3418_2015_93.
(60) Mannik, L.; Stryland, J. C.; Welsh, H. L. An Infrared Spectrum of CO_2 Dimers in the "Locked" Configuration. *Can. J. Phys.* **1971**, *49* (23), 3056–3057. https://doi.org/10.1139/p71-364.
(61) Novick, S. E.; Davies, P. B.; Dyke, T. R.; Klemperer, William. Polarity of van Der Waals Molecules. *J. Am. Chem. Soc.* **1973**, *95* (26), 8547–8550. https://doi.org/10.1021/ja00807a008.
(62) Barton, A. E.; Chablo, A.; Howard, B. J. On the Structure of the Carbon Dioxide Dimer. *Chem. Phys. Lett.* **1979**, *60* (3), 414–417. https://doi.org/10.1016/0009-2614(79)80600-4.
(63) Lobue, J. M.; Rice, J. K.; Novick, S. E. Qualitative Structure of $(CO_2)_2$ and $(OCS)_2$. *Chem. Phys. Lett.* **1984**, *112* (4), 376–380. https://doi.org/10.1016/0009-2614(84)85761-9.
(64) Harnes, J.; Winkler, M.; Lindblad, A.; Sæthre, L. J.; Børve, K. J. Size of Free Neutral CO_2 Clusters from Carbon 1s Ionization Energies. *J. Phys. Chem. A* **2011**, *115* (38), 10408–10415. https://doi.org/10.1021/jp206329m.
(65) Broekhuizen, F. A. van; Groot, I. M. N.; Fraser, H. J.; Dishoeck, E. F. van; Schlemmer, S. Infrared Spectroscopy of Solid CO–CO_2 Mixtures and Layers. *Astron. Astrophys.* **2006**, *451* (2), 723–731. https://doi.org/10.1051/0004-6361:20052942.
(66) Falk, M.; Miller, A. G. Infrared Spectrum of Carbon Dioxide in Aqueous Solution. *Vib. Spectrosc.* **1992**, *4* (1), 105–108. https://doi.org/10.1016/0924-2031(92)87018-B.
(67) Ma, Y.; Peng, L.; Zhang, H.; Yu, J.-G. The Potential Energy Surfaces of the Ground and Excited States of Carbon Dioxide Molecule. *Russ. J. Phys. Chem. A* **2014**, *88* (13), 2339–2347. https://doi.org/10.1134/S0036024414130287.
(68) Spielfiedel, A.; Feautrier, N.; Cossart-Magos, C.; Chambaud, G.; Rosmus, P.; Werner, H. -J.; Botschwina, P. Bent Valence Excited States of CO_2. *J. Chem. Phys.* **1992**, *97* (11), 8382–8388. https://doi.org/10.1063/1.463408.

(69) Dixon, R. N.; Porter, G. The Carbon Monoxide Flame Bands. *Proc. R. Soc. Lond. Ser. Math. Phys. Sci.* **1963**, *275* (1362), 431–446. https://doi.org/10.1098/rspa.1963.0178.
(70) Cossart-Magos, C.; Launay, F.; Parkin, J. E. High Resolution Absorption Spectrum of CO_2 between 1750 and 2000 Å. *Mol. Phys.* **1992**, *75* (4), 835–856. https://doi.org/10.1080/00268979200100641.
(71) Cossart-Magos, C.; Launay, F.; Parkin, J. E. High Resolution Absorption Spectrum of CO_2 between 1750 and 2000 Å. 2. Rotational Analysis of Two Parallel-Type Bands Assigned to the Lowest Electronic Transition $1^3B_2 \leftarrow X^1\Sigma_g^+$. *Mol. Phys.* **2005**, *103* (5), 629–641. https://doi.org/10.1080/00268970512331328668.
(72) Lin, M. C.; Bauer, S. H. Bimolecular Reaction of N_2O with CO and the Recombination of O and CO as Studied in a Single-Pulse Shock Tube. *J. Chem. Phys.* **1969**, *50* (8), 3377–3391. https://doi.org/10.1063/1.1671561.
(73) Okabe, H. *Photochemistry of Small Molecules*; Wiley New York, 1978; Vol. 431.
(74) Allan, C. J.; Gelius, U.; Allison, D. A.; Johansson, G.; Siegbahn, H.; Siegbahn, K. ESCA Studies of CO_2, CS_2 and COS. *J. Electron Spectrosc. Relat. Phenom.* **1972**, *1* (2), 131–151. https://doi.org/10.1016/0368-2048(72)80027-6.
(75) Mohammed, H. H.; Fournier, J.; Deson, J.; Vermeil, C. Matrix-Isolation Study of the CO_2 Lowest Triplet State. *Chem. Phys. Lett.* **1980**, *73* (2), 315–318. https://doi.org/10.1016/0009-2614(80)80380-0.
(76) Walsh, A. D. The Electronic Orbitals, Shapes, and Spectra of Polyatomic Molecules. Part II. Non-Hydride AB_2 and BAC Molecules. *J. Chem. Soc.* **1953**, No. 0, 2266–2288. https://doi.org/10.1039/JR9530002266.
(77) Bogey, M.; Demuynck, C.; Destombes, J. L.; Krupnov, A. Molecular Structure of $HOCO^+$. *J. Mol. Struct.* **1988**, *190*, 465–474. https://doi.org/10.1016/0022-2860(88)80305-3.
(78) Ovenall, D. W.; Whiffen, D. H. Electron Spin Resonance and Structure of the CO^-_2 Radical Ion. *Mol. Phys.* **1961**, *4*, 135–144. https://doi.org/10.1080/00268976100100181.
(79) Hartman, K. O.; Hisatsune, I. C. Infrared Spectrum of Carbon Dioxide Anion Radical. *J. Chem. Phys.* **1966**, *44* (5), 1913–1918. https://doi.org/10.1063/1.1726961.
(80) Gutsev, G. L.; Bartlett, R. J.; Compton, R. N. Electron Affinities of CO_2, OCS, and CS_2. *J. Chem. Phys.* **1998**, *108* (16), 6756–6762. https://doi.org/10.1063/1.476091.
(81) Compton, R. N.; Reinhardt, P. W.; Cooper, C. D. Collisional Ionization of Na, K, and Cs by CO_2, COS, and CS_2: Molecular Electron Affinities. *J. Chem. Phys.* **1975**, *63* (9), 3821. https://doi.org/10.1063/1.431875.
(82) Rauk, A.; Armstrong, D. A.; Yu, D. The Lifetimes of Gas Phase $CO_2^{\cdot -}$ and $N_2O^{\cdot -}$ Calculated from the Transition Probability of the Autodetachment Process $A^- \rightarrow A + e^-$. *Int. J. Chem. Kinet.* **1994**, *26* (1), 7–24. https://doi.org/10.1002/kin.550260104.
(83) Raarup, M. K.; Andersen, H. H.; Andersen, T. Metastable State of CO_2^- with Millisecond Lifetime. *J. Phys. B At. Mol. Opt. Phys.* **1999**, *32* (23), L659–L664. https://doi.org/10.1088/0953-4075/32/23/101.
(84) Dodson, L. G.; Thompson, M. C.; Weber, J. M. Characterization of Intermediate Oxidation States in CO_2 Activation. *Annu. Rev. Phys. Chem.* **2018**, *69* (1), 231–252. https://doi.org/10.1146/annurev-physchem-050317-021122.
(85) Pacansky, J.; Wahlgren, U.; Bagus, P. S. SCF Ab-initio Ground State Energy Surfaces for CO_2 and CO_2^-. *J. Chem. Phys.* **1975**, *62* (7), 2740–2744. https://doi.org/10.1063/1.430807.
(86) Simons, Jack.; Jordan, K. D. Ab Initio Electronic Structure of Anions. *Chem. Rev.* **1987**, *87* (3), 535–555. https://doi.org/10.1021/cr00079a004.
(87) Holroyd, R. A.; Itoh, K.; Nishikawa, M. Studies of $e^- + CO_2 \rightleftharpoons CO_2^-$ Equilibria in Hexamethyldisiloxane and Bis(Trimethylsilyl) Methane. *Chem. Phys. Lett.* **1997**, *266* (1), 227–232. https://doi.org/10.1016/S0009-2614(97)01536-4.
(88) Muraoka, A.; Inokuchi, Y.; Hammer, N. I.; Shin, J.-W.; Johnson, M. A.; Nagata, T. Structural Evolution of the $[(CO_2)_n(H_2O)]^-$ Cluster Anions: Quantifying the Effect of Hydration on the

Excess Charge Accommodation Motif. *J. Phys. Chem. A* **2009**, *113* (31), 8942–8948. https://doi.org/10.1021/jp903578e.
(89) Tsukuda, T.; Saeki, M.; Kimura, R.; Nagata, T. Electronic Isomers in $[(CO_2)_nROH]^-$ Cluster Anions. I. Photoelectron Spectroscopy. *J. Chem. Phys.* **1999**, *110* (16), 7846–7857. https://doi.org/10.1063/1.478691.
(90) Klots, C. E. Stable Gas Phase Hydrates of the CO^-_2 Anion. *J. Chem. Phys.* **1979**, *71* (10), 4172–4172. https://doi.org/10.1063/1.438193.
(91) Surber, E.; Mabbs, R.; Habteyes, T.; Sanov, A. Photoelectron Imaging of Hydrated Carbon Dioxide Cluster Anions. *J. Phys. Chem. A* **2005**, *109* (20), 4452–4458. https://doi.org/10.1021/jp050061p.
(92) DeLuca, M. J.; Niu, B.; Johnson, M. A. Photoelectron Spectroscopy of $(CO_2)_n^-$ Clusters with $2 \leq n \leq 13$: Cluster Size Dependence of the Core Molecular Ion. *J. Chem. Phys.* **1988**, *88* (9), 5857–5863. https://doi.org/10.1063/1.454548.
(93) Janik, I.; Tripathi, G. N. R. The Nature of the CO_2^- Radical Anion in Water. *J. Chem. Phys.* **2016**, *144* (15), 154307. https://doi.org/10.1063/1.4946868.
(94) Thompson, W. E.; Jacox, M. E. The Vibrational Spectra of CO_2^+, $(CO_2)_2^+$, CO_2^-, and $(CO_2)_2^-$ Trapped in Solid Neon. *J. Chem. Phys.* **1999**, *111* (10), 4487–4496. https://doi.org/10.1063/1.479212.
(95) Zhou, M.; Andrews, L. Infrared Spectra of the CO_2^- and $C_2O_4^-$ Anions Isolated in Solid Argon. *J. Chem. Phys.* **1999**, *110* (5), 2414–2422. https://doi.org/10.1063/1.477947.
(96) Corey, E. J.; Winter, R. A. E. A New, Stereospecific Olefin Synthesis from 1,2-Diols. *J. Am. Chem. Soc.* **1963**, *85* (17), 2677–2678. https://doi.org/10.1021/ja00900a043.
(97) Corey, E. J.; Carey, F. A.; Winter, R. A. E. Stereospecific Syntheses of Olefins from 1,2-Thionocarbonates and 1,2-Trithiocarbonates. Trans-Cycloheptene. *J. Am. Chem. Soc.* **1965**, *87* (4), 934–935. https://doi.org/10.1021/ja01082a057.
(98) Hoffmann, R. W.; Reiffen, M. Carben-Reaktionen, X. Ionische Zwischenstufen der Reaktion von Orthoameisensäure-trimethylester mit Arylisocyanat. *Chem. Ber.* **1977**, *110* (1), 49–52. https://doi.org/10.1002/cber.19771100106.
(99) Lakkaraju, P. S.; Askerka, M.; Beyer, H.; Ryan, C. T.; Dobbins, T.; Bennett, C.; Kaczur, J. J.; Batista, V. S. Formate to Oxalate: A Crucial Step for the Conversion of Carbon Dioxide into Multi-Carbon Compounds. *ChemCatChem* **2016**, *8* (22), 3453–3457. https://doi.org/10.1002/cctc.201600765.
(100) Paparo, A.; Silvia, J. S.; Kefalidis, C. E.; Spaniol, T. P.; Maron, L.; Okuda, J.; Cummins, C. C. A Dimetalloxycarbene Bonding Mode and Reductive Coupling Mechanism for Oxalate Formation from CO_2. *Angew. Chem. Int. Ed.* **2015**, *54* (31), 9115–9119. https://doi.org/10.1002/anie.201502532.
(101) Tanaka, K.; Kushi, Y.; Tsuge, K.; Toyohara, K.; Nishioka, T.; Isobe, K. Catalytic Generation of Oxalate through a Coupling Reaction of Two CO_2 Molecules Activated on $[(Ir(\eta^5\text{-}C_5Me_5))_2(Ir((\eta^4\text{-}C_5Me_5)CH_2CN)(\mu^3\text{-}S)_2]$. *Inorg. Chem.* **1998**, *37* (1), 120–126. https://doi.org/10.1021/ic9702328.
(102) Garron, A.; Epron, F. Use of Formic Acid as Reducing Agent for Application in Catalytic Reduction of Nitrate in Water. *Water Res.* **2005**, *39* (13), 3073–3081. https://doi.org/10.1016/j.watres.2005.05.012.
(103) Zimmermann, P.; Hoof, S.; Braun-Cula, B.; Herwig, C.; Limberg, C. A Biomimetic Nickel Complex with a Reduced CO_2 Ligand Generated by Formate Deprotonation and Its Behaviour towards CO_2. *Angew. Chem. Int. Ed.* **2018**, *57* (24), 7230–7233. https://doi.org/10.1002/anie.201802655.
(104) Schreiner, P. R.; Reisenauer, H. P. Spectroscopic Identification of Dihydroxycarbene. *Angew. Chem. Int. Ed.* **2008**, *47* (37), 7071–7074. https://doi.org/10.1002/anie.200802105.

(105) Bencivenni, L.; D'alessio, L.; Ramondo, F.; Pelino, M. Vibrational Spectra and Structure of $M(CO_2)$ and $M_2(CO_2)$ Molecules. *Inorganica Chim. Acta* **1986**, *121* (2), 161–166. https://doi.org/10.1016/S0020-1693(00)84515-6.

(106) Saouma, C. T.; Lu, C. C.; Day, M. W.; Peters, J. C. CO_2 Reduction by Fe(I): Solvent Control of C–O Cleavage versus C–C Coupling. *Chem. Sci.* **2013**, *4* (10), 4042–4051. https://doi.org/10.1039/C3SC51262B.

(107) Castro, L.; Mills, D. P.; Jones, C.; Maron, L. Activation of Heteroallenes CO_xS_{2-x} (x = 0–2): Experimental and Theoretical Evidence of the Synthetic Versatility of a Bulky Guanidinato Sm^{II} Complex. *Eur. J. Inorg. Chem.* **2016**, *2016* (6), 792–796. https://doi.org/10.1002/ejic.201501346.

(108) Tsoureas, N.; Castro, L.; Kilpatrick, A. F. R.; Cloke, F. G. N.; Maron, L. Controlling Selectivity in the Reductive Activation of CO_2 by Mixed Sandwich Uranium(III) Complexes. *Chem. Sci.* **2014**, *5* (10), 3777–3788. https://doi.org/10.1039/C4SC01401D.

(109) Herskovitz, T.; Guggenberger, L. J. Carbon Dioxide Coordination Chemistry. The Structure and Some Chemistry of the Novel Carbon Dioxide Addition Product Chlorobis(Carbon Dioxide)Tris(Trimethylphosphine)Iridium. *J. Am. Chem. Soc.* **1976**, *98* (6), 1615–1616. https://doi.org/10.1021/ja00422a074.

(110) Babaeva, M. A.; Tsyganenko, A. A. Infrared Spectroscopic Evidence for the Formation of Carbonite CO_2^{2-} Ions in CO Interaction with Basic Oxide Surfaces. *React. Kinet. Catal. Lett.* **1987**, *34* (1), 9–14. https://doi.org/10.1007/BF02069193.

(111) Babaeva, M. A.; Bystrov, D. S.; Kovalgin, A. Yu.; Tsyganenko, A. A. CO Interaction with the Surface of Thermally Activated CaO and MgO. *J. Catal.* **1990**, *123* (2), 396–416. https://doi.org/10.1016/0021-9517(90)90138-A.

(112) Binet, C.; Badri, A.; Boutonnet-Kizling, M.; Lavalley, J.-C. FTIR Study of Carbon Monoxide Adsorption on Ceria: CO_2^{2-} Carbonite Dianion Adsorbed Species. *J. Chem. Soc. Faraday Trans.* **1994**, *90* (7), 1023–1028. https://doi.org/10.1039/FT9949001023.

(113) Murphy, L. J.; Robertson, K. N.; Kemp, R. A.; Tuononen, H. M.; Clyburne, J. A. C. Structurally Simple Complexes of CO_2. *Chem. Commun.* **2015**, *51* (19), 3942–3956. https://doi.org/10.1039/C4CC08510H.

(114) Freund, H.-J.; Messmer, R. P. On the Bonding and Reactivity of CO_2 on Metal Surfaces. *Surf. Sci.* **1986**, *172* (1), 1–30. https://doi.org/10.1016/0039-6028(86)90580-7.

(115) Thomas, D. A.; Mucha, E.; Gewinner, S.; Schöllkopf, W.; Meijer, G.; von Helden, G. Vibrational Spectroscopy of Fluoroformate, FCO_2^-, Trapped in Helium Nanodroplets. *J. Phys. Chem. Lett.* **2018**, *9* (9), 2305–2310. https://doi.org/10.1021/acs.jpclett.8b00664.

(116) Weber, J. M.; Schneider, H. Infrared Spectra of $X^-{\cdot}CO2{\cdot}Ar$ Cluster Anions (X=Cl,Br,I). *J. Chem. Phys.* **2004**, *120* (21), 10056–10061. https://doi.org/10.1063/1.1736633.

(117) S. Bristow, G.; B. Hitchcock, P.; F. Lappert, M. A Novel Carbon Dioxide Complex: Synthesis and Crystal Structure of $[Nb(\eta\text{-}C_5H_4Me)_2(CH_2SiMe_3)(\eta^2\text{-}CO_2)]$. *J. Chem. Soc. Chem. Commun.* **1981**, *0* (21), 1145–1146. https://doi.org/10.1039/C39810001145.

(118) Kilpatrick, A. F. R.; Green, J. C.; Cloke, F. G. N. Bonding in Complexes of Bis(Pentalene)Dititanium, $Ti_2(C_8H_6)_2$. *Organometallics* **2015**, *34* (20), 4830–4843. https://doi.org/10.1021/acs.organomet.5b00363.

(119) Miedaner, A.; DuBois, D. L.; Curtis, C. J.; Haltiwanger, R. C. Generation of Metal Formyl Complexes Using Nickel and Platinum Hydrides as Reducing Agents. *Organometallics* **1993**, *12* (2), 299–303. https://doi.org/10.1021/om00026a014.

(120) Lee, C. H.; Laitar, D. S.; Mueller, P.; Sadighi, J. P. Generation of a Doubly Bridging CO_2 Ligand and Deoxygenation of CO_2 by an (NHC)Ni(0) Complex. *J. Am. Chem. Soc.* **2007**, *129* (45), 13802–13803. https://doi.org/10.1021/ja075630g.

(121) Rodríguez-Blanco, G.; Jobst, K. J.; Luider, T. M.; Terlouw, J. K.; Burgers, P. C. Generation and Dissociation of $RCOOCaCl_2^-$ and Other Carboxylate-Substituted Superhalogens: CO_2 Capture and Implications for Structure Analysis. *ChemPlusChem* **2013**, *78* (9), 1184–1189. https://doi.org/10.1002/cplu.201300161.

(122) Castro-Rodriguez, I.; Nakai, H.; Zakharov, L. N.; Rheingold, A. L.; Meyer, K. A Linear, O-Coordinated η^1-CO_2 Bound to Uranium. *Science* **2004**, *305* (5691), 1757–1759. https://doi.org/10.1126/science.1102602.
(123) Hwang, D.-Y.; Mebel, A. M. Theoretical Study on Reforming of CO_2 Catalyzed with Be. *Chem. Phys. Lett.* **2000**, *325* (5), 639–644. https://doi.org/10.1016/S0009-2614(00)00650-3.
(124) Hwang, D.-Y.; Mebel, A. M. Theoretical Study on the Reaction Mechanism of CO_2 with Mg. *J. Phys. Chem. A* **2000**, *104* (32), 7646–7650. https://doi.org/10.1021/jp0010839.
(125) Hwang, D.-Y.; Mebel, A. M. Reaction Mechanism of CO_2 with Ca Atom: A Theoretical Study. *Chem. Phys. Lett.* **2000**, *331* (5), 526–532. https://doi.org/10.1016/S0009-2614(00)01188-X.
(126) Liu, G.; Ciborowski, S. M.; Zhu, Z.; Chen, Y.; Zhang, X.; Bowen, K. H. The Metallo-Formate Anions, $M(CO_2)^-$, M = Ni, Pd, Pt, Formed by Electron-Induced CO_2 Activation. *Phys. Chem. Chem. Phys.* **2019**, *21* (21), 10955–10960. https://doi.org/10.1039/C9CP01915D.
(127) Calabrese, J. C.; Herskovitz, T.; Kinney, J. B. Carbon Dioxide Coordination Chemistry. 5. The Preparation and Structure of the Rhodium Complex Rh(η^1-CO_2)(Cl)(Diars)$_2$. *J. Am. Chem. Soc.* **1983**, *105* (18), 5914–5915. https://doi.org/10.1021/ja00356a033.
(128) Tanaka, H.; Nagao, H.; Peng, S. M.; Tanaka, K. Crystal Structure of Cis-(Carbonyl)(η^1-Carbon Dioxide)Bis(2,2'-Bipyridyl)Ruthenium, an Active Species in Catalytic Carbon Dioxide Reduction Affording Carbon Monoxide and $HCOO^-$. *Organometallics* **1992**, *11* (4), 1450–1451. https://doi.org/10.1021/om00040a010.
(129) Knurr, B. J.; Weber, J. M. Interaction of Nickel with Carbon Dioxide in $[Ni(CO_2)_n]^-$ Clusters Studied by Infrared Spectroscopy. *J. Phys. Chem. A* **2014**, *118* (38), 8753–8757. https://doi.org/10.1021/jp507149u.
(130) Knurr, B. J.; Weber, J. M. Infrared Spectra and Structures of Anionic Complexes of Cobalt with Carbon Dioxide Ligands. *J. Phys. Chem. A* **2014**, *118* (23), 4056–4062. https://doi.org/10.1021/jp503194v.
(131) Aresta, M.; Francesco Nobile, C.; G. Albano, V.; Forni, E.; Manassero, M. New Nickel–Carbon Dioxide Complex: Synthesis, Properties, and Crystallographic Characterization of (Carbon Dioxide)-Bis(Tricyclohexylphosphine)Nickel. *J. Chem. Soc. Chem. Commun.* **1975**, *0* (15), 636–637. https://doi.org/10.1039/C39750000636.
(132) Contreras, L.; Paneque, M.; Sellin, M.; Carmona, E.; J. Pérez, P.; Gutiérrez-Puebla, E.; Monge, A.; Ruiz, C. Novel Carbon Dioxide and Carbonyl Carbonate Complexes of Molybdenum. The X-Ray Structures of *Trans*-$[Mo(CO_2)_2\{HN(CH_2CH_2PMe_2)_2\}(PMe_3)]$ and $[Mo_3(\mu_2\text{-}CO_3)(\mu_2\text{-}O)_2(O)_2(CO)_2(H_2O)(PMe_3)_6]\cdot H_2O$. *New J. Chem.* **2005**, *29* (1), 109–115. https://doi.org/10.1039/B409385B.
(133) Ishida, T.; Hayashi, T.; Mizobe, Y.; Hidai, M. Preparation and Properties of Molybdenum and Tungsten Dinitrogen Complexes. 38. Hydrido-Carbonato, Hydrido-Carbamato, and Carbon Dioxide Complexes of Tungsten Derived from the Carbonyl-Dinitrogen Complex Trans-$[W(CO)(N_2)(Ph_2PCH_2CH_2PPh_2)_2]$. *Inorg. Chem.* **1992**, *31* (22), 4481–4485. https://doi.org/10.1021/ic00048a009.
(134) Thompson, M. C.; Ramsay, J.; Weber, J. M. Interaction of CO_2 with Atomic Manganese in the Presence of an Excess Negative Charge Probed by Infrared Spectroscopy of $[Mn(CO_2)_n]^-$ Clusters. *J. Phys. Chem. A* **2017**, *121* (40), 7534–7542. https://doi.org/10.1021/acs.jpca.7b06870.
(135) Thompson, M. C.; Dodson, L. G.; Weber, J. M. Structural Motifs of $[Fe(CO_2)_n]^-$ Clusters (n = 3–7). *J. Phys. Chem. A* **2017**, *121* (21), 4132–4138. https://doi.org/10.1021/acs.jpca.7b02742.
(136) Pilato, R. S.; Housmekerides, C. E.; Jernakoff, P.; Rubin, D.; Geoffroy, G. L.; Rheingold, A. L. Net [2 + 2] Cycloaddition Reactions of the Oxo Complexes $Cp_2M{=}O$ (M = Mo, W) with Electrophilic Organic and Organometallic Substrates. Formation of Bimetallic μ^2-η^3-CO_2 Complexes. *Organometallics* **1990**, *9* (8), 2333–2341. https://doi.org/10.1021/om00158a034.
(137) Green, A. E.; Justen, J.; Schöllkopf, W.; Gentleman, A. S.; Fielicke, A.; Mackenzie, S. R. IR Signature of Size-Selective CO_2 Activation on Small Platinum Cluster Anions, Pt_n^- (N=4–7). *Angew. Chem.* **2018**, *130* (45), 15038–15042. https://doi.org/10.1002/ange.201809099.

(138) Ricks, A. M.; Brathwaite, A. D.; Duncan, M. A. IR Spectroscopy of Gas Phase $V(CO_2)_n^+$ Clusters: Solvation-Induced Electron Transfer and Activation of CO_2. *J. Phys. Chem. A* **2013**, *117* (45), 11490–11498. https://doi.org/10.1021/jp4089035.
(139) Spreitzer, R. J.; Salvucci, M. E. RUBISCO: Structure, Regulatory Interactions, and Possibilities for a Better Enzyme. *Annu. Rev. Plant Biol.* **2002**, *53* (1), 449–475. https://doi.org/10.1146/annurev.arplant.53.100301.135233.
(140) Peltzer, R. M.; Gauss, J.; Eisenstein, O.; Cascella, M. The Grignard Reaction – Unraveling a Chemical Puzzle. *J. Am. Chem. Soc.* **2020**, *142* (6), 2984–2994. https://doi.org/10.1021/jacs.9b11829.
(141) Sun, X.-L.; Liu, D.-M.; Tian, D.; Zhang, X.-Y.; Wu, W.; Wan, W.-M. The Introduction of the Barbier Reaction into Polymer Chemistry. *Nat. Commun.* **2017**, *8* (1), 1210. https://doi.org/10.1038/s41467-017-01472-w.
(142) Xantheas, S. S.; Ruedenberg, K. Potential Energy Surfaces of Carbon Dioxide. *Int. J. Quantum Chem.* **1994**, *49* (4), 409–427. https://doi.org/10.1002/qua.560490408.
(143) Geppert, W. D.; Naulin, C.; Costes, M. Integral Cross-Section of the $C(^3P_J) + O_2(X^3\Sigma_g^-) \rightarrow CO(X^1\Sigma^+) + O(1D_2)$ Reaction between 0.41 and 12.0 KJ/Mol. *Chem. Phys. Lett.* **2002**, *364* (1), 121–126. https://doi.org/10.1016/S0009-2614(02)01251-4.
(144) Shortridge, R. G.; Lin, M. C. The Dynamics of the $O(^1D_2)+CO(X\ ^1\Sigma^+, V=0)$ Reaction. *J. Chem. Phys.* **1976**, *64* (10), 4076–4085. https://doi.org/10.1063/1.432017.
(145) Feller, D.; Katriel, J.; Davidson, E. R. The Cyclic Isomer of CO_2. *J. Chem. Phys.* **1980**, *73* (9), 4517–4520. https://doi.org/10.1063/1.440689.
(146) Tsukuda, T.; Saeki, M.; Iwata, S.; Nagata, T. Reaction of Negatively-Charged Clusters of Carbon Dioxide with CH_3I: Formation of Novel Molecular Anion $CH_3CO_2I^-$. *J. Phys. Chem. A* **1997**, *101* (28), 5103–5110. https://doi.org/10.1021/jp9708714.
(147) Tsukuda, T.; Nagata, T. Gas-Phase Reaction of Hydrated $CO_2^{\bullet-}$ Anion Radical with CH_3I. *J. Phys. Chem. A* **2003**, *107* (41), 8476–8483. https://doi.org/10.1021/jp0350767.
(148) Herman, J.; Foutch, J. D.; Davico, G. E. Gas-Phase Reactivity of Selected Transition Metal Cations with CO and CO_2 and the Formation of Metal Dications Using a Sputter Ion Source. *J. Phys. Chem. A* **2007**, *111* (13), 2461–2468. https://doi.org/10.1021/jp067777k.
(149) Koyanagi, G. K.; Bohme, D. K. Gas-Phase Reactions of Carbon Dioxide with Atomic Transition-Metal and Main-Group Cations: Room-Temperature Kinetics and Periodicities in Reactivity. *J. Phys. Chem. A* **2006**, *110* (4), 1232–1241. https://doi.org/10.1021/jp0526602.
(150) Sodupe, M.; Branchadell, V.; Rosi, M.; Bauschlicher, C. W. Theoretical Study of $M^+{-}CO_2$ and OM^+CO Systems for First Transition Row Metal Atoms. *J. Phys. Chem. A* **1997**, *101* (42), 7854–7859. https://doi.org/10.1021/jp9711252.
(151) Pápai, I.; Mascetti, J.; Fournier, R. Theoretical Study of the Interaction of the Ti Atom with CO_2: Cleavage of the C−O Bond. *J. Phys. Chem. A* **1997**, *101* (24), 4465–4471. https://doi.org/10.1021/jp970379k.
(152) Hwang, D.-Y.; Mebel, A. M. Ab Initio Study of the Reaction Mechanism of CO_2 with Ti Atom in the Ground and Excited Electronic States. *J. Chem. Phys.* **2002**, *116* (13), 5633–5642. https://doi.org/10.1063/1.1453954.
(153) Sun, Y.; Sun, X.; Huang, X. Reaction of CO_2 with Atomic Transition Metal $M^{+/0/-}$ Ions: A Theoretical Study. *J. Phys. Chem. A* **2018**, *122* (27), 5848–5860. https://doi.org/10.1021/acs.jpca.8b01917.
(154) Andrews, L.; Tague, T. J. Reactions of Pulsed-Laser-Evaporated Be Atoms with CO_2. Infrared Spectra of OCBeO and COBeO in Solid Argon. *J. Am. Chem. Soc.* **1994**, *116* (15), 6856–6859. https://doi.org/10.1021/ja00094a045.
(155) DiGiuseppe, T. G.; Davidovits, P. Boron Atom Reactions. II. Rate Constants with O_2, SO_2, CO_2, and N_2O. *J. Chem. Phys.* **1981**, *74* (6), 3287–3291. https://doi.org/10.1063/1.441534.

(156) Burkholder, T. R.; Andrews, L.; Bartlett, R. J. Reaction of Boron Atoms with Carbon Dioxide: Matrix and Ab Initio Calculated Infrared Spectra of OBCO. *J. Phys. Chem.* **1993**, *97* (14), 3500–3503.
(157) Sakai, S. Theoretical Studies on the Chemical Reaction Mechanisms of an Aluminum Atom with Carbon Dioxide Molecule. *J. Phys. Chem.* **1992**, *96* (1), 131–135. https://doi.org/10.1021/j100180a029.
(158) Clemmer, D. E.; Weber, M. E.; Armentrout, P. B. Reactions of $Al^+(^1S)$ with NO_2, N_2O, and CO_2: Thermochemistry of AlO and AlO^+. *J. Phys. Chem.* **1992**, *96* (26), 10888–10893. https://doi.org/10.1021/j100205a052.
(159) Kilpatrick, A. F. R.; Cloke, F. G. N. Reductive Deoxygenation of CO_2 by a Bimetallic Titanium Bis(Pentalene) Complex. *Chem. Commun.* **2014**, *50* (21), 2769–2771. https://doi.org/10.1039/C3CC48379G.
(160) Wang, T.-F.; Hwu, C.-C.; Tsai, C.-W.; Lin, K.-J. Formation of a Carbon Dioxide Complex of Rhenium via Formal Oxidation of a Carbon Monoxide Ligand. *Organometallics* **1997**, *16* (14), 3089–3090. https://doi.org/10.1021/om9702845.
(161) Wu, X.; Zhao, L.; Jin, J.; Pan, S.; Li, W.; Jin, X.; Wang, G.; Zhou, M.; Frenking, G. Observation of Alkaline Earth Complexes $M(CO)_8$ (M = Ca, Sr, or Ba) That Mimic Transition Metals. *Science* **2018**, *361* (6405), 912–916. https://doi.org/10.1126/science.aau0839.
(162) Wu, X.; Zhao, L.; Jiang, D.; Fernández, I.; Berger, R.; Zhou, M.; Frenking, G. Barium as Honorary Transition Metal in Action: Experimental and Theoretical Study of $Ba(CO)^+$ and $Ba(CO)^-$. *Angew. Chem. Int. Ed.* **2018**, *57* (15), 3974–3980. https://doi.org/10.1002/anie.201713002.
(163) Esrafilzadeh, D.; Zavabeti, A.; Jalili, R.; Atkin, P.; Choi, J.; Carey, B. J.; Brkljača, R.; O'Mullane, A. P.; Dickey, M. D.; Officer, D. L.; MacFarlane, D. R.; Daeneke, T.; Kalantar-Zadeh, K. Room Temperature CO_2 Reduction to Solid Carbon Species on Liquid Metals Featuring Atomically Thin Ceria Interfaces. *Nat. Commun.* **2019**, *10* (1), 865. https://doi.org/10.1038/s41467-019-08824-8.
(164) Yuasa, S.; Isoda, H. Ignition and Combustion of Metals in a Carbon Dioxide Stream. *Symp. Int. Combust.* **1989**, *22* (1), 1635–1641. https://doi.org/10.1016/S0082-0784(89)80175-4.
(165) Reddy, K. P.; Dama, S.; Mhamane, N. B.; Ghosalya, M. K.; Raja, T.; Satyanarayana, C. V.; Gopinath, C. S. Molybdenum Carbide Catalyst for the Reduction of CO_2 to CO: Surface Science Aspects by NAPPES and Catalysis Studies. *Dalton Trans.* **2019**, *48* (32), 12199–12209. https://doi.org/10.1039/C9DT01774G.
(166) Porosoff, M. D.; Kattel, S.; Li, W.; Liu, P.; Chen, J. G. Identifying Trends and Descriptors for Selective CO_2 Conversion to CO over Transition Metal Carbides. *Chem. Commun.* **2015**, *51* (32), 6988–6991. https://doi.org/10.1039/C5CC01545F.
(167) Hale, R. D.; Chan, C.-C.; Weisbecker, C. S.; Attygalle, A. B. Gas-Phase Fragmentation of Metal Adducts of Alkali-Metal Oxalate Salts. *J. Mass Spectrom.* **2014**, *49* (3), 195–200. https://doi.org/10.1002/jms.3322.
(168) Castro, L.; Labouille, S.; Kindra, D. R.; Ziller, J. W.; Nief, F.; Evans, W. J.; Maron, L. Insights into the Mechanism of Reaction of $[(C_5Me_5)_2Sm^{II}(Thf)_2]$ with CO_2 and COS by DFT Studies. *Chem. – Eur. J.* **2012**, *18* (25), 7886–7895. https://doi.org/10.1002/chem.201103192.
(169) Willauer, A. R.; Toniolo, D.; Fadaei-Tirani, F.; Yang, Y.; Laurent, M.; Mazzanti, M. Carbon Dioxide Reduction by Dinuclear Yb(II) and Sm(II) Complexes Supported by Siloxide Ligands. *Dalton Trans.* **2019**, *48* (18), 6100–6110. https://doi.org/10.1039/C9DT00554D.
(170) Formanuik, A.; Ortu, F.; Inman, C. J.; Kerridge, A.; Castro, L.; Maron, L.; Mills, D. P. Concomitant Carboxylate and Oxalate Formation From the Activation of CO_2 by a Thorium(III) Complex. *Chem. Weinh. Bergstr. Ger.* **2016**, *22* (50), 17976–17979. https://doi.org/10.1002/chem.201604622.

(171) Kégl, T.; Ponec, R.; Kollár, L. Theoretical Insights into the Nature of Nickel−Carbon Dioxide Interactions in $Ni(PH_3)_2(\eta^2\text{-}CO_2)$. *J. Phys. Chem. A* **2011**, *115* (45), 12463–12473. https://doi.org/10.1021/jp201140h.
(172) Guainazzi, M.; Filardo, G.; Silvestri, G.; Gambino, S.; Ercoli, R. Process for the Preparation of Squaric Acid by Reductive Cyclotetramerization of Carbon Monoxide. US3833489A, September 3, 1974.
(173) Barber, J. J. Process for the Preparation of Squaric Acid by the Electrolysis of Carbon Monoxide in Anhydrous Aliphatic Nitrile Solvent Media. US4461681A, July 24, 1984.
(174) Barber, J. J. Process for the Recovery of High Purity Squaric Acid. US4523980A, June 18, 1985.
(175) Frey, A. S.; Cloke, F. G. N.; Hitchcock, P. B.; Day, I. J.; Green, J. C.; Aitken, G. Mechanistic Studies on the Reductive Cyclooligomerisation of CO by U(III) Mixed Sandwich Complexes; the Molecular Structure of $[(U(\eta\text{-}C_8H_6\{Si^iPr_3\text{-}1,4\}_2)(\eta\text{-}Cp^*)]_2(\mu\text{-}\eta^1\text{:}\eta^1\text{-}C_2O_2)$. *J. Am. Chem. Soc.* **2008**, *130* (42), 13816–13817. https://doi.org/10.1021/ja8059792.
(176) McKay, D.; Frey, A. S. P.; Green, J. C.; Cloke, F. G. N.; Maron, L. Computational Insight into the Reductive Oligomerisation of CO at Uranium(III) Mixed-Sandwich Complexes. *Chem. Commun.* **2012**, *48* (34), 4118–4120. https://doi.org/10.1039/C2CC30864A.
(177) Menges, F. S.; Perez, E. H.; Edington, S. C.; Duong, C. H.; Yang, N.; Johnson, M. A. Integration of High-Resolution Mass Spectrometry with Cryogenic Ion Vibrational Spectroscopy. *J. Am. Soc. Mass Spectrom.* **2019**, *30* (9), 1551–1557. https://doi.org/10.1007/s13361-019-02238-y.
(178) Frisch, M. J.; Trucks, G. W.; Schlegel, H. B.; Scuseria, G. E.; Robb, M. A.; Cheeseman, J. R.; Scalmani, G.; Barone, V.; Petersson, G. A.; Nakatsuji, H.; Li, X.; Caricato, M.; Marenich, A. V.; Bloino, J.; Janesko, B. G.; Gomperts, R.; Mennucci, B.; Hratchian, H. P.; Ortiz, J. V.; Izmaylov, A. F.; Sonnenberg, J. L.; Williams-Young, D.; Ding, F.; Lipparini, F.; Egidi, F.; Goings, J.; Peng, B.; Petrone, A.; Henderson, T.; Ranasinghe, D.; Zakrzewski, V. G.; Gao, J.; Rega, N.; Zheng, G.; Liang, W.; Hada, M.; Ehara, M.; Toyota, K.; Fukuda, R.; Hasegawa, J.; Ishida, M.; Nakajima, T.; Honda, Y.; Kitao, O.; Nakai, H.; Vreven, T.; Throssell, K.; Montgomery, J. A., Jr; Peralta, J. E.; Ogliaro, F.; Bearpark, M.; Heyd, J. J.; Brothers, E.; Kudin, K. N.; Staroverov, V. N.; Keith, T. A.; Kobayashi, R.; Normand, J.; Raghavachari, K.; Rendell, A.; Burant, J. C.; Iyengar, S. S.; Tomasi, J.; Cossi, M.; Milliam, J. M.; Klene, M.; Adamo, C.; Cammi, R.; Ochterski, J. W.; Martin, R. L.; Morokuma, K.; Farkas, O.; Foresman, J. B.; Fox, D. J. Gaussian 16, Revision A. 03, Gaussian. *Inc Wallingford CT* **2016**.
(179) Valiev, M.; Bylaska, E. J.; Govind, N.; Kowalski, K.; Straatsma, T. P.; Van Dam, H. J. J.; Wang, D.; Nieplocha, J.; Apra, E.; Windus, T. L.; de Jong, W. A. NWChem: A Comprehensive and Scalable Open-Source Solution for Large Scale Molecular Simulations. *Comput. Phys. Commun.* **2010**, *181* (9), 1477–1489. https://doi.org/10.1016/j.cpc.2010.04.018.
(180) Skripnikov, L. V. *Chemissian Version 4.52, Visualization Computer Program*; 2017.
(181) Feller, D. The Role of Databases in Support of Computational Chemistry Calculations. *J. Comput. Chem.* **1996**, *17* (13), 1571–1586. https://doi.org/10.1002/(SICI)1096-987X(199610)17:13<1571::AID-JCC9>3.0.CO;2-P.
(182) Schuchardt, K. L.; Didier, B. T.; Elsethagen, T.; Sun, L.; Gurumoorthi, V.; Chase, J.; Li, J.; Windus, T. L. Basis Set Exchange: A Community Database for Computational Sciences. *J. Chem. Inf. Model.* **2007**, *47* (3), 1045–1052. https://doi.org/10.1021/ci600510j.
(183) Pritchard, B. P.; Altarawy, D.; Didier, B.; Gibson, T. D.; Windus, T. L. New Basis Set Exchange: An Open, Up-to-Date Resource for the Molecular Sciences Community. *J. Chem. Inf. Model.* **2019**, *59* (11), 4814–4820. https://doi.org/10.1021/acs.jcim.9b00725.
(184) Dole, M.; Mack, L. L.; Hines, R. L.; Mobley, R. C.; Ferguson, L. D.; Alice, M. B. Molecular Beams of Macroions. *J. Chem. Phys.* **1968**, *49* (5), 2240–2249. https://doi.org/10.1063/1.1670391.
(185) Iribarne, J. V.; Thomson, B. A. On the Evaporation of Small Ions from Charged Droplets. *J. Chem. Phys.* **1976**, *64*, 2287–2294. https://doi.org/10.1063/1.432536.

(186) Smith, D. P. H. The Electrohydrodynamic Atomization of Liquids. *IEEE Trans. Ind. Appl.* **1986**, *IA-22* (3), 527–535. https://doi.org/10.1109/TIA.1986.4504754.
(187) Hayati, I.; Bailey, A. I.; Tadros, Th. F. Investigations into the Mechanisms of Electrohydrodynamic Spraying of Liquids: I. Effect of Electric Field and the Environment on Pendant Drops and Factors Affecting the Formation of Stable Jets and Atomization. *J. Colloid Interface Sci.* **1987**, *117* (1), 205–221. https://doi.org/10.1016/0021-9797(87)90185-8.
(188) Ikonomou, M. G.; Blades, A. T.; Kebarle, Paul. Electrospray-Ion Spray: A Comparison of Mechanisms and Performance. *Anal. Chem.* **1991**, *63* (18), 1989–1998. https://doi.org/10.1021/ac00018a017.
(189) Tang, Liang.; Kebarle, Paul. Effect of the Conductivity of the Electrosprayed Solution on the Electrospray Current. Factors Determining Analyte Sensitivity in Electrospray Mass Spectrometry. *Anal. Chem.* **1991**, *63* (23), 2709–2715. https://doi.org/10.1021/ac00023a009.
(190) Mora, J. F. D. L. The Effect of Charge Emission from Electrified Liquid Cones. *J. Fluid Mech.* **1992**, *243*, 561–574. https://doi.org/10.1017/S0022112092002829.
(191) Tang, Liang.; Kebarle, Paul. Dependence of Ion Intensity in Electrospray Mass Spectrometry on the Concentration of the Analytes in the Electrosprayed Solution. *Anal. Chem.* **1993**, *65* (24), 3654–3668. https://doi.org/10.1021/ac00072a020.
(192) Gomez, A.; Tang, K. Charge and Fission of Droplets in Electrostatic Sprays. *Phys. Fluids* **1994**, *6* (1), 404–414. https://doi.org/10.1063/1.868037.
(193) Kebarle, P. A Brief Overview of the Present Status of the Mechanisms Involved in Electrospray Mass Spectrometry. *J. Mass Spectrom.* **2000**, *35* (7), 804–817. https://doi.org/10.1002/1096-9888(200007)35:7<804::AID-JMS22>3.0.CO;2-Q.
(194) Lord Rayleigh, F. R. S. XX. On the Equilibrium of Liquid Conducting Masses Charged with Electricity. *Lond. Edinb. Dublin Philos. Mag. J. Sci.* **1882**, *14* (87), 184–186. https://doi.org/10.1080/14786448208628425.
(195) Miller, P. E.; Denton, M. B. The Quadrupole Mass Filter: Basic Operating Concepts. *J. Chem. Educ.* **1986**, *63* (7), 617. https://doi.org/10.1021/ed063p617.
(196) March, R. E. An Introduction to Quadrupole Ion Trap Mass Spectrometry. *J. Mass Spectrom.* **1997**, *32* (4), 351–369. https://doi.org/10.1002/(SICI)1096-9888(199704)32:4<351::AID-JMS512>3.0.CO;2-Y.
(197) Gioumousis, G.; Stevenson, D. P. Reactions of Gaseous Molecule Ions with Gaseous Molecules. V. Theory. *J. Chem. Phys.* **1958**, *29* (2), 294–299. https://doi.org/10.1063/1.1744477.
(198) Su, T.; Bowers, M. T. Ion-Polar Molecule Collisions. Proton Transfer Reactions of H_3^+ and CH_5^+ to the Geometric Isomers of Difluoroethylene, Dichloroethylene, and Difluorobenzene. *J. Am. Chem. Soc.* **1973**, *95* (5), 1370–1373. https://doi.org/10.1021/ja00786a003.
(199) Su, T.; Bowers, M. T. Theory of Ion-Polar Molecule Collisions. Comparison with Experimental Charge Transfer Reactions of Rare Gas Ions to Geometric Isomers of Difluorobenzene and Dichloroethylene. *J. Chem. Phys.* **1973**, *58* (7), 3027–3037. https://doi.org/10.1063/1.1679615.
(200) Shukla, A. K.; Futrell, J. H. Tandem Mass Spectrometry: Dissociation of Ions by Collisional Activation. *J. Mass Spectrom.* **2000**, *35* (9), 1069–1090. https://doi.org/10.1002/1096-9888(200009)35:9<1069::AID-JMS54>3.0.CO;2-C.
(201) Göpel, W.; Hesse, J.; Zemel, J. N. *Sensors, Optical Sensors*; John Wiley & Sons, 2008.
(202) Miller, G. B. S. Intrinsic Reactivity of Reduced Mg and Zn with CO_2 – Relationships to Biological and Non-Biological C–C Bond Formation. PhD thesis, University of Oslo, Department of Chemistry, 2018.
(203) Błaziak, K.; Miller, G. B. S.; Ryding, M. J.; Uggerud, E. Reaction Model for the Formation of Benzene from Benzoates and Grignard Reagents. *Eur. J. Org. Chem.* **2017**, *2017* (29), 4272–4276. https://doi.org/10.1002/ejoc.201700816.
(204) Armentrout, P. B. Mass Spectrometry—Not Just a Structural Tool: The Use of Guided Ion Beam Tandem Mass Spectrometry to Determine Thermochemistry. *J. Am. Soc. Mass Spectrom.* **2002**, *13* (5), 419–434. https://doi.org/10.1016/S1044-0305(02)00347-1.

(205) Rodgers, M. T.; Ervin, K. M.; Armentrout, P. B. Statistical Modeling of Collision-Induced Dissociation Thresholds. *J. Chem. Phys.* **1997**, *106* (11), 4499–4508. https://doi.org/10.1063/1.473494.
(206) Narancic, S.; Bach, A.; Chen, P. Simple Fitting of Energy-Resolved Reactive Cross Sections in Threshold Collision-Induced Dissociation (T-CID) Experiments. *J. Phys. Chem. A* **2007**, *111* (30), 7006–7013. https://doi.org/10.1021/jp072092l.
(207) Goldberg, D. E. *Genetic Algorithms in Search, Optimization, and Machine Learning*, 1 edition.; Addison-Wesley Professional: Reading, Mass, 1989.
(208) Chantry, P. J. Doppler Broadening in Beam Experiments. *J. Chem. Phys.* **1971**, *55* (6), 2746. https://doi.org/10.1063/1.1676489.
(209) Graul, S. T.; Squires, R. R. Gas-Phase Acidities Derived from Threshold Energies for Activated Reactions. *J. Am. Chem. Soc.* **1990**, *112* (7), 2517–2529. https://doi.org/10.1021/ja00163a007.
(210) Dawson, P. H. A Study of the Collision-Induced Dissociation of $C_2H_5OH_2^+$ Using Various Target Gases. *Int. J. Mass Spectrom. Ion Phys.* **1983**, *50* (3), 287–297. https://doi.org/10.1016/0020-7381(83)87006-5.
(211) Bouchoux, G.; Hoppilliard, Y. Role of Ion-Neutral Complexes during Acid-Catalyzed Dehydration of Ethanol in the Gas Phase. *J. Am. Chem. Soc.* **1990**, *112* (25), 9110–9115. https://doi.org/10.1021/ja00181a012.
(212) Fairley, D. A.; Scott, G. B. I.; Freeman, C. G.; Maclagan, R. G. A. R.; McEwan, M. J. $C_2H_7O^+$ Potential Surface and Ion−Molecule Association between H_3O^+ and C_2H_4. *J. Phys. Chem. A* **1997**, *101* (15), 2848–2851. https://doi.org/10.1021/jp963294c.
(213) More, M. B.; Ray, D.; Armentrout, P. B. Intrinsic Affinities of Alkali Cations for 15-Crown-5 and 18-Crown-6: Bond Dissociation Energies of Gas-Phase M^+−Crown Ether Complexes. *J. Am. Chem. Soc.* **1999**, *121* (2), 417–423. https://doi.org/10.1021/ja9823159.
(214) Armentrout, P. B.; Austin, C. A.; Rodgers, M. T. Alkali Metal Cation Interactions with 15-Crown-5 in the Gas Phase: Revisited. *J. Phys. Chem. A* **2014**, *118* (37), 8088–8097. https://doi.org/10.1021/jp4116172.
(215) Harvey, D. J.; Hunter, A. P.; Bateman, R. H.; Brown, J.; Critchley, G. Relationship between In-Source and Post-Source Fragment Ions in the Matrix-Assisted Laser Desorption (Ionization) Mass Spectra of Carbohydrates Recorded with Reflectron Time-of-Flight Mass Spectrometers. *Int. J. Mass Spectrom.* **1999**, *188* (1), 131–146. https://doi.org/10.1016/S1387-3806(99)00014-7.
(216) Møller, Chr.; Plesset, M. S. Note on an Approximation Treatment for Many-Electron Systems. *Phys. Rev.* **1934**, *46* (7), 618–622. https://doi.org/10.1103/PhysRev.46.618.
(217) Čížek, J. On the Correlation Problem in Atomic and Molecular Systems. Calculation of Wavefunction Components in Ursell-Type Expansion Using Quantum-Field Theoretical Methods. *J. Chem. Phys.* **1966**, *45* (11), 4256–4266. https://doi.org/10.1063/1.1727484.
(218) Purvis, G. D.; Bartlett, R. J. A Full Coupled-cluster Singles and Doubles Model: The Inclusion of Disconnected Triples. *J. Chem. Phys.* **1982**, *76* (4), 1910–1918. https://doi.org/10.1063/1.443164.
(219) Pople, J. A.; Head-Gordon, M.; Raghavachari, K. Quadratic Configuration Interaction. A General Technique for Determining Electron Correlation Energies. *J. Chem. Phys.* **1987**, *87* (10), 5968–5975. https://doi.org/10.1063/1.453520.
(220) Langhoff, S. R.; Davidson, E. R. Configuration Interaction Calculations on the Nitrogen Molecule. *Int. J. Quantum Chem.* **1974**, *8* (1), 61–72. https://doi.org/10.1002/qua.560080106.
(221) Lee, T. J.; Taylor, P. R. A Diagnostic for Determining the Quality of Single-Reference Electron Correlation Methods. *Int. J. Quantum Chem.* **1989**, *36* (S23), 199–207. https://doi.org/10.1002/qua.560360824.
(222) Townsend, J.; Kirkland, J. K.; Vogiatzis, K. D. Chapter 3 - Post-Hartree-Fock Methods: Configuration Interaction, Many-Body Perturbation Theory, Coupled-Cluster Theory. In *Mathematical Physics in Theoretical Chemistry*; Blinder, S. M., House, J. E., Eds.; Developments in Physical & Theoretical Chemistry; Elsevier, 2019; pp 63–117. https://doi.org/10.1016/B978-0-12-813651-5.00003-6.

(223) Becke, A. D. Density-Functional Exchange-Energy Approximation with Correct Asymptotic Behavior. *Phys. Rev. A* **1988**, *38* (6), 3098–3100. https://doi.org/10.1103/PhysRevA.38.3098.
(224) Lee, C.; Yang, W.; Parr, R. G. Development of the Colle-Salvetti Correlation-Energy Formula into a Functional of the Electron Density. *Phys. Rev. B* **1988**, *37* (2), 785–789. https://doi.org/10.1103/PhysRevB.37.785.
(225) Curtiss, L. A.; Redfern, P. C.; Raghavachari, K. Gaussian-4 Theory. *J. Chem. Phys.* **2007**, *126* (8), 084108. https://doi.org/10.1063/1.2436888.
(226) Curtiss, L. A.; Redfern, P. C.; Raghavachari, K. Assessment of Gaussian-4 Theory for Energy Barriers. *Chem. Phys. Lett.* **2010**, *499* (1–3), 168–172. https://doi.org/10.1016/j.cplett.2010.09.012.
(227) Boys, S. F.; Bernardi, F. The Calculation of Small Molecular Interactions by the Differences of Separate Total Energies. Some Procedures with Reduced Errors. *Mol. Phys.* **1970**, *19* (4), 553–566. https://doi.org/10.1080/00268977000101561.
(228) Simon, S.; Duran, M.; Dannenberg, J. J. How Does Basis Set Superposition Error Change the Potential Surfaces for Hydrogen-bonded Dimers? *J. Chem. Phys.* **1996**, *105* (24), 11024–11031. https://doi.org/10.1063/1.472902.
(229) van Duijneveldt, F. B.; van Duijneveldt-van de Rijdt, J. G. C. M.; van Lenthe, J. H. State of the Art in Counterpoise Theory. *Chem. Rev.* **1994**, *94* (7), 1873–1885. https://doi.org/10.1021/cr00031a007.
(230) Xantheas, S. S. On the Importance of the Fragment Relaxation Energy Terms in the Estimation of the Basis Set Superposition Error Correction to the Intermolecular Interaction Energy. *J. Chem. Phys.* **1996**, *104* (21), 8821–8824. https://doi.org/10.1063/1.471605.
(231) Nemukhin, A. V.; Weinhold, F. Natural Bond Orbitals in Multiconfigurational Expansions: Local Treatment of Electron Correlation in Molecules. *J. Chem. Phys.* **1992**, *97* (2), 1095–1108. https://doi.org/10.1063/1.463289.
(232) Dean, P. A. W. The Oxalate Dianion, $C_2O_4^{2-}$: Planar or Nonplanar? *J. Chem. Educ.* **2012**, *89* (3), 417–418. https://doi.org/10.1021/ed200202r.
(233) Jestilä, J. S.; Denton, J. K.; Perez, E. H.; Khuu, T.; Aprà, E.; Xantheas, S. S.; Johnson, M. A.; Uggerud, E. Characterization of the Alkali Metal Oxalates ($MC_2O_4^-$) and Their Formation by CO_2 Reduction via the Alkali Metal Carbonites (MCO_2^-). *Phys. Chem. Chem. Phys.* **2020**, *22* (14), 7460–7473. https://doi.org/10.1039/D0CP00547A.
(234) Kaupp, M.; Schleyer, P. v. R.; Stoll, H.; Preuss, H. Pseudopotential Approaches to Ca, Sr, and Ba Hydrides. Why Are Some Alkaline Earth MX_2 Compounds Bent? *J. Chem. Phys.* **1991**, *94* (2), 1360–1366. https://doi.org/10.1063/1.459993.

8 Papers

Paper I.

PCCP

ROYAL SOCIETY OF CHEMISTRY

PAPER

View Article Online
View Journal | View Issue

Cite this: *Phys. Chem. Chem. Phys.*, 2020, **22**, 7460

Characterization of the alkali metal oxalates ($MC_2O_4^-$) and their formation by CO_2 reduction *via* the alkali metal carbonites (MCO_2^-)†

Joakim S. Jestilä, [a] Joanna K. Denton, [b] Evan H. Perez, [b] Thien Khuu, [b] Edoardo Aprà, [c] Sotiris S. Xantheas, [de] Mark A. Johnson [b] and Einar Uggerud *[a]

The reduction of carbon dioxide to oxalate has been studied by experimental Collisionally Induced Dissociation (CID) and vibrational characterization of the alkali metal oxalates, supplemented by theoretical electronic structure calculations. The critical step in the reductive process is the coordination of CO_2 to an alkali metal anion, forming a metal carbonite MCO_2^- able to subsequently receive a second CO_2 molecule. While the energetic demand for these reactions is generally low, we find that the degree of activation of CO_2 in terms of charge transfer and transition state energies is the highest for lithium and systematically decreases down the group (M = Li–Cs). This is correlated to the strength of the binding interaction between the alkali metal and CO_2, which can be related to the structure of the oxalate moiety within the product metal complexes evolving from a planar to a staggered conformer with increasing atomic number of the interacting metal. Similar structural changes are observed for crystalline alkali metal oxalates, although the $C_2O_4^{2-}$ moiety is in general more planar in these, a fact that is attributed to the increased number of interacting alkali metal cations compared to the gas-phase ions.

Received 31st January 2020,
Accepted 10th March 2020

DOI: 10.1039/d0cp00547a

rsc.li/pccp

I. Introduction

While methanol and carbon monoxide are widely used as C1 chemical feedstocks, methane and carbon dioxide have found limited uses as of today.[1–4] The utilization of simple molecular building blocks such as CO_2 in direct synthesis is of significant importance, as it has the potential to reduce the waste-to-product ratio of industrial processes by providing a more atom-efficient route to the desired products.[5–9] However, the stability and inertness of CO_2 pose significant challenges in terms of its chemical transformation. Consequently, although it already has various technological and chemical applications,[10–13] a significant fraction of these simply release it into the atmosphere in its original state at the end of the process.[14–16] Chemical transformation by reduction of CO_2 to oxalate,

$$2CO_2 + 2e^- \rightarrow C_2O_4^{2-} \quad (1)$$

has received much interest in recent years. It is most often carried out using oxophilic, electron-poor transition metals or lanthanide complexes.[17–23] This reaction can formally be thought of as either a two-step one-electron reduction, followed by the coupling of the reduced $CO_2^{\bullet-}$ species,

$$2CO_2 + 2e^- \rightarrow 2CO_2^{\bullet-} \quad (2)$$

$$CO_2^{\bullet-} + CO_2^{\bullet-} \rightarrow C_2O_4^{2-}, \quad (3)$$

or alternatively a one-step two-electron reduction followed by nucleophilic attack of CO_2^{2-} on the neutral counterpart,

$$CO_2 + 2e^- \rightarrow CO_2^{2-} \quad (4)$$

$$CO_2^{2-} + CO_2 \rightarrow C_2O_4^{2-}. \quad (5)$$

[a] *Department of Chemistry and Hylleraas Centre for Quantum Molecular Sciences, University of Oslo, P.O. Box 1033, Blindern, Oslo N-0135, Norway. E-mail: einar.uggerud@kjemi.uio.no*
[b] *Sterling Chemistry Laboratory, Yale University, New Haven, Connecticut 06520, USA*
[c] *Environmental Molecular Sciences Laboratory, Pacific Northwest National Laboratory, P.O. Box 999, Richland, Washington 99352, USA*
[d] *Advanced Computing, Mathematics and Data Division, Pacific Northwest National Laboratory, 902 Battelle Boulevard, P.O. Box 999, MS K1-83, Richland, Washington, USA*
[e] *Department of Chemistry, University of Washington, Seattle, Washington 98195, USA*

† Electronic supplementary information (ESI) available: SI-A. Mass spectra of oxalic acid and metal chlorides and hydroxides. SI-B. Validation of estimated threshold energies by known reaction energies. SI-C. Molecular orbitals of the alkali metals and metal carbonites. SI-D. Basis set superposition errors with fragment relaxation energy corrections. SI-E. Computational modeling of the unimolecular MOx^- dissociation. SI-F. Relative stabilities of the oxalate dianion conformers in different solvents. SI-G. Alkali metal carbonite (MCO_2^-) C(1s) energies and carboxylation barriers. SI-H. Alkali metal oxalate crystal structures. SI-I. Calculated IR spectra [MP2/def2-TZVPPD] for $MC_2O_4^-$. SI-J. Cartesian coordinates for the MCO_2^- geometries optimized at the [CCSD(T)/def2-TZVPPD] level of theory. SI-K. Cartesian coordinates for [MP2/def2-TZVPPD] optimized species formed during MOx^- dissociation. See DOI: 10.1039/d0cp00547a

Carbon dioxide has a negative electron affinity,[24–26] and its reduced intermediates must therefore be stabilized. This can be achieved through interactions with a metal,

$$CO_2 + M^- \rightarrow MCO_2^- \quad (6)$$

$$MCO_2^- + CO_2 \rightarrow MC_2O_4^-. \quad (7)$$

Here, M may represent a metal cathode, as for example in electrochemical reduction,[27–30] a coordinated metal in the case of reduction by organometallic complexes,[17–23] or simply a metal atom when isolated as a gas-phase species.[31–36] Of particular importance for the reduction reaction in terms of selectivity is the structure and electronic properties of the metal-coordinated CO_2 (eqn (6)), which constitutes the first intermediate in the formation of a covalent (C–C) bond. CO_2 is a versatile ligand, and several of its coordination modes have been described and characterized.[33–41] Although several recent studies have focused on transition or lanthanide metal catalysts, it has been shown that alkali metal atoms spontaneously reduce CO_2, forming metal–carbon dioxide complexes, $M^+CO_2^-$ and $(M^+)_2CO_2^{2-}$, as well as metal–oxalates, $M^+C_2O_4^-$ and $(M^+)_2C_2O_4^{2-}$.[42–45] The critical step in these reactions is the reduction of CO_2 to $CO_2^{\bullet-}$ by a neutral metal atom. A second metal atom is needed for the reduction to the oxalate dianion. The analogous two-electron reduction of CO_2 to oxalate stimulated by a single alkali metal anion has been studied through the corresponding reverse process, namely the decarboxylation of anionic metal oxalates, $MC_2O_4^-$.[46–48] The MCO_2^- anions formed by decarboxylation of $MC_2O_4^-$ can be formally viewed as complexes between carbonite, CO_2^{2-}, and a singly charged metal cation, M^+, the former assumed to be an important intermediate in the reductive activation of carbon dioxide to carbon monoxide, formic acid, methanol, formaldehyde or other products.[49–51]

The gas-phase oxalate dianion, $C_2O_4^{2-}$, hereafter denoted as Ox^{2-}, is unstable with respect to electron detachment due to Coulombic repulsion, but can be stabilized by a minimum of three water molecules.[52,53] The ion has a C–C single bond in the range 1.54–1.57 Å with a rotational barrier of 8–25 kJ mol^{-1}, depending on the local environment.[54–56] It is widely accepted that the most stable conformer in solution is staggered or slightly twisted, having D_{2d} or D_2/C_2 symmetries, respectively.[54,55,57–61] Similar geometries are adopted by Ox^{2-} when coordinated by metals, as observed in the crystal structures reported in the course of spectroscopic studies of solid and aqueous alkali metal oxalates, $M_2C_2O_4$, M = Li–Cs.[57,61–65] In general, it is seen that the planarity between the alkali metal cations and the oxalate anions in the crystals decreases down the alkali metal group. Thus, the interaction with a suitably polarizing metal, such as the lighter alkali metals Li–K, reduces the Coulombic repulsion between the two carboxylate groups sufficiently to allow for planarity in the oxalate scaffold.[54,55] Alternatively, the degree of planarity can be rationalized by noting that lighter metals fit better within the Ox^{2-} bite and interact more strongly with the anion.[54,55]

In this study we aim to characterize the structures of alkali metal oxalate complexes, $MC_2O_4^-$, as products of two-electron CO_2 reduction mediated by single metal anions, with particular attention on their connection to the structures of the intermediate metal carbonites, MCO_2^-. In addition, we examine whether the structure of oxalate in the solids is due to a crystal-packing effect, or is intrinsic to the nature of the coordinating ligand. This characterization is achieved by analyzing the results of both cryogenic ion vibrational spectroscopy and CID mass spectrometry with electronic structure calculations. With this joint experimental–theoretical approach, we reveal the factors that control the degree of carbon dioxide activation by the alkali metals.

II. Methods

a. Mass spectrometry

The formation of the metal oxalate complexes ($MC_2O_4^-$, MOx^-) was accomplished by electrospraying solutions with 1.0–4.0 mM oxalic acid and 1.0–6.0 mM metal chloride (M = Li, Rb and Cs) or metal hydroxide (M = Na and K). We used a Waters Micromass QTOF 2 MS with a modified custom collision gas inlet for precise control of the collision induced dissociation (CID) conditions. The capillary and time-of-flight detector were operated at 3 and −3 kV, and the multichannel plate detector was kept between 1.9 and 2.3 kV. The source and desolvation temperatures were 100 and 150 °C, respectively. The metal oxalate ions, MOx^-, were mass selected and subjected to CID under 2.0×10^{-4} mbar argon pressure in the collision cell. Breakdown curves were acquired by varying the collision energy during this process and used to estimate the binding energies of the metal oxalates and their metal carbonite fragments. In order to validate the threshold energies estimated by linear extrapolation of the breakdown curves, we applied the same methodology to two systems with well-characterized dissociation thresholds, namely protonated ethanol and deprotonated benzoic acid. Our procedure yields similar values to those reported in the literature.[66–68] More details are available in the ESI.† The uncertainties in the threshold energies due to the kinetic and thermal shifts as well as the kinetic energy release associated with the dissociation reactions are difficult to quantify for our experimental setup. For this reason we only report the threshold energies with the numerical uncertainty associated with the extrapolation procedure, ranging from 5–45 kJ mol^{-1}.

b. Cryogenic ion vibrational spectroscopy

The gas-phase metal oxalate vibrational spectra were obtained using the Yale hybrid Orbitrap/time-of-flight photofragmentation mass spectrometer described previously.[69,70] $M^+Oxalate^{2-}$ (M = Li, Na, K, Rb, Cs) ions were extracted from ~2 mM solutions of oxalic acid and solid metal hydroxide salts (obtained from Sigma Aldrich with no further purification and dissolved in methanol or methanol:H_2O mixtures) using electrospray ionization and mass selected in the quadrupole of a modified[69] Thermo Fisher Scientific Orbitrap Velos Pro. The selected ions were then accumulated in a (20–50 K) Paul trap where they were cooled by a buffer gas mixture of He and (~10%) hydrogen to provide the "messenger tags" (D_2 for Li, K, and Cs; H_2 for Na and Rb) weakly bound to the parent anions. The hydrogen molecules provide a low energy photofragmentation channel, which was

monitored to collect linear (*i.e.*, one-photon) vibrational spectra with a minimum of structural perturbation. The spectrum of D-oxalate was reproduced from a previous report.[71] In that case, a ~1 mM solution of oxalic acid in methanol was electrosprayed and deuterated by leaking D_2O vapor into the second differentially pumped stage before the condensation and photofragmentation of $2H_2$ tags.

c. Computational

We employed the Gaussian 09/16[72] software for the computational studies with the B3LYP density functional, the G4 composite method and second order Møller–Plesset perturbation theory (MP2),[73–77] and the NWChem[78] suite of electronic structure software for the Coupled Cluster Singles and Doubles with a perturbational estimate of triple excitations [CCSD(T)][79–81] calculations. For the MP2 and CCSD(T) calculations, the frozen-core approximation was deemed unsuitable due to certain alkali metal core orbitals being higher in energy than the lowest energy CO_2 valence orbitals in the complexes. This issue has been previously noted by Rassolov and coworkers,[82] as well as Petrie,[83] both suggesting feasible approaches to separate the core from the valence electrons. We chose to rearrange the active space manually on the basis of visual inspection of the orbitals. The frozen core of Na was therefore adjusted to the $[1s^2 2s^2]$ electrons and that of K to the $[1s^2 2s^2 2p^6 3s^2]$ electrons, see the ESI† (SI-C, Fig. S17 and S18). The Ahlrichs/Weigend basis set def2-TZVPPD was chosen for the calculations due to its versatility and availability over the periodic table (H–Rn), and was retrieved from the Basis Set Exchange Web portal.[84–88] For the heavier elements Rb and Cs, this basis set employs effective core potentials (ECP) accounting for scalar relativistic effects through a quasi-relativistic description of the core region.[87–89] The core potentials replace all electrons in the shells up to the penultimate one, *i.e.* 28 electrons for Rb and 46 electrons for Cs. For the Rb- and Cs-oxalate complexes, all electrons not described by the effective core potentials were included in the determination of electron correlation. The basis set superposition error was estimated for the metal carbonites using the function counterpoise method,[90–92] which includes the CO_2 deformation energy,[93] which is substantial since the CO_2 moiety is bent in the MCO_2^- complexes. A detailed procedure is contained in the ESI.† The BSSE correction amounts to a correction of 5–12 kJ mol^{-1} at the CCSD(T) level of theory with the triple-ζ basis set (see Table S5 in the ESI†). The B3LYP density functional was used for the initial survey of the reaction landscape, while the G4 composite and the CCSD(T) methods were used to refine the thermochemistry, the latter also to provide more reliable metal carbonite geometries.

III. Results and discussion

a. Mass spectrometric characterization

The primary fragmentation pathway of all the alkali metal oxalate anions occurs by two sequential decarboxylations, as indicated in Fig. 1 and eqn (8a) and (9a), the first one to produce MCO_2^- and the second M^-,

$$MC_2O_4^- \ (m/z\text{: } 95, 111, 127, 173, 221) \rightarrow MCO_2^- \ (m/z\text{: } 51, 67, 83, 129, 177) + CO_2 \quad (8a)$$

$$MCO_2^- \ (m/z\text{: } 51, 67, 83, 129, 177) \rightarrow M^- \ (m/z\text{: } —, 23, 39, 85, 133) + CO_2 \quad (9a)$$

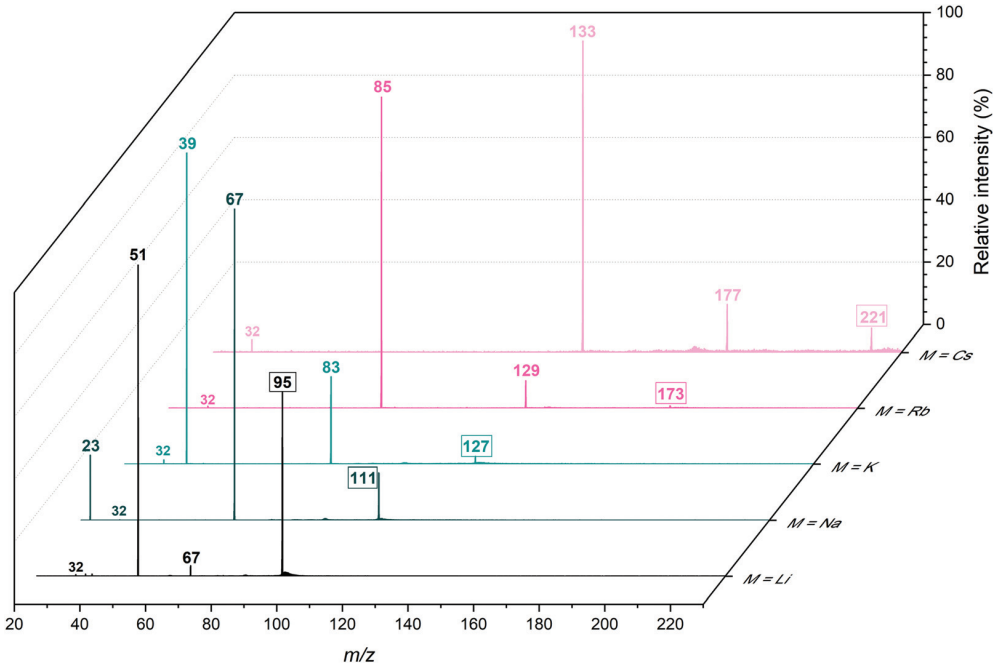

Fig. 1 Fragmentation mass spectra of $MC_2O_4^-$ recorded at a collision energy integrated over the range E_{COM} = 3.0–5.0 eV under 2.0×10^{-4} mbar collision gas (Ar) pressure. The *m/z* values of the mass selected parent ions are enclosed in frames.

For the lithium oxalate anion, the decarbonylation leading to lithium carbonate is also observed:

$$LiC_2O_4^- \ (m/z\ 95) \rightarrow LiCO_3^- \ (m/z\ 67) + CO. \qquad (10)$$

These observations are in good agreement with previous reports by Tian,[46] Attygalle[48] and Curtis *et al.*[47] as well as studies of thermal decomposition of solid alkali metal oxalates.[63,94–97] It should also be mentioned that the lithium anion, Li^- (m/z 7), is below the low mass cut-off of our QTOF 2 instrument. According to the MP2/6-311++G(d,p) calculations by Attygalle *et al.*[48] $LiCO_2^-$ has a lower electron detachment energy (47 kJ mol^{-1}) than the decarboxylation barrier (54 kJ mol^{-1}), suggesting that electron detachment yielding a neutral lithium carbonite radical, which occurs at the crossing of the neutral and ionic surfaces,

$$LiCO_2^- \rightarrow LiCO_2^{\bullet} + e^-, \qquad (11)$$

is the dominant decomposition channel. Our estimates for the electron detachment energy and the decarboxylation barrier of the Li system are 77 kJ mol^{-1} and 80 kJ mol^{-1} with the G4 composite method and 52 and 69 kJ mol^{-1} at the CCSD(T)/def2-TZVPPD level of theory (both using MP2 geometries), respectively. For the sodium analogue, the difference between the computed electron detachment energy and decarboxylation barrier for $NaCO_2^-$ was reported[48] to be 2.5 kJ mol^{-1} (67.0 and 69.5 kJ mol^{-1}), the former having the lowest energy value. However, Na^- (m/z 23) is observed in our experiments. The G4 (using MP2 geometries) results indicate that the vertical electron detachment of $NaCO_2^-$ requires 82 kJ mol^{-1}, while the decarboxylation has a barrier of 52 kJ mol^{-1}. The CCSD(T) calculations yield values of 67 kJ mol^{-1} and 38 kJ mol^{-1} for the electron detachment energy and decarboxylation barrier, respectively.

In order to probe the binding energies of the complexes, we measured the breakdown and appearance curves over an energy range from 0.4–8.0 eV in the center of mass (COM) frame (Fig. 2), and the resulting (estimated) threshold energies are shown in Table 1. It is important to emphasize that the threshold energies are less accurate for M^- than for MCO_2^-, since they are affected by secondary fragmentation. Therefore, we expect a closer correspondence between the theoretical and experimental values for the latter than for the former, given a reliable computational method. To the best of our knowledge, experimental threshold energies have not been reported to date for any of these systems.

The observation that M^- is increasingly more abundant than MCO_2^- for K, Rb and Cs (*cf.* Fig. 1) can be qualitatively attributed to the decreasing dissociation energy for $MCO_2^- \rightarrow M^- + CO_2$ going down the series from Li to Cs. A more quantitative assessment, however, will require explicit treatment of the electron detachment channel. The combined ion yields of MCO_2^- and M^- do not account for the total signal loss of the precursor oxalate complexes (*cf.* Fig. 2), which could be an artefact of electron detachment. However, a fraction of the total signal loss is inherent to the ion transport, making explicit treatment of the electron detachment channel difficult.

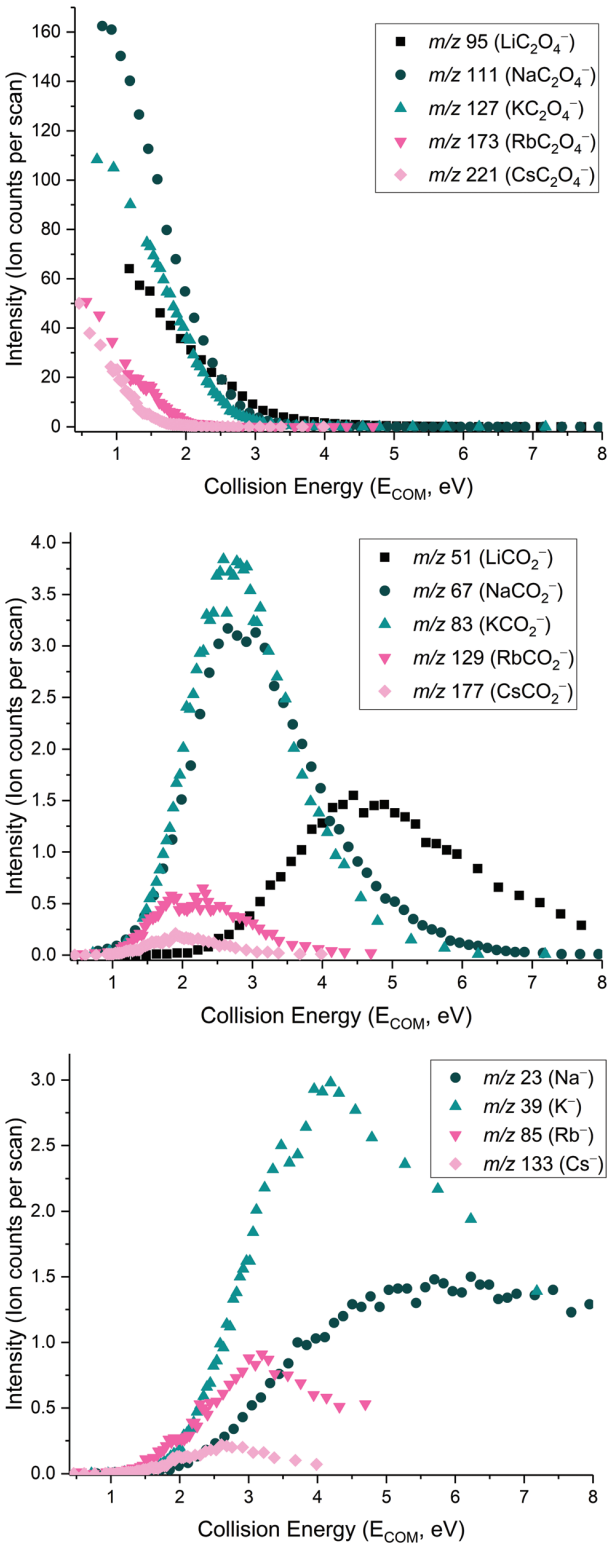

Fig. 2 Breakdown curves for the $MC_2O_4^-$ (M = Li, Na, K, Rb, Cs) complexes and appearance curves for MCO_2^- and M^- recorded for the collision energy interval E_{COM} = 0.4–8.0 eV under 2.0 × 10^{-4} mbar collision gas (Ar) pressure.

Table 1 Experimentally estimated threshold energies for MCO_2^- and M^- in kJ mol^{-1} and MP2/def2-TZVPPD barriers in parentheses. Uncertainties (one standard deviation) are associated with the linear extrapolation procedure outlined in the ESI, and only partly reflect the experimental uncertainty (*cf.* Experimental section)

	M = Li	M = Na	M = K	M = Rb	M = Cs
MCO_2^-	256 ± 14 (238)	157 ± 10 (150)	150 ± 9 (143)	110 ± 6 (145)	109 ± 11 (158)
M^-	n/a (317)	238 ± 45 (192)	200 ± 19 (176)	157 ± 16 (181)	139 ± 5 (195)

b. Computational modeling of the unimolecular MOx^- dissociation

A detailed computational survey was conducted to aid the understanding of the elementary reaction steps in the dissociation of the alkali metal oxalates into metal anions and carbon dioxide. Some of the key results are presented in Table 2, while more complete potential energy diagrams are reported in the ESI.† Attygalle *et al.*[48] have previously reported results at the MP2/6-311++G(d,p) level of theory for these reactions, yet several additions and refinements have been made herein, such as employing electronic structure methods of higher accuracy [*i.e.* CCSD(T) and the G4 composite methods] and using more detailed reaction models. We advise the reader that some of the notation in Table 2 is introduced in Section IIId.

Our calculations indicate that the energetic demands for the CO_2 loss from MOx^-,

$$MC_2O_4^- \rightarrow MCO_2^- + CO_2, \quad (8b)$$

decrease with the atomic number of the metal up to KOx^-, and subsequently increase slightly to $CsOx^-$. The same trend is observed for the decarboxylation of MCO_2^-,

$$MCO_2^- \rightarrow M^- + CO_2 \quad (9b)$$

Table 2 MP2/def2-TZVPPD and G4, CCSD(T)/def2-TZVPPD (EE + ZPVE) energies for the dissociation of MOx^- in kJ mol^{-1}, relative to $MC_2O_4^-$ (**1A**). **1A** corresponds to the optimum MOx^- geometries, notwithstanding KOx^-. The MOx^- complexes were optimized at the MP2/def2-TZVPPD level of theory and energies were subsequently refined at the CCSD(T)/def2-TZVPPD and G4 levels using these geometries. The MCO_2^- and CO_2 geometries were optimized at both the MP2 and CCSD(T) levels. The G4 energies are computed using the MP2/def2-TZVPPD geometries

	M = Li	M = Na	M = K	M = Rb	M = Cs	Method
$MC_2O_4^-$ (**1A**)	0	0	0	0	0	MP2
	0	0	0	—	—	G4
	0	0	0	0	0	CCSD(T)
$MC_2O_4^-$ (**1B**)	77	49	−3	—	—	MP2
	76	47	−1	—	—	G4
	76	48	−2	—	—	CCSD(T)
$M(\kappa^2\text{-}O_2C)^-$ (**2A**) + CO_2	238	150	137	141	154	MP2
	233	161	152	—	—	G4
	237	160	146	152	165	CCSD(T)
$M(\eta^2\text{-}CO_2)^-$ (**2B**) + CO_2	249	178	161	166	174	MP2
	238	181	172	—	—	G4
	248	180	164	171	183	CCSD(T)
M^- + $2CO_2$	317	189	169	174	188	MP2
	310	202	189	—	—	G4
	302	183	166	174	189	CCSD(T)
M + e^- + $2CO_2$	326	211	193	200	216	MP2
	372	255	236	—	—	G4
	346	230	209	216	230	CCSD(T)
EA(M)	9	22	24	26	28	MP2
	63	53	47	—	—	G4
	45	47	43	42	41	CCSD(T)
	60	53	48	46	46	Exp.[98–102]

This is in contrast to our experimental estimates, the accuracy of which depends on a multitude of factors, which are difficult to assess (*cf.* Experimental section IIa), making it unfeasible to assign higher validity to either of the experimental or theoretical energies. As a test of the reliability of our computational methods, the electron affinities of the metals were calculated. The experimental Electron Affinities (EA) decrease monotonically down the alkali metal group,[98–102] while MP2 yields an increasing trend down the series. CCSD(T) slightly underestimates the electron affinities of all alkali metals, but manages to reproduce the experimental trend, lithium notwithstanding, while the G4 results are best in agreement with the experimental Electron Affinities (EA) for the Li–K atoms.[98–105] Despite erroneous EAs for MP2, there is general qualitative agreement among all methods for the dissociation of MOx^-.

As regards the optimum geometries, the oxalate moiety is twisted from the planar to the staggered conformation with increasing metal atomic number from Li to Cs (Fig. 3).

Specifically, the lowest energy $LiOx^-$ complex is calculated to be planar (**1A**, C_{2v}), $NaOx^-$ is slightly twisted (**1A**, C_2), and KOx^- has both twisted (**1A**, C_2) and staggered (*i.e.*, with the metal ion bound closer to one –CO_2 group, **1B**, C_s) conformations that are close in energy, while $RbOx^-$ and $CsOx^-$ are both staggered (**1A**, C_s), similar to their crystalline counterparts.[57,62–65] The staggered MOx^- complexes may dissociate directly to the lowest energy carbonites, **2A**, $M(\kappa^2\text{-}O_2C)^-$ (*cf.* Fig. 5), while the planar ($LiOx^-$) and twisted ($NaOx^-$) complexes require metal migration to yield an end-on isomer (**1B**, C_{2v}) prior to dissociation. For all oxalates, the formation of the **2B** isomers $M(\eta^2\text{-}CO_2)$ is the most demanding pathway as discussed further in Section d.

c. Cryogenic ion vibrational spectroscopic characterization of the MOx^- complexes

The structural characterization of the alkali metal oxalates was achieved by acquiring vibrational spectra of the corresponding mass-selected, cryogenically cooled gas-phase ions with the results displayed in Fig. 4. We could not reach sufficient signal intensity to acquire spectra of the corresponding metal carbonites. The harmonic spectra of the calculated (at the MP2/def2-TZVPPD level of theory) $MC_2O_4^-$ structures feature four transitions in the fingerprint region between 1100 and 1900 cm^{-1}, resulting from combinations of carbonyl (C═O) displacements, which are in good agreement with the experimental band patterns. According to our MP2 calculations, the symmetry of the MOx^- complexes is reduced down the series, from C_{2v} for Li to C_2 for Na and K, and finally C_s for Rb and Cs. Note that for hydrogen/deuterium the point group is also C_s as the potential for proton transfer between O atoms has a double minimum shape.[71]

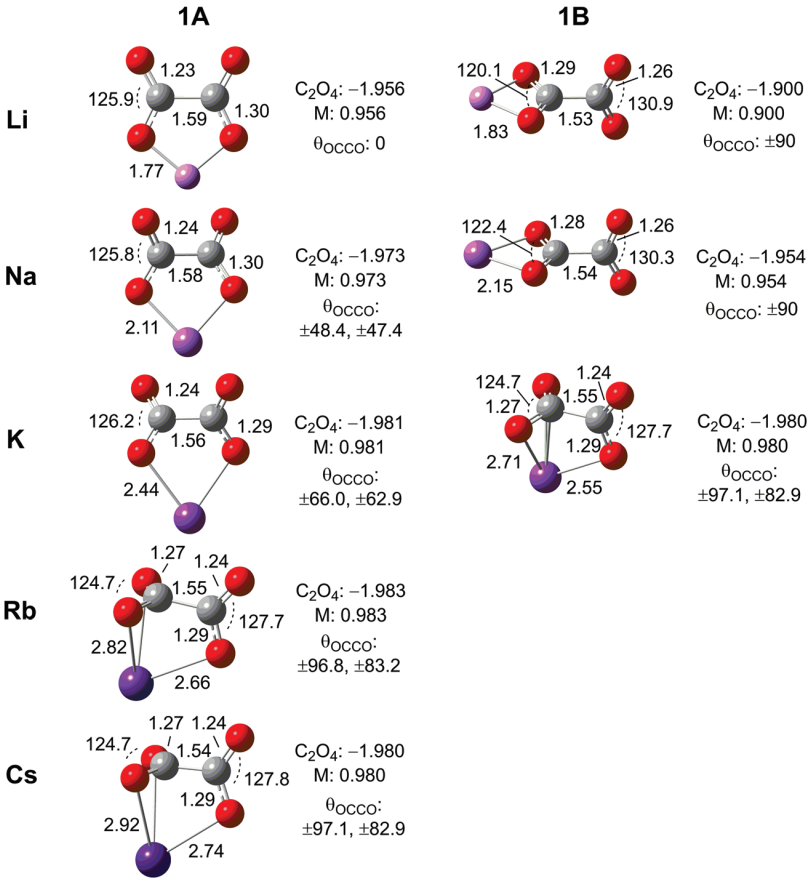

Fig. 3 MP2/def2-TZVPPD optimized geometries **1A** and **1B** of the MOx^- complexes with NBO partial charges on C_2O_4 and M indicated. Bond distances in Angstroms (Å), angles in degrees.

For the C_{2v} and C_2 metal oxalates (Li, Na and K), the strongest C═O stretching based fundamental is the in-phase combination of the unbound C═O displacements (ν_{15}), observed at 1683, 1652 and 1634 cm^{-1}, respectively. The out-of-phase combinations (ν_{14}) are found slightly lower in energy at 1661, 1625 and 1592 cm^{-1}, and exhibit different shifts relative to the in-phase bands with increasing ligand size ($\Delta\nu$: 22 to 43 cm^{-1}). As expected, the bound C═O displacements are lower in energy, with in-phase combinations (ν_{13}) at 1335, 1358 and 1381 cm^{-1} and out-of-phase combinations (ν_{12}) at 1220, 1232 and 1238 cm^{-1}. Although KOx^- appears well-characterized by a harmonic vibrational model, additional details are recovered from the calculated anharmonic spectra. The FWHM of the unbound C═O fundamental band centered at 1634 cm^{-1} in the K complex is slightly larger with an asymmetrical lineshape relative to the corresponding band for the other metal oxalates (20 cm^{-1} compared to 17 cm^{-1} ($LiOx^-$), 15 cm^{-1} ($NaOx^-$), 13 cm^{-1} ($RbOx^-$) and 11 cm^{-1} ($CsOx^-$)). This broadening can be traced to two combination bands with significant oscillator strength (~50% of the fundamental) within 11 cm^{-1} from the corresponding calculated transition (see the ESI†).

In the asymmetric (C_s) Ox complexes with D, Rb and Cs, the CO_2 moieties are distinguishable from each other. One of these has equivalent C═O bonds, most closely resembling a carboxylate group (CO_2^-), while the other has notably different C═O bond lengths, *i.e.* the structural features of a carboxyl group (M–O–C═O). The strongest oscillator is thus the unbound C═O displacement (ν_{15}) of the carboxyl group, observed at 1768, 1622 and 1626 cm^{-1} for D, Rb and Cs. Nearly as strong is the asymmetric CO_2 displacement of the carboxylate group (ν_{14}), located at 1683 cm^{-1} for the deuterium complex, and at 1528 cm^{-1} for both $RbOx^-$ and $CsOx^-$. The lowest frequency bands in the range 1200–1400 cm^{-1} are due to the in- and out-of-phase combinations of CO_2 bound in a symmetric motif as well as the bound C═O displacements (ν_{13}, ν_{12}). For the deuterium complex, the vibrational modes in this range involve the movement of the deuteron ligand to a higher degree than in the corresponding alkali metal oxalates.[71] Thus, the band at around 1200 cm^{-1} can be mainly attributed to the OD-bend, while the combination of out-of-phase symmetric CO_2 and bound C═O displacement modes makes a minor contribution to this feature, consistent with the previous assignment.[71]

In terms of overall trends, we observe a red-shift of the unbound C═O (ν_{14}, ν_{15}) stretches concurrent with the blue-shift of the bound C═O vibrations (ν_{12}, ν_{13}) with increasing metal size. In other words, the bound and unbound C═O displacement bands converge with the increasing atomic number of the metal ligand, a fact that can be attributed to the decreasing

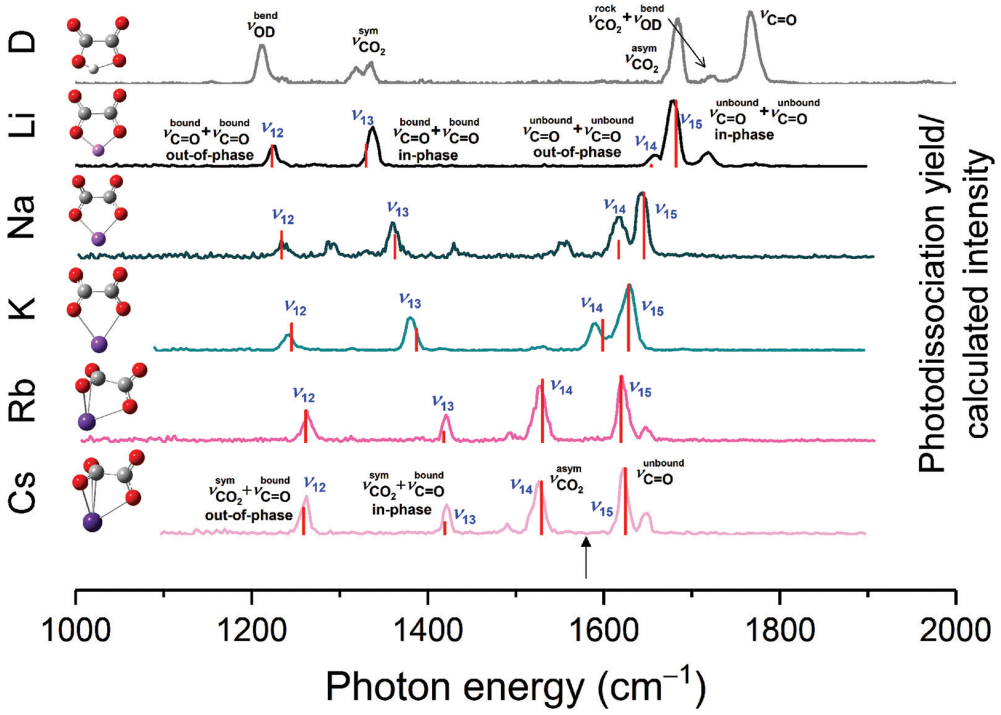

Fig. 4 Vibrational predissociation spectra for the $MC_2O_4^-$ (M = D, Li, Na, K, Rb and Cs) complexes "tagged" with either D_2 (M = Li, K and Cs) or H_2 (M = Na and Rb). The deuterium oxalate spectrum is adapted with permission from (C. T. Wolke, A. F. DeBlase, C. M. Leavitt, A. B. McCoy, M. A. Johnson, Diffuse Vibrational Signature of a Single Proton Embedded in the Oxalate Scaffold, $HO_2CCO_2^-$, *J. Phys. Chem. A*, 2015, **119**(52), 13018–13024).[71] Copyright (2020) American Chemical Society. The MP2/def2-TZVPPD minimum energy structures are shown to the left, and the corresponding computed vibrational frequencies (scaled by 0.990 for Li, Na and K, and by 0.985 for Rb and Cs) are denoted by sticks. The scaling has been determined according to the best fit to the experimental spectra.

covalence in the metal–oxalate bonding. At the same time, oxalate twists towards the most stable staggered configuration of the isolated dianion. For Ox^{2-} the antisymmetric carboxylate stretches are degenerate, with a transition at around 1580 cm^{-1}.[58,60,61] In comparison, we observe a splitting of the corresponding transition (symbolized by an arrow in the Cs trace, to ν_{14} and ν_{15}) due to the presence of the metal in the $RbOx^-$ and $CsOx^-$ spectra in Fig. 4. For the Li–K species, this effect manifests itself by the increasing splitting of the unbound C=O modes with the metal size, as the out-of-phase mode gradually transforms into the asymmetric CO_2 displacement mode in the $RbOx^-$ and $CsOx^-$ spectra. Note that while the DOx^- spectrum most closely resembles those of $RbOx^-$ and $CsOx^-$, in which oxalate is staggered, the oxalate moiety is planar in that complex. The asymmetry, or rather the non-equivalency of the two CO_2 moieties, is thus enforced by deuteron's smaller size and the double-minimum covalent bonding motif, while the large size of the Rb and Cs ions makes them unsuitable for symmetric accommodation within the oxalate scaffold. Additionally, the increasingly ionic bonding for the heavier alkali metal complexes increases the electron density on the oxalate, which in turn lessens the Coulombic repulsion by twisting about the C–C bond.

The geometry of Ox^{2-} in an aqueous solution with alkali metal counterions was previously studied by Kuroda *et al.*, who proposed the formation of contact ion pairs, $M^+\cdots Ox^{2-}$, in which oxalate assumes D_{2d} and D_{2h} conformations.[61] However, these authors suggested a different position for the metal, with a mixture of side- and end-on coordination being observed, which is likely due to the presence of solvent molecules and the formation of a fully connected hydrogen bonding network in the condensed phase, which is absent in the binary complex. We rather find that the gas-phase MOx^- geometries resemble those of the solid metal oxalate salts.[57,62–65] In that regime, however, Ox^{2-} is planar from Li to K, whereas the degree of coplanarity between the alkali metal cations and the oxalate dianion in the crystal lattice decreases with heavier counterions. Crystalline Rb oxalate has two isomeric forms (planar and staggered) with respect to oxalate at elevated temperatures, while in the Cs salt it is staggered.[62,63] The differences in the oxalate conformations between the gas-phase and the solid species could stem from the different numbers of interacting metal cations in the two cases. Indeed, for the gas-phase $MC_2O_4^-$ complexes, there is only one interacting cation, while the crystalline analogues have several. Thus, we surmise that the structure of oxalate in solid crystals is not solely governed by packing effects as suggested by Dinnebier *et al.*,[62] but also by the intrinsic nature of the interaction with the coordinating metal. This is partly supported by noting that the oxalate moiety in both $NaHC_2O_4{\cdot}H_2O$[106] and KHC_2O_4[107–109] salts is slightly twisted with an angle of $\angle OCCO = 13°$, and that Ox^{2-} is covalently interacting with a proton in addition to an alkali metal cation.

d. Activation of CO_2 and the formation of the MOx^- complexes

The activation of CO_2 as an isolated molecule can be accomplished by the addition of an alkali metal anion,

$$CO_2 + M^- \rightarrow MCO_2^-. \quad (6)$$

Although a barrier might be present for this reaction, the relevant barrier heights are low (1–15 kJ mol^{-1}). The addition reaction may lead to two different metal carbonite isomers, one with bidentate oxygen–metal coordination, **2A**, $M(\kappa^2\text{-}O_2C)^-$, and the other with mixed carbon–oxygen or acyl metal coordination, **2B**, $M(\eta^2\text{-}CO_2)^-$. Previous studies have shown that CO_2 forms metalloformates, $M(\eta^1\text{-}CO_2)^-$, with Ni, Cu, Pd, Pt, Au, Ag, and Bi.[31,32,36,110,111] For the alkali metal series, CCSD(T) calculations indicate that only $LiCO_2^-$ is stable as a metalloformate, with a BDE of 11 kJ mol^{-1} and C–M bond of 2.28 Å (not shown). We surmise that the alkali metals attain the bidentate oxygen–metal coordination due to being more oxophilic, as quantified by Kepp.[112] The abovementioned metals are among the least oxophilic (0.0–0.2 on the Kepp scale), favoring the metalloformate geometry. Interestingly, Li has a relatively low oxophilicity (0.3), which could partly explain its increased propensity towards the metalloformate structure.

Formation of the **2B** isomer should occur with the lowest barrier, and we expect it to be the initial product of reaction (6), similarly to what has been reported for the neutral reaction[43–45]

$$CO_2 + M \rightarrow MCO_2. \quad (12)$$

In order to assess the degree of CO_2 reduction in terms of charge transfer, we invoked the natural bond orbital (NBO)[113] analysis of the CCSD(T)/def2-TZVPPD optimized geometries of the metal carbonite anions shown in Fig. 5.

Going down the series from Li to Cs, the partial charge on the metal atom decreases, while it increases on the CO_2 moiety. At the same time, the M–O bond length increases, corresponding to a weaker interaction between CO_2 and M when going from Li to Cs. The ∠OCO bond angle ranges from 127°–133° in the **2A** isomers, while the corresponding angles for the **2B** isomers are wider, 134°–139°. These values are close to the reported bond angles for the analogous neutral MCO_2 species.[43,44] The partial charges on the CO_2 in the **2A** complexes are close to −1, suggesting that the electronic state resembles that of the isolated carbon dioxide radical anion, $CO_2^{\bullet-}$.[24] However, due to the metal–oxygen interaction, the C–O bonds are elongated (1.24–1.26 Å) and the ∠OCO angle is slightly narrowed when compared to the structure of the isolated $CO_2^{\bullet-}$ (1.23 Å and 138°).[35,114] Thus, the C–O bond lengths of the **2A** complexes range from that of $CO_2^{\bullet-}$ to those found in carboxylate groups (1.26 Å).[115] The **2B** isomers have slightly different C–O bond lengths due to the metal interacting with only one oxygen atom. The largest difference between the two C–O bonds is found in the lithium **2B** isomer, with this difference decreasing down the series from Li to Cs. The second order perturbation theory analysis on the NBO basis suggests that the M–C bond donates electron density to the C–O antibonding orbital, while the oxygen lone pair donates to the M–C antibonding orbital. The stabilization due to the former diminishes with increasing atomic number, while it increases for the latter. This is consistent with the observed C–O bond differences and the elongation of the M–C bond down the series.

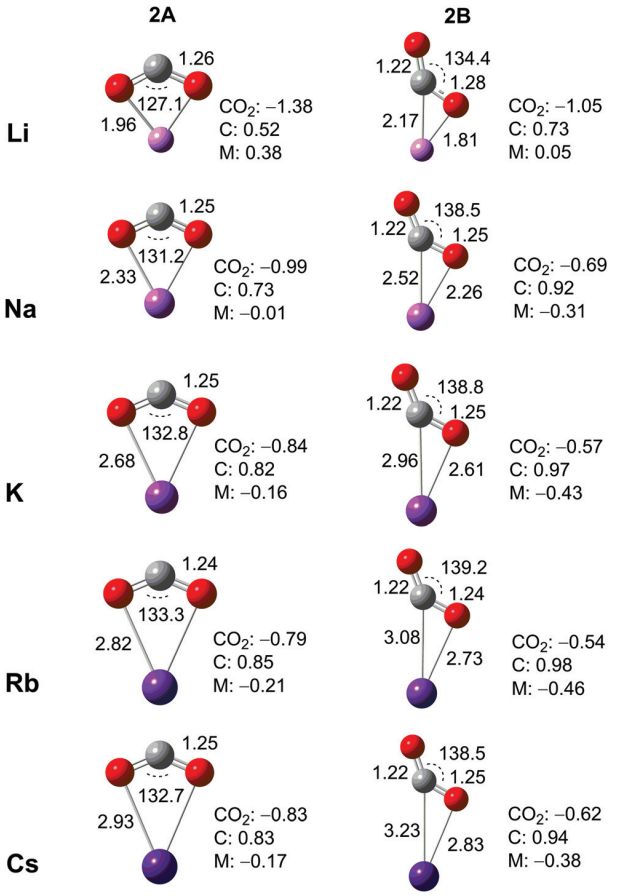

Fig. 5 CCSD(T)/def2-TZVPPD optimized geometries of the **2A** ($M(\kappa^2\text{-}O_2C)^-$, C_{2v}) and **2B** ($M(\eta^2\text{-}CO_2)^-$, C_s) alkali metal carbonites. Bond lengths are in Angstroms (Å) and angles in degrees. The NBO partial charges on the CO_2 moiety as well as the carbon and the metal atoms are also indicated.

The next step in the reduction of CO_2 to $C_2O_4^{2-}$ is the addition of a second carbon dioxide molecule to the metal carbonite,

$$MCO_2^- + CO_2 \rightarrow MC_2O_4^-. \quad (7)$$

This reaction provides a suitable test system to probe the extent of CO_2 activation in the intermediate MCO_2^- complex. Two phenomenologically different transition states, **TS1A** and **TS2A**, for the addition of a second CO_2 were found, differing according to whether C–C bond formation occurs with or without interaction between the incoming CO_2 and the metal, as shown in Fig. 6. The carboxylation of the lightest metal carbonites, Li and Na, is calculated to proceed exclusively *via* **TS1A**. Both reaction paths are accessible for the heaviest metal carbonites, K–Cs, with decreasing energetic demands for **TS2A** down the series as discussed further below.

The barrier for CO_2 addition is lowered when the reaction coordinate (primarily the C–C bond length) is elongated towards that of the separated reactants in the transition state. Following this deduction, the metal carbonite becomes a less efficient nucleophile down the alkali metal series, as seen by the decreasing

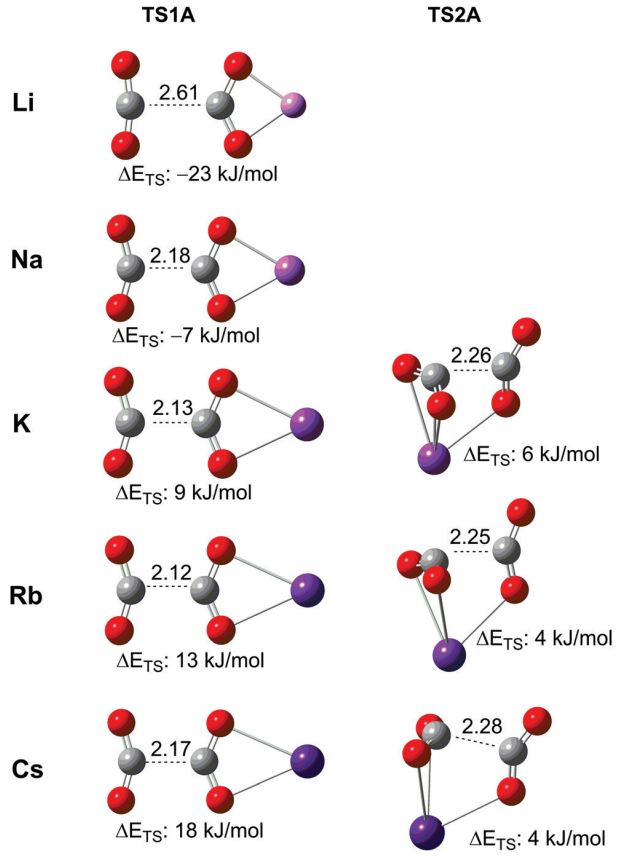

Fig. 6 Structures and energetics of transition states for the addition of CO_2 to MCO_2^- (**2A**) at the MP2/def2-TZVPPD level of theory. The C–C bond length (Å) corresponds to the reaction coordinate. ΔE_{TS} is the energy difference (E_e + ZPVE) between the transition state and the MCO_2^- + CO_2 asymptote.

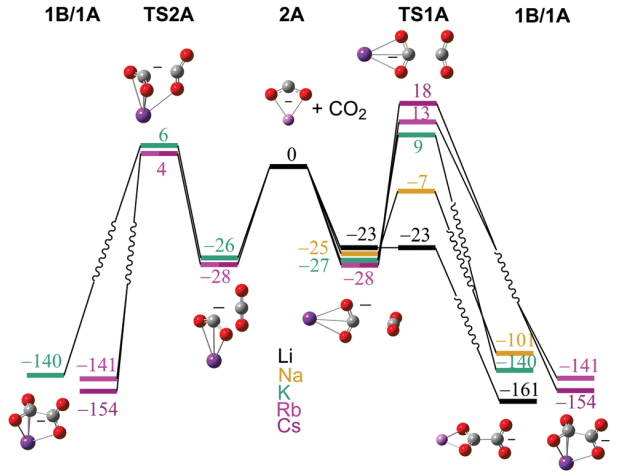

Fig. 7 Relative stabilities of isomers **1A/1B** and **2A** (kJ mol^{-1}) for the alkali metals considered in this study at the MP2/def2-TZVPPD level of theory.

C–C bond length and increasing barrier height in **TS1A**. However, the barriers are lowered when the addition proceeds through **TS2A** for the K, Rb and Cs species. We surmise that the energetic penalty is lowered due to the increasingly negative and larger metal participating in the activation of the incoming CO_2. Therefore, we observe mixed carbon and metal nucleophilicity in **TS2A** consistent with the fact that as the metal size increases, more of the negative charge remains on the metal in the MCO_2^- species.

The activation of CO_2 as a carbon nucleophile is more accurately assessed by considering the reaction path *via* **TS1A** in conjunction with the partial charges on the carbon. The energetic demands increase with the metal size for the addition proceeding over this barrier, congruent with the assumption that the lighter metals are more efficient in activating CO_2. We find some support in the literature on the relative reactivities of the neutral lithium and sodium carbonites, MCO_2, in that the latter exhibits lower reactivity towards CO_2 than the former.[45] In addition, we find that the order of reactivities of neutral alkali metals towards CO_2 have been reported as Li > Cs > K > Na.[44] This was rationalized by stating that the initial interaction between CO_2 and the alkali metal leads to the formation of a neutral **2B** analogue, and that its relative stability controls how readily the reaction sequence begins. We find that the interconversion between **2A** and **2B** ions requires less energy than the addition, except for Na. For the **2B** species, carboxylation occurs without a barrier for all metals according to our calculations, and we might expect this reaction to display significant metal activation of the incoming CO_2. This is supported by our calculations predicting a negative charge that is generally larger on the metal and lower on the CO_2 moiety in the **2B** carbonites.

The relative stabilities (in kJ mol^{-1}) of the various isomers **1A/1B** and **2A** and the paths connecting them *via* transition states **TS1A** and **TS2A** for all alkali metals are summarized in Fig. 7, which provides a global picture of the potential energy landscape for each system.

The core ionization energies, IE(1s), have been shown to correlate with properties such as Lewis acidity and basicity,[116,117] and the C(1s) energies of the MCO_2^- complexes (Table 3) could therefore prove to be useful descriptors of their carbon nucleophilicity.

The C(1s) energy is a diagnostic for the charge distribution around the nucleus, and it can be used to infer how well it interacts with positive or negative charges. A higher orbital energy implies more negative charge around the nucleus, favoring nucleophilicity. The near linear correlation (R^2 = 0.96, see the ESI†) of the C(1s) energies with the **2A** + CO_2 (**TS1A**) barrier heights strengthens the results obtained from the NBO analysis. The lower orbital energies of the **2B** species support the assumption that these are not as efficient carbon nucleophiles as **2A**.

Finally, we computed the partial charges on the MOx^- product complexes as a step towards validation of our simple model, where the two electrons needed for the formation of the C–C bond

Table 3 C(1s) energies (eV) of the MCO_2^- complexes at the CCSD(T)/def2-TZVPPD level of theory. The corresponding value for neutral CO_2 is −311.9 eV

MCO_2^-	2A	2B
Li	−302.40	−303.861
Na	−304.04	−305.608
K	−304.88	−306.204
Rb	−305.24	−306.487
Cs	−305.20	−306.348

between two CO_2 molecules are provided by the alkali metal anions, as implied by eqn (6) and (7). Fig. 3 in conjunction with Fig. 5 illustrates the expected charge reversal of the metal from −1 to +1 that would result from the stepwise reduction of CO_2 to $C_2O_4^{2-}$.

IV. Conclusions

Alkali metal oxalate and alkali metal carbonite binding energies decrease down the alkali metal series, as indicated by both approximate experimental dissociation thresholds and the results of electronic structure calculations. For the MOx^- complexes, this trend is evident in the evolution of the C═O stretching fundamentals in the IR spectra, specifically the blueshift of the bound C═O vibrational bands down the series. The size and binding strength of the interacting metal also determine the degree of planarity for the oxalate moiety, which evolves towards the most stable isolated (Ox^{2-}) D_{2d} isomer with increasing metal size. The change in planarity provides an additional transition state for the decarboxylation of the K–Cs alkali metal oxalates, which led us to propose two different types of nucleophilic reactivity for the intermediate MCO_2^- complexes. These intermediates may react either as pure carbon or mixed carbon–metal centered nucleophiles, with the smaller and more tightly bound metal complexes preferring the former, while those with larger, more polarizable metals favoring the latter. This difference can be attributed to more complete charge transfer from the metal to the CO_2 moiety in the more tightly bound species (*i.e.* Li). According to our proposed reaction model, the activation of CO_2 by the alkali metals proceeds energetically downhill when an additional electron is introduced.

Conflicts of interest

There are no conflicts to declare.

Acknowledgements

This work was supported by the Norwegian Research Council through Grant No. 249788 (The chemistry of CO_2 activation and fixation) to the Hylleraas Centre for Quantum Molecular Sciences No. 262695/F50 through their Centre of Excellence program, and the Norwegian Supercomputing Program (NOTUR) through a grant of computer time (Grant No. NN4654K). EA and SSX acknowledge support from the Center for Scalable Predictive methods for Excitations and Correlated phenomena (SPEC), which is funded by the U.S. Department of Energy, Office of Science, Basic Energy Sciences, Chemical Sciences, Geosciences and Biosciences Division, as part of the Computational Chemical Sciences Program at Pacific Northwest National Laboratory. Battelle operates the Pacific Northwest National Laboratory for the U.S. Department of Energy. This research also used computational resources provided by PNNL's Institutional Computing (PIC) and by the National Energy Research Scientific Computing Center, which is supported by the Office of Science of the U.S. Department of Energy under Contract No. DE-AC02-05CH11231. M. A. J. thanks the Air Force Office of Scientific Research (AFOSR) under grants FA9550-17-1-0267 (DURIP) and FA9550-18-1-0213.

References

1 C. Mesters, A Selection of Recent Advances in C1 Chemistry, *Annu. Rev. Chem. Biomol. Eng.*, 2016, **7**(1), 223–238, DOI: 10.1146/annurev-chembioeng-080615-034616.
2 P. Tian, Y. Wei, M. Ye and Z. Liu, Methanol to Olefins (MTO): From Fundamentals to Commercialization, *ACS Catal.*, 2015, **5**(3), 1922–1938, DOI: 10.1021/acscatal.5b00007.
3 A. de Klerk, Fischer–Tropsch Process, *Kirk-Othmer Encyclopedia of Chemical Technology*, American Cancer Society, 2013, pp. 1–20, DOI: 10.1002/0471238961.fiscdekl.a01.
4 M. Höök, D. Fantazzini, A. Angelantoni and S. Snowden, Hydrocarbon Liquefaction: Viability as a Peak Oil Mitigation Strategy, *Philos. Trans. R. Soc., A*, 2014, **372**(2006), 20120319, DOI: 10.1098/rsta.2012.0319.
5 M. Aresta, A. Dibenedetto and A. Angelini, Catalysis for the Valorization of Exhaust Carbon: From CO_2 to Chemicals, Materials, and Fuels. Technological Use of CO_2, *Chem. Rev.*, 2014, **114**(3), 1709–1742, DOI: 10.1021/cr4002758.
6 M. Aresta and A. Dibenedetto, Key Issues in Carbon Dioxide Utilization as a Building Block for Molecular Organic Compounds in the Chemical Industry, in *CO_2* Conversion and Utilization*, ed. C. Song, A. F. Gaffney and K. Fujimoto,* American Chemical Society, Washington, DC, 2002, vol. 809, pp. 54–70.
7 L. Plasseraud, Carbon Dioxide as Chemical Feedstock. Edited by Michele Aresta, *ChemSusChem*, 2010, **3**(5), 631–632, DOI: 10.1002/cssc.201000097.
8 E. A. Quadrelli, G. Centi, J.-L. Duplan and S. Perathoner, Carbon Dioxide Recycling: Emerging Large-Scale Technologies with Industrial Potential, *ChemSusChem*, 2011, **4**(9), 1194–1215, DOI: 10.1002/cssc.201100473.
9 T. Sakakura, J.-C. Choi and H. Yasuda, Transformation of Carbon Dioxide, *Chem. Rev.*, 2007, **107**(6), 2365–2387, DOI: 10.1021/cr068357u.
10 H. Kolbe, Ueber Synthese Der Salicylsäure, *Justus Liebigs Ann. Chem.*, 1860, **113**(1), 125–127, DOI: 10.1002/jlac.18601130120.
11 R. Schmitt and E. Burkard, *Ber. Dtsch. Chem. Ges.*, 1877, **20**, 2699.
12 B. Carl and M. Wilhelm, *Process of Manufacturing Urea*, US1429483A, 1922.
13 E. Solvay, US263981A, 1882.
14 M. Aresta, A. Dibenedetto and A. Dutta, Energy Issues in the Utilization of CO_2 in the Synthesis of Chemicals: The Case of the Direct Carboxylation of Alcohols to Dialkyl-Carbonates, *Catal. Today*, 2017, **281**, 345–351, DOI: 10.1016/j.cattod.2016.02.046.
15 M. Aresta, A. Dibenedetto and A. Angelini, The Changing Paradigm in CO_2 Utilization, *J. CO2 Util.*, 2013, **3–4**, 65–73, DOI: 10.1016/j.jcou.2013.08.001.
16 Q. Zhu, Developments on CO_2-Utilization Technologies, *Clean Energy*, 2019, **3**(2), 85–100, DOI: 10.1093/ce/zkz008.

17 U. R. Pokharel, F. R. Fronczek and A. W. Maverick, Reduction of Carbon Dioxide to Oxalate by a Binuclear Copper Complex, *Nat. Commun.*, 2014, **5**(1), 1–5, DOI: 10.1038/ncomms6883.

18 A. Paparo, J. S. Silvia, C. E. Kefalidis, T. P. Spaniol, L. Maron, J. Okuda and C. C. Cummins, A Dimetalloxycarbene Bonding Mode and Reductive Coupling Mechanism for Oxalate Formation from CO_2, *Angew. Chem., Int. Ed.*, 2015, **54**(31), 9115–9119, DOI: 10.1002/anie.201502532.

19 A. R. Willauer, D. Toniolo, F. Fadaei-Tirani, Y. Yang, M. Laurent and M. Mazzanti, Carbon Dioxide Reduction by Dinuclear Yb(II) and Sm(II) Complexes Supported by Siloxide Ligands, *Dalton Trans.*, 2019, **48**(18), 6100–6110, DOI: 10.1039/C9DT00554D.

20 A. Formanuik, F. Ortu, C. J. Inman, A. Kerridge, L. Castro, L. Maron and D. P. Mills, Concomitant Carboxylate and Oxalate Formation From the Activation of CO_2 by a Thorium(III) Complex, *Chem. Weinh. Bergstr. Ger.*, 2016, **22**(50), 17976–17979, DOI: 10.1002/chem.201604622.

21 L. J. Farrugia, S. Lopinski, P. A. Lovatt and R. D. Peacock, Fixing Carbon Dioxide with Copper: Crystal Structure of $[LCu(\mu\text{-}C_2O_4)CuL][Ph_4B]_2$ (L = *N*,*N*′,*N*″-triallyl-1,4,7-Triazacyclononane), *Inorg. Chem.*, 2001, **40**(3), 558–559, DOI: 10.1021/ic000418y.

22 K. Tanaka, Y. Kushi, K. Tsuge, K. Toyohara, T. Nishioka and K. Isobe, Catalytic Generation of Oxalate through a Coupling Reaction of Two CO_2 Molecules Activated on $[(Ir(\eta^5\text{-}C_5Me_5))_2(Ir((\eta^4\text{-}C_5Me_5)CH_2CN)(\mu^3\text{-}S)_2]$, *Inorg. Chem.*, 1998, **37**(1), 120–126, DOI: 10.1021/ic9702328.

23 B. Horn, C. Limberg, C. Herwig and B. Braun, Nickel(I)-Mediated Transformations of Carbon Dioxide in Closed Synthetic Cycles: Reductive Cleavage and Coupling of CO_2 Generating Ni^ICO, $Ni^{II}CO_3$ and $Ni^{II}C_2O_4Ni^{II}$ Entities, *Chem. Commun.*, 2013, **49**(93), 10923–10925, DOI: 10.1039/C3CC45407J.

24 D. Schröder, C. A. Schalley, J. N. Harvey and H. Schwarz, On the Formation of the Carbon Dioxide Anion Radical $CO_2^{-\bullet}$ in the Gas Phase, *Int. J. Mass Spectrom.*, 1999, **185**, 25–35.

25 G. L. Gutsev, R. J. Bartlett and R. N. Compton, Electron Affinities of CO_2, OCS, and CS_2, *J. Chem. Phys.*, 1998, **108**(16), 6756–6762, DOI: 10.1063/1.476091.

26 R. N. Compton, P. W. Reinhardt and C. D. Cooper, Collisional Ionization of Na, K, and Cs by CO_2, COS, and CS_2: Molecular Electron Affinities, *J. Chem. Phys.*, 1975, **63**(9), 3821, DOI: 10.1063/1.431875.

27 I. V. Chernyshova, P. Somasundaran and S. Ponnurangam, On the Origin of the Elusive First Intermediate of CO_2 Electroreduction, *Proc. Natl. Acad. Sci. U. S. A.*, 2018, **115**(40), E9261–E9270, DOI: 10.1073/pnas.1802256115.

28 Y. Hori, Electrochemical CO_2 Reduction on Metal Electrodes, in *Modern Aspects of Electrochemistry*, ed. C. G. Vayenas, R. E. White and M. E. Gamboa-Aldeco, Modern Aspects of Electrochemistry, Springer, New York, NY, 2008, pp. 89–189, DOI: 10.1007/978-0-387-49489-0_3.

29 J. T. Feaster, C. Shi, E. R. Cave, T. Hatsukade, D. N. Abram, K. P. Kuhl, C. Hahn, J. K. Nørskov and T. F. Jaramillo, Understanding Selectivity for the Electrochemical Reduction of Carbon Dioxide to Formic Acid and Carbon Monoxide on Metal Electrodes, *ACS Catal.*, 2017, **7**(7), 4822–4827, DOI: 10.1021/acscatal.7b00687.

30 S. A. Akhade, W. Luo, X. Nie, A. Asthagiri and M. J. Janik, Theoretical Insight on Reactivity Trends in CO_2 Electroreduction across Transition Metals, *Catal. Sci. Technol.*, 2016, **6**(4), 1042–1053, DOI: 10.1039/C5CY01339A.

31 M. C. Thompson, J. Ramsay and J. M. Weber, Solvent-Driven Reductive Activation of CO_2 by Bismuth: Switching from Metalloformate Complexes to Oxalate Products, *Angew. Chem., Int. Ed.*, 2016, **55**(48), 15171–15174, DOI: 10.1002/anie.201607445.

32 B. J. Knurr and J. M. Weber, Solvent-Mediated Reduction of Carbon Dioxide in Anionic Complexes with Silver Atoms, *J. Phys. Chem. A*, 2013, **117**(41), 10764–10771, DOI: 10.1021/jp407646t.

33 A. M. Ricks, A. D. Brathwaite and M. A. Duncan, IR Spectroscopy of Gas Phase $V(CO_2)_n^+$ Clusters: Solvation-Induced Electron Transfer and Activation of CO_2, *J. Phys. Chem. A*, 2013, **117**(45), 11490–11498, DOI: 10.1021/jp4089035.

34 G. B. S. Miller, T. K. Esser, H. Knorke, S. Gewinner, W. Schöllkopf, N. Heine, K. R. Asmis and E. Uggerud, Spectroscopic Identification of a Bidentate Binding Motif in the Anionic Magnesium-CO_2 Complex ($[ClMgCO_2]-$), *Angew. Chem.*, 2014, **126**(52), 14635–14638, DOI: 10.1002/ange.201409444.

35 K. Blaziak, D. Tzeli, S. S. Xantheas and E. Uggerud, The Activation of Carbon Dioxide by First Row Transition Metals (Sc–Zn), *Phys. Chem. Chem. Phys.*, 2018, **20**(39), 25495–25505, DOI: 10.1039/C8CP04231D.

36 E. Lim, S. K. Kim and K. H. Bowen, Photoelectron Spectroscopic and Computational Study of $(M–CO_2)^-$ Anions, M = Cu, Ag, Au, *J. Chem. Phys.*, 2015, **143**(17), 174305, DOI: 10.1063/1.4935061.

37 H.-J. Freund and R. P. Messmer, On the Bonding and Reactivity of CO_2 on Metal Surfaces, *Surf. Sci. Lett.*, 1986, **172**(1), A333, DOI: 10.1016/0167-2584(86)91274-0.

38 M. Aresta and A. Angelini, The Carbon Dioxide Molecule and the Effects of Its Interaction with Electrophiles and Nucleophiles, in *Carbon Dioxide and Organometallics*, ed. X.-B. Lu, Topics in Organometallic Chemistry, Springer International Publishing, Cham, 2016, pp. 1–38, DOI: 10.1007/3418_2015_93.

39 D. H. Gibson, Carbon Dioxide Coordination Chemistry: Metal Complexes and Surface-Bound Species. What Relationships?, *Coord. Chem. Rev.*, 1999, **185–186**, 335–355, DOI: 10.1016/S0010-8545(99)00021-1.

40 E. Barwa, M. Ončák, T. F. Pascher, A. Herburger, C. Linde and M. K. van der; Beyer, Infrared Multiple Photon Dissociation Spectroscopy of Hydrated Cobalt Anions Doped with Carbon Dioxide $CoCO_2(H_2O)N^-$, N = 1–10, in the C–O Stretch Region, *Chem. – Eur. J.*, 2020, **26**(5), 1074–1081, DOI: 10.1002/chem.201904182.

41 D. A. Thomas, E. Mucha, S. Gewinner, W. Schöllkopf, G. Meijer and G. von Helden, Vibrational Spectroscopy of

Fluoroformate, FCO_2^-, Trapped in Helium Nanodroplets, *J. Phys. Chem. Lett.*, 2018, **9**(9), 2305–2310, DOI: 10.1021/acs.jpclett.8b00664.

42 M. E. Jacox and D. E. Milligan, Vibrational Spectrum of CO_2^- in an Argon Matrix, *Chem. Phys. Lett.*, 1974, **28**(2), 163–168, DOI: 10.1016/0009-2614(74)80043-6.

43 Z. H. Kafafi, R. H. Hauge, W. E. Billups and J. L. Margrave, Carbon Dioxide Activation by Lithium Metal. 1. Infrared Spectra of Lithium Carbon Dioxide ($Li^+CO_2^-$), Lithium Oxalate ($Li^+C_2O_4^-$), and Lithium Carbon Dioxide ($Li_2^{2+}CO_2^{2-}$) in Inert-Gas Matrices, *J. Am. Chem. Soc.*, 1983, **105**(12), 3886–3893, DOI: 10.1021/ja00350a025.

44 Z. H. Kafafi, R. H. Hauge, W. E. Billups and J. L. Margrave, Carbon Dioxide Activation by Alkali Metals. 2. Infrared Spectra of $M^+CO_2^-$ and $M_2^{2+}CO_2^{2-}$ in Argon and Nitrogen Matrixes, *Inorg. Chem.*, 1984, **23**(2), 177–183, DOI: 10.1021/ic00170a013.

45 L. Manceron, A. Loutellier and J. P. Perchard, Reduction of Carbon Dioxide to Oxalate by Lithium Atoms: A Matrix Isolation Study of the Intermediate Steps, *J. Mol. Struct.*, 1985, **129**(1), 115–124, DOI: 10.1016/0022-2860(85)80197-6.

46 Z. Tian, B. Chan, M. B. Sullivan, L. Radom and S. R. Kass, Lithium Monoxide Anion: A Ground-State Triplet with the Strongest Base to Date, *Proc. Natl. Acad. Sci. U. S. A.*, 2008, **105**(22), 7647–7651, DOI: 10.1073/pnas.0801393105.

47 S. Curtis, J. Renaud, J. L. Holmes and P. M. Mayer, Old Acid, New Chemistry. Negative Metal Anions Generated from Alkali Metal Oxalates and Others, *J. Am. Soc. Mass Spectrom.*, 2010, **21**(11), 1944–1946, DOI: 10.1016/j.jasms.2010.08.003.

48 A. B. Attygalle, F. U. Axe and C. S. Weisbecker, Mild Route to Generate Gaseous Metal Anions, *Rapid Commun. Mass Spectrom.*, 2011, **25**(6), 681–688, DOI: 10.1002/rcm.4913.

49 A. Paparo and J. Okuda, Carbonite, the Dianion of Carbon Dioxide and Its Metal Complexes, *J. Organomet. Chem.*, 2018, **869**, 270–274, DOI: 10.1016/j.jorganchem.2017.10.005.

50 G. B. S. Miller and E. Uggerud, C–C Bond Formation of Mg- and Zn-Activated Carbon Dioxide, *Chem. – Eur. J.*, 2018, **24**(18), 4710–4717, DOI: 10.1002/chem.201706069.

51 H. Dossmann Soldi-Lose, C. Afonso, D. Lesage, J.-C. Tabet and E. Uggerud, Formation and Characterization of Gaseous Adducts of Carbon Dioxide to Magnesium, $(CO_2)MgX^-$ (X = OH, Cl, Br), *Angew. Chem., Int. Ed.*, 2012, **51**(28), 6938–6941, DOI: 10.1002/anie.201108477.

52 X.-B. Wang, X. Yang, J. B. Nicholas and L.-S. Wang, Photodetachment of Hydrated Oxalate Dianions in the Gas Phase, $C_2O_4^{2-}(H_2O)_n$ (N = 3–40): From Solvated Clusters to Nanodroplet, *J. Chem. Phys.*, 2003, **119**(7), 3631–3640, DOI: 10.1063/1.1590641.

53 X. Yang, X.-B. Wang and L.-S. Wang, Photodetachment of Hydrated Sulfate Doubly Charged Anions: $SO_4^{2-}(H_2O)_n$ (n = 4–40), *J. Phys. Chem. A*, 2002, **106**(33), 7607–7616, DOI: 10.1021/jp014632z.

54 M. J. S. Dewar and Y.-J. Zheng, Structure of the Oxalate Ion, *THEOCHEM*, 1990, **209**(1–2), 157–162, DOI: 10.1016/0166-1280(90)85053-P.

55 P. A. W. Dean, The Oxalate Dianion, $C_2O_4^{2-}$: Planar or Nonplanar?, *J. Chem. Educ.*, 2012, **89**(3), 417–418, DOI: 10.1021/ed200202r.

56 G. Zhou and W.-K. Li, The Abnormally Long C-C Bond in the Oxalate Ion, *J. Chem. Educ.*, 1989, **66**(7), 572, DOI: 10.1021/ed066p572.

57 K. I. Peterson and D. P. Pullman, Determining the Structure of Oxalate Anion Using Infrared and Raman Spectroscopy Coupled with Gaussian Calculations, *J. Chem. Educ.*, 2016, **93**(6), 1130–1133, DOI: 10.1021/acs.jchemed.6b00118.

58 R. J. H. Clark and S. Firth, Raman, Infrared and Force Field Studies of $K_2{}^{12}C_2O_4{\cdot}H_2O$ and $K_2{}^{13}C_2O_4{\cdot}H_2O$ in the Solid State and in Aqueous Solution, and of $(NH_4)_2{}^{12}C_2O_4{\cdot}H_2O$ and $(NH_4)_2{}^{13}C_2O_4{\cdot}H_2O$ in the Solid State, *Spectrochim. Acta, Part A*, 2002, **58**(8), 1731–1746, DOI: 10.1016/S1386-1425(01)00635-7.

59 G. M. Begun and W. H. Fletcher, Vibrational Spectra of Aqueous Oxalate Ion, *Spectrochim. Acta*, 1963, **19**(8), 1343–1349, DOI: 10.1016/0371-1951(63)80244-1.

60 D. G. Kuroda and R. M. Hochstrasser, Two-Dimensional Infrared Spectral Signature and Hydration of the Oxalate Dianion, *J. Chem. Phys.*, 2011, **135**(20), 204502, DOI: 10.1063/1.3658461.

61 D. G. Kuroda and R. M. Hochstrasser, Dynamic Structures of Aqueous Oxalate and the Effects of Counterions Seen by 2D IR, *Phys. Chem. Chem. Phys.*, 2012, **14**(18), 6219, DOI: 10.1039/c2cp23892f.

62 R. E. Dinnebier, S. Vensky, M. Panthöfer and M. Jansen, Crystal and Molecular Structures of Alkali Oxalates: First Proof of a Staggered Oxalate Anion in the Solid State, *Inorg. Chem.*, 2003, **42**(5), 1499–1507, DOI: 10.1021/ic0205536.

63 R. E. Dinnebier, S. Vensky, M. Jansen and J. C. Hanson, Crystal Structures and Topological Aspects of the High-Temperature Phases and Decomposition Products of the Alkali-Metal Oxalates $M_2[C_2O_4]$ (M = K, Rb, Cs), *Chem. – Eur. J.*, 2005, **11**(4), 1119–1129, DOI: 10.1002/chem.200400616.

64 D. A. Reed and M. M. Olmstead, Sodium Oxalate Structure Refinement, *Acta Crystallogr., Sect. B: Struct. Crystallogr. Cryst. Chem.*, 1981, **37**(4), 938–939, DOI: 10.1107/S0567740881004676.

65 B. Beagley and R. W. H. Small, The Structure of Lithium Oxalate, *Acta Crystallogr.*, 1964, **17**(6), 783–788, DOI: 10.1107/S0365110X64002079.

66 D. A. Fairley, G. B. I. Scott, C. G. Freeman, R. G. A. R. Maclagan and M. J. McEwan, $C_2H_7O^+$ Potential Surface and Ion–Molecule Association between H_3O^+ and C_2H_4, *J. Phys. Chem. A*, 1997, **101**(15), 2848–2851, DOI: 10.1021/jp963294c.

67 P. H. Dawson, A Study of the Collision-Induced Dissociation of $C_2H_5OH_2^+$ Using Various Target Gases, *Int. J. Mass Spectrom. Ion Phys.*, 1983, **50**(3), 287–297, DOI: 10.1016/0020-7381(83)87006-5.

68 S. T. Graul and R. R. Squires, Gas-Phase Acidities Derived from Threshold Energies for Activated Reactions, *J. Am. Chem. Soc.*, 1990, **112**(7), 2517–2529, DOI: 10.1021/ja00163a007.

69 F. S. Menges, E. H. Perez, S. C. Edington, C. H. Duong, N. Yang and M. A. Johnson, Integration of High-Resolution Mass Spectrometry with Cryogenic Ion Vibrational

Spectroscopy, *J. Am. Soc. Mass Spectrom*, 2019, **30**(9), 1551–1557, DOI: 10.1007/s13361-019-02238-y.

70 N. Yang, C. H. Duong, P. J. Kelleher, M. A. Johnson and A. B. McCoy, Isolation of Site-Specific Anharmonicities of Individual Water Molecules in the $I^-\cdot(H_2O)_2$ Complex Using Tag-Free, Isotopomer Selective IR-IR Double Resonance, *Chem. Phys. Lett.*, 2017, **690**, 159–171, DOI: 10.1016/j.cplett.2017.09.042.

71 C. T. Wolke, A. F. DeBlase, C. M. Leavitt, A. B. McCoy and M. A. Johnson, Diffuse Vibrational Signature of a Single Proton Embedded in the Oxalate Scaffold, $HO_2CCO_2^-$, *J. Phys. Chem. A*, 2015, **119**(52), 13018–13024, DOI: 10.1021/acs.jpca.5b10649.

72 M. J. Frisch, G. W. Trucks, H. B. Schlegel, G. E. Scuseria, M. A. Robb, J. R. Cheeseman, G. Scalmani, V. Barone, G. A. Petersson, H. Nakatsuji, X. Li, M. Caricato, A. V. Marenich, J. Bloino, B. G. Janesko, R. Gomperts, B. Mennucci, H. P. Hratchian, J. V. Ortiz, A. F. Izmaylov, J. L. Sonnenberg, D. Williams-Young, F. Ding, F. Lipparini, F. Egidi, J. Goings, B. Peng, A. Petrone, T. Henderson, D. Ranasinghe, V. G. Zakrzewski, J. Gao, N. Rega, G. Zheng, W. Liang, M. Hada, M. Ehara, K. Toyota, R. Fukuda, J. Hasegawa, M. Ishida, T. Nakajima, Y. Honda, O. Kitao, H. Nakai, T. Vreven, K. Throssell, J. A. Montgomery Jr, J. E. Peralta, F. Ogliaro, M. Bearpark, J. J. Heyd, E. Brothers, K. N. Kudin, V. N. Staroverov, T. A. Keith, R. Kobayashi, J. Normand, K. Raghavachari, A. Rendell, J. C. Burant, S. S. Iyengar, J. Tomasi, M. Cossi, J. M. Milliam, M. Klene, C. Adamo, R. Cammi, J. W. Ochterski, R. L. Martin, K. Morokuma, O. Farkas, J. B. Foresman and D. J. Fox, *Gaussian 16, Revision A. 03*, Gaussian. Inc, Wallingford CT, 2016.

73 A. D. Becke, Density-Functional Exchange-Energy Approximation with Correct Asymptotic Behavior, *Phys. Rev. A: At., Mol., Opt. Phys.*, 1988, **38**(6), 3098–3100, DOI: 10.1103/PhysRevA.38.3098.

74 C. Lee, W. Yang and R. G. Parr, Development of the Colle-Salvetti Correlation-Energy Formula into a Functional of the Electron Density, *Phys. Rev. B: Condens. Matter Mater. Phys.*, 1988, **37**(2), 785–789, DOI: 10.1103/PhysRevB.37.785.

75 L. A. Curtiss, P. C. Redfern and K. Raghavachari, Gaussian-4 Theory, *J. Chem. Phys.*, 2007, **126**(8), 084108, DOI: 10.1063/1.2436888.

76 L. A. Curtiss, P. C. Redfern and K. Raghavachari, Assessment of Gaussian-4 Theory for Energy Barriers, *Chem. Phys. Lett.*, 2010, **499**(1–3), 168–172, DOI: 10.1016/j.cplett.2010.09.012.

77 Chr. Møller and M. S. Plesset, Note on an Approximation Treatment for Many-Electron Systems, *Phys. Rev.*, 1934, **46**(7), 618–622, DOI: 10.1103/PhysRev.46.618.

78 M. Valiev, E. J. Bylaska, N. Govind, K. Kowalski, T. P. Straatsma, H. J. J. Van Dam, D. Wang, J. Nieplocha, E. Apra, T. L. Windus and W. A. de Jong, NWChem: A Comprehensive and Scalable Open-Source Solution for Large Scale Molecular Simulations, *Comput. Phys. Commun.*, 2010, **181**(9), 1477–1489, DOI: 10.1016/j.cpc.2010.04.018.

79 J. Čížek, On the Correlation Problem in Atomic and Molecular Systems. Calculation of Wavefunction Components in Ursell-Type Expansion Using Quantum-Field Theoretical Methods, *J. Chem. Phys.*, 1966, **45**(11), 4256–4266, DOI: 10.1063/1.1727484.

80 G. D. Purvis and R. J. Bartlett, A Full Coupled-cluster Singles and Doubles Model: The Inclusion of Disconnected Triples, *J. Chem. Phys.*, 1982, **76**(4), 1910–1918, DOI: 10.1063/1.443164.

81 J. A. Pople, M. Head-Gordon and K. Raghavachari, Quadratic Configuration Interaction. A General Technique for Determining Electron Correlation Energies, *J. Chem. Phys.*, 1987, **87**(10), 5968–5975, DOI: 10.1063/1.453520.

82 V. A. Rassolov, J. A. Pople, P. C. Redfern and L. A. Curtiss, The Definition of Core Electrons, *Chem. Phys. Lett.*, 2001, **350**(5–6), 573–576, DOI: 10.1016/S0009-2614(01)01345-8.

83 S. Petrie, Pitfalls for the Frozen-Core Approximation: Gaussian-2 Calculations on the Sodium Cation Affinities of Diatomic Fluorides, *J. Phys. Chem. A*, 1998, **102**(30), 6138–6151, DOI: 10.1021/jp9802432.

84 K. L. Schuchardt, B. T. Didier, T. Elsethagen, L. Sun, V. Gurumoorthi, J. Chase, J. Li and T. L. Windus, Basis Set Exchange: A Community Database for Computational Sciences, *J. Chem. Inf. Model.*, 2007, **47**(3), 1045–1052, DOI: 10.1021/ci600510j.

85 B. P. Pritchard, D. Altarawy, B. Didier, T. D. Gibson and T. L. Windus, New Basis Set Exchange: An Open, Up-to-Date Resource for the Molecular Sciences Community, *J. Chem. Inf. Model.*, 2019, **59**(11), 4814–4820, DOI: 10.1021/acs.jcim.9b00725.

86 D. Feller, The Role of Databases in Support of Computational Chemistry Calculations, *J. Comput. Chem.*, 1996, **17**(13), 1571–1586, DOI: 10.1002/(SICI)1096-987X(199610)17:13<1571::AID-JCC9>3.0.CO;2-P.

87 F. Weigend and R. Ahlrichs, Balanced Basis Sets of Split Valence, Triple Zeta Valence and Quadruple Zeta Valence Quality for H to Rn: Design and Assessment of Accuracy, *Phys. Chem. Chem. Phys.*, 2005, **7**(18), 3297, DOI: 10.1039/b508541a.

88 D. Rappoport and F. Furche, Property-Optimized Gaussian Basis Sets for Molecular Response Calculations, *J. Chem. Phys.*, 2010, **133**(13), 134105, DOI: 10.1063/1.3484283.

89 M. Kaupp, P. v. R. Schleyer, H. Stoll and H. Preuss, Pseudopotential Approaches to Ca, Sr, and Ba Hydrides. Why Are Some Alkaline Earth MX_2 Compounds Bent?, *J. Chem. Phys.*, 1991, **94**(2), 1360–1366, DOI: 10.1063/1.459993.

90 S. F. Boys and F. Bernardi, The Calculation of Small Molecular Interactions by the Differences of Separate Total Energies. Some Procedures with Reduced Errors, *Mol. Phys.*, 1970, **19**(4), 553–566, DOI: 10.1080/00268977000101561.

91 S. Simon, M. Duran and J. J. Dannenberg, How Does Basis Set Superposition Error Change the Potential Surfaces for Hydrogen-bonded Dimers?, *J. Chem. Phys.*, 1996, **105**(24), 11024–11031, DOI: 10.1063/1.472902.

92 F. B. van Duijneveldt, J. G. C. M. van Duijneveldt-van de Rijdt and J. H. van Lenthe, State of the Art in Counterpoise Theory, *Chem. Rev.*, 1994, **94**(7), 1873–1885, DOI: 10.1021/cr00031a007.

93 S. S. Xantheas, On the Importance of the Fragment Relaxation Energy Terms in the Estimation of the Basis Set Superposition

Error Correction to the Intermolecular Interaction Energy, *J. Chem. Phys.*, 1996, **104**(21), 8821–8824, DOI: 10.1063/1.471605.

94 D. Dollimore and D. Tinsley, The Thermal Decomposition of Oxalates. Part XII. The Thermal Decomposition of Lithium Oxalate, *J. Chem. Soc. A*, 1971, 3043–3047, DOI: 10.1039/J19710003043.

95 R. Ito, Y. Masuda and Y. Ito, Thermal Analyses of Rubidium and Cesium Oxalate Monohydrates, *Thermochim. Acta*, 1988, **127**, 159–170, DOI: 10.1016/0040-6031(88)87492-6.

96 I. A. Kahwa and A. M. Mulokozi, The Thermal Decomposition Temperatures of Ionic Metal Oxalates, *J. Therm. Anal.*, 1981, **22**(1), 61–65, DOI: 10.1007/BF01915696.

97 T. Higashiyama and S. Hasegawa, The Differential Thermal Analysis of Potassium Oxalate, *Bull. Chem. Soc. Jpn.*, 1971, **44**(7), 1727–1730, DOI: 10.1246/bcsj.44.1727.

98 G. Haeffler, D. Hanstorp, I. Kiyan, A. E. Klinkmüller, U. Ljungblad and D. J. Pegg, Electron Affinity of Li: A State-Selective Measurement, *Phys. Rev. A: At., Mol., Opt. Phys.*, 1996, **53**(6), 4127–4131, DOI: 10.1103/PhysRevA.53.4127.

99 H. Hotop and W. C. Lineberger, Binding Energies in Atomic Negative Ions: II, *J. Phys. Chem. Ref. Data*, 1985, **14**(3), 731–750, DOI: 10.1063/1.555735.

100 K. T. Andersson, J. Sandström, I. Yu. Kiyan, D. Hanstorp and D. J. Pegg, Measurement of the Electron Affinity of Potassium, *Phys. Rev. A: At., Mol., Opt. Phys.*, 2000, **62**(2), 022503, DOI: 10.1103/PhysRevA.62.022503.

101 P. Frey, F. Breyer and H. Holop, High Resolution Photodetachment from the Rubidium Negative Ion around the Rb(5p1/2) Threshold, *J. Phys. B: At. Mol. Phys.*, 1978, **11**(19), L589–L594, DOI: 10.1088/0022-3700/11/19/005.

102 M. Scheer, J. Thøgersen, R. C. Bilodeau, C. A. Brodie, H. K. Haugen, H. H. Andersen, P. Kristensen and T. Andersen, Experimental Evidence That the $6s6p^3$ States of Cs^- Are Shape Resonances, *Phys. Rev. Lett.*, 1998, **80**(4), 684–687, DOI: 10.1103/PhysRevLett.80.684.

103 T. Andersen, Atomic Negative Ions: Structure, Dynamics and Collisions, *Phys. Rep.*, 2004, **394**(4), 157–313, DOI: 10.1016/j.physrep.2004.01.001.

104 H. Pathak, S. Sasmal, M. K. Nayak, N. Vaval and S. Pal, Relativistic Equation-of-Motion Coupled-Cluster Method for the Electron Attachment Problem, *Comput. Theor. Chem.*, 2016, **1076**, 94–100, DOI: 10.1016/j.comptc.2015.12.015.

105 S. Salomonson, H. Warston and I. Lindgren, Many-Body Calculations of the Electron Affinity for Ca and Sr, *Phys. Rev. Lett.*, 1996, **76**(17), 3092–3095, DOI: 10.1103/PhysRevLett.76.3092.

106 R. Tellgren and I. Olovsson, Hydrogen Bond Studies. XXXXVI. The Crystal Structures of Normal and Deuterated Sodium Hydrogen Oxalate Monohydrate $NaHC_2O_4{\cdot}H_2O$ and $NaDC_2O_4{\cdot}D_2O$, *J. Chem. Phys.*, 1971, **54**(1), 127–134, DOI: 10.1063/1.1674582.

107 B. F. Pedersen, The Crystal Structure of Potassium Hydrogen Oxalate, *Acta Chem. Scand.*, 1968, **22**(9), 2953–2964, DOI: 10.3891/acta.chem.scand.22-2953.

108 H. Einspahr, R. E. Marsh and J. Donohue, The Crystal Structure of Potassium Binoxalate, *Acta Crystallogr., Sect. B: Struct. Crystallogr. Cryst. Chem.*, 1972, **28**(7), 2194–2198, DOI: 10.1107/S0567740872005783.

109 L. N. Kholodkovskaya, V. K. Trunov and N. B. Tskhelashvili, Refinement of the Crystal Structures of Potassium and Rubidium Hydrogen Oxalates MHC_2O_4 (M = K, Rb), *J. Struct. Chem.*, 1990, **31**(3), 509–511, DOI: 10.1007/BF00743603.

110 G. Liu, S. M. Ciborowski, Z. Zhu, Y. Chen, X. Zhang and K. H. Bowen, The Metallo-Formate Anions, $M(CO_2)^-$, M = Ni, Pd, Pt, Formed by Electron-Induced CO_2 Activation, *Phys. Chem. Chem. Phys.*, 2019, **21**(21), 10955–10960, DOI: 10.1039/C9CP01915D.

111 B. J. Knurr and J. M. Weber, Solvent-Driven Reductive Activation of Carbon Dioxide by Gold Anions, *J. Am. Chem. Soc.*, 2012, **134**(45), 18804–18808, DOI: 10.1021/ja308991a.

112 K. P. Kepp, A Quantitative Scale of Oxophilicity and Thiophilicity, *Inorg. Chem.*, 2016, **55**(18), 9461–9470, DOI: 10.1021/acs.inorgchem.6b01702.

113 E. D. Glendening, A. E. Reed, J. E. Carpenter and F. Weinhold, *NBO Version 3.1*, 1990.

114 M. Zhou and L. Andrews, Infrared Spectra of the CO_2- and C_2O_4- Anions Isolated in Solid Argon, *J. Chem. Phys.*, 1999, **110**(5), 2414–2422, DOI: 10.1063/1.477947.

115 A. J. Gordon and R. A. Ford, *The Chemist's Companion: A Handbook of Practical Data, Techniques, and References*, Wiley, New York, 1972.

116 L. J. Saethre and T. D. Thomas, On the Origin of Substituent Effects in Electrophilic Addition: Evidence from Core-Electron Spectroscopy, *J. Org. Chem.*, 1991, **56**(12), 3935–3942, DOI: 10.1021/jo00012a029.

117 I. Fernández, G. Frenking and E. Uggerud, Rate-Determining Factors in Nucleophilic Aromatic Substitution Reactions, *J. Org. Chem.*, 2010, **75**(9), 2971–2980, DOI: 10.1021/jo100195w.

Paper II.

ORGANOMETALLICS

pubs.acs.org/Organometallics

Article

Computational Exploration of the Direct Reduction of CO_2 to CO Mediated by Alkali Metal and Alkaline Earth Metal Chloride Anions

Joakim S. Jestilä and Einar Uggerud*

Cite This: *Organometallics* 2021, 40, 1735−1743

Read Online

ACCESS | Metrics & More | Article Recommendations | Supporting Information

ABSTRACT: We present a computational survey of the reduction of CO_2 to CO by alkali metal and alkaline earth metal chloride anions in the gas phase, uncovering also mechanistic aspects on the selective tuning between oxalate and carbonate products relevant to chemical or electrochemical processes. The reduction of a single CO_2 molecule is typically endothermic, whereas the corresponding disproportionation reaction involving two molecules is exothermic. Our computational results suggest consistent periodic trends with reaction energies being highest for elements toward the center of each group. The factors governing these trends are discussed, in particular, the covalent contributions to bonding in these highly ionic species.

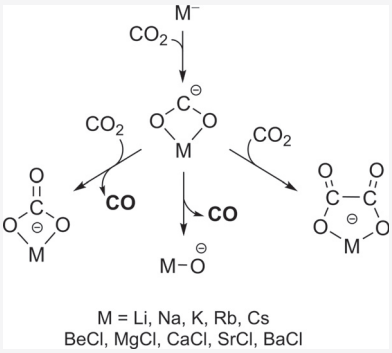

INTRODUCTION

From a circular economy perspective, the use of CO_2 as feedstock for synthetic fuels or commodity chemicals is an attractive prospect. In practice, the first step in such processes will be the reduction of CO_2 to CO. Once formed, CO may then serve as a reactant, for example, in the Fischer−Tropsch synthesis of hydrocarbons[1] and the Cativa/Monsanto processes for production of acetic acid.[2,3] Obviously, direct reduction of CO_2 to CO is an endothermic reaction:

$$CO_2(g) \rightarrow CO(g) + {}^1/_2O_2(g) \quad \Delta H^\circ_{rxn} = 283\ \text{kJ/mol} \tag{i}$$

The required energy can be obtained either electrochemically, e.g.,

$$2H^+(aq) + 2e^-(aq) + CO_2(g) \rightleftharpoons CO(g) + H_2O(l), \tag{ii}$$

or by using a suitable reducing agent, with the following reaction acting as a prototype example (ignoring the fact that the water−gas shift reaction, actually used for producing H_2 in industry, is the reverse of this):

$$CO_2(g) + H_2(g) \rightleftharpoons CO(g) + H_2O(l) \tag{iii}$$

It is well established that metal atoms and anions may add CO_2 to form complexes in gas phase reactions, formally metal carbonites (MCO_2). Their preferred structures are shown in Scheme 1, which in the case of alkali and alkaline earth metals is the bidentate coordination of the metal to both oxygen atoms (κ^2-O_2C),[4−12] while for transition metals, the metal typically binds to the carbon atom (η^1-CO_2) or in a side-on fashion (η^2-CO_2).[13−19] Early transition metals, M = Sc, Ti, V, and Cr,[14,15,20−29] even insert into one of the C−O bonds with subsequent CO elimination:

$$MCO_2 \rightarrow OMCO \rightarrow MO + CO. \tag{iv}$$

Metal carbonites, formed by the addition of alkali and alkaline metal anions to one CO_2 molecule, may in turn add a second CO_2, giving rise to metal oxalate complexes by C−C coupling:

$$M^- \xrightarrow{+CO_2} MCO_2^- \xrightarrow{+CO_2} MC_2O_4^-. \tag{v}$$

In association with this observation, we recently found from an energy resolved collisional activation study that metal

Scheme 1. Structural Motifs of Metal Carbonites (MO_2C)

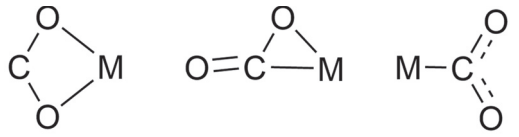

Received: April 6, 2021
Published: May 19, 2021

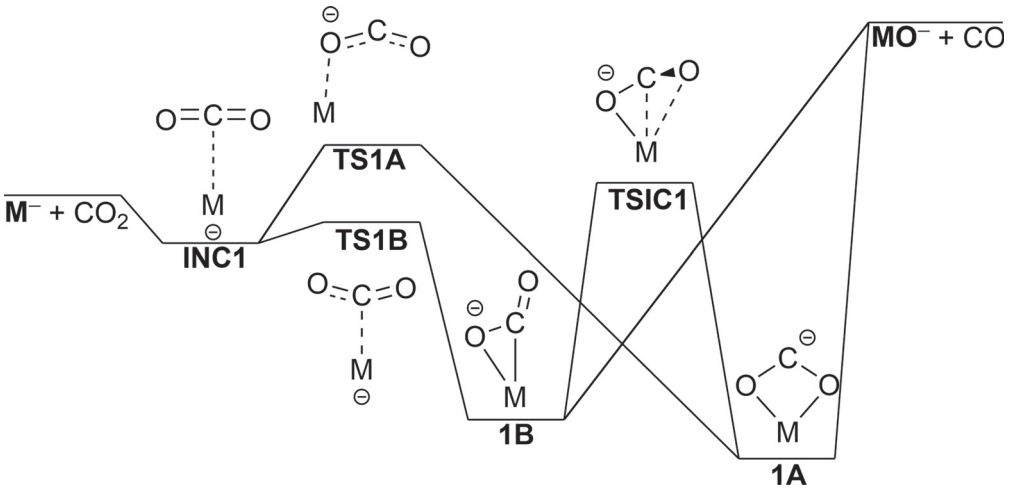

Figure 1. Schematic potential energy diagram of reactions between a CO_2 molecule and alkali (M = Li−Cs) and chloride-tagged alkaline earth (M = BeCl−BaCl) metal anions, M^-. **1A** is the κ^2-O_2C isomer, while **1B** is the η^2-CO_2 coordinated metal carbonite.

Table 1A. Relative ZPVE-Corrected [MP2/def2-TZVPPD] Electronic Energies for $M^- + CO_2 \rightarrow MO^- + CO$, in kJ/mol

	Li	Na	K	Rb	Cs	BeCl	MgCl	CaCl	SrCl	BaCl
$M^- + CO_2$	0[a]	0[a]	0[a]	0[a]	0[a]	0	0	0	0	0
INC1	−15[a]	−10[a]	−7[a]	−7[a]	−5[a]	−22	−15	−13	−11	−9
TS1A	1[a]	13[a]	14[a]	12[a]	15[a]	*n.e.*[c]	20	6	3	0
TS1B	−4[a]	3[a]	7[a]	7[a]	7[a]	−23	−9	1	−6	*n.e.*
1A	−79[a]	−39[a]	−33[a]	−33[a]	−34[a]	−247	−102	−103	−73	−85
TSIC1	−44[a]	9[a]	2[a]	2[a]	−3[a]	*n.e.*[b]	6	−35	−32	−45
1B	−68[a]	−11[a]	−9[a]	−8[a]	−14[a]	−248	−84	−96	−76	−82
$MO^- + CO$	160	228	213	213	191	−181	66	86	104	41

[a]From ref 12. [b]Proceeds by dissociation and reattachment via **INC1**. [c]The designation *n.e.* indicates either nonexistent minima or, in the case of transition states, that the reaction proceeds with a monotonic increase in potential energy in both directions along the reaction coordinate.

oxalate complexes of this kind provide an alternative route to CO formation since the disproportionation reaction

$$MC_2O_4^- \rightarrow MCO_3^- + CO \quad \text{(vi)}$$

was observed for M = Li but not for M = Na−Cs.[12] It turned out that the same type of decarbonylation had previously been seen by other authors.[30−32] Closely related to this, Miller and Uggerud observed the formation of metal carbonates accompanied by the expulsion of CO, i.e., reductive disproportionation, in S_E2-type reactions between MCO_2^- (M = ZnCl, MgCl) and CO_2 at near-thermal energies:

$$MCO_2^- + CO_2 \rightarrow MCO_3^- + CO.^{11} \quad \text{(vii)}$$

The intermediacy of a metal oxalate complex was inferred in these reactions. Reductive disproportionation of CO_2 along this pathway has also been reported for several low valent transition metal systems, typically initiated by the formation of corresponding metal carbonites.[33−37] Furthermore, carbonate formation is an unwanted byproduct since it results in both energy and carbon loss during electrolytic CO_2 reduction to CO, for which oxalate production is another competing process.[38]

Studying elementary reactions in the isolated gas phase provides fundamental insights into the physicochemical factors that determine chemical reactivity.

In particular, it would be useful to understand how different metal anions interact with the CO_2 molecule and how this in turn determines which reaction pathways toward CO formation are available for a given metal anion. Based upon the discussion above, we are interested in obtaining comprehensive pictures of the following two reactions:

$$M^- + CO_2 \rightarrow MO^- + CO \quad \text{(viii)}$$

$$M^- + 2CO_2 \rightarrow MCO_3^- + CO. \quad \text{(ix)}$$

Here, we limit ourselves to investigating periodic trends for the anionic alkali metals (M = Li, Na, K, Rb, and Cs) and the isovalent chloride-bonded alkaline earth metals (M = BeCl, MgCl, CaCl, SrCl, and BaCl), identifying relevant intermediates and key transition structures based upon quantum chemical calculations. Our efforts in isolating some of these intermediates experimentally have turned out rather unsuccessfully, probably due to their low inherent stabilities—which are not a limitation for theoretical calculations. Despite the fundamental objective of our study, we hope that the results and insights may be of use for practical purposes, for example, providing insights into electrochemical and chemical reduction of CO_2 as already mentioned.

RESULTS AND DISCUSSION

The reaction mechanisms relevant for reduction of CO_2 to CO mediated by a single anionic metal center, M^-, are illustrated in Figure 1, and the corresponding computed [MP2/def2-TZVPPD] energies are presented in Table 1A. The fully metal inserted complex $OMCO^-$ is reported as a key intermediate for the early transition metals[14,15,20−29] but

https://doi.org/10.1021/acs.organomet.1c00213
Organometallics 2021, 40, 1735−1743

Table 1B. [MP2/def2-TZVPPD] NBO Partial Charges and Other Relevant Data on the Reactants, Intermediates, and Products of the $M^- + CO_2 \rightarrow MO^- + CO$ Reaction

		Li	Na	K	Rb	Cs	BeCl	MgCl	CaCl	SrCl	BaCl
M^-	M	−1.0	−1.0	−1.0	−1.0	−1.0	−0.2	−0.1	−0.1	−0.1	−0.1
	Cl	*n.a.*	*n.a.*	*n.a.*	*n.a.*	*n.a.*	−0.8	−0.9	−0.9	−0.9	−0.9
1A	M	0.4	0.0	−0.2	−0.2	−0.2	1.1	1.5	1.5	1.4	1.4
	C	0.5	0.7	0.8	0.8	0.8	0.5	0.4	0.4	0.5	0.5
	O	−0.9	−0.9	−0.8	−0.8	−0.8	−1.0	−1.0	−1.1	−1.0	−1.0
	Cl	*n.a.*	*n.a.*	*n.a.*	*n.a.*	*n.a.*	−0.6	−0.8	−0.8	−0.9	−0.9
1B	M	0.0	−0.3	−0.4	−0.5	−0.4	0.9	1.2	1.3	1.3	1.3
	C	0.7	0.9	1.0	1.0	0.9	0.5	0.5	0.4	0.4	0.5
	O_{Bridge}	−1.0	−0.9	−0.8	−0.8	−0.8	−1.0	−1.0	−1.1	−1.1	−1.0
	$O_{Terminal}$	−0.8	−0.8	−0.7	−0.7	−0.7	−0.8	−0.8	−0.8	−0.8	−0.8
	Cl	*n.a.*	*n.a.*	*n.a.*	*n.a.*	*n.a.*	−0.6	−0.8	−0.8	−0.9	−0.9
MO^-	M	0.9	0.5	0.4	0.4	0.5	1.6	1.8	1.8	1.8	1.7
	O	−1.9	−1.5	−1.4	−1.4	−1.5	−1.8	−1.9	−1.8	−1.8	−1.7
	Cl	*n.a.*	*n.a.*	*n.a.*	*n.a.*	*n.a.*	−0.8	−0.9	−1.0	−1.0	−1.0
	r_{M-O} (Å)	1.69	1.94	2.23	2.32	2.62	1.39	1.80	1.99	2.04	2.08

Table 2A. Relative ZPVE-Corrected [MP2/def2-TZVPPD] Electronic Energies for $M^- + 2\ CO_2 \rightarrow MCO_3^- + CO$ in kJ/mol

	Li	Na	K	Rb	Cs	BeCl	MgCl	CaCl	SrCl	BaCl
$M^- + 2\ CO_2$	0[a]	0[a]	0[a]	0[a]	0[a]	0	0	0	0	0
1A + CO_2	−79[a]	−39[a]	−33[a]	−33[a]	−34[a]	−247	−102	−103	−73	−85
TSIC1 + CO_2	−44[a]	9[a]	2[a]	2[a]	−3[a]	*n.e.*[b,c]	6	−35	−32	−45
1B + CO_2	−68[a]	−11[a]	−9[a]	−8[a]	−14[a]	−248	−84	−96	−76	−82
INC2A	−102[a]	−64[a]	−60[a]	−61[a]	−62[a]	*n.e.*	*n.e.*	*n.e.*	*n.e.*	*n.e.*
INC2B	−92[a]	−32[a]	−34[a]	−36[a]	*n.e.*	−273	−110	−134	−117	−126
TS2A	−102[a]	−46[a]	−26[a]	−29[a]	−30[a]	*n.e.*	*n.e.*	*n.e.*	*n.e.*	*n.e.*
TS2B	−84[a]	*n.e.*	−34[a]	−36[a]	*n.e.*	−244	−105	−130	−113	−123
2A	−317[a]	−189[a]	−169[a]	*n.e.*	*n.e.*	−504	−334	−344	−323	−334
TSIC2	−226[a]	−134[a]	−168[a]	*n.e.*	*n.e.*	−266	−198	−254	−307	−327
2B	−241[a]	−140[a]	−172[a]	−174[a]	−188[a]	−357	−232	−315	−312	−335
TS3A	*n.e.*	5	24	11	9	*n.e.*	−120	−140	−121	−127
TS3B	−88	5	*n.e.*	*n.e.*	*n.e.*	*n.e.*	−107	−110	−118	−127
TS3C	−28	84	79	76	56	−198	−41	−66	−63	−89
INC3	−200	−70	−52	−47	−70	−411	−243	−272	−251	−246
MCO_3^- + CO	−181	−48	−20	−14	−41	−399	−228	−239	−216	−226

[a]From ref 12. [b]Proceeds by dissociation and reattachment via **INC1**. [c]The designation *n.e.* indicates either nonexistent minima or, in the case of transition states, that the reaction proceeds with a monotonic increase in potential energy in both directions along the reaction coordinate.

turned out not to correspond to a stable minimum energy structure for any of the metal anions studied here. Consequently, we will only need to consider $[M,CO_2]^-$ intermediates with intact CO_2 cores, consistent with previously published literature on reactions between these metals and CO_2.[4−9,11,12]

The formation of the intermediate metal carbonites[39,40] **1A**/**1B** via a weakly bonded ion−molecule complex **INC1** is always exothermic and facile. Small or negligible barriers separate **INC1** from **1A** and **1B**, respectively. The bidentate structure **1A** is typically the more stable isomer. It should also be noted that the barrier for interconversion between the two isomers, **TSIC1**, is usually close to or lower in potential energy than the separated reactants, $M^- + CO_2$, and always lower than the separated products $MO^- + CO$, with the exception of M = BeCl. The formation of the products from both **1A** and **1B** occurs without a reverse barrier.

Before continuing, it should be mentioned that the reverse reaction, adsorption of CO to alkaline earth metal oxide surfaces, has been reported to lead to the initial formation of MCO_2 surface species, acting as precursors to a range of products.[41−45]

According to our calculations, the reduction of CO_2 to CO is endothermic for all systems, except for M = BeCl, giving rise to a significantly exothermic reaction ($\Delta H°_{rxn,\ 0K} = -181$ kJ/mol). Unfortunately, experimental reaction energies are not directly available for all species from the literature for comparison since complete Born−Haber cycles cannot be established without making assumptions including theoretical data, and some of the experimental data are affected with considerable uncertainties. Despite this, we have made such "experimental" estimates; see Supporting Information (SI) and further in the text. Although there is considerable scatter, the relatively uncertain estimates show essentially the same periodic trends as the computed data.

From Table 1A, it can be seen that the reduction of CO_2 to CO is more endothermic for the alkali metals anions than for the alkaline earth metal chloride anions. This can be rationalized by using the reactions of Li^- and $BeCl^-$ as illustrative examples by employing Natural Bond Orbital (NBO) analysis,[46] providing localized Lewis-type structures

https://doi.org/10.1021/acs.organomet.1c00213
Organometallics 2021, 40, 1735−1743

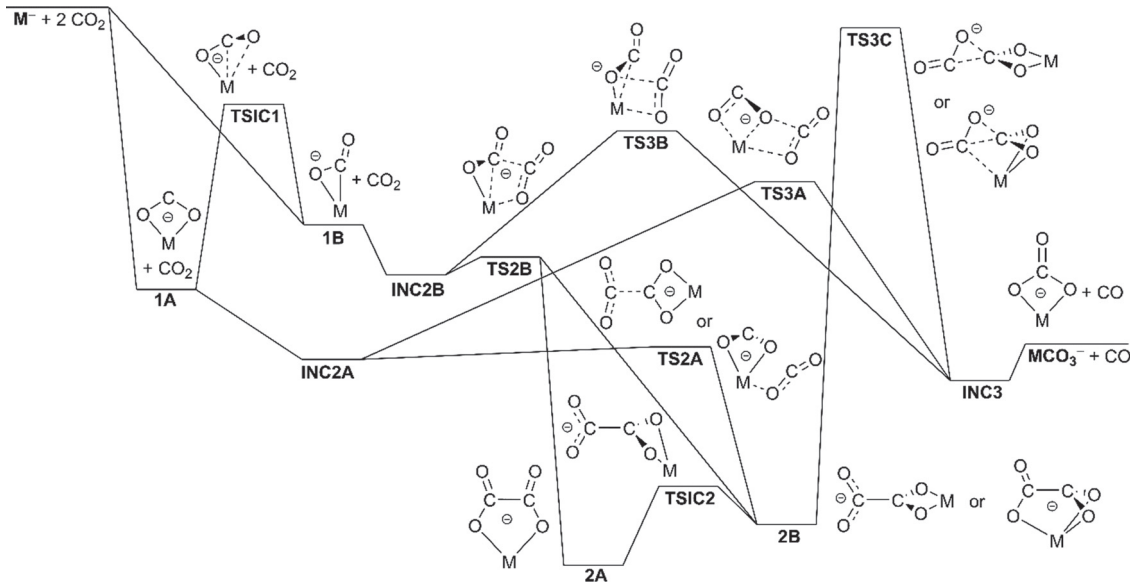

Figure 2. Schematic potential energy diagram for the reactions between two CO_2 molecules and alkali (M = Li − Cs) and chloride-tagged alkaline earth (M = BeCl−BaCl) metal anions, M^-.

Table 2B. [MP2/def2-TZVPPD] NBO Partial Charges and Other Relevant Data for $MC_2O_4^-$ and MCO_3^-

		Li	Na	K	Rb	Cs	BeCl	MgCl	CaCl	SrCl	BaCl
2A	**M**	1.0	1.0	1.0	*n.a.*	*n.a.*	1.7	1.8	1.9	1.9	1.9
2B	**M**	0.9	1.0	1.0	1.0	1.0	1.6	1.8	1.9	1.9	1.9
MCO_3^-	**M**	0.9	1.0	1.0	1.0	1.0	1.7	1.8	1.9	1.9	1.9
	r_{M-O} (Å)	1.78	2.10	2.41	2.52	2.58	1.57	1.92	2.16	2.28	2.42

and partial charges for the reactants and products (Table 1B). In the product LiO^-, the metal atom has an NBO charge of 0.9, indicating a Li−O bond (1.69 Å) with an extensive polar character with Li almost devoid of 2s electrons. The metal−oxygen bond in the isovalent $ClBeO^-$ also has a polar character but with a clearly more covalent contribution—seen from the higher relative electron density at the metal—giving rise to a much stronger bond. This observation is obviously correlated to a much shorter M−O bond length for Be (1.39 Å), corresponding to the smaller atom/ion radius. Similar comparisons can be made for the bond lengths of pairs of alkali and alkaline earth metals as one goes down in the periodic table. The effect is the same, but generally, the difference in metal−oxygen dissociation energies becomes smaller down the group.

The reaction mechanisms relevant for the reduction of two CO_2 molecules to CO leaving the complementary CO_3 moiety in the form of a metal complex are illustrated in Figure 2, and the corresponding computed energies are presented in Table 2A. Following the initial reaction between CO_2 and the metal, there are two potential routes for the subsequent reaction between **1A**/**1B** and a second CO_2 molecule, one being carboxylation to form the metal oxalates **2A**/**2B** and the other reductive disproportionation to MCO_3^- + CO.

The formation of the oxalates **2A**/**2B** is exothermic and constitutes the global potential energy minima for all metals considered. In analogy with carbonite formation, this reaction can proceed via the ion−molecule complexes **INC2A** and **INC2B** separated from the products by the small or negligible barriers **TS2A** and **TS2B**, respectively. Notably, carboxylation proceeds monotonically downhill for the alkaline earth metal carbonites—without forming an intermediate ion−molecule complex, **INC2A**.

Decarbonylation of **1A**/**1B** competes directly with carboxylation, and the same ion−molecule complex can act as the first step in both reactions. Although the total reaction leading to MCO_3^- + CO is exothermic for all metal species, the corresponding barriers **TS3A** and **TS3B** are higher in potential energy than the separated reactants M^- + 2 CO_2 for the alkali metals, except for lithium. In contrast, the barriers for the alkaline earth metals are well below the separated reactants and also the **1A**/**1B** + CO_2 asymptote in energy.

In the isolated gas phase, without a surrounding thermal bath, oxalates first formed in this way keep their total energy, which either back-dissociates reforming the reactants or gives rise to decarbonylation via **TS3C** leading to MCO_3^- + CO. Regardless, decarbonylation of the oxalates is seen to be energetically more demanding than decarbonylation of the ion−molecule complexes **INC2A**/**INC2B**, yet both display similar periodic trends. Notably, **TS3C** is lower in energy than the M^- + 2 CO_2 asymptote for the alkaline earth metals and lithium, incidentally also explaining why, among the alkali metals, decarbonylation is only observed for the lithium oxalate complex upon collisional activation, whereas the rest dissociate solely by consecutive decarboxylations.[12,30−32]

Oxalate formation as described in Table 2A is particularly facile for the alkaline earth metal carbonites due to the absence of potential energy barriers. The degree of charge transfer from the metal to CO_2 during complexation is a useful metric for the activation of the latter.[12,13,22] Our NBO analysis, outlined in Table 1B, suggests that while CO_2 receives almost two electrons from the alkaline earth metal chlorides, the alkalis

https://doi.org/10.1021/acs.organomet.1c00213
Organometallics 2021, 40, 1735−1743

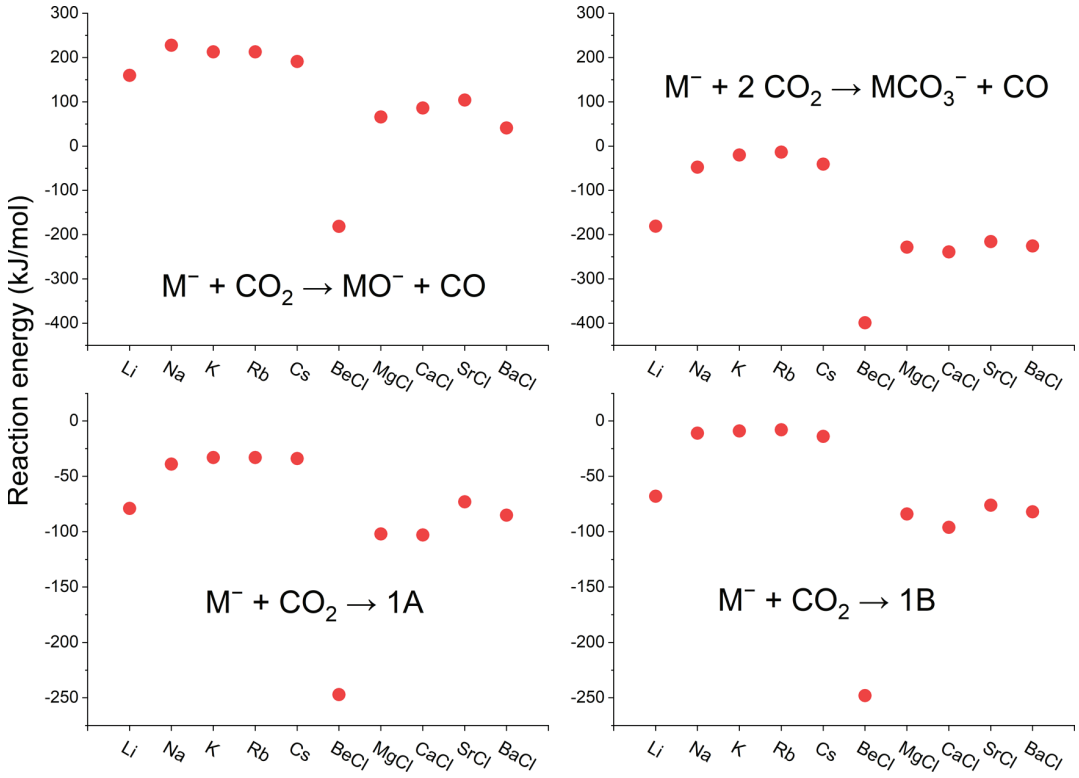

Figure 3. [MP2/def2-TZVPPD] reaction energies in kJ/mol (EE + ZPVE).

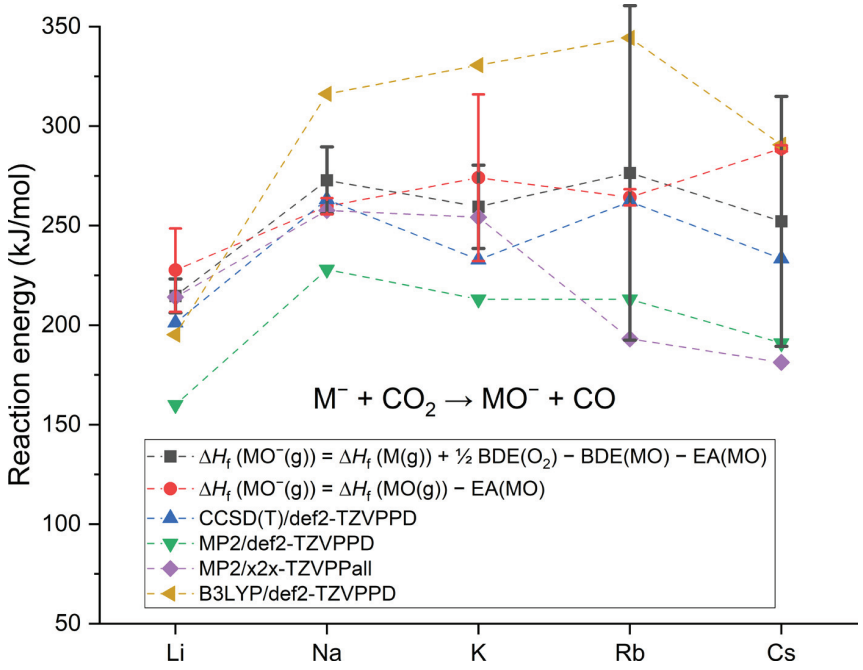

Figure 4. Comparison of "experimental" and computational reaction energies for the reduction of CO_2 to CO by the alkali metals. The connecting lines are meant as a guide to the eye and carry no further significance. For the "experimental" values, the error bars indicate uncertainties.

donate less than one. This leads to noticeable differences in how the second CO_2 moiety binds to alkali and alkaline earth metals, the former displaying generally wider OCO angles and shorter C−O bonds than the latter—more closely resembling the structure of the isolated molecule—in turn affecting the reaction energetics; see SI-C for geometries.

The reactivity trends are similar as for the reduction of one CO_2 to CO. The same reasoning applies for the relative stabilities of the carbonate products as the oxides, and the

https://doi.org/10.1021/acs.organomet.1c00213
Organometallics 2021, 40, 1735−1743

reactions of Li^- and $BeCl^-$ can conveniently be used to illustrate this once more. Table 2B shows that the M−O bonds in the product $LiCO_3^-$ are close to completely ionic (1.78 Å) due to the positive NBO charge on the metal, whereas they are more covalent (1.57 Å) in the corresponding $ClBeCO_3^-$ species. The bond lengths thus decrease across periods. Meanwhile, the M−O bond lengths of $\mathbf{MCO_3^-}$ increase down each group in parallel with increasing atom/ion radius; see SI-C for further details.

The overall reaction energies for both decarbonylation reactions, as well as formation of the intermediary carbonites **1A** and **1B**, are shown in Figure 3, illustrating their periodic trends. The alkaline earth metals generally display lower reaction energies than the alkali metals, which are consistent with the contraction of M−O bond lengths along periods. The trends are similar throughout groups, but there is some variation. The stabilities of the products decrease with increasing bond lengths for the first two or three members of each group. However, when moving toward the heavier elements, the bond distances continue to increase, now accompanied by an increase in product stabilities (from Rb to Cs and SrCl to BaCl, respectively). At the same time, any physical quantities controlling the stabilities of the products, such as the atomic/ionic radii or electron affinities/ionization potentials, decrease monotonously down each respective group; see SI. The expectation of a monotonous trend builds upon the assumption that bonding evolves in a monotonous manner, for instance, that the lighter elements form bonds with higher covalent contributions than the heavier elements. Notwithstanding, increasing evidence suggests that compounds of the heavier alkaline earth metals are not always accurately described as purely ionic. The dihalides of Ca (CaF_2), Sr (SrF_2, $SrCl_2$), and Ba (BaF_2, $BaCl_2$, BaI_2) and other compounds with these metals are bent, whereas corresponding ionic compounds are linear.[47,48] A possible explanation invokes that the $(n-1)$ p- and d-orbitals are involved in bonding.[49] On a related note, formation of carbonyl complexes $M(CO)_n$ with M = Ca, Sr, and Ba has recently been reported, where d-orbital participation is deemed important for their stabilities.[50] In our computations, bending of the MCO_2^-, MO^-, and MCO_3^- complexes with M = SrCl and BaCl is observed. A more acute angle is seen for the BaCl-complexes, consistent with the higher polarizability of barium; see SI-C. Increased d-orbital participation, and hence covalency, could therefore contribute to the deviation from the expected trends.

As mentioned earlier in the discussion, we strove to verify the computational results by comparing them with experimental reaction energies procured via Born−Haber cycles. Complete estimates for both groups were impossible since there are no published data on the novel alkaline earth metal oxochlorides, but estimates were still made for the alkali metals, specifically for the $M^- + CO_2 \rightarrow MO^- + CO$ reaction as visualized in Figure 4.

Along with the "experimental" estimates, we supplemented these with energies from additional computational methods, B3LYP and CCSD(T). Two separate methods were used to calculate the "experimental" reaction energy, only differing in how ΔH°_f ($MO^-(g)$) is determined. While one estimates the latter through ΔH°_f (M(g)) using a Born−Haber cycle involving the BDEs of O_2 and MO (in black), the second method goes more directly via ΔH°_f (MO(g)) (in red); the full details are provided in SI-A. Notwithstanding, both of these depend on the electron affinities of the metal and the metal oxide. We were unable to find the literature EA of $RbO^\bullet$; hence, it was estimated using CCSD(T), giving a value of EA($RbO^\bullet$) = 43 kJ/mol. Furthermore, the literature EAs of $LiO^\bullet$, $NaO^\bullet$, and $KO^\bullet$ are also computational.[51] Hence, to the best of our knowledge, an experimental EA has only been reported for $CsO^\bullet$ in the alkali monoxide series.[52]

Generally, the uncertainties of the "experimental" estimates increase with atomic number and overlap for all metals. The largest uncertainties are associated with the BDEs of the heavier metal oxides, $RbO^\bullet$ and $CsO^\bullet$, hampering the definitive determination of trends down groups. Still, the more direct method is less uncertain, suggesting that the reaction energy increases down the group. Barring few exceptions, the [CCSD(T)/def2-TZVPPD] energies agree most closely with the "experimental" estimates. Meanwhile, [MP2/def2-TZVPPD] yields systematically lower energies but is offset from the [CCSD(T)/def2-TZVPPD] values by a fairly constant value. Thus, while the absolute energies provided by [MP2/def2-TZVPPD] are obviously too low, the periodic trends follow closely those of the more accurate estimates. Notably, [MP2/x2c-TZVPPall] performs well for M = Li, Na, and K, as indicated by its proximity to the "experimental" estimates, whereas the energies for M = Rb and Cs are anomalously low when considering the general trends of the other methods. [B3LYP/def2-TZVPPD] performs fairly well for M = Li and Cs, overestimating the energies of the mid-group metals, yet to some extent reproduces the periodic trends.

It is relevant to point out that our reaction models are based on single-reference methods, while KO^- ($^1\Sigma^+$) is reported to have a significant multireference character, determined by the T1 diagnostic of CCSD and the percent SCF contribution to the total atomization energy.[51,53] Application of single-reference methods for species with a multireference character can lead to significant errors in energies as illustrated by the reported ΔH°_f values for KO^-, where 100 kJ/mol separates the single-reference and multireference estimates.[51] Hence, we applied the T1 diagnostic to the MO^- species on the [CCSD(T)/def2-TZVPPD] level of theory, yielding 0.073, 0.046, 0.075, 0.046, and 0.063 for M = Li, Na, K, Rb, and Cs, respectively (all in the $^1\Sigma^+$ state). Meanwhile, the diagnostic yields lower values for the alkaline earth MO^- species: 0.013, 0.020, 0.016, 0.017, and 0.018 for M = BeCl ($^1\Sigma^+$), MgCl ($^1\Sigma^+$), CaCl ($^1\Sigma^+$), SrCl (^{1}A'), and BaCl (^{1}A'), respectively. A value greater than 0.020 is often considered to indicate that multireference methods should preferably be used but does not necessarily imply failure of single-reference procedures. This is exemplified by a computational study on the first three alkali metal oxides, LiO^-, NaO^-, and KO^-, where the single-reference method only fails for the latter. Meanwhile, the alkaline earth metal species are likely adequately described by a single-reference procedure, according to the low T1-diagnostic values.

Furthermore, LiO^- and NaO^- were treated as being singlets rather than having triplet $^3\Pi$ ground states since coherence between reactant and product spin states was deemed more relevant for our reactivity models. However, the [CCSD(T)/def2-TZVPPD] energy difference between the triplet and singlet is only 7 and 1 kJ/mol, respectively.

Consequently, although we realize that there may be inherent systematic errors associated with our computational model that affect the absolute values, they are seen to be

https://doi.org/10.1021/acs.organomet.1c00213
Organometallics 2021, 40, 1735−1743

qualitatively correct compared to the "experimental" trends of the alkali metals, although the uncertainty in the latter is high.

CONCLUSIONS

In this study, we have surveyed the reduction of one and two CO_2 to CO by anionic alkali and alkaline earth metal chlorides, leading to MO^- + CO and MCO_3^- + CO, respectively. While the first reaction series is generally endothermic (with the exception of M = BeCl), the second is exothermic. For the second series, decarbonylation is energetically favored for the reaction between CO_2 and carbonites over the reaction proceeding via the oxalates. We find that the energetics are generally more favorable for alkaline earth metals than for alkali metals but that lithium displays reactivity closer to the former. Generally, the energies increase toward the middle of the groups, indicating that the covalent contributions to the bonding grow toward the heavier elements. Still, we realize that our main single-reference-based computational method is prone to failure for some of the relevant species and, furthermore, that the experimental estimates of the reaction energies are highly uncertain. Hence, further work is needed to reaffirm the results presented herein. Nevertheless, we hope that, ultimately, these theoretical reaction models provide additional insight to the reductive chemistry of the alkali and alkaline earth metals and prove useful for practical applications of electrochemical and chemical reduction of CO_2.

METHODS

All computations were conducted using the Gaussian 16[54] software suite.[55−59] We chose to use the second-order Møller−Plesset perturbation theory (MP2) as it provided energies close to CCSD(T) in a previous study involving similar oxocarbon species.[12] As noted in this study, the default frozen-core approximation for MP2 placed certain metal core orbitals higher in energy than the lowest CO_2 valence orbitals in the carbonites, leading to an unbalanced description of the complexes relative to unbound fragments M^- + CO_2, a problem that has been elaborated on in the past.[60,61] The frozen cores were thus adjusted as follows for the lighter elements: C, O, Li, Be, and Mg = [1 s^2]; Na = [$1s^2 2s^2$]; Cl and Ca = [$1s^2 2s^2 2p^6$]; and K = [$1s^2 2s^2 2p^6 3s^2$]. Most of the computations were carried out using the def2-TZVPPD basis set, retrieved from the Basis Set Exchange Web portal.[62−66] This basis set employs effective core potentials (ECPs) to account for scalar relativistic effects,[49,65,66] which describe electrons up to the penultimate shell: 28 electrons for Sr and Rb and 46 electrons for Ba and Cs. For these heavy elements, the electrons not described by the ECP were included in the determination of electron correlation. Due to the exclusion of the inner shells by the ECPs, we also used the all-electron counterpart to the def2 basis set, x2c-TZVPPall, for selected computations to check for consistency between basis sets.[67] The frozen cores of the heavy elements in computations with the all-electron basis set were adjusted to [$1s^2 2s^2 2p^6 3s^2 3p^6$] for Rb and Sr and to [$1s^2 2s^2 2p^6 3s^2 3p^6 4s^2 3d^{10} 4p^6$] for Cs and Ba. The results of these calculations are listed in the SI. The differences between the two basis sets stem from the core of the larger elements being more accurately described using the all-electron basis, while the lighter elements are in principle more accurately described with def2-TZVPPD, having more diffuse outer shells. We also employed B3LYP[55,56] and CCSD(T)[68−70] computations to further reaffirm the consistency of our models.

Vibrational frequencies were computed to ensure the correct number of imaginary frequencies for all minima and transition states (TS)—zero and one—respectively. The minima were connected by following the minimum energy paths over each TS using intrinsic reaction coordinate (IRC) computations. Relaxed potential energy scans were used to map reaction profiles in cases where transition structures were not found.

It should be noted that while LiO^- and NaO^- have triplet ground states ($^3\Pi$),[51] we only considered singlet MO^- species ($^1\Sigma^+$) in our reaction models, ensuring coherence between reactant and product spin states. Furthermore, the singlet−triplet state separations are only a few kJ/mol, reflecting a minor correction to the energies presented.

ASSOCIATED CONTENT

Supporting Information

The Supporting Information is available free of charge at https://pubs.acs.org/doi/10.1021/acs.organomet.1c00213.

Supporting information is available and contains the following: data relevant for Born−Haber cycles, additional computational details, and figures of the optimized [MP2/def2-TZVPPD] geometries for MCO_2^-, MO^-, and MCO_3^- (PDF)

Optimized geometries (XYZ)

AUTHOR INFORMATION

Corresponding Author

Einar Uggerud − *Department of Chemistry and Hylleraas Centre for Quantum Molecular Sciences, University of Oslo, N-0315 Oslo, Norway;* orcid.org/0000-0003-2732-2336; Email: einar.uggerud@kjemi.uio.no

Author

Joakim S. Jestilä − *Department of Chemistry and Hylleraas Centre for Quantum Molecular Sciences, University of Oslo, N-0315 Oslo, Norway;* orcid.org/0000-0002-7233-2093

Complete contact information is available at: https://pubs.acs.org/10.1021/acs.organomet.1c00213

Notes

The authors declare no competing financial interest.

ACKNOWLEDGMENTS

This work has received funding and support from the Norwegian Research Council through Grant No. 249788 (The chemistry of CO_2 activation and fixation), the Hylleraas Centre for Quantum Molecular Sciences No. 262695/F50 through their Centre of Excellence program, and the Norwegian Supercomputing Program (NOTUR) through a grant of computer time (Grant NN4654K). The authors would like to acknowledge Sotiris S. Xantheas for providing valuable suggestions during the final phases of this study.

REFERENCES

(1) Fischer, F.; Tropsch, H. Über Die Direkte Synthese von Erdöl-Kohlenwasserstoffen Bei Gewöhnlichem Druck. (Erste Mitteilung). *Ber. Dtsch. Chem. Ges.* **1926**, *59*, 830−831.

(2) Paulik, F. E.; Roth, J. F. Novel Catalysts for the Low-Pressure Carbonylation of Methanol to Acetic Acid. *Chem. Commun. Lond.* **1968**, *24*, 1578a.

(3) Sunley, G. J.; Watson, D. J. High Productivity Methanol Carbonylation Catalysis Using Iridium: The Cativa™ Process for the Manufacture of Acetic Acid. *Catal. Today* **2000**, *58*, 293−307.

(4) Setton, R. THE REACTION BETWEEN CESIUM AND CARBON DIOXIDE. *Bull. Soc. Chim. Fr.* **1958**, 11−12.

(5) Jacox, M. E.; Milligan, D. E. Vibrational Spectrum of CO_2^- in an Argon Matrix. *Chem. Phys. Lett.* **1974**, *28*, 163−168.

(6) Kafafi, Z. H.; Hauge, R. H.; Billups, W. E.; Margrave, J. L. Carbon Dioxide Activation by Lithium Metal. 1. Infrared Spectra of Lithium Carbon Dioxide ($Li^+CO_2^-$), Lithium Oxalate ($Li^+C_2O_4^-$),

and Lithium Carbon Dioxide ($Li_2^{2+}CO_2^{2-}$) in Inert-Gas Matrices. *J. Am. Chem. Soc.* **1983**, *105*, 3886−3893.
(7) Kafafi, Z. H.; Hauge, R. H.; Billups, W. E.; Margrave, J. L. Carbon Dioxide Activation by Alkali Metals. 2. Infrared Spectra of $M^+CO_2^-$ and $M_2^{2+}CO_2^{2-}$ in Argon and Nitrogen Matrixes. *Inorg. Chem.* **1984**, *23*, 177−183.
(8) Bencivenni, L.; D'alessio, L.; Ramondo, F.; Pelino, M. Vibrational Spectra and Structure of $M(CO_2)$ and $M_2(CO_2)$ Molecules. *Inorganica Chim. Acta* **1986**, *121*, 161−166.
(9) Soldi-Lose, H. D.; Afonso, C.; Lesage, D.; Tabet, J.-C.; Uggerud, E. Formation and Characterization of Gaseous Adducts of Carbon Dioxide to Magnesium, $(CO_2)MgX^-$ (X=OH, Cl, Br). *Angew. Chem., Int. Ed.* **2012**, *51*, 6938−6941.
(10) Miller, G. B. S.; Esser, T. K.; Knorke, H.; Gewinner, S.; Schöllkopf, W.; Heine, N.; Asmis, K. R.; Uggerud, E. Spectroscopic Identification of a Bidentate Binding Motif in the Anionic Magnesium-CO_2 Complex ($[ClMgCO_2]^-$). *Am. Ethnol.* **2014**, *126*, 14635−14638.
(11) Miller, G. B. S.; Uggerud, E. C−C Bond Formation of Mg- and Zn-Activated Carbon Dioxide. *Chem. − Eur. J.* **2018**, *24*, 4710−4717.
(12) Jestilä, J. S.; Denton, J. K.; Perez, E. H.; Khuu, T.; Aprà, E.; Xantheas, S. S.; Johnson, M. A.; Uggerud, E. Characterization of the Alkali Metal Oxalates ($MC_2O_4^-$) and Their Formation by CO_2 Reduction via the Alkali Metal Carbonites (MCO_2^-). *Phys. Chem. Chem. Phys.* **2020**, *22*, 7460−7473.
(13) Blaziak, K.; Tzeli, D.; Xantheas, S. S.; Uggerud, E. The Activation of Carbon Dioxide by First Row Transition Metals (Sc−Zn). *Phys. Chem. Chem. Phys.* **2018**, *20*, 25495−25505.
(14) Mascetti, J.; Tranquille, M. Fourier Transform Infrared Studies of Atomic Titanium, Vanadium, Chromium, Iron, Cobalt, Nickel and Copper Reactions with Carbon Dioxide in Low-Temperature Matrices. *J. Phys. Chem.* **1988**, *92*, 2177−2184.
(15) Mascetti, J.; Galan, F.; Pàpai, I. Carbon Dioxide Interaction with Metal Atoms: Matrix Isolation Spectroscopic Study and DFT Calculations. *Coord. Chem. Rev.* **1999**, *190*−*192*, 557−576.
(16) Boese, A. D.; Schneider, H.; Glöß, A. N.; Weber, J. M. The Infrared Spectrum of Au^-CO_2. *J. Chem. Phys.* **2005**, *122*, 154301.
(17) Knurr, B. J.; Weber, J. M. Solvent-Driven Reductive Activation of Carbon Dioxide by Gold Anions. *J. Am. Chem. Soc.* **2012**, *134*, 18804−18808.
(18) Knurr, B. J.; Weber, J. M. Solvent-Mediated Reduction of Carbon Dioxide in Anionic Complexes with Silver Atoms. *J. Phys. Chem. A* **2013**, *117*, 10764−10771.
(19) Lim, E.; Kim, S. K.; Bowen, K. H. Photoelectron Spectroscopic and Computational Study of $(M-CO_2)^-$ Anions, M = Cu, Ag, Au. *J. Chem. Phys.* **2015**, *143*, 174305.
(20) Zhou, M.; Andrews, L. Infrared Spectra of the CO_2^- and $C_2O_4^-$ Anions Isolated in Solid Argon. *J. Chem. Phys.* **1999**, *110*, 2414−2422.
(21) Hwang, D.-Y.; Mebel, A. M. Theoretical Study on the Reaction Mechanism of Sc Atoms with Carbon Dioxide. *Chem. Phys. Lett.* **2002**, *357*, 51−58.
(22) Dodson, L. G.; Thompson, M. C.; Weber, J. M. Titanium Insertion into CO Bonds in Anionic Ti−CO_2 Complexes. *J. Phys. Chem. A* **2018**, *122*, 2983−2991.
(23) Pápai, I.; Mascetti, J.; Fournier, R. Theoretical Study of the Interaction of the Ti Atom with CO_2: Cleavage of the C−O Bond. *J. Phys. Chem. A* **1997**, *101*, 4465−4471.
(24) Hwang, D.-Y.; Mebel, A. M. Ab Initio Study of the Reaction Mechanism of CO_2 with Ti Atom in the Ground and Excited Electronic States. *J. Chem. Phys.* **2002**, *116*, 5633−5642.
(25) Sievers, M. R.; Armentrout, P. B. Potential Energy Surface for Carbon-dioxide Activation by V^+: A Guided Ion Beam Study. *J. Chem. Phys.* **1995**, *102*, 754−762.
(26) Lessen, D. E.; Asher, R. L.; Brucat, P. J. Energy Dependent Photochemistry in the Predissociation of $V(OCO)^+$. *J. Chem. Phys.* **1991**, *95*, 1414−1416.
(27) Pápai, I.; Hannachi, Y.; Gwizdala, S.; Mascetti, J. Vanadium Insertion into CO_2, CS_2 and OCS: A Comparative Theoretical Study. *J. Phys. Chem. A* **2002**, *106*, 4181−4186.
(28) Zhang, Q.; Chen, M.; Zhou, M. Infrared Spectra and Structures of the Neutral and Charged $CrCO_2$ and $Cr(CO_2)_2$ Isomers in Solid Neon. *J. Phys. Chem. A* **2014**, *118*, 6009−6017.
(29) Schwarz, H. Metal-Mediated Activation of Carbon Dioxide in the Gas Phase: Mechanistic Insight Derived from a Combined Experimental/Computational Approach. *Coord. Chem. Rev.* **2017**, *334*, 112−123.
(30) Tian, Z.; Chan, B.; Sullivan, M. B.; Radom, L.; Kass, S. R. Lithium Monoxide Anion: A Ground-State Triplet with the Strongest Base to Date. *Proc. Natl. Acad. Sci.* **2008**, *105*, 7647−7651.
(31) Curtis, S.; Renaud, J.; Holmes, J. L.; Mayer, P. M. Old Acid, New Chemistry. Negative Metal Anions Generated from Alkali Metal Oxalates and Others. *J. Am. Soc. Mass Spectrom.* **2010**, *21*, 1944−1946.
(32) Attygalle, A. B.; Axe, F. U.; Weisbecker, C. S. Mild Route to Generate Gaseous Metal Anions. *Rapid Commun. Mass Spectrom.* **2011**, *25*, 681−688.
(33) Chatt, J.; Kubota, M.; Leigh, G. J.; March, F. C.; Mason, R.; Yarrow, D. J. A Possible Carbon Dioxide Complex of Molybdenum and Its Rearrangement Product Di-μ-Carbonato-Bis{carbonyltris-(Dimethylphenylphosphine)Molybdenum}: X-Ray Crystal Structure. *J. Chem. Soc., Chem. Commun.* **1974**, *24*, 1033−1034.
(34) Karsch, H. H. Funktionelle Trimethylphosphinderivate, III. Ambivalentes Verhalten von Tetrakis(trimethylphosphin)eisen: Reaktion mit CO_2. *Chem. Ber.* **1977**, *110*, 2213−2221.
(35) Fachinetti, G.; Floriani, C.; Chiesi-Villa, A.; Guastini, C. Carbon Dioxide Activation. Deoxygenation and Disproportionation of Carbon Dioxide Promoted by Bis(Cyclopentadienyl)Titanium and -Zirconium Derivatives. A Novel Bonding Mode of the Carbonato and a Trimer of the Zirconyl Unit. *J. Am. Chem. Soc.* **1979**, *101*, 1767−1775.
(36) Tetrick, S. M.; Cutler, A. R. Reactivity of the Metallocarboxylates $Cp(NO)(PPh_3)ReCO_2^-M^+$ toward Excess Carbon Dioxide: Degradation to a Bimetallic μ-[η^1-C(Re):η^1-O,O'(Re')] Carbon Dioxide Complex $Cp(NO)(PPh_3)ReCO_2Re(NO)(CO)(PPh_3)(\eta^1$-$C_5H_5)$. *Organometallics* **1999**, *18*, 1741−1746.
(37) Jurd, P. M.; Li, H. L.; Bhadbhade, M.; Field, L. D. Fe(0)-Mediated Reductive Disproportionation of CO_2. *Organometallics* **2020**, *39*, 2011−2018.
(38) Rabinowitz, J. A.; Kanan, M. W. The Future of Low-Temperature Carbon Dioxide Electrolysis Depends on Solving One Basic Problem. *Nat. Commun.* **2020**, *11*, 5231.
(39) Paparo, A.; Okuda, J. Carbon Dioxide Complexes: Bonding Modes and Synthetic Methods. *Coord. Chem. Rev.* **2017**, *334*, 136−149.
(40) Paparo, A.; Okuda, J. Carbonite, the Dianion of Carbon Dioxide and Its Metal Complexes. *J. Organomet. Chem.* **2018**, *869*, 270−274.
(41) Coluccia, S.; Garrone, E.; Guglielminotti, E.; Zecchina, A. Infrared Study of Carbon Monoxide Adsorption on Calcium and Strontium Oxides. *J. Chem. Soc. Faraday Trans. 1 Phys. Chem. Condens. Phases* **1981**, *77*, 1063.
(42) Babaeva, M. A.; Tsyganenko, A. A. Infrared Spectroscopic Evidence for the Formation of Carbonite CO_2^{2-} Ions in CO Interaction with Basic Oxide Surfaces. *React. Kinet. Catal. Lett.* **1987**, *34*, 9−14.
(43) Garrone, E.; Zecchina, A.; Stone, F. S. CO Adsorption on MgO and CaO. Spectroscopic Investigations of Stages Prior to Cyclic Anion Cluster Formation. *J. Chem. Soc. Faraday Trans. 1 Phys. Chem. Condens. Phases* **1988**, *84*, 2843.
(44) Babaeva, M. A.; Bystrov, D. S.; Kovalgin, A. Y.; Tsyganenko, A. A. CO Interaction with the Surface of Thermally Activated CaO and MgO. *J. Catal.* **1990**, *123*, 396−416.
(45) Zecchina, A.; Coluccia, S.; Spoto, G.; Scarano, D.; Marchese, L. Revisiting MgO−CO Surface Chemistry: An IR Investigation. *J. Chem. Soc., Faraday Trans.* **1990**, *86*, 703−709.
(46) Glendening, E. D.; Badenhoop, J. K.; Reed, A. E.; Carpenter, J. E.; Bohmann, J. A.; Morales, C. M.; Karafiloglou, P.; Landis, C. R.; Weinhold, F. NBO 7.0. 2018, Software.

https://doi.org/10.1021/acs.organomet.1c00213
Organometallics 2021, 40, 1735−1743

(47) Buchler, A.; Stauffer, J. L.; Klemperer, W. The Determination of the Geometry of High-Temperature Species by Electric Deflection and Mass Spectrometric Detection. *J. Am. Chem. Soc.* **1964**, *86*, 4544−4550.
(48) Burns, C. J.; Andersen, R. A. Organometallic Coordination Complexes of the Bis(Pentamethylcyclopentadienyl)-Alkaline Earth Compounds, $(Me_5C_5)_2MLn$, Where M IS Mg, Ca, Sr, OR Ba and Me_5C_5BeCl. *J. Organomet. Chem.* **1987**, *325*, 31−37.
(49) Kaupp, M.; Schleyer, P. v. R.; Stoll, H.; Preuss, H. Pseudopotential Approaches to Ca, Sr, and Ba Hydrides. Why Are Some Alkaline Earth MX_2 Compounds Bent? *J. Chem. Phys.* **1991**, *94*, 1360−1366.
(50) Wu, X.; Zhao, L.; Jin, J.; Pan, S.; Li, W.; Jin, X.; Wang, G.; Zhou, M.; Frenking, G. Observation of Alkaline Earth Complexes $M(CO)_8$ (M = Ca, Sr, or Ba) That Mimic Transition Metals. *Science* **2018**, *361*, 912−916.
(51) Mintz, B.; Chan, B.; Sullivan, M. B.; Buesgen, T.; Scott, A. P.; Kass, S. R.; Radom, L.; Wilson, A. K. Structures and Thermochemistry of the Alkali Metal Monoxide Anions, Monoxide Radicals, and Hydroxides. *J. Phys. Chem. A* **2009**, *113*, 9501−9510.
(52) Sarkas, H. W.; Hendricks, J. H.; Arnold, S. T.; Slager, V. L.; Bowen, K. H. Measurement of the $X\ ^2\Sigma^+-A\ ^2\Pi$ Splitting in CsO via Photoelectron Spectroscopy of CsO^-. *J. Chem. Phys.* **1994**, *100*, 3358−3360.
(53) Lee, T. J.; Taylor, P. R. A Diagnostic for Determining the Quality of Single-Reference Electron Correlation Methods. *Int. J. Quantum Chem.* **1989**, *36*, 199−207.
(54) Frisch, M. J.; Trucks, G. W.; Schlegel, H. B.; Scuseria, G. E.; Robb, M. A.; Cheeseman, J. R.; Scalmani, G.; Barone, V.; Petersson, G. A.; Nakatsuji, H.; Li, X.; Caricato, M.; Marenich, A. V.; Bloino, J.; Janesko, B. G.; Gomperts, R.; Mennucci, B.; Hratchian, H. P.; Ortiz, J. V.; Izmaylov, A. F.; Sonnenberg, J. L.; Williams-Young, D.; Ding, F.; Lipparini, F.; Egidi, F.; Goings, J.; Peng, B.; Petrone, A.; Henderson, T.; Ranasinghe, D.; Zakrzewski, V. G.; Gao, J.; Rega, N.; Zheng, G.; Liang, W.; Hada, M.; Ehara, M.; Toyota, K.; Fukuda, R.; Hasegawa, J.; Ishida, M.; Nakajima, T.; Honda, Y.; Kitao, O.; Nakai, H.; Vreven, T.; Throssell, K.; Montgomery, J. A., Jr; Peralta, J. E.; Ogliaro, F.; Bearpark, M.; Heyd, J. J.; Brothers, E.; Kudin, K. N.; Staroverov, V. N.; Keith, T. A.; Kobayashi, R.; Normand, J.; Raghavachari, K.; Rendell, A.; Burant, J. C.; Iyengar, S. S.; Tomasi, J.; Cossi, M.; Milliam, J. M.; Klene, M.; Adamo, C.; Cammi, R.; Ochterski, J. W.; Martin, R. L.; Morokuma, K.; Farkas, O.; Foresman, J. B.; Fox, D. J. *Gaussian 16*, Revision A. 03, Gaussian: Inc Wallingford CT 2016.
(55) Becke, A. D. Density-Functional Exchange-Energy Approximation with Correct Asymptotic Behavior. *Phys. Rev. A* **1988**, *38*, 3098−3100.
(56) Lee, C.; Yang, W.; Parr, R. G. Development of the Colle-Salvetti Correlation-Energy Formula into a Functional of the Electron Density. *Phys. Rev. B* **1988**, *37*, 785−789.
(57) Curtiss, L. A.; Redfern, P. C.; Raghavachari, K. Gaussian-4 Theory. *J. Chem. Phys.* **2007**, *126*, No. 084108.
(58) Curtiss, L. A.; Redfern, P. C.; Raghavachari, K. Assessment of Gaussian-4 Theory for Energy Barriers. *Chem. Phys. Lett.* **2010**, *499*, 168−172.
(59) Møller, C.; Plesset, M. S. Note on an Approximation Treatment for Many-Electron Systems. *Phys. Rev.* **1934**, *46*, 618−622.
(60) Rassolov, V. A.; Pople, J. A.; Redfern, P. C.; Curtiss, L. A. The Definition of Core Electrons. *Chem. Phys. Lett.* **2001**, *350*, 573−576.
(61) Petrie, S. Pitfalls for the Frozen-Core Approximation: Gaussian-2 Calculations on the Sodium Cation Affinities of Diatomic Fluorides. *J. Phys. Chem. A* **1998**, *102*, 6138−6151.
(62) Schuchardt, K. L.; Didier, B. T.; Elsethagen, T.; Sun, L.; Gurumoorthi, V.; Chase, J.; Li, J.; Windus, T. L. Basis Set Exchange: A Community Database for Computational Sciences. *J. Chem. Inf. Model.* **2007**, *47*, 1045−1052.
(63) Pritchard, B. P.; Altarawy, D.; Didier, B.; Gibson, T. D.; Windus, T. L. New Basis Set Exchange: An Open, Up-to-Date Resource for the Molecular Sciences Community. *J. Chem. Inf. Model.* **2019**, *59*, 4814−4820.
(64) Feller, D. The Role of Databases in Support of Computational Chemistry Calculations. *J. Comput. Chem.* **1996**, *17*, 1571−1586.
(65) Weigend, F.; Ahlrichs, R. Balanced Basis Sets of Split Valence, Triple Zeta Valence and Quadruple Zeta Valence Quality for H to Rn: Design and Assessment of Accuracy. *Phys. Chem. Chem. Phys.* **2005**, *7*, 3297.
(66) Rappoport, D.; Furche, F. Property-Optimized Gaussian Basis Sets for Molecular Response Calculations. *J. Chem. Phys.* **2010**, *133*, 134105.
(67) Pollak, P.; Weigend, F. Segmented Contracted Error-Consistent Basis Sets of Double- and Triple-ζ Valence Quality for One- and Two-Component Relativistic All-Electron Calculations. *J. Chem. Theory Comput.* **2017**, *13*, 3696−3705.
(68) Čížek, J. On the Correlation Problem in Atomic and Molecular Systems. Calculation of Wavefunction Components in Ursell-Type Expansion Using Quantum-Field Theoretical Methods. *J. Chem. Phys.* **1966**, *45*, 4256−4266.
(69) Purvis, G. D., III; Bartlett, R. J. A Full Coupled-cluster Singles and Doubles Model: The Inclusion of Disconnected Triples. *J. Chem. Phys.* **1982**, *76*, 1910−1918.
(70) Pople, J. A.; Head-Gordon, M.; Raghavachari, K. Quadratic Configuration Interaction. A General Technique for Determining Electron Correlation Energies. *J. Chem. Phys.* **1987**, *87*, 5968−5975.

https://doi.org/10.1021/acs.organomet.1c00213
Organometallics 2021, 40, 1735−1743

Paper IV.

Organic & Biomolecular Chemistry

ROYAL SOCIETY OF CHEMISTRY

PAPER

View Article Online
View Journal | View Issue

Cite this: *Org. Biomol. Chem.*, 2020, **18**, 9499

The unimolecular dissociation of magnesium chloride squarate ($ClMgC_4O_4^-$) and reductive cyclooligomerisation of CO on magnesium†

Joakim S. Jestilä, [a] Zsuzsanna Iker,[b] Mauritz J. O. Ryding [a] and Einar Uggerud *[a]

Received 29th September 2020,
Accepted 9th November 2020

DOI: 10.1039/d0ob01994a

rsc.li/obc

In this paper, we present an investigation of the unimolecular dissociation of an anionic magnesium chloride squarate complex, $ClMgC_4O_4^-$ using mass spectrometry supported by theoretical reaction models based on quantum chemical calculations. Sequential decarbonylation is the main fragmentation pathway leading to the deltate and ethenedione complexes, $ClMgC_3O_3^-$ and $ClMgC_2O_2^-$, and $MgCl^-$—yet the monomer, $ClMgCO^-$, is not observed. Calculations using the G4 composite method show that the latter is unstable with respect to further dissociation. The implications for the reverse reaction sequence, cyclooligomerisation of CO on $MgCl^-$, are discussed in detail and also compared with recent results from synthetic efforts in finding benign and efficient metal catalysed pathways to squaric acid from CO by reduction. It appears that the first step in these reactions, the formation of the first C–C bond by coupling of two CO molecules on $MgCl^-$, is the most critical. The role of electron transfer in step-by-step stabilising the nascent C_nO_n centre is highlighted.

Introduction

Activation of CO as a pathway to synthetic alternatives to fossil fuels has been a topic of research for many years.[1–6] The main challenge for the conversion of CO is related to its high bond dissociation energy (BDE) of 1071 kJ mol^{-1},[7] manifested in the high operational pressures and elevated temperatures required for the commercial processes utilising it as feedstock.[5,8–10] Nevertheless, it is well established that the CO molecule coordinates to transition metals (TM), a process that usually weakens the C–O bond as indicated through redshifted infrared stretch frequencies, with reduced low valent metal centres effecting larger shifts. Recently, the late alkaline earth metals (Ca–Ba) have been shown to form carbonyl compounds typically observed with the TMs, such as octacarbonyls, $M(CO)_8$, thus earning them the moniker "honorary transition metals".[11,12] Metal carbonyls usually serve as a starting point in synthetic reactions involving CO;[10,13–16] to this end, the reductive C–C bond formation by reactions between CO and f-block metal or Mg(II) hydrides has been studied by several authors.[17–22] These papers outline the formation of various C–C and C–H coupled species, such as free ethene ($CH_2{=}CH_2$) and propene ($CH_3CH{=}CH_2$), in addition to metal-complexed ethenediolate ($^-OCH{=}CHO^-$), ethenolate ($CH_2{=}CHO^-$), oxomethylene (OCH_2^-) and propenolate ($CH_2{=}CHCH_2O^-$). Also, for metal complexes involving U(III), Sm(II) and Mg(I), pure C–C coupling in the form of reductive cyclooligomerisation of CO has been reported, leading to oxocarbons such as deltate ($C_3O_3^{2-}$) and squarate ($C_4O_4^{2-}$):

$$n\mathrm{CO} + \mathrm{M} \rightarrow \mathrm{M}^{2+}(\mathrm{CO})_n^{2-}, \quad (1)$$

where M = U(III), Sm(II) and Mg(I).[1,2,17,23–25]

The cyclic oxocarbons, $C_3O_3^{2-}$, $C_4O_4^{2-}$, $C_5O_5^{2-}$ and $C_6O_6^{2-}$ represent an interesting class of compounds. These molecules are highly symmetric and stable due to aromaticity, resulting in unusually strong corresponding acids, $H_2C_3O_3$, $H_2C_4O_4$, $H_2C_5O_5$ and $H_2C_6O_6$, respectively; at variance, the corresponding neutral cyclic oxocarbons, *i.e.*, C_3O_3, C_4O_4, C_5O_5 and C_6O_6, are generally unstable.[26–31] Squarate ($C_4O_4^{2-}$) is a potential anode material for lithium batteries due to its electrochemical properties.[32] Contemporary electrode materials are often expensive and produced in a non-sustainable manner,[33] making it desirable to devise alternatives that mitigate these issues.

Given the background outlined above, it is of interest to further investigate the nature of the CO cyclooligomerisation processes with simple model systems. In a recent study[34] on

[a]*Department of Chemistry and Hylleraas Centre for Quantum Molecular Sciences, University of Oslo, PO Box 1033, Blindern, Oslo N-0135, Norway. E-mail: einar.uggerud@kjemi.uio.no*
[b]*Budapest University of Technology and Economics, Department of Organic Chemistry and Technology, Műegyetem rkp. 3, H1111 Budapest, Hungary*

†Electronic supplementary information (ESI) available: SI-A. Energy-resolved cross-sections and pressure extrapolation, SI-B. Metastable fragmentation, SI-C. G4 (0 K) $ClMgC_4O4^-$ singlet PES, SI-D. G4 (0 K) $ClMgC_4O4^-$ triplet PES and SI-E. Optimized geometries and G4 (0 K) energies. See DOI: 10.1039/d0ob01994a

the fragmentation of $HC_4O_4^-$ and $C_4O_4^{\bullet-}$, we inferred that one electron is necessary to initiate the cyclooligomerisation of CO,

$$n\mathrm{CO} + \mathrm{e}^{\bullet-} \rightarrow \mathrm{C}_n\mathrm{O}_n^{\bullet-}, \quad (2)$$

while a second electron terminates the reaction,

$$\mathrm{C}_n\mathrm{O}_n^{\bullet-} + \mathrm{e}^{\bullet-} \rightarrow \mathrm{C}_n\mathrm{O}_n^{2-}. \quad (3)$$

In this way, the process is analogous to the radical polymerisation of alkenes. It was also found that in the case of the isolated gas-phase, the first step in the electron initiated reaction is the association of two CO molecules with the electron,

$$2\mathrm{CO} + \mathrm{e}^{\bullet-} \rightarrow \mathrm{C}_2\mathrm{O}_2^{\bullet-}, \quad (4)$$

as CO by itself has a negative electron affinity. In contrast, during collision induced dissociation (CID) of the hydride bound tetramer, $HC_4O_4^-$, the HCO^- fragment was observed, suggesting that the initial step of the formation of $HC_4O_4^-$ from CO could be one-electron reduction of CO mediated by H^-.

As mentioned above, uranium, samarium and magnesium have previously been used for the cyclooligomerisation of CO, and although all three metals are effective reductants, magnesium stands out as being neither radioactive nor toxic. Furthermore, as an example of the ongoing shift towards more sustainable commercial processes, the chemistry of low-valent magnesium (Mg(I)) compounds has developed rapidly in recent years. A prerequisite for a Mg(I) compound is a Mg–Mg metal bond, leading to the characterisation of several dimeric LMgMgL complexes, where L is a bulky, monoanionic ligand providing a kinetic barrier against disproportionation.[23,35,36] We find it of interest to further investigate the use of magnesium as a reducing agent, and in particular the effect it has on the potential energy surface (PES) for the reductive cyclooligomerisation of CO.

In the present study, we have expanded upon our previous work[34] by substituting $MgCl^-$ for H^-. The cyclooligomerisation of CO thus becomes

$$n\mathrm{CO} + \mathrm{MgCl}^- \rightarrow \mathrm{ClMgC}_n\mathrm{O}_n^-, \quad (5)$$

where we have magnesium formally as Mg(0) bonded to Cl^- with the latter acting as a charge carrier. Of particular interest is the number of CO molecules involved in the first step of the oligomerisation as well as the energetic demands.

In practice, we investigate the oligomerisation reaction through its reverse process, *i.e.*, the unimolecular dissociation; we use the squarate complex as the starting point. Thus, the subject of this study is the reaction

$$\mathrm{ClMgC}_4\mathrm{O}_4^- \rightarrow \mathrm{MgCl}^- + 4\mathrm{CO}. \quad (6)$$

The experimental studies are conducted using mass spectrometry techniques and corresponding potential energy landscapes are computed using quantum chemical methods.

Methods

Experimental methods

All experiments were conducted using a Waters/Micromass QTOF 2 mass spectrometer. Ions were produced by electrospray ionisation (ESI) from a solution of 0.2 mM squaric acid and 0.5 mM $MgCl_2$ in 50/50 (v/v) H_2O/CH_3OH. The ESI source was operated with a capillary voltage of 3.0 kV and a cone voltage of 50 V; the source and desolvation temperatures were 100 °C and 150 °C, respectively. Once inside the high vacuum chamber of the instrument, the ions of interest, that is $ClMgC_4O_4^-$, were mass selected by a quadrupole mass filter (with better than unit mass resolution) and transferred into the collision cell. In the collision cell, fitted with a hexapole ion guide, the ions were subjected to CID at a range of centre-of-mass frame collision energies (E_{COM}). Argon was used as the collision gas and introduced into the collision cell *via* a high-vacuum leak valve; measurements were done at four different collision gas pressures: 9.45×10^{-4}, 6.66×10^{-4}, 4.73×10^{-4} and 2.76×10^{-4} mbar, plus one background pressure (3.78×10^{-5} mbar). After exiting the collision cell, intact parent ions (PI) and fragments were detected by a time-of-flight (TOF) mass analyser fitted with a microchannel plate detector. The TOF voltage was set to −3.0 kV, which allows the detection of ions having a lower mass-to-charge ratio (m/z) than the standard setting (cut-off around $m/z = 50$). Before and after the CID measurement at a given centre-of-mass energy, a reference measurement at a fixed E_{COM} = 10 eV was performed. This allowed us to monitor any changes in the collision gas pressure and to compensate for any drift in the amount of ions produced in the ion source. Both the reactant ion intensity and the fragment ion intensities were expressed relative to the references in order to ensure that different measurements were comparable with each other.

The cross section (σ) for producing a particular fragment ion can be calculated from the Lambert–Beer law analogy $\sigma = -\ln(1 - \varphi)/(Lc)$, where φ is the intensity of the fragment ion relative to the reactant ion intensity, L is the length of the flight path through the collision cell, and c is the concentration of the collision gas. Plotting σ as a function of E_{COM} yields the "breakdown curve" or "appearance curve" from which the energetic threshold for the production of the fragment in question can be estimated.

Due to factors that are difficult to control or assess with this type of instrumentation, the overall procedure will by necessity be semi-quantitative. The foremost of these factors is the pressure-independent thermal shift, *i.e.*, the apparent lowering of threshold energies due to the non-zero internal energy content of the ions. The second most important factor is the kinetic shift, *i.e.*, the necessity of increased collision energy relative to the actual energetic threshold in order to observe the fragments in the limited experimental time frame. In addition, kinetic energy is distributed between dissociating fragments, affecting the apparent thresholds for secondary fragmentation. To account for the kinetic shift, to which the thresholds for producing the secondary and third fragments,

$ClMgC_2O_2^-$ and $MgCl^-$, are the most sensitive, additional measurements were conducted by subjecting $ClMgC_3O_3^-$ (m/z 143) to CID using a single collision gas pressure of 4.63×10^{-4} mbar argon.

Given the semi-quantitative nature of the experiments, we employed two different but internally consistent methods for estimating the threshold energies: the first being a linear extrapolation of the appearance curve while the second was the more sophisticated L-CID deconvolution procedure developed by the Chen group.[37]

Appearance curves are generally sigmoidal in shape and threshold energy estimation by linear extrapolation amount to following the tangent of the inflection point to the abscissa, with the corresponding E_{COM} value being interpreted as the threshold energy. Fitting an (asymmetric double) sigmoidal function to the experimental curve provides a consistent and simple method for finding the inflection point. This is a straightforward method for estimating the threshold energy; given that it does not compensate for kinetic and thermal shifts, the method works best when these are small.

Bypassing the need of explicit knowledge of the kinetic and thermal shifts, L-CID utilises Monte-Carlo simulations to model collision events, resulting in a fit to the experimental breakdown curve.[37,38] These simulations account for critical factors in the CID process from collision to dissociation with physically realistic models. The collision event is modelled according to the electrostatic theory by Gioumousis and Stevenson,[39] including additional terms for the internal energy of the ions, their kinetic energy distribution and the effects of Doppler broadening on the appearance curve. The dissociation event is modelled accounting for the collisional energy transfer and the kinetic shift, resulting in the reaction cross section by fitting of the threshold energy with a genetic algorithm. However, L-CID has been developed and written for a specific instrumental configuration in which the ions are thermalised prior to collisional activation; this is not possible in our instrument, and we might therefore expect systematic errors to manifest in our L-CID threshold energies. The thermalisation stage assumed in L-CID uses the same gas as for the CID; hence, the temperature of the ions and collision gas is equal. In our L-CID analysis, we utilised the approximate temperature in our collision cell, 298 K, as the input parameter. This will lead to an under- or overestimation of the threshold energies depending upon whether the effective temperature of the ions is greater or smaller than 298 K, respectively. Since the actual internal energy of the ions might vary from case to case, determining it from benchmarking using known systems is rather unfeasible.

In addition, it should be pointed out that for the calculation of the density-of-states, L-CID circumvents the need to know explicitly the vibrational frequencies by replacing them with a single effective frequency. The premise of this approximation is that the vibrational modes will be sufficiently averaged for larger molecules to be represented by a single (fitted) parameter. The smallest reference molecule used in the development of the approximation was toluene with 15 atoms, which is somewhat larger than the 10 atoms of $ClMgC_4O_4^-$, studied here.

Breakdown curves were—as mentioned above—measured at four different pressures of collision gas. In order to compensate for the effects of the pressure-dependent thermal shift as well as minimising the effect of double collisions, the threshold energies obtained were plotted against the pressure and extrapolated to vacuum.

As a step towards validation of our results, we performed separate measurements and analyses—following the procedures outlined above—using two reference reactions: the decarboxylation of benzoate and the dissociation of the caesium–15-crown-5 complex (xenon was used as collision gas for the latter). The former reaction, $C_6H_5CO_2^- \rightarrow C_6H_5^- + CO_2$, has previously been analysed by Graul and Squires.[40] In addition, all reaction partners have well-known thermodynamic parameters, facilitating comparison of reaction energies determined from multiple sources. The latter reaction, Cs^+(15-crown-5) $\rightarrow Cs^+$ + 15-crown-5, has previously been subjected to threshold energy extraction methods such as L-CID[37] used herein as well as CRUNCH and T-CID developed by Armentrout *et al.*[41–43]

Plots of breakdown curves at various pressures, the corresponding extracted threshold energies, as well as threshold energies in the limit of zero pressure are shown in section SI-A of the ESI.†

In pursuit of additional information on the reaction kinetics and dynamics, we conducted an analysis of metastable fragment peaks according to methodology by Harvey *et al.*[44] This method is based on the analysis of the kinematics of dissociating ions within the reflectron time-of-flight mass analyser, taking the geometry and the electric fields explicitly into account. See SI-B† for more details.

Computational methods

Gaussian 16 (rev. A.03 and C.01) and the Gaussview 6.0.16 software were utilised for the computational part of this study.[45] Our investigation was twofold: the initial survey of the potential energy landscape for $ClMgC_4O_4^- \rightarrow MgCl^- + 4CO$ was done using density functional theory with the B3LYP functional and the aug-cc-pVTZ basis set; following the initial survey, the energies were refined with the G4 composite method.[46–51] The same computational methodology was applied to the reference reaction, $C_6H_5CO_2^- \rightarrow C_6H_5^- + CO_2$. Optimization of all structures was followed by computation of vibrational frequencies, ensuring that all PES minima and transition states have the correct number of imaginary frequencies, zero and one, respectively. Intrinsic reaction coordinate calculations were employed to connect all reactions proceeding over a transition state, and by relaxed potential energy scans where a TS was not found. We benchmarked the computed G4 (0 K) BDE of CO, MgCl and $MgCl^-$ against values in the literature. For MgCl, our computed value is 323 kJ mol^{-1}, while the literature value is 324 kJ mol^{-1}.[52] For the anion, the corresponding values are 138 kJ mol^{-1} and 123 ± 10 kJ mol^{-1}, respectively.[53] We also found fair agreement between our computed and the literature BDE for CO, 1076 kJ mol^{-1} *vs.* 1071 kJ mol^{-1},[7] respectively.

Note that G4 uses B3LYP with a smaller basis set, 6-31G(2df,p), for geometries compared to our initial survey, where aug-cc-pVTZ was used; yet, this has a minor effect (~1 kJ mol^{-1}) on the computed energies as determined by using G4 on the aug-cc-pVTZ geometries without optimisation.

We surveyed both singlet and triplet PESs for the reaction system in question, and while our calculations generally place the triplets higher in energy, intersystem crossing is possible due to relatively low (52–60 kJ mol^{-1}) singlet–triplet gaps for certain ions (SI-D, S32–S33†). Notwithstanding, we have not attempted to locate avoided crossings between the singlet and triplet species.

The sufficiency of the single reference (SR) character of our reaction model system was inferred by employing the T1 diagnostic of CCSD on the singlet $ClMgC_nO_n^-$ fragments and their relevant isomers (n = 1–4) and verifying that T1 < 0.02 in all cases; the figures are 0.0177/0.0181 for n = 4, 0.0171/0.0193 for n = 3, 0.0186 for n = 2 and 0.0175 for n = 1.[54]

Results and discussion

Dissociation of magnesium chloride squarate, $ClMgC_4O_4^-$ (m/z 171)

Collision induced dissociation of magnesium chloride squarate, $ClMgC_4O_4^-$ (m/z 171), yielded the mass spectrum in Fig. 1; specifically the figure shows the combined spectrum of CID integrated over E_{COM} = 300–900 kJ mol^{-1}. The peaks at m/z 143 and m/z 115 suggest that $ClMgC_4O_4^-$ undergoes two decarbonylations; however, there is no peak corresponding to a third CO loss at m/z 87. For the integrated range of collision energies in Fig. 1, the base peak is due to $MgCl^-$ (m/z 59), resulting from the loss of four CO; there is also a significant peak for Cl^- (m/z 35). The latter likely stems from the former by heterolytic cleavage, since this takes only 123 ± 10 kJ mol^{-1} (ref. 53) (experimental value, the corresponding G4 (0 K) from this work is 138 kJ mol^{-1}). Consistent with this assumption is that the computed Mg–Cl$^-$ bond strength increases when the metal chloride is bound to oxocarbons: 335 kJ mol^{-1} in $ClMgC_2O_2^-$, 397 kJ mol^{-1} in $ClMgC_3O_3^-$ and 429 kJ mol^{-1} in $ClMgC_4O_4^-$.

Minor peaks are observed at m/z 135, 99, 75, 56 and 37. The peak at m/z 99 could potentially be $ClMgCCO^-$, while m/z 75 could be due to $ClMgO^-$. The ethenedione radical anion, $C_2O_2^{\bullet-}$ can be observed at m/z 56. The peak at m/z 37 likely corresponds to the heavier chloride isotope $^{37}Cl^-$, but its origin is unknown. In summary, the unimolecular dissociation of $ClMgC_4O_4^-$ can be described by the following reactions, assuming that the loss of CO is sequential, with the notable exception of the last step:

$$ClMgC_4O_4^-(m/z\ 171) \rightarrow ClMgC_3O_3^-(m/z\ 143) + CO \quad (7)$$

$$ClMgC_3O_3^-(m/z\ 143) \rightarrow ClMgC_2O_2^-(m/z\ 115) + CO \quad (8)$$

$$ClMgC_2O_2^-(m/z\ 115) \rightarrow MgCl^-(m/z\ 59) + 2CO. \quad (9)$$

In addition, based on the mass difference between precursor and fragments, two minor channels are ostensibly observed:

$$ClMgC_4O_4^-(m/z\ 171) \rightarrow ClMgC_2O^-(m/z\ 99) + CO_2 + CO \quad (10)$$

$$ClMgC_4O_4^-(m/z\ 171) \rightarrow ClMgO^-(m/z\ 75) + C_2O + 2CO. \quad (11)$$

Threshold energies for the various fragments were extracted from their corresponding appearance curves using extrapolation and the L-CID software,[37] as illustrated in Fig. 2 and fully described in SI-A;† the values were extrapolated to vacuum and are given in Table 1. As mentioned in the section Experimental methods, in order to elucidate the effects of kinetic shift on

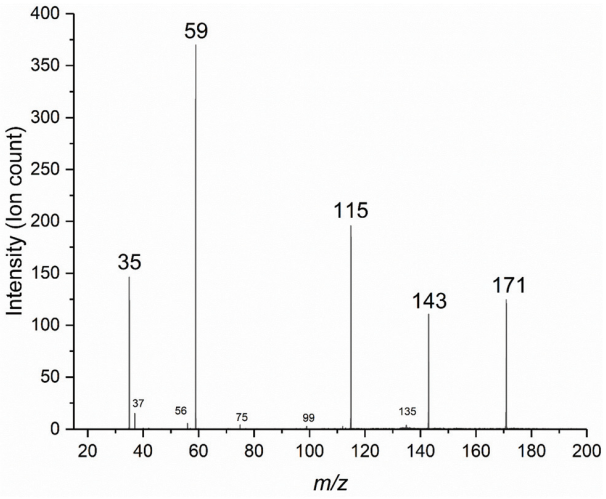

Fig. 1 Mass spectrum of resulting from CID of mass selected (MSMS) m/z 171 ($ClMgC_4O_4^-$) integrated over a collision energy range of 300–900 kJ mol^{-1} (E_{COM}) at 5.3 × 10^{-4} mbar collision gas (Ar) pressure.

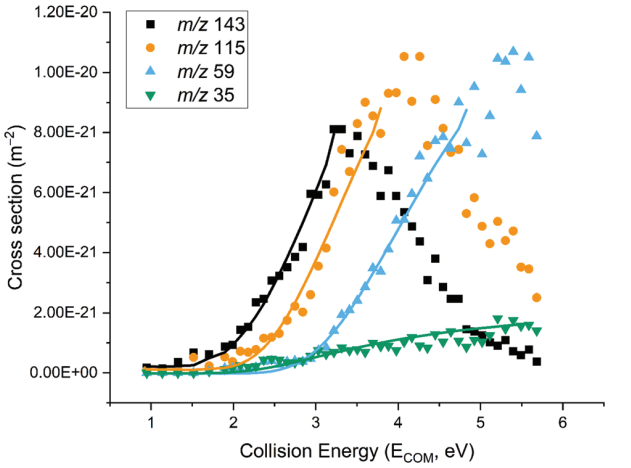

Fig. 2 Energy-resolved CID cross sections and L-CID fits for the dissociation of $ClMgC_4O_4^-$ (m/z 171) at 9.45 × 10^{-4} mbar Ar pressure.

Table 1 Threshold energies (E_T) of $ClMgC_nO_n^-$ fragments in kJ mol^{-1} estimated using two different methods. For the $ClMgC_4O_4^-$ precursor ion, the values are extrapolated to vacuum, while the $ClMgC_3O_3^-$ values are from measurements with 4.63 × 10^{-4} mbar collision gas (Ar) pressure. Uncertainties (one standard deviation) are derived from the pressure extrapolation procedure (for precursor $ClMgC_4O_4^-$), alternatively from repeated L-CID analysis and from the error of the fitted function for linear extrapolation (for precursor $ClMgC_3O_3^-$). It must be stressed that these methods of error estimation only capture the uncertainty associated with the numerical methods used to determine the energies, and therefore only part of the experimental uncertainty

	Fragment ion (m/z)		
Precursor ion (m/z)	$ClMgC_3O_3^-$ (143)	$ClMgC_2O_2^-$ (115)	$MgCl^-$ (59)
Linear extrapolation			
$ClMgC_4O_4^-$ (171)	211 ± 6	252 ± 15	374 ± 26
$ClMgC_3O_3^-$ (143)	—	127 ± 3	208 ± 2
L-CID			
$ClMgC_4O_4^-$ (171)	181 ± 4	206 ± 13	277 ± 16
$ClMgC_3O_3^-$ (143)	—	110 ± 1	161 ± 1

the secondary fragmentation reactions (reactions (8) and (9)), we also measured the appearance curves for the fragments produced by CID of mass selected $ClMgC_3O_3^-$ (m/z 143). These threshold energies are also given in Table 1; however, it should be noted that repeated experiments to extrapolate these values to vacuum was not done. Based on the observations for the vacuum-extrapolations done (see Fig. S6–S8 in SI-A†), the threshold energies at zero pressure are likely higher than these values.

With $ClMgC_4O_4^-$ as the precursor, the L-CID threshold energies indicate that the first decarbonylation has the lowest energy demand of 181 ± 4 kJ mol^{-1}; the trend continues with the second and third decarbonylation events requiring 206 ± 13 kJ mol^{-1} and 277 ± 16 kJ mol^{-1}, respectively. The corresponding thresholds from linear extrapolation are slightly higher in absolute values at, respectively, 211 ± 6 kJ mol^{-1}, 252 ± 15 kJ mol^{-1} and 374 ± 26 kJ mol^{-1}; however, the differences in threshold energies have overlapping uncertainties between the two methods as shown in the next section.

We note from Table 1 that in the sequential decay $ClMgC_4O_4^- \rightarrow ClMgC_3O_3^- \rightarrow ClMgC_2O_2^- \rightarrow MgCl^-$, the threshold energies of the second and third step represent only a minor increase compared to the threshold energy of the first step: (206 ± 13)–(181 ± 4) = 25 ± 14 kJ mol^{-1} and (277 ± 16)–(181 ± 4) = 96 ± 12 kJ mol^{-1}, respectively (L-CID values). In comparison, with $ClMgC_3O_3^-$ as the precursor ion, the threshold energies extracted from the appearance curves of $ClMgC_2O_2^-$ and $MgCl^-$ are, respectively, 110 ± 1 kJ mol^{-1} and 161 ± 1 kJ mol^{-1} when using L-CID; with linear extrapolation the corresponding threshold energies are 127 ± 3 kJ mol^{-1} and 208 ± 2 kJ mol^{-1}.

Both $ClMgC_2O_2^-$ and $MgCl^-$ can be said to display higher threshold energies relative to $ClMgC_3O_3^-$ when $ClMgC_3O_3^-$ is the reactant ion rather than a product of $ClMgC_4O_4^-$ decarbonylation. This could imply a different isomer (or mixture of isomers) of $ClMgC_3O_3^-$ when it is formed in the ion source compared to when formed from CID of $ClMgC_4O_4^-$. In addition, there is likely a difference in the internal energy of $ClMgC_3O_3^-$ between the two cases, and, of course, the aforementioned influence of the kinetic shift for the latter case. Alternatively, there might exist an activated pathway to $ClMgC_2O_2^-$ such that it is easier to form from the squarate complex than from the trimer. To assess whether this could be the case or not, we conducted a separate analysis of metastable fragmentation within the TOF (SI-B, S27–S30†) as described by Harvey *et al.*[44] Consistent with there being such a pathway, a peak corresponding to $ClMgC_4O_4^- \rightarrow ClMgC_2O_2^- + 2CO$, *i.e.*, the double decarbonylation of the squarate complex, is observed (SI-B, Fig. S22†); in contrast, the peak for the single decarbonylation has a higher intensity when $ClMgC_3O_3^-$ is mass selected as the precursor (SI-B, Fig. S23†). However, the presence of a peak corresponding to a specific neutral loss cannot be used to confirm a reaction pathway, as it does not distinguish between single step and sequential reactions. We will continue the discussion on $ClMgC_3O_3^-$ after presenting our computational reaction model in the next section.

Computational model for the dissociation of $ClMg(\kappa^2\text{-}C_4O_4)^-$

The singlet G4 (0 K) PES for the fragmentation of $ClMgC_4O_4^-$, **1A**, is displayed in Fig. 3. The kinetically favoured pathway is marked by bold lines in order to distinguish it from the alternative high-energy routes.

For the decarbonylation of $ClMgC_4O_4^-$, opening the cyclic squarate moiety prior to dissociation,

$$ClMg(\kappa^2\text{-}C_4O_4)^-(\mathbf{1A}) \rightarrow TS1A \rightarrow ClMg(\kappa^2\text{-}C_4O_4)^-(1B) \rightarrow TS2A \rightarrow ClMg(\kappa^2\text{-}C_3O_3)^-(2B) + CO \quad (12)$$

has a lower barrier than direct decarbonylation,

$$ClMg(\kappa^2\text{-}C_4O_4)^-(\mathbf{1A}) \rightarrow \mathbf{TS1B} \rightarrow ClMg(\kappa^2\text{-}C_3O_3)^-(\mathbf{2A}) + CO, \quad (13)$$

by 83 kJ mol^{-1}. The kinetically favoured pathway (12) leads to the open $ClMg(\kappa^2\text{-}C_3O_3)^-$ isomer, **2B**, which has a 3 kJ mol^{-1} barrier for interconversion to the thermodynamic product, **2A**. The second decarbonylation occurs without a reverse barrier,

$$ClMg(\kappa^2\text{-}C_3O_3)^-(\mathbf{2B}) \rightarrow ClMg(\eta^2\text{-}C_2O_2)^-(\mathbf{3A}) + CO, \quad (14)$$

unlike the last step,

$$ClMg(\eta^2\text{-}C_2O_2)^-(\mathbf{3A}) \rightarrow \mathbf{TS4A} \rightarrow MgCl^-(\mathbf{4A}) + 2CO, \quad (15)$$

where **TS4A** lies 50 kJ mol^{-1} above the separated products in energy. Following the intrinsic reaction coordinate of **TS4A** leads to the full dissociation of the squarate complex into $MgCl^-$ and 4 CO molecules. While $ClMgCO^-$ is a minimum on the singlet electronic G4 (0 K) PES (bound by ~5 kJ mol^{-1}), the zero-point vibrational correction places it higher in energy than the CO + $MgCl^-$ asymptote (by 5 kJ mol^{-1}). We did not find any transition states for the dissociation of the singlet monomer, the absence of which was supported by relaxed potential energy scans. Nonetheless, we found three high-

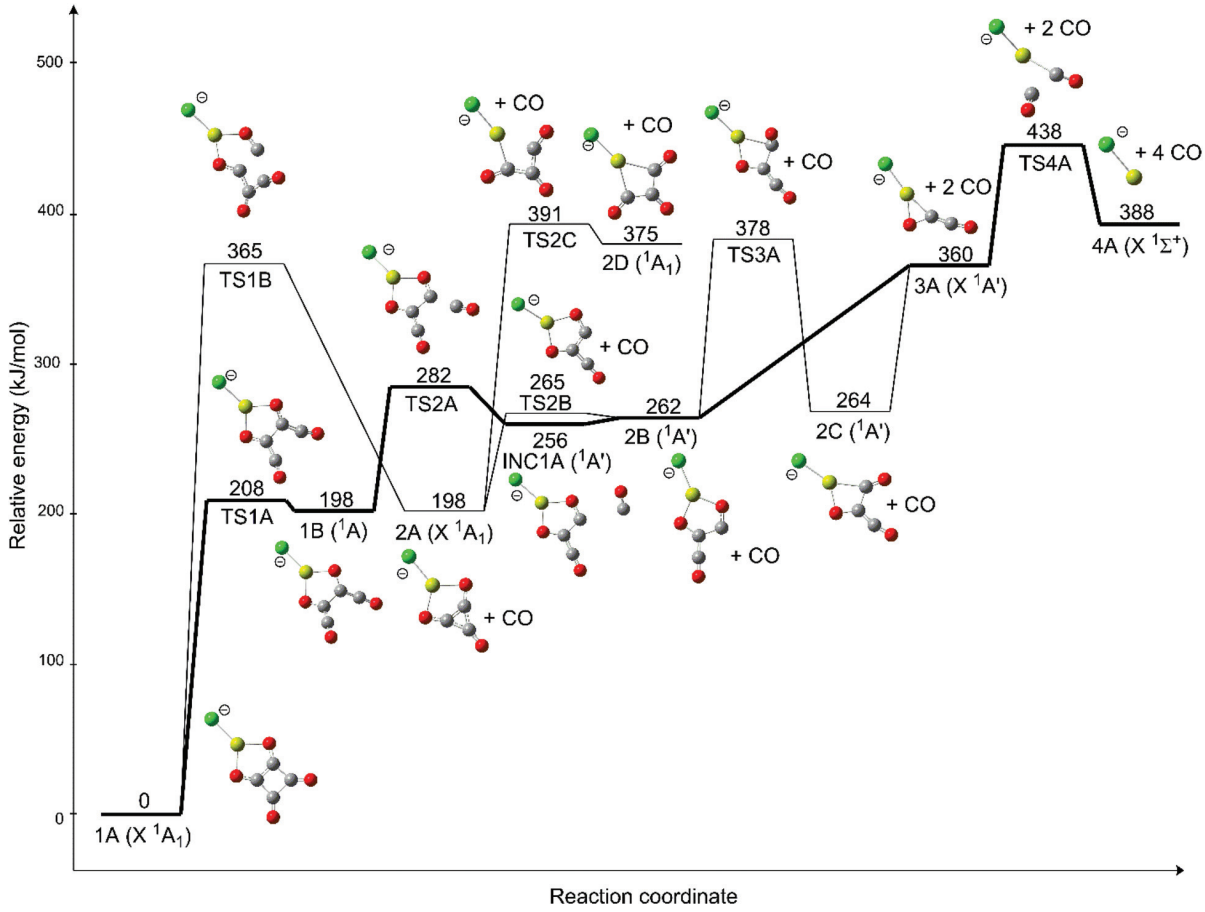

Fig. 3 The singlet G4 (0 K) potential energy (electronic + zero-point vibrational energy) diagram for the dissociation of $ClMgC_4O_4^-$ (**1A**) into $MgCl^-$ + 4CO (**4A**). The lowest energy pathway is indicated by bold lines.

energy triplet isomers with stronger Mg–C bonding interactions, $^3ClMg(\eta^1\text{-}CO)^-$, $^3ClMg(\eta^2\text{-}CO)^-$ and $^3ClMg(\eta^1\text{-}OC)^-$, discussed later in the text. These results suggest that two CO molecules are lost simultaneously from the dimer complex, $ClMgC_2O_2^-$ (*m*/*z* 115), consistent with the fact that we do not observe a signal corresponding to $ClMgCO^-$ (*m*/*z* 87) in the CID mass spectrum in Fig. 1.

The energy difference for formation of **2B** *via* **TS2A** and formation of **3A** is 78 kJ mol^{-1} in Fig. 3; this might be compared to the difference in threshold energy between $ClMgC_3O_3^-$ and $ClMgC_2O_2^-$ with $ClMgC_4O_4^-$ as the reactant ion. From Table 1, we get these values as 25 ± 14 kJ mol^{-1} for L-CID and 41 ± 15 kJ mol^{-1} for the linear extrapolation; both lower than the aforementioned 78 kJ mol^{-1}, yet with overlapping uncertainties. However, considering that the suggested mechanism for the first decarbonylation of $ClMgC_4O_4^-$ involves two discrete transition states while the second decarbonylation leading to **3A** proceeds asymptotically in one step, a kinetic elevation of **2B** relative to the intermediate following it is expected. In this case, once the energy of the system is sufficiently high to reach the subsequent intermediate (*i.e.* **3A**), it will likely also be enough to counteract the kinetic effect. Also note the activated pathway over **TS1B**, higher in energy than $ClMgC_2O_2^-$ + 2CO (**3A**), the possibility of which was suggested earlier.

More accurate experimental estimates of the threshold energies for the formation of **3A** and **4A** can be found by the collisional activation of $ClMgC_3O_3^-$, although we will point out that the values presented here are likely underestimated. For the first loss of CO, L-CID and linear extrapolation yield threshold energies of 110 ± 1 kJ mol^{-1} and 127 ± 3 kJ mol^{-1}, respectively; this is in fair agreement with the computed 98 kJ mol^{-1} energy difference between **2B** and **3A**. Notwithstanding, the experiments could also indicate that the $ClMgC_3O_3^-$ structure depends upon the location of its formation, be it in-source or following CID of a precursor in the high-vacuum region. This is not an unlikely case given the results in Fig. 3 clearly showing the preferred reaction pathway from $ClMgC_4O_4^-$ to $ClMgC_3O_3^-$ landing in the thermodynamically less favourable isomer **2B**, whereas the more stable isomer **2A** can be expected to be formed in the source. For comparison, the energy difference between **2A** and **3A** is 162 kJ mol^{-1} in Fig. 3.

For the final step of the dissociation, **3A** → **TS4A** → **4A**, the energy difference is 78 kJ mol^{-1} between **3A** and **TS4A**. The

difference in L-CID threshold energies between $ClMgC_2O_2^-$ and $MgCl^-$ are 71 ± 21 kJ mol^{-1} or 51 ± 6 kJ mol^{-1} depending upon if respectively $ClMgC_4O_4^-$ or $ClMgC_3O_3^-$ was used as the reactant ion; the corresponding values from linear extrapolation are 122 ± 30 kJ mol^{-1} and 81 ± 8 kJ mol^{-1}.

As mentioned in the section Experimental methods, we subjected two reference reactions to our analyses in order to test their accuracies (SI-A, S18–S26†). The reference reaction,

$$C_6H_5CO_2^- \rightarrow C_6H_5^- + CO_2, \quad (16)$$

has a computed 0 K reaction energy of 234 kJ mol^{-1}, slightly closer to the L-CID threshold of 205 ± 1 kJ mol^{-1} than to the threshold determined by linear extrapolation: 265 ± 4 kJ mol^{-1}. For the second reference reaction,

$$Cs^+(15\text{-Crown-5}) \rightarrow Cs^+ + 15\text{-Crown-5}, \quad (17)$$

L-CID gives a threshold energy of 154 ± 3 kJ mol^{-1}, while linear extrapolation again yields a higher value at 201 ± 5 kJ mol^{-1}. The former is closer to the values determined by both Narancic *et al.* and Armentrout *et al.* at 138 ± 5 and 159 ± 10 kJ mol^{-1}, respectively.[37,43]

Although the absolute threshold energies are generally lower than the computational energies for the formation of various intermediates, we find acceptable agreement between experiment and theory for the relative energies, *i.e.*, when comparing the difference in threshold energies to the computed energy difference between intermediates, as shown in Fig. 4. In particular, L-CID provides systematically lower threshold energies than G4 (0 K), which could be connected to the assumption in the program code that the ions are thermalised to the temperature of the collision gas (usually close to room temperature) prior to CID, as hinted at in the Experimental methods section.[37] Another possibility is that the experimental energies are lowered by tunnelling, shown to be significant even for heavier atoms.[55,56] The probability of tunnelling increases with the curvature of the potential energy surface along the reaction coordinate, and the largest effect would therefore be expected for **TS1A** and **TS1B** with imaginary frequencies **i**·408 and **i**·385 cm^{-1}, respectively.

Reductive activation and cyclooligomerisation of CO to squarate

Now, we will look at the reverse reactions to those discussed above, namely the cyclooligomerisation of CO starting with $MgCl^-$. The computed potential energy diagram is included in Fig. 5, with the same designation for the ions as in Fig. 3. The first and most demanding step in the activation of CO by $MgCl^-$ is the termolecular reaction,

$$MgCl^-(\mathbf{4A}) + 2CO \rightarrow ClMg(\eta^2\text{-}C_2O_2)^-(\mathbf{3A}), \quad (18)$$

proceeding through the transition state **TS4A** 50 kJ mol^{-1} higher in energy than the separated reactants. This is comparable to the 41 kJ mol^{-1} needed for the incorporation of one CO molecule into the dimeric Mg(I) complex, [{(^{Dip}Nacnac)(D)Mg–Mg(^{Dip}Nacnac)}] (where Nacnac = $[(NCMe)_2CH]^-$; Dip = 2,6-diisopropylphenyl; D = :C{N(Me)C(Me)}$_2$), as reported by Yuvaraj *et al.*,[23] denoted $[Mg]_2$ hereafter. Similar values, 46 and 54 kJ mol^{-1}, are reported for the analogous incorporation of one and two CO molecules, respectively, into a U(III) mixed-sandwich model complex, [U] = U(η-C_8H_6{SiH_3-1,4}$_2$)(η-Cp).[2,24,57] However, direct comparison should be made with care, as our system is monometallic, while these involve two metals. Another distinction regards the electronic states of the metals, since the magnesium centre is formally Mg(0) in $MgCl^-$, Mg(I) in $[Mg]_2$, and uranium is U(III) in [U].

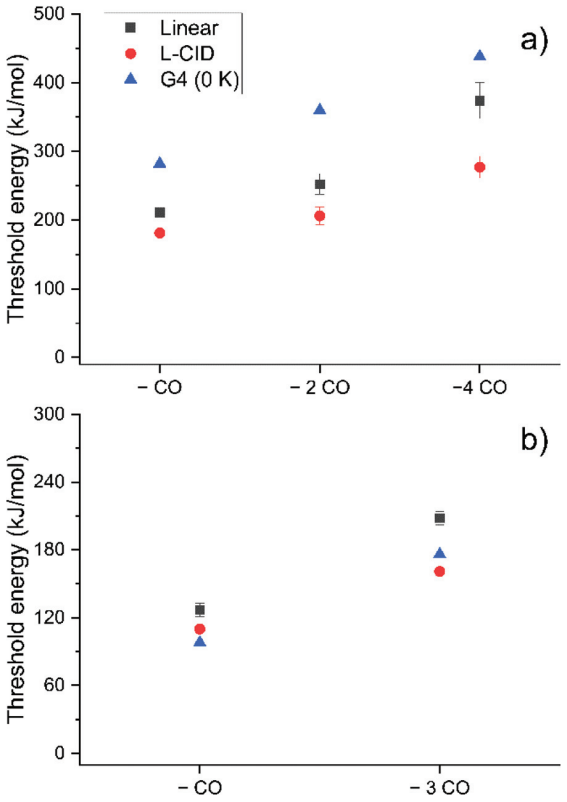

Fig. 4 Comparison of threshold energies determined by linear extrapolation, L-CID and G4 (0 K) computations. (a) Energies required for the dissociation of $ClMgC_4O_4^-$ into $ClMgC_3O_3^-$, $ClMgC_2O_2^-$, and $MgCl^-$ by loss of one, two and four COs, respectively. (b) Energies required for the dissociation of $ClMgC_3O_3^-$ into $ClMgC_2O_2^-$ and $MgCl^-$ by loss of one and three COs, respectively.

The magnesium chloride ethenedione complex, **3A**, can receive a third CO molecule in a barrierless reaction,

$$ClMg(\eta^2\text{-}C_2O_2)^-(\mathbf{3A}) + CO \rightarrow ClMg(\kappa^2\text{-}C_3O_3)^-(\mathbf{2B}). \quad (19)$$

The resulting open deltate isomer, **2B**, has a negligible barrier for ring-closing to **2A** and a 20 kJ mol^{-1} barrier for further CO incorporation. The latter finally results in the cyclotetramerisation of CO to **1A** *via* an open squarate isomer, **1B**, with a 10 kJ mol^{-1} barrier for ring-closing, 388 kJ mol^{-1} lower than the separated reactants. In comparison, formation of deltate from $[Mg]_2$-(μ-η^2:η^2-CO)$^{2-}$ proceeds downhill by

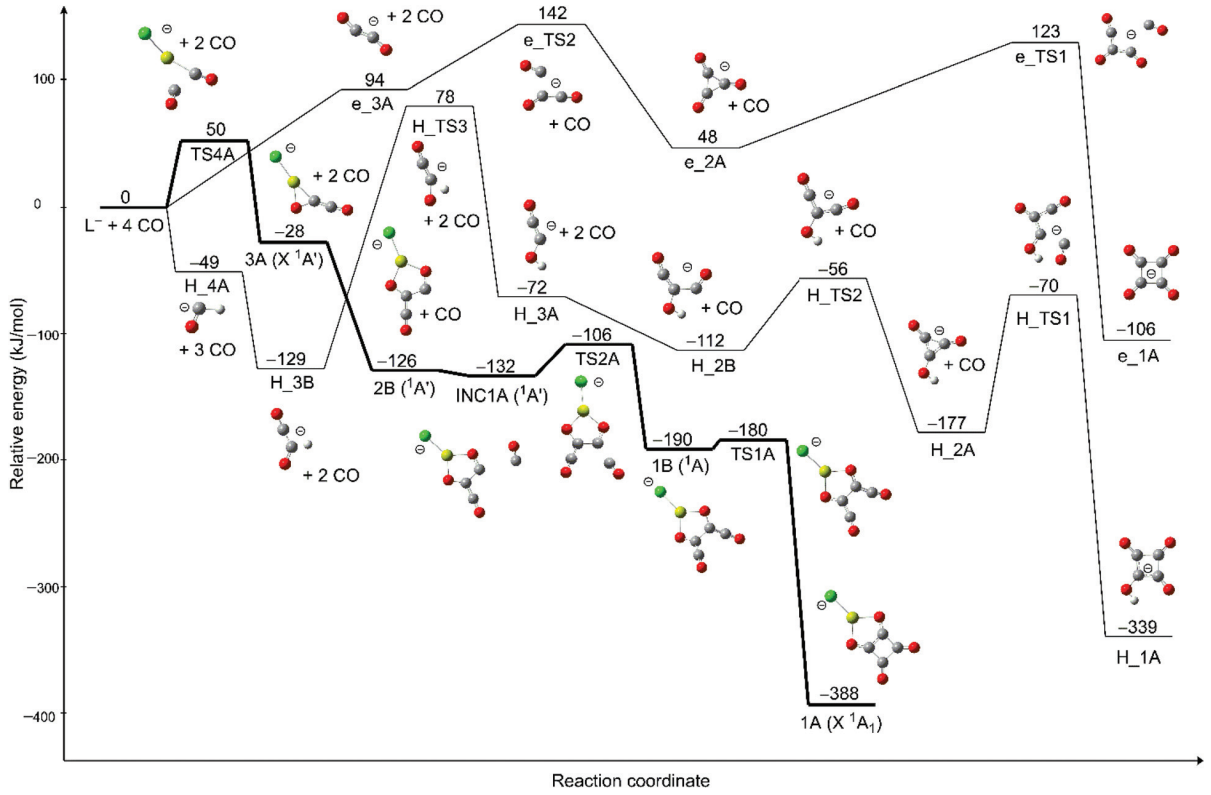

Fig. 5 The singlet G4 (0 K) potential energy (electronic + zero-point vibrational energy) diagram for the $L^- + nCO \rightarrow LC_nO_n^-$ reactions (L = e^-, H^- or $MgCl^-$). The lowest energy $ClMgC_4O_4^-$ (L = $MgCl^-$) pathway is indicated by lines in bold, while the lowest energy $C_4O_4^{\bullet-}$ and $HC_4O_4^-$ pathways (from ref. 34) are indicated by prefixes e and H in the labels, respectively.

403 kJ mol^{-1} (ref. 23) with small barriers separating product ions from the CO and precursor ion complexes.

McKay *et al.*[57] suggest that a symmetric $[U]_2$-$(\mu\text{-}\eta^2\text{:}\eta^2\text{-}C_2O_2)^{2-}$ isomer with inequivalent carbon centres is responsible for the reactivity of the diuranium ethenedione complex. Formation of this complex,

$$[U]_2\text{-}(\mu\text{-}\eta^2 : \eta^2\text{-}CO)^{2-} + CO \rightarrow [U]_2\text{-}(\mu\text{-}\eta^2 : \eta^2\text{-}C_2O_2)^{2-} \quad (20)$$

requires 72 kJ mol^{-1}, while the next step in the cyclooligomerisation,

$$[U]_2\text{-}(\mu\text{-}\eta^2 : \eta^2\text{-}C_2O_2)^{2-} + CO \rightarrow [U]_2\text{-}(\mu\text{-}\eta^2 : \kappa^2\text{-}C_3O_3)^{2-}, \quad (21)$$

needs 100 kJ mol^{-1} to proceed.[57] In contrast, the symmetry-enforced equivalence of the CO units in the kinetic zig-zag isomer $[U]_2$-$(\mu\text{-}\eta^3\text{:}\eta^3\text{-}C_2O_2)^{2-}$ hampers its reactivity; hence, it only undergoes isomerisation to the inert ethynedione isomer, $[U]_2$-$(\mu\text{-}\eta^1\text{:}\eta^1\text{-}C_2O_2)^{2-}$. However, due to the asymmetric bonding moiety inherent to a single Mg-centre in the coordination sphere, the carbon centres in our system (**3A**) are inequivalent. A study by Arnold and coworkers[25] on a uranium(III) trisamide complex, N''_3U ($N'' = N(SiMe_3)_2^-$)—which couples CO in a similar manner to the above $[U]_2$ complex—corroborates the inertness of the ethynedione isomer, $^-OC{\equiv}CO^-$, but shows that it can be functionalised through heating, supporting the assumptions we made in an earlier publication[34] about the isomeric dependency on the reactivity of the CO-dimer.

Direct comparison of reaction dynamics is simpler between relevant gas-phase $LC_nO_n^-$ species (L = e^-, H^- or $MgCl^-$) than with the Mg(I) or U(III) complexes mentioned above. Fig. 5 shows that while cyclooligomerisation is initiated with the association of two CO molecules when L = e^- or $MgCl^-$, H^- can form a bond directly with one CO, leading to the formyl anion, **H_4A**. Subsequently, the formyl anion can add to another CO without a barrier, yielding **H_3B**. Although both of these steps proceed downhill in energy, isomerisation of **H_3B** to the more reactive ethenedione isomer, **H_3A**, requires crossing a barrier, **H_TS3**, of 207 kJ mol^{-1} (78 kJ mol^{-1} higher than the separated reactants). Each CO-addition leads to species lower in energy than the separated reactants for both L = H^- and $MgCl^-$, while the radical anions **e_3A** and **e_2A** reside uphill in energy. Only formation of the squarate radical anion, **e_1A**, amounts to a moderate stabilisation of 106 kJ mol^{-1} compared to four CO molecules and a free electron, while the formation of $HC_4O_4^-$ and $ClMgC_4O_4^-$ are exothermic by 339 and 388 kJ mol^{-1}, respectively. This is consistent with the fact that the only stable corresponding neutral species is C_4O_4, in addition to the higher oligomers C_5O_5 and C_6O_6, while C_2O_2 and C_3O_3 are unstable.[31,58] Overall, in terms of the energetics, the efficiency of activation and cyclooligomerisation is in the

order $MgCl^-$ > H^- > e^- for our computational models, determined by comparing the highest barriers for the process. The highest barrier is 50 kJ mol^{-1} for $MgCl^-$, 78 kJ mol^{-1} for H^-, and 142 kJ mol^{-1} for e^-.

Unfortunately, we are not aware of any single study containing the corresponding value for cyclotetramerisation by the model complex [U],[2,24,57] while only cyclotrimerisation has been reported for $[Mg]_2$.[23] Nonetheless, formation of $[U]_2$-$(\mu\text{-}\eta^1\text{:}\kappa^2\text{-}C_3O_3)^{2-}$ lowers the energy by 162 kJ mol^{-1} (ref. 57) while an additional lowering of 136 kJ mol^{-1} (ref. 2) is provided through the formation of $[U]_2\text{-}(\mu\text{-}\kappa^2\text{:}\kappa^2\text{-}C_4O_4)^{2-}$, amounting to a total of 298 kJ mol^{-1} for the whole process. The total stabilisation of the system by the formation $[Mg]_2\text{-}(\mu\text{-}\eta^1\text{:}\eta^1\text{-}C_3O_3)^{2-}$ is 432 kJ mol^{-1}, and given the low barriers involved, this implies that the $[Mg]_2$ complex is the most efficient reductant of CO among the dimeric metal complexes reported in literature. The relative efficiency of Mg(I) and Mg(0) compared to U(III) is consistent with their lower ionisation energies of 1451 and 738 against 3540 kJ mol^{-1}, respectively.[59] Still, this does not account for the influence of the molecular structures on the propensity for reduction, evident from comparing Mg(I) and Mg(0).

In the previous study on $HC_4O_4^-$ and $C_4O_4^{\bullet-}$, we surmised that the charge-bearing electron initiates the cyclooligomerisation process, while a second one terminates it. Expanding on this admittedly simple scheme, we computed the natural partial charges in each $ClMgC_nO_n^-$ oligomer along the pathway (Fig. 6). For the first step, the partial charge on the ethenedione moiety in **3A** is −1.835, indicating that close to two electrons have been transferred from $MgCl^-$ and addition of a third CO proceeds without a barrier. In the next step, the **2B** and **2A** isomers of $ClMgC_3O_3^-$ have slightly increased negative partial charges on the C_3O_3 moiety, −1.897 and −1.915, respectively, and further CO addition has a higher barrier for the latter than the former. Finally, squarate has a computed charge of −1.903 in **1A**. Thus, a more negative partial charge on the C_nO_n moieties is generally consistent with higher barriers towards further reaction.

Magnesium monocarbonyls

To elucidate why the $ClMgCO^-$ monomer is missing in our experiments, we optimized the neutral, cationic and anionic $ClMgCO^{-/+}$ species, as well as the corresponding $MgCO^{+/2+}$ complexes (Fig. 7). We advise that in the notation used in this section, $^{2S+1}MCO^{charge}$, 2S + 1 describes spin multiplicity, not to be confused with isotopes.

The carbonyl vibrational frequency (νC═O) for free CO is 2205 cm^{-1} on the G4 level of theory, while the experimental value is 2143 cm^{-1}.[7,60] According to the calculations, the νC═O for $^1ClMgCO^-$ is slightly redshifted at 2110 cm^{-1}, consistent with the weak interaction between Mg and CO. This consists of donation of the Mg lone pair to the antibonding π*-

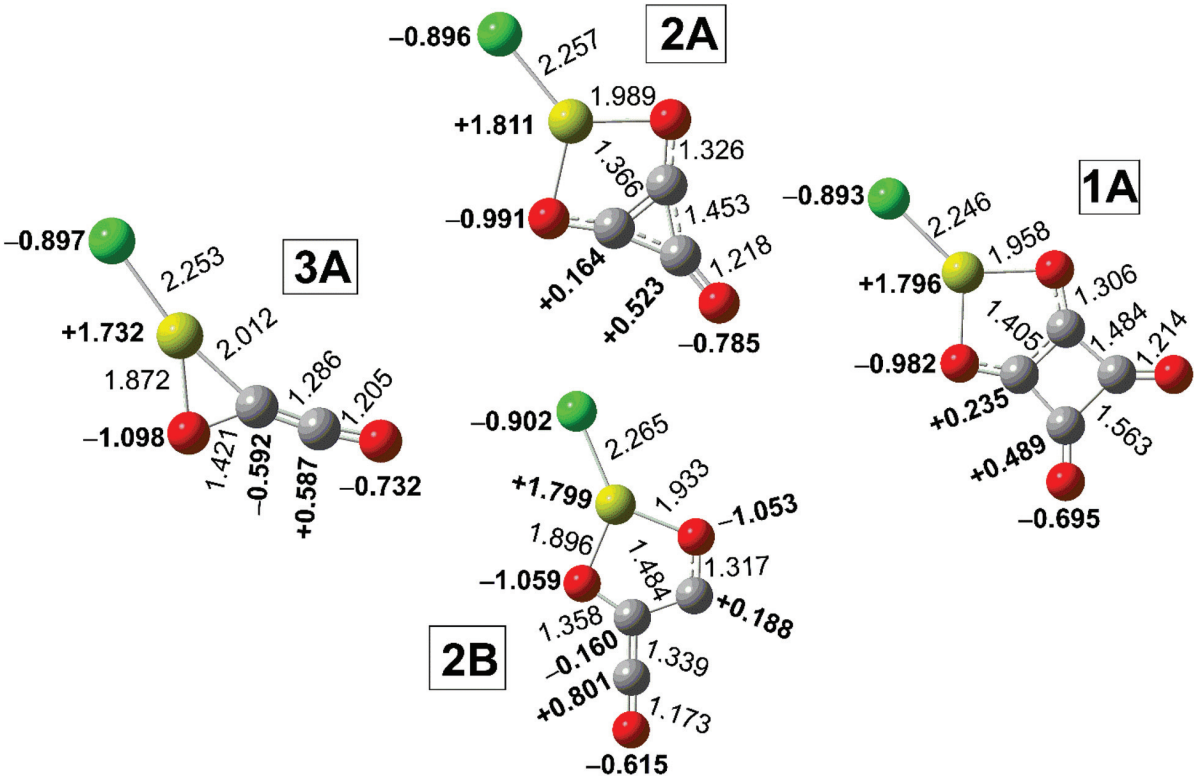

Fig. 6 Natural partial charges (in bold) and bond lengths (Å) of the main species in the cyclooligomerisation sequence computed on the G4 level of theory (B3LYP/6-31G(2df,p) geometries).

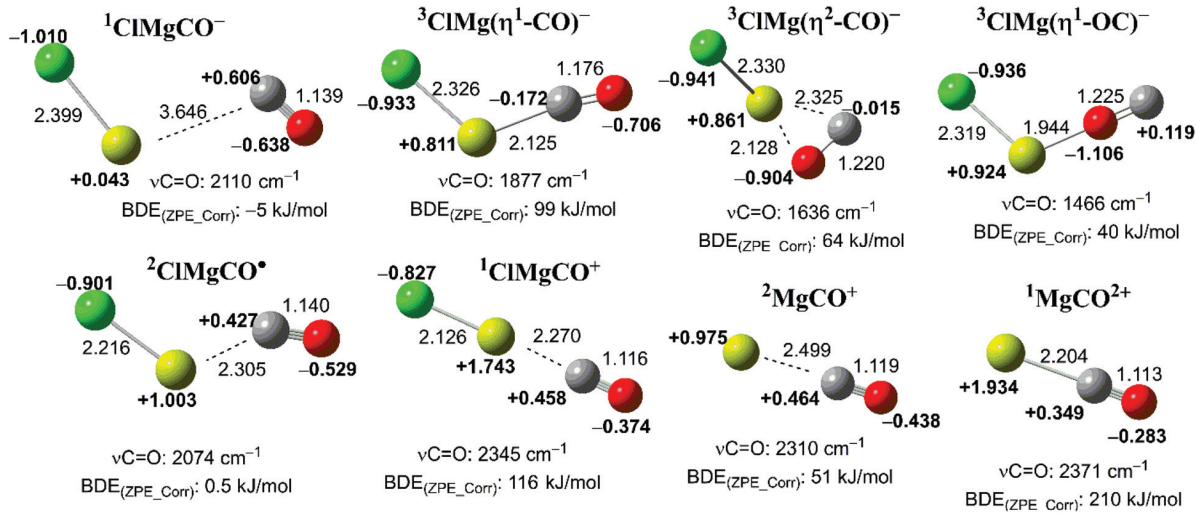

Fig. 7 Magnesium chloride monocarbonyls, ClMgCO$^{-//+}$, and magnesium monocarbonyls, MgCO$^{+/2+}$, computed on the G4 level of theory (B3LYP/6-31G(2df,p) geometries).

orbital of CO, leading to a stabilization of 4.7 kJ mol^{-1}. However, as already stated, ZPE-correction leads to destabilization of the complex compared to dissociated CO + MgCl$^-$, making the latter more stable and thus we do not observe the complex. Changing the multiplicity of the ClMgCO$^-$ to triplet leads to a larger redshift of the νC≡Os in general. This can be explained by the fact that in order to attain triplet multiplicity, one of the Mg valence electrons is transferred to the π*-antibonding orbital on CO. We find three triplet monocarbonyl isomers, ^{3}ClMg(η^1-CO)$^-$, ^{3}ClMg(η^2-CO)$^-$, and ^{3}ClMg(η^1-OC)$^-$. The carbonyl stretching frequencies decrease going from the former to the latter, consistent with an increase in the polarization of the π- and σ-bonds of C–O towards oxygen, accompanied by an elongation of the bond distance from 1.18 Å to 1.23 Å. The BDEs decrease with the increasing distance to the carbon centered π-SOMO, which donates significantly towards magnesium according to second order perturbation theory analysis in the NBO basis.

For ^{2}ClMgCO$^•$, NBO analysis indicates that a one-electron bond is formed, heavily polarized towards magnesium. Still, the calculated C–Mg BDE is only 0.5 kJ mol^{-1} and the redshift of the carbonyl stretching frequency is 2074 cm^{-1}. Removing an additional electron leads to cationic ^{1}ClMgCO$^+$, and at this point the carbonyl stretching frequency is blue-shifted to 2345 cm^{-1}, consistent with the change in polarization of the CO π- and σ-bonds towards carbon. This leads to an increased BDE compared to the anions.

While the neutral MgCO complex does not form according to our calculations, ^{2}MgCO$^+$ and ^{1}MgCO^{2+} display blue-shifted νC≡Os characteristic to non-classical carbonyls. The monocationic complex has a BDE of 51 kJ mol^{-1}, while the dicationic species is bonded by 210 kJ mol^{-1}. The second perturbation theory analysis indicates that donation of the CO σ-lone pair leads to a larger stabilization of the dication than the monocation, 148 and 85 kJ mol^{-1}, respectively. However, most of the increased BDE can likely be attributed to the higher polarizing power of Mg^{2+}. This is further supported by the fact that while CO σ-lone pair donation leads to a comparable stabilization of ^{1}ClMgCO$^+$ and ^{1}MgCO^{2+}, the former has a lower partial charge (1.74 *vs.* 1.93) due to the presence of Cl. Otherwise, ^{1}ClMgCO$^+$ and ^{1}MgCO^{2+}, have similar geometries, with CO bond lengths of 1.116 and 1.113 Å, and C–Mg bonds of 2.270 and 2.204 Å.

Some similarities are observed between the monocarbonyls and the formyl anion, radical and cation. The formyl cation, HCO$^+$, is linear, while HCO$^•$ and HCO$^-$ are bent. The former bonds through the carbon σ-lone pair (HOMO), while the two latter interact through the π*-antibonding orbital on CO. The calculated C≡O stretch is redshifted in the formyl anion (1868 cm^{-1}),[61] while it is blue-shifted in the cation (2184 cm^{-1}).[62] While the triplet monocarbonyls, ^{1}ClMgCO$^-$ and ^{2}ClMgCO$^•$ are similar to HCO$^-$ and HCO$^•$, and ^{1}ClMgCO$^+$, ^{2}MgCO$^+$ and ^{1}MgCO^{2+} resemble HCO$^+$.

The two preceding sections provides a rationale to why singlet ClMgCO$^-$ cannot be the first step in the cyclooligomerisation reaction sequence, while in principle, the triplet species could, conforming to our surmised one-electron initiation of the cyclooligomerisation. Analysis of the partial charges on CO in the monomer complexes (Fig. 7) shows that although the singlet has the negative charge on MgCl$^-$, the triplet species are more stable with the charge on CO. Placement of the charge-bearing electron on the CO moiety in the triplet species can be rationalised by comparison of the energy difference between triplet and singlet MgCl$^-$ to the energy difference between anionic and neutral CO; these differences are calculated to 162 kJ mol^{-1} and 139 kJ mol^{-1}, respectively. Nevertheless, the absence of a signal for ClMgCO$^-$ (*m*/z 87) in our experiments supports the assumption that the dissociation of the squarate complex occurs on the singlet PES in our experiments, consistent with the triplet species being higher in energy.

Conclusions

In conclusion, we have investigated the unimolecular dissociation of $ClMgC_4O_4^-$ to reveal mechanistic details about the reverse reaction, *i.e.* cyclotetramerisation of CO, and found that with the exception of the first step, where two CO molecules is associated on $MgCl^-$, each subsequent CO addition proceeds downhill in energy with relatively low barriers. The most important result of this study is that L = $MgCl^-$ provides an energetically more facile pathway to $LC_4O_4^-$ than L = H^- or e^-. A signal corresponding to $ClMgCO^-$ was not observed in our CID-experiments, consistent with the fact that this species is unstable with respect to dissociation according to computations. We have also assessed the degree of reduction through the natural partial charges on the $C_nO_n^-$ moiety and its effects on the stability of the MgCl-bound oligomers, and found that these correlate with the barrier heights for CO addition. Generally, a more negative partial charge implies a higher barrier (up to −2), consistent with the conclusion of a previous study[34] that transfer of two electrons to the oxocarbon moiety terminates the cyclooligomerisation process.

Conflicts of interest

The authors declare no conflicts of interest.

Acknowledgements

This work has been supported by the Norwegian Research Council through Grant No. 249788 (The chemistry of CO_2 activation and fixation), the Hylleraas Centre for Quantum Molecular Sciences No. 262695/F50 through their Centre of Excellence program, and the Norwegian Supercomputing Program (NOTUR) through a grant of computer time (Grant No. NN4654 K).

References

1 W. J. Evans, J. W. Grate, L. A. Hughes, H. Zhang and J. L. Atwood, *J. Am. Chem. Soc.*, 1985, **107**, 3728–3730.
2 O. T. Summerscales, F. G. N. Cloke, P. B. Hitchcock, J. C. Green and N. Hazari, *J. Am. Chem. Soc.*, 2006, **128**, 9602–9603.
3 M. Aresta, in *Activation of Small Molecules*, John Wiley & Sons, Ltd, 2006, pp. 1–41.
4 B. L. Conley, W. J. Tenn, K. J. H. Young, S. Ganesh, S. Meier, V. Ziatdinov, O. Mironov, J. Oxgaard, J. Gonzales, W. A. Goddard and R. A. Periana, in *Activation of Small Molecules*, John Wiley & Sons, Ltd, 2006, pp. 235–285.
5 P. W. N. M. van Leeuwen and Z. Freixa, in *Activation of Small Molecules*, John Wiley & Sons, Ltd, 2006, pp. 319–356.
6 C. Mesters, *Annu. Rev. Chem. Biomol. Eng.*, 2016, **7**, 223–238.
7 G. Frenking, C. Loschen, A. Krapp, S. Fau and S. H. Strauss, *J. Comput. Chem.*, 2007, **28**, 117–126.
8 A. Y. Khodakov, W. Chu and P. Fongarland, *Chem. Rev.*, 2007, **107**, 1692–1744.
9 F. Fischer and H. Tropsch, *Ber. Dtsch. Chem. Ges. B*, 1926, **59**, 830–831.
10 G. J. Sunley and D. J. Watson, *Catal. Today*, 2000, **58**, 293–307.
11 X. Wu, L. Zhao, J. Jin, S. Pan, W. Li, X. Jin, G. Wang, M. Zhou and G. Frenking, *Science*, 2018, **361**, 912–916.
12 X. Wu, L. Zhao, D. Jiang, I. Fernández, R. Berger, M. Zhou and G. Frenking, *Angew. Chem., Int. Ed.*, 2018, **57**, 3974–3980.
13 E. W. Abel and F. G. A. Stone, *Q. Rev., Chem. Soc.*, 1970, **24**, 498.
14 F. E. Paulik and J. F. Roth, *Chem. Commun.*, 1968, 1578a.
15 N. V. Kutepow, W. Himmele and H. Hohenschutz, *Chem. Ing. Tech.*, 1965, **37**, 383–388.
16 G. Wilke, *Pure Appl. Chem.*, 1978, **50**, 677–690.
17 R. Lalrempuia, C. E. Kefalidis, S. J. Bonyhady, B. Schwarze, L. Maron, A. Stasch and C. Jones, *J. Am. Chem. Soc.*, 2015, **137**, 8944–8947.
18 W. J. Evans, J. W. Grate and R. J. Doedens, *J. Am. Chem. Soc.*, 1985, **107**, 1671–1679.
19 G. M. Ferrence, R. McDonald and J. Takats, *Angew. Chem., Int. Ed.*, 1999, **38**, 2233–2237.
20 E. L. Werkema, L. Maron, O. Eisenstein and R. A. Andersen, *J. Am. Chem. Soc.*, 2007, **129**, 2529–2541.
21 D. A. Katahira, K. G. Moloy and T. J. Marks, *Organometallics*, 1982, **1**, 1723–1726.
22 T. Shima and Z. Hou, *J. Am. Chem. Soc.*, 2006, **128**, 8124–8125.
23 K. Yuvaraj, I. Douair, A. Paparo, L. Maron and C. Jones, *J. Am. Chem. Soc.*, 2019, **141**, 8764–8768.
24 A. S. Frey, F. G. N. Cloke, P. B. Hitchcock, I. J. Day, J. C. Green and G. Aitken, *J. Am. Chem. Soc.*, 2008, **130**, 13816–13817.
25 P. L. Arnold, Z. R. Turner, R. M. Bellabarba and R. P. Tooze, *Chem. Sci.*, 2010, **2**, 77–79.
26 S. Cohen, J. R. Lacher and J. D. Park, *J. Am. Chem. Soc.*, 1959, **81**, 3480–3480.
27 R. West, *Oxocarbons*, Elsevier, 1980.
28 S. Cohen and S. G. Cohen, *J. Am. Chem. Soc.*, 1966, **88**, 1533–1536.
29 D. Eggerding and R. West, *J. Am. Chem. Soc.*, 1976, **98**, 3641–3644.
30 L. M. Schwartz and L. O. Howard, *J. Phys. Chem.*, 1971, **75**, 1798–1803.
31 H. Jiao and H.-S. Wu, *J. Org. Chem.*, 2003, **68**, 1475–1479.
32 A. Ghosh and S. Mitra, *ChemElectroChem*, 2018, **5**, 159–165.
33 A. Manthiram, *J. Phys. Chem. Lett.*, 2011, **2**, 176–184.
34 J. S. Jestilä and E. Uggerud, *J. Org. Chem.*, 2019, **84**, 14005–14014.
35 A. Stasch and C. Jones, *Dalton Trans.*, 2011, **40**, 5659–5672.
36 S. P. Green, C. Jones and A. Stasch, *Science*, 2007, **318**, 1754–1757.

37 S. Narancic, A. Bach and P. Chen, *J. Phys. Chem. A*, 2007, **111**, 7006–7013.
38 D. E. Goldberg, *Genetic Algorithms in Search, Optimization, and Machine Learning*, Addison-Wesley Professional, Reading, Mass, 1st edn, 1989.
39 G. Gioumousis and D. P. Stevenson, *J. Chem. Phys.*, 1958, **29**, 294–299.
40 S. T. Graul and R. R. Squires, *J. Am. Chem. Soc.*, 1990, **112**, 2517–2529.
41 M. B. More, D. Ray and P. B. Armentrout, *J. Am. Chem. Soc.*, 1999, **121**, 417–423.
42 M. T. Rodgers, K. M. Ervin and P. B. Armentrout, *J. Chem. Phys.*, 1997, **106**, 4499–4508.
43 P. B. Armentrout, C. A. Austin and M. T. Rodgers, *J. Phys. Chem. A*, 2014, **118**, 8088–8097.
44 D. J. Harvey, A. P. Hunter, R. H. Bateman, J. Brown and G. Critchley, *Int. J. Mass Spectrom.*, 1999, **188**, 131–146.
45 M. J. Frisch, G. W. Trucks, H. B. Schlegel, G. E. Scuseria, M. A. Robb, J. R. Cheeseman, G. Scalmani, V. Barone, G. A. Petersson, H. Nakatsuji, X. Li, M. Caricato, A. V. Marenich, J. Bloino, B. G. Janesko, R. Gomperts, B. Mennucci, H. P. Hratchian, J. V. Ortiz, A. F. Izmaylov, J. L. Sonnenberg, D. Williams-Young, F. Ding, F. Lipparini, F. Egidi, J. Goings, B. Peng, A. Petrone, T. Henderson, D. Ranasinghe, V. G. Zakrzewski, J. Gao, N. Rega, G. Zheng, W. Liang, M. Hada, M. Ehara, K. Toyota, R. Fukuda, J. Hasegawa, M. Ishida, T. Nakajima, Y. Honda, O. Kitao, H. Nakai, T. Vreven, K. Throssell, J. A. Montgomery Jr., J. E. Peralta, F. Ogliaro, M. Bearpark, J. J. Heyd, E. Brothers, K. N. Kudin, V. N. Staroverov, T. A. Keith, R. Kobayashi, J. Normand, K. Raghavachari, A. Rendell, J. C. Burant, S. S. Iyengar, J. Tomasi, M. Cossi, J. M. Milliam, M. Klene, C. Adamo, R. Cammi, J. W. Ochterski, R. L. Martin, K. Morokuma, O. Farkas, J. B. Foresman and D. J. Fox, Inc, Wallingford CT.
46 A. D. Becke, *Phys. Rev. A*, 1988, **38**, 3098–3100.
47 C. Lee, W. Yang and R. G. Parr, *Phys. Rev. B: Condens. Matter Mater. Phys.*, 1988, **37**, 785–789.
48 T. H. Dunning, *J. Chem. Phys.*, 1989, **90**, 1007.
49 R. A. Kendall, T. H. Dunning and R. J. Harrison, *J. Chem. Phys.*, 1992, **96**, 6796–6806.
50 L. A. Curtiss, P. C. Redfern and K. Raghavachari, *J. Chem. Phys.*, 2007, **126**, 084108.
51 L. A. Curtiss, P. C. Redfern and K. Raghavachari, *Chem. Phys. Lett.*, 2010, **499**, 168–172.
52 M. Farber and R. D. Srivastava, *Chem. Phys. Lett.*, 1976, **42**, 567–569.
53 T. M. Miller and W. C. Lineberger, *Chem. Phys. Lett.*, 1988, **146**, 364–366.
54 T. J. Lee and P. R. Taylor, *Int. J. Quantum Chem.*, 2009, **36**, 199–207.
55 S. Karmakar and A. Datta, *J. Phys. Chem. B*, 2016, **120**, 945–950.
56 S. Karmakar and A. Datta, *J. Org. Chem.*, 2017, **82**, 1558–1566.
57 D. McKay, A. S. P. Frey, J. C. Green, F. G. N. Cloke and L. Maron, *Chem. Commun.*, 2012, **48**, 4118–4120.
58 D. Schröder, C. Heinemann, H. Schwarz, J. N. Harvey, S. Dua, S. J. Blanksby and J. H. Bowie, *Chem. – Eur. J.*, 1998, **4**, 2550–2557.
59 J. Emsley, *The elements*, Clarendon Press, Oxford University Press, Oxford, New York, 1998.
60 K. P. Huber and G. Herzberg, in *Molecular Spectra and Molecular Structure: IV. Constants of Diatomic Molecules*, ed. K. P. Huber and G. Herzberg, Springer US, Boston, MA, 1979, pp. 8–689.
61 K. K. Murray, T. M. Miller, D. G. Leopold and W. C. Lineberger, *J. Chem. Phys.*, 1986, **84**, 2520–2525.
62 S. C. Foster, A. R. W. McKellar and T. J. Sears, *J. Chem. Phys.*, 1984, **81**, 578–579.

9 Supporting information for the papers

Supporting information for Paper I.

Electronic Supplementary Material (ESI) for Physical Chemistry Chemical Physics.

Characterization of the Alkali Metal Oxalates ($MC_2O_4^-$) and their formation by CO_2 reduction via the Alkali Metal Carbonites (MCO_2^-)

Joakim S. Jestilä[1], Joanna K. Denton[2], Evan H. Perez[2], Thien Khuu[2], Edoardo Apra[3], Sotiris S. Xantheas[4,5], Mark A. Johnson[2] and Einar Uggerud[1]

[1] Department of Chemistry and Hylleraas Centre for Quantum Molecular Sciences, University of Oslo, PO Box 1033, Blindern, Oslo N-0135, Norway

[2] Sterling Chemistry Laboratory, Yale University, New Haven, Connecticut 06520, United States

[3] Environmental Molecular Sciences Laboratory, Pacific Northwest National Laboratory, P.O. Box 999, Richland, Washington 99352, United States

[4] Advanced Computing, Mathematics and Data Division, Pacific Northwest National Laboratory, 902 Battelle Boulevard, P.O. Box 999, MS K1-83, Richland, Washington United States

[5] Department of Chemistry, University of Washington, Seattle, Washington 98195, United States

Supporting information

Table of Contents

SI-A. Mass spectra of oxalic acid and metal chlorides and hydroxides

Mass spectra of oxalic acid and metal chloride/hydroxide dissolved in water-methanol solutions are presented in Figure S1 –Figure ***S5***, whence the following are induced.

- Addition of triethylamine (TEA) or use of the metal hydroxide (MOH) as the source for the metal cations generally leads to improved metal oxalate peak intensities relative to the deprotonated oxalate peak.
- The base peak is most often due to the deprotonated acid, hydrogen oxalate ($HC_2O_4^-$), followed by the metal oxalate ($MC_2O_4^-$) or the metal hydrogen oxalate dimer ($M^+(HC_2O_4^-)_2$) peaks in terms of decreasing intensity. The dimer peak intensities relative to the base and monomer peaks tend to increase with metal size.
- Use of metal hydroxides generally yield "cleaner" mass spectra with fewer and higher peaks compared to the metal chlorides.
- TEA (10%) effectively removes the $RbCl_2^-$ peak from the mass spectrum of oxalic acid and RbCl.

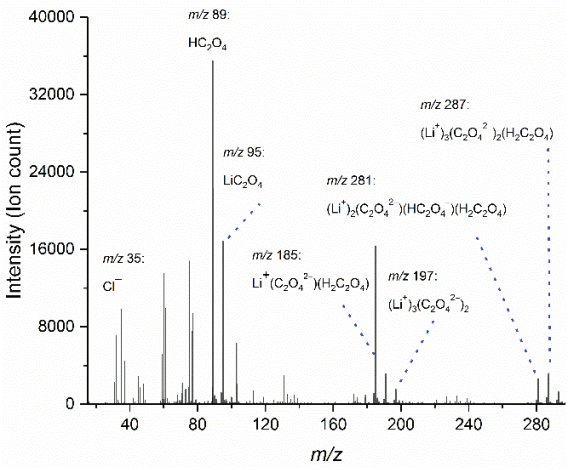

Figure S1. MS of 4mM Oxalic acid and 6 mM LiCl in 50/50 water/methanol with 1 % triethylamine (TEA).

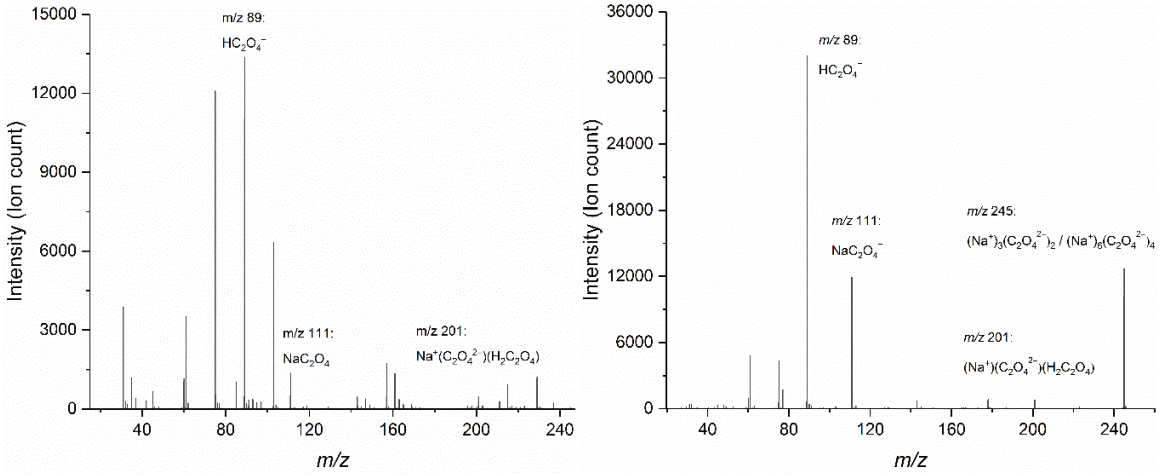

Figure S2. MS of 3.3 mM oxalic acid and 1.3 mM NaCl in 40/60 water/methanol (*left*), and of 2.9 mM oxalic acid and 5.3 mM NaOH in 50/50 water/methanol (*right*).

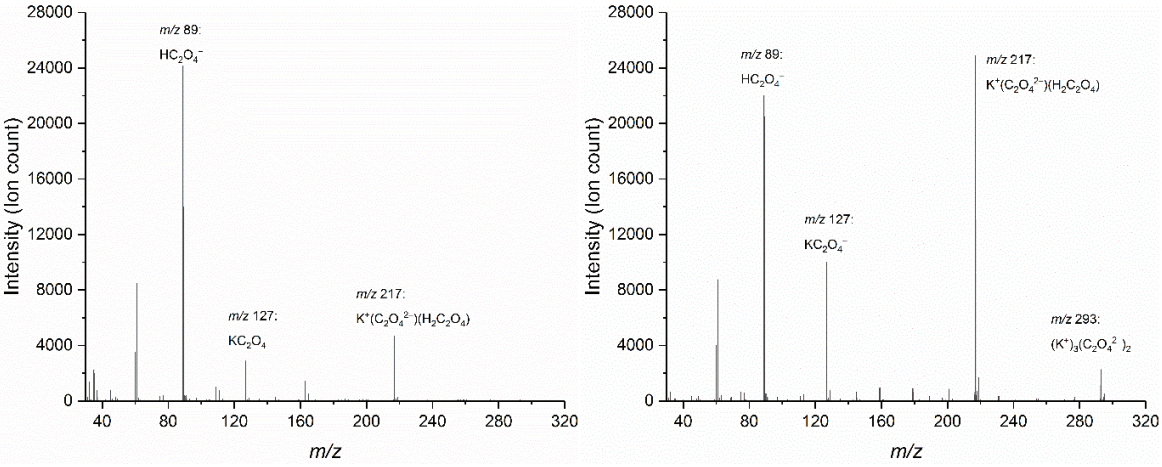

Figure S3. MS of 3.0 mM oxalic acid and 3.0 mM KCl in 50/50 water/methanol (*left*), and of 3.0 mM oxalic acid and 5.0 mM KOH in 50/50 water/methanol (*right*).

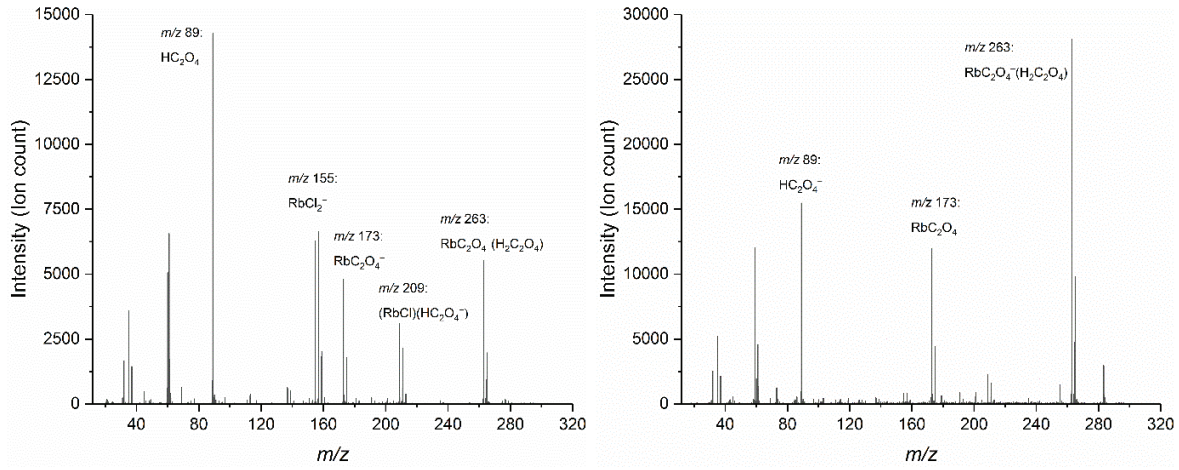

Figure S4. MS of 3.0 mM oxalic acid and 5.0 mM RbCl in 50/50 water/methanol (*left*), and of 3.0 mM oxalic acid and 5.0 mM RbCl in 50/50 water/methanol with 10% TEA (*right*).

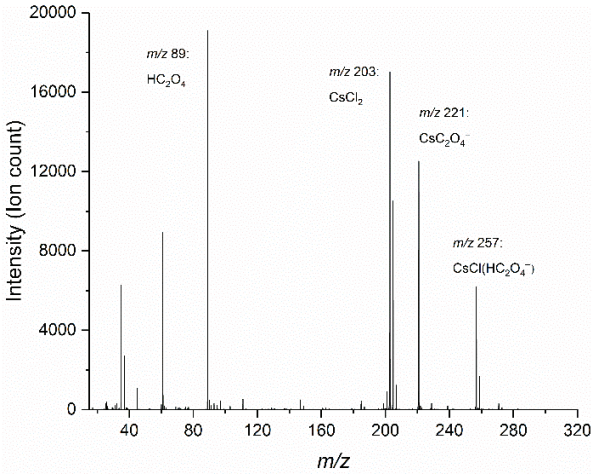

Figure S5. MS of 3.0 mM oxalic acid and 5.0 mM CsCl in 50/50 water/methanol.

SI-B. Validation of estimated threshold energies by known reaction energies

i. Dissociation of protonated ethanol, $C_2H_5OH_2^+$

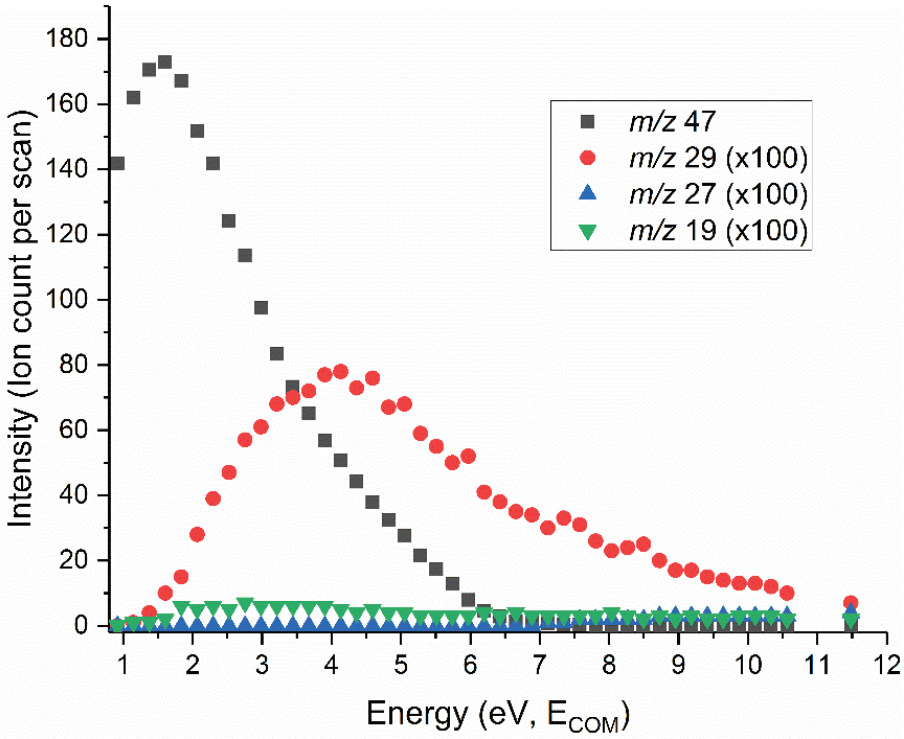

Figure S6. Breakdown curve of protonated ethanol, $C_2H_5OH_2^+$, *m/z* 47, recorded over a collision energy range from 0.9 to 11.5 eV (E_{COM}), 2.0 $\times 10^{-4}$ mbar Ar. *m/z* 29 corresponds to $C_2H_5^+$, *m/z* 27 to $C_2H_3^+$ and *m/z* 19 to H_3O^+. The intensities of the two smallest ions, *m/z* 19 and 27 were too low to yield reliable threshold energy estimates.

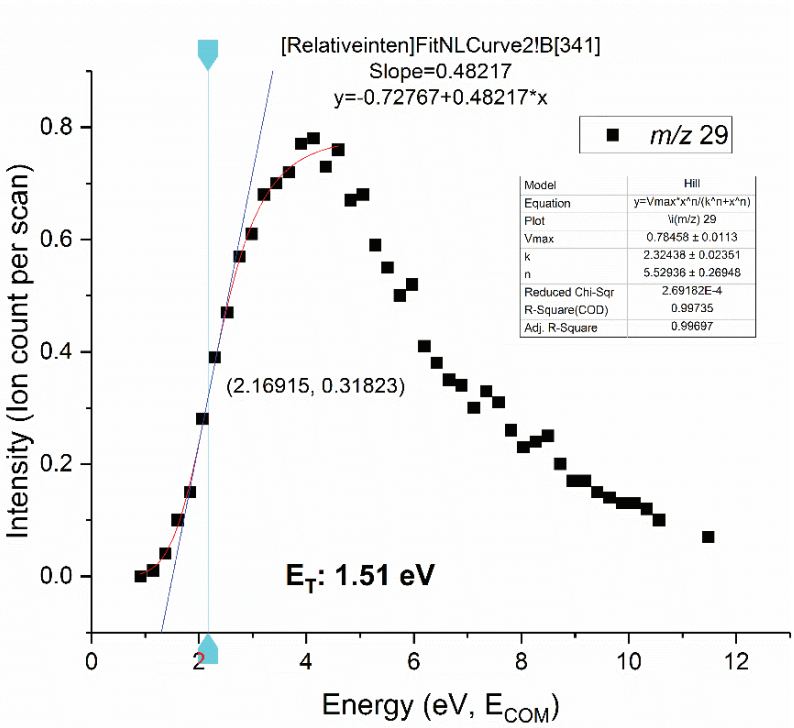

Figure S7. Appearance curve of ethyl cation, $C_2H_5^+$, *m/z* 29, recorded over a collision energy range from 0.9 to 11.5 eV (E_{COM}), 2.0 · 10^{-4} mbar Ar. The curve has been fitted to a Hill function, and extrapolated to baseline in order to estimate the threshold energy (E_T) for its formation.

Table S1. Experimental and calculated reaction enthalpies ($\Delta_rH°$) and threshold energies (E_T) for $C_2H_5OH_2^+ \rightarrow C_2H_5^+ + H_2O$ in eV (kJ/mol in parentheses). Our estimate in **bold** (our calculations on the G4 level of theory, also in **bold**).

Exp		Calc	
$\Delta_rH°$	E_T	$\Delta_rH°$	E_T
	1.51 (146)		**1.45 (140)**
1.60 (154)[1]		1.48 (143)[1]	
	1.70 (164)[2]		1.76 (170)[3]

ii. Decarboxylation of benzoate, $C_6H_5CO_2^-$

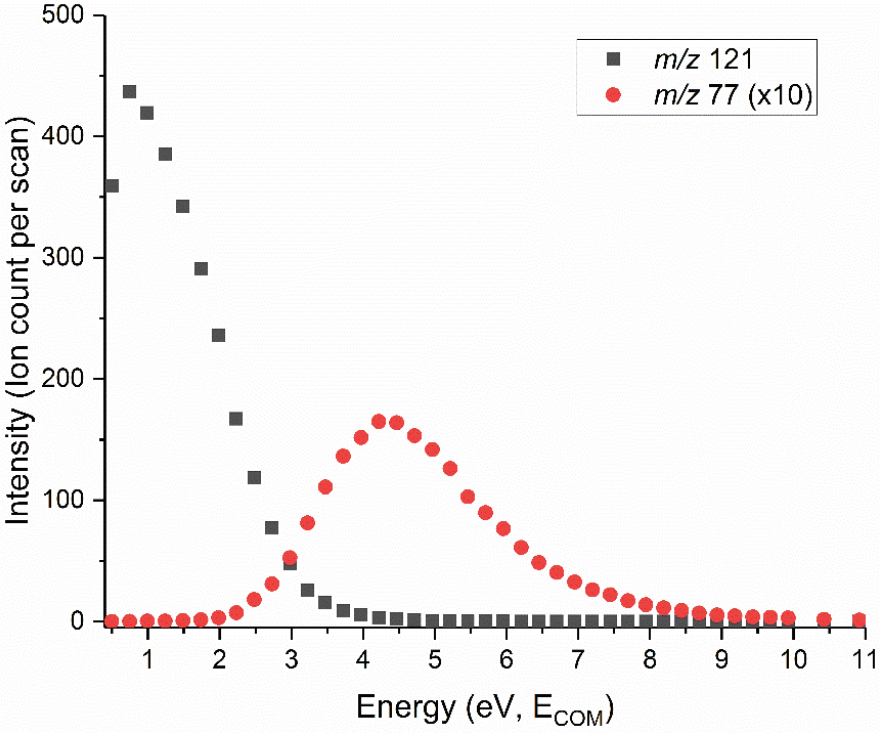

Figure S8. Breakdown curve of benzoate, $C_6H_5CO_2^-$, *m/z* 121, recorded over a collision energy range from 0.5 to 11.0 eV (E_{COM}), $2.0 \cdot 10^{-4}$ mbar Ar. *m/z* 77 corresponds to the product of decarboxylation, $C_6H_5^-$.

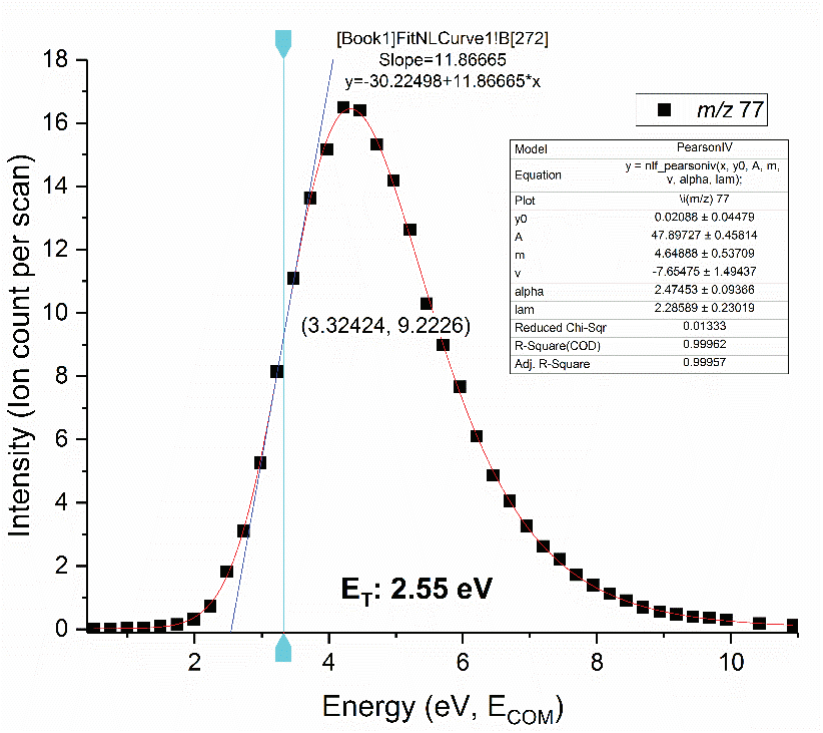

Figure S9. Appearance curve of the phenyl anion, $C_6H_5^-$, *m/z* 77, recorded over a collision energy range from 0.5 to 11.0 eV (E_{COM}), 2.0 · 10^{-4} mbar Ar. The curve has been fitted to a Pearson function, and extrapolated to baseline in order to estimate the threshold energy (E_T) for its formation.

Table S2. Experimental and calculated reaction enthalpies ($\Delta_rH°$) and threshold energies (E_T) for $C_6H_5CO_2^-$ → $C_6H_5^-$ + CO_2 in eV (kJ/mol in parentheses). Our estimate in **bold** (our calculations on the G4 level of theory, also in **bold**).

Exp		Calc	
$\Delta_rH°$	E_T	$\Delta_rH°$	E_T
	2.55 (246)		**2.43**
	2.63 ± 0.15 (254 ± 14)[4]		

SI-C. Molecular orbitals of the alkali metals and metal carbonites

The molecular orbital diagrams in this section were prepared using the Chemissian 4.52 software.[5]

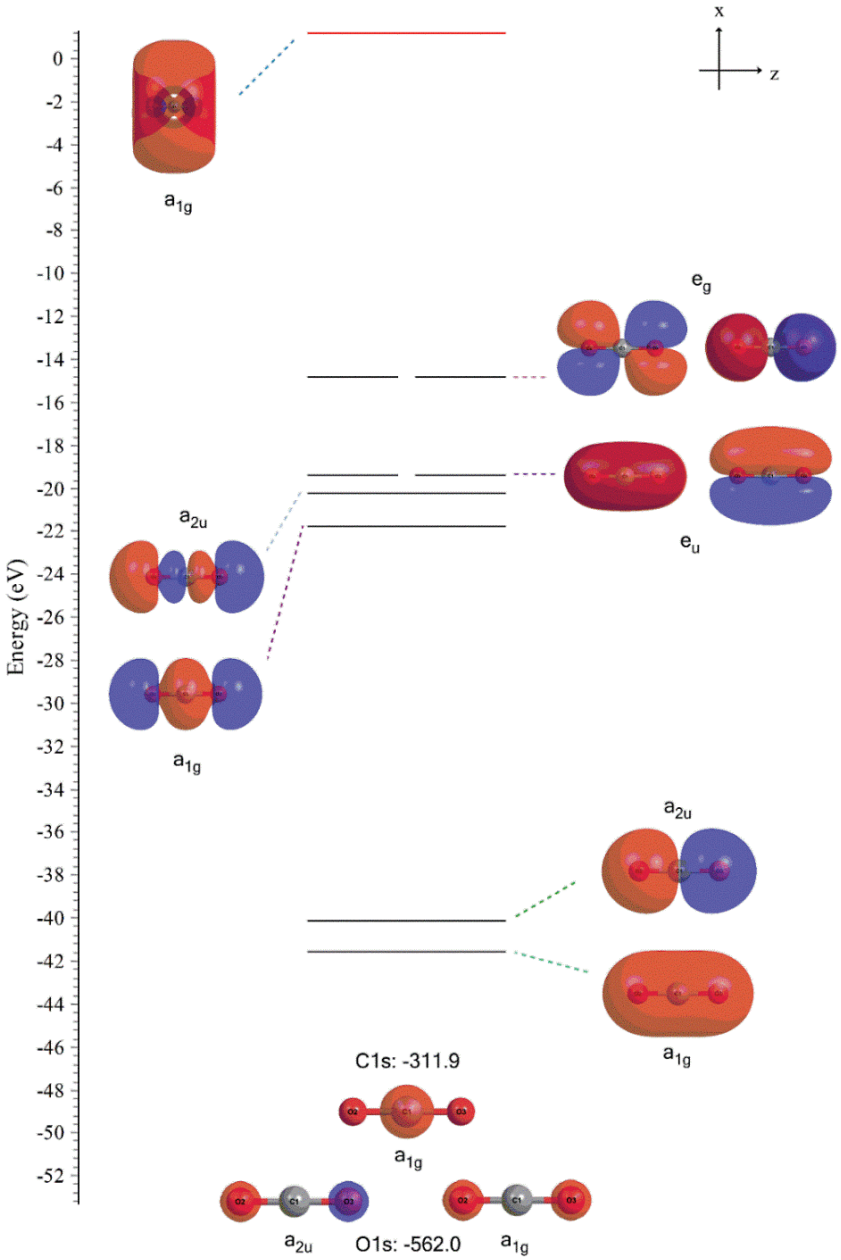

Figure S10. Molecular orbital diagram for CO_2 at the CCSD(T)/def2-TZVPPD optimized geometry (black lines = doubly occupied/red lines = virtual orbitals). The three lowest orbitals are frozen.

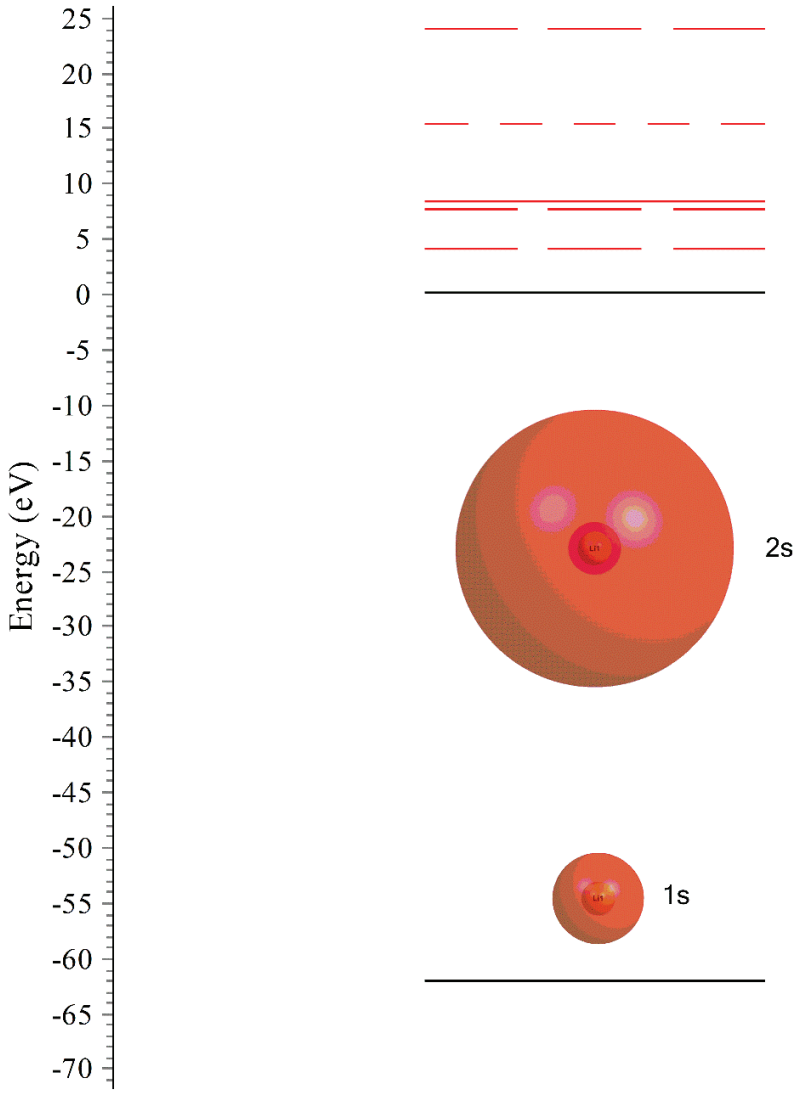

Figure S11. Atomic orbital diagram for Li^- computed at the CCSD(T)/def2-TZVPPD level of theory (black lines = doubly occupied/red lines = virtual orbitals). The 1s orbital is frozen in the frozen core approximation.

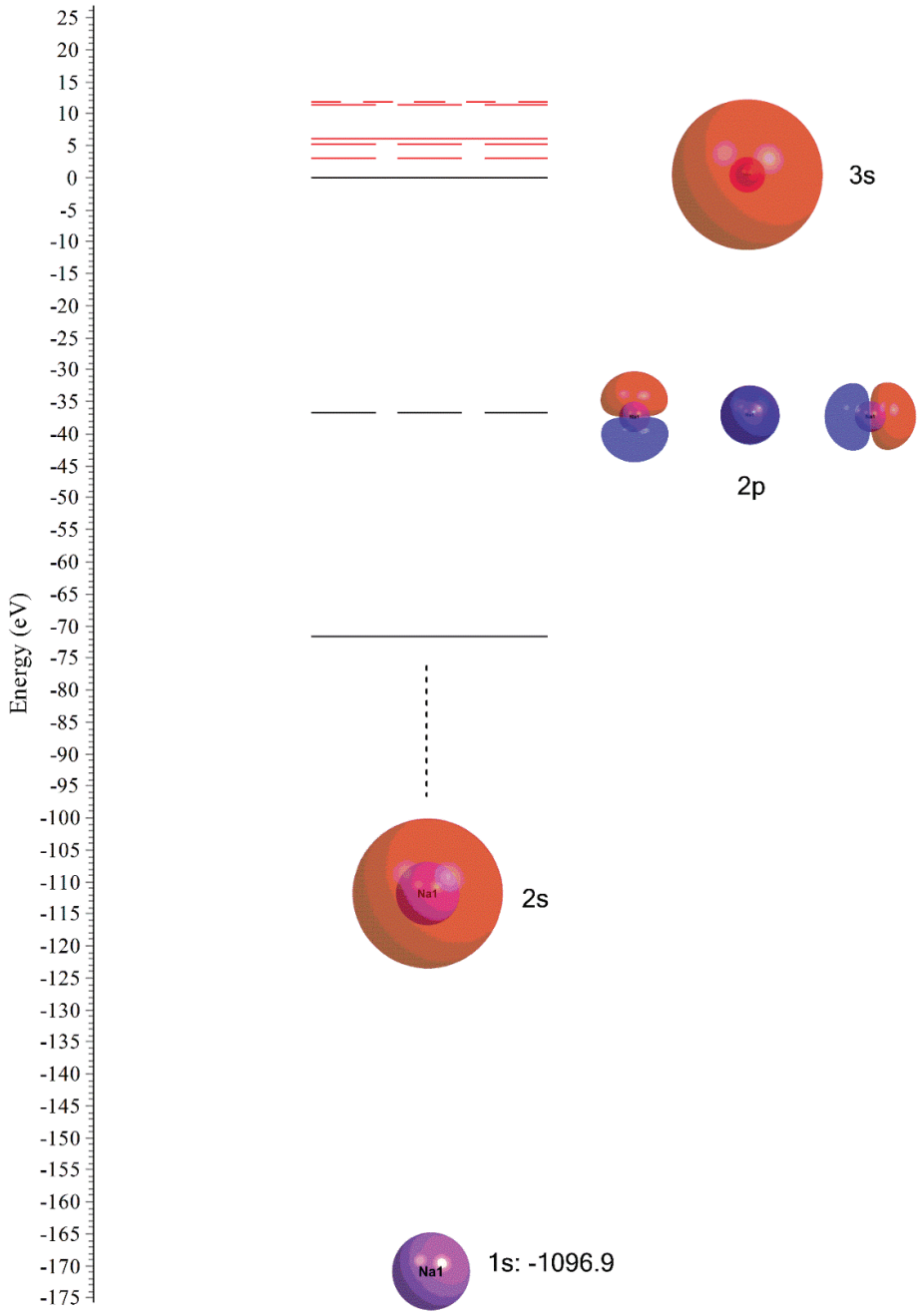

Figure S12. Atomic orbital diagram for Na^- computed at the CCSD(T)/def2-TZVPPD level of theory (black lines = doubly occupied/red lines = virtual orbitals). The five lowest orbitals are frozen in the frozen core approximation, while we have frozen the two lowest.

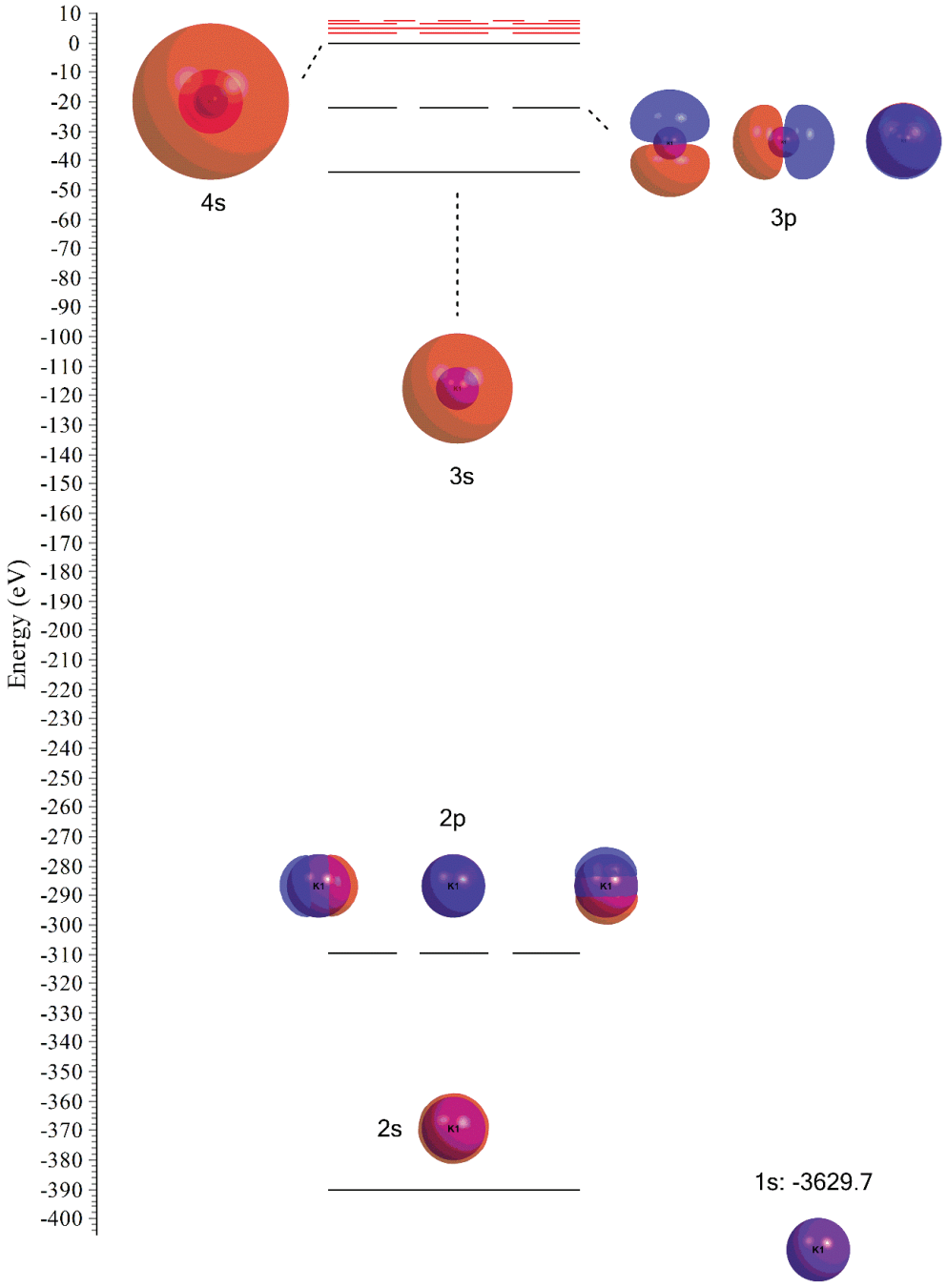

Figure S13. Atomic orbital diagram for K^- computed at the CCSD(T)/def2-TZVPPD level of theory (black lines = doubly occupied/red lines = virtual orbitals). The nine lowest orbitals are frozen in the frozen core approximation, while we have frozen the six lowest.

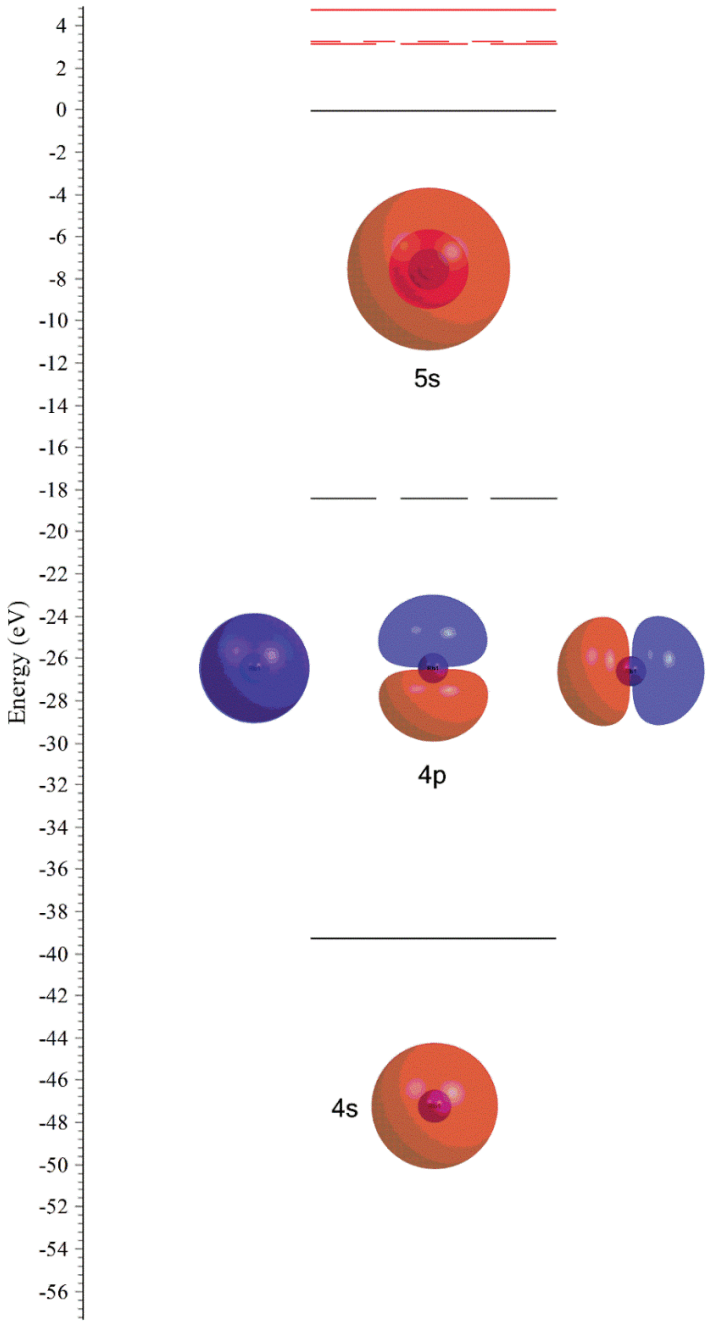

Figure S14. Atomic orbital diagram for Rb^- computed at the CCSD(T)/def2-TZVPPD level of theory (black lines = doubly occupied/red lines = virtual orbitals). The 28 inner electrons have been replaced by an ECP.

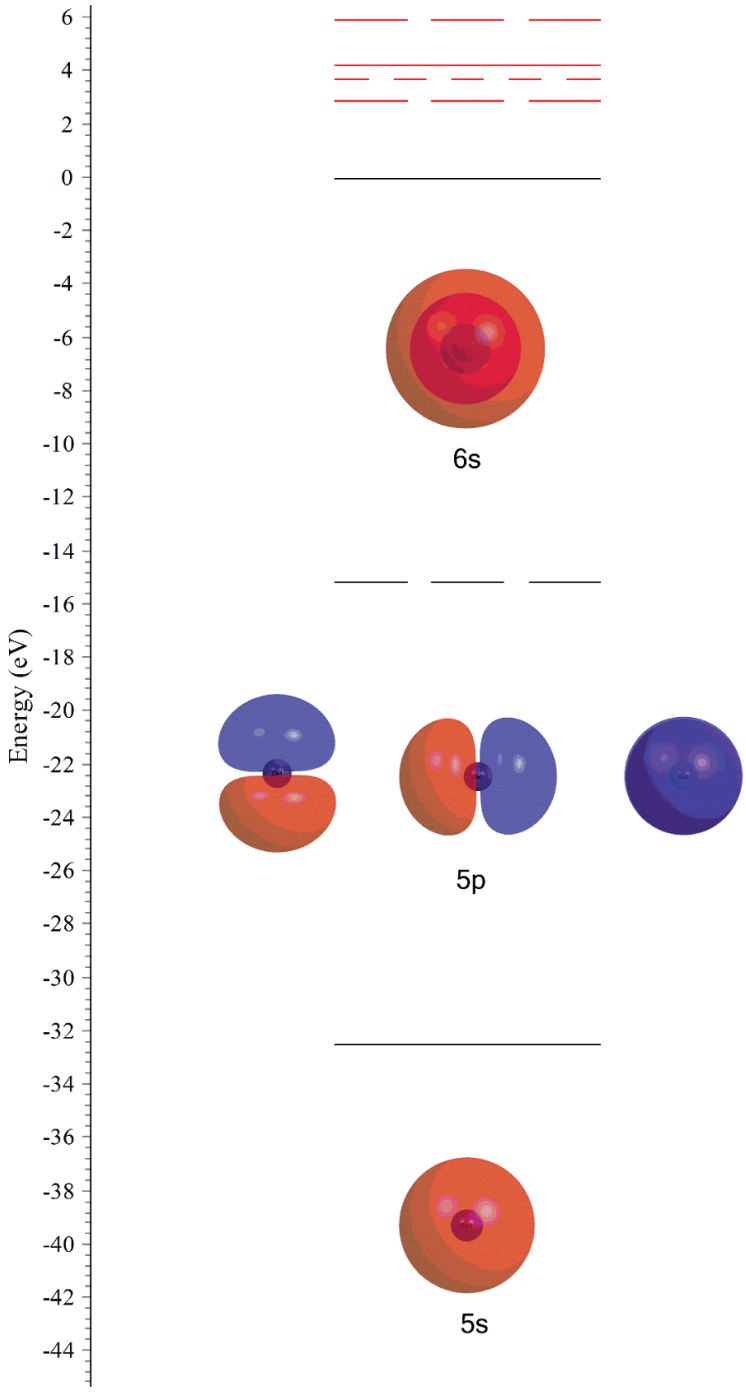

Figure S15. Atomic orbital diagram for Cs^- computed at the CCSD(T)/def2-TZVPPD level of theory (black lines = doubly occupied/red lines = virtual orbitals). The 46 inner electrons have been replaced by an ECP.

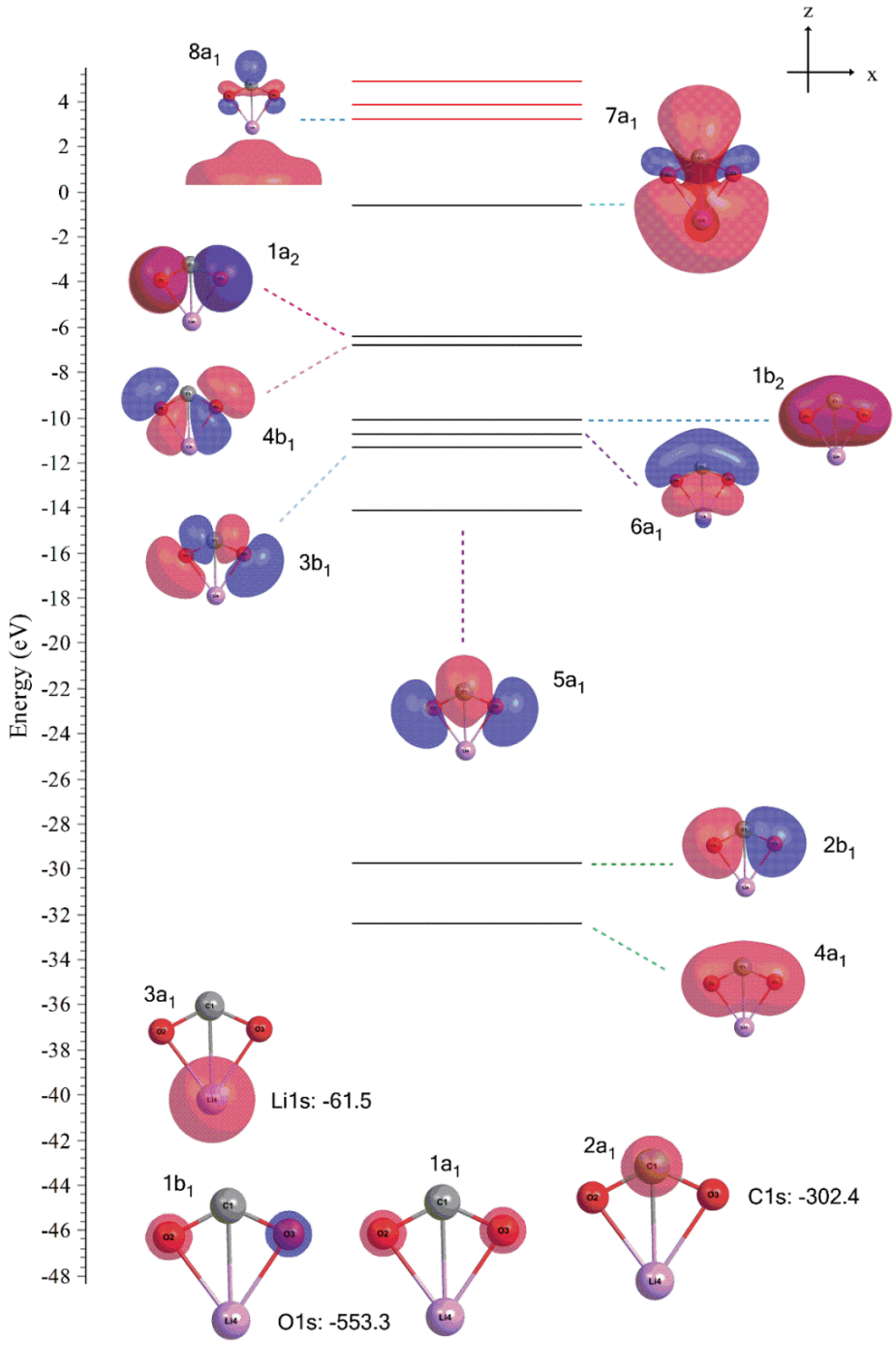

Figure S16. Molecular orbital diagram for $Li(\kappa^2\text{-}O_2C)^-$ (A isomer) at the CCSD(T)/def2-TZVPPD optimized geometry (black lines = doubly occupied/red lines = virtual orbitals). The four lowest orbitals are frozen.

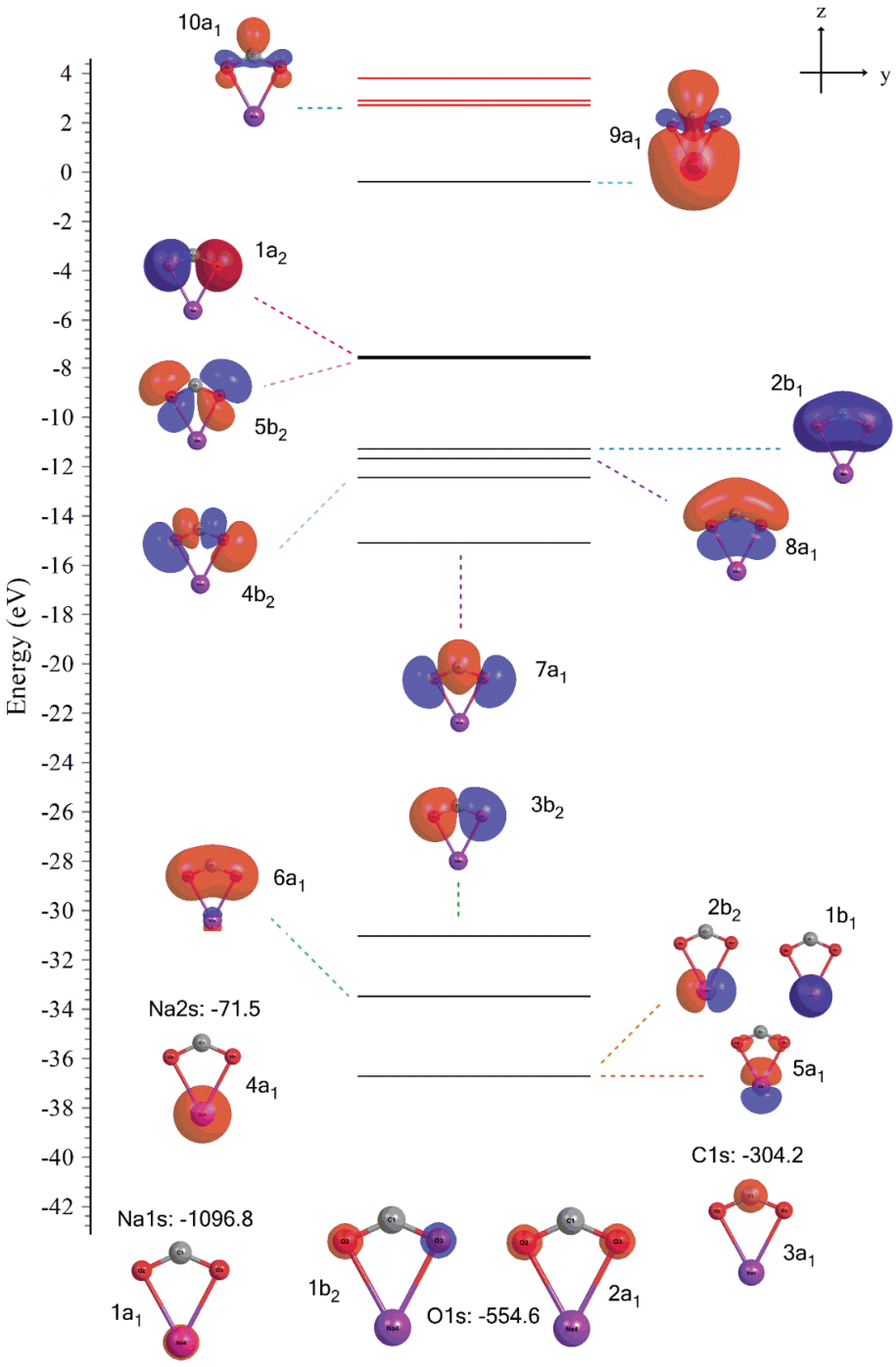

Figure S17. Molecular orbital diagram for Na(κ^2-O_2C)$^-$ (A isomer) at the CCSD(T)/def2-TZVPPD optimized geometry (black lines = doubly occupied/red lines = virtual orbitals). The eight lowest orbitals are frozen in the frozen core approximation, while we froze the five lowest orbitals.

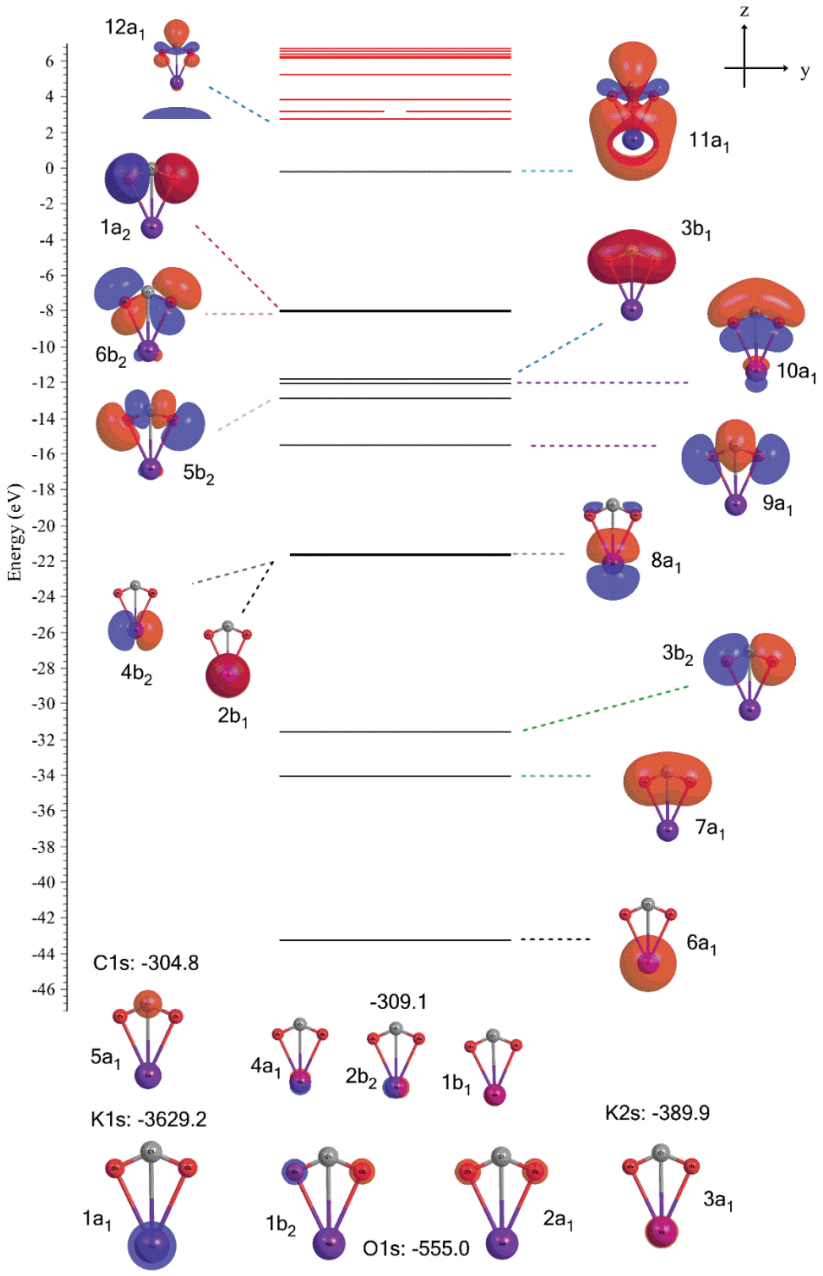

Figure S18. Molecular orbital diagram for $K(\kappa^2\text{-}O_2C)^-$ (A isomer) at the CCSD(T)/def2-TZVPPD optimized geometry (black lines = doubly occupied/red lines = virtual orbitals). The twelve lowest orbitals are frozen in the frozen core approximation, while we froze the nine lowest orbitals. Note how the carbon/oxygen 2s MOs ($7a_1$ and $3b_2$) are lower in energy than K 2p AOs ($2b_1$, $4b_2$ and $8a_1$).

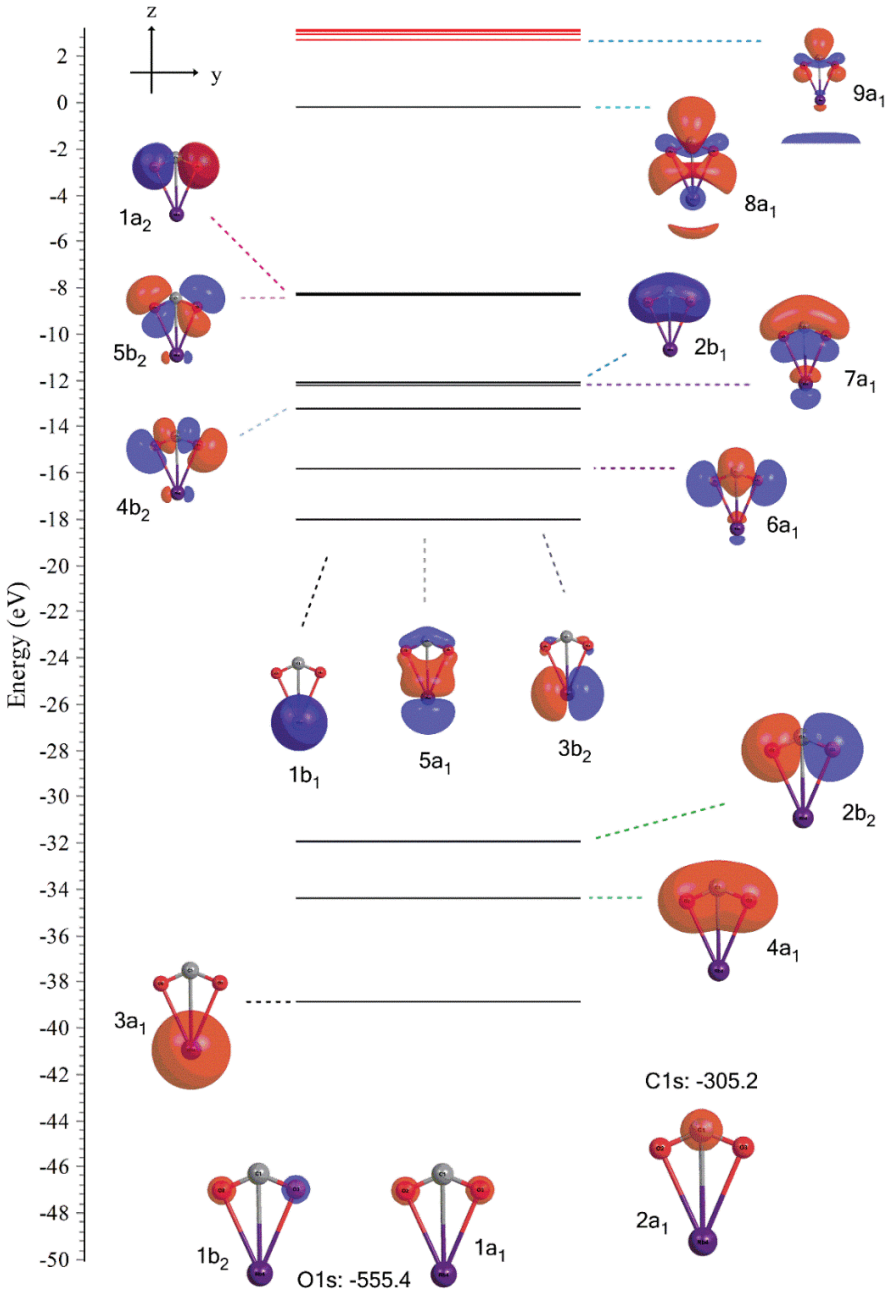

Figure S19. Molecular orbital diagram for Rb(κ^2-O_2C)$^-$ (A isomer) at the CCSD(T)/def2-TZVPPD optimized geometry (black lines = doubly occupied/red lines = virtual orbitals). The 28 inner electrons on Rb have been replaced by an ECP, and the three lowest orbitals are frozen in the complex.

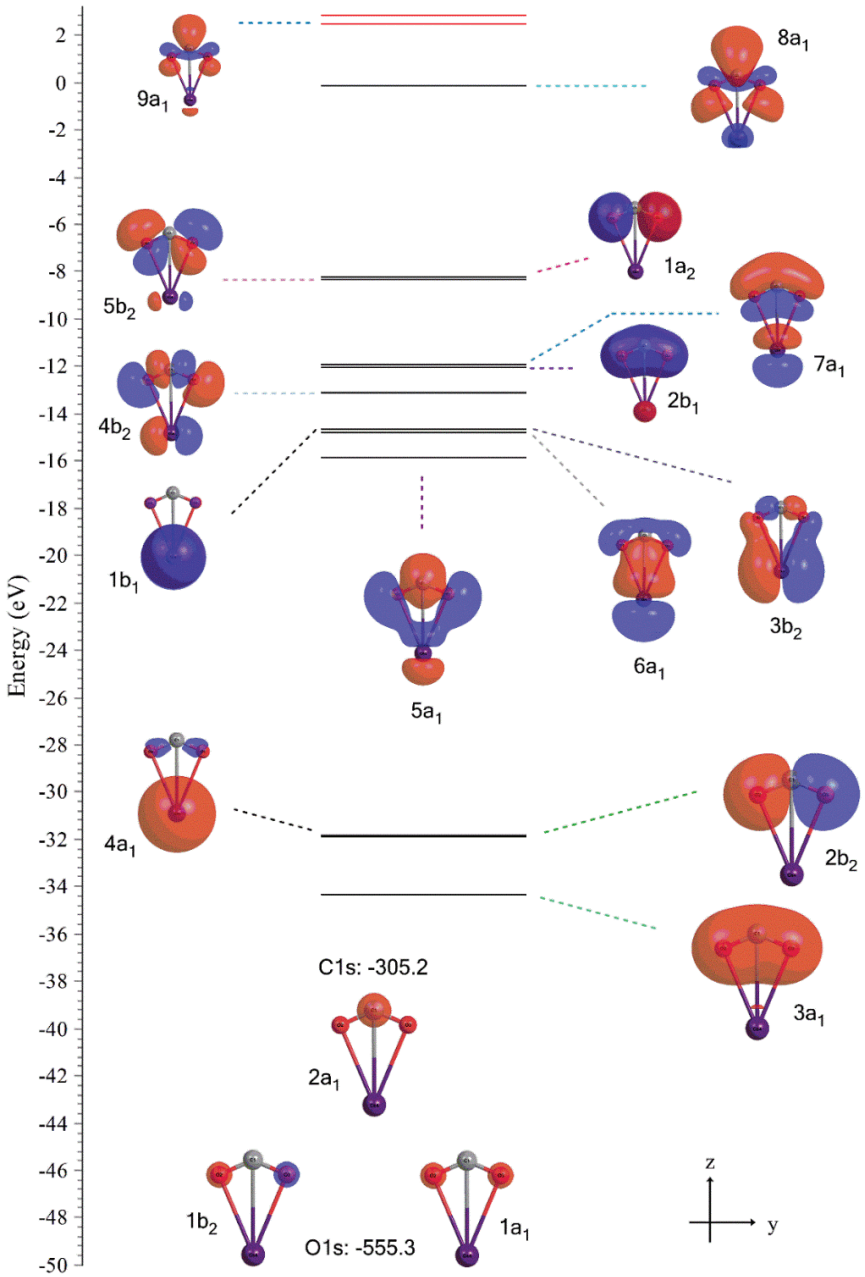

Figure S20. Molecular orbital diagram for $Cs(\kappa^2\text{-}O_2C)^-$ (A isomer) at the CCSD(T)/def2-TZVPPD optimized geometry (black lines = doubly occupied/red lines = virtual orbitals). The 46 inner electrons on Cs have been replaced by an ECP, and the three lowest orbitals are frozen in the complex,

SI-D. Calculation of the Basis Set Superposition Error (BSSE) correction

The uncorrected, ΔE, and BSSE-corrected, $\Delta E(BSSE)$, interaction energies are estimated using a procedure reported earlier[6] according to

$$\Delta E = E_{AB}^{\alpha\cup\beta}(AB) - E_{A}^{\alpha}(A) - E_{B}^{\beta}(B) \quad \text{(S1)}$$

$$\Delta E(BSSE) = \Delta E - \left\{E_{AB}^{\alpha\cup\beta}(A) - E_{AB}^{\alpha}(A)\right\} - \left\{E_{AB}^{\alpha\cup\beta}(B) - E_{AB}^{\beta}(B)\right\}, \quad \text{(S2)}$$

where $E_{AB}^{\alpha\cup\beta}(A)$ denotes the energy of fragment (A) in the dimer geometry AB using the combined basis sets of both the alkali metal (α) and the CO_2 fragment (β). The BSSE correction thus includes the deformation energy of the CO_2 fragment (B), which is substantial as the geometry of this fragment is bent in the dimer optimal geometry. Since fragment (A) is a monatomic cation, it is obvious that $E_{AB}^{\alpha}(A) = E_{A}^{\alpha}(A)$. i.e. its deformation energy is zero. The magnitudes of the various energy terms that are needed to estimate the uncorrected and BSSE-corrected interaction energies via equations (S1) and (S2) for isomers **A** and **B** for all alkali metal systems are listed in Tables S3 and S4.

Table S3. Energies (in a.u.) of the various terms of equations (S1) and (S2) needed to calculate the uncorrected and BSSE-corrected interaction energies of the **A isomer** of the alkali metal carbonites at the CCSD(T)/def2-TZVPPD level of theory. Here, the electronic energy of a molecule M at geometry G computed with basis set σ is defined as $E_{G}^{\sigma}(M)$. α is the basis set of the alkali metal, β is the basis set of CO_2 and $\alpha\cup\beta$ is the basis set of the dimer.

	$E_{MCO_2}^{\alpha\cup\beta}(MCO_2^-)$	$E_{CO_2}^{\beta}(CO_2)$	$E_{M}^{\alpha}(M^-)$	$E_{MCO_2}^{\alpha\cup\beta}(CO_2)$	$E_{MCO_2}^{\alpha\cup\beta}(M^-)$	$E_{MCO_2}^{\beta}(CO_2)$	ΔE	$\Delta E(BSSE)$
Li	−195.80034	−188.32603	−7.44970	−188.24346	−7.45194	−188.24294	−0.024615	−0.021861
Na	−350.33935	−188.32603	−162.00462	−188.25889	−162.00667	−188.25847	−0.008703	−0.006231

K	−787.64906	−188.32603	−599.31520	−188.26367	−599.31673	−188.26334	−0.007839	−0.005977
Rb	−212.26058	−188.32603	−23.92619	−188.26549	−23.93043	−188.26518	−0.008364	−0.003817
Cs	−208.36501	−188.32603	−20.02985	−188.26315	−20.03317	−188.2629	−0.009135	−0.005547

Table S4. Energies (in a.u.) of the various terms of equations (S1) and (S2) needed to calculate the uncorrected and BSSE-corrected interaction energies of the **B isomer** of the alkali metal carbonites at the CCSD(T)/def2-TZVPPD level of theory. Here, the electronic energy of a molecule M at geometry G computed with basis set σ is defined as $E_G^{\sigma}(M)$. α is the basis set of the alkali metal, β is the basis set of CO_2 and $\alpha \cup \beta$ is the basis set of the dimer.

	$E_{MCO_2}^{\alpha\cup\beta}(MCO_2^-)$	$E_{CO_2}^{\beta}(CO_2)$	$E_M^{\alpha}(M^-)$	$E_{MCO_2}^{\alpha\cup\beta}(CO_2)$	$E_{MCO_2}^{\alpha\cup\beta}(M^-)$	$E_{MCO_2}^{\beta}(CO_2)$	ΔE	$\Delta E(BSSE)$
Li	−195.79613	−188.32603	−7.44970	−188.26631	−7.45179	−188.26583	−0.020404	−0.017833
Na	−350.33193	−188.32603	−162.00462	−188.28015	−162.00647	−188.27978	−0.001286	0.000933
K	−787.64231	−188.32603	−599.31520	−188.28129	−599.3165	−188.28101	−0.001091	0.000508
Rb	−212.25331	−188.32603	−23.92619	−188.28245	−23.92974	−188.28219	−0.001097	0.002713
Cs	−208.35816	−188.32603	−20.02985	−188.28062	−20.03268	−188.28039	−0.002282	0.000781

Table S5. Uncorrected [ΔE] and BSSE-Corrected [$\Delta E(BSSE)$**]** (in parentheses) interaction energies (kJ/mol) for both **A** and **B** alkali metal carbonite isomers at the CCSD(T)/def2-TZVPPD level of theory.

	A	**B**
Li	−64.6 (−57.4)	−53.6 (−46.8)
Na	−22.9 (−16.4)	−3.4 (2.4)
K	−20.6 (−15.7)	−2.9 (1.3)
Rb	−22.0 (−10.0)	−2.9 (7.1)
Cs	−24.0 (−14.6)	−6.0 (2.1)

SI-E. Computational modeling of the unimolecular MOx^- dissociation

A detailed computational survey was conducted to aid the understanding of the elementary reaction steps constituting the full dissociation of metal oxalates into metal anions and carbon dioxide, the results of which were used to construct the potential energy diagrams in this section.

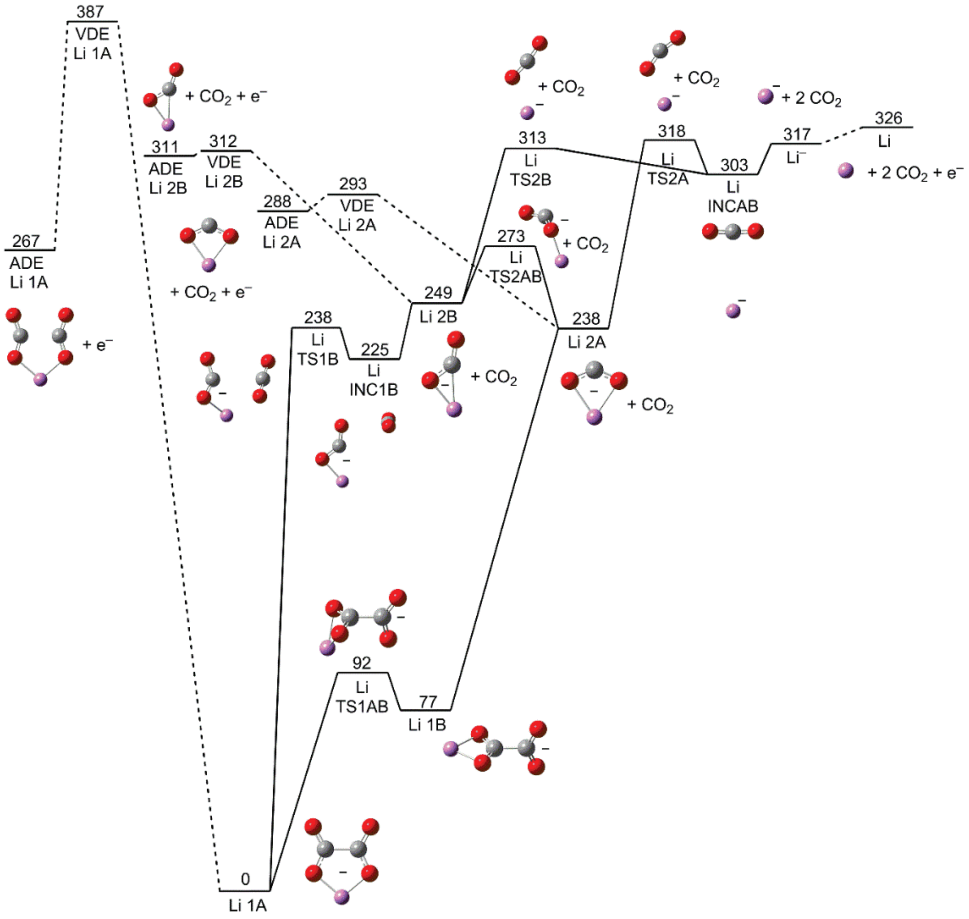

Figure S21. MP2/Def2-TZVPPD potential energy diagram for the dissociation of $LiC_2O_4^-$. The numbers are zero-point corrected electronic energies. Electron detachment of the MCO_2^- species is indicated by dashed (---) lines, while chemical transformations are drawn with full lines (—).

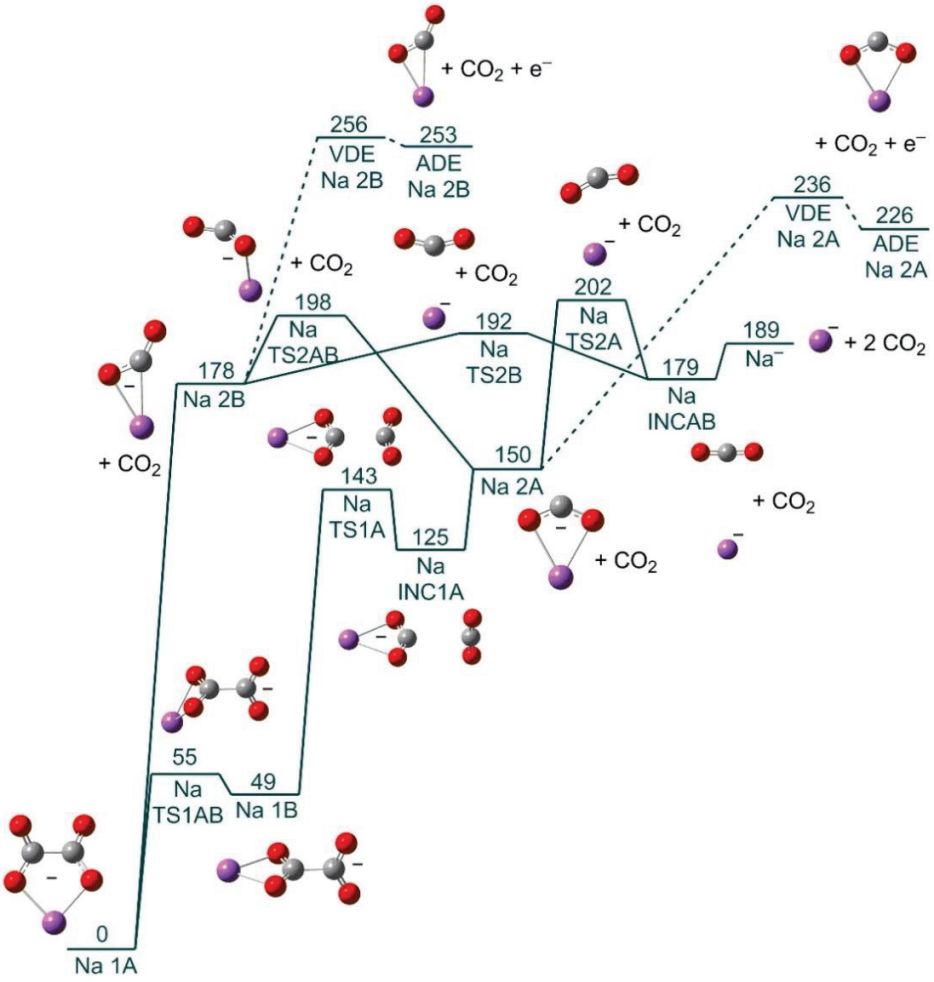

Figure S22. MP2/Def2-TZVPPD potential energy diagram for the dissociation of $NaC_2O_4^-$. The numbers are zero-point corrected electronic energies. Electron detachment of the MCO_2^- species is indicated by dashed (---) lines, while chemical transformations are drawn with full lines (—).

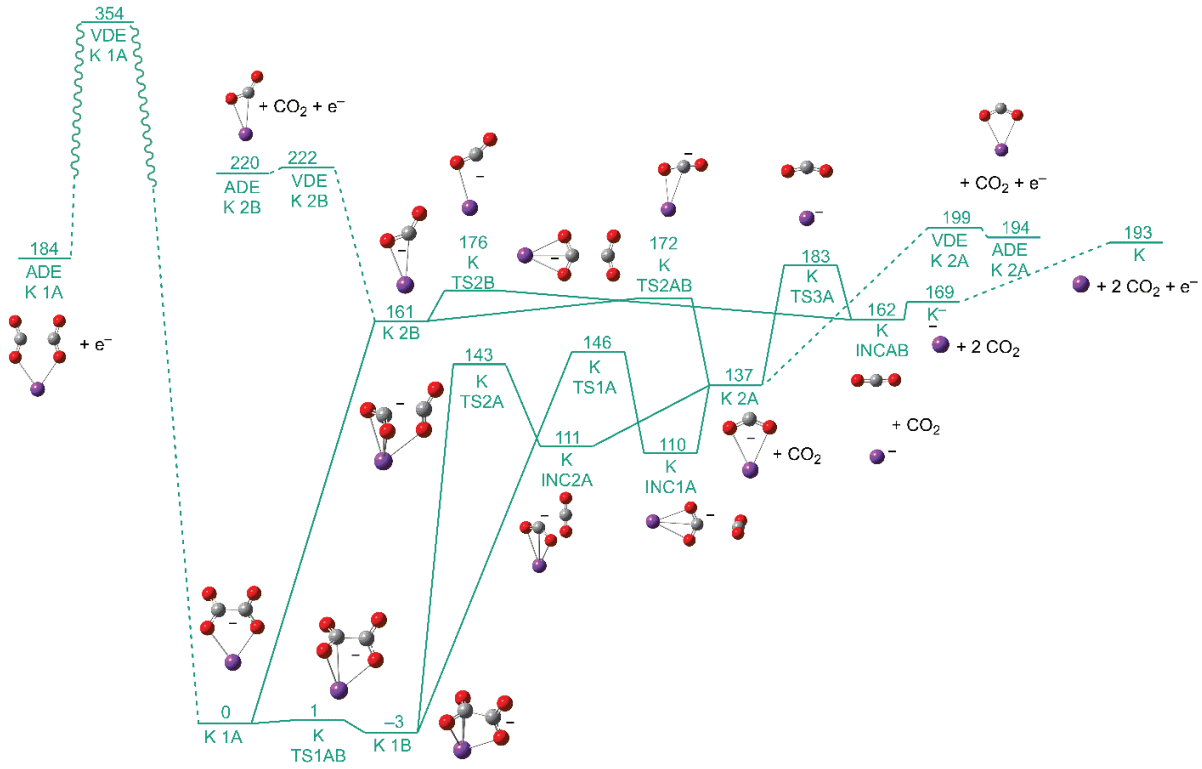

Figure S23. MP2/Def2-TZVPPD potential energy diagram for the dissociation of $KC_2O_4^-$. The numbers are zero-point corrected electronic energies. Electron detachment of the MCO_2^- species is indicated by dashed (---) lines, while chemical transformations are drawn with full lines (—).

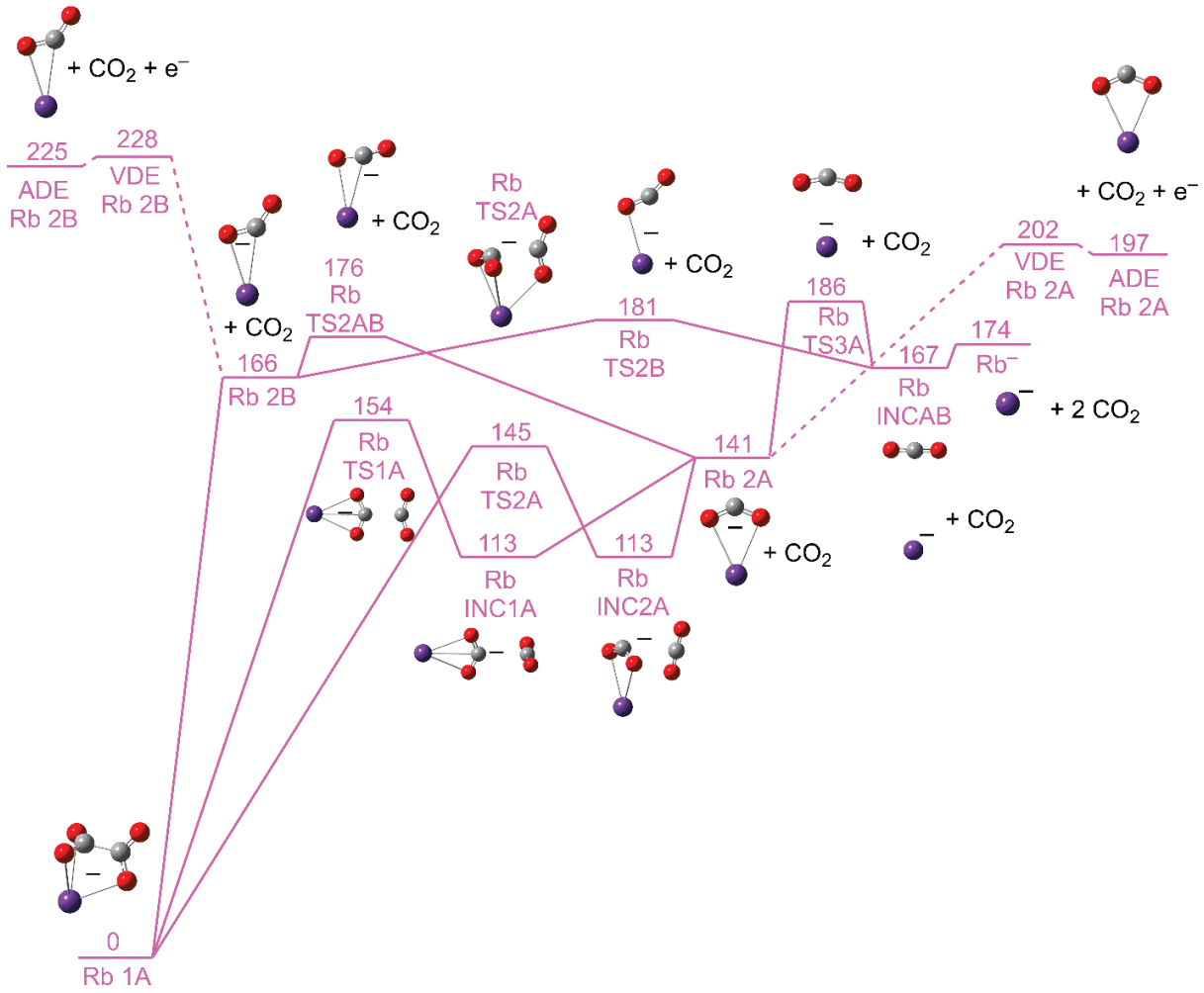

Figure S24. MP2/Def2-TZVPPD potential energy diagram for the dissociation of $RbC_2O_4^-$. The numbers are zero-point corrected electronic energies. Electron detachment of the MCO_2^- species is indicated by dashed (---) lines, while chemical transformations are drawn with full lines (—).

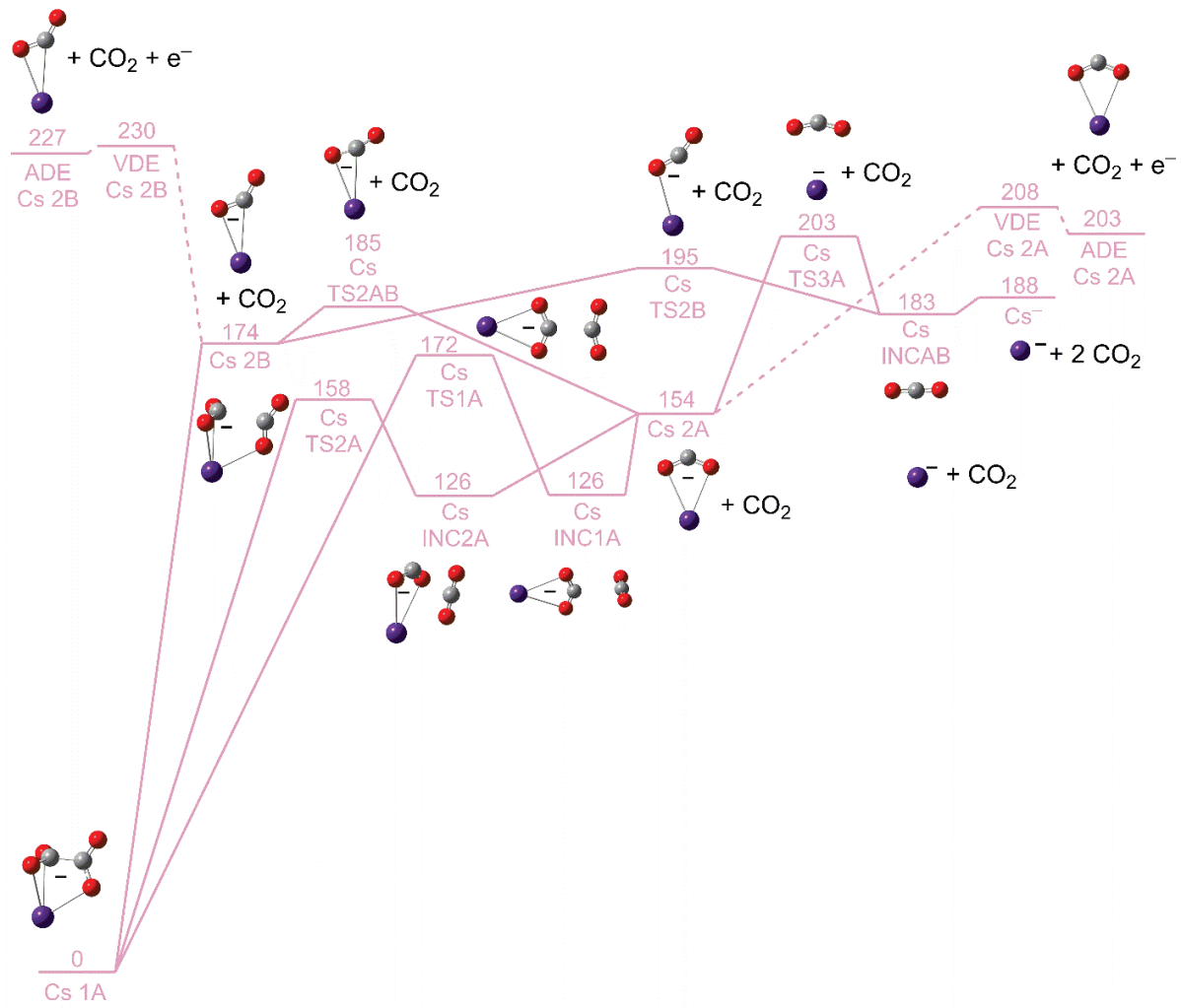

Figure S25. MP2/Def2-TZVPPD potential energy diagram for the dissociation of $CsC_2O_4^-$. The numbers are zero-point corrected electronic energies. Electron detachment of the MCO_2^- species is indicated by dashed (---) lines, while chemical transformations are drawn with full lines (—).

SI-F. Relative stabilities of the oxalate dianion conformers in different solvents

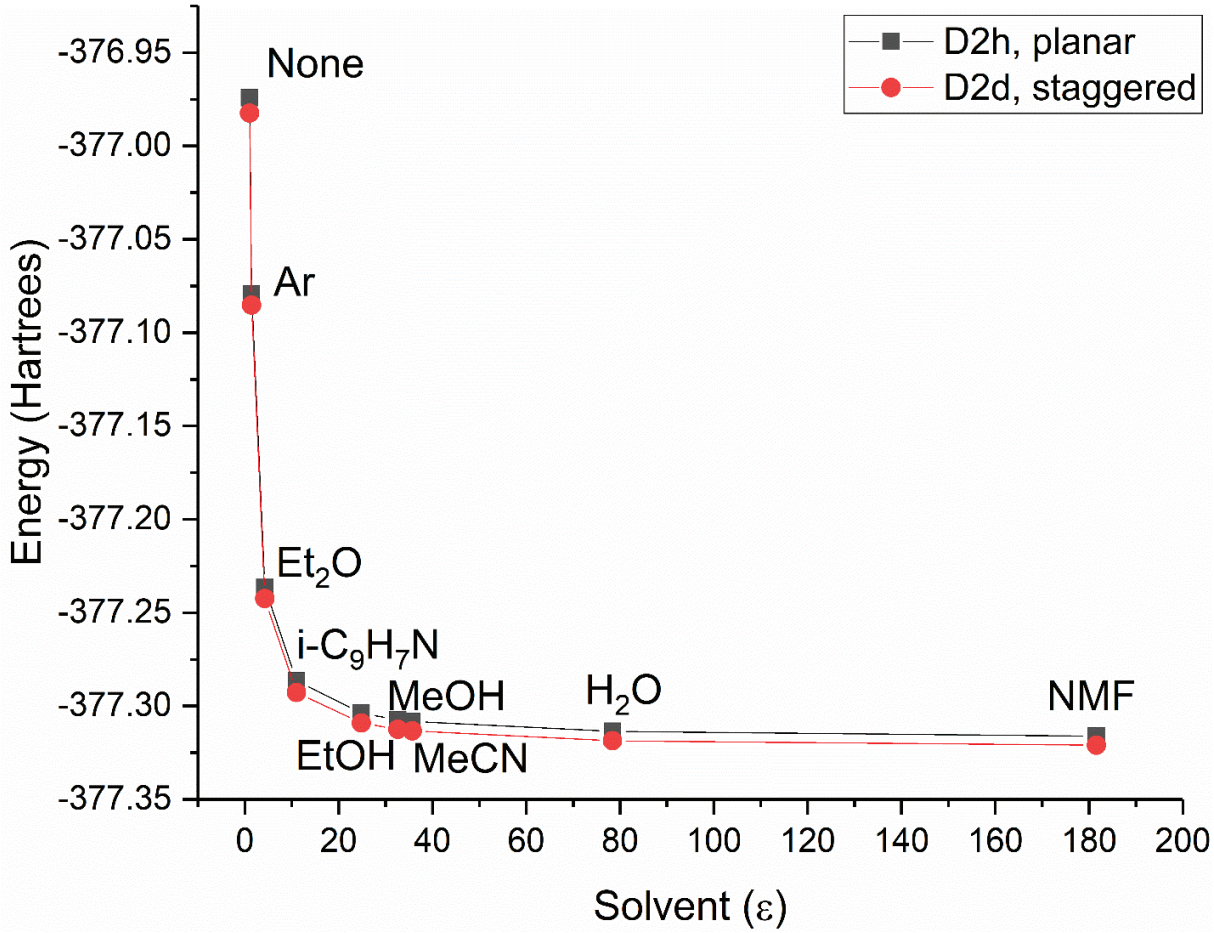

Figure S26. Stabilities of the staggered and planar Ox^{2-} by solvent on the MP2/def2-TZVPPD level of theory.

SI-G. Alkali metal carbonite (MCO_2^-) C(1s) energies and carboxylation barriers

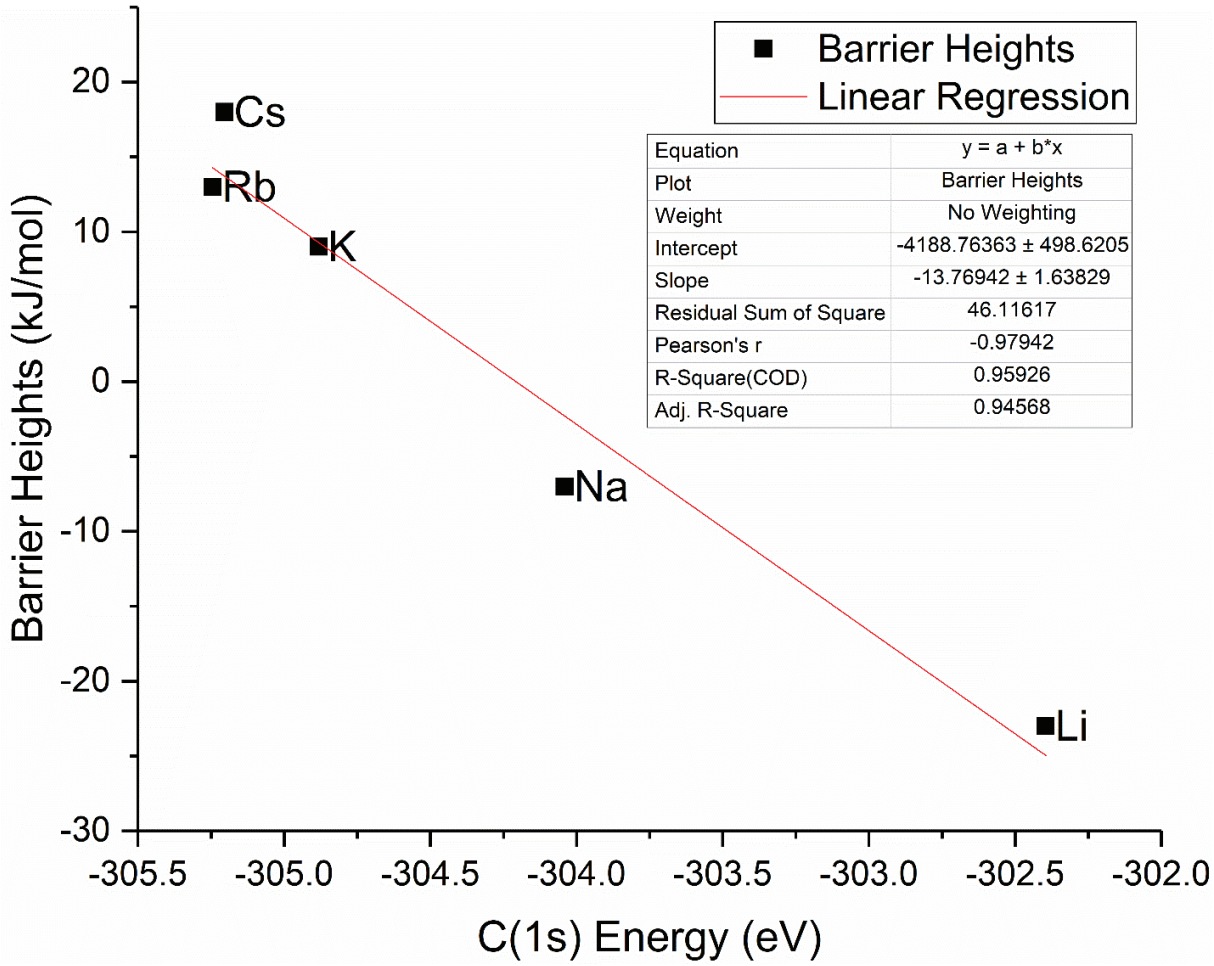

Figure S27. Correlation between the alkali metal carbonite (MCO_2^-) C(1s) energy and the barrier heights for CO_2 addition.

SI-H. Alkali metal oxalate crystal structures

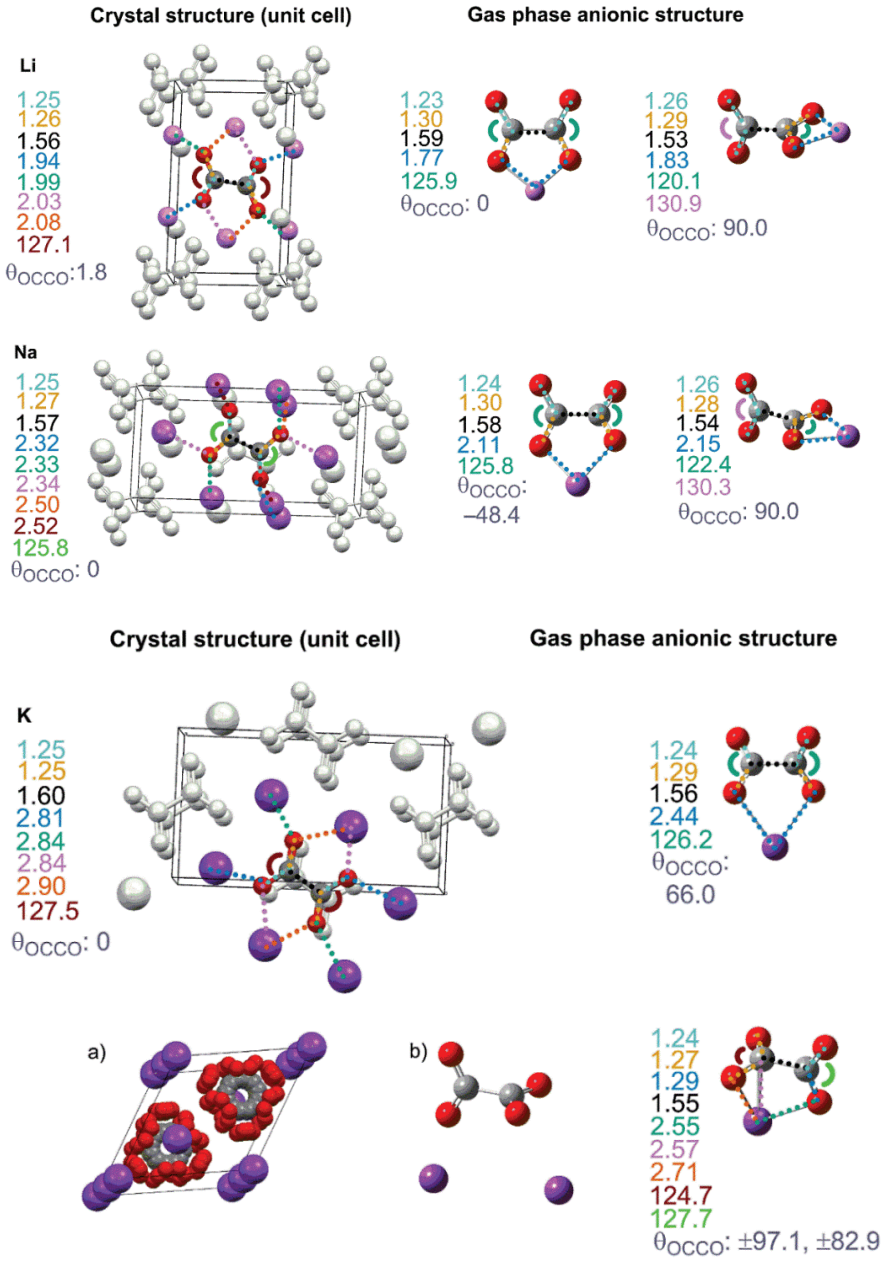

Figure S28. Reported crystal structures and computed MP2/def2-TZVPPD gas-phase ion structures for the alkali metal oxalates (Li – K).

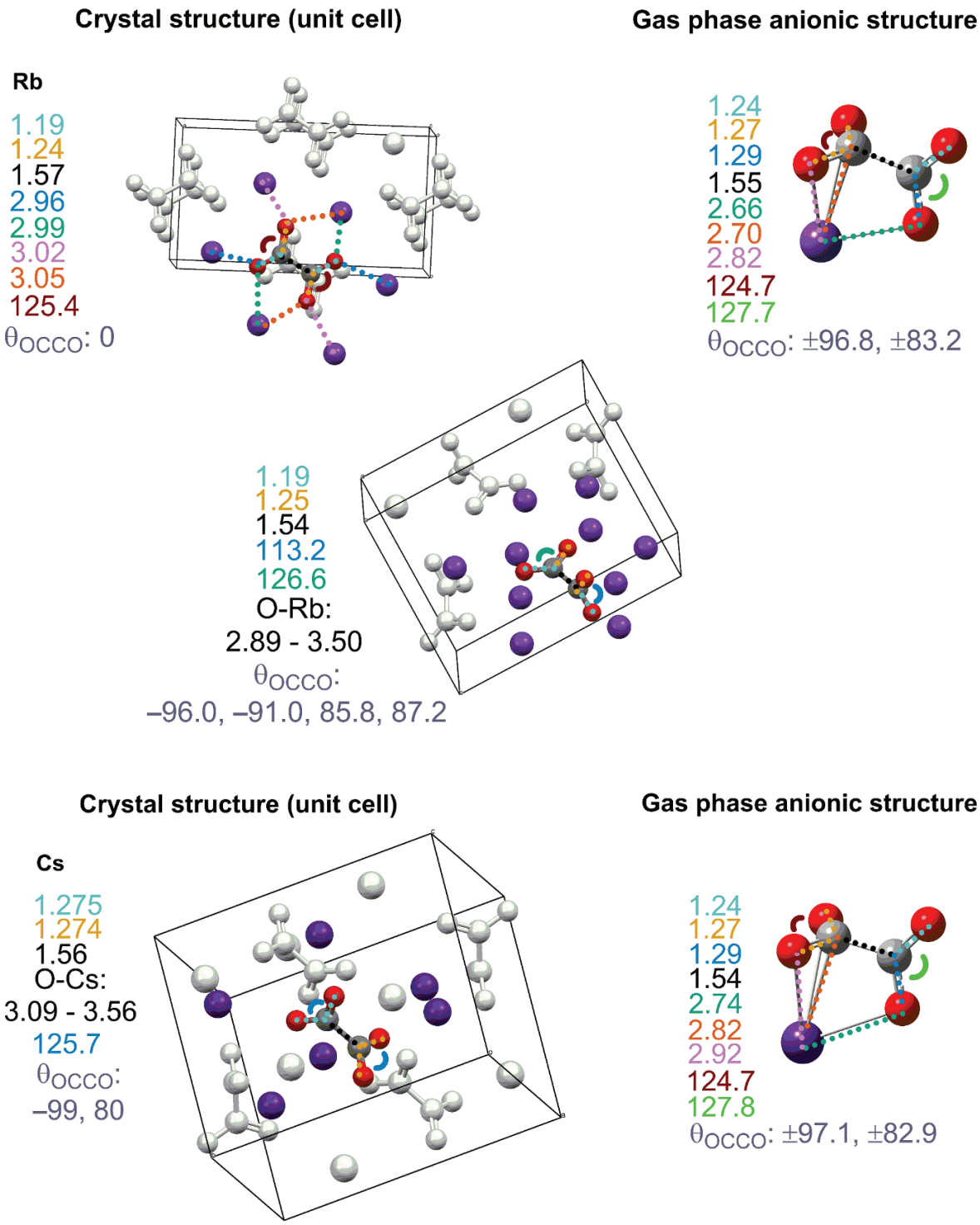

Figure S29. Reported crystal structures and computed MP2/def2-TZVPPD gas-phase ion structures for the alkali metal oxalates (Rb – Cs).

SI-I. Calculated [MP2/def2-TZVPPD] and observed IR spectra for $MC_2O_4^-$

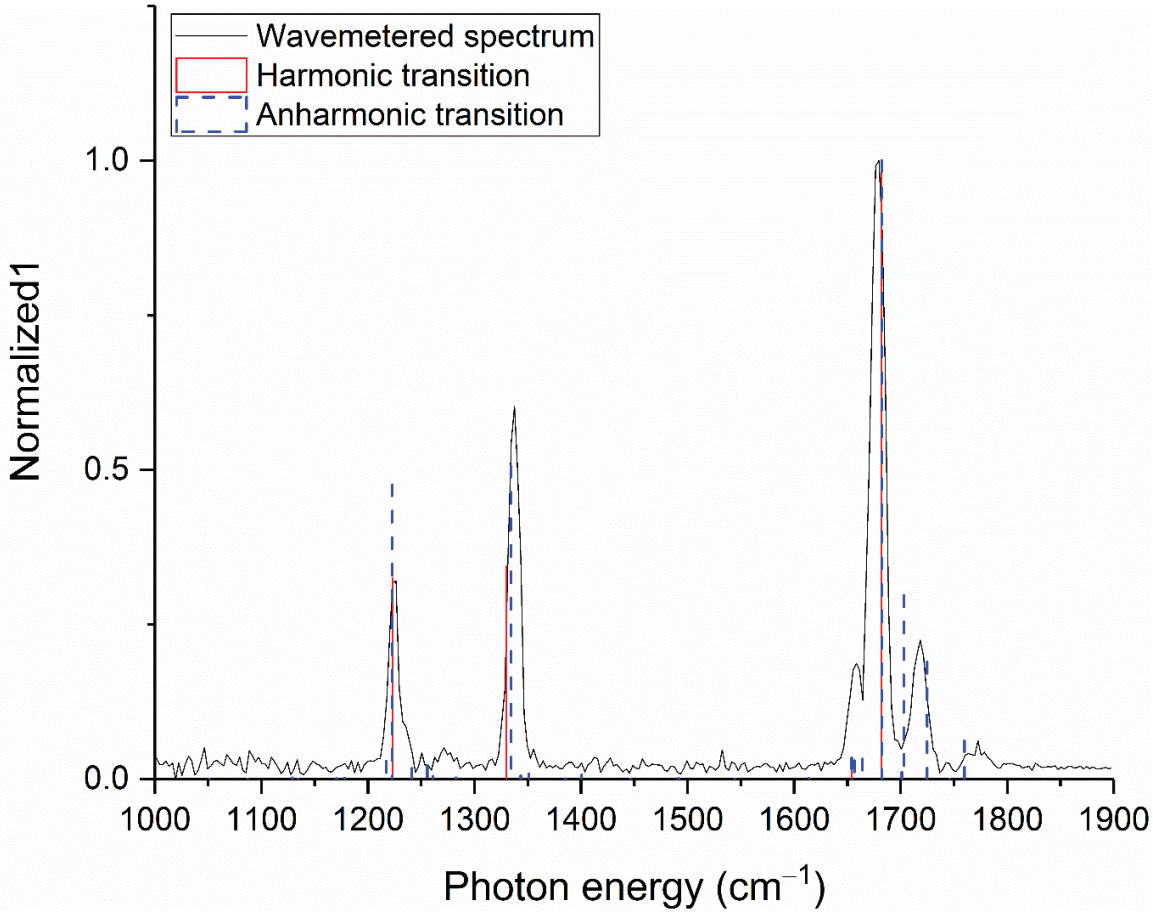

Figure S30. Calculated [MP2/def2-TZVPPD] vs. observed IR-spectra for $LiOx^-$.

Table S6. Calculated [MP2/def2-TZVPPD] and observed transitions for $LiOx^-$.

Description	Normal mode	Calculated transition (cm^{-1})	Scaled (×0.99) transition (cm^{-1})	Observed transition (cm^{-1})
Out-of-phase bound C=O stretch	ν_{12}	1235.36	1223.01	1219.96
In-phase bound C=O stretch	ν_{13}	1343.36	1329.93	1334.68
Out-of-phase unbound C=O stretch	ν_{14}	1670.67	1653.97	1661.11
In-phase unbound C=O stretch	ν_{15}	1698.96	1681.97	1682.86

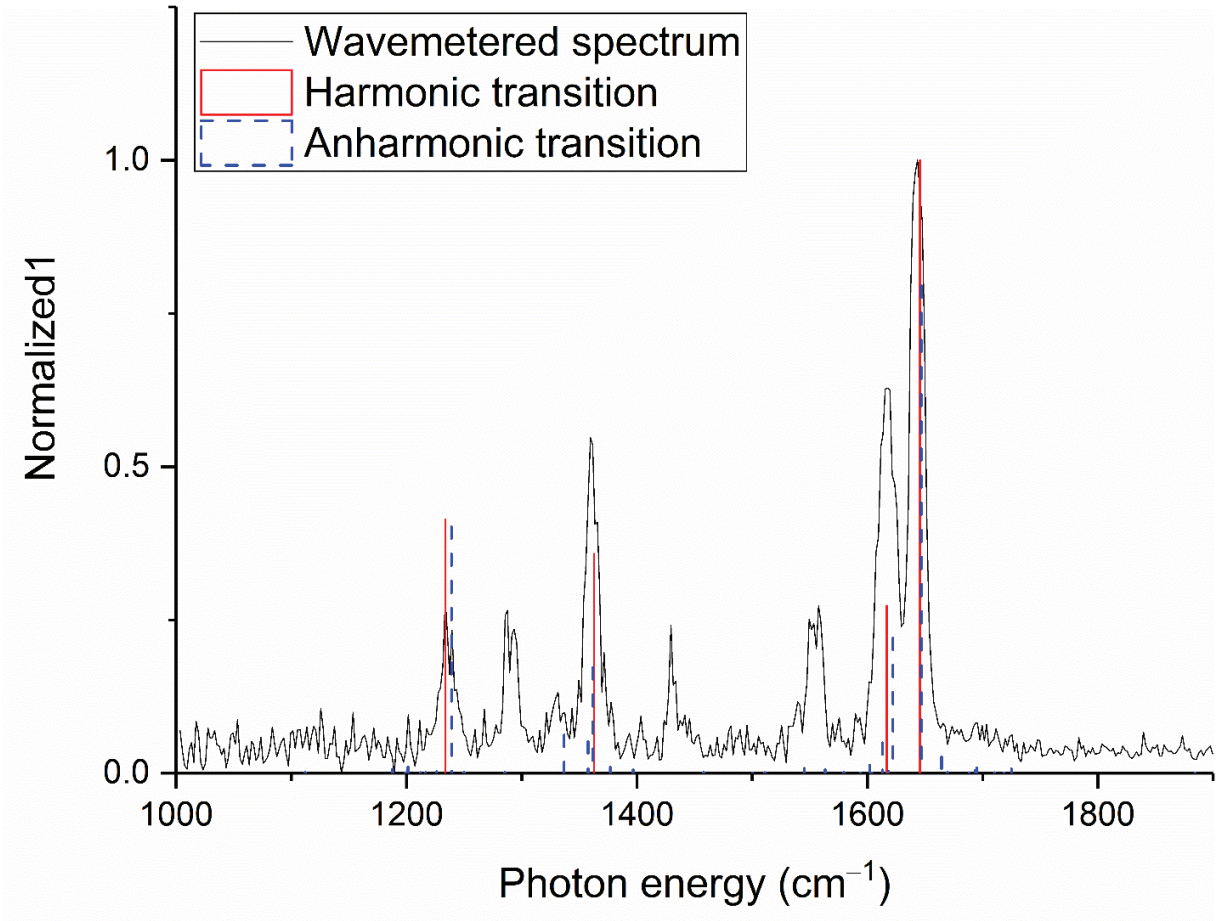

Figure S31. Calculated [MP2/def2-TZVPPD] vs. observed IR-spectra for $NaOx^-$.

Table S7. Calculated [MP2/def2-TZVPPD] and observed transitions for $NaOx^-$.

Description	Normal mode	Calculated transition (cm^{-1})	Scaled (×0.99) transition (cm^{-1})	Observed transition (cm^{-1})
Out-of-phase bound C=O stretch	ν_{12}	1246.27	1233.81	1232.46
In-phase bound C=O stretch	ν_{13}	1376.49	1362.72	1358.13
Out-of-phase unbound C=O stretch	ν_{14}	1633.11	1616.78	1624.62
In-phase unbound C=O stretch	ν_{15}	1662.17	1645.54	1651.57

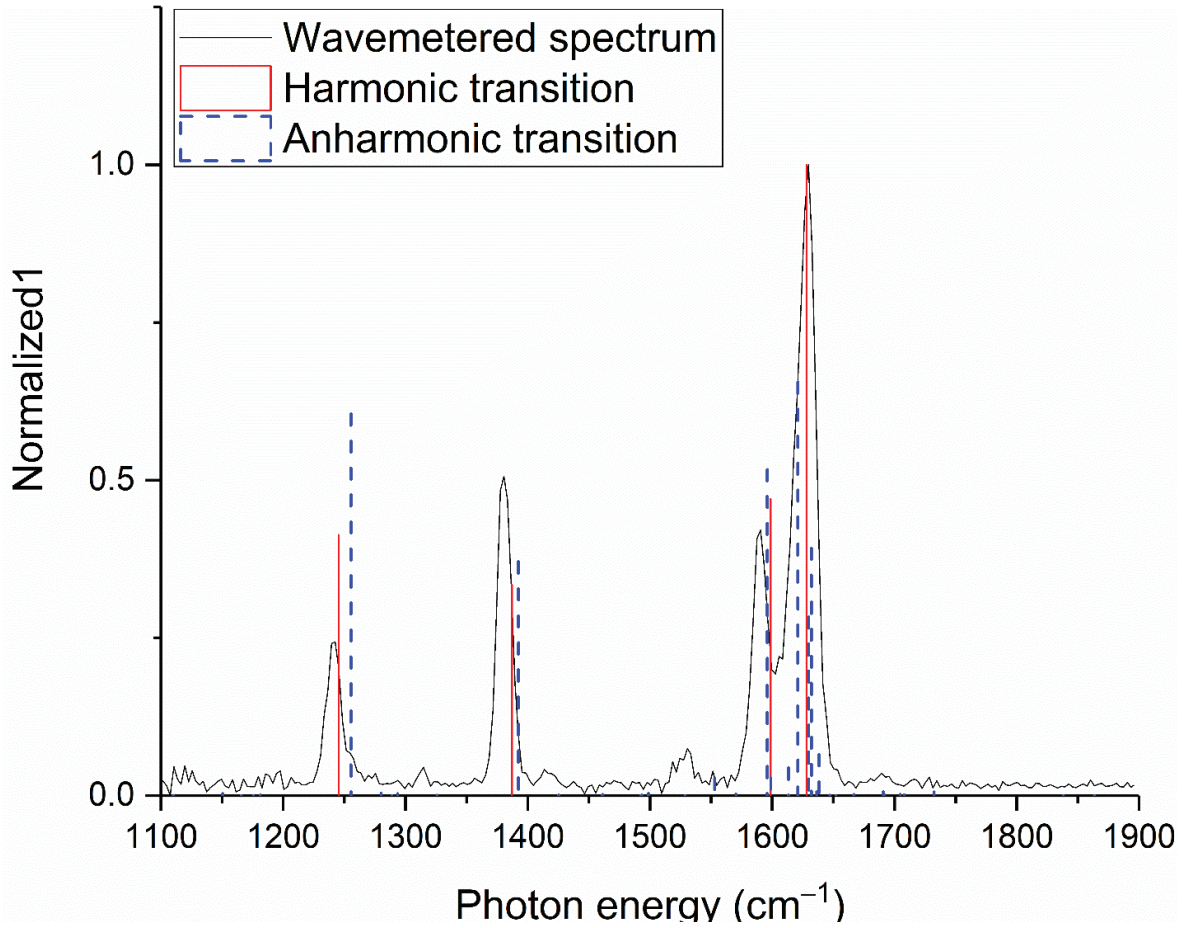

Figure S32. Calculated [MP2/def2-TZVPPD] vs. observed IR-spectra for KOx^-.

Table S8. Calculated [MP2/def2-TZVPPD] and observed transitions for KOx^-.

Description	Normal mode	Calculated transition (cm^{-1})	Scaled (×0.99) transition (cm^{-1})	Observed transition (cm^{-1})
Out-of-phase bound C=O stretch	ν_{12}	1257.86	1245.29	1238.45
In-phase bound C=O stretch	ν_{13}	1401.10	1387.09	1380.96
Out-of-phase unbound C=O stretch	ν_{14}	1614.80	1598.65	1591.95
In-phase unbound C=O stretch	ν_{15}	1644.55	1628.11	1634.49

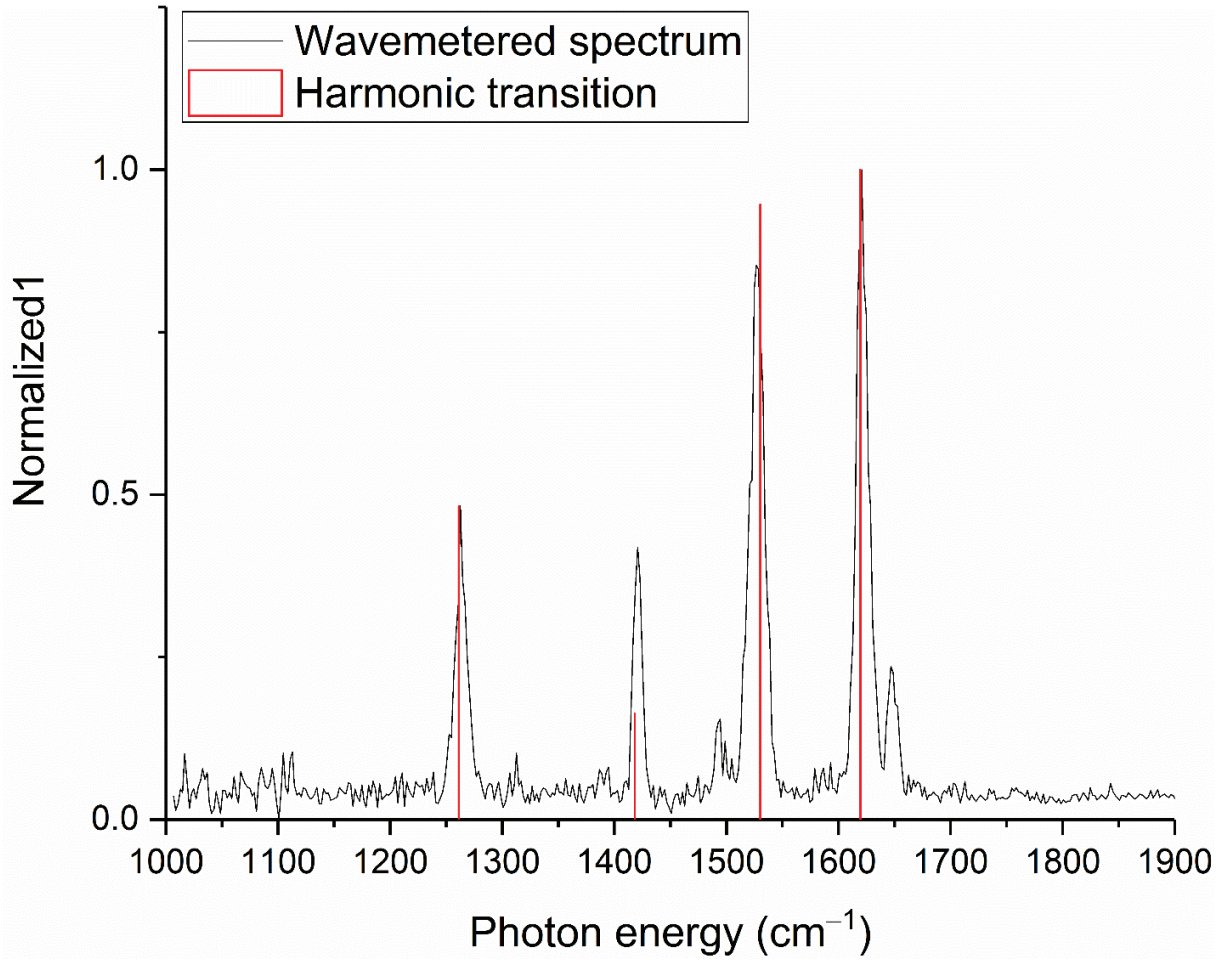

Figure S33. Calculated [MP2/def2-TZVPPD] vs. observed IR-spectra for $RbOx^-$.

Table S9. Calculated [MP2/def2-TZVPPD] and observed transitions for $RbOx^-$.

Description	Normal mode	Calculated transition (cm^{-1})	Scaled (×0.985) transition (cm^{-1})	Observed transition (cm^{-1})
Out-of-phase bound C=O and symmetric CO_2 stretch	ν_{12}	1280.41	1261.20	1250.65
In-phase bound C=O and symmetric CO_2 stretch	ν_{13}	1439.79	1418.20	1424.82
Antisymmetric CO_2 stretch	ν_{14}	1553.61	1530.30	1528.18
Unbound C=O stretch	ν_{15}	1644.12	1619.46	1622.89

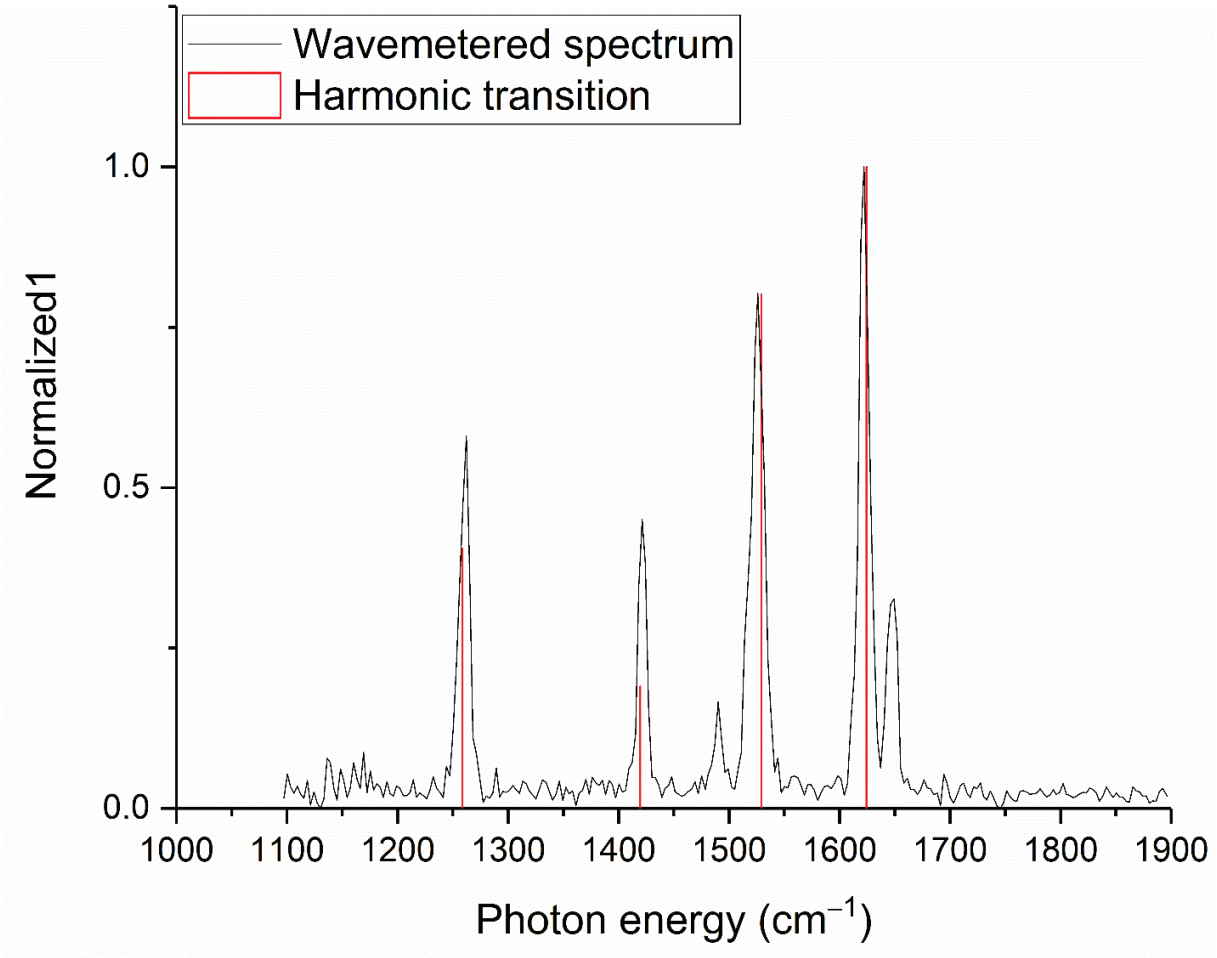

Figure S34. Calculated [MP2/def2-TZVPPD] vs. observed IR-spectra for $CsOx^-$.

Table S10. Calculated [MP2/def2-TZVPPD] and observed transitions for $CsOx^-$.

Description	Normal mode	Calculated transition (cm^{-1})	Scaled (×0.985) transition (cm^{-1})	Observed transition (cm^{-1})
Out-of-phase bound C=O and symmetric CO_2 stretch	ν_{12}	1278.03	1258.86	1257.94
In-phase bound C=O and symmetric CO_2 stretch	ν_{13}	1441.01	1419.40	1420.74
Antisymmetric CO_2 stretch	ν_{14}	1552.45	1529.16	1528.29
Unbound C=O stretch	ν_{15}	1649.14	1624.40	1625.78

SI-J. Cartesian coordinates for the MCO_2^- geometries optimized on the [CCSD(T)/def2-TZVPPD] level of theory

Lithium A isomer

C	0.00000000	0.00000000	-0.62166437
O	-1.12949325	0.00000000	-0.05993573
O	1.12949325	0.00000000	-0.05993573
Li	0.00000000	0.00000000	1.54016564

Lithium B isomer

C	-0.22916797	0.17526263	0.00000000
O	-0.12015001	1.38742865	0.00000000
O	0.59818564	-0.79518546	0.00000000
Li	-0.81697026	-1.91688324	0.00000000

Sodium A isomer

C	0.00000000	0.00000000	1.10447983
O	0.00000000	1.13664696	0.58893580
O	0.00000000	-1.13664696	0.58893580
Na	0.00000000	0.00000000	-1.44592518

Sodium B isomer

C	0.00000000	0.72189100	0.00000000
O	-0.18939800	1.92319000	0.00000000
O	0.96504500	-0.07450400	0.00000000
Na	-0.56410700	-1.73825700	0.00000000

Potassium A isomer

C	0.00000000	0.00000000	-1.55114100
O	0.00000000	1.14170200	-1.05253300
O	0.00000000	-1.14170200	-1.05253300
K	0.00000000	0.00000000	1.37617700

Potassium B isomer

C	0.10454624	-1.26957068	0.00000000
O	0.49883946	-2.42203076	0.00000000
O	-0.97608899	-0.64823564	0.00000000
K	0.18028146	1.68802389	0.00000000

Rubidium A isomer

C	0.00000000	0.00000000	2.07313321
O	0.00000000	1.14211461	1.58028214
O	0.00000000	-1.14211461	1.58028214
Rb	0.00000000	0.00000000	-0.99308527

Rubidium B isomer

C	0.10486370	-1.87607566	0.00000000
O	0.55761475	-3.00661055	0.00000000
O	-1.00061520	-1.30458889	0.00000000
Rb	0.08027922	1.20584642	0.00000000

Cesium A isomer

C	0.00164000	2.40405600	-0.00076400
O	1.14250300	1.90272700	0.00141700
O	-1.14023000	1.90507400	0.00141800
Cs	-0.00172400	-0.79794800	-0.00118600

Cesium B isomer

C	0.12137171	-2.25809424	0.00000000
O	0.54232712	-3.40141016	0.00000000
O	-0.97617654	-1.66635471	0.00000000
Cs	0.04115927	0.97001573	0.00000000

Carbon dioxide

C	0.00000000	0.00000000	0.00000000
O	0.00000000	0.00000000	-1.16594614
O	0.00000000	0.00000000	1.16594614

SI-K. Cartesian coordinates for [MP2/def2-TZVPPD] optimized species formed during MOx^- dissociation

The nomenclature for the structures reported in this section is equivalent to that used in section SI-E and Figure S21 to Figure S25.

Lithium

1A

Center Number	Atomic Number	Atomic Type	Coordinates (Angstroms) X	Y	Z
1	6	0	-2.913516	0.403028	-0.031874
2	6	0	-4.513180	0.409636	-0.031874
3	8	0	-2.315120	1.478354	-0.031874
4	8	0	-2.363210	-0.775792	-0.031874
5	8	0	-5.102672	1.489869	-0.031874
6	8	0	-5.073206	-0.764598	-0.031874
7	3	0	-3.722924	-1.911928	-0.031873

TS1AB

Center Number	Atomic Number	Atomic Type	Coordinates (Angstroms) X	Y	Z
1	6	0	-3.018513	0.303670	0.001620
2	6	0	-4.550213	0.316007	0.031460
3	8	0	-2.390083	1.216404	0.644954
4	8	0	-2.433512	-0.334683	-0.942924
5	8	0	-4.916118	1.193686	-0.815874
6	8	0	-5.219687	-0.424161	0.772786
7	3	0	-2.060248	1.499084	-1.192304

1B

Center Number	Atomic Number	Atomic Type	Coordinates (Angstroms) X	Y	Z
1	6	0	-3.036136	0.339363	-0.032358
2	6	0	-4.569781	0.375282	-0.030070
3	8	0	-2.374792	1.101320	0.766521
4	8	0	-2.413574	-0.452664	-0.833152
5	8	0	-5.073642	1.206038	-0.824883
6	8	0	-5.109610	-0.431029	0.766299
7	3	0	-0.948534	0.290469	-0.035472

2A

Center Number	Atomic Number	Atomic Type	Coordinates (Angstroms) X	Y	Z
1	6	0	-0.487526	1.028670	0.955446
2	8	0	0.704030	1.325256	0.738651
3	8	0	-1.559853	1.568233	0.618167
4	3	0	-0.229522	2.838036	-0.243532

TS2A

Center Number	Atomic Number	Atomic Type	Coordinates (Angstroms) X	Y	Z
1	6	0	-0.467241	1.028733	0.955030
2	8	0	0.530846	0.493903	1.290364
3	8	0	-1.230990	1.804392	0.456568
4	3	0	-0.405486	3.433167	-0.633230

INCAB

Center Number	Atomic Number	Atomic Type	Coordinates (Angstroms) X	Y	Z
1	6	0	-0.129154	-0.437278	0.290938
2	8	0	1.004247	-0.690963	0.438288
3	8	0	-1.275448	-0.229750	0.174285
4	3	0	0.789570	2.851852	-1.896513

TS1B

Center Number	Atomic Number	Atomic Type	Coordinates (Angstroms) X	Y	Z
1	6	0	-1.640336	0.295600	0.102543
2	6	0	-4.608578	0.290276	-0.161056
3	8	0	-1.472439	1.330849	-0.416351
4	8	0	-1.664947	-0.731343	0.677554
5	8	0	-4.938003	1.454514	-0.127763
6	8	0	-4.974621	-0.787279	0.406295
7	3	0	-3.896093	-1.702683	-0.704337

INC1B

Center Number	Atomic Number	Atomic Type	Coordinates (Angstroms) X	Y	Z
1	6	0	-1.425993	0.698642	0.220128
2	6	0	-4.512886	-0.132798	-0.058198
3	8	0	-1.429187	1.217086	-0.827947
4	8	0	-1.343643	0.196235	1.272773
5	8	0	-4.169717	0.921440	0.440132
6	8	0	-5.631681	-0.698840	-0.287704
7	3	0	-4.685610	-2.053230	-0.984398

2B

Center Number	Atomic Number	Atomic Type	Coordinates (Angstroms) X	Y	Z
1	6	0	-0.595109	0.943437	0.520284
2	8	0	0.264499	1.004550	1.374773
3	8	0	-1.696449	1.549757	0.294234
4	3	0	-1.860841	0.517723	-1.163922

TS2AB

Center Number	Atomic Number	Atomic Type	Coordinates (Angstroms) X	Y	Z
1	6	0	-0.282073	0.933572	0.709019
2	8	0	0.734269	0.769646	1.366935
3	8	0	-1.128714	1.875727	0.600340
4	3	0	-0.896354	3.181249	-0.607562

TS2B

Center Number	Atomic Number	Atomic Type	Coordinates (Angstroms) X	Y	Z
1	6	0	-0.593271	1.157204	0.793201
2	8	0	0.375647	0.959831	1.418487
3	8	0	-1.610995	1.472137	0.272976
4	3	0	-2.059281	0.426294	-1.459293

Sodium

1A

Center Number	Atomic Number	Atomic Type	Coordinates (Angstroms) X	Y	Z
1	6	0	-2.926594	0.435793	-0.103358
2	6	0	-4.497768	0.452100	0.007287
3	8	0	-2.360228	1.397091	-0.639375
4	8	0	-2.341514	-0.616460	0.380437
5	8	0	-5.050694	1.470511	0.442360
6	8	0	-5.097377	-0.635883	-0.367380
7	11	0	-3.729989	-2.179325	0.085724

TS1AB

Center Number	Atomic Number	Atomic Type	Coordinates (Angstroms) X	Y	Z
1	6	0	-3.167487	0.432222	-0.115388
2	6	0	-4.686703	0.287978	0.050149
3	8	0	-2.564079	1.345703	0.548325
4	8	0	-2.589244	-0.223923	-1.050360
5	8	0	-5.292496	1.087250	-0.725059
6	8	0	-5.141553	-0.539168	0.869419
7	11	0	-1.770451	1.749223	-1.430441

1B

Center Number	Atomic Number	Atomic Type	Coordinates (Angstroms) X	Y	Z
1	6	0	-3.076309	0.341085	-0.031494
2	6	0	-4.614724	0.372893	-0.033545
3	8	0	-2.443725	1.111067	0.774991
4	8	0	-2.473946	-0.454431	-0.836334
5	8	0	-5.124787	1.201488	-0.829008
6	8	0	-5.160718	-0.433868	0.760512
7	11	0	-0.631861	0.290544	-0.028237

TS1A

Center Number	Atomic Number	Atomic Type	Coordinates (Angstroms) X	Y	Z
1	6	0	-2.834763	0.336068	-0.031178
2	6	0	-5.014469	0.381229	-0.034059
3	8	0	-2.348918	0.290378	1.106157
4	8	0	-2.344439	0.361533	-1.167223
5	8	0	-5.313381	0.423763	-1.194065
6	8	0	-5.317950	0.351177	1.125151
7	11	0	-0.352151	0.284631	-0.027897

INC1A

Center Number	Atomic Number	Atomic Type	Coordinates (Angstroms) X	Y	Z
1	6	0	-2.646852	0.332173	-0.030928
2	6	0	-5.446729	0.390181	-0.034636
3	8	0	-2.156383	1.119544	0.792129
4	8	0	-2.187236	-0.474881	-0.852726
5	8	0	-5.486471	1.231066	-0.848993
6	8	0	-5.523421	-0.448291	0.779566
7	11	0	-0.079580	0.278986	-0.027526

2A

Center Number	Atomic Number	Atomic Type	Coordinates (Angstroms) X	Y	Z
1	6	0	-0.486115	0.959057	1.009797
2	8	0	0.703206	1.267713	0.801795
3	8	0	-1.571719	1.466528	0.667812
4	11	0	-0.218244	3.066894	-0.410671

TS2A

Center Number	Atomic Number	Atomic Type	Coordinates (Angstroms) X	Y	Z
1	6	0	-0.435706	0.981976	0.994339
2	8	0	0.741732	0.837699	1.091859
3	8	0	-1.455741	1.504846	0.641726
4	11	0	-0.423157	3.435671	-0.659191

INCAB

Center Number	Atomic Number	Atomic Type	Coordinates (Angstroms) X	Y	Z
1	6	0	-0.066758	-1.185066	0.798593
2	8	0	1.100718	-1.253699	0.845135
3	8	0	-1.236680	-1.156943	0.779351
4	11	0	0.146330	2.345232	-1.580403

2B

Center Number	Atomic Number	Atomic Type	Coordinates (Angstroms) X	Y	Z
1	6	0	0.081715	-0.688035	0.000000
2	8	0	0.496386	-1.835928	-0.000000
3	8	0	-1.020467	-0.086226	-0.000000
4	11	0	0.350644	1.731656	-0.000000

TS2B

Center Number	Atomic Number	Atomic Type	Coordinates (Angstroms) X	Y	Z
1	6	0	-0.503999	-0.476056	0.002649
2	8	0	0.694486	-0.851011	-0.002052
3	8	0	-1.617842	-0.974998	0.007917
4	11	0	1.049959	1.398073	-0.005949

TS2AB

Center Number	Atomic Number	Atomic Type	Coordinates (Angstroms) X	Y	Z
1	6	0	-0.314403	1.008034	0.652266
2	8	0	0.709968	0.866770	1.314753
3	8	0	-1.378446	1.674150	0.752164
4	11	0	-0.589990	3.211238	-0.650449

Potassium

1A

Center Number	Atomic Number	Atomic Type	Coordinates (Angstroms) X	Y	Z
1	6	0	-2.937092	0.500535	-0.009708
2	6	0	-4.495008	0.495148	-0.071514
3	8	0	-2.355978	1.422288	0.586701
4	8	0	-2.374587	-0.514255	-0.582699
5	8	0	-5.081008	1.390001	-0.703076
6	8	0	-5.052107	-0.499726	0.540365
7	19	0	-3.708067	-2.469831	0.016815

TS1AB

Center Number	Atomic Number	Atomic Type	Coordinates (Angstroms) X	Y	Z
1	6	0	-2.989603	0.540985	-0.044171
2	6	0	-4.536146	0.672197	0.014496
3	8	0	-2.278399	1.160038	0.762738
4	8	0	-2.586689	-0.251509	-0.984123
5	8	0	-5.072298	1.688186	-0.479875
6	8	0	-5.154718	-0.364742	0.463315
7	19	0	-4.554595	-1.618663	-1.592475

1B

Center Number	Atomic Number	Atomic Type	Coordinates (Angstroms) X	Y	Z
1	6	0	-3.039535	-0.151920	0.452911
2	6	0	-4.374600	0.406195	-0.094189
3	8	0	-2.483219	0.504529	1.387554
4	8	0	-2.475327	-1.062417	-0.230194
5	8	0	-4.159556	1.320270	-0.978503
6	8	0	-5.471356	-0.015658	0.309059
7	19	0	-1.522476	1.427779	-1.069753

TS1A

Center Number	Atomic Number	Atomic Type	Coordinates (Angstroms) X	Y	Z
1	6	0	-2.344751	0.439743	-0.055094
2	6	0	-4.475404	0.484399	0.062018
3	8	0	-2.006719	1.564570	-0.318501
4	8	0	-2.027181	-0.698824	0.172277
5	8	0	-4.938930	1.609901	-0.153842
6	8	0	-4.959100	-0.621250	0.329944
7	19	0	-7.303488	0.543673	0.217466

INC1A

Center Number	Atomic Number	Atomic Type	Coordinates (Angstroms) X	Y	Z
1	6	0	2.772944	-0.058118	-0.152417
2	6	0	0.052071	-0.001092	-0.002862
3	8	0	2.802073	0.587120	-1.130416
4	8	0	2.882061	-0.706253	0.817984
5	8	0	-0.361068	0.967017	0.656728
6	8	0	-0.470919	-0.949580	-0.610998
7	19	0	-2.870549	0.060163	0.157781

2A

Center Number	Atomic Number	Atomic Type	Coordinates (Angstroms) X	Y	Z
1	6	0	-0.486452	1.242447	-0.488211
2	8	0	0.666485	1.234348	-0.006517
3	8	0	-1.629261	1.233867	0.017036
4	19	0	-0.456488	1.193109	2.431398

TS3A

Center Number	Atomic Number	Atomic Type	Coordinates (Angstroms) X	Y	Z
1	6	0	-0.486317	1.240415	-0.409047
2	8	0	0.686382	1.235780	-0.179900
3	8	0	-1.653681	1.237244	-0.154096
4	19	0	-0.452099	1.190332	2.696748

INCAB

Center Number	Atomic Number	Atomic Type	Coordinates (Angstroms) X	Y	Z
1	6	0	-0.023617	0.034568	-2.143644
2	8	0	1.146176	0.034121	-2.174239
3	8	0	-1.193800	0.035585	-2.148435
4	19	0	0.029368	-0.042985	2.665626

TS2A

Center Number	Atomic Number	Atomic Type	Coordinates (Angstroms) X	Y	Z
1	6	0	-2.912510	-0.294876	0.594856
2	6	0	-4.797871	0.598683	-0.284507
3	8	0	-2.486431	0.529823	1.395312
4	8	0	-2.477015	-1.069179	-0.249656
5	8	0	-4.232441	1.378197	-1.039066
6	8	0	-5.842538	0.178498	0.118035
7	19	0	-1.614169	1.432071	-1.076422

INC2A

Center Number	Atomic Number	Atomic Type	Coordinates (Angstroms) X	Y	Z
1	6	0	0.375976	-1.052663	1.114643
2	6	0	-2.010621	0.129509	-0.188209
3	8	0	0.754132	0.006231	1.647807
4	8	0	0.503461	-1.558539	-0.017013
5	8	0	-1.354175	0.894577	-0.784961
6	8	0	-2.706344	-0.609096	0.391819
7	19	0	1.688385	0.772365	-0.801779

2B

Center Number	Atomic Number	Atomic Type	Coordinates (Angstroms) X	Y	Z
1	6	0	0.081991	-1.214525	-0.000000
2	8	0	0.545537	-2.349656	0.000000
3	8	0	-1.049414	-0.671473	0.000000
4	19	0	0.229465	1.583840	0.000000

TS2B

Center Number	Atomic Number	Atomic Type	Coordinates (Angstroms) X	Y	Z
1	6	0	-0.020257	-1.353245	0.001104
2	8	0	0.593435	-2.374603	-0.000425
3	8	0	-1.013044	-0.668321	0.005341
4	19	0	0.247443	1.744356	-0.006020

TS2AB

Center Number	Atomic Number	Atomic Type	Coordinates (Angstroms) X	Y	Z
1	6	0	-0.356942	1.510654	-0.190608
2	8	0	0.707759	1.043349	-0.604937
3	8	0	-1.480378	1.046046	0.129924
4	19	0	-0.776155	1.303722	2.619327

Rubidium

1A

Center Number	Atomic Number	Atomic Type	Coordinates (Angstroms) X	Y	Z
1	6	0	-2.862757	0.558561	-0.260334
2	6	0	-4.395250	0.375034	-0.169524
3	8	0	-2.353809	1.592874	-0.722504
4	8	0	-2.254949	-0.483017	0.198243
5	8	0	-4.939918	0.642045	0.946429
6	8	0	-4.952472	-0.270937	-1.110554
7	37	0	-4.245007	-2.090733	0.923940

TS1A

Center Number	Atomic Number	Atomic Type	Coordinates (Angstroms) X	Y	Z
1	6	0	-2.459258	0.993948	-0.456723
2	6	0	-4.094376	-0.240256	0.102260
3	8	0	-2.733394	1.438202	-1.542336
4	8	0	-1.672470	0.936647	0.453633
5	8	0	-3.936490	-0.763012	1.210863
6	8	0	-4.982344	-0.268580	-0.756757
7	37	0	-6.374640	-1.961530	0.881766

INC1A

Center Number	Atomic Number	Atomic Type	Coordinates (Angstroms) X	Y	Z
1	6	0	2.755493	2.079942	-0.941977
2	6	0	0.679447	0.512885	-0.232269
3	8	0	2.790913	1.664109	-2.037532
4	8	0	2.833979	2.581755	0.114639
5	8	0	1.050929	-0.580647	0.226610
6	8	0	-0.416339	1.059691	-0.443540
7	37	0	-1.671605	-1.261756	0.571451

2A

Center Number	Atomic Number	Atomic Type	Coordinates (Angstroms) X	Y	Z
1	6	0	-0.000000	-0.000000	2.070993
2	8	0	0.000000	1.147492	1.573315
3	8	0	0.000000	-1.147492	1.573315
4	37	0	-0.000000	0.000000	-0.977010

TS3A

Center Number	Atomic Number	Atomic Type	Coordinates (Angstroms) X	Y	Z
1	6	0	0.000000	0.000000	1.979162
2	8	0	-0.000000	1.169644	1.729549
3	8	0	-0.000000	-1.169644	1.729549
4	37	0	0.000000	-0.000000	-1.197647

INCAB

Center Number	Atomic Number	Atomic Type	Coordinates (Angstroms) X	Y	Z
1	6	0	-0.000000	0.000000	2.924511
2	8	0	0.000000	1.170044	2.940626
3	8	0	0.000000	-1.170044	2.940626
4	37	0	0.000000	-0.000000	-1.994718

TS2A

Center Number	Atomic Number	Atomic Type	Coordinates (Angstroms) X	Y	Z
1	6	0	-2.523854	0.628253	-0.291761
2	6	0	-4.757001	0.397515	-0.178770
3	8	0	-2.106016	1.652330	-0.748360
4	8	0	-2.240608	-0.460620	0.190293
5	8	0	-5.072893	0.603203	0.986693
6	8	0	-5.082810	-0.327836	-1.110494
7	37	0	-4.220979	-2.169017	0.958095

INC2A

Center Number	Atomic Number	Atomic Type	Coordinates (Angstroms) X	Y	Z
1	6	0	1.782012	1.547272	-0.665927
2	6	0	-1.161376	1.362671	-0.660087
3	8	0	1.743390	2.653091	-1.041879
4	8	0	1.873674	0.439263	-0.296976
5	8	0	-0.976655	1.458066	0.569811
6	8	0	-1.227556	0.410528	-1.460389
7	37	0	-0.449433	-1.335661	0.646678

2B

Center Number	Atomic Number	Atomic Type	Coordinates (Angstroms) X	Y	Z
1	6	0	0.082164	-1.815632	0.000000
2	8	0	0.602822	-2.928218	-0.000000
3	8	0	-1.078740	-1.337813	-0.000000
4	37	0	0.135896	1.100234	-0.000000

TS2B

Center Number	Atomic Number	Atomic Type	Coordinates (Angstroms) X	Y	Z
1	6	0	-0.003457	-1.956323	-0.001177
2	8	0	0.642306	-2.960438	0.002503
3	8	0	-1.032163	-1.322724	-0.009430
4	37	0	0.135458	1.258056	0.008104

TS2AB

Center Number	Atomic Number	Atomic Type	Coordinates (Angstroms) X	Y	Z
1	6	0	0.272045	0.119899	1.747857
2	8	0	-0.198876	1.187960	2.155257
3	8	0	-0.186221	-1.020143	1.484280
4	37	0	0.113052	-0.287715	-1.146781

Cesium

1A

Center Number	Atomic Number	Atomic Type	Coordinates (Angstroms) X	Y	Z
1	6	0	-2.863666	0.581661	-0.265974
2	6	0	-4.392577	0.393441	-0.173796
3	8	0	-2.349487	1.616204	-0.718524
4	8	0	-2.262480	-0.467984	0.185482
5	8	0	-4.934034	0.644017	0.947409
6	8	0	-4.948185	-0.251665	-1.116240
7	55	0	-4.253735	-2.191845	0.947338

TS1A

Center Number	Atomic Number	Atomic Type	Coordinates (Angstroms) X	Y	Z
1	6	0	-2.458203	1.043363	-0.475196
2	6	0	-4.101864	-0.250428	0.105426
3	8	0	-2.764160	1.480966	-1.552117
4	8	0	-1.671937	0.983830	0.432057
5	8	0	-3.921947	-0.776813	1.208652
6	8	0	-4.997378	-0.287319	-0.745017
7	55	0	-6.438447	-2.089646	0.930821

INC1A

Center Number	Atomic Number	Atomic Type	Coordinates (Angstroms) X	Y	Z
1	6	0	3.134081	2.466960	-1.107111
2	6	0	1.078290	0.848765	-0.380905
3	8	0	3.157341	2.052687	-2.202922
4	8	0	3.207432	2.957280	-0.045427
5	8	0	1.473897	-0.240974	0.066870
6	8	0	-0.028571	1.378648	-0.577430
7	55	0	-1.330224	-1.047073	0.469900

2A

Center Number	Atomic Number	Atomic Type	Coordinates (Angstroms) X	Y	Z
1	6	0	-2.382375	0.000023	0.000207
2	8	0	-1.884071	-1.147556	0.000135
3	8	0	-1.884038	1.147588	0.000135
4	55	0	0.788498	-0.000023	-0.000248

TS3A

Center Number	Atomic Number	Atomic Type	Coordinates (Angstroms) X	Y	Z
1	6	0	-2.300623	0.000022	0.000195
2	8	0	-2.040143	-1.169538	0.000157
3	8	0	-2.040109	1.169574	0.000157
4	55	0	1.018888	-0.000026	-0.000282

INCAB (not converged)

Center Number	Atomic Number	Atomic Type	Coordinates (Angstroms) X	Y	Z
1	6	0	-3.235214	0.000047	0.000464
2	8	0	-3.246891	-1.170962	0.000466
3	8	0	-3.246857	1.171056	0.000466
4	55	0	1.073625	-0.000016	-0.000154

TS2A

Center Number	Atomic Number	Atomic Type	Coordinates (Angstroms) X	Y	Z
1	6	0	-2.158527	0.761492	-0.353733
2	6	0	-4.414574	0.484196	-0.209810
3	8	0	-1.767357	1.796397	-0.808050
4	8	0	-1.857740	-0.326466	0.116529
5	8	0	-4.710348	0.677567	0.961369
6	8	0	-4.732070	-0.238602	-1.144312
7	55	0	-3.803465	-2.210392	0.956286

INC2A

Center Number	Atomic Number	Atomic Type	Coordinates (Angstroms) X	Y	Z
1	6	0	1.822962	2.005103	-0.847653
2	6	0	-1.078955	1.678492	-0.816626
3	8	0	1.751722	3.129239	-1.159410
4	8	0	1.949391	0.880341	-0.545817
5	8	0	-0.891326	1.793911	0.411061
6	8	0	-1.237533	0.716788	-1.590941
7	55	0	-0.382207	-1.112981	0.574040

2B

Center Number	Atomic Number	Atomic Type	Coordinates (Angstroms) X	Y	Z
1	6	0	0.091493	-2.193041	0.000000
2	8	0	0.597483	-3.310963	-0.000000
3	8	0	-1.062710	-1.697859	-0.000000
4	55	0	0.102417	0.846020	-0.000000

TS2B

Center Number	Atomic Number	Atomic Type	Coordinates (Angstroms) X	Y	Z
1	6	0	0.012376	-2.352642	0.000265
2	8	0	0.617137	-3.380621	0.000323
3	8	0	-0.983810	-1.670951	0.000584
4	55	0	0.082980	1.048372	-0.001171

TS2AB

Center Number	Atomic Number	Atomic Type	Coordinates (Angstroms) X	Y	Z
1	6	0	-2.064700	-0.115780	-0.278036
2	8	0	-2.465967	-1.184099	0.198318
3	8	0	-1.780059	1.018185	0.187371
4	55	0	0.948740	0.281726	-0.107423

Carbon dioxide

Center Number	Atomic Number	Atomic Type	Coordinates (Angstroms) X	Y	Z
1	6	0	0.345953	2.167102	0.000000
2	8	0	-0.823110	2.167102	0.000000
3	8	0	1.515016	2.167102	0.000000

References

(1) Fairley, D. A.; Scott, G. B. I.; Freeman, C. G.; Maclagan, R. G. A. R.; McEwan, M. J. C $_2$ H $_7$ O $^+$ Potential Surface and Ion−Molecule Association between H_3O^+ and C_2H_4. *J. Phys. Chem. A* **1997**, *101* (15), 2848–2851. https://doi.org/10.1021/jp963294c.

(2) Dawson, P. H. A Study of the Collision-Induced Dissociation of $C_2H_5OH_2^+$ Using Various Target Gases. *Int. J. Mass Spectrom. Ion Phys.* **1983**, *50* (3), 287–297. https://doi.org/10.1016/0020-7381(83)87006-5.

(3) Bouchoux, G.; Hoppilliard, Y. Role of Ion-Neutral Complexes during Acid-Catalyzed Dehydration of Ethanol in the Gas Phase. *J. Am. Chem. Soc.* **1990**, *112* (25), 9110–9115. https://doi.org/10.1021/ja00181a012.

(4) Graul, S. T.; Squires, R. R. Gas-Phase Acidities Derived from Threshold Energies for Activated Reactions. *J. Am. Chem. Soc.* **1990**, *112* (7), 2517–2529. https://doi.org/10.1021/ja00163a007.

(5) Skripnikov, L. V. *Chemissian Version 4.52, Visualization Computer Program*; 2017.

(6) Xantheas, S. S. On the Importance of the Fragment Relaxation Energy Terms in the Estimation of the Basis Set Superposition Error Correction to the Intermolecular Interaction Energy. *J. Chem. Phys.* **1996**, *104* (21), 8821–8824. https://doi.org/10.1063/1.471605.

Supporting information for Paper II.

Supporting Information – Computational Exploration of the Direct Reduction of CO_2 to CO Mediated by Alkali Metal and Alkaline Earth Metal Chloride Anions

Joakim S. Jestilä and Einar Uggerud*

Department of Chemistry and Hylleraas Centre for Quantum Molecular Sciences, University of Oslo, P. O. Box 1033 Blindern, N-0315 OSLO, Norway

SI-A. Data relevant for Born Haber cycles

Table SI-1A. Born Haber cycle parameters and estimated "experimental" enthalpies ($\Delta H^\circ_{rxn,\,MP2}$) for $M^- + CO_2 \rightarrow MO^- + CO$ in kJ/mol. Experimental ΔH°_f (M(g)), ΔH°_f (MO(g)), ΔH°_f (CO_2(g)) and ΔH°_f (CO(g)) retrieved from thermochemical tables (NIST-JANAF).[1] Computational adiabatic electron affinities (EA_{MP2}) and bond dissociation (ZPE + EE) energies (BDE_{MP2}) from the [MP2/def2-TZVPPD] level of theory. Values from or based exclusively on literature, computational and experimental, in **bold**. Estimates based on a combination of literature values and MP2 calculations in normal text.

	Li	**Na**	**K**	**Rb**	**Cs**	**BeCl**	**MgCl**	**CaCl**	**SrCl**	**BaCl**
$\Delta H^\circ_{f,\,298K}$ (M(g))	**159.3**	**107.5**	**89.0**	**80.9**	**76.5**	**60.7**	**−43.5**	**−104.6**	**−123.8**	**−142.3**
$\Delta H^\circ_{f,\,0K}$ (M(g))	**157.7**	**107.5**	**89.9**	**82.2**	**78.0**					
EA_{MP2}(M)	9.1	22.3	23.8	26.2	28.0	85.7	125.0	101.1	99.6	83.2
EA(M)	**60** [g]	**53** [h]	**48** [i]	**46** [j]	**46** [k]		**153.3** [l]			
$\Delta H^\circ_{f,\,MP2}(M^-(g))$[a]	150.2	85.2	65.2	54.7	48.5	−25.0	−168.5	−205.7	−223.4	−225.5
$\Delta H^\circ_{f,\,298K}$ (M^-(g))[1b]	**99.3**	**54.5**	**41**	**34.9**	**30.5**		**−196.8**			
$\Delta H^\circ_{f,\,0K}$ (M^-(g))[2b]	**97.7**	**54.5**	**41.9**	**36.2**	**32.0**					
$\Delta H^\circ_{f,\,298K}$ (MO(g))*	**84.1**	**83.7**	**71.1**	**59.0** [m]	**62.8**	**136.4**	**58.2**	**43.9**	**−13.4**	**−123.8**
BDE_{MP2}(Cl—MO)	*n.a.*	*n.a.*	*n.a.*	*n.a.*	*n.a.*	279.6	394.6	353.3	324.7	258.7
BDE(M—O)	**333.5**	**256.1**	**277.8**	**255**	**295.8**					
EA_{MP2}(MO)	74.1	99.3	112.5	115.6	108.1	345.5	258.5	226.3	207.2	228.6
EA(MO)	**40.1** [n]	**52.4** [n]	**39.0** [n]	42.8**	**26.3** [o]					
$\Delta H^\circ_{f,\,MP2}(MO^-(g))$[c]	10.0	−15.6	−41.3	−40.7	−45.4	−367.7	−474.0	−414.7	−424.3	−490.1
$\Delta H^\circ_{f,\,298K^1}$ (MO^-(g))[1d]	**44.0**	**31.3**	**32.1**	16.2	**36.4**					
$\Delta H^\circ_{f,\,298K^2}$ (MO^-(g))[2d]	**34.7**	**48**	**21.2**	32.1	**3.4**					
$\Delta H^\circ_{f,\,0K^2}$ (MO^-(g))[2d]	**33.1**	**48.0**	**22.1**	33.4	**4.9**					

$\Delta H^\circ_{rxn,\,MP2}$[e]	142.7	182.1	176.4	187.5	189.1	−59.7	−22.5	74.0	82.1	18.3
$\Delta H^\circ_{rxn,\,298K}$[1] [1f]	**227.6**	**259.7**	**274.1**	264.2	**288.9**					
$\Delta H^\circ_{rxn,\,298K}$[2] [2f]	**218.3**	**276.4**	**263.1**	280.1	**255.8**					
$\Delta H^\circ_{rxn,\,0K}$[2] [2f]	**214.7**	**272.8**	**259.5**	276.5	**252.2**					
$\Delta H^\circ_{f,\,298K}$ (CO_2(g))	**−393.5**									
$\Delta H^\circ_{f,\,0K}$ (CO_2(g))	**−393.1**									
$\Delta H^\circ_{f,\,298K}$ (CO(g))	**−110.5**									
$\Delta H^\circ_{f,\,0K}$ (CO(g))	**−113.8**									
BDE(Cl_2)	**242.0**									
BDE(O_2)	**498.0**									

***** ΔH°_f of the metal oxide without chloride

****** CCSD(T)/def2-TZVPPD (this work)

[g] From ref 2

[h] From ref 3

[i] From ref 4

[j] From ref 5

[k] From ref 6

[l] From ref 7

[m] From ref 8

[n] From ref 9

[o] From ref 10

[a] $\Delta H^\circ_{f,\,MP2}(M^-(g)) = \mathbf{\Delta H^\circ_{f,\,298K}(M(g))} - EA_{MP2}(M)$

[1b] $\mathbf{\Delta H^\circ_{f,\,298K}(M^-(g)) = \Delta H^\circ_{f,\,298K}(M(g)) - EA(M)}$

[2b] $\mathbf{\Delta H^\circ_{f,\,0K}(M^-(g)) = \Delta H^\circ_{f,\,0K}(M(g)) - EA(M)}$

For M = Li – Cs:

[c] $\Delta H^\circ_{f,\,MP2}(MO^-(g)) = \mathbf{\Delta H^\circ_{f,\,298K}(MO(g))} - EA_{MP2}(MO)$

For M = BeCl – BaCl:

[c] $\Delta H^\circ_{f,\,MP2}(MO^-(g)) = \mathbf{\Delta H^\circ_{f,\,298K}(MO(g))} + \frac{1}{2}\,\mathbf{BDE(Cl_2)} - BDE_{MP2}(Cl—MO) - EA_{MP2}(MO)$

[1d] $\mathbf{\Delta H^\circ_{f,\,298K}{}^{1}\,(MO^-(g)) = \Delta H^\circ_{f,\,298K}\,(MO(g)) - EA(MO)}$

[2d] $\mathbf{\Delta H^\circ_{f,\,0K/298K}{}^{2}\,(MO^-(g)) = \Delta H^\circ_{f,\,0K/298K}\,(M(g)) + \tfrac{1}{2}\,BDE(O_2) - BDE(M{-}O) - EA(MO)}$

[e] $\Delta H^\circ_{rxn,\,MP2} = [\Delta H^\circ_{f,\,MP2}\,(MO^-(g)) + \mathbf{\Delta H^\circ_{f,\,298K}\,(CO(g))}] - [\Delta H^\circ_{f,\,MP2}\,(M^-(g)) + \mathbf{\Delta H^\circ_{f,\,298K}\,(CO_2(g))}]$

[1f] $\mathbf{\Delta H^\circ_{rxn,\,298K}{}^{1} = [\Delta H^\circ_{f,\,298K}\,(MO^-(g)) + \Delta H^\circ_{f,\,298K}\,(CO(g))] - [\Delta H^\circ_{f,\,298K}\,(M^-(g)) + \Delta H^\circ_{f,\,298K}\,(CO_2(g))]}$

[2f] $\mathbf{\Delta H^\circ_{rxn,\,0K/298K}{}^{2} = [\Delta H^\circ_{f,\,0K/298K}\,(MO^-(g)) + \Delta H^\circ_{f,\,0K}\,(CO(g))] - [\Delta H^\circ_{f,\,0K}\,(M^-(g)) + \Delta H^\circ_{f,\,0K}\,(CO_2(g))]}$

SI-B. Additional computational details

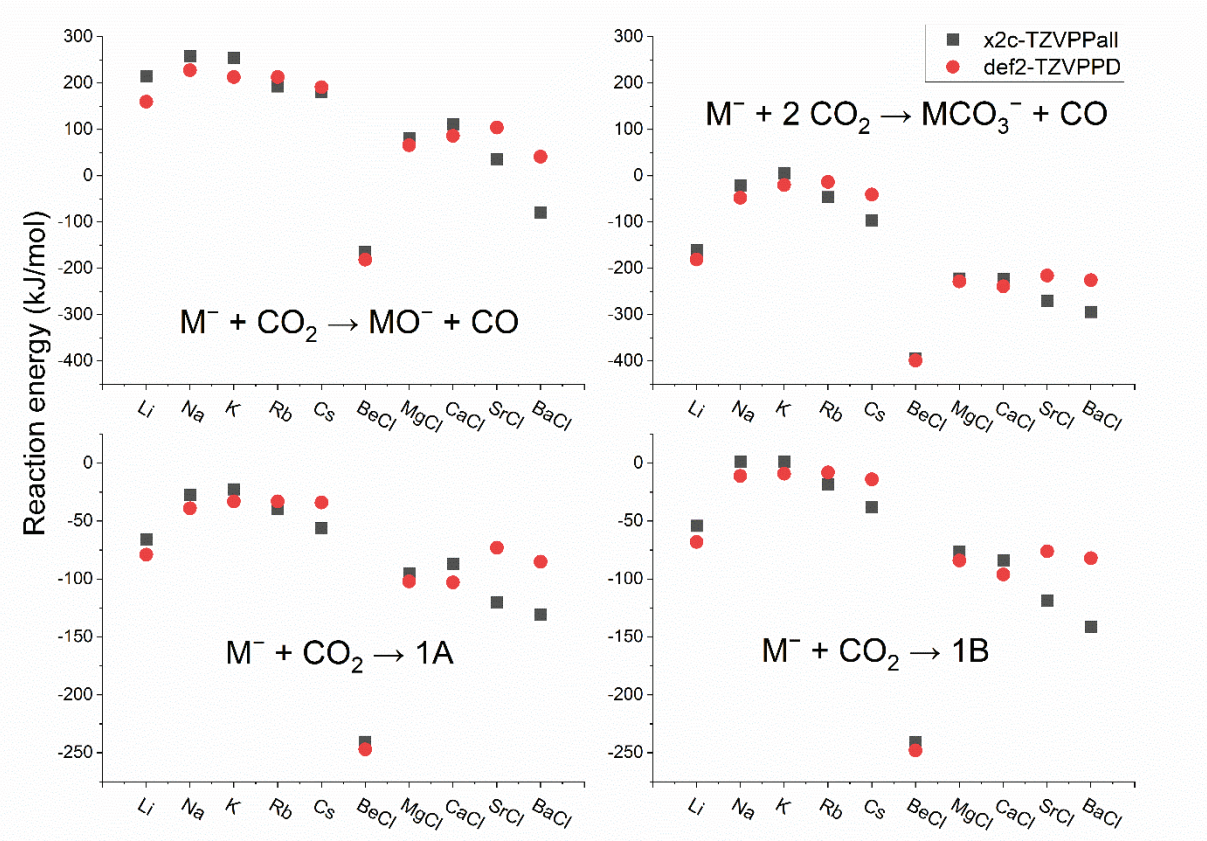

Figure SI-1. Reaction energies (in kJ/mol) for the pseudopotential [MP2/def2-TZVPPD] and all-electron [MP2/x2c-TZVPPall] treatments.

The pseudopotential [MP2/def2-TZVPPD] and the all-electron [MP2/x2c-TZVPPall] treatments for the reduction of both one and two CO_2 to CO are compared in Figure SI-1, and the corresponding numbers are presented in Table SI-1B. The all-electron treatment slightly increases the endothermicity of the reactions for M = Li – K and M = BeCl – MgCl, while decreasing it for the heavy elements M = Rb – Cs and M = SrCl – BaCl compared to the pseudopotential treatment. We assume that this is due to the lower flexibility of the all-electron basis set for the lighter elements, having fewer diffuse basis functions, whereas it is more flexible for the heavier elements, which have moderately diffuse functions and accessible inner shells. Notwithstanding, the periodic trends are qualitatively the same, with decreasing

exothermicity when going down towards the middle of the groups, followed by an increase towards the heavy elements. It is worth noting that this leads to the $M^- + CO_2 \rightarrow MO^- + CO$ reaction for M = BaCl being exothermic with the all-electron treatment, whereas it is slightly endothermic with the pseudopotential treatment.

Table SI-1B. Relative ZPVE-corrected [MP2/def2-TZVPPD] (**def2**) and [MP2/x2c-TZVPPall] (**x2c**) electronic energies in kJ/mol.

		Li	**Na**	**K**	**Rb**	**Cs**	**BeCl**	**MgCl**	**CaCl**	**SrCl**	**BaCl**
M^- + 2 CO_2	**def2**	0*	0*	0*	0*	0*	0	0	0	0	0
	x2c	0*	0*	0*	0*	0*	0	0	0	0	0
1A + CO_2	**def2**	−79*	−39*	−33*	−33*	−34*	−247	−102	−103	−73	−85
	x2c	−66	−27	−23	−40	−56	−240	−95	−87	−120	−131
1B + CO_2	**def2**	−68*	−11*	−9*	−8*	−14*	−248	−84	−96	−76	−82
	x2c	−54	1	1	−18	−38	−241	−77	−84	−118	−141
MO^- + CO	**def2**	160	228	213	213	191	−181	66	86	104	41
	x2c	214	258	254	193	181	−165	80	111	36	−79
MCO_3^- + CO	**def2**	−181	−48	−20	−14	−41	−399	−228	−239	−216	−226
	x2c	−161	−21	5	−46	−97	−394	−222	−223	−270	−294

* from reference [11]

The calculations above and those described in the main text generally follow the frozen core formalism introduced therein, that is C, O, Li, Be, Mg = [$1s^2$]; Na = [$1s^2 2s^2$]; Cl, Ca = [$1s^2 2s^2 2p^6$]; and K = [$1s^2 2s^2 2p^6 3s^2$]. For the heavier elements, Rb, Sr, Cs and Ba in the def2-TZVPPD basis set, all electrons not described by the pseudopotential are correlated, while the frozen cores for these metals in x2c-TZVPPall are adjusted to Rb, Sr = [$1s^2 2s^2 2p^6 3s^2 3p^6$], and for Cs, Ba = [$1s^2 2s^2 2p^6 3s^2 3p^6 4s^2 3d^{10} 4p^6$]. Hence, to elucidate the errors associated with the use of these limited correlation spaces, denoted **FC**, we computed the corresponding full-correlation space energies for a subset of reactions, denoted **Full**. This was done for the x2c-TZVPPall basis set due to its core-electron availability, enabling comparison between

computations involving all electrons for the heavier elements, not solely those not described by the pseudopotential.

Table SI-2B. Relative ZPVE-corrected [MP2=Full/x2c-TZVPPall] and [MP2=FC/x2c-TZVPPall] electronic energies in kJ/mol, denoted **Full** and **FC**, respectively.

		Li	**Na**	**K**	**Rb**	**Cs**	**BeCl**	**MgCl**	**CaCl**	**SrCl**	**BaCl**
M^- + 2 CO_2	**FC**	0	0	0	0	0	0	0	0	0	0
	Full	0	0	0	0	0	0	0	0	0	0
1A + CO_2	**FC**	−66	−27	−23	−40	−56	−240	−95	−87	−120	−131
	Full	−66	−26	−22	−40	−57	−240	−93	−86	−120	−134
1B + CO_2	**FC**	−54	1	1	−18	−38	−241	−77	−84	−118	−141
	Full	−55	2	1	−19	−40	−242	−75	−83	−120	−146
MO^- + CO	**FC**	214	258	254	193	181	−165	80	111	36	−79
	Full	216	261	256	195	179	−163	84	114	35	−83
MCO_3^- + CO	**FC**	−161	−21	5	−46	−97	−394	−222	−223	−270	−294
	Full	−160	−19	6	−47	−99	−393	−219	−222	−270	−298

Finally, we compared MP2 with CCSD(T) and B3LYP (using the def2-TZVPPD basis set) for a selection of reactions to elucidate trends across methods, Table SI-3B. The energies are based on geometries optimized at each respective level of theory.

Table SI-3B. Relative ZPVE-corrected [MP2/def2-TZVPPD], [B3LYP/def2-TZVPPD] and [CCSD(T)=Full/def2-TZVPPD] optimized electronic energies in kJ/mol.

		Li	**Na**	**K**	**Rb**	**Cs**	**BeCl**	**MgCl**	**CaCl**	**SrCl**	**BaCl**
M^- + $2CO_2$	**MP2**	0*	0*	0*	0*	0*	0	0	0	0	0
	B3LYP	0	0	0	0	0	0	0	0	0	0
	CCSD(T)	0	0	0	0	0	0	0	0	0	0
1A + CO_2	**MP2**	−79*	−39*	−33*	−33*	−34*	−247	−102	−103	−73	−85
	B3LYP	−87	−15	−8	−1	−1	−247	−92	−119	−88	−77
	CCSD(T)										
1B + CO_2	**MP2**	−68*	−11*	−9*	−8*	−14*	−248	−84	−96	−76	−82
	B3LYP	−79	*n.e.*	*n.e.*	*n.e.*	*n.e.*	−248	−70	−111	−83	−77

	CCSD(T)										
MO^- + CO	**MP2**	160	228	213	213	191	−181	66	86	104	41
	B3LYP	195	316	331	344	291	−167	111	84	118	77
	CCSD(T)	201	263	233	262	233	−160	93	116	134	70
MCO_3^- + CO	**MP2**	−181	−48	−20	−14	−41	−399	−228	−239	−216	−226
	B3LYP	−183	−33	−17	6	−30	−385	−196	−238	−203	−199

* from reference [11]

Table SI-4B. [MP2/x2c-TZVPPall] NBO partial charges on the reactants, intermediates and products of the $M^- + CO_2 \rightarrow MO^- + CO$ reaction.

		Li	**Na**	**K**	**Rb**	**Cs**	**BeCl**	**MgCl**	**CaCl**	**SrCl**	**BaCl**
M^-	**M**	−1.0	−1.0	−1.0	−1.0	−1.0	0.0	0.0	0.0	0.0	0.0
	Cl	*n.a.*	*n.a.*	*n.a.*	*n.a.*	*n.a.*	−1.0	−1.0	−1.0	−1.0	−1.0
1A	**M**	0.1	−0.2	−0.2	−0.2	−0.2	1.6	1.7	1.8	1.8	1.8
	C	0.7	0.8	0.9	0.9	0.8	0.4	0.4	0.4	0.4	0.4
	O	−0.9	−0.8	−0.8	−0.8	−0.8	−1.1	−1.1	−1.1	−1.1	−1.1
	Cl	*n.a.*	*n.a.*	*n.a.*	*n.a.*	*n.a.*	−0.8	−0.9	−1.0	−1.0	−1.0
1B	**M**	0.0	−0.4	−0.4	−0.3	−0.3	1.5	1.5	1.6	1.6	1.7
	C	0.8	1.0	1.0	0.9	0.9	0.3	0.3	0.3	0.3	0.2
	O_{Bridge}	−1.0	−0.9	−0.8	−0.9	−0.9	−1.1	−1.1	−1.1	−1.1	−1.1
	$O_{Terminal}$	−0.8	−0.7	−0.7	−0.7	−0.7	−0.8	−0.8	−0.8	−0.8	−0.8
	Cl	*n.a.*	*n.a.*	*n.a.*	*n.a.*	*n.a.*	−0.8	−0.9	−0.9	−1.0	−1.0
MO^-	**M**	0.8	0.3	0.3	0.4	0.6	1.6	1.7	1.7	1.7	1.5
	O	−1.8	−1.3	−1.3	−1.4	−1.6	−1.7	−1.8	−1.8	−1.7	−1.6
	Cl	*n.a.*	*n.a.*	*n.a.*	*n.a.*	*n.a.*	−0.8	−0.9	−1.0	−1.0	−1.0

SI-C. Optimized [MP2/def2-TZVPPD] geometries for MCO_2^-, MO^- and MCO_3^-

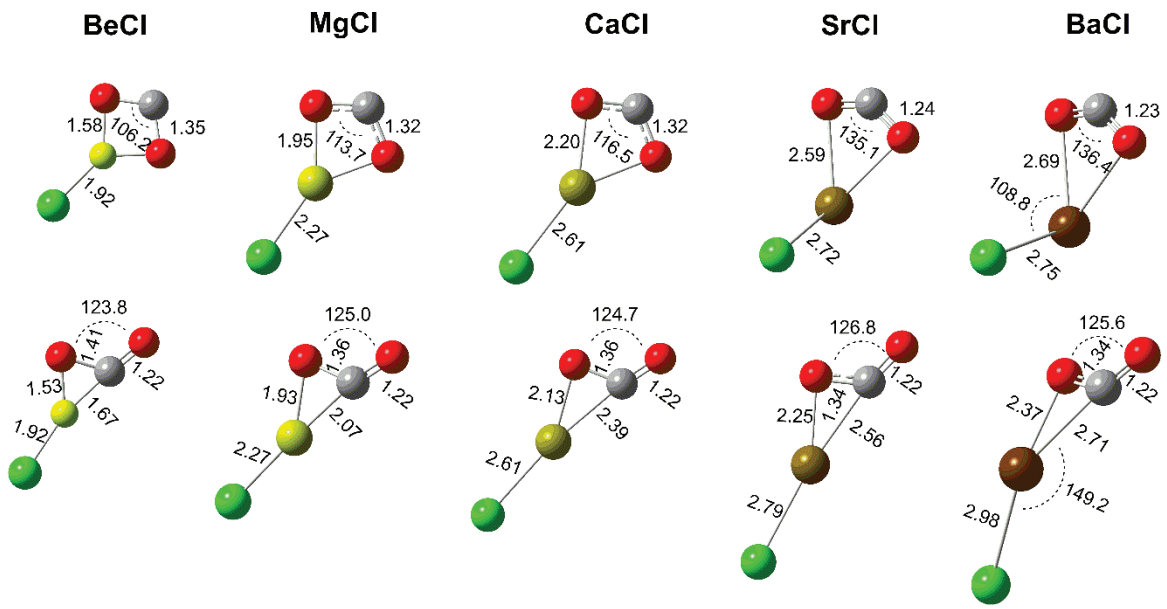

Figure SI-2. [MP2/def2-TZVPPD] optimized MCO_2^- geometries (**1A** on top, **1B** below). The corresponding alkali metal series is reported in reference 11.

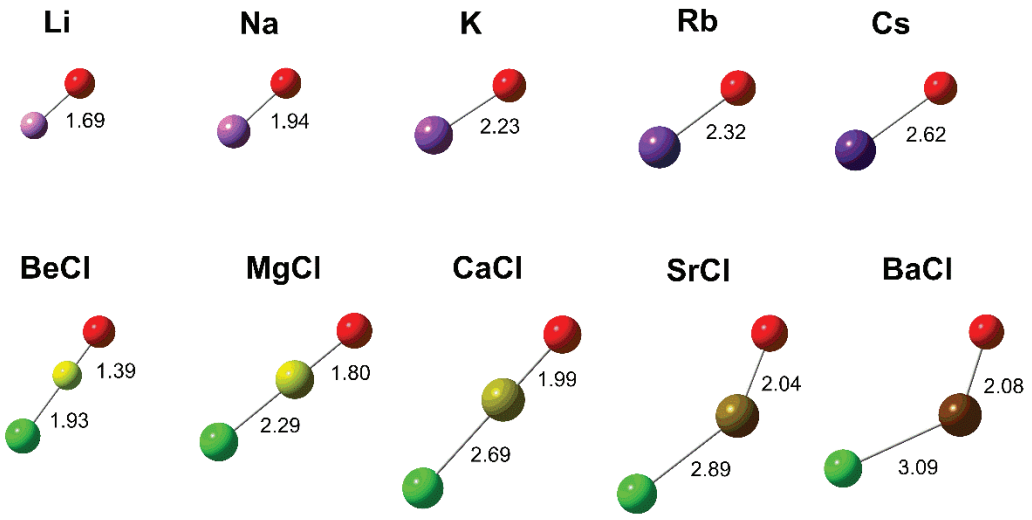

Figure SI-3. [MP2/def2-TZVPPD] optimized MO^- geometries.

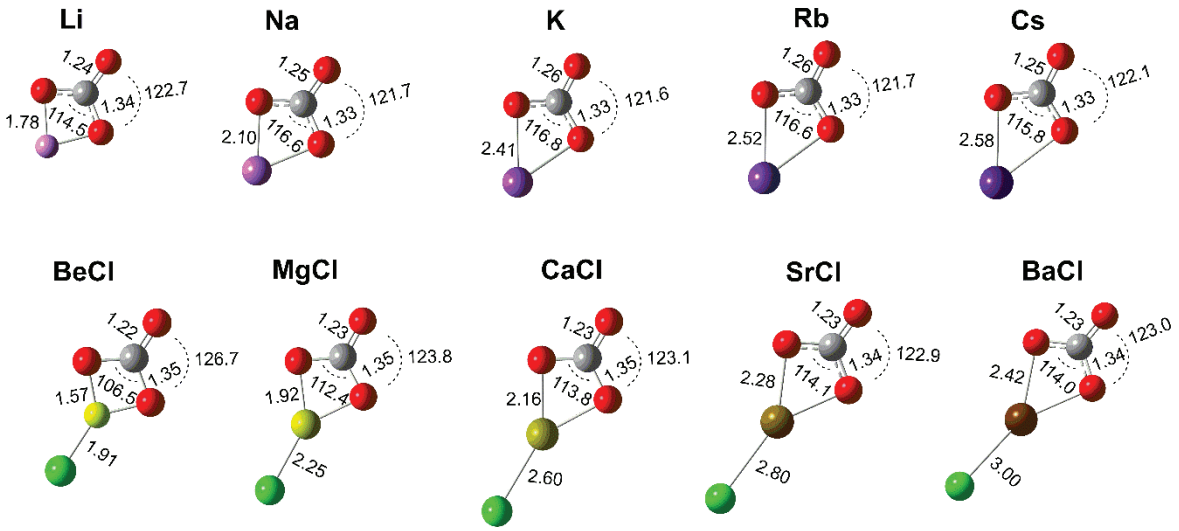

Figure SI-4. [MP2/def2-TZVPPD] optimized MCO_3^- geometries.

SI-F. References

(1) Chase, M. *NIST-JANAF Thermochemical Tables, 4th Edition*; American Institute of Physics, -1, 1998.

(2) Haeffler, G.; Hanstorp, D.; Kiyan, I.; Klinkmüller, A. E.; Ljungblad, U.; Pegg, D. J. Electron Affinity of Li: A State-Selective Measurement. *Phys. Rev. A* **1996**, *53* (6), 4127–4131.

(3) Hotop, H.; Lineberger, W. C. Binding Energies in Atomic Negative Ions: II. *J. Phys. Chem. Ref. Data* **1985**, *14* (3), 731–750.

(4) Andersson, K. T.; Sandström, J.; Kiyan, I. Yu.; Hanstorp, D.; Pegg, D. J. Measurement of the Electron Affinity of Potassium. *Phys. Rev. A* **2000**, *62* (2), 022503.

(5) Frey, P.; Breyer, F.; Holop, H. High Resolution Photodetachment from the Rubidium Negative Ion around the Rb($5p_{1/2}$) Threshold. *J. Phys. B At. Mol. Phys.* **1978**, *11* (19), L589–L594.

(6) Scheer, M.; Thøgersen, J.; Bilodeau, R. C.; Brodie, C. A.; Haugen, H. K.; Andersen, H. H.; Kristensen, P.; Andersen, T. Experimental Evidence That the $6s6p^3$ States of Cs^- Are Shape Resonances. *Phys. Rev. Lett.* **1998**, *80* (4), 684–687.

(7) Miller, T. M.; Lineberger, W. C. Electron Affinity Of MgCl. *Chem. Phys. Lett.* **1988**, *146* (5), 364–366.

(8) Lamoreaux, R. H.; Hildenbrand, D. L. High Temperature Vaporization Behavior of Oxides. I. Alkali Metal Binary Oxides. *J. Phys. Chem. Ref. Data* **1984**, *13* (1), 151–173.

(9) Mintz, B.; Chan, B.; Sullivan, M. B.; Buesgen, T.; Scott, A. P.; Kass, S. R.; Radom, L.; Wilson, A. K. Structures and Thermochemistry of the Alkali Metal Monoxide Anions, Monoxide Radicals, and Hydroxides. *J. Phys. Chem. A* **2009**, *113* (34), 9501–9510.

(10) Sarkas, H. W.; Hendricks, J. H.; Arnold, S. T.; Slager, V. L.; Bowen, K. H. Measurement of the X $^2\Sigma^+$–A $^2\Pi$ Splitting in CsO via Photoelectron Spectroscopy of CsO^-. *J. Chem. Phys.* **1994**, *100* (4), 3358–3360.

(11) Jestilä, J. S.; Denton, J. K.; Perez, E. H.; Khuu, T.; Aprà, E.; Xantheas, S. S.; Johnson, M. A.; Uggerud, E. Characterization of the Alkali Metal Oxalates ($MC_2O_4^-$) and Their Formation by CO_2 Reduction via the Alkali Metal Carbonites (MCO_2^-). *Phys. Chem. Chem. Phys.* **2020**, *22* (14), 7460–7473.

Supporting information for Paper III.

The Unimolecular Dissociation of Hydrogen Squarate ($HC_4O_4^-$) and the Squarate Radical Anion ($C_4O_4^{\bullet-}$) in the Gas Phase and Relationship to CO Cyclooligomerization.

Joakim S. Jestilä and Einar Uggerud*.

Supporting Information

Table of Contents

SI-A. Metastable fragmentation

$$M^* = M_p \left[\frac{1 + \left(\frac{M_f}{M_p}\right) r}{(1 + r)} \right]^2$$

In the above expression[1], r is an instrumental value describing the ratio between time spent in the reflectron and the field-free region for a given ion. The r-value is calibrated by assigning a metastable fragment signal to a given precursor and focused fragment. Unfortunately, the above equation only covers fragmentation in the first field-free region of the flight tube; thereby we wish to expand upon it (yet we do not consider fragmentation in the acceleration region). Depending on the kinetics, fragmentation may occur anywhere inside the reflectron. The peak position will vary depending on the location of the fragmentation, as the fragment ion will not penetrate to the same depth in the reflectron as the stable ions due to loss of kinetic energy. However, the region where stable ions are slowed down and turned around should be the most likely place to expect fragmentation within the mirror. A metastable ion dissociating at the turning point penetrates the mirror to the same depth as a stable ion, given equal kinetic energies, and the following expression describes its mass assignment

$$M_{tp}^* = M_p \left[\frac{1 + \sqrt{\frac{M_f}{M_p}}}{2} \right]^2$$

We have used this expression along with the Harvey equation to calculate regions where unfocused fragments can be expected (Figure S1 & S2).

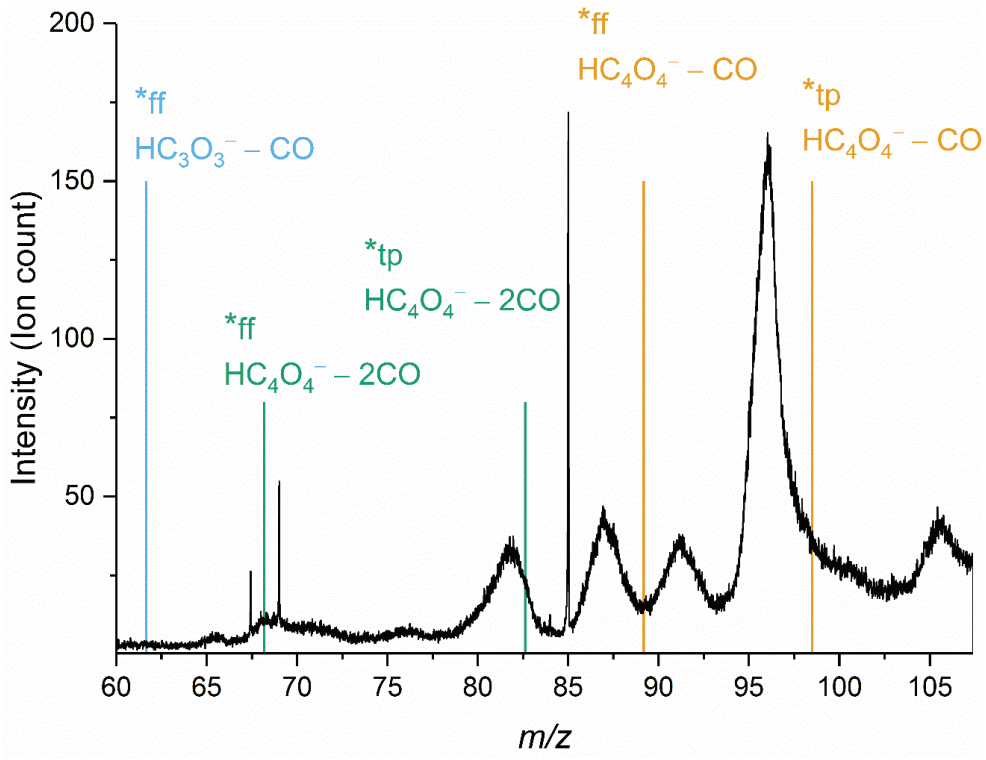

Figure S1. Metastable peaks between *m/z* 60 – 106 from the MSMS of *m/z* 113, averaged over collision energies between 300 – 1400 kJ/mol in the center of mass frame. The intensity of *m/z* 113 is $5.2 \cdot 10^5$ counts. Location of fragmentation within the TOF is indicated by subscripts ff and tp, denoting (1st) field-free region and turning point, respectively. The calibrated instrumental r-value is r = 0.82.

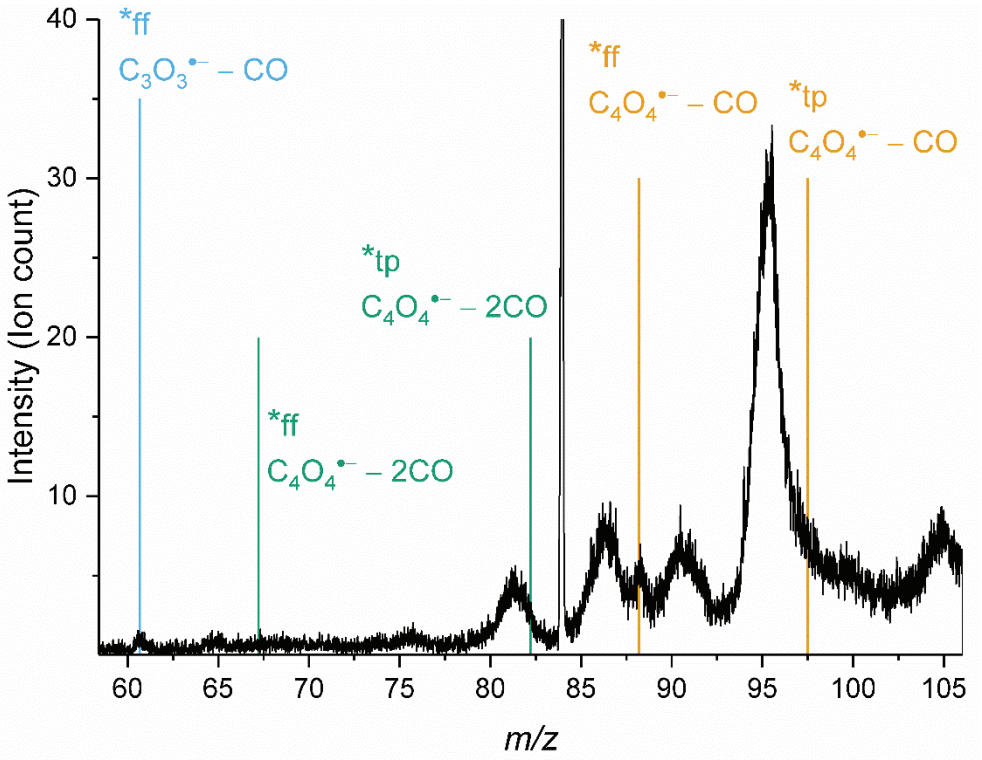

Figure S2. Metastable ion fragmentation from the MSMS of *m/z* 112 averaged over collision energies from 130 kJ/mol to 1015 kJ/mol in the center of mass frame. Intensity of *m/z* 112 is $1.2 \cdot 10^5$ counts, while *m/z* 84 amounts to 944 counts. Location of fragmentation within the TOF is indicated by subscripts ff and tp, denoting (1st) field-free region and turning point, respectively. The calibrated instrumental r-value is r = 0.82.

SI-B. G4 (0 K) Potential energy diagram for the dissociation of HSq^-

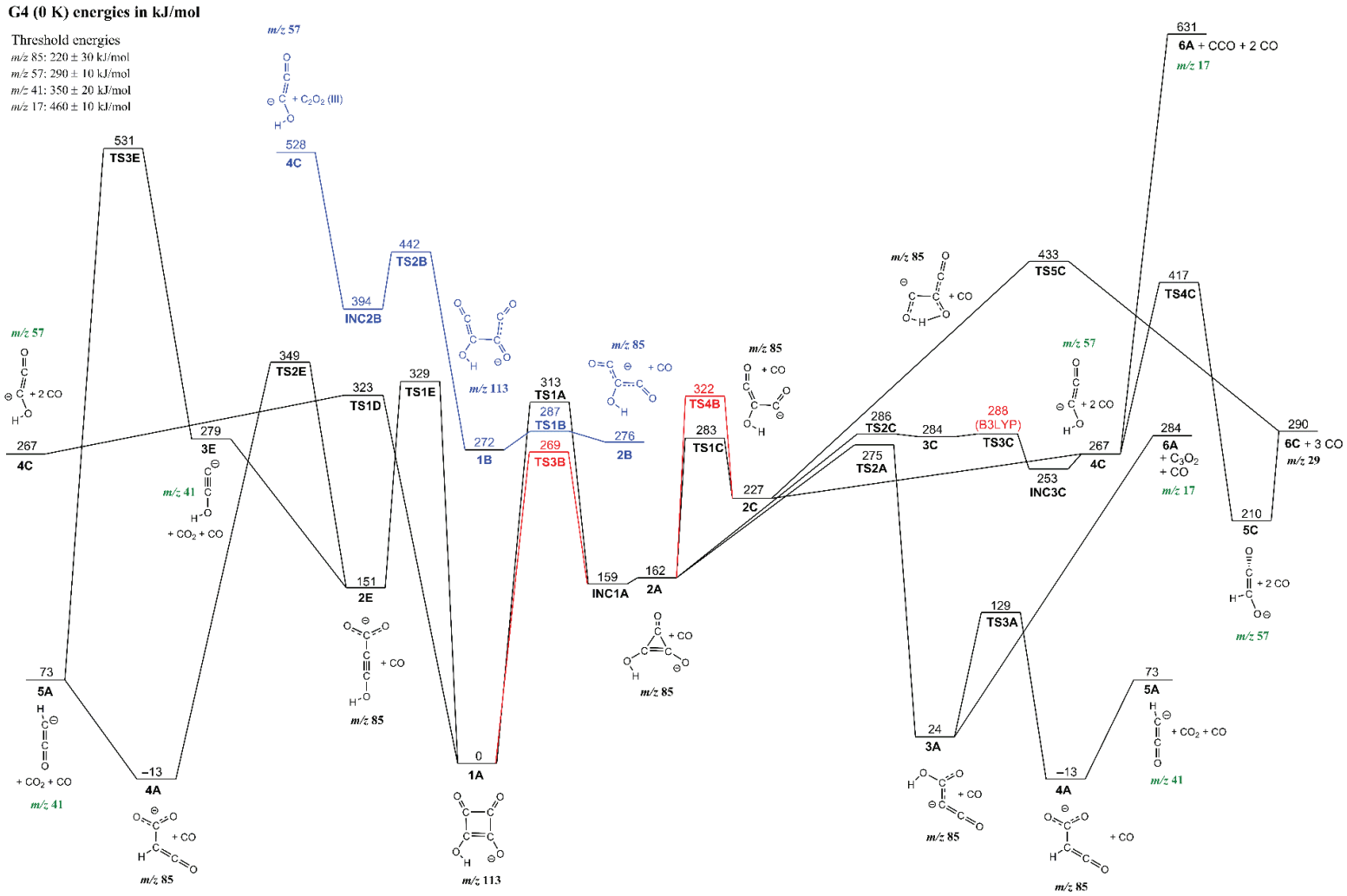

Figure S3. G4 (0 K) potential energy diagram for the fragmentation of hydrogen squarate (*m/z* 113) in kJ/mol. The blue part corresponds to the triplet surface. CASSCF(4,4)/6-311+G(d,p) energies in red.

SI-C. B3LYP and CASSCF Optimized Geometries in Cartesian Coordinates and G4 (0 K) Energies

HSq^{-}

1A

Center Number	Atomic Number	Atomic Type	Coordinates (Angstroms) X	Y	Z
1	8	0	-4.824858	-8.285855	-1.292075
2	8	0	-7.254785	-9.961281	0.321348
3	8	0	-8.436316	-10.978810	-2.329373
4	1	0	-8.773747	-11.172632	-1.439868
5	8	0	-6.108808	-9.388723	-4.101105
6	6	0	-6.870586	-9.749455	-0.835629
7	6	0	-6.378748	-9.514351	-2.911430
8	6	0	-5.769368	-8.991292	-1.582798
9	6	0	-7.362885	-10.183200	-2.100468

G4(0 K)= -453.801659

1B

Center Number	Atomic Number	Atomic Type	Coordinates (Angstroms) X	Y	Z
1	8	0	-4.748537	-8.219187	-0.825076
2	8	0	-7.344111	-10.049726	0.142815
3	8	0	-8.431123	-10.959233	-2.221976
4	1	0	-8.580161	-11.017353	-1.256493
5	8	0	-6.290106	-9.522580	-4.439529
6	6	0	-6.804092	-9.714764	-0.948361
7	6	0	-6.609088	-9.694473	-3.292867
8	6	0	-5.666135	-8.902751	-1.190954
9	6	0	-7.306748	-10.145532	-2.238957

G4(0 K)= -453.697943

2A

Center Number	Atomic Number	Atomic Type	Coordinates (Angstroms) X	Y	Z
1	8	0	-5.143697	-8.541960	-1.895078
2	8	0	-7.202102	-9.915768	0.832359
3	8	0	-7.999322	-10.670410	-2.665563
4	1	0	-8.673270	-11.139371	-2.160571
5	6	0	-6.927731	-9.773351	-0.364866
6	6	0	-6.090333	-9.214751	-1.480324
7	6	0	-7.198362	-10.037364	-1.712577

G4(0 K)= -340.450361

2B

Center Number	Atomic Number	Atomic Type	Coordinates (Angstroms) X	Y	Z
1	8	0	-7.549554	-10.335333	0.192986
2	8	0	-8.520854	-10.827887	-2.435774
3	1	0	-8.854574	-11.028395	-1.551795
4	8	0	-6.564688	-9.707161	-4.411416
5	6	0	-6.942575	-9.980673	-0.814414
6	6	0	-6.486547	-9.685394	-3.194427
7	6	0	-7.286577	-10.147859	-2.154943

G4(0 K)= -340.407164

2C

Center Number	Atomic Number	Atomic Type	Coordinates (Angstroms) X	Y	Z
1	8	0	-7.818419	-8.372243	-0.934208
2	8	0	-6.313781	-11.571368	-1.425323
3	1	0	-8.469699	-9.104688	-1.026455
4	8	0	-4.220570	-8.706529	-1.055333
5	6	0	-7.045428	-10.624061	-1.274106
6	6	0	-5.422348	-8.733736	-1.034866
7	6	0	-6.656731	-9.135026	-1.067602

G4(0 K)= -340.425950

2E

Center Number	Atomic Number	Atomic Type	Coordinates (Angstroms) X	Y	Z
1	8	0	1.966846	1.452670	-0.153974
2	8	0	-1.805349	-1.356664	-0.155680
3	1	0	-1.894855	-1.348077	0.804965
4	8	0	1.631102	1.029880	-2.360418
5	6	0	0.194669	0.083775	-0.781357
6	6	0	1.394965	0.949514	-1.140842
7	6	0	-0.754427	-0.598874	-0.472952

G4(0 K)= -340.454899

3A

Center Number	Atomic Number	Atomic Type	Coordinates (Angstroms) X	Y	Z
1	8	0	-4.870072	-8.109224	-2.200027
2	8	0	-7.434887	-10.472094	0.511573
3	8	0	-8.538626	-11.062338	-1.334063
4	1	0	-8.416293	-10.836076	-2.265028
5	6	0	-7.502332	-10.352343	-0.701390
6	6	0	-5.755346	-8.842870	-1.842373
7	6	0	-6.717761	-9.618030	-1.611813

G4(0 K)= -340.502996

3C

Center Number	Atomic Number	Atomic Type	Coordinates (Angstroms) X	Y	Z
1	8	0	1.982155	1.444370	-0.086380
2	8	0	-0.617459	-0.436582	1.338038
3	8	0	-1.637746	-1.202140	-0.716517
4	1	0	-1.570704	-1.142485	0.327812
5	6	0	-0.039732	-0.026524	0.228701
6	6	0	1.033108	0.753838	0.061524
7	6	0	-0.609099	-0.455638	-1.098236

G4(0 K)= -340.404215

3E

Center Number	Atomic Number	Atomic Type	Coordinates (Angstroms) X	Y	Z
1	8	0	-6.925548	-9.691419	0.715764
2	6	0	-7.091158	-9.921356	-0.626933
3	6	0	-7.262783	-10.130104	-1.841376
4	1	0	-5.975660	-9.633035	0.865859

G4(0 K)= -151.870628

4A

Center Number	Atomic Number	Atomic Type	Coordinates (Angstroms) X	Y	Z
1	8	0	1.775957	1.312817	-0.095464
2	8	0	-1.761109	-1.417229	-1.396306
3	1	0	-0.165447	-0.051752	1.002946
4	8	0	0.987245	0.577530	-2.095261
5	6	0	-0.125746	-0.101968	-0.076187
6	6	0	1.022310	0.694929	-0.861160
7	6	0	-1.000260	-0.802104	-0.738826

G4(0 K)= -340.517215

4C

Center Number	Atomic Number	Atomic Type	Coordinates (Angstroms) X	Y	Z
1	8	0	-6.878450	-9.682154	0.601961
2	8	0	-8.182210	-10.805755	-2.626077
3	1	0	-7.859910	-10.654315	-3.515308
4	6	0	-7.163069	-9.961440	-0.557124
5	6	0	-7.241679	-10.108715	-1.814751

G4(0 K)= -227.121067

5A

Center Number	Atomic Number	Atomic Type	Coordinates (Angstroms) X	Y	Z
1	8	0	-7.018786	-9.823369	0.579079
2	6	0	-7.073065	-9.898844	-0.638842
3	6	0	-7.028033	-9.843028	-1.894369
4	1	0	-7.453880	-10.408926	-2.700036

G4(0 K)= -151.949354

5C

Center Number	Atomic Number	Atomic Type	Coordinates (Angstroms) X	Y	Z
1	8	0	-6.858110	-9.843986	0.600987
2	8	0	-8.147557	-10.803985	-2.522286
3	6	0	-7.255405	-9.702760	-0.541328
4	6	0	-7.249655	-10.219007	-1.847664
5	1	0	-6.437669	-9.619661	-2.379065

G4(0 K)= -227.142886

6A

Center Number	Atomic Number	Atomic Type	Coordinates (Angstroms) X	Y	Z
1	8	0	-3.145243	-0.541712	-1.347132
2	1	0	-4.041141	-0.151622	-1.320815

G4(0 K)= -75.778356

6C

Center Number	Atomic Number	Atomic Type	Coordinates (Angstroms) X	Y	Z
1	8	0	-8.037531	-11.109940	-2.858216
2	6	0	-7.298093	-10.261322	-2.360033
3	1	0	-6.639534	-9.653697	-3.333056

G4(0 K)= -113.822848

TS1A

Center Number	Atomic Number	Atomic Type	Coordinates (Angstroms) X	Y	Z
1	8	0	-4.898058	-8.340111	-1.068334
2	8	0	-7.447528	-10.108183	0.380537
3	8	0	-8.241526	-10.840284	-2.552566
4	1	0	-8.104149	-10.793988	-3.545605
5	8	0	-6.991813	-10.041761	-4.542736
6	6	0	-6.988121	-9.836721	-0.761703
7	6	0	-6.308677	-9.502129	-3.704041
8	6	0	-5.840595	-9.018934	-1.003149
9	6	0	-7.241661	-10.092775	-2.114518

G4(0 K)= -453.682520

TS1B

Center Number	Atomic Number	Atomic Type	Coordinates (Angstroms) X	Y	Z
1	8	0	-4.876299	-7.730985	-0.969404
2	8	0	-7.484933	-10.298589	0.218781
3	8	0	-8.543563	-10.831683	-2.446112
4	1	0	-8.887744	-11.054171	-1.572381
5	8	0	-6.526232	-9.685760	-4.395943
6	6	0	-6.952156	-9.984065	-0.830322
7	6	0	-6.499569	-9.695194	-3.184555
8	6	0	-4.803546	-8.866351	-1.157000
9	6	0	-7.311171	-10.163240	-2.159251

G4(0 K)= -453.692229

TS1C

Center Number	Atomic Number	Atomic Type	Coordinates (Angstroms) X	Y	Z
1	8	0	-7.892890	-8.335293	-0.927386
2	8	0	-6.442398	-11.719410	-1.443990
3	1	0	-8.614170	-8.981695	-1.005837
4	8	0	-4.235126	-8.596217	-1.039180
5	6	0	-6.659747	-10.536637	-1.269312
6	6	0	-5.416682	-8.865259	-1.053932
7	6	0	-6.685964	-9.213140	-1.078255

G4(0 K)= -340.404510

TS1D

Center Number	Atomic Number	Atomic Type	Coordinates (Angstroms) X	Y	Z
1	8	0	-3.921447	-7.656377	-1.539064
2	8	0	-7.545984	-10.102582	0.461375
3	8	0	-8.132502	-10.806947	-2.950776
4	1	0	-8.812180	-11.255905	-2.440620
5	8	0	-6.213895	-9.513546	-4.035823
6	6	0	-7.474643	-10.149606	-0.732089
7	6	0	-6.088016	-9.325589	-2.856706
8	6	0	-4.812217	-8.262975	-1.120053
9	6	0	-7.311323	-10.138227	-2.019783

G4(0 K)= -453.678634

TS1E

Center Number	Atomic Number	Atomic Type	Coordinates (Angstroms) X	Y	Z
1	8	0	-4.397056	-7.991951	-2.147539
2	8	0	-8.245240	-10.676270	0.169199
3	8	0	-8.279770	-10.889552	-2.225363
4	1	0	-8.664614	-11.102162	-1.280865
5	8	0	-5.946758	-9.280709	-3.867738
6	6	0	-7.265364	-9.975190	-0.195989
7	6	0	-6.375062	-9.497804	-2.566678
8	6	0	-5.312127	-8.690048	-2.360085
9	6	0	-7.294109	-10.121916	-1.796342

G4(0 K)= -453.676220

TS2A

Center Number	Atomic Number	Atomic Type	Coordinates (Angstroms) X	Y	Z
1	8	0	-5.113316	-8.300757	-2.339229
2	8	0	-7.464029	-10.207110	0.956959
3	8	0	-8.082373	-11.293169	-2.277850
4	1	0	-8.752912	-10.630462	-2.489895
5	6	0	-7.130387	-10.019944	-0.155383
6	6	0	-5.882553	-8.985532	-1.732898
7	6	0	-6.809249	-9.856001	-1.408325

G4(0 K)= -340.407384

TS2B

Center Number	Atomic Number	Atomic Type	Coordinates (Angstroms) X	Y	Z
1	8	0	-4.717998	-8.094483	-0.757604
2	8	0	-7.538262	-10.305596	0.019982
3	8	0	-8.494694	-10.764865	-2.322548
4	1	0	-8.302781	-10.829976	-1.348011
5	8	0	-6.172396	-9.506167	-4.855071
6	6	0	-6.664441	-9.599735	-0.498193
7	6	0	-6.859720	-9.880454	-3.937275
8	6	0	-5.629446	-8.825441	-0.451799
9	6	0	-7.330014	-10.406676	-2.871409

G4(0 K)= -453.633231

TS2C

Center Number	Atomic Number	Atomic Type	Coordinates (Angstroms) X	Y	Z
1	8	0	-4.797683	-8.278044	-1.690708
2	8	0	-7.335459	-10.075354	0.092391
3	8	0	-8.270959	-10.838132	-2.328404
4	1	0	-8.450427	-10.937774	-1.359218
5	6	0	-6.802569	-9.721999	-1.019981
6	6	0	-5.727730	-8.948867	-1.409750
7	6	0	-7.168253	-10.033105	-2.363557

G4(0 K)= -340.403404

TS2E

Center Number	Atomic Number	Atomic Type	Coordinates (Angstroms) X	Y	Z
1	8	0	1.763811	1.347147	0.060389
2	8	0	-1.951146	-1.490431	-0.345020
3	1	0	-1.228638	-0.852418	0.582085
4	8	0	1.638383	1.024474	-2.187129
5	6	0	0.094302	-0.000803	-0.837695
6	6	0	1.298486	0.889518	-0.996607
7	6	0	-0.882246	-0.705263	-0.536277

G4(0 K)= -340.379185

TS3A

Center Number	Atomic Number	Atomic Type	Coordinates (Angstroms) X	Y	Z
1	8	0	-4.916502	-8.144164	-2.206133
2	8	0	-7.427144	-10.477051	0.588767
3	8	0	-8.472609	-11.006194	-1.370679
4	1	0	-7.751004	-10.322205	-2.268943
5	6	0	-7.556506	-10.405517	-0.621095
6	6	0	-5.801854	-8.873526	-1.879323
7	6	0	-6.782362	-9.661308	-1.658354

G4(0 K)= -340.463016

TS3B

Center Number	Atomic Number	Atomic Type	Coordinates (Angstroms) X	Y	Z
1	8	0	-4.900287	-8.334417	-0.934966
2	8	0	-7.423096	-10.094755	0.303499
3	8	0	-8.268546	-10.856730	-2.496600
4	1	0	-8.251219	-10.895085	-3.447793
5	8	0	-6.927089	-9.999100	-4.620154
6	6	0	-6.956905	-9.817927	-0.831061
7	6	0	-6.286516	-9.490052	-3.774546
8	6	0	-5.811484	-8.995010	-0.950873
9	6	0	-7.236986	-10.091809	-2.159620

CASSCF(4,4) (0 K) = -451.504406

TS3C

Center Number	Atomic Number	Atomic Type	Coordinates (Angstroms) X	Y	Z
1	8	0	1.982972	1.448263	-0.042532
2	8	0	-0.660884	-0.441698	1.273075
3	8	0	-1.638238	-1.220652	-0.705975
4	1	0	-1.507151	-1.088520	0.409662
5	6	0	-0.031897	-0.017742	0.169877
6	6	0	1.034817	0.759337	0.086643
7	6	0	-0.639094	-0.504149	-1.135807

B3LYP/aug-cc-pVTZ (0 K) = -340.626574

TS3E

Center Number	Atomic Number	Atomic Type	Coordinates (Angstroms) X	Y	Z
1	8	0	-6.957574	-9.696703	0.690917
2	6	0	-7.834411	-9.929799	-0.521140
3	6	0	-6.594698	-9.971692	-1.032899
4	1	0	-5.868467	-9.777720	-0.023564

G4(0 K)= -151.774499

TS4B

Center Number	Atomic Number	Atomic Type	Coordinates (Angstroms) X	Y	Z
1	8	0	-7.863087	-8.370855	-0.933125
2	8	0	-6.390155	-11.672576	-1.438308
3	1	0	-8.603067	-8.955124	-1.002221
4	8	0	-4.276159	-8.620219	-1.041797
5	6	0	-6.665174	-10.515492	-1.266161
6	6	0	-5.437297	-8.922154	-1.061704
7	6	0	-6.712037	-9.191230	-1.074576

CASSCF(4,4) (0 K) = -338.751114

TS4C

Center Number	Atomic Number	Atomic Type	Coordinates (Angstroms) X	Y	Z
1	8	0	-6.858110	-9.843986	0.600987
2	8	0	-8.147557	-10.803985	-2.522286
3	6	0	-7.255405	-9.702760	-0.541328
4	6	0	-7.249655	-10.219007	-1.847664
5	1	0	-6.437669	-9.619661	-2.379065

G4(0 K)= -227.142886

TS5C

Center Number	Atomic Number	Atomic Type	Coordinates (Angstroms) X	Y	Z
1	8	0	-8.141034	-8.322794	-1.389519
2	8	0	-5.974415	-11.316380	-1.492418
3	1	0	-7.682617	-8.920053	-0.262817
4	8	0	-4.596544	-9.289230	-0.978423
5	6	0	-6.926720	-10.591176	-1.501477
6	6	0	-5.616198	-8.663108	-1.012617
7	6	0	-7.009446	-9.144907	-1.180622

G4(0 K)= -340.347153

Sq•⁻

1F ($^2A_{2u}$)

Center Number	Atomic Number	Atomic Type	Coordinates (Angstroms) X	Y	Z
1	8	0	-4.836599	-8.292309	-1.288498
2	8	0	-7.136260	-9.871127	0.378689
3	8	0	-8.405723	-10.963051	-2.406412
4	8	0	-6.106062	-9.384233	-4.073599
5	6	0	-6.861927	-9.741471	-0.806917
6	6	0	-6.380395	-9.513888	-2.887993
7	6	0	-5.787026	-9.003504	-1.586189
8	6	0	-7.455296	-10.251855	-2.108721

G4(0 K)= -453.198205

1F ($^2B_{2g}$)

Center Number	Atomic Number	Atomic Type	Coordinates (Angstroms) X	Y	Z
1	8	0	-4.845797	-8.299171	-1.291379
2	8	0	-7.133604	-9.869881	0.367228
3	8	0	-8.396543	-10.956160	-2.403533
4	8	0	-6.108714	-9.385494	-4.062138
5	6	0	-6.860883	-9.740991	-0.811393
6	6	0	-6.381420	-9.514393	-2.883512
7	6	0	-5.790617	-9.006187	-1.587315
8	6	0	-7.451705	-10.249166	-2.107597

G4(0 K)= -453.195262

1H

Center Number	Atomic Number	Atomic Type	Coordinates (Angstroms) X	Y	Z
1	8	0	-7.063060	-7.449637	-0.338746
2	8	0	-5.047257	-10.124699	-0.462897
3	8	0	-7.593987	-8.805444	-2.223806
4	8	0	-6.815179	-11.757355	-4.057403
5	6	0	-5.983518	-9.618366	-1.090385
6	6	0	-6.837767	-10.874360	-3.261999
7	6	0	-6.839106	-8.439666	-0.997391
8	6	0	-6.789709	-9.951813	-2.346915

G4(0 K)= -453.137096

2F

Center Number	Atomic Number	Atomic Type	Coordinates (Angstroms) X	Y	Z
1	8	0	-5.137994	-8.536849	-1.848121
2	8	0	-7.165390	-9.890881	0.826099
3	8	0	-7.974849	-10.647158	-2.618908
4	6	0	-6.925781	-9.773283	-0.377766
5	6	0	-6.094964	-9.218403	-1.473654
6	6	0	-7.257502	-10.083193	-1.789517

G4(0 K)= -339.850095

2H

Center Number	Atomic Number	Atomic Type	Coordinates (Angstroms) X	Y	Z
1	8	0	-2.169635	3.339330	-0.715753
2	8	0	-1.000794	1.421838	-0.730551
3	8	0	0.758832	-1.655586	-0.656796
4	6	0	0.016304	-0.713739	-0.508608
5	6	0	-1.954751	2.218096	-0.332088
6	6	0	-0.898239	0.113523	-0.158829

G4(0 K)= -339.790512

2G

Center Number	Atomic Number	Atomic Type	Coordinates (Angstroms) X	Y	Z
1	8	0	1.520029	1.077533	-0.681228
2	8	0	0.141968	0.198983	1.968703
3	8	0	-1.397552	-1.073429	-1.082725
4	6	0	-0.363396	-0.218785	0.965124
5	6	0	0.560854	0.370457	-0.811999
6	6	0	-0.541210	-0.415679	-0.419306

G4(0 K)= -339.821266

3F

Center Number	Atomic Number	Atomic Type	Coordinates (Angstroms) X	Y	Z
1	8	0	-6.791333	-9.680271	0.575923
2	8	0	-7.969550	-10.620709	-2.812225
3	6	0	-7.235273	-9.850913	-0.568920
4	6	0	-7.525610	-10.450067	-1.667382

G4(0 K)= -226.543367

3G

Center Number	Atomic Number	Atomic Type	Coordinates (Angstroms) X	Y	Z
1	8	0	1.410900	0.971535	-1.262206
2	8	0	-1.795086	-1.235824	1.481314
3	8	0	-2.108334	-1.582790	-0.724372
4	6	0	-1.513667	-1.092667	0.286289
5	6	0	0.520667	0.345430	-0.749477
6	6	0	-0.394373	-0.295609	-0.175917

G4(0 K)= -339.866470

4F

Center Number	Atomic Number	Atomic Type	Coordinates (Angstroms) X	Y	Z
1	8	0	-1.754056	0.161929	-0.002120
2	6	0	-2.986125	0.161929	-0.002120

G4(0 K)= -113.234172

4G

Center Number	Atomic Number	Atomic Type	Coordinates (Angstroms) X	Y	Z
1	8	0	-6.224276	-9.870362	0.950064
2	6	0	-6.890169	-9.732099	-0.066306
3	6	0	-7.596822	-9.585376	-1.144921

G4(0 K)= -151.290021

5F

Center Number	Atomic Number	Atomic Type	Coordinates (Angstroms) X	Y	Z
1	8	0	-1.804635	0.161929	-0.002120
2	6	0	-2.935546	0.161929	-0.002120

G4(0 K)= -113.289425

TS1F

Center Number	Atomic Number	Atomic Type	Coordinates (Angstroms) X	Y	Z
1	8	0	-4.932624	-8.343532	-0.942065
2	8	0	-7.459767	-10.177615	0.376437
3	8	0	-8.198901	-10.835596	-2.703047
4	8	0	-6.428830	-9.595233	-4.922717
5	6	0	-6.980023	-9.861009	-0.762826
6	6	0	-5.897404	-9.170047	-3.999740
7	6	0	-5.875882	-9.046358	-0.985431
8	6	0	-7.377354	-10.202988	-2.098569

G4(0 K)= -453.111173

TS1H

Center Number	Atomic Number	Atomic Type	Coordinates (Angstroms) X	Y	Z
1	8	0	-6.173865	-7.253077	-0.712469
2	8	0	-5.990383	-10.732326	-0.347353
3	8	0	-8.460862	-9.356266	-2.451468
4	8	0	-5.831719	-11.169722	-3.890541
5	6	0	-6.470953	-9.768068	-1.007336
6	6	0	-6.491245	-10.434893	-3.237665
7	6	0	-6.223280	-8.425802	-0.848476
8	6	0	-7.326976	-9.881287	-2.284333

G4(0 K)= -453.098764

TS1G

Center Number	Atomic Number	Atomic Type	Coordinates (Angstroms) X	Y	Z
1	8	0	-5.106434	-8.539609	-2.368061
2	8	0	-6.585388	-9.482492	0.475758
3	8	0	-8.034048	-10.691678	-2.641338
4	6	0	-6.970998	-9.816845	-0.612222
5	6	0	-6.077196	-9.247016	-2.330867
6	6	0	-7.176257	-10.032836	-1.976790

G4(0 K)= -339.817538

TS2F

Center Number	Atomic Number	Atomic Type	Coordinates (Angstroms) X	Y	Z
1	8	0	1.520029	1.077533	-0.681228
2	8	0	0.141968	0.198983	1.968703
3	8	0	-1.397552	-1.073429	-1.082725
4	6	0	-0.363396	-0.218785	0.965124
5	6	0	0.560854	0.370457	-0.811999
6	6	0	-0.541210	-0.415679	-0.419306

G4(0 K)= -339.821266

TS2G

Center Number	Atomic Number	Atomic Type	Coordinates (Angstroms) X	Y	Z
1	8	0	1.444712	0.936347	-0.591543
2	8	0	-1.644386	-1.240683	1.389569
3	8	0	-1.657480	-1.053031	-1.323839
4	6	0	-1.169155	-0.854431	0.375039
5	6	0	0.513768	0.363632	-1.147081
6	6	0	-0.567495	-0.379630	-0.712908

G4(0 K)= -339.796875

TS2H

Center Number	Atomic Number	Atomic Type	Coordinates (Angstroms) X	Y	Z
1	8	0	-2.617778	2.947743	-0.689840
2	8	0	-0.897311	1.454009	-0.867929
3	8	0	-1.395175	-1.756485	0.806493
4	6	0	-1.241025	-0.617286	0.437550
5	6	0	-1.712999	2.305345	-0.213846
6	6	0	-0.995097	0.635980	0.324193

G4(0 K)= -339.775180

TS3H

Center Number	Atomic Number	Atomic Type	Coordinates (Angstroms) X	Y	Z
1	8	0	-1.689985	3.376423	-0.649316
2	8	0	-1.694284	1.108208	-1.015884
3	8	0	1.008634	-0.913267	-0.767208
4	6	0	-0.083465	-0.618458	-0.371006
5	6	0	-1.517426	2.190125	-0.464487
6	6	0	-1.271759	-0.419570	0.165275

G4(0 K)= -339.750345

SI-D. Potential energy scans for the two lowest radical anion and the lowest dianion electronic states and symmetry analysis

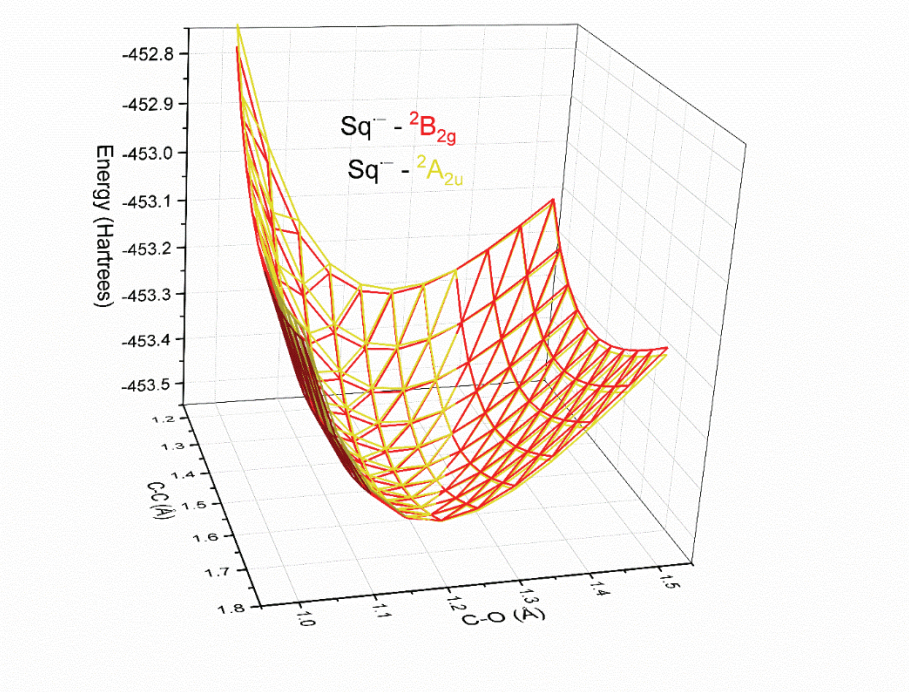

Figure S4. B3LYP/aug-cc-pVTZ potential energy scan of the $^2B_{2g}$ and $^2A_{2u}$ electronic states of the squarate radical anion at different C-C and C-O bond lengths.

In order to elucidate the relative energies of the two lowest electronic states of the radical anion, $^2B_{2g}$ and $^2A_{2u}$, we scanned the energy while varying the C-O and C-C bond lengths and ensuring that the SCF procedure retained orbital symmetry throughout the scans (Figure S4). Scanning all four C-O and C-C bonds simultaneously correspond to the totally symmetric a_{1g} vibrational mode (Figure S5). According to B3LYP, crossing between the two states following this motion is possible close to the equilibrium geometries.

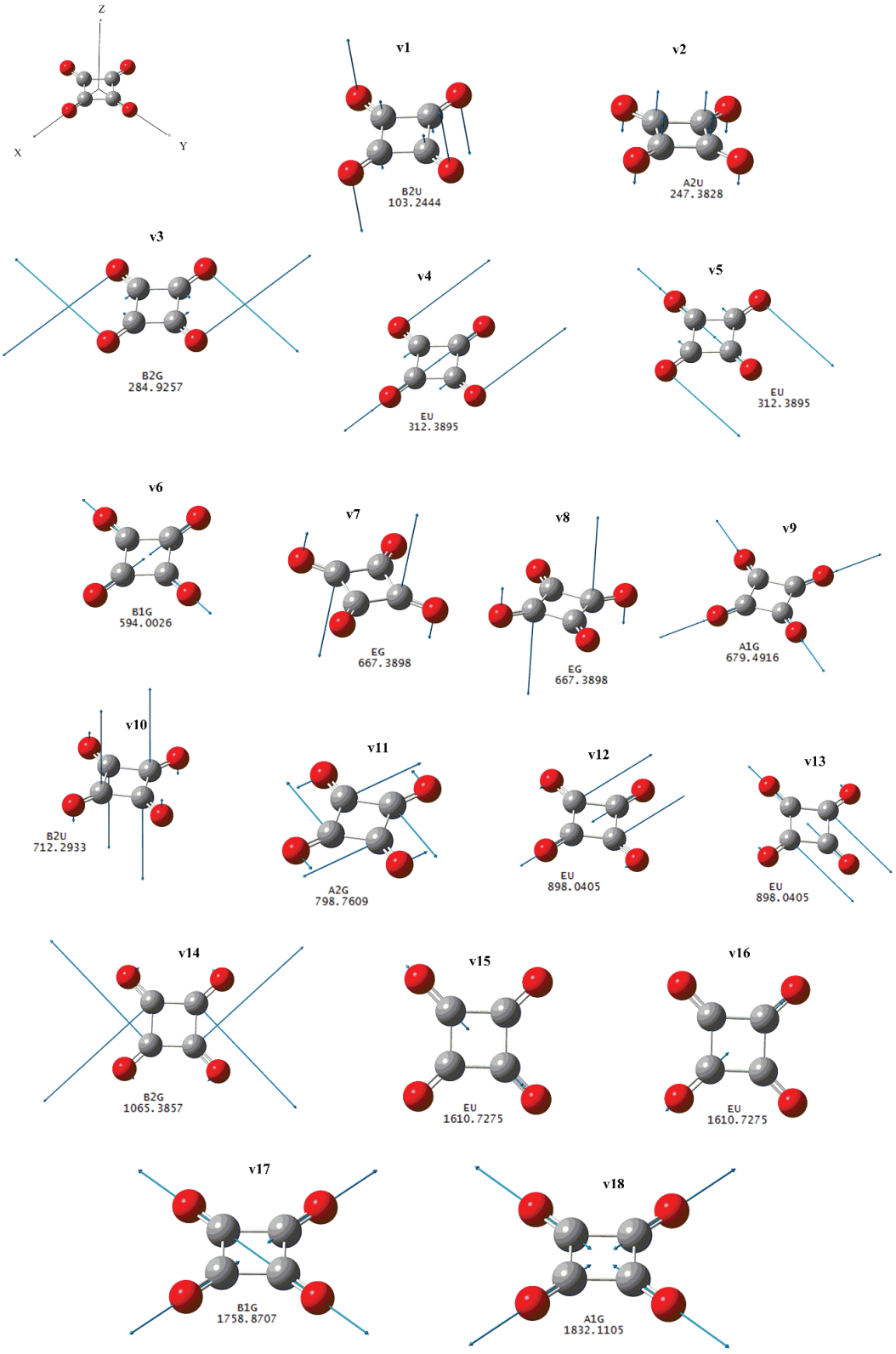

Figure S5. Normal modes of the squarate radical anion ($^2B_{2g}$) calculated at the B3LYP/aug-cc-pVTZ level of theory. Analogous modes are found at the G4 level of theory.

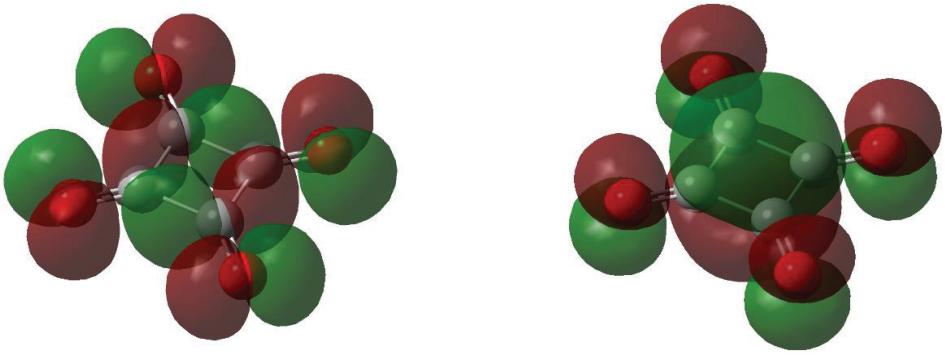

Figure S6. The frontier b_{2g} and a_{2u} (in standard orientation) orbitals of Sq^{2-} and $Sq^{\bullet-}$.

The direct product of the two highest occupied orbitals is (Figure S6): $\mathbf{b_{2g} \times a_{2u} = B_{1u}}$. The transition dipole moment integral,

$$\vec{M} = \int \psi^f * \vec{\mu} \psi^i d\tau,$$

should be non-zero for an allowed transition, a condition that is met when the direct product of the initial and final state symmetries with the transition moment operator, $\vec{\mu}$, contains the totally symmetric representation, A_{1g}. The symmetry of the transition moment operator is that of the x, y and z operators from the character table. For the D_{4h} group these are A_{2u} and E_u.

The electronic transition from $^2B_{2g}$ to $^2A_{2u}$ has the direct product:

$$A_{2u} \times \begin{pmatrix} A_{2u} \\ E_u \end{pmatrix} \times B_{2g} = \begin{pmatrix} B_{2g} \\ E_g \end{pmatrix}.$$

The electronic transition is thus not allowed, as A_{1g} is not present in the product. However, the vibrational irreducible representation of the D_{4h} group contains the b_{2g} and e_g modes that can generate the totally symmetric representation (Figure S6). This means that vibronic coupling can lead to an allowed transition between the $^2B_{2g}$ and $^2A_{2u}$ states.

$$\begin{pmatrix} B_{2g} \\ E_g \end{pmatrix} \times \left\{ A_{2u} \times \begin{pmatrix} A_{2u} \\ E_u \end{pmatrix} \times B_{2g} \right\} = \begin{pmatrix} \boldsymbol{A_{1g}} \\ \boldsymbol{A_{1g}} + [A_{2g}] + B_{1g} + B_{2g} \end{pmatrix}$$

The lowest energy b_{2g} mode, v3, at 285 cm^{-1} (3.4 kJ/mol) should be significantly populated even at low temperatures, facilitating the transition, especially considering the near degeneracy of the states.

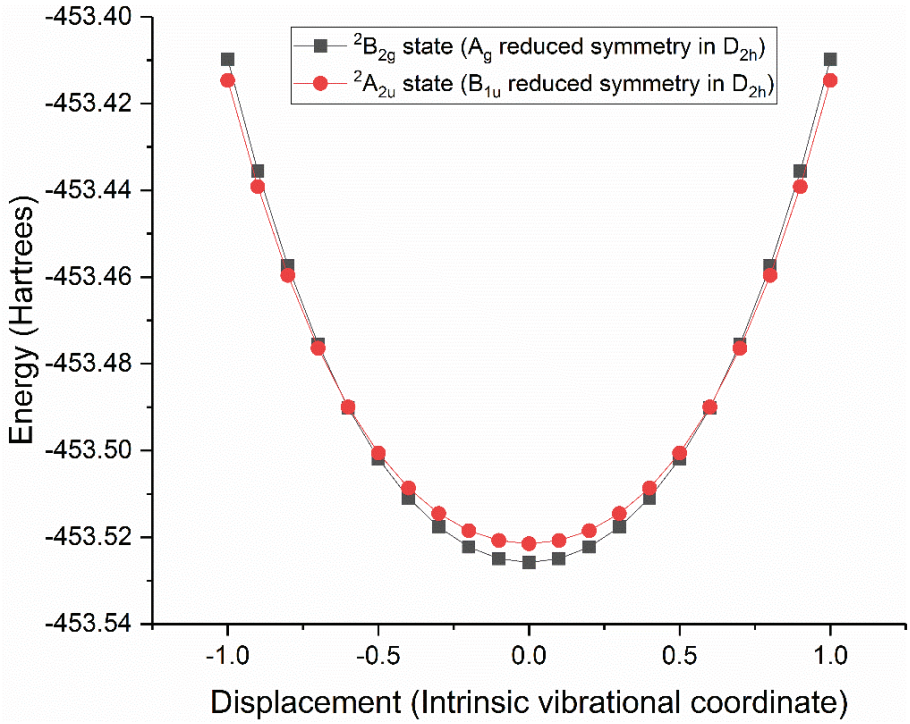

Figure S7. B3LYP/aug-cc-pVTZ potential energy scan of the lowest energy b_{2g} vibrational mode for the $^2B_{2g}$ and $^2A_{2u}$ electronic states of the squarate radical anion

We computed the displacement energies for the b_{2g} vibrational mode for the two electronic states of the squarate radical anion (Figure S7), and found that the potential energies cross at 90 kJ/mol relative to the lowest $^2B_{2g}$ state at the B3LYP/aug-cc-pVTZ level of theory.

The same symmetry arguments may be applied to the transition between the two radical anion states, $^2B_{2g}$ to $^2A_{2u}$, and the dianion $^1A_{1g}$ ground state. The direct product between ground state $^2B_{2g}$ and $^1A_{1g}$ is:

$$B_{2g} \times \begin{pmatrix} A_{2u} \\ E_u \end{pmatrix} \times A_{1g} = \begin{pmatrix} B_{1u} \\ E_u \end{pmatrix}.$$

The transition is not allowed. However, the direct product between the excited state $^2A_{2u}$ and $^1A_{1g}$ is:

$$A_{2u} \times \begin{pmatrix} A_{2u} \\ E_u \end{pmatrix} \times A_{1g} = \begin{pmatrix} \boldsymbol{A_{1g}} \\ E_g \end{pmatrix}.$$

Thus, the transition between the $^2A_{2u}$ excited state of the squarate radical anion and $^1A_{1g}$ state of the dianion is allowed by symmetry arguments, and can be promoted by the a_{1g} and e_g vibrational modes.

$$\begin{pmatrix} A_{1g} \\ E_g \end{pmatrix} \times \left\{ A_{2u} \times \begin{pmatrix} A_{2u} \\ E_u \end{pmatrix} \times A_{1g} \right\} = \begin{pmatrix} \boldsymbol{A_{1g}} \\ \boldsymbol{A_{1g}} + [A_{2g}] + B_{1g} + B_{2g} \end{pmatrix}$$

The non-allowed transition between the squarate radical anion ground state and the dianion can be promoted by the e_u vibrational mode.

On the G4 level of theory, the $^2A_{2u}$ state is the ground state of the squarate radical anion, and thus the transition to the dianion ground state is an allowed transition. As for the transition between the two radical anion states, $^2B_{2g}$ and $^2A_{2u}$, the potential energy surface overlap is not present in the lowest b_{2g} mode at the geometries explored (Figure S8). This can be rationalized by the fact that the vibrational modes able to promote the electronic transition are consistently higher for the $^2B_{2g}$ state. However, this analysis does not account for anharmonicities in the vibrational modes.

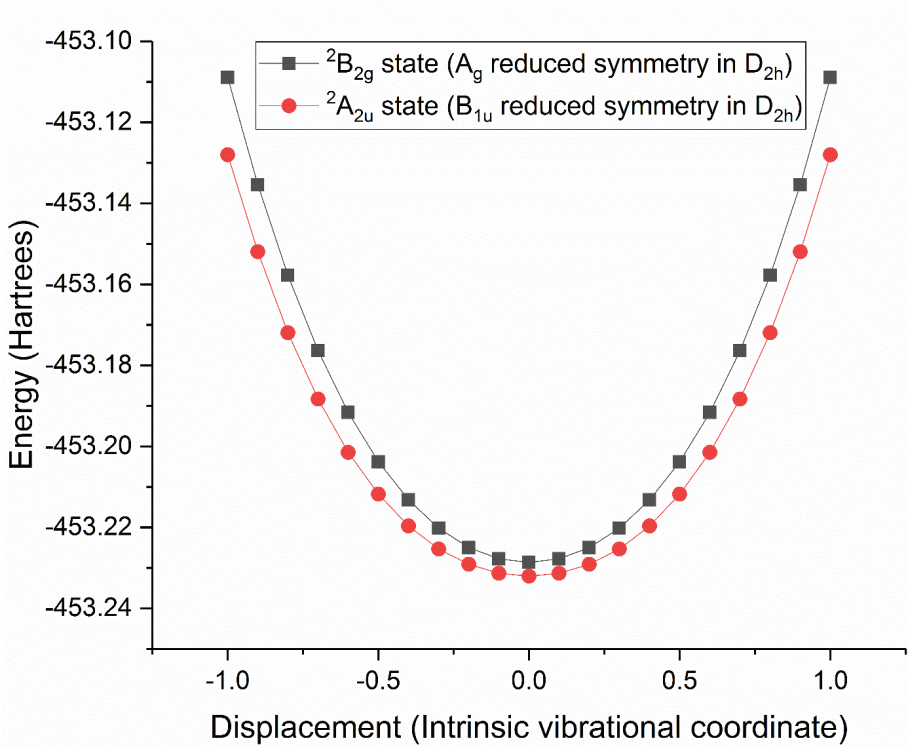

Figure S8. G4 potential energy scan of the lowest energy b_{2g} vibrational mode for the $^2B_{2g}$ and $^2A_{2u}$ electronic states of the squarate radical anion

SI-E. Potential energy scans for the lowest dianion electronic state and coulomb barrier towards electron detachment

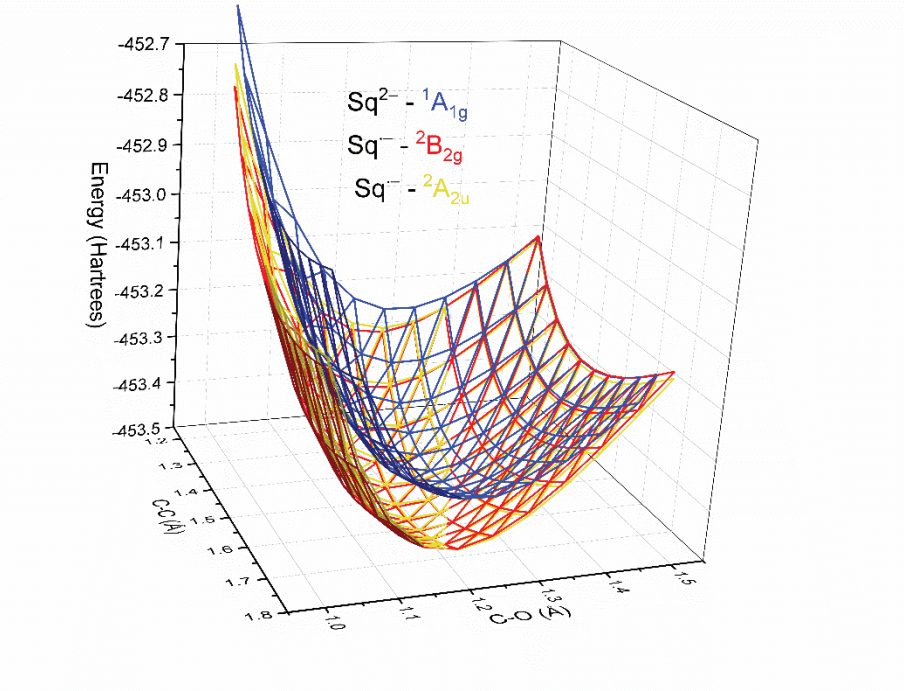

Figure S9. B3LYP/aug-cc-pVTZ potential energy scan of the $^1A_{1g}$, $^2B_{2g}$ and $^2A_{2u}$ electronic states of the squarate di- and radical anions at different C-C and C-O bond lengths.

Although the electron binding energy of the second electron in the squarate dianion is negative, it can be stabilized against electron ejection in the gas phase by the reverse Coulomb barrier (RCB).[2] In order to assess the barrier height for electron ejection from $C_4O_4^{2-}$, we employed a Marcus-Hush approach as reported by Poad et al.[3,4] The barrier ΔG^* is estimated with the following expression:

$$\Delta G^* = \frac{\lambda}{4}\left(1 + \left(\frac{\Delta G^\circ}{\lambda}\right)\right)^2$$

where λ, the reorganization energy, is the energy needed to distort the dianion equilibrium geometry into that of the radical anion ($^2A_{2u}$), while ΔG° is the adiabatic electron detachment energy. Based on this we find that the RCB for the dianion is 454 kJ/mol. However, the Marcus-Hush approach requires that the two intersecting potential energy surfaces are strictly parabolic, a situation that may or may not be true. The deviation from strictly parabolic surfaces can be

expressed by the difference in the reorganization energies on the dianion and radical anion surfaces. For the squarate dianion and radical anion surfaces, this difference is 0.6 kJ/mol, amounting to a difference of 33 kJ/mol for the calculated RCB barrier. Thus, the intersecting potentials are sufficiently parabolic to meet the underlying assumptions of the Marcus-Hush approach.

REFERENCES

(1) Harvey, D. J.; Hunter, A. P.; Bateman, R. H.; Brown, J.; Critchley, G. Relationship between In-Source and Post-Source Fragment Ions in the Matrix-Assisted Laser Desorption (Ionization) Mass Spectra of Carbohydrates Recorded with Reflectron Time-of-Flight Mass Spectrometers. *Int. J. Mass Spectrom.* **1999**, *188* (1–2), 131–146.

(2) Wang, X.-B.; Wang, L.-S. Observation of Negative Electron-Binding Energy in a Molecule. *Nature* **1999**, *400* (6741), 245–248.

(3) Poad, B. L. J.; Reed, N. D.; Hansen, C. S.; Trevitt, A. J.; Blanksby, S. J.; Mackay, E. G.; Sherburn, M. S.; Chan, B.; Radom, L. Preparation of an Ion with the Highest Calculated Proton Affinity: Ortho-Diethynylbenzene Dianion. *Chem. Sci.* **2016**, *7* (9), 6245–6250.

(4) Grampp, G. The Marcus Inverted Region from Theory to Experiment. *Angew. Chem. Int. Ed. Engl.* **1993**, *32* (5), 691–693.

Supporting information for Paper IV.

Electronic Supplementary Material (ESI) for Organic & Biomolecular Chemistry.

The unimolecular dissociation of magnesium chloride squarate ($ClMgC_4O_4^-$) and reductive cyclooligomerisation of CO on magnesium – Supporting Information

Joakim S. Jestilä[1], Zsuzsanna Iker[2], Mauritz J. O. Ryding[1] and Einar Uggerud[1*]

[1] Department of Chemistry and Hylleraas Centre for Quantum Molecular Sciences, University of Oslo, PO Box 1033, Blindern, Oslo N-0135, Norway

[2] Budapest University of Technology and Economics, Department of Organic Chemistry and Technology, Műegyetem rkp. 3., H1111, Budapest, Hungary

Table of Contents

SI-A. Energy-resolved cross-sections and pressure extrapolation

All appearance curves were acquired by measuring 150, 250 or 300 scans on each collision energy increment. For the linear extrapolation, the threshold energies were estimated by fitting asymmetric double sigmoidal functions to the curves, and subsequently extrapolating the linear portion (assumed to be the inflection point) of the fitted function to baseline. In addition, we utilized the L-CID software of Chen and coworkers[1] to further refine the results. The following parameters were used for all dissociation reactions:

Temperature	298 K
TS (0 = loose)(1 = tight)	0
FWHM of ion beam kin. E	2
Corr. for Elab to reach detector	0
Free rotors	0
Degrees of freedom	3N − 6

The analysis was conducted three times on each curve to estimate the numerical error of the procedure.

The measurements were done at four different plus one background collision gas (Ar) pressures, in order to extrapolate the threshold energies to vacuum. To account for the decreasing signal-to-noise ratio with pressure, the threshold energies are weighted by their relative signal intensities in the linear extrapolation procedure, giving lower priority to more uncertain measurements. For calibration, the same analysis was done on two reference systems with known reaction energetics, the decarboxylation of benzoate, $C_6H_5CO_2^- \rightarrow C_6H_5^- + CO_2$, and the dissociation of the Cs^+(15-crown-5) complex, Cs^+(15-crown-5) → Cs^+ + (15-crown-5).

Linear extrapolation example: threshold energy of $ClMgC_3O_3^-$ (*m/z* 143)

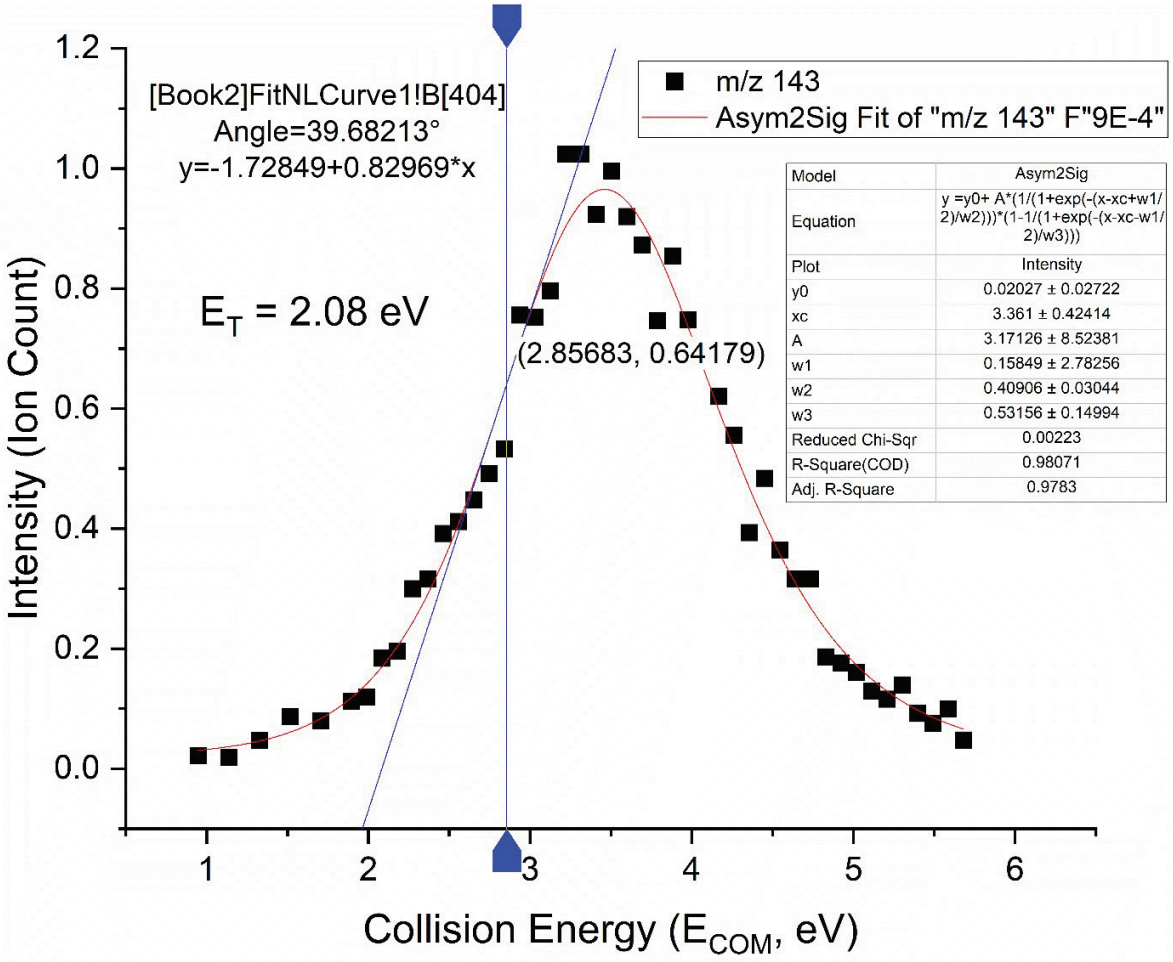

Figure S1. Appearance curve of $ClMgC_3O_3^-$ (*m/z* 143) taken at 9.45×10^{-4} mbar Ar pressure with fitted asymmetric double sigmoidal function. Threshold energy is determined by following the tangent line of the inflection point (2.86, 0.64) to the abscissa.

Threshold energies for dissociation of $ClMgC_4O_4^-$ (*m/z* 171)

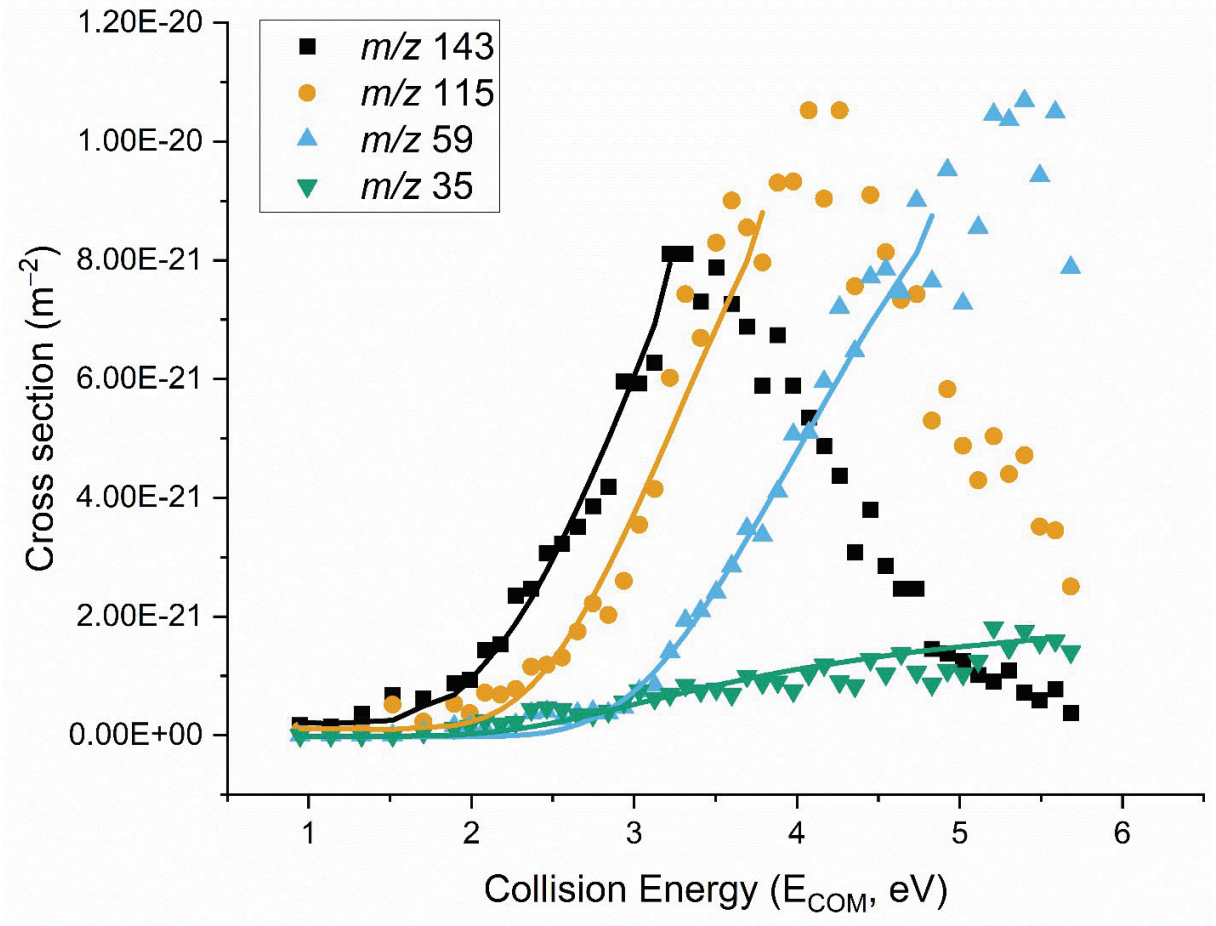

Figure S2. Energy-resolved CID cross sections and L-CID fits for the dissociation of $ClMgC_4O_4^-$ (*m/z* 171) at 9.45×10^{-4} mbar Ar pressure.

Table S1. L-CID output and results of linear extrapolation (9.45×10^{-4} mbar Ar pressure).

	***m/z* 143**	***m/z* 115**	***m/z* 59**	***m/z* 35**
E_{0_Linear} (eV)	2.08	2.32	3.12	1.76
E_{0_LCID} (eV)	1.61 ± 0.02	2.00 ± 0.02	2.39 ± 0.01	1.77 ± 0.11
ν_{eff} (cm^{-1})	1003 ± 5	744 ± 39	807 ± 71	813 ± 192
a' (cm^{-1})	5733 ± 574	5747 ± 423	5853 ± 12	5713 ± 241

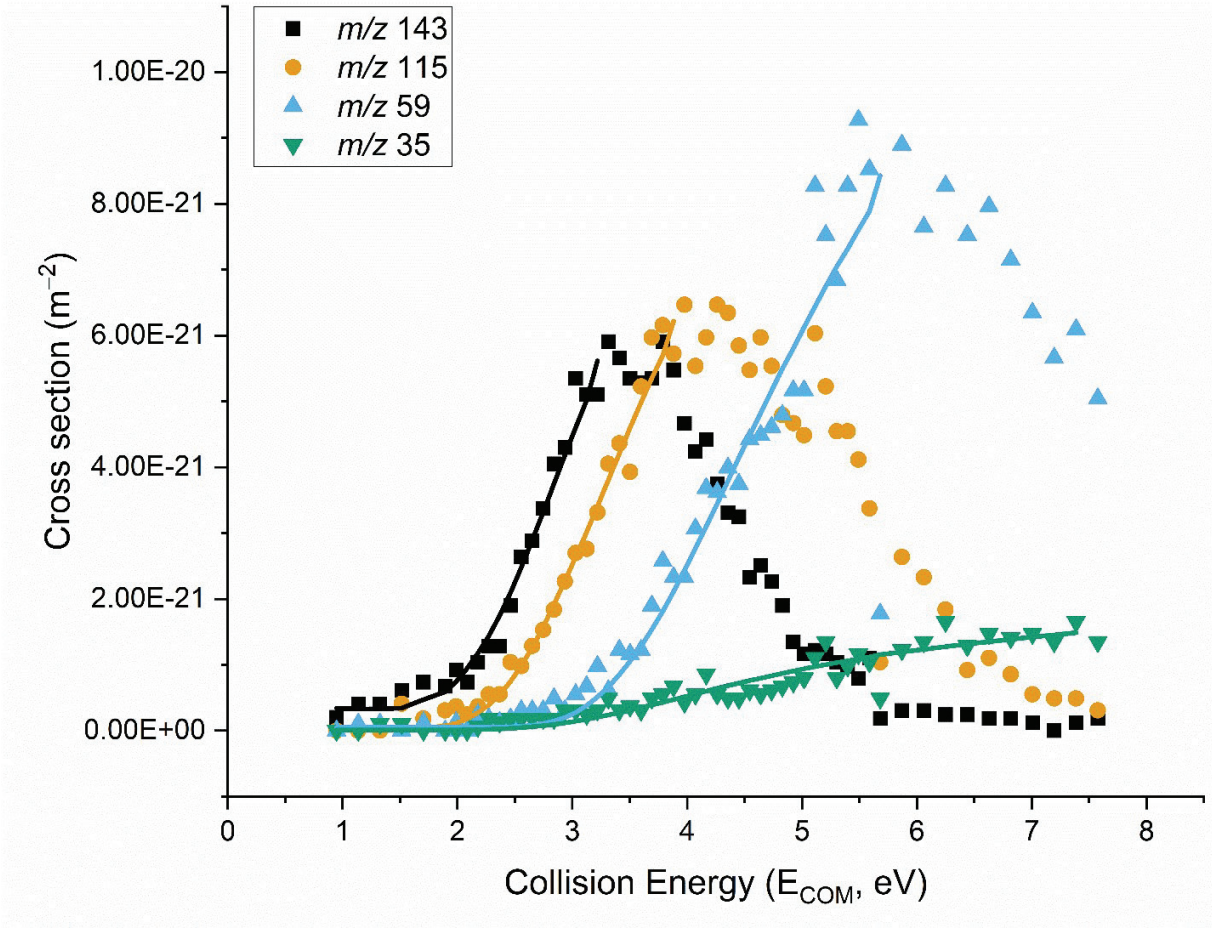

Figure S3. Energy-resolved CID cross sections and L-CID fits for the dissociation of $ClMgC_4O_4^-$ (*m/z* 171) at 6.66×10^{-4} mbar Ar pressure.

Table S2. L-CID output and results of linear extrapolation (6.66×10^{-4} mbar Ar pressure).

	***m/z* 143**	***m/z* 115**	***m/z* 59**	***m/z* 35**
E_{0_Linear} (eV)	2.15	2.52	3.15	2.63
E_{0_LCID} (eV)	1.78 ± 0.05	1.97 ± 0.01	2.59 ± 0.01	2.09 ± 0.01
ν_{eff} (cm^{-1})	771 ± 126	811 ± 74	799 ± 54	1004 ± 3
a' (cm^{-1})	5733 ± 272	5580 ± 420	5800 ± 193	5987 ± 194

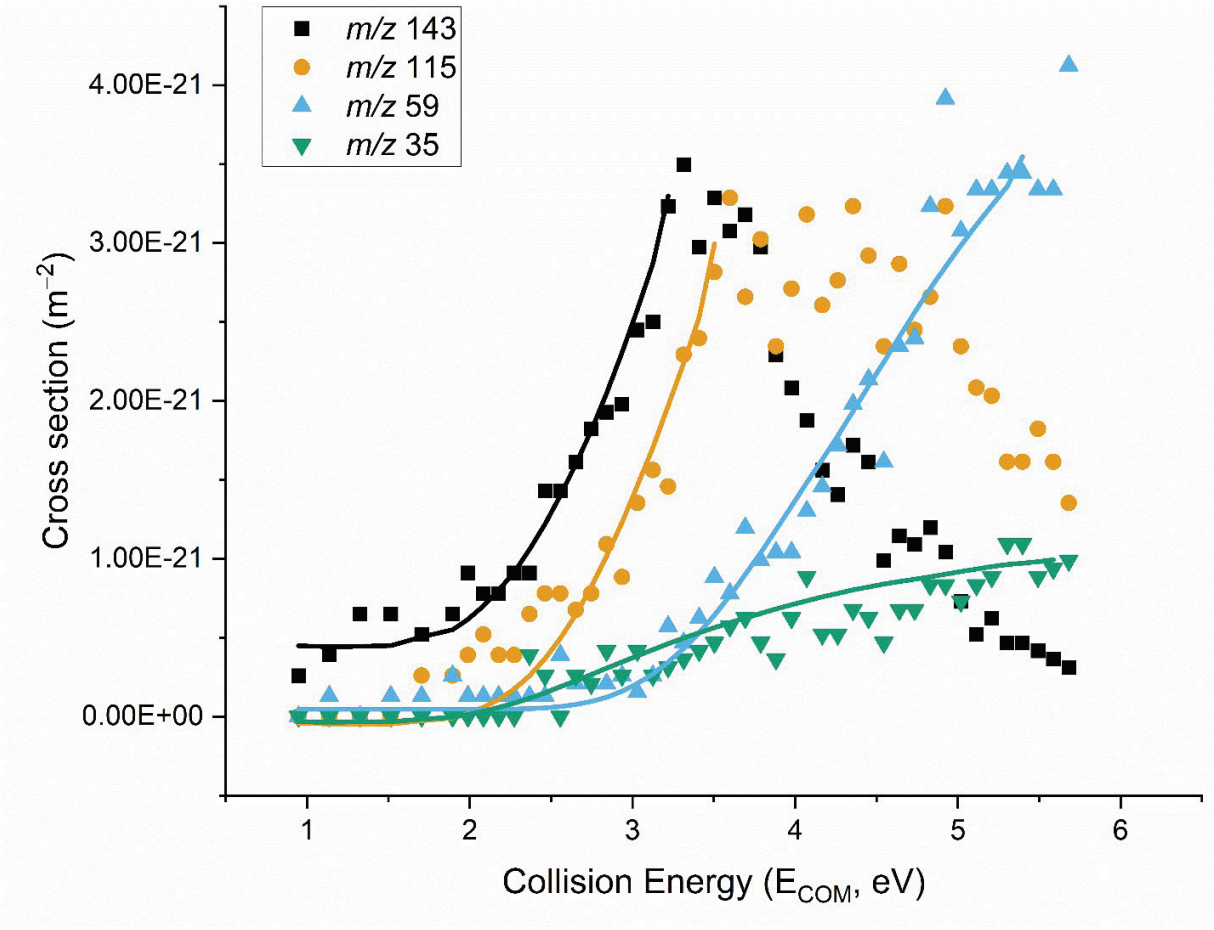

Figure S4. Energy-resolved CID cross sections and L-CID fits for the dissociation of $ClMgC_4O_4^-$ (*m/z* 171) at 4.73×10^{-4} mbar Ar pressure.

Table S3. L-CID output and results of linear extrapolation (4.73×10^{-4} mbar Ar pressure).

	***m/z* 143**	***m/z* 115**	***m/z* 59**	***m/z* 35**
$E_{0\ Linear}$ (eV)	2.10	2.45	3.43	2.08
$E_{0\ LCID}$ (eV)	1.74 ± 0.01	1.90 ± 0.05	2.50 ± 0.03	1.75 ± 0.08
ν_{eff} (cm^{-1})	1004 ± 4	1002 ± 3	770 ± 32	889 ± 101
a' (cm^{-1})	5593 ± 110	5627 ± 549	5827 ± 361	5513 ± 280

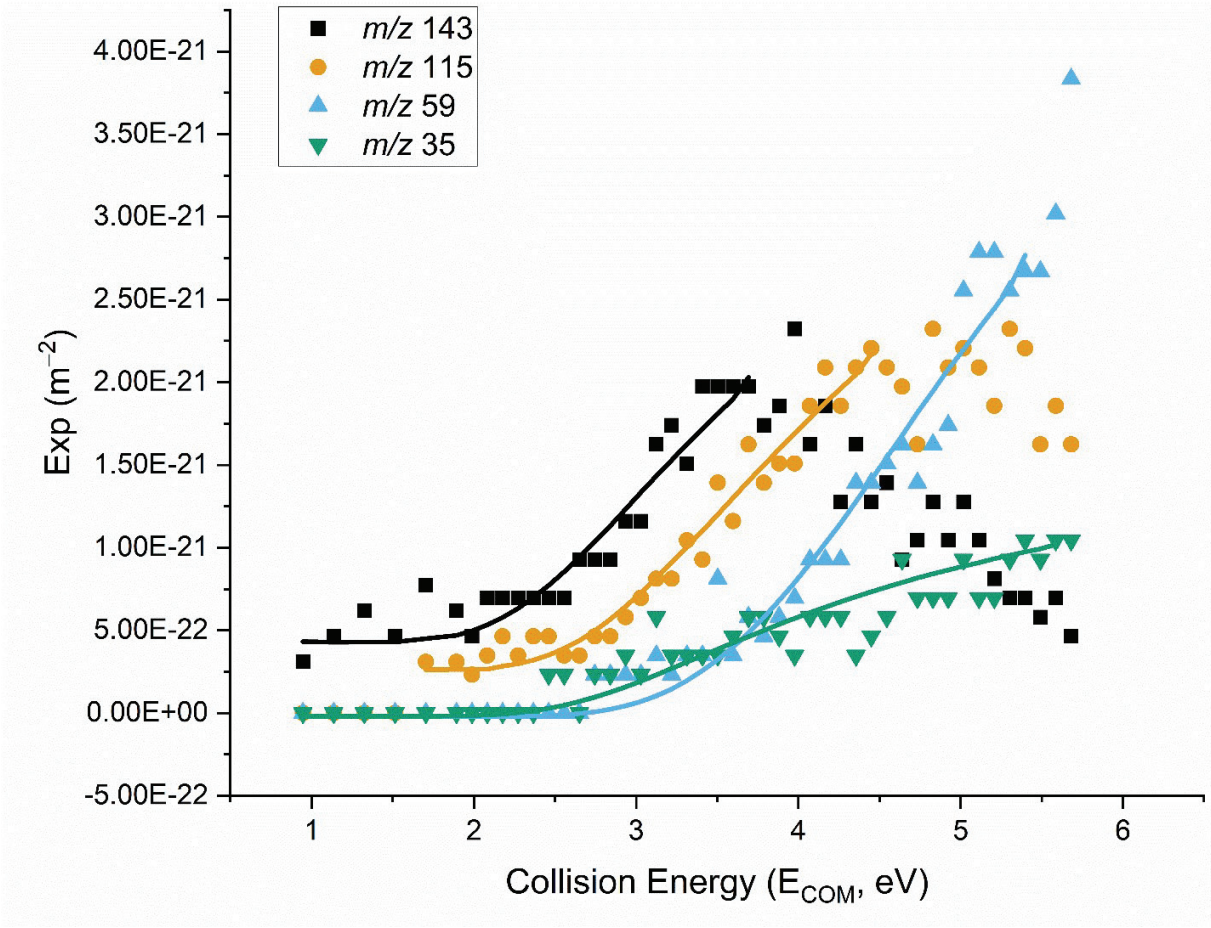

Figure S5. Energy-resolved CID cross sections and L-CID fits for the dissociation of $ClMgC_4O_4^-$ (*m/z* 171) at 2.76×10^{-4} mbar Ar pressure.

Table S4. L-CID output and results of linear extrapolation (2.76×10^{-4} mbar Ar pressure).

	***m/z* 143**	***m/z* 115**	***m/z* 59**	***m/z* 35**
$E_{0\ Linear}$ **(eV)**	2.17	2.40	3.90	2.86
$E_{0\ LCID}$ **(eV)**	1.77 ± 0.04	2.16 ± 0.02	2.54 ± 0.06	2.02 ± 0.04
ν_{eff} **(cm^{-1})**	938 ± 118	715 ± 125	986 ± 20	735 ± 76
a' (cm^{-1})	5880 ± 505	5660 ± 314	5573 ± 560	5720 ± 191

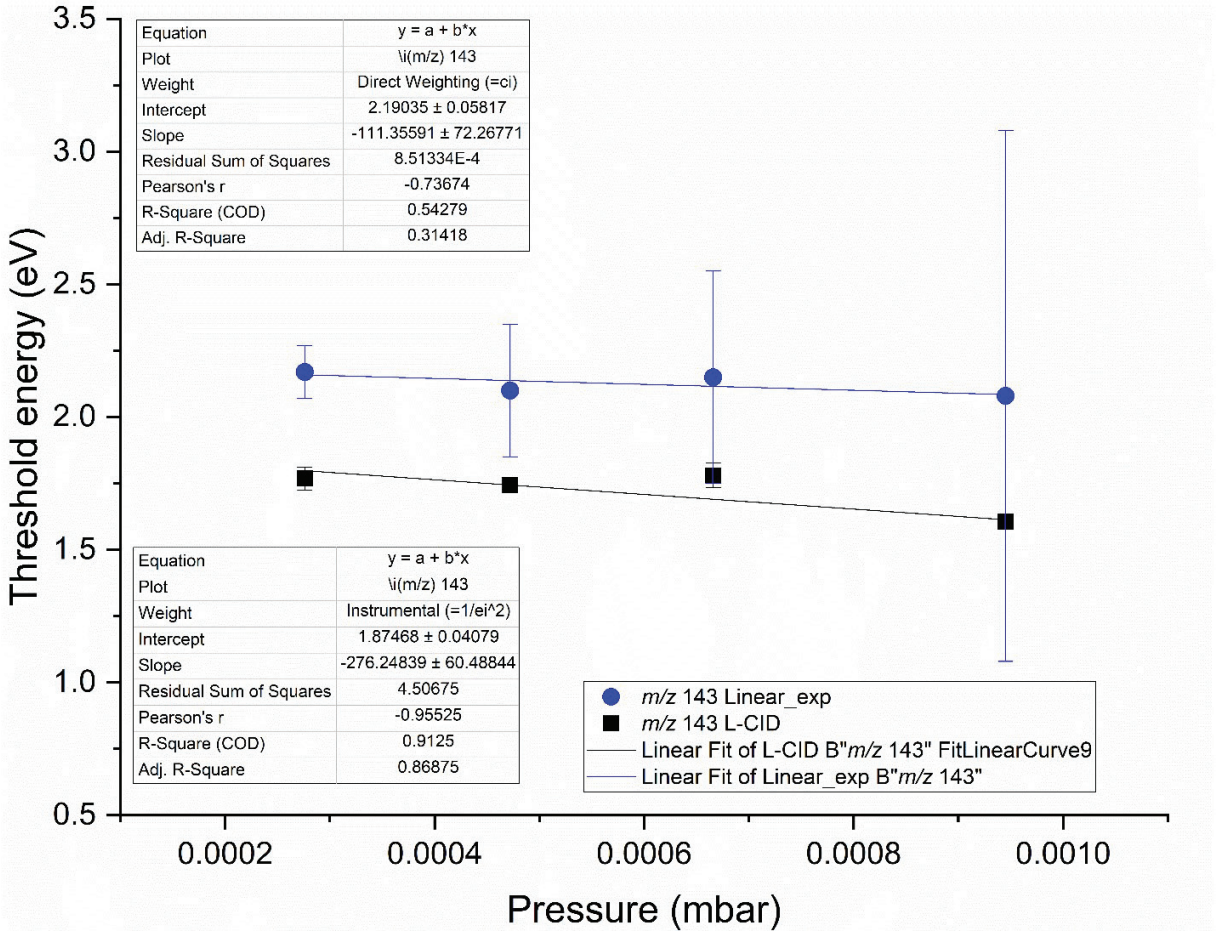

Figure S6. Pressure extrapolation of $ClMgC_3O_3^-$ (*m/z* 143) threshold energies (linear and L-CID) to zero pressure. The fitting of the linearly extrapolated energies uses direct weighing ($w_i = c_i$) as represented by error bars corresponding to the highest signal intensity in each experiment, while the error bars on the L-CID energies are used in instrumental weighing ($w_i = 1/e_i^2$).

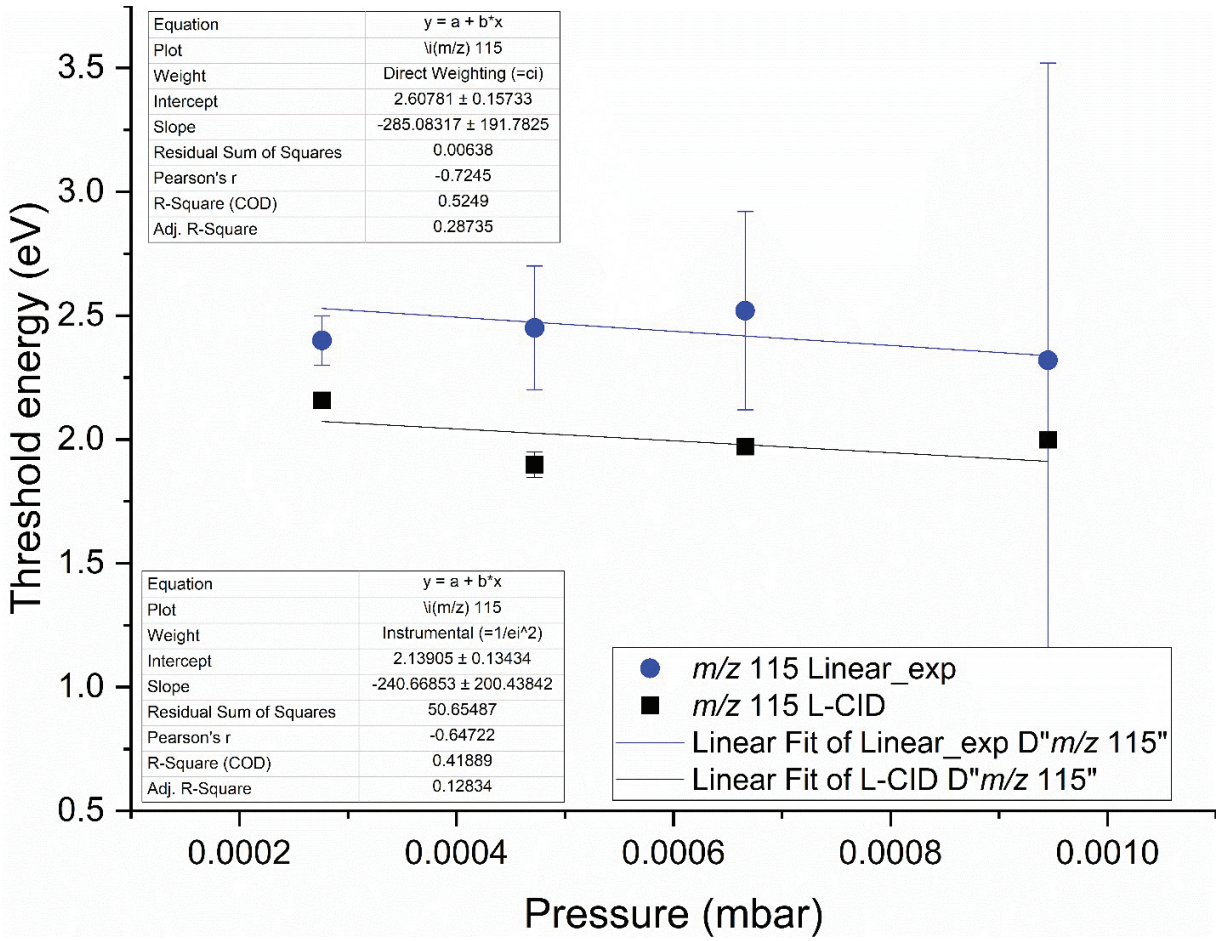

Figure S7. Pressure extrapolation of $ClMgC_2O_2^-$ (*m/z* 115) threshold energies (linear and L-CID) to zero pressure. The fitting of the linearly extrapolated energies uses direct weighing ($w_i = c_i$) as represented by error bars corresponding to the highest signal intensity in each experiment, while the error bars on the L-CID energies are used in instrumental weighing ($w_i = 1/e_i^2$).

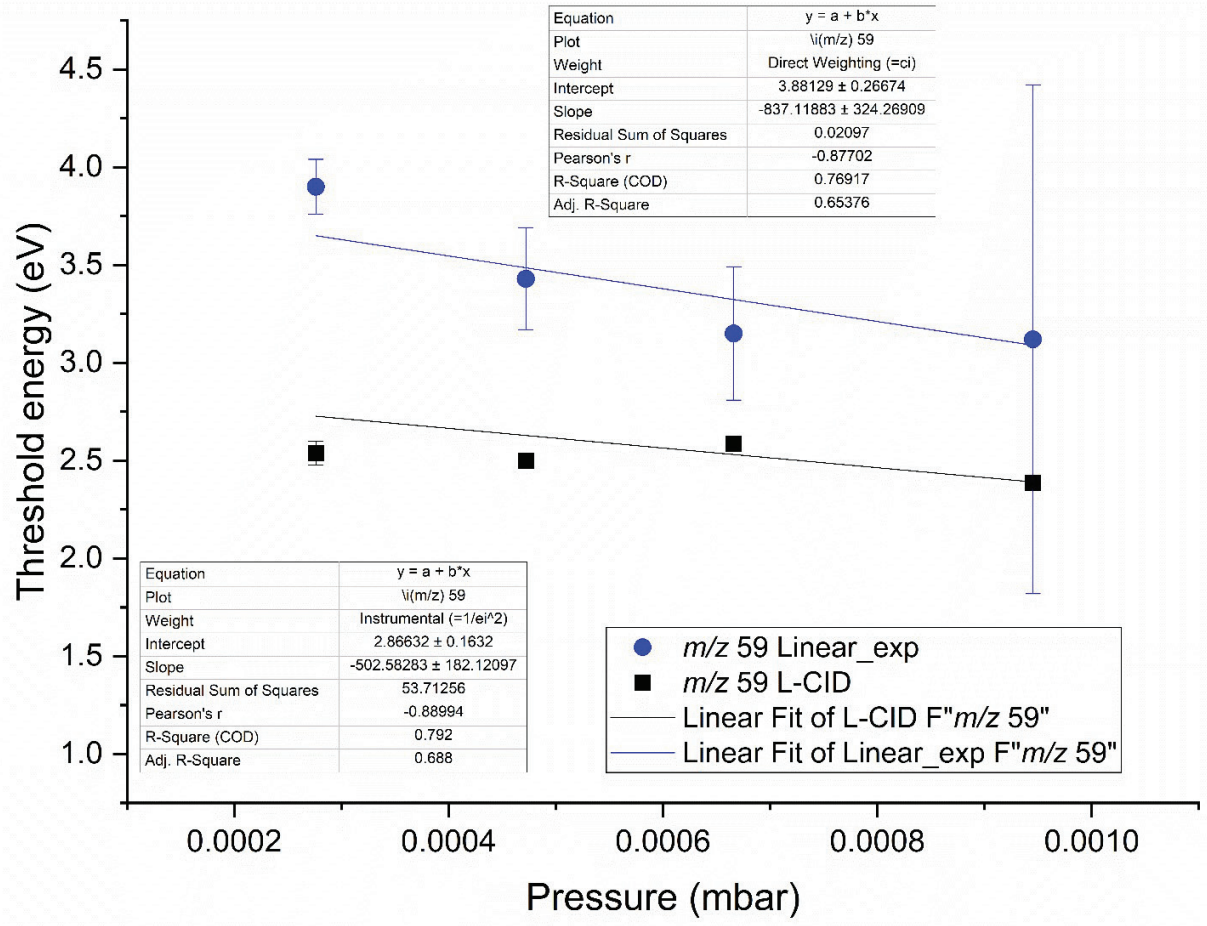

Figure S8. Pressure extrapolation of $ClMg^-$ (*m/z* 59) threshold energies (linear and L-CID) to zero pressure. The fitting of the linearly extrapolated energies uses direct weighing ($w_i = c_i$) as represented by error bars corresponding to the highest signal intensity in each experiment, while the error bars on the L-CID energies are used in instrumental weighing ($w_i = 1/e_i^2$).

Threshold energies for dissociation of $ClMgC_3O_3^-$ (*m/z* 143)

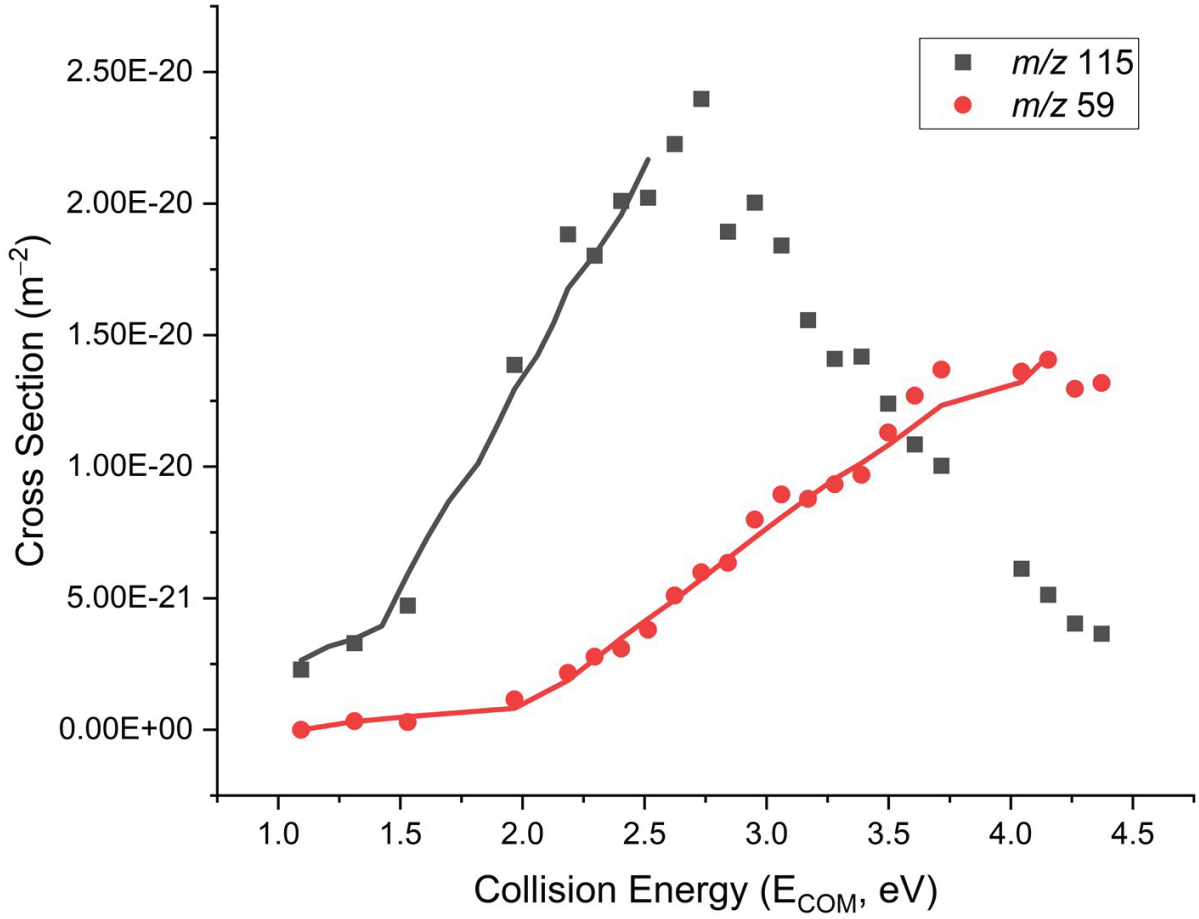

Figure S9. Energy-resolved CID cross sections and L-CID fits for the dissociation of $ClMgC_3O_3^-$ (*m/z* 143) at 4.63×10^{-4} mbar Ar pressure. Extra arbitrary points were added for the *m/z* 115 curve between 1.5 and 2.0 eV to enable L-CID fitting.

Table S5. L-CID output and results of linear extrapolation (4.63×10^{-4} mbar Ar pressure).

	***m/z* 115**	***m/z* 59**
E_{0_Linear} (eV)	1.32	2.16
E_{0_LCID} (eV)	1.14 ± 0.01	1.67 ± 0.01
ν_{eff} (cm^{-1})	671 ± 22	715 ± 58
a' (cm^{-1})	5620 ± 322	5593 ± 269

Threshold energies for the reference system, $C_6H_5^-$ (*m/z* 121) → $C_6H_5^-$ (*m/z* 77) + CO_2

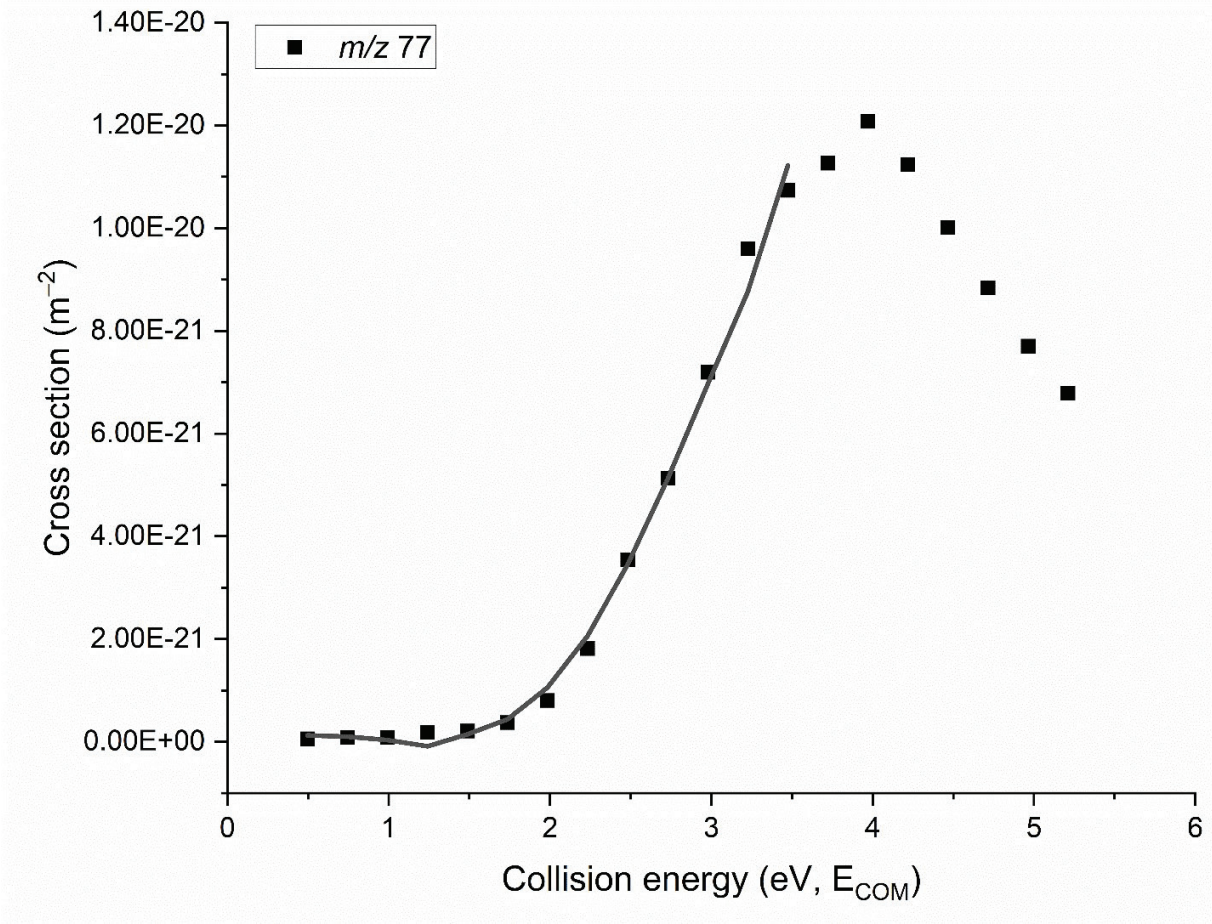

Figure S10. Energy-resolved CID cross sections and L-CID fits for the dissociation of benzoate (*m/z* 121) at 5.35×10^{-4} mbar Ar pressure.

Table S6. L-CID output and results of linear extrapolation (5.35×10^{-4} mbar Ar pressure).

	***m/z* 77**
E_{0_Linear} (eV)	2.17
E_{0_LCID} (eV)	1.73 ± 0.01
ν_{eff} (cm^{-1})	776 ± 39
a' (cm^{-1})	5833 ± 133

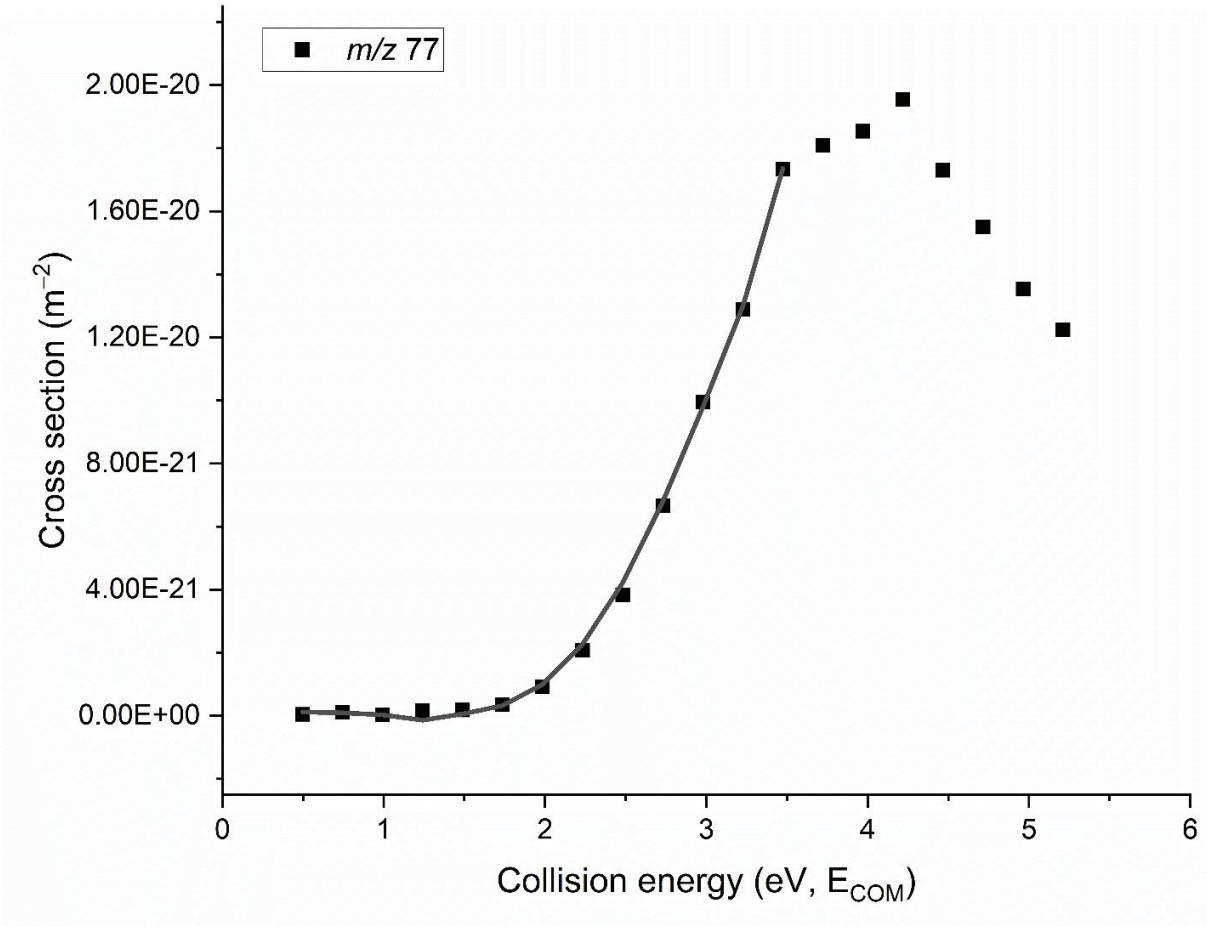

Figure S11. Energy-resolved CID cross sections and L-CID fits for the dissociation of benzoate (*m/z* 121) at 4.00×10^{-4} mbar Ar pressure.

Table S7. L-CID output and results of linear extrapolation (4.00×10^{-4} mbar Ar pressure).

	***m/z* 77**
$E_{0\ Linear}$ (eV)	2.32
E_{0_LCID} (eV)	1.86 ± 0.03
ν_{eff} (cm^{-1})	786 ± 132
a' (cm^{-1})	5900 ± 265

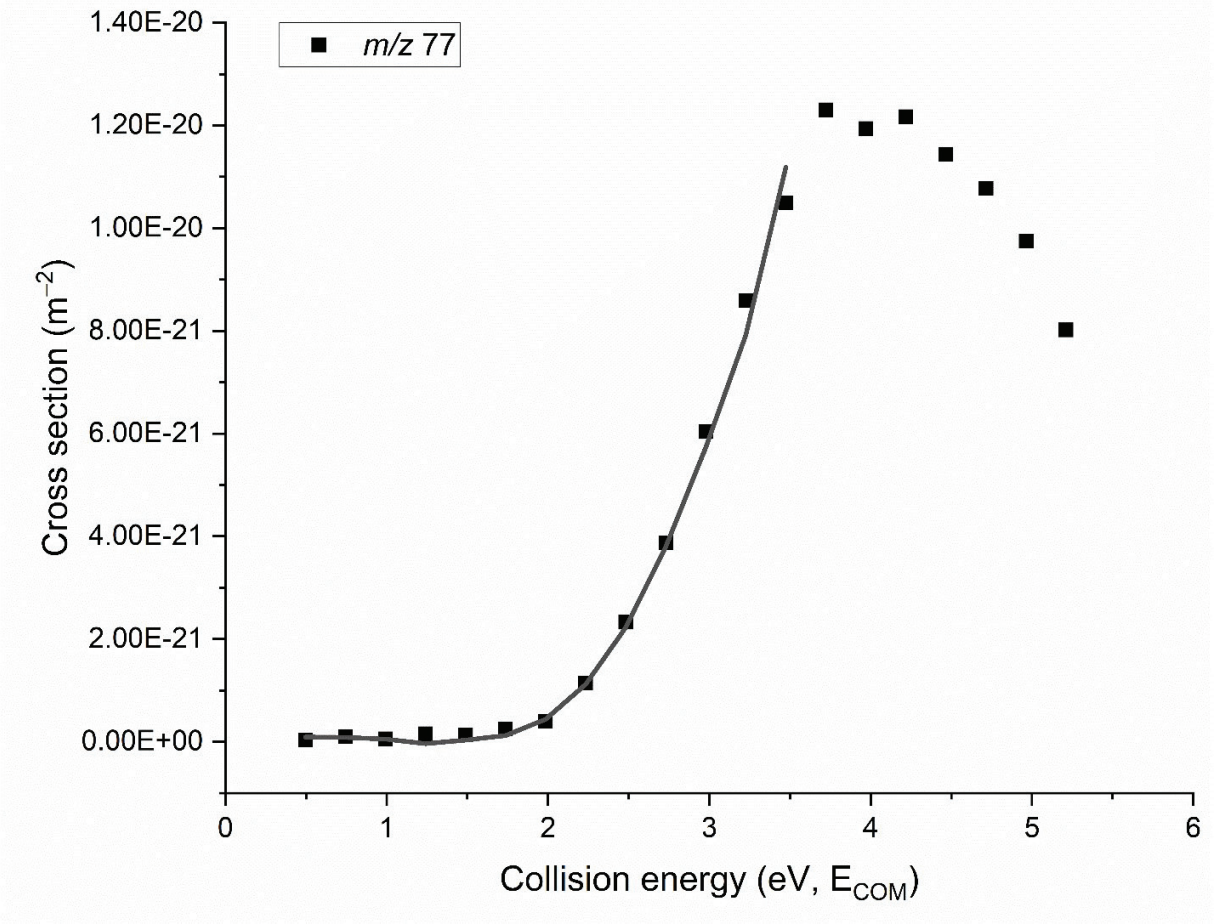

Figure S12. Energy-resolved CID cross sections and L-CID fits for the dissociation of benzoate (*m/z* 121) at 3.02×10^{-4} mbar Ar pressure.

Table S8. L-CID output and results of linear extrapolation (3.02×10^{-4} mbar Ar pressure).

	***m/z* 77**
$E_{0\ Linear}$ (eV)	2.37
E_{0_LCID} (eV)	1.88 ± 0.02
ν_{eff} (cm^{-1})	864 ± 67
a' (cm^{-1})	5800 ±72

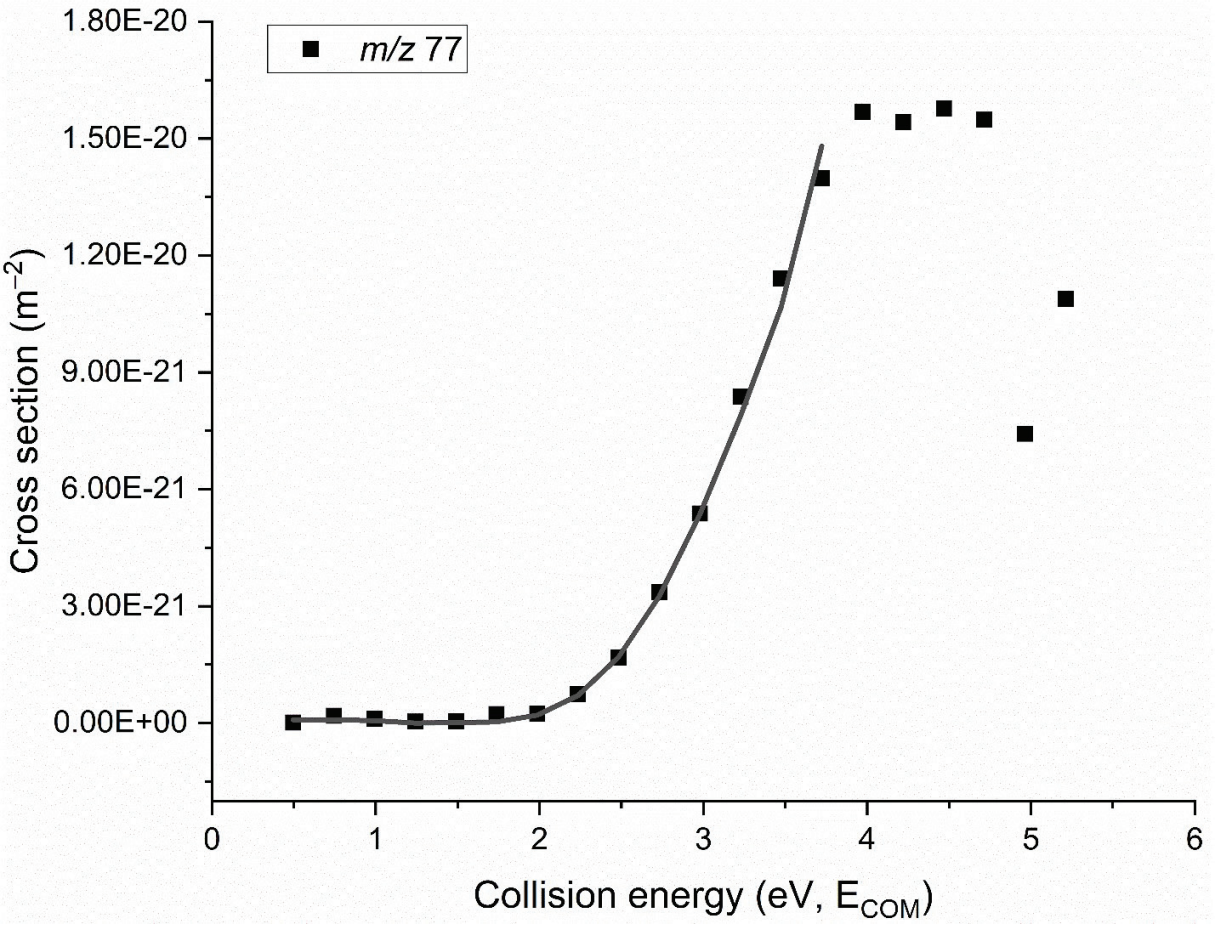

Figure S13. Energy-resolved CID cross sections and L-CID fits for the dissociation of benzoate (*m/z* 121) at 1.97×10^{-4} mbar Ar pressure.

Table S9. L-CID output and results of linear extrapolation (1.97×10^{-4} mbar Ar pressure).

	***m/z* 77**
$E_{0\ Linear}$ (eV)	2.57
E_{0_LCID} (eV)	1.99 ± 0.01
ν_{eff} (cm^{-1})	833 ± 29
a' (cm^{-1})	5687 ± 273

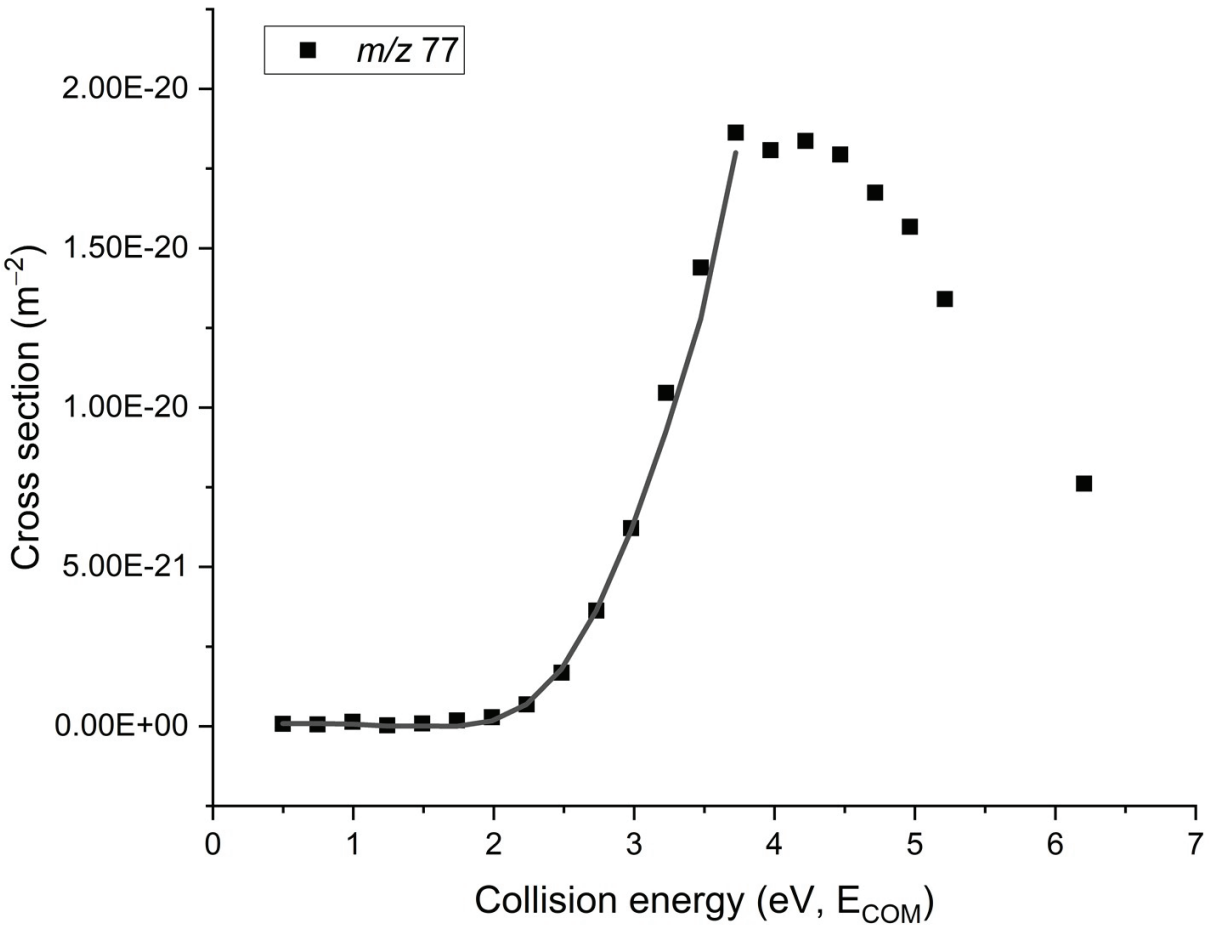

Figure S14. Energy-resolved CID cross sections and L-CID fits for the dissociation of benzoate (*m/z* 121) at 1.04×10^{-4} mbar Ar pressure.

Table S10. L-CID output and results of linear extrapolation (1.04×10^{-4} mbar Ar pressure).

	***m/z* 77**
$E_{0\ Linear}$ (eV)	2.65
E_{0_LCID} (eV)	2.03 ± 0.01
ν_{eff} (cm^{-1})	896 ± 13
a' (cm^{-1})	5847 ± 253

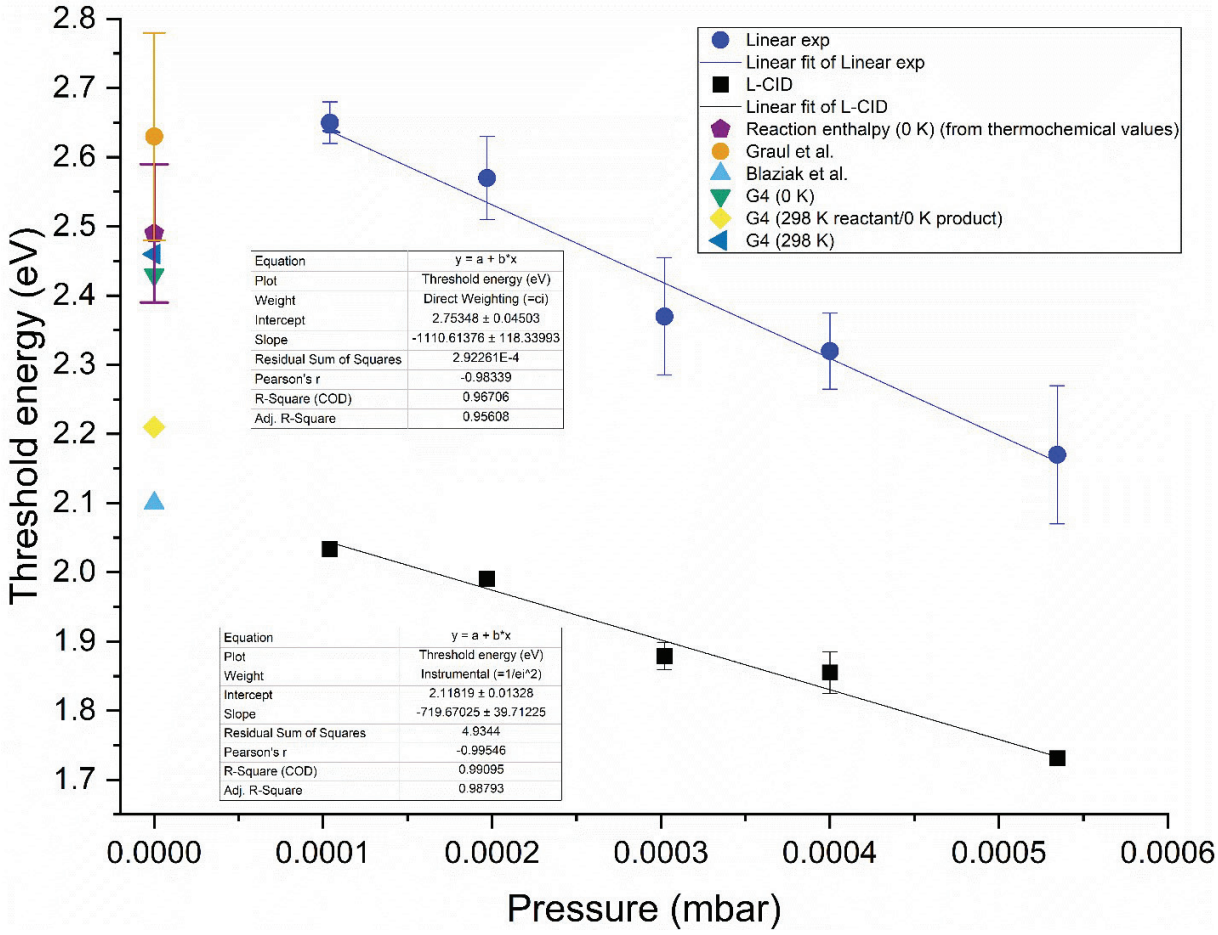

Figure S15. Pressure extrapolation of $C_6H_5^-$ (*m*/z 77) threshold energies (Linear and L-CID) to zero pressure. The fitting of the linearly extrapolated energies uses direct weighing ($w_i = c_i$) as represented by error bars corresponding to the highest signal intensity in each experiment, while the error bars on the L-CID energies are used in instrumental weighing ($w_i = 1/e_i^2$).

Table S11. Experimental and calculated reaction enthalpies ($\Delta_rH°$) and threshold energies (E_T) for $C_6H_5CO_2^- \rightarrow C_6H_5^- + CO_2$ in eV (kJ/mol in parentheses). Our estimates in **bold** (experimental and computational G4 (0 K)).

Experimental		
$\Delta_rH°$ (298 K)	E_T (linear extrapolation)	E_T (L-CID)
2.49 ± 0.1 (240 ± 10)	**2.75 ± 0.05 (265 ± 4)**	**2.12 ± 0.01 (205 ± 1)**
	2.63 ± 0.15 (254 ± 14)[2]	
	2.10 (203)[3]	
Computational		
$\Delta_rH°$ (298 K)	$\Delta_rH°$ (298 K reactant /0 K product)	E_T (0 K)
2.46 (237)	**2.21 (213)**	**2.43 (234)**
2.27 (219)[3]		2.37 (229)[3]

Calculation of reaction enthalpy for $C_6H_5CO_2^- \rightarrow C_6H_5^- + CO_2$ at 0 K

$\Delta_{f,gas}H°_{,\ 0K}(C_6H_5CO_2^-) = -381.8 \pm 10$ kJ/mol

$\Delta_{f,gas}H°_{,\ 0K}(C_6H_5^-) = 244.9 \pm 0.5$ kJ/mol[4]

$\Delta_{f,gas}H°_{,\ 0K}(CO_2) = -393.11 \pm 0.02$ kJ/mol

$\Delta_{decarb,gas}H°_{,\ 0K}$ = (244.9 kJ/mol + (−393.1 kJ/mol)) – (−381.8 kJ/mol)

$\Delta_{decarb,gas}H°_{,\ 0K}$ = **233.7 ± 10.0 kJ/mol**

Thermochemical parameters used in the calculation of the enthalpy of formation for benzoate:

PA = $-\Delta_{rxn}H°$ = 1423 ± 9 kJ/mol[5] for $C_6H_5CO_2^- + H^+ \rightarrow C_6H_5CO_2H$

$\Delta_fH°_{,\ 0K}(H^+)$ = 1528.03 kJ/mol

$\Delta_{Sub}H°(C_6H_5CO_2H)$ = 90 ± 4 kJ/mol (NIST database, average of 13 values)

$\Delta_{f,solid}H°_{,\ 0K}(C_6H_5CO_2H)$ = −366.8 ± 0.5 kJ/mol (NIST database)

$\Delta_{f,gas}H°_{,\ 0K}(C_6H_5CO_2H)$ = −366.8 kJ/mol + $\Delta_{Sub}H°(C_6H_5CO_2H)$ = −276.8 ± 4 kJ/mol

$\Delta_{f,gas}H°_{,\ 0K}(C_6H_5CO_2^-) = \Delta_{f,gas}H°_{,\ 0K}(C_6H_5CO_2H) - \Delta_fH°_{,\ 0K}(H^+) + PA$

Calculation of reaction enthalpy for $C_6H_5CO_2^- \rightarrow C_6H_5^- + CO_2$ at 298 K

$\Delta_{f,gas}H°_{,\ 298K}(C_6H_5CO_2^-) = -401.9 \pm 10$ kJ/mol

$\Delta_{f,gas}H°_{,\ 298K}(C_6H_5^-) = 232.0 \pm 0.5$ kJ/mol[4]

$\Delta_{f,gas}H°_{,\ 298K}(CO_2) = -393.50 \pm 0.02$ kJ/mol

$\Delta_{decarb,gas}H°_{,\ 298K} = (232.0 \text{ kJ/mol} + (-393.5 \text{ kJ/mol})) - (-401.9 \text{ kJ/mol})$

$\Delta_{decarb,gas}H°_{,\ 298K} =$ **240.4 ± 10.0 kJ/mol**

Thermochemical parameters used in the calculation of the enthalpy of formation for benzoate:

$PA = -\Delta_{rxn}H° = 1423 \pm 9$ kJ/mol[5] for $C_6H_5CO_2^- + H^+ \rightarrow C_6H_5CO_2H$

$\Delta_fH°_{,\ 298K}(H^+) = 1530.05$ kJ/mol

$\Delta_{Sub}H°(C_6H_5CO_2H) = 90 \pm 4$ kJ/mol (NIST database, average of 13 values)

$\Delta_{f,solid}H°_{,\ 298K}(C_6H_5CO_2H) = -384.8 \pm 0.5$ kJ/mol (NIST database)

$\Delta_{f,gas}H°_{,\ 298K}(C_6H_5CO_2H) = -384.8 \text{ kJ/mol} + \Delta_{Sub}H°(C_6H_5CO_2H) = -294.8 \pm 4$ kJ/mol

$\Delta_{f,gas}H°_{,\ 298K}(C_6H_5CO_2^-) = \Delta_{f,gas}H°_{,\ 298K}(C_6H_5CO_2H) - \Delta_fH°_{,\ 298K}(H^+) + PA$

Threshold energies for the reference system, Cs^+(15-crown-5) (*m/z* 353) → Cs^+ (*m/z* 133) + 15-crown-5

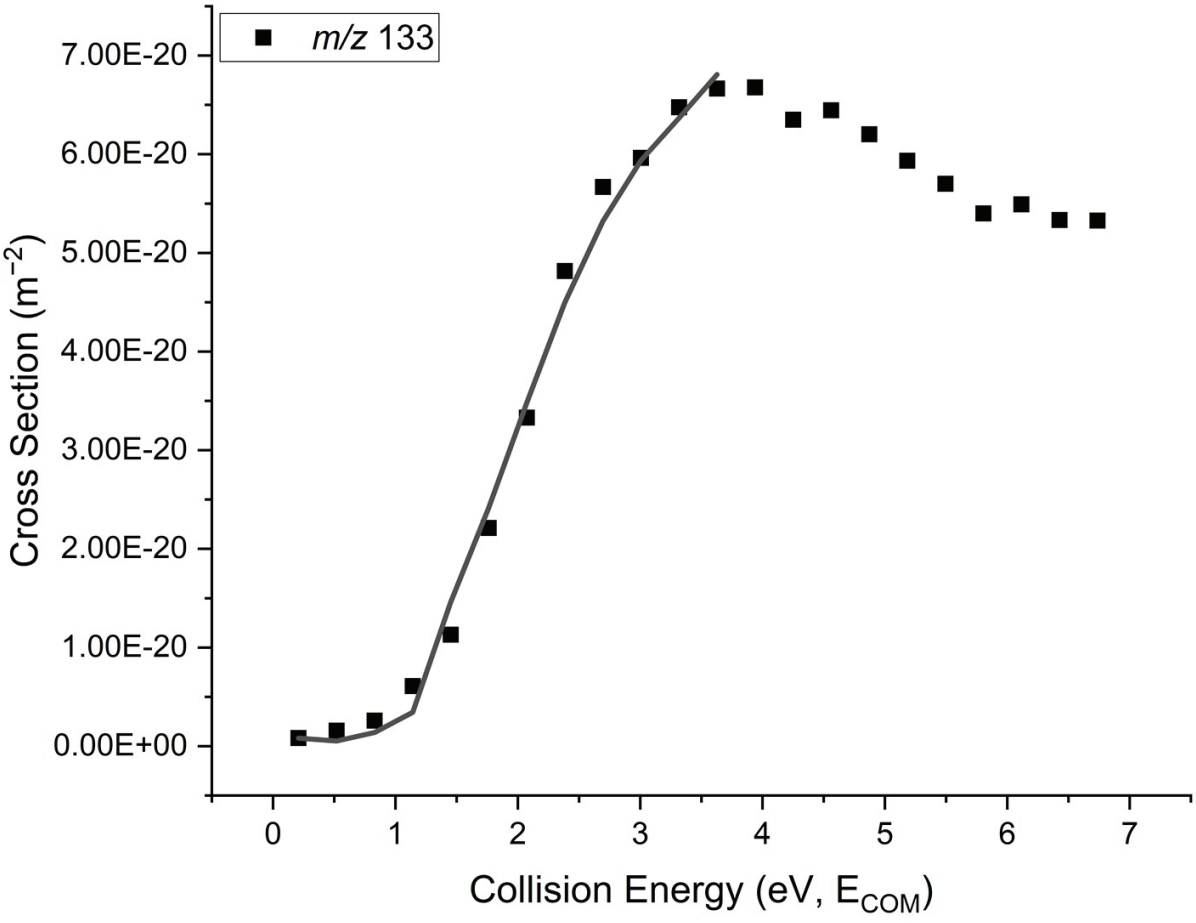

Figure S16. Energy-resolved CID cross sections and L-CID fit for the dissociation of Cs^+(15-crown-5) (*m/z* 353) at 4.95×10^{-4} mbar Xe pressure.

Table S12. L-CID output and results of linear extrapolation (4.95×10^{-4} mbar Xe pressure).

	***m/z* 77**
$E_{0\ Linear}$ (eV)	1.26
$E_{0\ LCID}$ (eV)	1.19
ν_{eff} (cm^{-1})	962
a' (cm^{-1})	5760

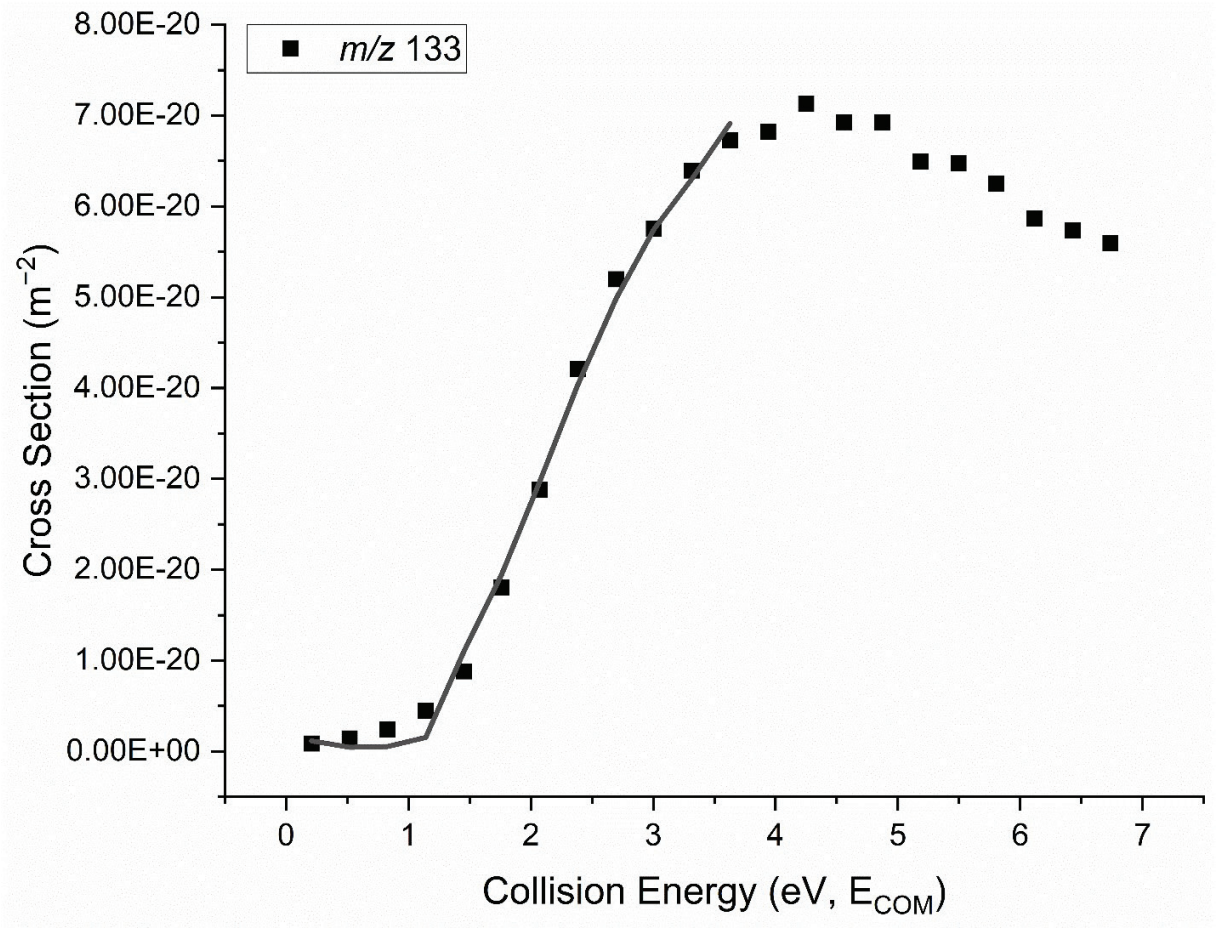

Figure S17. Energy-resolved CID cross sections and L-CID fit for the dissociation of Cs^+(15-crown-5) (*m/z* 353) at 4.00×10^{-4} mbar Xe pressure.

Table S13. L-CID output and results of linear extrapolation (4.00×10^{-4} mbar Xe pressure).

	***m/z* 77**
E_{0_Linear} (eV)	1.34
E_{0_LCID} (eV)	1.32 ± 0.01
ν_{eff} (cm^{-1})	769 ± 51
a' (cm^{-1})	6170 ± 41

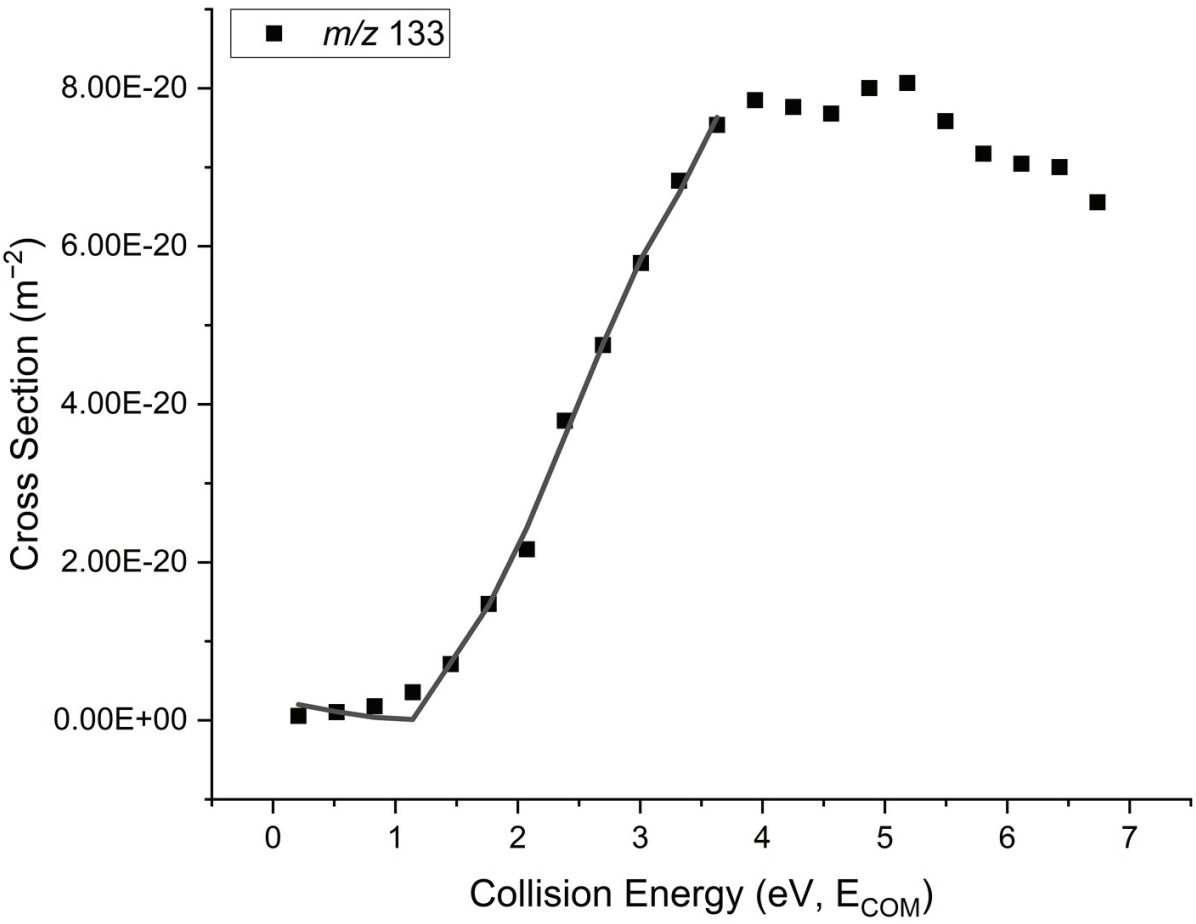

Figure S18. Energy-resolved CID cross sections and L-CID fit for the dissociation of Cs^+(15-crown-5) (*m/z* 353) at 3.00×10^{-4} mbar Xe pressure.

Table S14. L-CID output and results of linear extrapolation (3.00×10^{-4} mbar Xe pressure).

	***m/z* 77**
E_{0_Linear} (eV)	1.54
E_{0_LCID} (eV)	1.40 ± 0.02
ν_{eff} (cm^{-1})	806 ± 44
a' (cm^{-1})	6030 ± 282

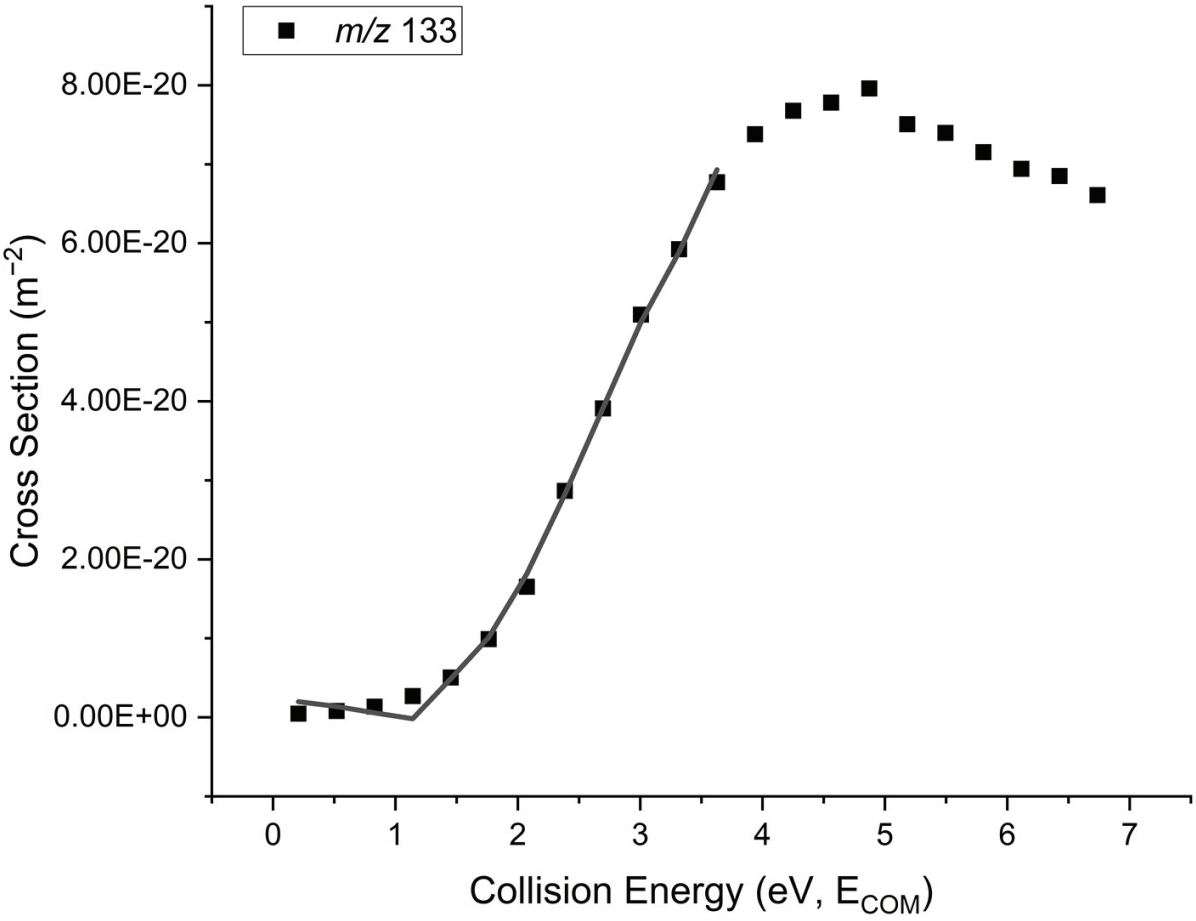

Figure S19. Energy-resolved CID cross sections and L-CID fit for the dissociation of Cs^+(15-crown-5) (*m/z* 353) at 2.00×10^{-4} mbar Xe pressure.

Table S15. L-CID output and results of linear extrapolation (2.00×10^{-4} mbar Xe pressure).

	***m/z* 77**
E_{0_Linear} (eV)	1.70
E_{0_LCID} (eV)	1.45 ± 0.02
ν_{eff} (cm^{-1})	614 ± 69
a' (cm^{-1})	5680 ± 220

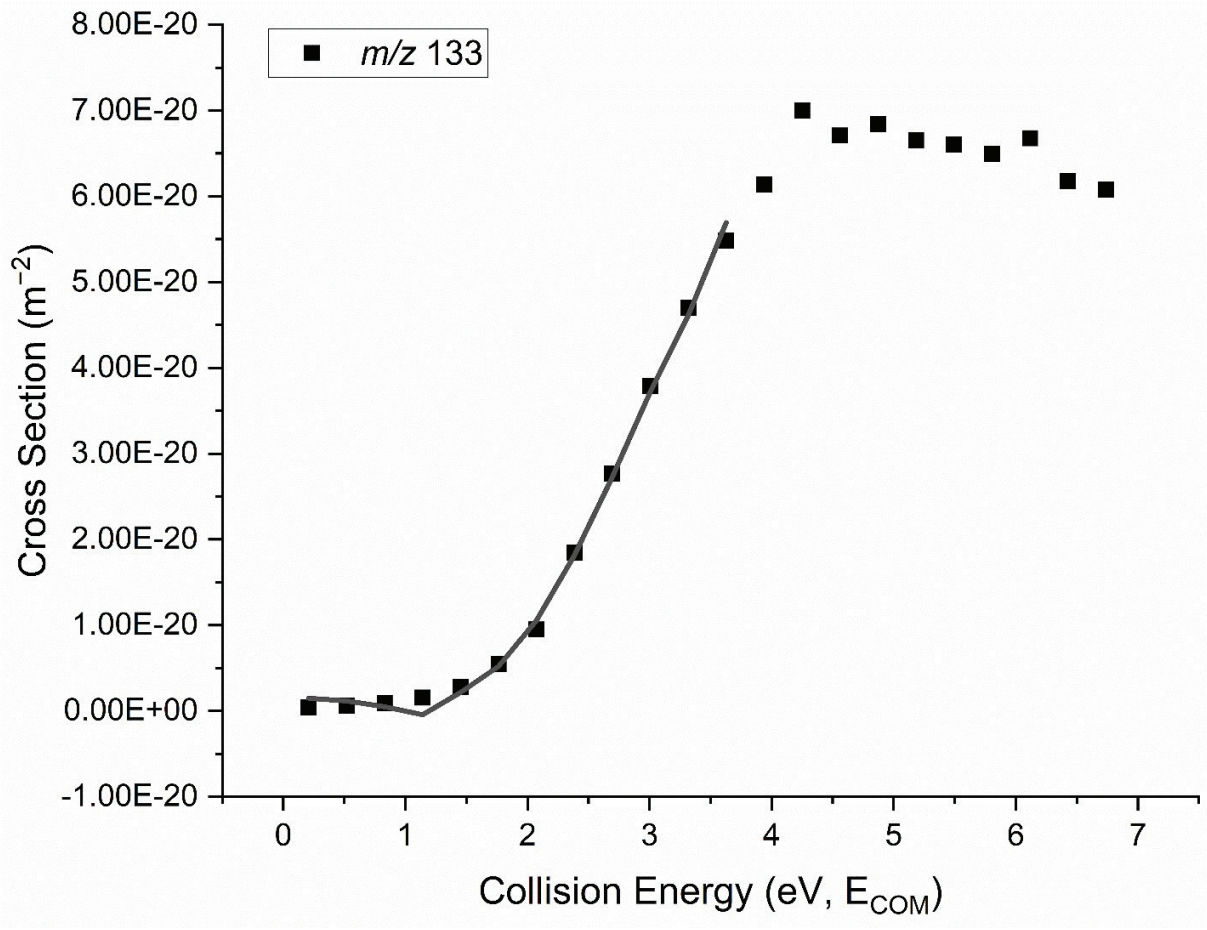

Figure S20. Energy-resolved CID cross sections and L-CID fit for the dissociation of Cs^+(15-crown-5) (*m/z* 353) at 1.00×10^{-4} mbar Xe pressure.

Table S16. L-CID output and results of linear extrapolation (1.00×10^{-4} mbar Xe pressure).

	***m/z* 77**
E_{0_Linear} (eV)	1.94
E_{0_LCID} (eV)	1.51 ± 0.01
ν_{eff} (cm^{-1})	655 ± 43
a' (cm^{-1})	5540 ± 140

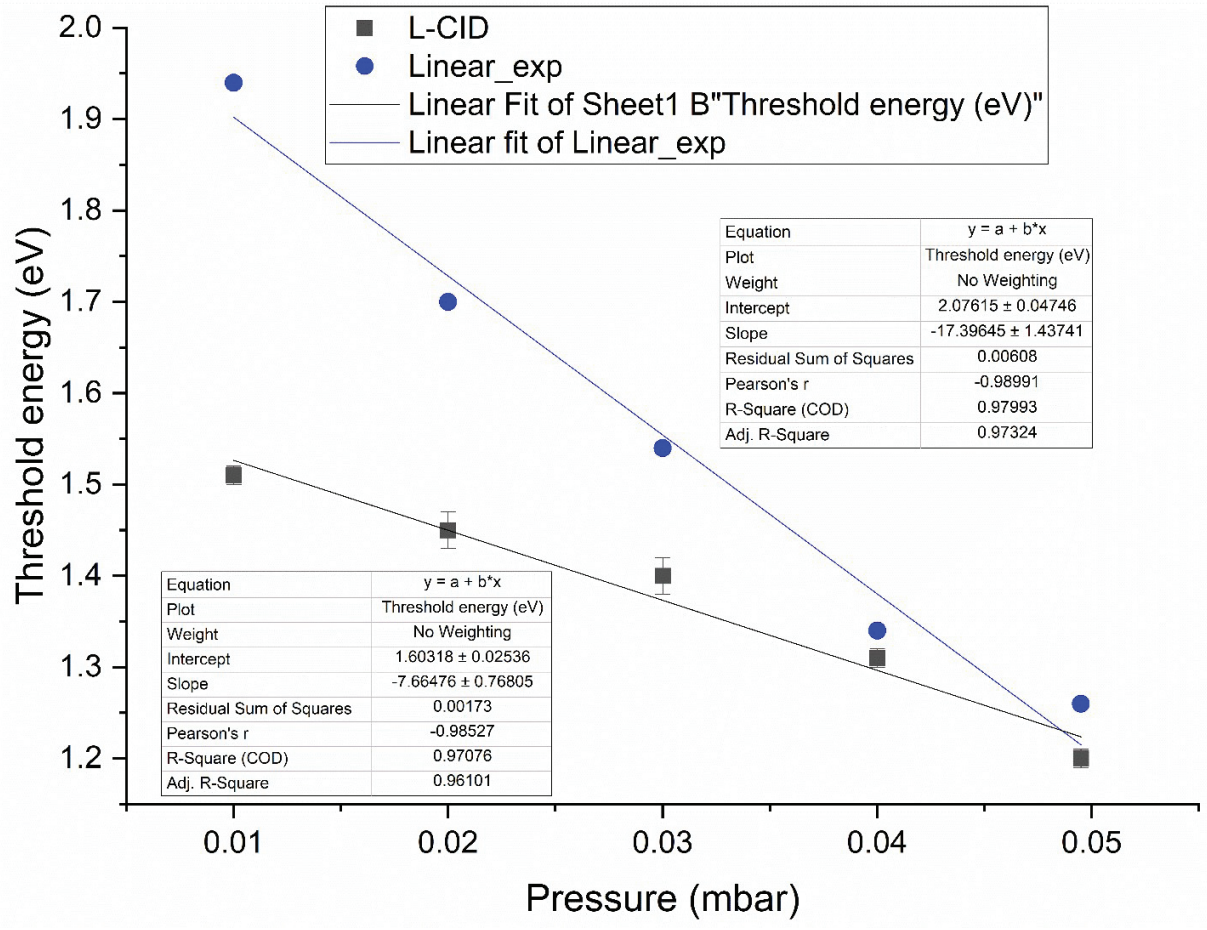

Figure S21. Pressure extrapolation of Cs^+ (*m/z* 133) threshold energies (Linear and L-CID) to zero pressure. The L-CID energies are instrumentally weighed ($w_i = 1/e_i^2$).

Table S17. Threshold energies of Cs^+ (*m/z* 133) extrapolated to vacuum and corresponding literature values.

	***m/z* 77**
E_{0_Linear} **(eV)**	2.08 ± 0.05
E_{0_LCID} **(eV)**	1.60 ± 0.03
$E_{0\_LCID\_CHEN}$ **(eV)**[1]	1.43 ± 0.05
$E_{0\_CRUNCH\_CHEN}$ **(eV)**[1]	1.45
$E_{0\_CRUNCH\_ARMENTROUT}$ **(eV)**[6]	1.04 ± 0.06
$E_{0\_TCID\_ARMENTROUT}$ **(eV)**[7]	1.65 ± 0.10

SI-B. Metastable fragmentation

We calculated peak corresponding to metastable fragmentation in the first field-free region of the TOF as described by Harvey and coworkers[8] and done in a previous study by us.[9] The following expression provides the apparent mass of the metastable ion,

$$M^* = M_p\left[\frac{1+\left(\frac{M_f}{M_p}\right)r}{(1+r)}\right]^2$$

where r is an instrumental parameter describing the relative traversal times of an ion through the field-free and the ion mirror (reflectron) regions. This is calibrated by assigning a metastable peak, M^*, to a specific precursor-fragment ion (M_p-M_f) transition. For our instrument, r = 0.82, calibrated through the spontaneous metastable fragmentation of water clusters, providing known precursor-fragment transitions. The results of this analysis are shown in Figures S22 – S23 and Table S18.

Table S18. Precursor (M_p), fragment (M_f) and calculated metastable (M^*) peak positions with r = 0.82

M_p	M_f	M^*
170.92	142.93	*146.63*
	114.94	*124.20*
	98.94	*112.21*
	58.96	*84.92*
	34.98	*70.37*
142.93	114.94	*118.82*
	98.94	*106.04*
	58.96	*77.28*
	34.98	*62.21*
114.94	58.96	*70.03*
	34.98	*54.18*
58.96	34.98	*39.33*

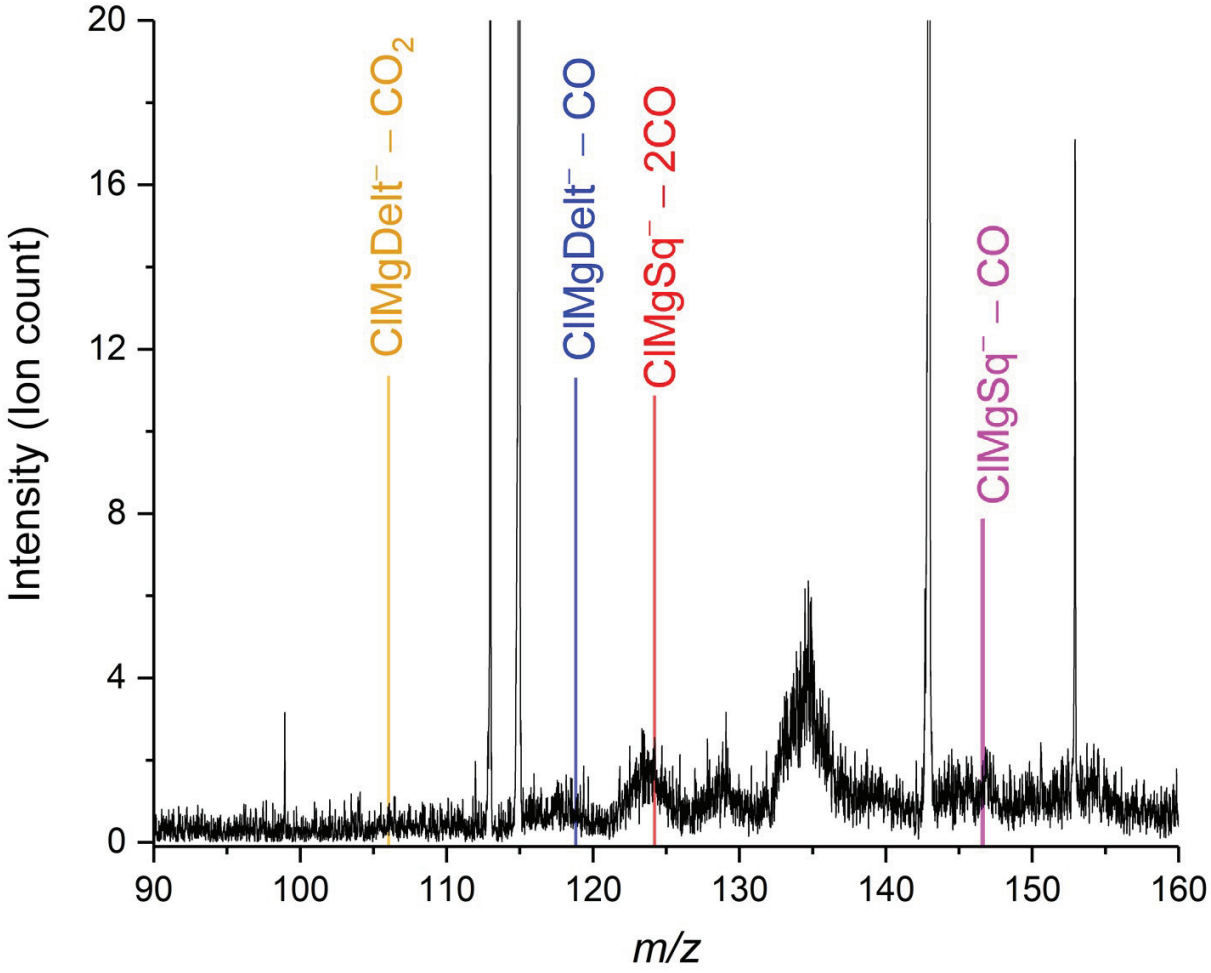

Figure S22. Metastable peaks between *m/z* 90 and 160 from the MSMS of *m/z* 171 ($ClMgSq^-$, $ClMgC_4O_4^-$), combined and averaged three times over collision energies between 90 – 550 kJ/mol in the center of mass frame. The instrumental r-value used in the calculation of the metastable peaks is 0.82.

The strongest metastable signals in Figure S22 correspond to the following dissociation reactions

$$ClMgC_4O_4^- \ (m/z\ 171) \rightarrow ClMgC_3O_3^- \ (m/z\ 143) + CO \qquad \text{(SI-1)}$$

$$ClMgC_4O_4^- \ (m/z\ 171) \rightarrow ClMgC_2O_2^- \ (m/z\ 115) + 2CO. \qquad \text{(SI-2)}$$

In addition, we have indicated the calculated metastable positions for

$$ClMgC_3O_3^- \ (m/z\ 143) \rightarrow ClMgC_2O_2^- \ (m/z\ 115) + CO \quad \text{(SI-3)}$$

$$ClMgC_3O_3^- \ (m/z\ 143) \rightarrow ClMgC_2O^- \ (m/z\ 99) + CO_2. \quad \text{(SI-4)}$$

The signal corresponding to SI-3 can be discerned from the noise-level, while the SI-4 metastable signal is too weak. We speculate that the origin of the two broad peaks at *m/z* 130 and 135 is from metastable fragmentation in the ion-mirror region, but have not made specific assignments.

The analysis was repeated for the MSMS of *m/z* 143 ($ClMgC_3O_3^-$) shown in Figure S23, further strengthening the assignments made above. Unsurprisingly, we do not observe the transitions corresponding to SI-1 and SI-2 here, but we do observe those corresponding to SI-3 and SI-4. The latter has a relatively high metastable signal compared to the focused fragment at *m/z* 99, which could be connected to the high stability of the neutral fragment CO_2.

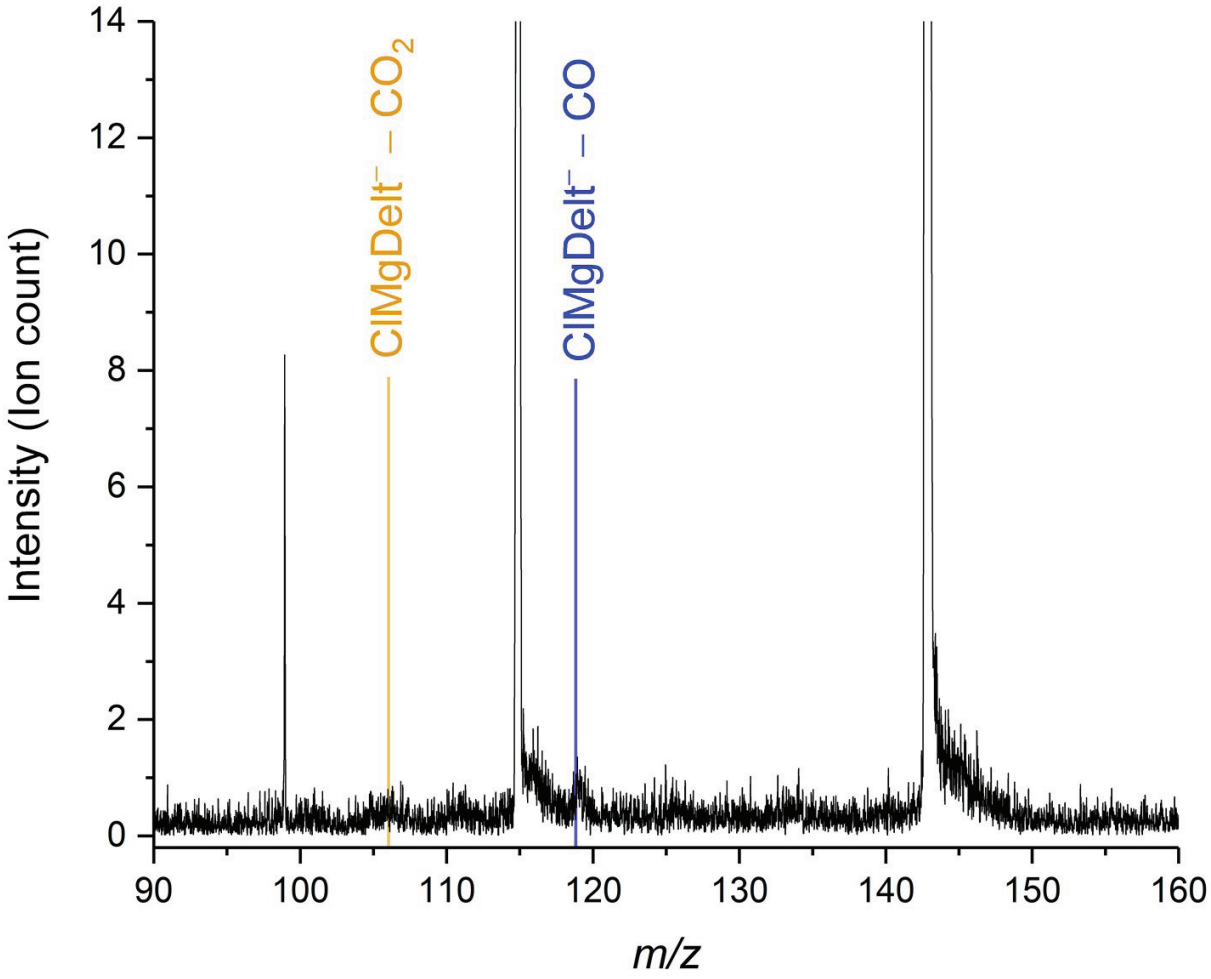

Figure S23. Metastable peaks between *m/z* 90 and 160 from the MSMS of *m/z* 143 ($ClMgDelt^-$, $ClMgC_3O_3^-$), combined and averaged three times over collision energies between 130 – 420 kJ/mol in the center of mass frame. The instrumental r-value used in the calculation of the metastable peaks is 0.82.

SI-C. G4 (0 K) $ClMgC_4O_4^-$ singlet potential energy surface

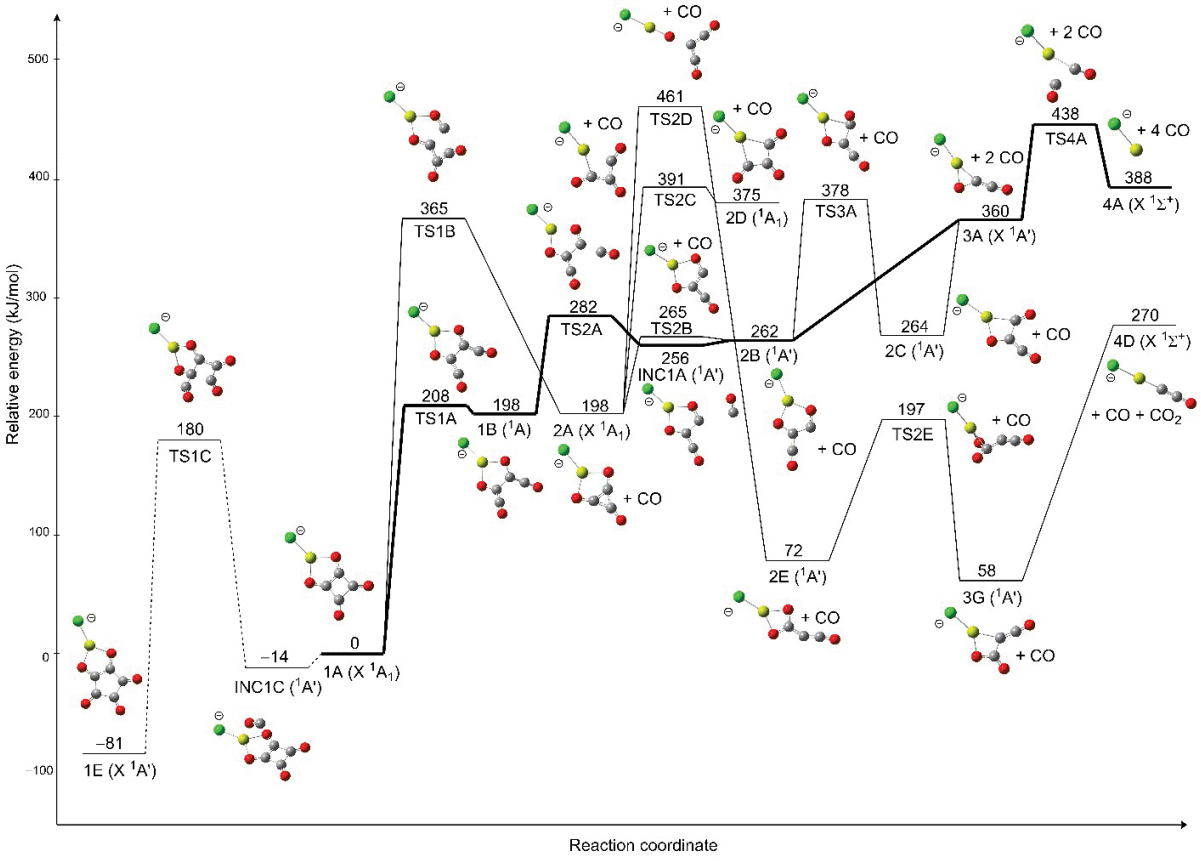

Figure S24. G4 (0 K) singlet PES for the dissociation of $ClMgC_4O_4^-$ and the formation of magnesium chloride croconate (1E) denoted by dashed lines.

SI-D. G4 (0 K) $ClMgC_4O_4^-$ triplet potential energy surface

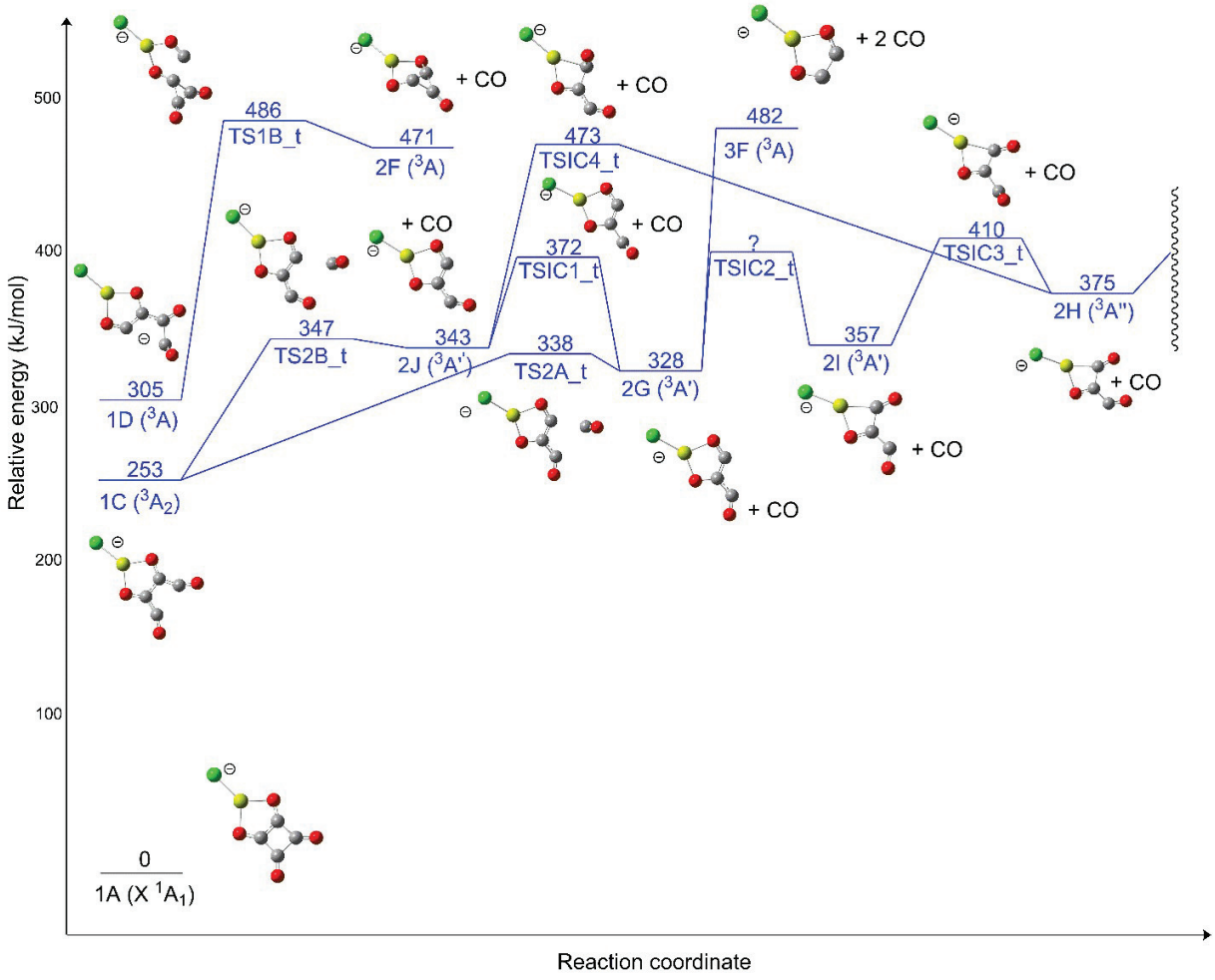

Figure S25. Part one of the G4 (0 K) triplet PES for the dissociation of $ClMgC_4O_4^-$.

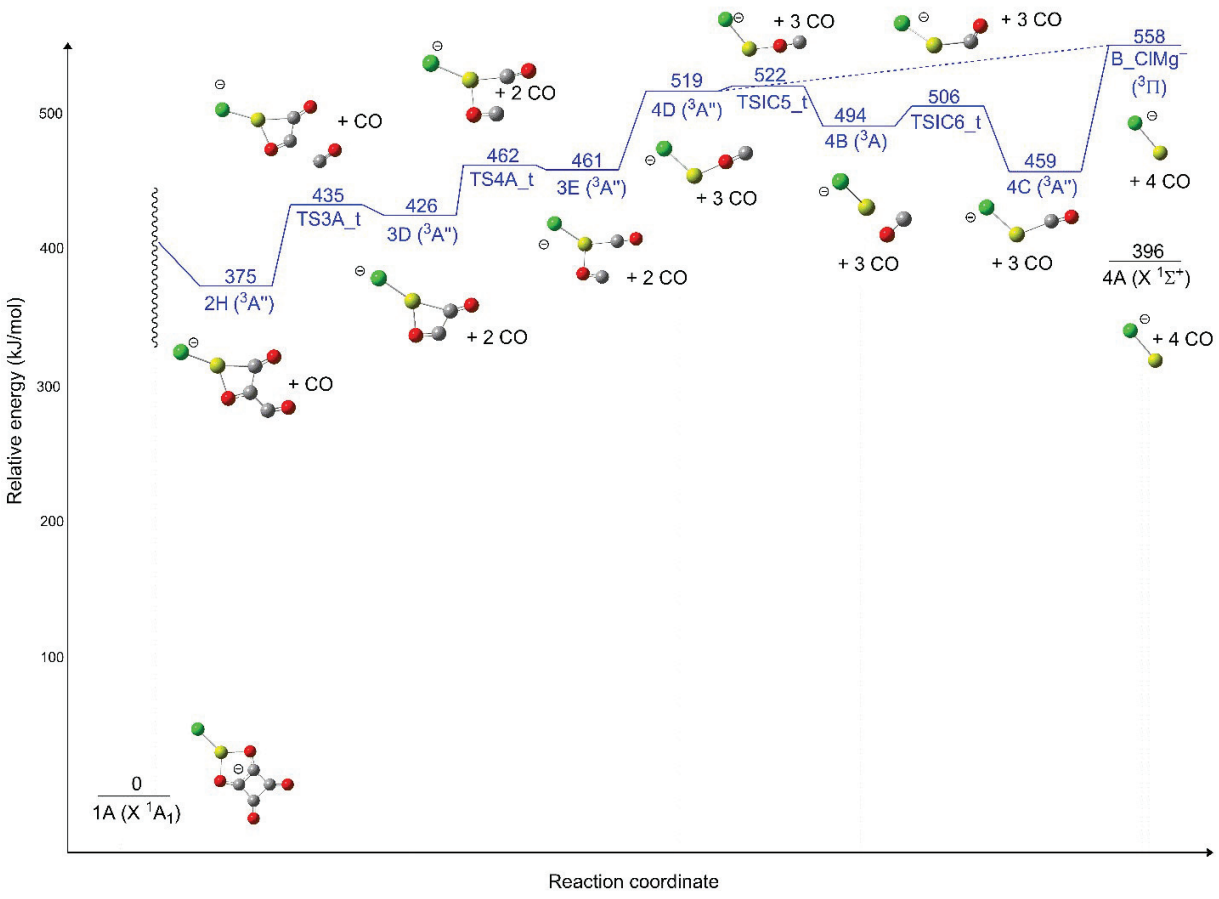

Figure S26. Part two of the G4 (0 K) triplet PES for the dissociation of $ClMgC_4O_4^-$.

SI-E. Optimized geometries and G4 (0 K) energies

Singlet PES

CO

Center Number	Atomic Number	Atomic Type	Coordinates (Angstroms) X	Y	Z
1	8	0	-1.804635	0.161929	-0.002120
2	6	0	-2.935546	0.161929	-0.002120

G4 (0 K)= -113.289425

CO_2

Center Number	Atomic Number	Atomic Type	Coordinates (Angstroms) X	Y	Z
1	6	0	0.000000	0.000000	0.000000
2	8	0	0.000000	0.000000	1.162879
3	8	0	0.000000	0.000000	-1.162879

G4(0 K)= -188.535267

1A

Center Number	Atomic Number	Atomic Type	Coordinates (Angstroms) X	Y	Z
1	8	0	-4.783019	-8.295918	-1.296009
2	8	0	-7.330509	-9.952772	0.284349
3	8	0	-8.456376	-10.920653	-2.175016
4	8	0	-6.068524	-9.401037	-4.104092
5	6	0	-6.838649	-9.698325	-0.897928
6	6	0	-6.351271	-9.510336	-2.929011
7	6	0	-5.738550	-8.983595	-1.590572
8	6	0	-7.389469	-10.171852	-2.101150
9	12	0	-8.853585	-11.054676	-0.262593
10	17	0	-10.474229	-12.097750	0.889818

G4 (0 K)= -1113.416747

1B

Center Number	Atomic Number	Atomic Type	Coordinates (Angstroms) X	Y	Z
1	6	0	1.003923	0.711277	0.186470
2	8	0	-0.139274	1.202480	0.734488
3	6	0	0.991049	-0.729326	-0.185634
4	8	0	-0.160389	-1.199774	-0.734609
5	6	0	2.040310	-1.454272	0.177438
6	8	0	3.001620	-2.078268	0.477469
7	6	0	2.066428	1.417123	-0.175721
8	8	0	3.039118	2.023626	-0.474945
9	17	0	-3.707298	0.033529	-0.001545
10	12	0	-1.450045	0.013113	-0.000603

G4 (0 K)= -1113.341335

1E

Center Number	Atomic Number	Atomic Type	Coordinates (Angstroms) X	Y	Z
1	6	0	2.693907	-0.000003	-0.000093
2	6	0	1.794751	-1.236290	0.000028
3	6	0	0.428350	-0.706764	0.000195
4	6	0	0.428353	0.706768	0.000195
5	6	0	1.794756	1.236288	0.000028
6	8	0	-0.693721	-1.370214	0.000339
7	8	0	-0.693715	1.370223	0.000339
8	8	0	2.166652	2.397731	-0.000030
9	8	0	3.905448	-0.000005	-0.000252
10	8	0	2.166642	-2.397734	-0.000030
11	12	0	-2.065339	0.000007	0.000504
12	17	0	-4.301745	0.000012	0.000780

G4(0 K)= -1226.737095

2A

Center Number	Atomic Number	Atomic Type	Coordinates (Angstroms) X	Y	Z
1	8	0	-7.307236	-9.814109	0.375905
2	8	0	-8.417444	-11.028977	-2.295036
3	8	0	-5.336506	-8.807006	-2.743825
4	6	0	-6.905820	-9.700130	-0.882982
5	6	0	-6.218714	-9.370922	-2.120629
6	6	0	-7.389254	-10.229138	-2.046029
7	12	0	-8.748155	-10.987764	-0.333823
8	17	0	-10.382134	-12.032219	0.820427

G4 (0 K)= -1000.051874

2B

Center Number	Atomic Number	Atomic Type	Coordinates (Angstroms) X	Y	Z
1	6	0	-0.087202	-2.096198	-1.147287
2	8	0	-0.133796	-3.188411	-1.571651
3	6	0	0.030008	-0.981105	0.849319
4	8	0	0.084475	0.219481	1.388718
5	6	0	-0.032824	-0.862927	-0.628488
6	8	0	-0.035946	0.286273	-1.352680
7	12	0	0.058333	1.587789	0.023051
8	17	0	0.116095	3.852434	0.030786

G4 (0 K)= -1000.027669

2C

Center Number	Atomic Number	Atomic Type	Coordinates (Angstroms) X	Y	Z
1	6	0	-2.441987	-1.080218	-0.043508
2	8	0	-3.619215	-1.210990	-0.066585
3	6	0	-1.004280	0.853341	-0.005017
4	8	0	-1.847041	1.721778	-0.015947
5	6	0	-1.192819	-0.670812	-0.017448
6	8	0	-0.023669	-1.372206	0.000640
7	12	0	1.104686	0.168002	0.030981
8	17	0	3.344444	0.569630	0.075774

G4 (0 K)= -1000.026735

2D

Center Number	Atomic Number	Atomic Type	Coordinates (Angstroms) X	Y	Z
1	6	0	1.008018	-1.706959	0.467325
2	8	0	1.964633	-2.248125	0.960887
3	6	0	0.390636	-1.699291	-0.889593
4	8	0	0.747048	-2.295448	-1.905015
5	6	0	-0.769887	-0.783134	-0.699098
6	8	0	-1.650019	-0.369899	-1.410563
7	12	0	-0.431577	-0.324009	1.452899
8	17	0	-1.088777	0.775264	3.325270

G4 (0 K)= -999.984644

2E

Center Number	Atomic Number	Atomic Type	Coordinates (Angstroms) X	Y	Z
1	8	0	0.275208	-0.929512	-0.000000
2	8	0	0.054246	1.283056	0.000000
3	8	0	4.562267	-0.411792	0.000000
4	6	0	0.885179	0.250263	-0.000000
5	6	0	3.410921	-0.081830	0.000000
6	6	0	2.249981	0.406085	-0.000000
7	12	0	-1.395554	0.021261	0.000000
8	17	0	-3.627271	-0.190368	0.000000

G4(0 K)= -1000.099991

3A

Center Number	Atomic Number	Atomic Type	Coordinates (Angstroms) X	Y	Z
1	8	0	-5.748239	-8.991157	-0.396043
2	8	0	-8.504720	-10.809861	-2.070600
3	6	0	-6.705304	-9.630948	-0.752703
4	6	0	-7.757309	-10.341187	-0.956318
5	12	0	-9.377958	-11.462076	-0.548228
6	17	0	-11.063400	-12.645908	0.365531

G4 (0 K)= -886.700913

3G

Center Number	Atomic Number	Atomic Type	Coordinates (Angstroms) X	Y	Z
1	8	0	-7.224149	-9.501035	-0.081727
2	8	0	-7.521886	-10.932590	-1.802547
3	8	0	-4.357863	-7.366628	-1.808303
4	6	0	-6.942748	-9.895331	-1.199628
5	6	0	-5.107854	-8.274807	-1.905750
6	6	0	-5.890311	-9.278520	-2.095715
7	12	0	-6.483734	-10.781989	-3.405546
8	17	0	-6.289816	-11.828558	-5.392886

G4(0 K)= -1000.105378

4A

Center Number	Atomic Number	Atomic Type	Coordinates (Angstroms) X	Y	Z
1	12	0	-0.058895	1.442929	0.442729
2	17	0	0.992001	2.812604	-1.238758

G4 (0 K)= -660.111153

4D

Center Number	Atomic Number	Atomic Type	Coordinates (Angstroms) X	Y	Z
1	8	0	0.000000	0.000000	-3.824627
2	6	0	0.000000	0.000000	-1.348044
3	6	0	0.000000	0.000000	-2.619200
4	12	0	0.000000	0.000000	0.552145
5	17	0	0.000000	0.000000	2.810278

G4 (0 K)= -811.489181

INC1A

Center Number	Atomic Number	Atomic Type	Coordinates (Angstroms) X	Y	Z
1	6	0	-2.039063	-1.752948	0.000000
2	8	0	-3.070401	-2.305372	0.000000
3	6	0	-1.123976	0.354720	0.000000
4	8	0	-0.000835	1.022966	0.000000
5	6	0	-0.869757	-1.096390	0.000000
6	8	0	0.349796	-1.692173	0.000000
7	12	0	1.513427	-0.192652	0.000000
8	17	0	3.757123	0.059620	0.000000
9	6	0	-3.005861	2.370830	0.000000
10	8	0	-2.254491	3.231392	0.000000

G4 (0 K)= -1113.319085

INC1C

Center Number	Atomic Number	Atomic Type	Coordinates (Angstroms) X	Y	Z
1	8	0	-4.781684	-8.341947	-1.266281
2	8	0	-7.219223	-10.076881	0.392033
3	8	0	-8.662150	-10.691434	-2.020560
4	8	0	-6.427647	-9.042975	-4.018351
5	6	0	-6.846144	-9.710357	-0.799908
6	6	0	-6.579598	-9.288414	-2.839984
7	6	0	-5.795466	-8.954447	-1.528905
8	6	0	-7.552965	-10.011397	-1.981722
9	12	0	-8.939332	-10.905055	-0.084305
10	17	0	-10.468507	-12.033074	1.117604
11	6	0	-9.380482	-7.546865	-0.675884
12	8	0	-9.799119	-8.481672	-0.187384

G4(0 K)= -1226.711648

TS1A

Center Number	Atomic Number	Atomic Type	Coordinates (Angstroms) X	Y	Z
1	6	0	-0.918528	-0.711647	0.172406
2	8	0	0.191512	-1.227426	0.722632
3	6	0	-0.918528	0.711647	-0.172406
4	8	0	0.191512	1.227426	-0.722632
5	6	0	-2.134268	1.243605	0.068372
6	8	0	-3.024354	1.929843	0.458588
7	6	0	-2.134268	-1.243605	-0.068372
8	8	0	-3.024355	-1.929843	-0.458588
9	17	0	3.750389	-0.000000	0.000000
10	12	0	1.497567	0.000000	0.000000

G4 (0 K)= -1113.337434

TS1B

Center Number	Atomic Number	Atomic Type	Coordinates (Angstroms) X	Y	Z
1	6	0	-0.873648	0.820230	0.033040
2	8	0	0.306965	1.395889	-0.312174
3	6	0	-1.004042	-0.579944	0.506023
4	8	0	0.162619	-1.144920	0.641760
5	6	0	-2.233900	-1.699263	-0.584696
6	8	0	-3.274258	-2.049206	-0.189318
7	6	0	-2.030646	1.490332	0.053490
8	8	0	-3.058452	2.051636	0.066601
9	17	0	3.815403	-0.150700	-0.122889
10	12	0	1.574716	0.028882	0.032251

G4 (0 K)= -1113.309172

TS1C

Center Number	Atomic Number	Atomic Type	Coordinates (Angstroms) X	Y	Z
1	8	0	-5.257081	-8.241925	-1.072012
2	8	0	-7.730882	-9.979323	0.492177
3	8	0	-8.819981	-10.849503	-1.984113
4	8	0	-6.468729	-9.412863	-3.870122
5	6	0	-7.621255	-9.225336	-0.625370
6	6	0	-6.870467	-9.337812	-2.715150
7	6	0	-6.281618	-8.737941	-1.455627
8	6	0	-7.936393	-9.906775	-1.918085
9	12	0	-8.809845	-11.445957	-0.109691
10	17	0	-9.771092	-13.231632	0.847522
11	6	0	-8.341688	-7.907930	-0.582816
12	8	0	-8.543294	-6.807507	-0.900357

G4 (0 K)= -1226.637653

TS2A

Center Number	Atomic Number	Atomic Type	Coordinates (Angstroms) X	Y	Z
1	6	0	-0.873648	0.820230	0.033040
2	8	0	0.306965	1.395889	-0.312174
3	6	0	-1.004042	-0.579944	0.506023
4	8	0	0.162619	-1.144920	0.641760
5	6	0	-2.233900	-1.699263	-0.584696
6	8	0	-3.274258	-2.049206	-0.189318
7	6	0	-2.030646	1.490332	0.053490
8	8	0	-3.058452	2.051636	0.066601
9	17	0	3.815403	-0.150700	-0.122889
10	12	0	1.574716	0.028882	0.032251

G4 (0 K)= -1113.309172

TS2B

Center Number	Atomic Number	Atomic Type	Coordinates (Angstroms) X	Y	Z
1	8	0	-1.662766	0.041496	-0.000000
2	8	0	1.120090	-0.509361	-0.000000
3	8	0	0.267509	-3.944331	-0.000000
4	6	0	-1.288857	-1.232519	-0.000000
5	6	0	0.149130	-2.775941	-0.000000
6	6	0	0.123376	-1.421532	-0.000000
7	12	0	0.000081	1.043944	0.000000
8	17	0	0.488095	3.255902	0.000000

G4 (0 K)= -1000.026288

TS2C

Center Number	Atomic Number	Atomic Type	Coordinates (Angstroms) X	Y	Z
1	6	0	0.918337	-1.697051	0.296948
2	8	0	1.736251	-2.017179	1.152368
3	6	0	0.463034	-1.815909	-1.082277
4	8	0	0.807078	-2.407564	-2.111694
5	6	0	-0.584985	-0.907554	-0.663964
6	8	0	-1.599563	-0.243511	-0.913579
7	12	0	-0.464820	-0.321158	1.387283
8	17	0	-1.105296	0.758378	3.237101

G4 (0 K)= -999.978400

TS2D

Center Number	Atomic Number	Atomic Type	Coordinates (Angstroms) X	Y	Z
1	8	0	-7.652162	-8.786852	0.164180
2	8	0	-6.093175	-9.916667	-3.099784
3	8	0	-3.657051	-7.859547	-1.030348
4	6	0	-6.734540	-8.826451	-0.583950
5	6	0	-4.720587	-8.358419	-1.185041
6	6	0	-5.829644	-8.972797	-1.522953
7	12	0	-6.180449	-10.778630	-4.652422
8	17	0	-6.255618	-11.868960	-6.642282

G4(0 K)= -999.951598

TS2E

Center Number	Atomic Number	Atomic Type	Coordinates (Angstroms) X	Y	Z
1	8	0	-7.767004	-9.618933	-0.370434
2	8	0	-7.547121	-11.235648	-1.895125
3	8	0	-4.611394	-7.496616	-2.385363
4	6	0	-7.113732	-10.089259	-1.343449
5	6	0	-5.432212	-8.346226	-2.213369
6	6	0	-6.267134	-9.301979	-2.177450
7	12	0	-8.770314	-9.926789	-2.575202
8	17	0	-10.614729	-9.338641	-3.671011

G4(0 K)= -1000.052407

TS3A

Center Number	Atomic Number	Atomic Type	Coordinates (Angstroms) X	Y	Z
1	6	0	-2.817745	-0.351495	-0.076316
2	8	0	-4.006910	-0.263744	-0.193515
3	6	0	-0.759591	1.051380	0.619387
4	8	0	-0.254929	1.689367	-0.317307
5	6	0	-1.543156	-0.275250	0.125824
6	8	0	-0.505602	-1.161448	0.029494
7	12	0	1.060801	-0.083695	0.132853
8	17	0	3.293380	-0.212915	-0.091238

G4 (0 K)= -999.983457

TS4A

Center Number	Atomic Number	Atomic Type	Coordinates (Angstroms) X	Y	Z
1	6	0	-1.678455	-0.669996	0.344752
2	8	0	-2.020541	-1.620063	-0.270132
3	6	0	-1.480292	1.030942	-0.247728
4	8	0	-2.276220	1.900752	-0.134529
5	12	0	0.528465	0.233852	0.591377
6	17	0	2.535925	-0.529811	-0.323272

G4 (0 K)= -886.670962

Triplet PES

1C

Center Number	Atomic Number	Atomic Type	Coordinates (Angstroms) X	Y	Z
1	8	0	-4.690309	-8.210133	-0.934837
2	8	0	-7.321351	-9.953905	0.233366
3	8	0	-8.419643	-10.889733	-2.155867
4	8	0	-6.276506	-9.561693	-4.385462
5	6	0	-6.758157	-9.647025	-0.935294
6	6	0	-6.571784	-9.683590	-3.233129
7	6	0	-5.638270	-8.888164	-1.202353
8	6	0	-7.324545	-10.129631	-2.167419
9	12	0	-8.829089	-11.038599	-0.279018
10	17	0	-10.454526	-12.084441	0.877811

G4 (0 K)= -1113.321382

1D

Center Number	Atomic Number	Atomic Type	Coordinates (Angstroms) X	Y	Z
1	8	0	2.792470	1.051170	-1.168891
2	8	0	-0.767623	-1.271759	0.932522
3	8	0	-0.146561	0.681202	-0.910208
4	8	0	3.871031	-0.264941	1.371224
5	6	0	0.437083	-0.966881	0.656172
6	6	0	3.126554	-0.591482	0.505342
7	6	0	2.224376	0.286244	-0.398594
8	6	0	0.829248	0.000957	-0.255661
9	12	0	-1.764155	-0.027025	-0.242851
10	17	0	-3.981029	0.218016	-0.493406

G4(0 K)= -1113.301923

2F

Center Number	Atomic Number	Atomic Type	Coordinates (Angstroms) X	Y	Z
1	8	0	-7.125756	-9.989199	0.277979
2	8	0	-8.304066	-11.089367	-2.275301
3	8	0	-5.253233	-9.074159	-2.672029
4	6	0	-7.211776	-9.247295	-0.845665
5	6	0	-6.261640	-9.429918	-2.081551
6	6	0	-7.518000	-10.079869	-2.100838
7	12	0	-8.694164	-10.985289	-0.310954
8	17	0	-10.336671	-12.075148	0.782381

G4 (0 K)= -999.949647

2G

Center Number	Atomic Number	Atomic Type	Coordinates (Angstroms) X	Y	Z
1	6	0	-0.046732	2.992124	0.000000
2	8	0	0.921430	3.714334	0.000000
3	6	0	-1.459725	1.027910	0.000000
4	8	0	-1.732961	-0.218774	0.000000
5	6	0	-0.194193	1.577488	0.000000
6	8	0	0.868301	0.690340	0.000000
7	12	0	0.075571	-1.014019	0.000000
8	17	0	0.650653	-3.194063	-0.000000

G4 (0 K)= -1000.003886

2H

Center Number	Atomic Number	Atomic Type	Coordinates (Angstroms) X	Y	Z
1	6	0	0.981514	-2.599149	0.002986
2	8	0	0.348433	-3.626070	0.001310
3	6	0	-0.986836	-0.856387	-0.002821
4	8	0	-1.910054	-1.644426	-0.005351
5	6	0	0.480391	-1.234628	0.001397
6	8	0	1.293510	-0.205705	0.003584
7	12	0	-0.139098	1.160134	-0.000654
8	17	0	0.029170	3.428535	-0.000449

G4 (0 K)= -999.986576

2I

Center Number	Atomic Number	Atomic Type	Coordinates (Angstroms) X	Y	Z
1	6	0	2.680515	-0.588608	-0.354766
2	8	0	3.205776	-1.662488	-0.511926
3	6	0	0.777713	1.146565	-0.025813
4	8	0	1.510833	2.121765	0.030790
5	6	0	1.270379	-0.255929	-0.217308
6	8	0	0.318418	-1.163093	-0.250748
7	12	0	-1.157002	0.146235	0.000291
8	17	0	-3.404185	-0.182538	0.123538

G4(0 K)= -999.984404

2J

Center Number	Atomic Number	Atomic Type	Coordinates (Angstroms) X	Y	Z
1	6	0	-0.776745	0.941916	0.002245
2	8	0	0.474627	1.524030	0.063092
3	6	0	-0.822208	-0.432006	-0.078386
4	8	0	0.183743	-1.221353	-0.102357
5	6	0	-1.955034	1.745435	0.023304
6	8	0	-3.135079	1.485459	-0.017324
7	17	0	3.888388	-0.318784	0.030202
8	12	0	1.669146	0.076299	0.005039

G4 (0 K)= -999.998314

3D

Center Number	Atomic Number	Atomic Type	Coordinates (Angstroms) X	Y	Z
1	6	0	1.796148	0.496919	0.000000
2	8	0	2.683728	1.335070	0.000000
3	6	0	1.801627	-0.964478	0.000000
4	8	0	0.709609	-1.648786	0.000000
5	12	0	-0.345883	0.025279	0.000000
6	17	0	-2.620564	0.284813	0.000000

G4 (0 K)= -886.678168

3E

Center Number	Atomic Number	Atomic Type	Coordinates (Angstroms) X	Y	Z
1	6	0	1.616855	0.918365	0.081700
2	8	0	2.615219	1.529092	0.116896
3	6	0	1.735521	-1.506220	0.083684
4	8	0	0.572700	-1.803202	0.040124
5	12	0	-0.238166	0.058270	-0.593803
6	17	0	-2.360258	0.295999	0.289639

G4(0 K)= -886.657801

3F

Center Number	Atomic Number	Atomic Type	Coordinates (Angstroms) X	Y	Z
1	8	0	0.036274	1.369884	0.202394
2	8	0	-0.059349	-1.387360	0.239377
3	6	0	-0.098730	0.734296	-0.975664
4	6	0	0.106317	-0.704937	-0.856374
5	12	0	0.024782	0.031116	1.548961
6	17	0	-0.009293	-0.042998	3.812127

G4 (0 K)= -886.656641

4B

Center Number	Atomic Number	Atomic Type	Coordinates (Angstroms) X	Y	Z
1	6	0	2.043455	-0.452419	0.671385
2	8	0	1.901949	-0.351104	-0.536169
3	12	0	0.244817	0.865493	0.013939
4	17	0	-1.780178	-0.286909	0.004739

G4 (0 K)= -773.363545

4C

Center Number	Atomic Number	Atomic Type	Coordinates (Angstroms) X	Y	Z
1	6	0	1.723584	-0.220853	-0.041277
2	8	0	2.803600	-0.685306	-0.083932
3	12	0	-0.065144	0.925663	-0.012788
4	17	0	-2.051996	-0.244443	0.291893

G4 (0 K)= -773.376632

4D

Center Number	Atomic Number	Atomic Type	Coordinates (Angstroms) X	Y	Z
1	6	0	-2.833757	-0.490514	-0.000000
2	8	0	-1.738934	0.059456	-0.000000
3	12	0	-0.000069	0.928775	-0.000000
4	17	0	1.818508	-0.510469	0.000000

G4 (0 K)= -773.354250

B_ClMg

Center Number	Atomic Number	Atomic Type	Coordinates (Angstroms) X	Y	Z
1	12	0	-2.684820	0.334925	-1.890217
2	17	0	-3.500909	0.575753	-4.060963

G4 (0 K)= -660.049294

TS1B_t

Center Number	Atomic Number	Atomic Type	Coordinates (Angstroms) X	Y	Z
1	8	0	3.102466	-1.146241	-1.417539
2	8	0	-0.764036	-1.134228	1.443897
3	8	0	0.067277	0.541162	-0.700023
4	8	0	3.089185	1.653078	0.784835
5	6	0	0.458032	-1.160975	1.471889
6	6	0	2.454301	0.820679	0.148970
7	6	0	2.459500	-0.336170	-0.761254
8	6	0	1.195147	0.108903	-0.144333
9	12	0	-1.554685	-0.009538	0.009288
10	17	0	-3.748177	0.263089	-0.334180

G4 (0 K)= -1113.233171

TS2A_t

Center Number	Atomic Number	Atomic Type	Coordinates (Angstroms) X	Y	Z
1	6	0	0.873927	0.655607	0.066305
2	8	0	-0.305519	1.347436	-0.087184
3	6	0	0.785474	-0.712986	0.207366
4	8	0	-0.282881	-1.399916	0.238473
5	6	0	3.059212	-1.362681	0.429044
6	8	0	3.525335	-1.805977	-0.523028
7	6	0	2.171351	1.226455	0.070072
8	8	0	2.622259	2.336228	-0.031321
9	17	0	-3.885078	-0.174092	-0.086613
10	12	0	-1.647250	0.024918	0.005015

G4 (0 K)= -1113.289940

TS2B_t

Center Number	Atomic Number	Atomic Type	Coordinates (Angstroms) X	Y	Z
1	6	0	-0.784180	0.907044	-0.001520
2	8	0	0.444124	1.522975	0.078871
3	6	0	-0.780646	-0.469192	-0.017126
4	8	0	0.242450	-1.228954	0.000150
5	6	0	-2.854667	-1.531594	-0.485740
6	8	0	-3.348613	-1.967193	0.450402
7	6	0	-1.989115	1.666851	-0.078439
8	8	0	-3.154787	1.351225	-0.123845
9	17	0	3.917102	-0.204667	0.203433
10	12	0	1.693089	0.116440	0.097902

G4 (0 K)= -1113.286591

TS3A_t

Center Number	Atomic Number	Atomic Type	Coordinates (Angstroms) X	Y	Z
1	6	0	-0.788027	-3.235941	-0.000059
2	8	0	0.215480	-3.806732	-0.000027
3	6	0	1.021711	-0.691766	0.000036
4	8	0	2.038362	-1.365702	0.000068
5	6	0	-0.383034	-1.065882	-0.000022
6	8	0	-1.330088	-0.202077	-0.000048
7	12	0	0.017050	1.263531	0.000020
8	17	0	-0.302014	3.517413	0.000033

G4 (0 K)= -999.964566

TS4A_t

Center Number	Atomic Number	Atomic Type	Coordinates (Angstroms) X	Y	Z
1	6	0	1.684955	0.782587	0.082088
2	8	0	2.682509	1.421510	0.045968
3	6	0	1.780411	-1.306105	-0.001684
4	8	0	0.640648	-1.729477	0.062753
5	12	0	-0.261580	0.099029	-0.329779
6	17	0	-2.502280	0.261273	0.140654

G4(0 K)= -886.657325

TSIC1_t

Center Number	Atomic Number	Atomic Type	Coordinates (Angstroms) X	Y	Z
1	6	0	0.205405	1.497044	0.139238
2	8	0	1.095898	0.449619	0.131940
3	6	0	-1.130001	1.226070	-0.002528
4	8	0	-1.650178	0.035149	-0.049760
5	6	0	0.766920	2.836499	-0.004365
6	8	0	1.185755	3.666959	0.750731
7	17	0	0.216865	-3.299942	-0.076697
8	12	0	-0.040214	-1.058850	-0.007342

G4 (0 K)= -999.986876

TSIC2_t

n.a.

TSIC3_t

Center Number	Atomic Number	Atomic Type	Coordinates (Angstroms) X	Y	Z
1	6	0	-0.384292	-2.764351	-0.326621
2	8	0	-0.625537	-3.530665	0.552995
3	6	0	1.183124	-0.683285	-0.104562
4	8	0	2.252312	-1.295191	-0.211132
5	6	0	-0.145659	-1.262057	-0.111680
6	8	0	-1.196342	-0.485280	-0.018905
7	12	0	-0.019390	1.116006	0.042238
8	17	0	-0.574774	3.317668	0.177667

G4 (0 K)= -999.972844

TSIC4_t

Center Number	Atomic Number	Atomic Type	Coordinates (Angstroms) X	Y	Z
1	6	0	0.357861	1.595570	0.038195
2	8	0	1.168474	0.546899	0.054776
3	6	0	-1.062049	1.036214	-0.089134
4	8	0	-1.589879	0.636230	0.975022
5	6	0	0.807697	2.935591	-0.012458
6	8	0	0.179945	3.981449	-0.057415
7	17	0	-0.114464	-3.150928	0.106385
8	12	0	-0.132016	-0.907881	0.016335

G4 (0 K)= -999.948828

TSIC5_t

Center Number	Atomic Number	Atomic Type	Coordinates (Angstroms) X	Y	Z
1	6	0	2.608779	-0.632640	0.531596
2	8	0	1.665281	-0.233214	-0.179947
3	12	0	0.077808	0.884025	-0.100519
4	17	0	-1.941824	-0.243111	-0.097237

G4 (0 K)= -773.352323

TSIC6_t

Center Number	Atomic Number	Atomic Type	Coordinates (Angstroms) X	Y	Z
1	6	0	1.926881	-0.320302	0.536834
2	8	0	2.360246	-0.542559	-0.568996
3	12	0	0.082909	0.867471	0.160173
4	17	0	-1.959993	-0.229550	0.025882

G4 (0 K)= -773.358559

^{1}ClMgCO^{-}

Center Number	Atomic Number	Atomic Type	Coordinates (Angstroms) X	Y	Z
1	6	0	2.802740	0.662951	-0.000000
2	8	0	3.741089	0.017820	-0.000000
3	12	0	-0.405933	-1.068977	-0.000000
4	17	0	-2.163548	0.563681	-0.000000

G4 (0 K)= -773.400143

^{3}ClMg(η^{2}-CO)$^{-}$ (4B)

Center Number	Atomic Number	Atomic Type	Coordinates (Angstroms) X	Y	Z
1	6	0	2.043455	-0.452419	0.671385
2	8	0	1.901949	-0.351104	-0.536169
3	12	0	0.244817	0.865493	0.013939
4	17	0	-1.780178	-0.286909	0.004739

G4 (0 K)= -773.363545

^{3}ClMg(η^{1}-CO)$^{-}$ (4C)

Center Number	Atomic Number	Atomic Type	Coordinates (Angstroms) X	Y	Z
1	6	0	1.723584	-0.220853	-0.041277
2	8	0	2.803600	-0.685306	-0.083932
3	12	0	-0.065144	0.925663	-0.012788
4	17	0	-2.051996	-0.244443	0.291893

G4 (0 K)= -773.376632

$^{3}ClMg(\eta^{1}\text{-}OC)^{-}$ (4D, triplet PES)

Center Number	Atomic Number	Atomic Type	Coordinates (Angstroms) X	Y	Z
1	6	0	-2.833757	-0.490514	-0.000000
2	8	0	-1.738934	0.059456	-0.000000
3	12	0	-0.000069	0.928775	-0.000000
4	17	0	1.818508	-0.510469	0.000000

G4 (0 K)= -773.354250

$^{2}ClMgCO^{\bullet}$

Center Number	Atomic Number	Atomic Type	Coordinates (Angstroms) X	Y	Z
1	6	0	1.909909	0.322045	-0.000000
2	8	0	3.048324	0.262074	-0.000000
3	12	0	-0.106281	-0.795499	-0.000000
4	17	0	-2.015083	0.330433	-0.000000

G4 (0 K)= -773.340061

$^{1}ClMgCO^{+}$

Center Number	Atomic Number	Atomic Type	Coordinates (Angstroms) X	Y	Z
1	6	0	-0.000000	0.000000	2.166158
2	8	0	-0.000000	0.000000	3.282055
3	12	0	-0.000000	0.000000	-0.103750
4	17	0	-0.000000	0.000000	-2.229463

G4 (0 K)= -773.099110

$^{2}MgCO^{+}$

Center Number	Atomic Number	Atomic Type	Coordinates (Angstroms) X	Y	Z
1	6	0	-0.000000	0.000000	-0.674818
2	8	0	-0.000000	0.000000	-1.787617
3	12	0	-0.000000	0.000000	1.529344

G4 (0 K)= -312.448896

$^{1}MgCO^{+}$

Center Number	Atomic Number	Atomic Type	Coordinates (Angstroms) X	Y	Z
1	6	0	1.990471	-1.126181	0.005310
2	8	0	2.833852	-1.861895	0.018243
3	12	0	0.107680	0.516249	-0.023564

G4 (0 K)= -312.939271

SI-F. REFERENCES

1 S. Narancic, A. Bach and P. Chen, *J. Phys. Chem. A*, 2007, **111**, 7006–7013.

2 S. T. Graul and R. R. Squires, *J. Am. Chem. Soc.*, 1990, **112**, 2517–2529.

3 K. Błaziak, G. B. S. Miller, M. J. Ryding and E. Uggerud, *Eur. J. Org. Chem.*, 2017, **2017**, 4272–4276.

4 W. R. Stevens, B. Ruscic and T. Baer, *J. Phys. Chem. A*, 2010, **114**, 13134–13145.

5 G. Caldwell, R. Renneboog and P. Kebarle, *Can. J. Chem.*, 1989, **67**, 611–618.

6 M. B. More, D. Ray and P. B. Armentrout, *J. Am. Chem. Soc.*, 1999, **121**, 417–423.

7 P. B. Armentrout, C. A. Austin and M. T. Rodgers, *J. Phys. Chem. A*, 2014, **118**, 8088–8097.

8 D. J. Harvey, A. P. Hunter, R. H. Bateman, J. Brown and G. Critchley, *Int. J. Mass Spectrom.*, 1999, **188**, 131–146.

9 J. S. Jestilä and E. Uggerud, *J. Org. Chem.*, 2019, **84**, 14005–14014.

10 G. Frenking, C. Loschen, A. Krapp, S. Fau and S. H. Strauss, *J. Comput. Chem.*, 2007, **28**, 117–126.

11 K. P. Huber and G. Herzberg, in *Molecular Spectra and Molecular Structure: IV. Constants of Diatomic Molecules*, eds. K. P. Huber and G. Herzberg, Springer US, Boston, MA, 1979, pp. 8–689.

12 K. K. Murray, T. M. Miller, D. G. Leopold and W. C. Lineberger, *J. Chem. Phys.*, 1986, **84**, 2520–2525.

13 S. C. Foster, A. R. W. McKellar and T. J. Sears, *J. Chem. Phys.*, 1984, **81**, 578–579.